MOLECULAR CATALYSTS FOR CO_2 FIXATION/REDUCTION

EDITED BY: Hitoshi Ishida, Charles Machan, Marc Robert and Nobuharu Iwasawa

PUBLISHED IN: Frontiers in Chemistry

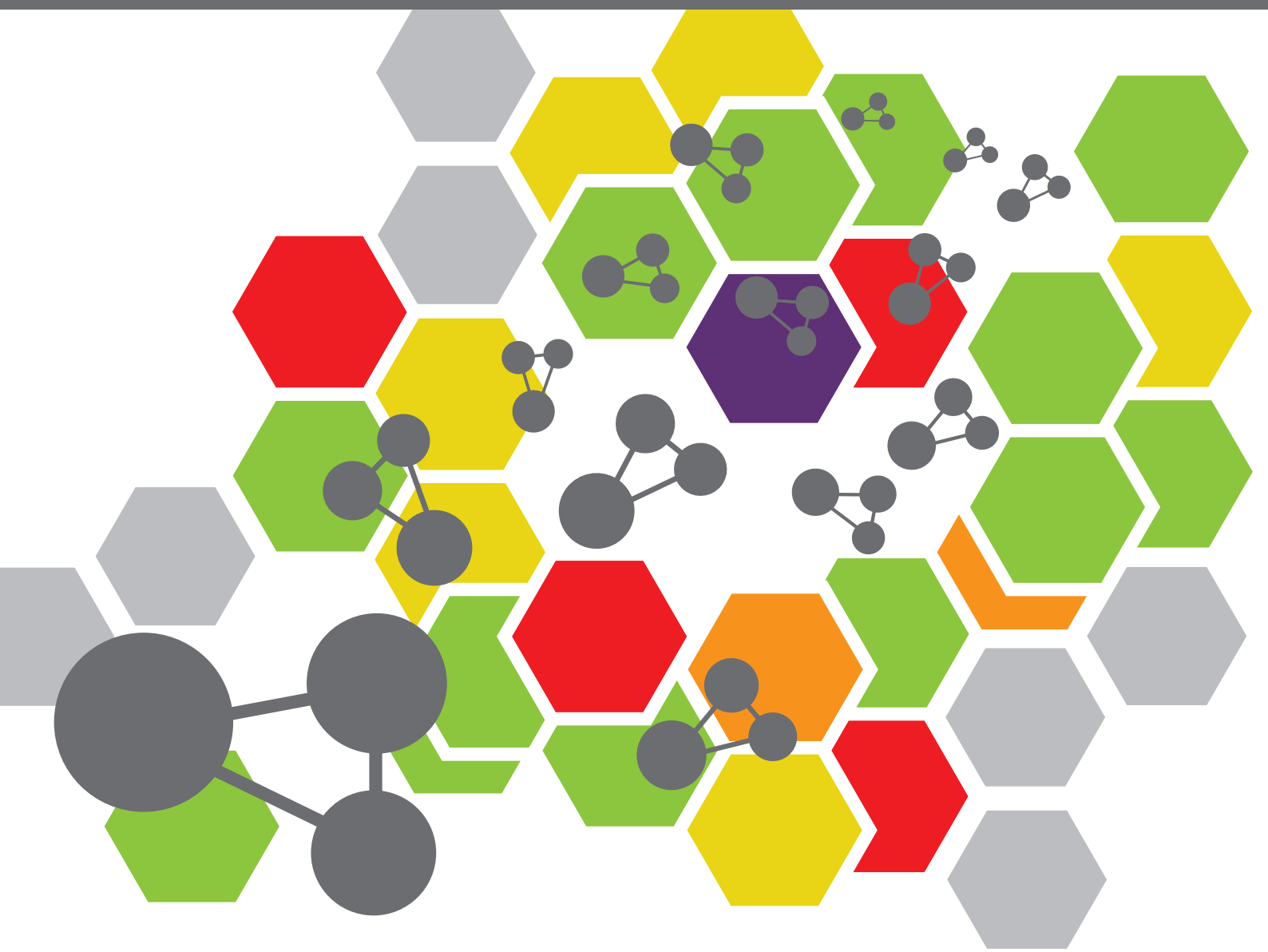

frontiers Research Topics

Frontiers eBook Copyright Statement

The copyright in the text of individual articles in this eBook is the property of their respective authors or their respective institutions or funders. The copyright in graphics and images within each article may be subject to copyright of other parties. In both cases this is subject to a license granted to Frontiers.

The compilation of articles constituting this eBook is the property of Frontiers.

Each article within this eBook, and the eBook itself, are published under the most recent version of the Creative Commons CC-BY licence. The version current at the date of publication of this eBook is CC-BY 4.0. If the CC-BY licence is updated, the licence granted by Frontiers is automatically updated to the new version.

When exercising any right under the CC-BY licence, Frontiers must be attributed as the original publisher of the article or eBook, as applicable.

Authors have the responsibility of ensuring that any graphics or other materials which are the property of others may be included in the CC-BY licence, but this should be checked before relying on the CC-BY licence to reproduce those materials. Any copyright notices relating to those materials must be complied with.

Copyright and source acknowledgement notices may not be removed and must be displayed in any copy, derivative work or partial copy which includes the elements in question.

All copyright, and all rights therein, are protected by national and international copyright laws. The above represents a summary only. For further information please read Frontiers' Conditions for Website Use and Copyright Statement, and the applicable CC-BY licence.

ISSN 1664-8714
ISBN 978-2-88963-622-8
DOI 10.3389/978-2-88963-622-8

About Frontiers

Frontiers is more than just an open-access publisher of scholarly articles: it is a pioneering approach to the world of academia, radically improving the way scholarly research is managed. The grand vision of Frontiers is a world where all people have an equal opportunity to seek, share and generate knowledge. Frontiers provides immediate and permanent online open access to all its publications, but this alone is not enough to realize our grand goals.

Frontiers Journal Series

The Frontiers Journal Series is a multi-tier and interdisciplinary set of open-access, online journals, promising a paradigm shift from the current review, selection and dissemination processes in academic publishing. All Frontiers journals are driven by researchers for researchers; therefore, they constitute a service to the scholarly community. At the same time, the Frontiers Journal Series operates on a revolutionary invention, the tiered publishing system, initially addressing specific communities of scholars, and gradually climbing up to broader public understanding, thus serving the interests of the lay society, too.

Dedication to Quality

Each Frontiers article is a landmark of the highest quality, thanks to genuinely collaborative interactions between authors and review editors, who include some of the world's best academicians. Research must be certified by peers before entering a stream of knowledge that may eventually reach the public - and shape society; therefore, Frontiers only applies the most rigorous and unbiased reviews.
Frontiers revolutionizes research publishing by freely delivering the most outstanding research, evaluated with no bias from both the academic and social point of view. By applying the most advanced information technologies, Frontiers is catapulting scholarly publishing into a new generation.

What are Frontiers Research Topics?

Frontiers Research Topics are very popular trademarks of the Frontiers Journals Series: they are collections of at least ten articles, all centered on a particular subject. With their unique mix of varied contributions from Original Research to Review Articles, Frontiers Research Topics unify the most influential researchers, the latest key findings and historical advances in a hot research area! Find out more on how to host your own Frontiers Research Topic or contribute to one as an author by contacting the Frontiers Editorial Office: researchtopics@frontiersin.org

MOLECULAR CATALYSTS FOR CO_2 FIXATION/REDUCTION

Topic Editors:
Hitoshi Ishida, Kitasato University, Japan
Charles Machan, University of Virginia, United States
Marc Robert, Université Paris Diderot, France
Nobuharu Iwasawa, Tokyo Institute of Technology, Japan

Citation: Ishida, H., Machan, C., Robert, M., Iwasawa, N., eds. (2020). Molecular Catalysts for CO_2 Fixation/Reduction. Lausanne: Frontiers Media SA.
doi: 10.3389/978-2-88963-622-8

Table of Contents

frontiers in Chemistry

EDITORIAL
published: 25 February 2020
doi: 10.3389/fchem.2020.00059

Editorial: Molecular Catalysts for CO_2 Fixation/Reduction

Hitoshi Ishida[1], Charles Machan[2], Marc Robert[3] and Nobuharu Iwasawa[4]*

[1] Department of Chemistry, Graduate School of Science, Kitasato University, Sagamihara, Japan, [2] Department of Chemistry, University of Virginia, Charlottesville, VA, United States, [3] Laboratoire d'Electrochimie Moléculaire (LEM), Université de Paris, Paris, France, [4] School of Science and Engineering, Tokyo Institute of Technology, Tokyo, Japan

Keywords: CO_2 reduction, CO_2 fixation, electrocatalysis, photocatalysis, artificial photosynthesis

Editorial on the Research Topic

Molecular Catalysts for CO_2 Fixation/Reduction

Conversion of CO_2 into useful chemicals and fuels becomes more and more important as increasing CO_2 emissions continue to worsen the effects of climate change. Catalytic CO_2 reduction and fixation are important components of artificial photosynthesis (the use of renewable energy to generate useful chemicals and fuels), which is vigorously studied as part of the solution to the environmental and energy problems that arise from its continuously elevating atmospheric concentration. However, the development of chemical processes remains a significant challenge for chemists. Molecular inorganic complexes, which can be utilized as homogeneous catalysts, have several advantages: well-defined structures that are readily characterized, catalytic mechanisms that can be elucidated with high fidelity, and the opportunity to optimize catalytic activities through molecular design. In this Research Topic, we present ten original research articles and three review articles dealing with electrochemical and photochemical catalysis for CO_2 reduction or fixation.

The metal complexes, *fac*-[Mn(bpy)$(CO)_3$Br] and *fac*-[Re(bpy)$(CO)_3$Cl] (bpy = 2,2′-bipyridine), are known to be excellent catalysts for electrochemical CO_2 reduction. Rotundo et al. synthesized 14 new Mn(I) and Re(I) complexes with structurally diverse 2,2′-bipyridyl derivatives and examined their catalytic activities by using cyclic voltammetry and controlled potential electrolysis. They reported that the complexes with only electron-withdrawing groups (e.g., $-CF_3$, -CN) lost their catalytic activities. On the other hand, the complexes with the symmetric $-NMe_2$ substituted and push–pull systems (containing both $-NMe_2$ and $-CF_3$) displayed electrocatalytic current enhancement. McKinnon et al. synthesized the manganese(I) complex *fac*-[Mn(bqn)$(CO)_3(CH_3CN)]^+$ with a 2,2′-biquinoline (bqn) ligand, which had unique steric and electronic properties. They examined the catalytic activities for electrochemical CO_2 reduction and further compared them to the efficiencies of the corresponding bpy, 1,10-phenanthroline (phen), and 2,9-dimethyl-1,10-phenanthroline (dmphen) derivatives. In the reaction mechanisms, the one-electron reduced species of the bpy complex dimerized, but the bqn ligand hindered the dimer formation to favorably afford two-electron reduced species. Talukdar et al. synthesized a new NNP-type pincer ligand, 8-(diphenylphosphaneyl)-2-(pyridin-2′-yl)quinolone, and the corresponding Fe, Co, Ni, and Zn complexes. Due to earth abundance, the development of molecular catalysts with first-row transition metals is desirable. They reported that the cobalt(II) complex showed the catalytic efficiency to produce CO in CO_2-saturated DMF containing 5% water; the catalytic efficiencies for CO of the active complexes in descending order were $Co^{2+} >> Ni^{2+} > Fe^{2+}$. The Zn(II) complex did not show catalytic activity. Nichols and Machan reviewed the secondary-sphere effects in the enzymes and the molecular catalysts for electrochemical CO_2 reduction. In the CO_2-related enzymes (e.g., carbon monoxide dehydrogenase, formic acid dehydrogenase), some amino acid residues around the catalytic centers can act as the

OPEN ACCESS

Edited and reviewed by:
Luís D. Carlos,
University of Aveiro, Portugal

****Correspondence:***
Hitoshi Ishida
ishida@sci.kitasato-u.ac.jp

Specialty section:
This article was submitted to Inorganic Chemistry, a section of the journal Frontiers in Chemistry

Received: *06 January 2020*
Accepted: *17 January 2020*
Published: *25 February 2020*

Citation:
Ishida H, Machan C, Robert M and Iwasawa N (2020) Editorial: Molecular Catalysts for CO_2 Fixation/Reduction. Front. Chem. 8:59. doi: 10.3389/fchem.2020.00059

pendent proton donors/shuttles, charged groups, etc. They discussed standard methodologies for estimating the effective catalytic overpotential and the maximal turnover frequency, and reviewed the development of secondary-sphere strategies for the classic molecular electrocatalysts, $[Fe(tetraphenylporphyrin)]^+$, $[Ni(cyclam)]^{2+}$, $Mn(bpy)(CO)_3X$, and $Re(bpy)(CO)_3X$ (X = solvent or halide). Igarashi et al. reported the surface modification of copper cathodes with ethynyl and azide monomers. Metal copper cathodes are known to be effective for electrochemical CO_2 reduction. The introduction of organic structures onto catalytically active metal surfaces has recently received attention because it often enhances activity and selectivity for specific products. They reported that an increase in ethylene production was observed for the organic molecule-modified copper electrodes in electrochemical CO_2 reduction.

Photocatalytic CO_2 reduction can be accomplished with the same molecular catalysts employed in electrochemistry by using appropriate redox photosensitizers and sacrificial electron donors instead of an electrode. The most widely used redox photosensitizer is $[Ru(bpy)_3]^{2+}$, which exhibits strong absorption in the visible light region and has a long lifetime in the triplet metal-to-ligand charge transfer (^{3}MLCT) excited state. Tamaki et al. synthesized a new ruthenium(II) picolinate complex, $[Ru(dmb)_2(pic)]^+$ (dmb = 4,4′-dimethyl-2,2′-bipyridine; Hpic = picolinic acid), with a wider wavelength range of visible-light absorption ($\lambda_{abs} < 670$ nm) and a strong reduction ability in the one-electron reduced state ($E_{red} = -1.86$ V vs. $Ag/AgNO_3$). They demonstrated that photocatalysis using $[Ru(dmb)_2(pic)]^+$ as the redox photosensitizer combined with a Re(I) catalyst reduced CO_2 to CO under red-light irradiation ($\lambda_{ex} > 600$ nm). In contrast, $[Ru(dmb)_3]^{2+}$, which could not absorb light at $\lambda > 560$ nm, was not capable of working as the redox photosensitizer under the same conditions. The molar extinction coefficient is also an important factor for a redox photosensitizer. A cyclometalated iridium(III) complex having 2-(pyren-1-yl)-4-methylquinoline ligands [Ir(pyr)] has a strong absorption band in the visible region (ε at 444 nm = 67,000 M^{-1} cm^{-1}) but does not act as a photosensitizer for photochemical CO_2 reduction reactions in the presence of triethylamine as an electron donor. Kuramochi and Ishitani report that the photochemical CO_2 reduction catalyzed by *trans*(Cl)-$Ru(dmb)(CO)_2Cl_2$ could proceed in a combination of [Ir(pyr)] as the photosensitizer and 1,3-dimethyl-2-(*o*-hydroxyphenyl)-2,3-dihydro-1*H*-benzo[d]imidazole (BI(OH)H) as the electron donor. They further synthesized a binuclear complex in which Ir(pyr) and Ru combined via an ethylene bridge. The development of efficient redox photosensitizers based on the earth-abundant metal ions as an alternative toward noble- and/or rare-metal-based photosensitizers is of continuing interest for the field. The heteroleptic Cu(I) phenanthroline complexes, such as $[Cu^I(dmp)(P)_2]^+$ (dmp = 2,9-dimethyl-1,10-phenanthroline, P = phosphine ligand), are known to have long lifetimes and show strong MLCT excited state emission even in a solution at room temperature due to the Cu(I) center's d^{10} configuration. Yamazaki et al. synthesized heteroleptic diimine-diphosphine Cu(I) complexes, $[Cu^I(dmpp)(diphos)]^+$ [dmpp = 2,9-dimethyl-4,7-diphenyl-1,10-phenanthroline; diphos = methylene chains (n = 2–4) linked bis(diphenyl phosphine)]. They investigated the effects of the number of methylene chains on the photocatalytic CO_2 reduction by using *fac*-$[Re(bpy)(CO)_3Br]$ as a catalyst and 1,3-dimethyl-2-phenyl-2,3-dihydro-1*H*-benzo[d]imidazole (BIH) as an electron donor. The most effective redox photosensitizer was the 1,4-bis(diphenylphosphino)butane (dppb; n = 4) complex. They discussed the photocatalytic results in the context of the P–Cu–P angles in the photosensitizer. Takeda et al. developed visible-light responsive Cu(I)-complex photosensitizers by introducing various aromatic substituents at the 4,7-positions of a 2,9-dimethyl-1,10-phenanthroline (dmp) ligand in a heteroleptic $[Cu^I(dmp)(DPEphos)]^+$-type complexes (DPEphos = [2-(diphenylphosphino)phenyl]ether). Introduction of biphenyl groups on the dmp ligand enhanced the molar extinction coefficient of the MLCT band. They further performed the photocatalyzed CO_2 reduction by an earth-abundant metal complex, $[Fe(dmp)_2(NCS)_2]$. Ohtsu et al. synthesized a ruthenium(II) NAD^+-type complex, $[Ru(bpy)_2(Me\text{-}pn)]^{2+}$ (Me-pn = 2-Methyl-6-(pyridin-2-yl)-1,5-naphthyridine). The common photosensitizers act as a one-electron reservoir. But they demonstrated the formation of the corresponding two-electron reduced ruthenium(II) complex, $[Ru(bpy)_2(Me\text{-}pnHH)]^{2+}$ (Me-pnHH (2-methyl-6-(pyridin-2-yl)-1,4-dihydro-1,5-naphthyridine) is the NADH-type ligand), by the photo-induced hydrogenation reaction of $[Ru(bpy)_2(Me\text{-}pn)]^{2+}$. The complex is a two-electron reservoir and will be applicable to photocatalytic CO_2 reduction as an efficient redox photosensitizer.

Fixation of CO_2 into organic molecules is important to obtain useful and valuable chemicals. Fujihara and Tsuji reviewed the transition metal-catalyzed carboxylation reactions of organic substrates with CO_2 via allyl metal intermediates. They summarized the carboxylation reactions via transmetalation, catalytic carboxylation reactions using allyl electrophiles and suitable reducing agents, and then the catalytic carboxylation reactions via additional reactions affording allyl metal intermediates. Murata et al. reported the visible-light-driven hydrocarboxylation of alkenes with CO_2 by a Rh(I) catalyst with $[Ru(bpy)_3]^{2+}$ (a redox photosensitizer) and BIH or BI(OH)H (an electron donor). The mechanistic study revealed that the catalysis required two photon-driven steps: the carboxylation of the hydrometalated Rh(I) complex on one hand, and the photo-induced generation of the Rh(III) dihydride complex on the other hand. The latter is an electron transfer process that requires the electron donor. The former is an energy transfer step, which would be sensitized by $[Ru(bpy)_3]^{2+}$. Interestingly, they found that the incorporation of the cyclometalated Ir(III) complex as a second photosensitizer with $[Ru(bpy)_3]^{2+}$ photosensitizer also resulted in the promotion of the reduction process. Fu et al. reviewed carbon capture and utilization (CCU) strategies. Although carbon capture and storage (CCS) strategies have been regarded as one of the promising options for controlling continuously elevating atmospheric CO_2 concentrations, desorption and compression

of CO_2 need extra energy input. In the CCU strategy, the CO_2 absorbents trap CO_2 to yield the CO_2 adducts, which can be reacted as transcarboxylation and transformation agents. For example, CO_2 capture and Rh- or Ru-catalyzed CO_2 adducts hydrogenation was introduced.

Conversion of CO_2 into useful chemicals by CO_2 reduction/fixation continues to attract significant interest and research effort. Through the remarkable creativity demonstrated by the authors, this collection of papers (and beyond) is clear evidence that CO_2 fixation and molecular catalysis of CO_2 reduction are and will remain very active and promising fields, promoting fundamental advances. To discover more efficient catalysts, mechanistic investigations on ligand effects, as well as the modification of the second sphere in the metal complexes, will continue to expand the impact of these efforts, with the help of many various complementary *in situ* spectroscopic techniques, such as IR, Raman, EPR, mass, and X-ray absorption spectroscopies. Developing new hybrid systems, such as those that combine the most promising molecular catalysts with semiconductor materials, will also be important developments in the near future, merging the best attributes of homogeneous and heterogeneous catalysis. We hope that this Research Topic will contribute to stimulating the next wave of research efforts in the construction of new artificial photosynthetic systems.

AUTHOR CONTRIBUTIONS

All authors listed have made a substantial, direct and intellectual contribution to the work, and approved it for publication.

FUNDING

HI was supported by a Grant-in-Aid for Scientific Research (C) from the Ministry of Education, Culture, Sports, Science and Technology (17K05815), and a Grant-in-Aid for Scientific Research on Innovative Areas, Innovations for Light-Energy Conversion (18H05176), from the Japan Society for the Promotion of Science (JSPS).

Conflict of Interest: The authors declare that the research was conducted in the absence of any commercial or financial relationships that could be construed as a potential conflict of interest.

Copyright © 2020 Ishida, Machan, Robert and Iwasawa. This is an open-access article distributed under the terms of the Creative Commons Attribution License (CC BY). The use, distribution or reproduction in other forums is permitted, provided the original author(s) and the copyright owner(s) are credited and that the original publication in this journal is cited, in accordance with accepted academic practice. No use, distribution or reproduction is permitted which does not comply with these terms.

frontiers in Chemistry

ORIGINAL RESEARCH
published: 30 April 2019
doi: 10.3389/fchem.2019.00288

Photocatalytic CO_2 Reduction Using Various Heteroleptic Diimine-Diphosphine Cu(I) Complexes as Photosensitizers

*Yasuomi Yamazaki, Takayuki Onoda, Jun Ishikawa, Shota Furukawa, Chinatsu Tanaka, Tomoya Utsugi and Taro Tsubomura**

Department of Materials and Life Science, Seikei University, Musashino-shi, Japan

The development of efficient redox-photosensitizers based on the earth-abundant metal ions as an alternative toward noble- and/or rare-metal based photosensitizers is very desirable. In recent years, heteroleptic diimine-diphosphine Cu(I) complexes have been well investigated as one of the most remarkable candidates because of their great potentials as efficient photosensitizers. Here, we investigated the effects of the structure of the diphosphine ligands on the photosensitizing abilities using a series of Cu(I) complexes bearing 2,9-dimethyl-4,7-diphenyl-1,10-phenanthroline (dmpp) and various diphosphine ligands in order to explore the suitable structure for the photosensitizing reactions. The number of methylene chains between the two phosphorous atoms in the diphosphine ligands was systematically changed from two to four, and the relationship between the length of the carbon chains and the photosensitizing abilities were investigated by conducting photocatalytic CO_2 reduction with the Cu(I) complexes as photosensitizers. Turnover frequencies of the CO_2 reduction drastically increased with increasing the length of the carbon chains. The systematic study herein reported suggests that the large P-Cu-P angles should be one of the most important factors for enhancing the photosensitizing abilities.

Keywords: CO_2 reduction, photocatalytic reaction, Cu(I) complexes, redox-photosensitizer, diphosphine ligands

OPEN ACCESS

Edited by:
Hitoshi Ishida,
Kitasato University, Japan

Reviewed by:
Yi Du,
University of Wollongong, Australia
Francesco Nastasi,
University of Messina, Italy

****Correspondence:***
Taro Tsubomura
tsubomura@st.seikei.ac.jp

Specialty section:
This article was submitted to Inorganic Chemistry, a section of the journal Frontiers in Chemistry

Received: *30 January 2019*
Accepted: *08 April 2019*
Published: *30 April 2019*

Citation:
Yamazaki Y, Onoda T, Ishikawa J, Furukawa S, Tanaka C, Utsugi T and Tsubomura T (2019) Photocatalytic CO_2 Reduction Using Various Heteroleptic Diimine-Diphosphine Cu(I) Complexes as Photosensitizers. Front. Chem. 7:288. doi: 10.3389/fchem.2019.00288

INTRODUCTION

In the last few decades, photocatalytic CO_2 reduction has been widely investigated due to emerging concerns about the serious environmental problems, e.g., global warming and depletion of carbon and energy resources. Metal complexes have played an important role both as photosensitizers and as CO_2 reduction catalysts in this research area, owing to their suitable photophysical and photochemical properties, high reaction selectivity, and flexibility in the molecular design (Morris et al., 2009; Windle and Perutz, 2012; Sahara and Ishitani, 2015; Yamazaki et al., 2015; Kuramochi et al., 2018). Noble- and/or rare-metal complexes in particular have shown quite high efficiency and durability. For instance, the photocatalytic systems constructed with a Re(I) tricarbonyl complex as a CO_2-reduction catalyst and a ring-shaped Re(I) multinuclear complex as a photosensitizer, can trigger CO_2 reduction with tremendously high quantum yield ($\Phi_{CO} = 82\%$) (Morimoto et al., 2013; Rohacova and Ishitani, 2016, 2017). Another example is a system using a Ru(II)-Re(I) multinuclear complexes, (Gholamkhass et al., 2005; Sato et al., 2007; Koike et al., 2009; Tamaki et al., 2012;

Tamaki et al., 2013a; Kato et al., 2015; Ohkubo et al., 2016; Tamaki and Ishitani, 2017; Yamazaki and Ishitani, 2018) which shows both high efficiency and durability, i.e., up to 50% of Φ_{CO} and more than 3,000 of the turnover number (TON_{CO}) (Tamaki et al., 2013a; Tamaki and Ishitani, 2017; Yamazaki and Ishitani, 2018). Though the fundamental researches using noble- and/or rare-metals must be quite important in order to fully understand the reaction mechanism of the CO_2 reduction and to explore strategies of molecular design for efficient components in photocatalytic systems, in the future, such metals which lie under the ground in small amounts should be replaced by earth-abundant elements because the amount of emission of CO_2 relating to consumption of fossil fuels is quite large and is increasing year by year (Takeda et al., 2016a).

In recent years, heteroleptic diimine-diphosphine Cu(I) complexes have been reported as an alternative toward noble- and/or rare-metal based photosensitizers (Takeda et al., 2016b, 2018; Heberle et al., 2017; Rosas-Hernández et al., 2017; McCullough et al., 2018; Zhang et al., 2018). Some of them show not only high efficiency but also high durability equal to or higher than those of noble- and/or rare-metal complexes, and the highest Φ_{CO} and TON_{CO} in the photocatalytic systems for CO_2 reduction using Cu(I) photosensitizers were 57% and >1,300, respectively (Takeda et al., 2018). These reports clearly indicate that Cu(I) complexes should be powerful candidates not just as an alternative toward photosensitizers based on noble- and/or rare-metal ions, but as one of the most efficient photosensitizers. Therefore, further investigation using series of Cu(I) complexes to clarify the relationship between the molecular structure and photosensitizing abilities should be useful to explore the suitable molecular design for the efficient Cu(I)-complex photosensitizers.

We previously reported photophysical properties of series of diimine-diphosphine Cu(I) complexes bearing 1,10-phenanthroline derivatives and various bidentate phosphine ligands (Saito et al., 2006; Tsubomura et al., 2015; Nishikawa et al., 2017). In particular, a series of the Cu(I) complexes having 2,9-dimethyl-4,7-diphenyl-1,10-phenanthroline (dmpp) showed high molar extinction coefficients and emission quantum yields compared with those without phenyl groups at 4,7 positions (Tsubomura et al., 2015). The photophysical properties of the dmpp complexes were strongly affected by the structure of the bidentate phosphine ligands; wavelength of both absorption bands and emission maxima were blue-shifted and emission lifetimes became longer with increasing the length of the methylene chains between the two phosphorous atoms, likely due to the difference in the bite angles of the chelate-phosphine ligands (P-Cu-P angles). The strong absorption abilities and long emission lifetimes should be useful not only as photo-luminescent materials but also as photosensitizers for photochemical reactions. Therefore, in this study, we examined the effects of diphosphine ligands in detail on the photosensitizing abilities using a series of Cu(I) complexes bearing dmpp ligands shown in **Chart 1**, i.e., dmpp complexes with 3 types of diphosphine ligands with different length of carbon chains: dppe (1,2-bis(diphenylphosphino)ethane), dppp (1,3-bis(diphenylphosphino)propane), and dppb (1,4-bis(diphenylphosphino)butane). The dmpp complex bearing Xantphos (4,5-Bis(diphenylphosphino)-9,9-dimethylxanthene), which is often used as a diphosphine ligand of Cu(I) photosensitizers, was also investigated for comparison. The systematic study herein reported suggests that the P-Cu-P angles should be one of the most important factors which determines the photosensitizing abilities.

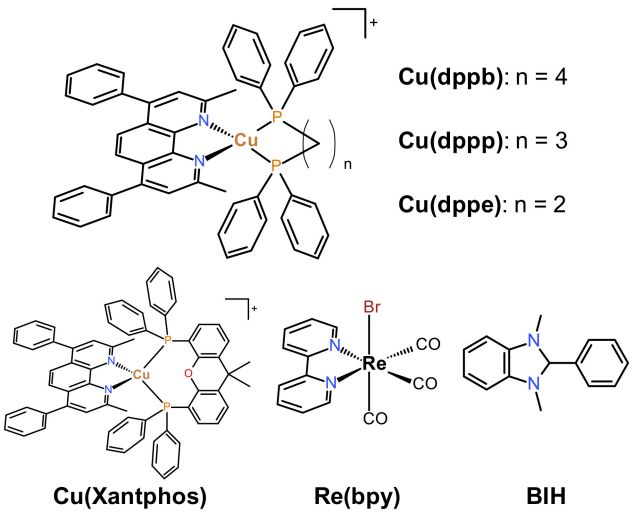

CHART 1 | Structures and abbreviations of the Cu(I) complexes, the Re(I) complex and the electron donor used in this study.

RESULTS AND DISCUSSION

Photocatalytic CO_2 Reduction Using Cu(I) Complexes as Photosensitizers

In a typical run of photocatalytic reactions, a mixed solution of MeCN-TEOA (TEOA = triethanolamine, 4:1 v/v) containing **Cu(dppb)** (0.5 mM) as a photosensitizer, Re(2,2'-bipyridine)$(CO)_3$Br (**Re(bpy)**, 0.05 mM) as a CO_2-reduction catalyst and 1,3-dimethyl-2-phenyl-2,3-dihydro-1*H*-benzo[*d*]imidazole (BIH, 0.1 M) as an electron donor was irradiated under a CO_2 atmosphere using a high-pressure mercury-lamp equipped with a UV-cut filter (>370 nm, **Figure 1**). **Re(bpy)** is well known not only as a photocatalyst for CO_2 reduction (Hawecker et al., 1983, 1986; Kutal et al., 1985) but also as a CO_2-reduction catalyst in photocatalytic systems, which can produce CO with high selectivity; (Gholamkhass et al., 2005; Sato et al., 2007; Kiyosawa et al., 2009; Koike et al., 2009; Morris et al., 2009; Tamaki et al., 2012, 2013a,b; Kou et al., 2014; Kato et al., 2015; Ohkubo et al., 2016). Therefore, we measured the gaseous products of the photocatalysis using gas-chromatography. CO was selectively produced and no hydrogen was detected over 30-min irradiation. TON_{CO} after 30-min irradiation was 40. Though various other CO_2-reduction catalysts, i.e., Re(4,4'-dimethyl-2,2'-bipyridine)$(CO)_3$Br, Re(1,10-phenanthroline)$(CO)_3$Br, and Ru(6,6'-dimethyl-2,2'-bipyridine)$(CO)_2Cl_2$, were also used

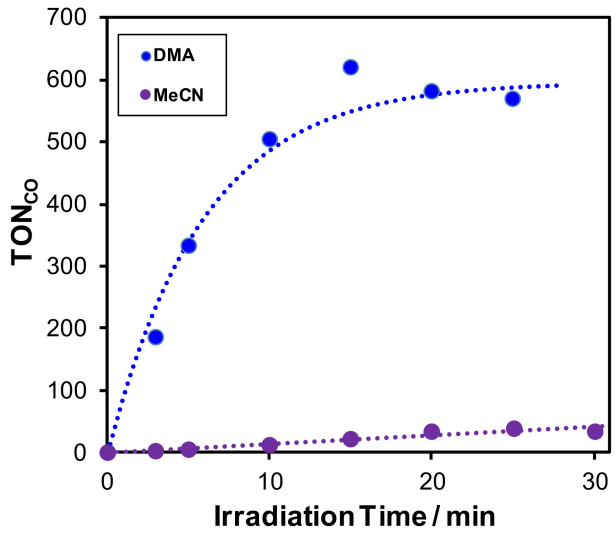

FIGURE 1 | Time courses of the TON of CO formation during photocatalytic reactions (λ_{ex} > 370 nm) using a mixture of MeCN and TEOA (4:1 v/v, purple) or a mixture of DMA and TEOA (4: 1 v/v, blue) containing 0.5 mM **Cu(dppb)**, 0.05 mM **Re(bpy)**, and 0.1 M BIH.

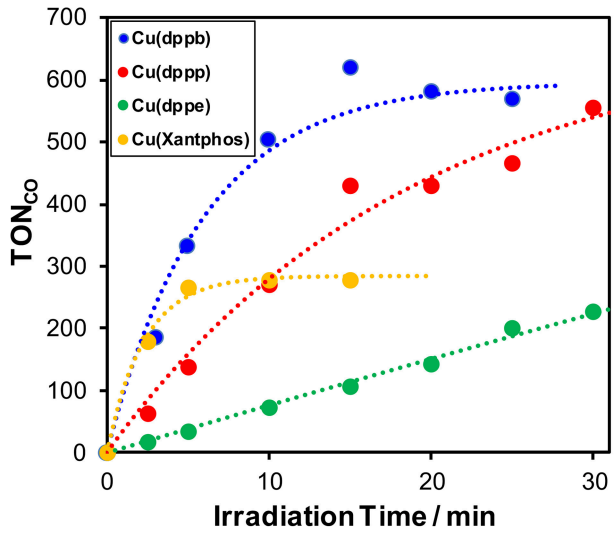

FIGURE 2 | Time courses of the TON of CO formation during photocatalytic reactions (λ_{ex} > 370 nm) using a mixture of DMA and TEOA (4:1 v/v) containing 0.05 mM **Re(bpy)**, 0.1 M BIH, and various Cu(I) complexes [blue: **Cu(dppb)**, red: **Cu(dppp)**, green: **Cu(dppe)**, orange: **Cu(Xantphos)**]. The concentration of each Cu(I) complex is 0.5 mM.

instead of **Re(bpy)**, the system using **Re(bpy)** showed the highest TON_{CO} in this reaction condition (**Figure S1**).

In the case of using a mixed solvent of DMA-TEOA (DMA = *N*,*N*-dimethylacetamide, 4:1 v/v) instead of that of MeCN-TEOA (4:1 v/v), TON_{CO} increased and reached 580 after 25-min irradiation (**Figure 1**). The turnover frequency (TOF), which was determined from the slopes of the fitting curves of the time course in the initial stage of the photocatalysis, was relatively high (65 min^{-1}, **Figure S2**). This result suggests that DMA should be more preferable solvent for the efficient photocatalytic reaction using **Cu(dppb)** and **Re(bpy)**. In the absence of **Cu(dppb)**, TON_{CO} after 1-h irradiation were 20; thus, the photocatalysis by only **Re(bpy)** should be not sufficient under the condition. In addition, in the absence of **Re(bpy)** or BIH, TON_{CO} were 0 or 7, respectively. These results clearly indicate that **Cu(dppb)** has relatively high photosensitizing ability and promoted CO_2 reduction on **Re(bpy)** using BIH as an electron donor. From these results, we concluded the photocatalyses using **Re(bpy)** as a CO_2-reduction catalyst and a mixed solvent of DMA-TEOA as a reaction solvent are suitable for the investigation to clarify the photosensitizing abilities of the series of the Cu(I) complexes shown in **Chart 1**.

Mixed solutions of DMA-TEOA (4:1 v/v) containing **Re(bpy)** (0.05 mM), BIH (0.1 M), and various Cu(I) complexes (0.5 mM) were shined under the same condition described above. **Figure 2** shows the time-courses of the CO production and both TON_{CO} and TOF are summarized in **Table 1** and **Figure S2**. Interestingly, both TON_{CO} and TOF strongly depended on the structure of the diphosphine ligands. When comparing **Cu(dppb)**, **Cu(dppp),** and **Cu(dppe)**, TOF drastically increased with increasing the length of the methylene chains between the two phosphorous atoms in the diphosphine ligands. In the case using **Cu(Xantphos)**, TOF was quite high and almost equal to that of **Cu(dppb)**. In contrast, TON_{CO} of **Cu(Xantphos)** was low, and the time course of CO formation reached plateau within 5-min of irradiation. The absorption spectral changes of the reaction solutions after irradiation are shown in **Figure S3**. In all cases, the metal-to-ligand charge transfer (MLCT) absorption bands of the Cu(I) complexes decreased gradually; therefore, one of the main reasons for the decreasing of the reaction rate with increasing the irradiation time should be the photo-decomposition of the Cu(I) complexes. Curiously, in the case using **Cu(Xantphos),** the photocatalytic CO formation stopped within 5 min even though the MLCT absorption band was obviously observed in the absorption spectrum of the reaction solution after 5-min irradiation. Though the reason for the low TON_{CO} when using **Cu(Xantphos)** is not clear at this stage, the degradation of **Re(bpy)** possibly proceeded more rapidly than the other cases. As described later, **Cu(Xantphos)** showed quite small absorption in the longer wavelength region (>430 nm) compared to the other Cu(I) complexes. It has been recently reported that the irradiation with short wavelength light (<450 nm) drastically lowered the photo-stability of Re(I) complexes; (Lang et al., 2019) thus, it is expected that **Re(bpy)** could absorb the irradiation light in the longer wavelength region, e.g., the emission line at 436 nm from the high-pressure mercury lamp, more frequently and photo-decomposition of **Re(bpy)** proceeded rapidly. Since the analysis of the Re(I) complexes, e.g., measurement of FT-IR spectra of the reaction solutions, was difficult because of the low concentration of the Re(I) complexes, further investigation is now undergoing.

In order to precisely evaluate the efficiency of CO_2 reduction, the quantum yield for CO formation (Φ_{CO}) was determined

TABLE 1 | Photocatalytic properties using the mixed system of the Cu(I) photosensitizers and **Re(bpy)**[a].

Photosensitizer	TON[b]		TOF[c]/min^{-1}	η_q/%	Φ_{CO}[g]/%
	CO	H_2			
Cu(dppb)	580	n.d.	65	99[e]	37
	40[d]	n.d.[d]	1.4[d]	99[e]	–
Cu(dppp)	560	n.d.	27	99[f]	–
Cu(dppe)	230	n.d.	7.3	98[f]	–
Cu(Xantphos)	240	n.d.	72	99[f]	–

[a] *A CO_2-saturated DMA-TEOA (4:1 v/v) mixed solution containing the Cu(I) photosensitizer (0.5 mM),* ***Re(bpy)*** *(0.05 mM), and BIH (0.1 M) was irradiated.*
[b] *Maximum TON_{CO} within 30-min irradiation calculated as [product (mol)]/[added* ***Re(bpy)*** *(mol)].*
[c] *TOF was determined by the slopes of the fitting curves over 5 min (**Figure S2**).*
[d] *A mixed solution of MeCN-TEOA (4:1 v/v) was used instead.*
[e] *Quenching fractions of emission from Cu(I) photosensitizers by BIH determined from Stern-Volmer analyses in a mixture of MeCN-TEOA (4:1 v/v).*
[f] *Quenching fractions of emission from Cu(I) photosensitizers by BIH determined from Stern-Volmer analyses in a mixture of DMA-TEOA (4:1 v/v).*
[g] *Quantum yield of CO production calculated as [CO (mol)]/[absorbed photon (einstein)] (λ_{ex} = 430 nm, light intensity: 1.0 × 10^{-8} einstein/s).*

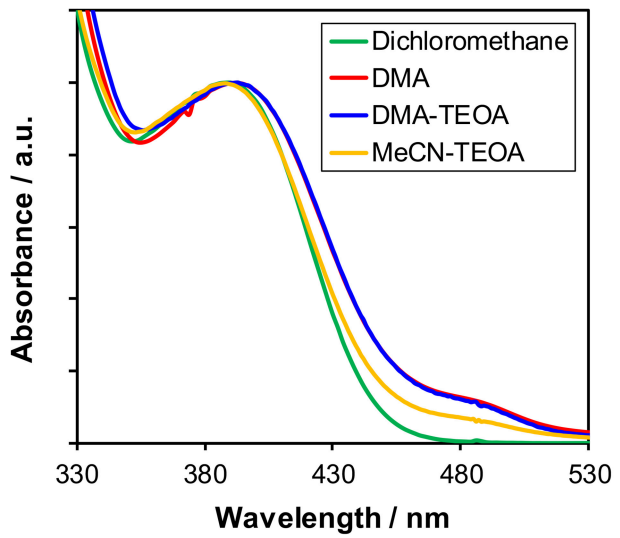

FIGURE 3 | UV-Vis absorption spectra of **Cu(dppb)** in various solutions: dichloromethane (green), DMA (red), a mixture of DMA-TEOA (4:1 v/v, blue), and a mixture of MeCN-TEOA (4:1 v/v, orange).

using the system of **Cu(dppb)** as a typical example. BIH is well known as a two-electron donor, which can induce the second-electron injection even to ground-state of photosensitizers and/or CO_2-reduction catalysts owing to the quite strong reducing power of the radical species produced after oxidation by the excited state of photosensitizers and subsequent deprotonation by TEOA (Equation 1); (Tamaki et al., 2013a). Thus, the maximum Φ_{CO} of this system should be 100%. A mixture of DMA and TEOA (4:1 v/v) containing 0.5 mM **Cu(dppb)**, 0.05 mM **Re(bpy)**, and 0.1 M BIH was irradiated with 430-nm monochromic light. CO was linearly produced over 1-h irradiation, and Φ_{CO} was determined to be 37% from the slopes of the fitting curves (**Figure S4**). This value is relatively high among the photocatalytic systems for CO_2 reduction using Cu(I)-complex photosensitizers.

spectra of **Cu(dppb)** in various solutions, i.e., dichloromethane, DMA, a mixture of DMA-TEOA and that of MeCN-TEOA. The shapes of the spectra at around 330–450 nm were similar. Except the spectrum in dichloromethane, small absorption bands were observed at around 450–530 nm. This is probably due to the formation of $[Cu(dmpp)_2]^+$-type complex produced by the disproportionation reaction after dissolving in solvents having coordination ability (Kaeser et al., 2013). Since the molar extinction coefficient of $[Cu(dmpp)_2]^+$ was large (ε_{484} = 10,300 in a DMA-TEOA mixed solution, **Figure S5**), the amount of the $[Cu(dmpp)_2]^+$ should not be large. ^{1}H NMR analyses of **Cu(dppb)** using CD_2Cl_2 or CD_3CN also revealed that the structure in CD_3CN is almost identical to that in CD_2Cl_2, though a few mol-percent of $[Cu(dmpp)_2]^+$ were observed. The

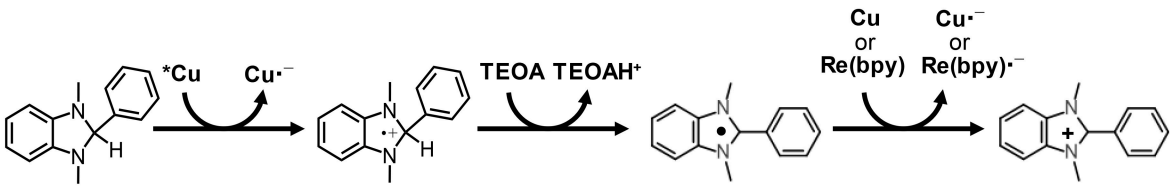

(1)

Properties of Cu(I) Complexes

Structure of Cu(I) Complexes in Solutions

As described above, the Cu(I) complexes, in particular **Cu(dppb)**, showed relatively high photosensitizing ability. In order to clarify the reason for the difference in the photosensitizing abilities of the Cu(I) complexes, we firstly investigated the molecular structure of the Cu(I) complexes in the reaction solutions in detail because it is known that Cu(I) complexes often cause structural changes in solutions due to the ligand-exchange reactions. **Figure 3** illustrates the UV-vis absorption

other complexes also showed similar spectrum-pattern in both absorption spectra and ^{1}H NMR spectra regardless of solvents (**Figure S6**). Therefore, the main species should be the diimine-diphosphine type complexes even in the reaction solutions for the photocatalytic reactions, and the solvent molecules do not strongly affect the structure and the electronic properties of the ground state of the Cu(I) complexes.

We previously clarified that **Cu(dppb)** is dimerized by bridging with two bidentate phosphine ligands in the solid state using single crystal X-ray structure analyses. The dimerization

might be a reason for the higher photosensitizing ability of **Cu(dppb)**; Thus, we measured diffusion-ordered NMR spectroscopy (DOSY-NMR) in order to clarify whether **Cu(dppb)** is dimerized even in solutions. The obtained DOSY-NMR spectra of **Cu(dppb)**, **Cu(dppp)**, **Cu(dppe)**, **Cu(Xantphos),** and $[Cu(dmpp)_2](PF_6)$ measured in CD_2Cl_2 solutions are illustrated in **Figure S7**. The diffusion coefficients of **Cu(dppb)**, **Cu(dppp)**, **Cu(dppe)**, **Cu(Xantphos),** and $[Cu(dmpp)_2](PF_6)$ in the solutions were determined to be 7.5 $\times 10^{-10}$, 7.9 $\times 10^{-10}$, 8.0 $\times 10^{-10}$, 7.0 $\times 10^{-10}$ and 8.4 $\times 10^{-10}$ [m^2/s], respectively. These obtained values were quite similar though they gradually decreased with increasing the molecular weight calculated as mononuclear complexes. Hence, the molecular sizes of the Cu(I) complexes might be almost the same in solutions. Since **Cu(dppp)** and **Cu(dppe)** were reported as mononuclear complexes in the solid state, **Cu(dppb)** in the reaction solutions is regarded as a mononuclear complex in this paper and the dimerization should not be the main reason for the high TOF of the system using **Cu(dppb)**.

Absorption Abilities of the Cu(I) Complexes

Figure 4A shows the UV-vis absorption spectra of **Cu(dppb)** and **Re(bpy)** in a DMA-TEOA mixed solution. Both complexes showed MLCT absorption bands at similar region with similar molar extinction coefficients. However, in the reaction condition, **Cu(dppb)** can absorb visible light more efficiently than **Re(bpy)** because the used concentration of **Cu(dppb)** was 10-times higher than that of **Re(bpy)** (**Figure 4B**). The light source was a high-pressure mercury lamp equipped with a UV-cut filter (>370 nm); Therefore, the main wavelength of the excitation light should be 405 and 436 nm. At 405 and 436 nm, more than 96% of absorbed photons should excite **Cu(dppb)** [Abs_{405}(**Cu(dppb)**): Abs_{405}(**Re(bpy)**) = 2.3: 0.10, Abs_{436}(**Cu(dppb)**): Abs_{436}(**Re(bpy)**) = 1.1: 0.03]. This means **Cu(dppb)** was selectively excited by the excitation light under the reaction condition.

The UV-Vis absorption spectra of the series of the Cu(I) complexes in DMA-TEOA mixed solutions are illustrated in **Figure 5**. All of the Cu(I) complexes showed MLCT absorption bands at around 350–450 nm. When comparing **Cu(dppb)**, **Cu(dppp)**, and **Cu(dppe)**, the absorption maxima of the MLCT absorption bands were gradually blue-shifted with increasing the length of the carbon chains [λ_{abs}(**Cu(dppe)**) = 417 nm, λ_{abs}(**Cu(dppp)**) = 410 nm, λ_{abs}(**Cu(dppb)**) = 391 nm]. Similar blue-shift of the absorption maxima was also observed in the reported system using dichloromethane solutions (Tsubomura et al., 2015). It is reported that the shift was strongly related to the bite angles of the diphosphine ligands, which were determined using the single crystal X-ray diffraction, i.e., the absorption energy became larger as bite angle became larger. The wavelength of the absorption maximum of **Cu(Xantphos)** was the shortest (388 nm); thus, the bite angle of Xantphos in **Cu(Xantphos)** might be larger than those in the other complexes. It should be noted that the absorbance at the irradiation wavelength (405, 436 nm) are relatively high (Abs > 0.86). Therefore, the total of the absorbed photon number of each reaction solution for the photocatalyses should be almost identical regardless of the structure of the diphosphine ligands, and TOFs should reflect the relative quantum yields for the photocatalytic CO_2 reduction.

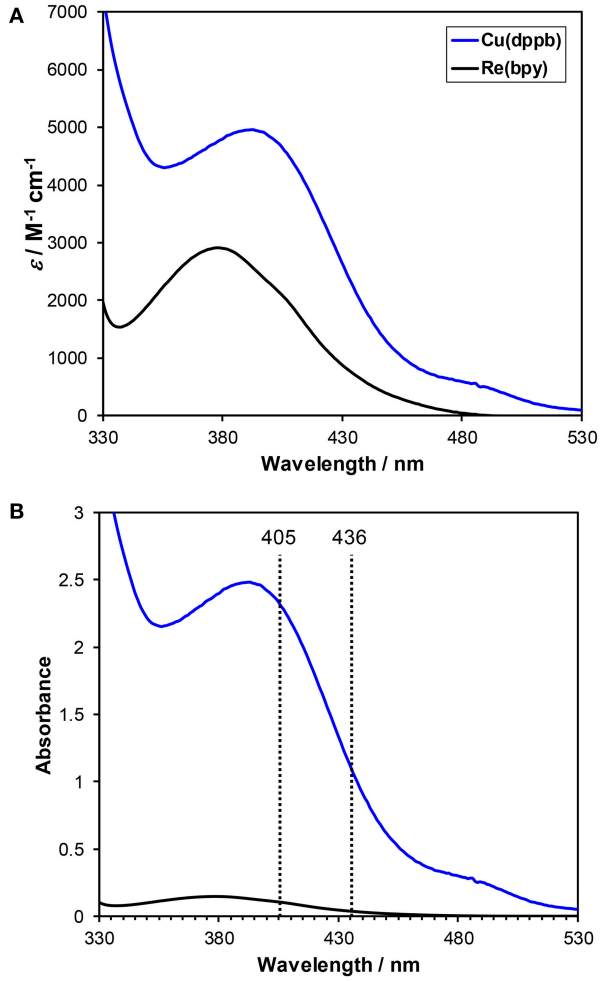

FIGURE 4 | (A) UV-Vis absorption spectra of **Cu(dppb)** (blue) and **Re(bpy)** (black). The solvent was DMA-TEOA mixed solutions (4:1 v/v). **(B)** Normalized spectra by the concentration of the reaction condition for the photocatalytic reactions ([**Cu(dppb)**] = 0.5 mM, [**Re(bpy)**] = 0.05 mM).

Photophysical and Photochemical Properties

In order to investigate the efficiencies of the initial steps of the photosensitizing reactions, we tried to measure the photophysical properties of Cu(I) complexes in the main solvent for the photocatalyses, i.e., DMA-TEOA mixed solutions. Interestingly, however, the Cu(I) complexes showed quite low luminescence properties in DMA-TEOA mixed solutions, even though the photocatalytic reactions proceeded efficiently in them. In particular, the emission quantum yield (Φ_{em}) of **Cu(dppb)** in the DMA-TEOA solutions was <0.01% and emission lifetime (τ_{em}) was shorter than 30 ns in contrast to those in other solvents (Φ_{em} in CH_2Cl_2 = 16%, τ_{em} in CH_2Cl_2 = 10 μs). The reason for the quite low luminescence properties of **Cu(dppb)** in DMA-TEOA solutions is now under investigation, but it

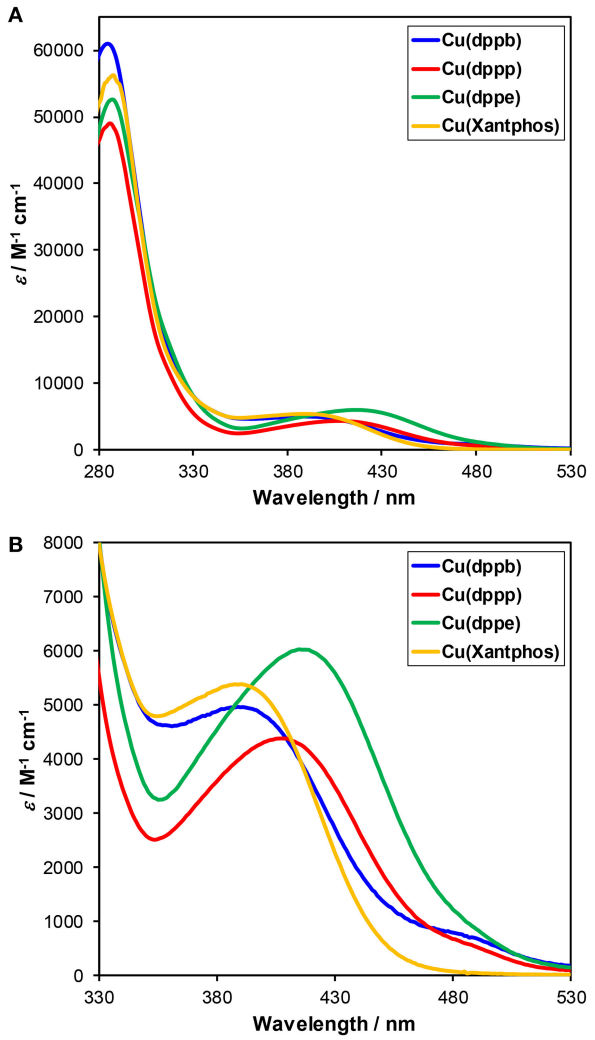

FIGURE 5 | (A) UV-Vis absorption spectra of Cu(I) complexes, i.e., **Cu(dppb)** (blue), **Cu(dppp)** (red), **Cu(dppb)** (green), and **Cu(Xantphos)** (orange). The solvent was DMA-TEOA mixed solutions (4:1 v/v). **(B)** Enlarged spectra at λ_{abs} = 330–530 nm.

TABLE 2 | Photophysical properties of Cu(I) complexes in a mixed solution of MeCN-TEOA (4:1 v/v)[a].

Complex	λ_{abs}[b]/nm (ε/$M^{-1}s^{-1}$)	λ_{em}/nm	Φ_{em}	τ_{em}[f]/μs
Cu(dppb)	387 (4,700)	605[c]	0.003[c]	0.24
	388 (5,000)[g]	585[g]	0.16[g]	10[g]
Cu(dppp)	400 (4,000)	608[d]	<0.001[d]	0.015
Cu(dppe)	411 (5,200)	608[e]	<0.001[e]	0.004
Cu(Xantphos)	388 (5,200)	577[c]	0.007[c]	0.36

[a] *Measured in a mixture of MeCN-TEOA.*
[b] *The molar extinction normalized by the number of the Cu centers. The UV-Vis absorption spectra are shown in* ***Figure S8****.*
[c] *Excitation wavelength: 390 nm.*
[d] *Excitation wavelength: 400 nm.*
[e] *Excitation wavelength: 410 nm.*
[f] *Excitation wavelength: 337 nm.*
[g] *The repoted values measured in dichloromethane (Tsubomura et al., 2015).*

might be caused by an efficient exciplex-quenching by DMA molecules (McMillin and McNett, 1998; Kuang et al., 2002). The detection of the luminescence from the DMA-TEOA solutions containing **Cu(dppb)** was difficult; therefore, we decided to compare the photophysical and photochemical properties of the series of Cu(I) complexes in the other solvents for the catalyses, i.e., a mixture of MeCN-TEOA. The emission properties of the Cu(I) complexes in a mixture of MeCN-TEOA (4:1 v/v) are summarized in **Table 2** and the emission spectra are shown in **Figure S8**. All of the complexes showed weak emission intensity and short emission lifetimes in a mixture of MeCN-TEOA compared with those in dichloromethane likely due to the exciplex-quenching by the MeCN molecules. In fact, the emission intensity of **Cu(dppb)** in MeCN solutions was almost identical to that in MeCN-TEOA solutions. Hence, the low emission intensity observed should not be derived from the quenching by TEOA (**Figure S9**). In accordance with the blue-shift of the MLCT absorption bands in the absorption spectra, the wavelength of the emission maxima of the three complexes, i.e., **Cu(dppb)**, **Cu(dppp)**, and **Cu(dppe)**, gradually decreased as the number of the methylene chains in the diphosphine ligands increased. The emission lifetimes became longer with increasing the length of the carbon chains. This is likely because the steric hindrance of the phenyl groups on the phosphorous atoms became larger with increasing the bite-angle of the diphosphine ligands, which resulted in inhibiting the attack of the solvent molecules in the excited state and decreasing non-radiative decay constants. **Cu(Xantphos)** showed the shortest wavelength of the emission maximum and the longest emission lifetime.

Since the reactions between the excited state of the Cu(I) complexes and BIH compete with the radiative and non-radiative deactivation processes, the shorter lifetime might lower the efficiencies of the quenching by BIH. Thus, we conducted quenching experiments using BIH to check whether the excited state of the Cu(I) complexes can be quenched by BIH. We measured emission intensity in the presence of various amounts of BIH. As shown in **Figure 6A**, the emission intensities became smaller with increasing the concentrations of BIH, indicating the excited state of **Cu(dppb)** was efficiently quenched by BIH. The Stern–Volmer analysis showed linear plots with an intercept at 1 (**Figure 6B**). From the slope of the fitting curve ($K_{SV} = k_q\tau_{em} = 0.71$ mM^{-1}) and the emission lifetime $\tau_{em} = 240$ ns, the quenching rate constant (k_q) was determined to be 3.0×10^9 M^{-1} s^{-1}. From these values, the quenching fraction (η_q) is estimated to be larger than 98% under the reaction condition (Equation 2) and the excited state of **Cu(dppb)** is expected to be quenched by BIH almost quantitatively, even though the emission lifetime is not so long. Moreover, in the presence of **Re(bpy)**, the emission intensity was almost identical to that in the absence of **Re(bpy)** (**Figure S10**); therefore, oxidative quenching, i.e., the electron transfer from the excited state of **Cu(dppb)** to **Re(bpy)** should be negligible. These results suggest that the photosensitizing reaction by **Cu(dppb)** mainly

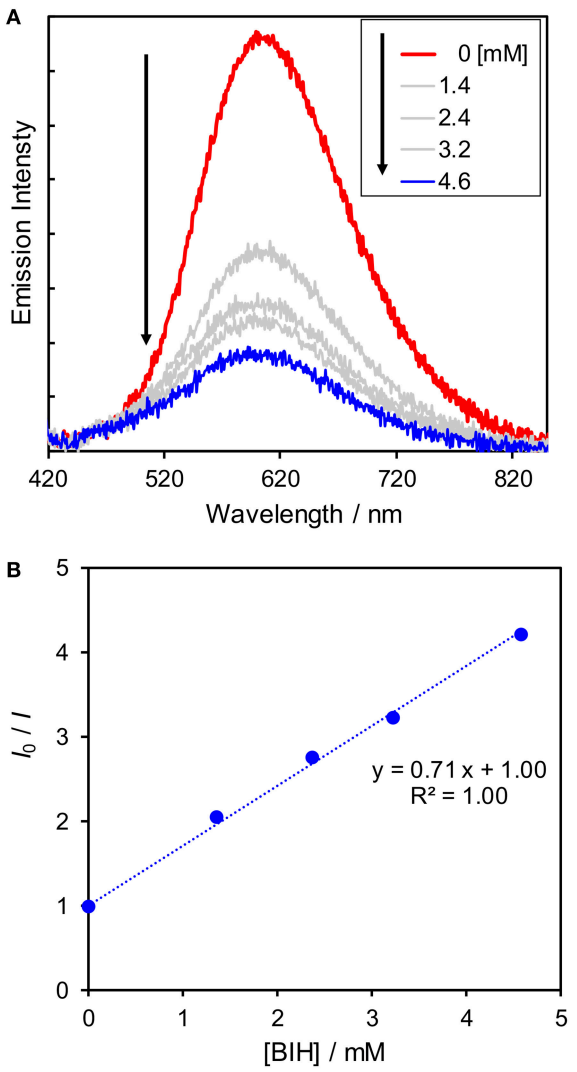

FIGURE 6 | (A) Emission spectra (excitation 410 nm) of **Cu(dppb)** in MeCN-TEOA under an Ar atmosphere in the presence of various amounts of BIH and **(B)** the Stern-Volmer plot using emission intensity (*I*) and the emission intensity without any BIH (I_0).

proceeds via the reductive quenching by BIH.

$$\eta_q = [\mathrm{BIH}]\times K_{SV}/(1+[\mathrm{BIH}]\times K_{SV}) \quad (2)$$

In the case using the other Cu(I) complexes, the emission intensity also decreased drastically by adding BIH, and emission from the Cu(I) complexes could not be detected in the presence of 0.1 M BIH. The Stern–Volmer analysis using the other Cu(I) complexes not only in a mixture of MeCN-TEOA but also in a mixture of DMA-TEOA could also be conducted owing to the larger emission intensities and the longer emission lifetimes in DMA-TEOA mixed solutions than those of **Cu(dppb)**. The Stern–Volmer analysis showed linear plots with an intercept at 1 in all cases (**Figure S11**). From the slope of the fitting curve, the quenching fractions of **Cu(dppp)**, **Cu(dppe)**, and **Cu(Xantphos)** were estimated to be larger than 99, 98, and 99%, respectively. These results clearly indicate that all of the Cu(I) complexes used in this study have relatively strong oxidizing power in the excited state and the efficiencies of the initial stage of the photosensitizing reaction, i.e., reductive quenching, should be almost identical regardless of the structure of the diphosphine ligands.

Spectral Changes During Irradiation

As mentioned above, the excited state of the Cu(I) complexes was efficiently quenched by BIH. To clarify the produced species of the quenching, UV-vis absorption spectral changes during photo-irradiation of a DMA-TEOA mixed solution (4:1 v/v) containing **Cu(dppb)** (0.1 mM) and BIH (0.1 M) under Ar were measured (**Figure 7A**). After an induction period over a few minutes, a new absorption bands at around 350–450 nm was observed. The new band increased continuously and linearly over 30-min irradiation. After irradiation, the solution was exposed to an ambient air. The solution color was immediately changed from deep-yellow to light-yellow. In the absorption spectrum measured after exposure to air, the new absorption band was completely disappeared and the original spectrum-shape was recovered (**Figure 7C**). These results clearly indicate that the quenching of the excited state of **Cu(dppb)** is a reductive quenching process, which gives one-electron reduced species (OERS) of **Cu(dppb)**. In contrast, when using **Cu(dppe)** the observed spectral changes were much smaller than **Cu(dppb)** though the shape of the new absorption band was similar to those of **Cu(dppb)** (**Figure 7B**). This difference should be derived from the difference of efficiencies for production of OERS between **Cu(dppb)** and **Cu(dppe)**. **Cu(Xantphos)** also showed rapid accumulation of OERS under the same condition, and **Cu(dppp)**, in contrast, showed slow accumulation as well as **Cu(dppe)** (**Figure S12**). Though the determination of the exact rate of production of OERS requires a spectrum obtained by electrochemical spectroscopy technics, such big difference in spectral changes and similarity of the shapes of the new absorption bands should suggest that the efficiency for production of OERS of **Cu(dppb)** and **Cu(Xantphos)** should be much larger than those of **Cu(dppp)** and **Cu(dppe)**. The tendency of the degree of the spectral changes corresponded reasonably well with that of TOF described above.

Electrochemical Properties

Figure 8 shows the cyclic voltammograms of **Cu(dppb)** and **Re(bpy)** measured in DMA-TEOA solutions and their redox potentials are summarized in **Table 3**. Both **Cu(dppb)** and **Re(bpy)** exhibited a quasi-reversible reduction wave as a first reduction wave at −1.96 and −1.70 V (vs. $Ag/AgNO_3$), respectively. These waves are attributable to the reduction of the diimine ligands. The reduction potential of **Cu(dppb)** is more negative than that of **Re(bpy)**; thus, OERS of **Cu(dppb)** has relatively strong reducing power and the electron transfer process from OERS of **Cu(dppb)** to **Re(bpy)** occurs exothermically when using **Cu(dppb)** as a photosensitizer and **Re(bpy)** as a catalyst. Interestingly, when using an MeCN-TEOA solution, the first reduction wave of **Cu(dppb)** became irreversible, though

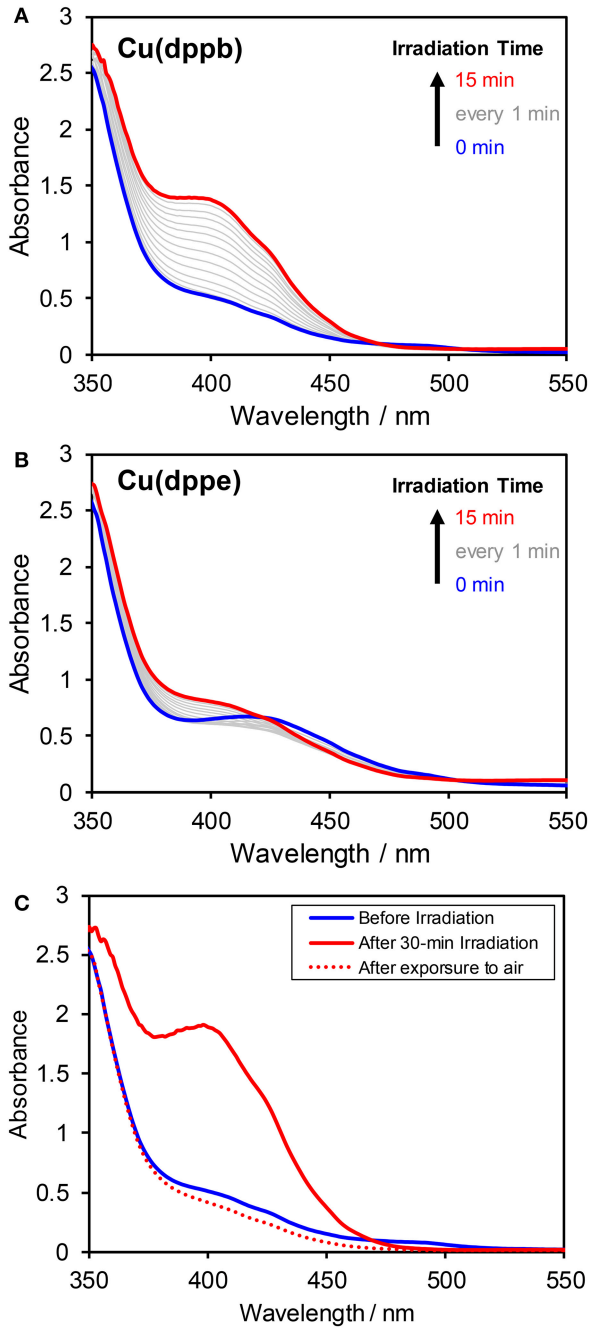

FIGURE 7 | Absorption spectral changes of DMA–TEOA (4:1 v/v) solutions containing BIH (0.1 M) and 0.1 mM of **(A) Cu(dppb)** or **(B) Cu(dppe)** under an argon atmosphere. The solution was irradiated with 430-nm monochromic light. **(C)** Absorption spectral changes of the reaction solution of **Cu(dppb)** measured before irradiation (blue solid line), just after 30-min irradiation (red solid line), and after irradiation and subsequent exposure to an ambient air (red dotted line).

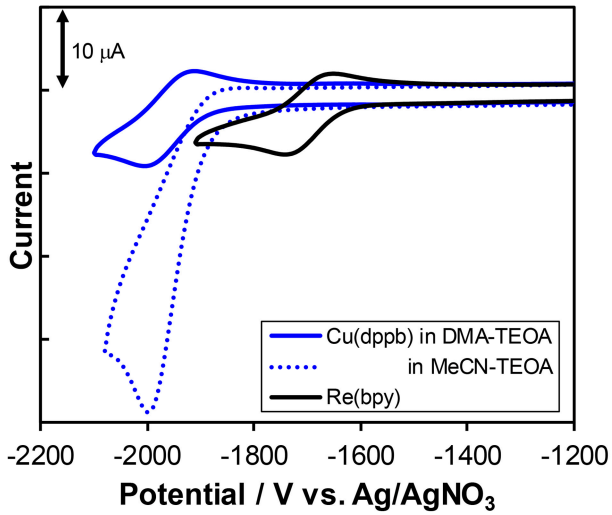

FIGURE 8 | Cyclic voltammograms of **Cu(dppb)** (blue solid line) and **Re(bpy)** (black solid line) a mixture of DMA and TEOA (4:1 v/v) containing Et_4NPF_6 (0.1 M) as a supporting electrolyte with a $Ag/AgNO_3$ (0.01M) reference electrode. The voltammogram of **Cu(dppb)** measured in a mixture of MeCN and TEOA (4:1 v/v) is also illustrated as a blue dotted line.

TABLE 3 | Electrochemical properties of the metal complexes in DMA-TEOA[a].

Complex	$E_{1/2}$/V vs. $Ag/AgNO_3$ (ΔE/mV)	
	M(N^N/N^N⁻) (M = Cu or Re)	$Cu^{I/II}$
Cu(dppb)	−1.96 (93)	–
	−1.91 (76)[b]	+0.80[b,c]
Cu(dppp)	−1.95 (84)	–
Cu(dppe)	−1.93 (78)	–
Cu(Xantphos)	−1.96 (79)	–
Re(bpy)	−1.70 (78)	–

[a] *Measured in a DMA-TEOA mixed solution containing the complex (0.5 mM) and Et_4NPF_6 (0.1 M) with a scan rate of 100 mV·s^{-1} under an Ar atmosphere.*
[b] *A DMA solution was used instead.*
[c] *Peak potential.*

the peak potential was almost identical to that in the DMA-TEOA solution. This means OERS of **Cu(dppb)** is not stable in an MeCN-TEOA solution and might be one of the reasons for the low TON_{CO} in the case using MeCN-TEOA solutions. Even though the oxidation potentials of the complexes could not be observed due to the potential window narrowed by oxidation of TEOA, the irreversible oxidation wave was observed at +0.80 V when using a DMA solution instead of the DMA-TEOA solutions. The first reduction potential observed in the DMA solution was almost identical to that in the presence of TEOA (−1.91 V). **Cu(dppb)** showed more negative reduction potential than Ru(II) tris-diimine complexes, which are typical redox-photosensitizers in the photocatalytic systems for CO_2 reduction. On the other hand, the oxidation potential was similar to those of the Ru(II) complexes; (Yamazaki et al., 2015) thus, **Cu(dppb)** should have both high reducing power in the reduced state and relatively high oxidizing power in the excited state.

The other Cu(I) complexes also showed reversible or quasi-reversible waves in the cyclic voltammograms measured in DMA-TEOA solutions (**Figure S13**). The reduction potentials were

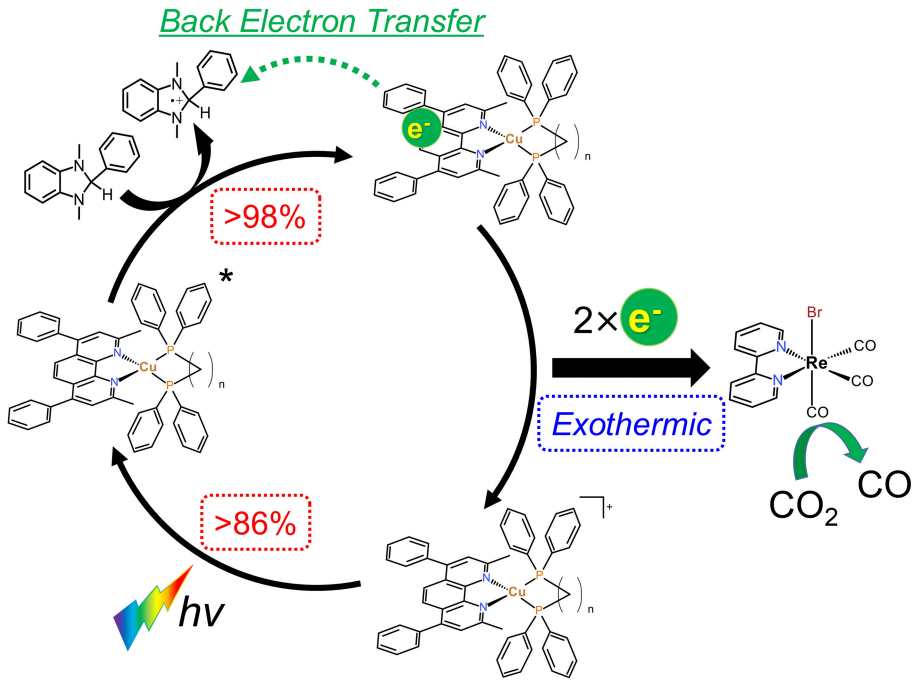

FIGURE 9 | Expected reaction mechanism of the CO_2 reduction using the Cu(I) complexes, **Re(bpy)** and BIH.

almost identical (−1.93 to −1.96 V); the reduction potentials were not strongly affected by the structure of the diphosphine ligands. These results are reasonable because it is well known that the lowest-unoccupied molecular orbitals (LUMO) of the Cu(I) complexes are mainly derived from the π*-orbitals of diimine ligands and the series of Cu(I) complexes have the same diimine ligands. Therefore, all of the Cu(I) complexes should have high reducing power in the reduced state enough to smoothly trigger the electron transfer from OERS of the Cu(I) complexes to **Re(bpy)**.

Expected Reaction Mechanism and Relationship Between the Molecular Structure and the Photosensitizing Abilities

From the results in the previous sections, the expected reaction mechanism of the photocatalytic systems in this study can be summarized as follows (**Figure 9**): (1) almost all of the irradiated photons are absorbed by the Cu(I) complexes; (2) the excited states of the Cu(I) complexes are reductively quenched by BIH to give OERS with high efficiencies; (3) the electron transfer from the OERS of the Cu(I) complexes to **Re(bpy)** proceeds exothermically; (4) CO_2 reduction takes place on **Re(bpy)** using the obtained electrons.

As described in section Photocatalytic CO_2 reduction using Cu(I) complexes as photosensitizers, TOFs were drastically changed by changing the structure of the diphosphine ligands. In contrast, all of the Cu(I) complexes showed quite similar absorbance, quenching fractions and reduction potentials; therefore, we could not observe a big difference in the efficiency of each step illustrated in **Figure 9**. However, only the efficiencies of the production of OERS strongly depended on the molecular structure even though the preceding process, i.e., the reductive quenching, proceeded almost quantitatively in all cases. It is reported that the efficiencies for the production of OERS strongly affected not only by the quenching fractions but also by the rate of the back electron transfer processes, i.e., the electron transfer from the OERS of the Cu(I) complexes to the one-electron oxidized species of BIH ($BIH^{\cdot+}$) produced by the reductive quenching processes (Tamaki et al., 2013a). This charge-recombination process forms the ground states of the Cu(I) complexes and BIH, resulting in wasting absorbed photons. The low efficiencies for the production of OERS in the case using **Cu(dppe)** should indicate that the back electron transfer proceeded more rapidly than the case using **Cu(dppb)** (**Figure 10**). The reason for the great difference in the rate of the back electron transfer is unclear at the moment, but the difference in the bite angles of the diphosphine ligands might be an important factor. The orientation of the four phenyl groups on the two phosphorous atoms is affected by changing the bite angles of the diphosphine ligands. Along with this, the distance between the phenyl groups on the phosphine ligands and the dmpp ligands will decrease by increasing the bite angles. The electrons obtained photochemically should mainly localize on the π* orbital in the dmpp ligands; thus, the back electron transfer process should proceed via the attack of $BIH^{\cdot+}$ to the π* orbital. If the phenyl groups exist nearby the dmpp ligands and cause the steric hindrance, the access of $BIH^{\cdot+}$ will be suppressed. As a result, the large P-Cu-P angles might suppress the charge-recombination and enhanced the efficiencies for OERS production. In fact, not only the photophysical properties

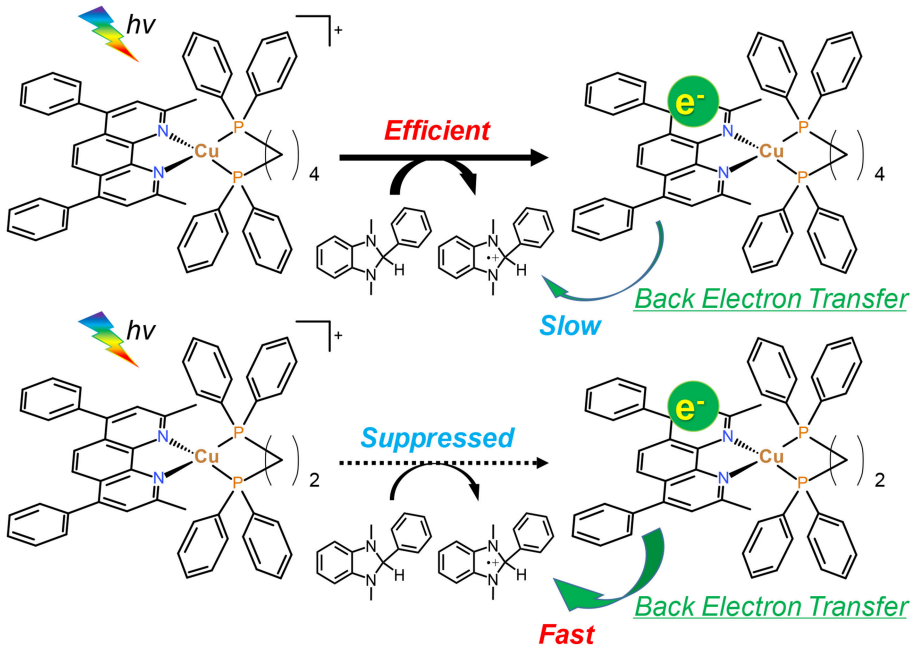

FIGURE 10 | The one-electron reduction processes of **Cu(dppb)** and **Cu(dppe)**.

TABLE 4 | Relationship between P-Cu-P angles in the solid state of the Cu(I) complexes and photosensitizing abilities[a].

Complex	P-Cu-P angles[a]/°	TOF/min^{-1}	λabs^d/nm	τ_{em^e}/μs
Cu(dppb)	120[b]	65	391	0.24
Cu(dppp)	105[b]	27	410	0.015
Cu(dppe)	91[b]	7.3	417	0.004
Cu(Xantphos)	113[c]	72	388	0.36

[a] *The angles are the reported values determined by single crystal X-ray diffraction studies. TOF was determined by the slope of the fitting curves over 5 min (**Figure S2**).*
[b] *The values from the reported literature (Tsubomura et al., 2015).*
[c] *The values from the reported literature (Heberle et al., 2017). The value in [Cu(2,9-dimethyl-1,10-phenanthroline)(Xantphos)]$^+$ instead of **Cu(Xantphos)**.*
[d] *Measured in a mixture of DMA-TEOA (4:1 v/v).*
[e] *Measured in a mixture of MeCN-TEOA (4:1 v/v).*

but also TOFs have good correlation with the reported bite angles determined using the single crystal X-ray diffraction (**Table 4**); (Tsubomura et al., 2015; Heberle et al., 2017) in other words, not only long emission lifetimes but also high photosensitizing abilities will be obtained by increasing the bite angles of the diphosphine ligands likely due to the steric hindrance of the phenyl groups to suppress the approach of the solvent molecules to the Cu(I) center and $BIH^{\cdot+}$ to the dmpp ligands.

EXPERIMENTS

General Procedure

NMR spectra were recorded on a JEOL ECA500 (500 MHz) spectrometer. The spectra were analyzed by Delta version 5. Transmission UV-vis (ultraviolet-visible light) absorption spectra were recorded on an Agilent 8453 spectrometer. Emission spectra were obtained in a solvent degassed by bubbling with argon. Emission spectra and emission lifetimes were recorded on a laboratory-made apparatus. The samples were excited by a monochromated xenon light source and the emission was analyzed by using a cooled CCD spectrometer. For the lifetime measurement, a nitrogen laser (USHO AN-200) was used to excite the samples, and the emission was detected by a monochromator equipped with a photomultiplier tube, and the signal was analyzed by using a digital oscilloscope. Emission quantum yields in solution were determined a combination of an integrating sphere, a monochromated xenon light source and a cooled CCD spectrometer.

Electrochemical Measurement

Cyclic voltammograms were conducted using an electrochemical analyzer, EC-stat 100 (EC Frontier CO., Ltd), using an electrochemical cell equipped with working (glassy carbon, $\varphi = 3$ mm), auxiliary (platinum wire), and reference ($Ag/AgNO_3$, 10 mM) electrodes. The solution containing a Cu(I) complex (0.5 mM) and Et_4NPF_6 (0.1 M) was bubbled with argon before the measurements.

Materials

Cu(dppb), **Cu(dppp)**, **Cu(dppe)**, **Re(bpy)**, and BIH were prepared according to reported methods with some modifications (Hawecker et al., 1986; Tamaki et al., 2013a; Tsubomura et al., 2015). **Cu(Xantphos)** were synthesized using dmpp instead of the corresponding diimine ligand according to the method for [Cu(2,2′-biquinoline)(Xantphos)](PF_6) (McCullough et al., 2018). Other chemicals were used as purchased without further purification.

Photocatalytic Reactions

The photocatalytic reactions were performed in a 15 mL test tube (i.d. = 11 mm) containing a 2 mL DMA–TEOA (4:1 v/v) solution of **Re(bpy)** (0.05 mM), BIH (0.1 M), and a Cu(I) complex (0.5 mM) after purging with CO_2 for more than 20 min. The solution was irradiated using a laboratory-made merry-go-round irradiation apparatus at $\lambda > 370$ nm with a high-pressure mercury lamp (SEN LIGHT Co.) combined with a UV-cut filter (Lintec Commerce. Inc.). During irradiation, the tube was cooled with a thermostatic bath (20°C). The gaseous reaction products (CO and H_2) were analyzed using a GC-TCD instrument (Shimadzu GC-8A).

Measurement of the Absorption Spectrum of the OERS

A DMA–TEOA (4:1 v/v) solution (2 mL) containing the Cu(I) complex (0.1 mM) and BIH (0.1 M) in a 7 mL quartz cell (light-pass length: 1 cm) was purged with Ar for over 20 min. The solution was irradiated with 430-nm monochromic light derived from an LED lamp purchased from CELL System Co. UV-Vis absorption spectral changes during irradiation were recorded using a Shimadzu QYM-01 system.

Measurement of Quantum Yields of Photocatalytic CO Formation

A DMA–TEOA (4:1 v/v) solution (2 mL) containing **Cu(dppb)** (0.5 mM), **Re(bpy)** (0.05 mM), and BIH (0.1 M) in a quartz cell (light-pass length: 1 cm, volume: 7 mL, light intensity: 1×10^{-8} einstein per s) was purged with CO_2 for 30 min. The solution was irradiated at $\lambda_{ex} = 430$ nm derived from an LED lamp purchased from CELL System Co. UV-Vis absorption spectral changes during irradiation were recorded using a Shimadzu QYM-01 system. During irradiation, the cell was cooled at 25°C with a thermostatic bath. The gaseous reaction products (CO and H_2) were analyzed using a GC-TCD instrument (Shimadzu GC-8A).

CONCLUSION

We investigated in detail the effects of the structure of the diphosphine ligands on the photosensitizing abilities of heteroleptic diimine-diphosphine Cu(I) complexes using a series of Cu(I) complexes bearing dmpp ligands and 4 types of diphosphine ligands by conducting photocatalytic CO_2 reduction using the Cu(I) complexes as photosensitizers. Turnover frequencies of the CO_2 reduction drastically increased up to ∼70 min^{-1} with increase of the P-Cu-P angles, even though all of the Cu(I) complexes showed similar photophysical, photochemical and electrochemical properties. In the case using **Cu(dppb)**, rapid accumulation of OERS was observed. On the contrary, when using **Cu(dppe)**, the apparent rate of the production of the OERS was quite slow. The low efficiency for the production of the OERS should be derived from the rapid charge-recombination with $BIH^{\cdot+}$. The large bite angles make the orientation of the phenyl groups on the phosphorous atoms toward the dmpp ligands, resulting in suppression of the attack by $BIH^{\cdot+}$ to the dmpp ligands. This might be one of the reasons for the high efficiencies of both the production of OERS and photocatalytic reactions when using the Cu(I) complexes connecting with the diphosphine ligands with the large bite angles.

AUTHOR CONTRIBUTIONS

YY and TT designed the study and YY wrote the initial draft of the manuscript. TO and TU investigated the photosensitizing abilities of the Cu(I) complexes. JI contributed to analyses of the structure of the Cu(I) complexes in solutions using NMR spectroscopy. SF measured the photophysical properties of the Cu(I) complexes in detail. The electrochemical properties of the Cu(I) complexes were checked by CT. All authors approved the final version of the manuscript, and agree to be accountable for all aspects of the work.

FUNDING

This work was supported by JSPS KAKENHI Grant Number 17K05816 and Grant from Seikei University.

SUPPLEMENTARY MATERIAL

The Supplementary Material for this article can be found online at: https://www.frontiersin.org/articles/10.3389/fchem.2019.00288/full#supplementary-material

REFERENCES

Gholamkhass, B., Mametsuka, H., Koike, K., Tanabe, T., Furue, M., and Ishitani, O. (2005). Architecture of supramolecular metal complexes for photocatalytic CO_2 reduction: ruthenium–rhenium Bi- and tetranuclear complexes. *Inorg. Chem.* 44, 2326–2336. doi: 10.1021/ic048779r

Hawecker, J., Lehn, J.-M., and Ziessel, R. (1983). Efficient photochemical reduction of CO_2 to CO by visible light irradiation of systems containing $Re(bipy)(CO)_3X$ or $Ru(bipy)_3^{2+}$-Co^{2+} combinations as homogeneous catalysts. *J. Chem. Soc. Chem. Commun.* 536–538. doi: 10.1039/C39830000536

Hawecker, J., Lehn, J.-M., and Ziessel, R. (1986). Photochemical and electrochemical reduction of carbon dioxide to carbon monoxide mediated by (2,2'-Bipyridine)tricarbonylchlororhenium(I) and related complexes as homogeneous catalysts. *Helv. Chim. Acta* 69, 1990–2012. doi: 10.1002/hlca.19860690824

Heberle, M., Tschierlei, S., Rockstroh, N., Ringenberg, M., Frey, W., Junge, H., et al. (2017). Heteroleptic copper photosensitizers: why an extended p-system does not automatically lead to enhanced hydrogen production. *Chem. Eur. J.* 23, 312–319. doi: 10.1002/chem.201604005

Kaeser, A., Mohankumar, M., Mohanraj, J., Monti, F., Holler, M., Cid, J. J., et al. (2013). Heteroleptic copper(I) complexes prepared from phenanthroline and bis-phosphine ligands. *Inorg. Chem.* 52, 12140–12151. doi: 10.1021/ic4020042

Kato, E., Takeda, H., Koike, K., Ohkubo, K., and Ishitani, O. (2015). Ru(II)–Re(I) binuclear photocatalysts connected by $-CH_2XCH_2-$ (X = O, S, CH_2) for CO_2reduction. *Chem. Sci.* 6, 3003–3012. doi: 10.1039/c4sc03710c

Kiyosawa, K., Shiraishi, N., Shimada, T., Masui, D., Tachibana, H., Takagi, S., et al. (2009). Electron transfer from the porphyrin S2 state in a zinc porphyrin-rhenium bipyridyl dyad having carbon dioxide reduction activity. *J. Phys. Chem. C* 113, 11667–11673. doi: 10.1021/jp901548y

Koike, K., Naito, S., Sato, S., Tamaki, Y., and Ishitani, O. (2009). Architecture of supramolecular metal complexes for photocatalytic CO_2 reduction III: effects of length of alkyl chain connecting photosensitizer to catalyst. *J. Photochem. Photobiol. A* 207, 109–114. doi: 10.1016/j.jphotochem.2008.12.014

Kou, Y., Nakatani, S., Sunagawa, G., Tachikawa, Y., Masui, D., Shimada, T., et al. (2014). Visible light-induced reduction of carbon dioxide sensitized by a porphyrin–rhenium dyad metal complex on p-type semiconducting NiO as the reduction terminal end of an artificial photosynthetic system. *J. Catal.* 310, 57–66. doi: 10.1016/j.jcat.2013.03.025

Kuang, S.-M., Cuttell, D. G., McMillin, D. R., Fanwick, P. E., and Walton, R. A. (2002). Synthesis and structural characterization of Cu(I) and Ni(II) complexes that contain the Bis[2-(diphenylphosphino)phenyl]ether ligand. Novel emission properties for the Cu(I) species. *Inorg. Chem.* 41, 3313–3322. doi: 10.1021/ic0201809

Kuramochi, Y., Ishitani, O., and Ishida, H. (2018). Reaction mechanisms of catalytic photochemical CO_2 reduction using Re(I) and Ru(II) complexes. *Coord. Chem. Rev.* 373, 333–356. doi: 10.1016/j.ccr.2017.11.023

Kutal, C., Weber, M. A., Ferraudi, G., and Geiger, D. (1985). A mechanistic investigation of the photoinduced reduction of carbon dioxide mediated by tricarbonylbromo(2,2'-bipyridine)rhenium(I). *Organometallics* 4, 2161–2166. doi: 10.1021/om00131a016

Lang, P., Giereth, R., Tschierlei, S., and Schwalbe, M. (2019). Unexpected wavelength dependency of the photocatalytic CO_2 reduction performance of the well-known (bpy)Re(CO)$_3$Cl complex. *Chem. Commun.* 55, 600–603. doi: 10.1039/c8cc08742c

McCullough, B. J., Neyhouse, B. J., Schrage, B. R., Reed, D. T., Osinski, A. J., Ziegler, C. J., et al. (2018). Visible-light-driven photosystems using heteroleptic Cu(I) photosensitizers and Rh(III) catalysts to produce H_2. *Inorg. Chem.* 57, 2865–2875. doi: 10.1021/acs.inorgchem.7b03273

McMillin, D. R., and McNett, K. M. (1998). Photoprocesses of copper complexes that bind to DNA. *Chem. Rev.* 98, 1201–1220. doi: 10.1021/cr9601167

Morimoto, T., Nishiura, C., Tanaka, M., Rohacova, J., Nakagawa, Y., Funada, Y., et al. (2013). Ring-shaped Re(I) multinuclear complexes with unique photofunctional properties. *J. Am. Chem. Soc.* 135, 13266–13269. doi: 10.1021/ja406144h

Morris, A. J., Meyer, G. J., and Fujita, E. (2009). Molecular approaches to the photocatalytic reduction of carbon dioxide for solar fuels. *Acc. Chem. Res.* 42, 1983–1994. doi: 10.1021/ar9001679

Nishikawa, M., Kakizoe, D., Saito, Y., Ohishi, T., and Tsubomura, T. (2017). Redox properties of Copper(I) complex bearing 4,7-Diphenyl-2,9-dimethyl-1,10-phenanthroline and 1,4-Bis(diphenylphosphino)butane ligands and effects of light in the presence of chloroform. *Bull. Chem. Soc. Jpn.* 90, 286–288. doi: 10.1246/bcsj.20160339

Ohkubo, K., Yamazaki, Y., Nakashima, T., Tamaki, Y., Koike, K., and Ishitani, O. (2016). Photocatalyses of Ru(II)–Re(I) binuclear complexes connected through two ethylene chains for CO_2 reduction. *J. Catal.* 343, 278–289. doi: 10.1016/j.jcat.2015.12.025

Rohacova, J., and Ishitani, O. (2016). Rhenium(I) trinuclear rings as highly efficient redox photosensitizers for photocatalytic CO_2 reduction. *Chem. Sci.* 7, 6728–6739. doi: 10.1039/c6sc01913g

Rohacova, J., and Ishitani, O. (2017). Photofunctional multinuclear rhenium(I) diimine carbonyl complexes. *Dalton Trans.* 46, 8899–8919. doi: 10.1039/c7dt00577f

Rosas-Hernández, A., Steinlechner, C., Junge, H., and Beller, M. (2017). Earth-abundant photocatalytic systems for the visible-light-driven reduction of CO_2 to CO. *Green Chem.* 19, 2356–2360. doi: 10.1039/c6gc03527b

Sahara, G., and Ishitani, O. (2015). Efficient photocatalysts for CO_2 reduction. *Inorg. Chem.* 54, 5096–5104. doi: 10.1021/ic502675a

Saito, K., Arai, T., Takahashi, N., Tsukuda, T., and Tsubomura, T. (2006). A series of luminescent Cu(I) mixed-ligand complexes containing 2,9-dimethyl-1,10-phenanthroline and simple diphosphine ligands. *Dalton Trans.* 4444–4448. doi: 10.1039/b608641a

Sato, S., Koike, K., Inoue, H., and Ishitani, O. (2007). Highly efficient supramolecular photocatalysts for CO_2 reduction using visible light. *Photochem. Photobiol. Sci.* 6, 454–461. doi: 10.1039/b613419j

Takeda, H., Cometto, C., Ishitani, O., and Robert, M. (2016a). Electrons, Photons, protons and earth-abundant metal complexes for molecular catalysis of CO_2 reduction. *ACS Catal.* 7, 70–88. doi: 10.1021/acscatal.6b02181

Takeda, H., Kamiyama, H., Okamoto, K., Irimajiri, M., Mizutani, T., Koike, K., et al. (2018). Highly efficient and robust photocatalytic systems for CO_2 reduction consisting of a Cu(I) photosensitizer and Mn(I) catalysts. *J. Am. Chem. Soc.* 140, 17241–17254. doi: 10.1021/jacs.8b10619

Takeda, H., Ohashi, K., Sekine, A., and Ishitani, O. (2016b). Photocatalytic CO_2 reduction using Cu(I) photosensitizers with a Fe(II) catalyst. *J. Am. Chem. Soc.* 138, 4354–4357. doi: 10.1021/jacs.6b01970

Tamaki, Y., and Ishitani, O. (2017). Supramolecular photocatalysts for the reduction of CO_2. *ACS Catal.* 7, 3394–3409. doi: 10.1021/acscatal.7b00440

Tamaki, Y., Koike, K., Morimoto, T., and Ishitani, O. (2013a). Substantial improvement in the efficiency and durability of a photocatalyst for carbon dioxide reduction using a benzoimidazole derivative as an electron donor. *J. Catal.* 304, 22–28. doi: 10.1016/j.jcat.2013.04.002

Tamaki, Y., Koike, K., Morimoto, T., Yamazaki, Y., and Ishitani, O. (2013b). Red-light-driven photocatalytic reduction of CO_2 using Os(II)–Re(I) supramolecular complexes. *Inorg. Chem.* 52, 11902–11909. doi: 10.1021/ic4015543

Tamaki, Y., Watanabe, K., Koike, K., Inoue, H., Morimoto, T., and Ishitani, O. (2012). Development of highly efficient supramolecular CO_2 reduction photocatalysts with high turnover frequency and durability. *Faraday Discuss.* 155, 115–127. doi: 10.1039/c1fd00091h

Tsubomura, T., Kimura, K., Nishikawa, M., and Tsukuda, T. (2015). Structures and photophysical properties of copper(I) complexes bearing diphenylphenanthroline and bis(diphenylphosphino)alkane: the effect of phenyl groups on the phenanthroline ligand. *Dalton Trans.* 44, 7554–7562. doi: 10.1039/c5dt00835b

Windle, C. D., and Perutz, R. N. (2012). Advances in molecular photocatalytic and electrocatalytic CO_2 reduction. *Coord. Chem. Rev.* 256, 2562–2570. doi: 10.1016/j.ccr.2012.03.010

Yamazaki, Y., and Ishitani, O. (2018). Synthesis of Os(II)–Re(I)–Ru(II) hetero-trinuclear complexes and their photophysical properties and photocatalytic abilities. *Chem. Sci.* 9, 1031–1041. doi: 10.1039/c7sc04162d

Yamazaki, Y., Takeda, H., and Ishitani, O. (2015). Photocatalytic reduction of CO_2 using metal complexes. *J. Photochem. Photobiol. C* 25, 106–137. doi: 10.1016/j.jphotochemrev.2015.09.001

Zhang, Y., Schulz, M., Wächtler, M., Karnahl, M., and Dietzek, B. (2018). Heteroleptic diimine–diphosphine Cu(I) complexes as an alternative towards noble-metal based photosensitizers: design strategies, photophysical properties and perspective applications. *Coord. Chem. Rev.* 356, 127–146. doi: 10.1016/j.ccr.2017.10.016

Conflict of Interest Statement: The authors declare that the research was conducted in the absence of any commercial or financial relationships that could be construed as a potential conflict of interest.

Copyright © 2019 Yamazaki, Onoda, Ishikawa, Furukawa, Tanaka, Utsugi and Tsubomura. This is an open-access article distributed under the terms of the Creative Commons Attribution License (CC BY). The use, distribution or reproduction in other forums is permitted, provided the original author(s) and the copyright owner(s) are credited and that the original publication in this journal is cited, in accordance with accepted academic practice. No use, distribution or reproduction is permitted which does not comply with these terms.

frontiers in Chemistry

ORIGINAL RESEARCH
published: 01 May 2019
doi: 10.3389/fchem.2019.00259

An Ir(III) Complex Photosensitizer With Strong Visible Light Absorption for Photocatalytic CO_2 Reduction

Yusuke Kuramochi[*†] and Osamu Ishitani*[*]

Department of Chemistry, Graduate School of Science and Engineering, Tokyo Institute of Technology, Tokyo, Japan

A cyclometalated iridium(III) complex having 2-(pyren-1-yl)-4-methylquinoline ligands [**Ir(pyr)**] has a strong absorption band in the visible region (ε_{444nm} = 67,000 M^{-1} cm^{-1}) but does not act as a photosensitizer for photochemical reduction reactions in the presence of triethylamine as an electron donor. Here, 1,3-dimethyl-2-(o-hydroxyphenyl)-2,3-dihydro-1H-benzo[d]imidazole (BI(OH)H) was used instead of the amine, demonstrating that BI(OH)H efficiently quenched the excited state of **Ir(pyr)** and can undergo the photochemical carbon dioxide (CO_2) reduction catalyzed by *trans*(Cl)-Ru(dmb)$(CO)_2Cl_2$ (dmb = 4,4′-dimethyl-2,2′-bipyridine, **Ru**) to produce formate as the main product. We also synthesized a binuclear complex combining **Ir(pyr)** and **Ru** *via* an ethylene bridge and investigated its photochemical CO_2 reduction activity in the presence of BI(OH)H.

Keywords: strong visible-light absorption, metal complex, photocatalyst, electron donor, rhenium, CO_2 reduction, photosensitizer, iridium

OPEN ACCESS

Edited by:
Hitoshi Ishida,
Kitasato University, Japan

Reviewed by:
Zhong Jin,
Nanjing University, China
Luca Conti,
University of Florence, Italy

****Correspondence:***
Yusuke Kuramochi
kuramochiy@rs.tus.ac.jp
Osamu Ishitani
ishitani@chem.titech.ac.jp

†Present Address:
Yusuke Kuramochi,
Department of Chemistry, Faculty of Science Division II, Tokyo University of Science, Tokyo, Japan

Specialty section:
This article was submitted to Inorganic Chemistry, a section of the journal Frontiers in Chemistry

Received: *31 January 2019*
Accepted: *01 April 2019*
Published: *01 May 2019*

Citation:
Kuramochi Y and Ishitani O (2019) An Ir(III) Complex Photosensitizer With Strong Visible Light Absorption for Photocatalytic CO_2 Reduction. Front. Chem. 7:259. doi: 10.3389/fchem.2019.00259

INTRODUCTION

Today, the consumption of fossil resources releases a tremendous amount of carbon dioxide (CO_2), which has had a serious impact on global climate change. The reduction in fossil resources in the future will induce shortages in both energy and carbon sources. To resolve these serious problems, the development of alternative energy systems that produce reduced volumes of CO_2 by using solar light as an energy source is desirable. To utilize a wider range of visible light from the sun, nature-inspired artificial Z-scheme systems have been developed by using semiconductors modified with metal complexes (Sato et al., 2011; Sekizawa et al., 2013; Kuriki et al., 2016, 2017; Sahara et al., 2016; Kumagai et al., 2017). Some metal complex photocatalytic systems that consist of a photosensitizer (PS) and a catalyst (CAT) can selectively induce CO_2 reduction and suppress hydrogen (H_2) evolution. These systems require a sacrificial electron donor due to the relatively low oxidation power of the PS unit in the excited state (Yamazaki et al., 2015; Tamaki and Ishitani, 2017; Kuramochi et al., 2018a) Step-by-step excitation of both the semiconductor and the metal complex produces an electron with high reducing power and a hole with high oxidizing power, allowing for CO_2 reduction by weaker electron donors such as methanol (**Figure 1**; Sekizawa et al., 2013).

Ru(II) tris-diimine complexes $[Ru(N^\wedge N)_3]^{2+}$ have been frequently used as the PS unit of supramolecular photocatalysts, which have strong absorption in the visible region, a long lifetime of the ^{3}MLCT excited state, and a stable one-electron reduced state. However, $[Ru(N^\wedge N)_3]^{2+}$ has a problem in that one of the N^N ligands is relatively easily released during the photocatalytic reaction to give $[Ru(N^\wedge N)_2(Solvent)_2]^{2+}$-type complexes that work as catalysts for CO_2 reduction

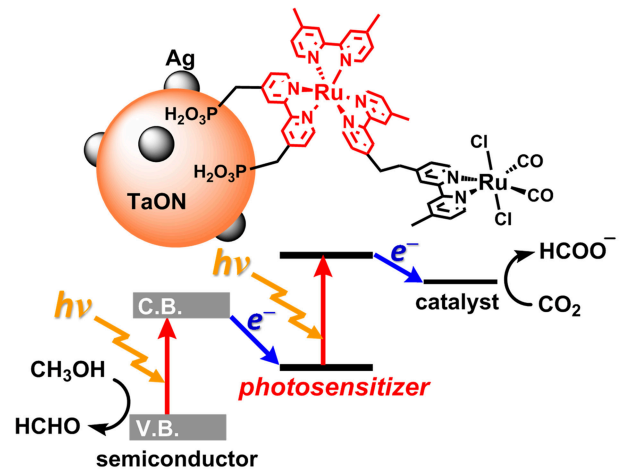

FIGURE 1 | The artificial Z-scheme system for CO_2 (carbon dioxide) reduction, consisting of a semiconductor (TaON) and a Ru(II) binuclear complex **(RuRu')** (Sekizawa et al., 2013).

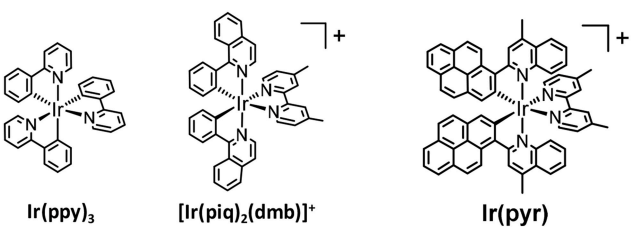

FIGURE 2 | Structures of iridium(III) complexes.

(Lehn and Ziessel, 1990; Yamazaki et al., 2015; Kuramochi et al., 2018a). In addition, a PS unit with stronger absorption in the visible region compared to $[Ru(N^\wedge N)_3]^{2+}$ should be more favorable for constructing new photocatalytic systems.

In recent years, cyclometalated iridium(III) complexes, such as $Ir(ppy)_3$ (ppy = 2-phenylpyridine) and $[Ir(ppy)_2(N^\wedge N)]^+$, have been used as PSs in various photocatalytic reactions, such as H_2 evolution (Goldsmith et al., 2005; Lowry and Bernhard, 2006), CO_2 reduction (Thoi et al., 2013; Bonin et al., 2014; Chen et al., 2015; Rao et al., 2017, 2018), and organic synthesis (**Figure 2**; Prier et al., 2013; Schultz and Yoon, 2014; Shaw et al., 2016), even though the absorption by $Ir(ppy)_3$ and $[Ir(ppy)_2(N^\wedge N)]^+$ is relatively weak in the visible region. We already reported that $[Ir(piq)_2(dmb)]^+$ (piq = 1-phenylisoquinoline, dmb = 4,4′-dimethyl-2,2′-bipyridine), which has a stronger absorption in the visible region (ε_{444nm} = 7,800 M^{-1} cm^{-1}) than $Ir(ppy)_3$, acts as a PS for CO_2 reduction without forming decomposed species that catalyze CO_2 reduction (**Figure 2**; Kuramochi and Ishitani, 2016). The intense absorption at the longer wavelength allowed for the selective excitation of the PS without exciting the CAT, such as *fac*-Re(dmb)(CO)$_3$Br (dmb = 4,4′-dimethyl-2,2′-bipyridine). In addition, the supramolecular photocatalyst, where $[Ir(piq)_2(BL)]^+$ (BL = bridging ligand) is connected with *fac*-Re(BL)(CO)$_3$Br, works as a better photocatalyst for CO_2 reduction compared to the mixed system of the corresponding mononuclear complexes, i.e., $[Ir(piq)_2(dmb)]^+$ and *fac*-Re(dmb)(CO)$_3$Br. Although $[Ir(piq)_2(dmb)]^+$ has a stronger absorption in the visible region compared to $Ir(ppy)_3$ and the advantages over $[Ru(N^\wedge N)_3]^{2+}$ as mentioned above, its absorption in the visible region is weaker than that of $[Ru(N^\wedge N)_3]^{2+}$. It has been reported that several Ir(III) complexes that have stronger absorption bands in the visible region than $[Ru(N^\wedge N)_3]^{2+}$ can act as PSs for H_2 evolution (Takizawa et al., 2012, 2014, 2018; Fan et al., 2014). Fan et al. reported that an Ir(III) complex with 2-(pyren-1-yl)-4-methylquinoline ligands [**Ir(pyr)**, **Figure 2**] showed a very strong absorption band in the visible region, ε(450 nm) > 60,000 M^{-1} cm^{-1}. Unfortunately, it could not photocatalyze H_2 evolution using K_2PtCl_4 as CAT in the presence of triethylamine (TEA). This inactivity was explained by the lack of photoinduced electron transfer from TEA to the excited state of **Ir(pyr)**, as the reduction potential of the excited state of **Ir(pyr)** is less than the oxidation potential of TEA (Fan et al., 2014). We reported that the Ru(II)–Ru(II) supramolecular photocatalyst can selectively reduce CO_2 to formic acid (HCOOH) by using 1,3-dimethyl-2-(*o*-hydroxyphenyl)-2,3-dihydro-1H-benzo[d]imidazole (BI(OH)H) as an electron donor (ED) with a high turnover number (TON_{HCOOH}) and a high quantum yield (Φ_{HCOOH}; Tamaki et al., 2015). This photocatalytic reaction does not proceed in the absence of BI(OH)H even if triethanolamine (TEOA), which has a similar oxidation potential to TEA, is used. This is because BI(OH)H has a much stronger reducing power ($E^{\circ x}_{1/2}$ = +0.02 V *vs.* Ag/$AgNO_3$) (Hasegawa et al., 2006; Elgrishi et al., 2017; Kuramochi et al., 2018a) than TEA ($E^{\circ x}_{p}$ = +0.67 V *vs.* Ag/$AgNO_3$) (Yamazaki et al., 2015; Elgrishi et al., 2017).

Herein, we report the successful use of **Ir(pyr)** as a PS for CO_2 reduction by using BI(OH)H as ED and *trans*(Cl)-Ru(dmb)(CO)$_2$Cl$_2$ (**Ru**) as CAT. We also synthesized a supramolecular photocatalyst from **Ir(pyr)** (**Ir(pyr)–Ru**; **Scheme 1**) and investigated its photocatalytic activity for CO_2 reduction.

RESULTS AND DISCUSSION

Synthesis of the Binuclear Complex, Ir(pyr)–Ru

Ir(pyr)–Ru was synthesized according to **Scheme 1**. The di-μ-chloride-iridium dimer (Fan et al., 2014) was reacted with $AgPF_6$ in acetonitrile to give the mononuclear acetonitrile–iridium complex. This complex was reacted with 1,2-bis(4′-methyl-[2,2′-bipyridin]-4-yl)ethane (BL), and the crude product was isolated using a silica gel column giving $[Ir(pyr\text{-}mq)_2(BL)](PF_6)$ in 43% yield, based on the acetonitrile–iridium complex. This was reacted with $[Ru(CO)_2Cl_2]_n$, which was pretreated by refluxing in the solvent (Kuramochi et al., 2015), giving the desired binuclear complex **Ir(pyr)–Ru** as a PF_6 salt in 87% yield.

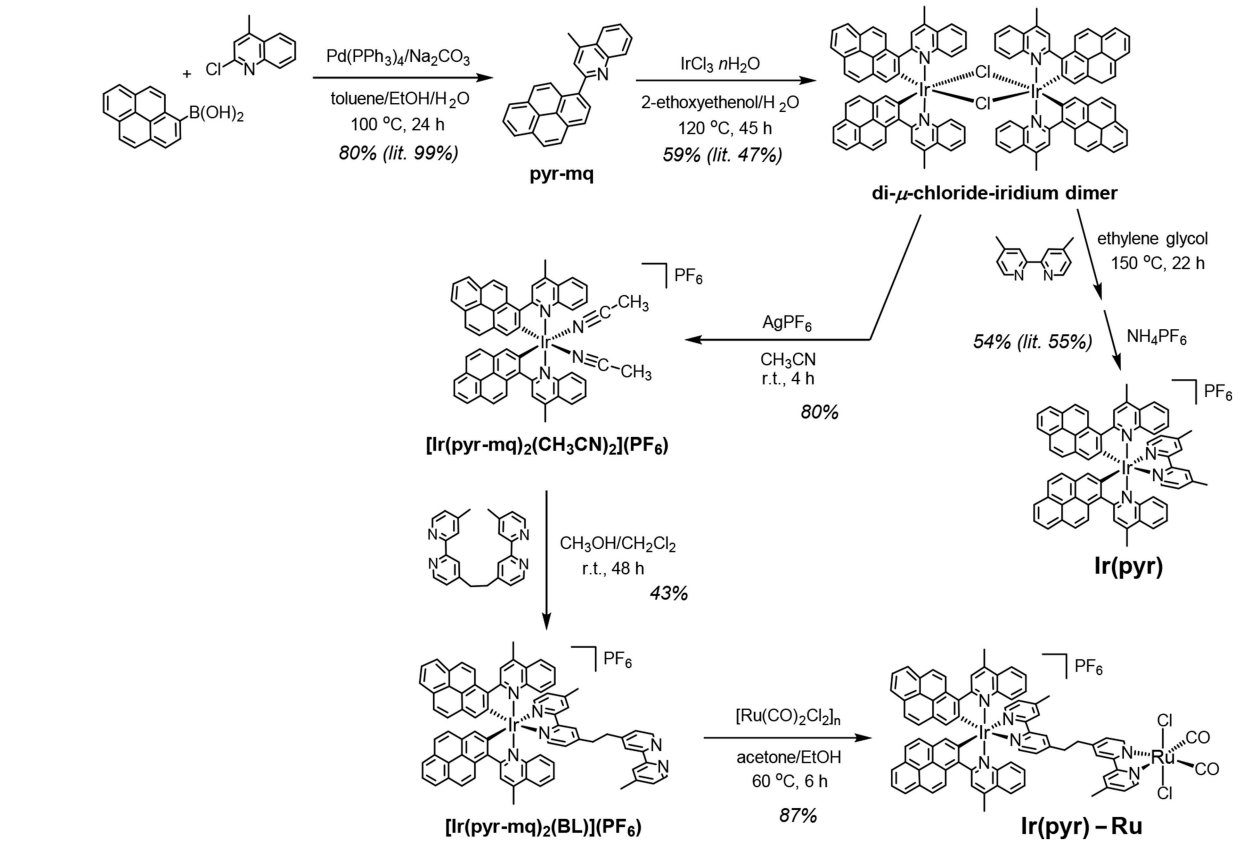

SCHEME 1 | Synthetic routes to Ir(pyr)–Ru and Ir(pyr).

Photophysical and Electrochemical Properties

Fan et al. reported the photophysical and electrochemical properties of **Ir(pyr)** in dichloromethane or tetrahydrofuran (Fan et al., 2014). Since these solvents are less polar than the solvents suitable for CO_2 reduction, such as *N,N*-dimethylacetamide (DMA), we measured the photophysical and electrochemical properties of **Ir(pyr)** in DMA (Kuramochi et al., 2014). **Figure 3** shows the ultraviolet–visible (UV–vis) absorption spectrum of **Ir(pyr)** in DMA, which shows a much stronger absorption in the visible region ($\varepsilon_{444\text{nm}} = 67{,}000\ \text{M}^{-1}\ \text{cm}^{-1}$) compared to $[\text{Ir(piq)}_2\text{(dmb)}]^+$ and $[\text{Ru(dmb)}_3]^{2+}$. According to the time-dependent density functional theory (TD-DFT) calculation of the UV–vis spectrum of **Ir(pyr)** in DMA (**Figure 4**, red bars), the strong absorption band at 444 nm is due to the transitions from the highest occupied molecular orbital (HOMO)-1 to the lowest unoccupied molecular orbital (LUMO)+2 and from HOMO to LUMO+1, which correspond to the $\pi - \pi^*$ transitions of the pyrene moieties. The absorption at a wavelength >500 nm is assigned to the transition from HOMO-1 to LUMO and corresponds to the transition from the interligand transition from the dmb to the pyrene moieties and might include some

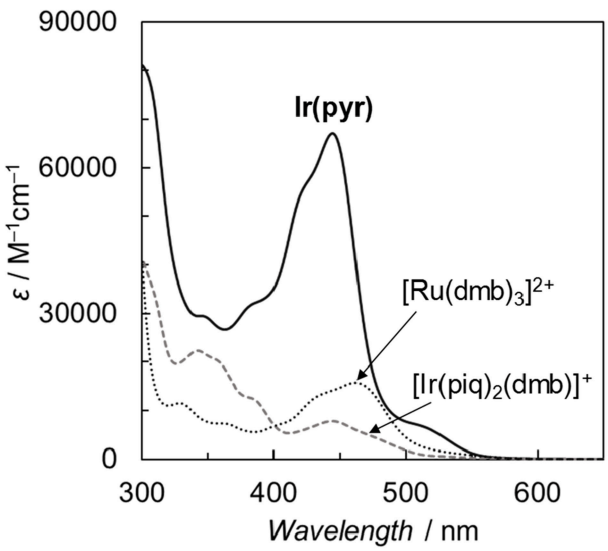

FIGURE 3 | Comparison of the ultraviolet–visible (UV–vis) absorption spectra of **Ir(pyr)**, $[\text{Ir(piq)}_2\text{(dmb)}](\text{PF}_6)$, and $[\text{Ru(dmb)}_3](\text{PF}_6)_2$ in *N,N*-dimethylacetamide (DMA) at 298 K.

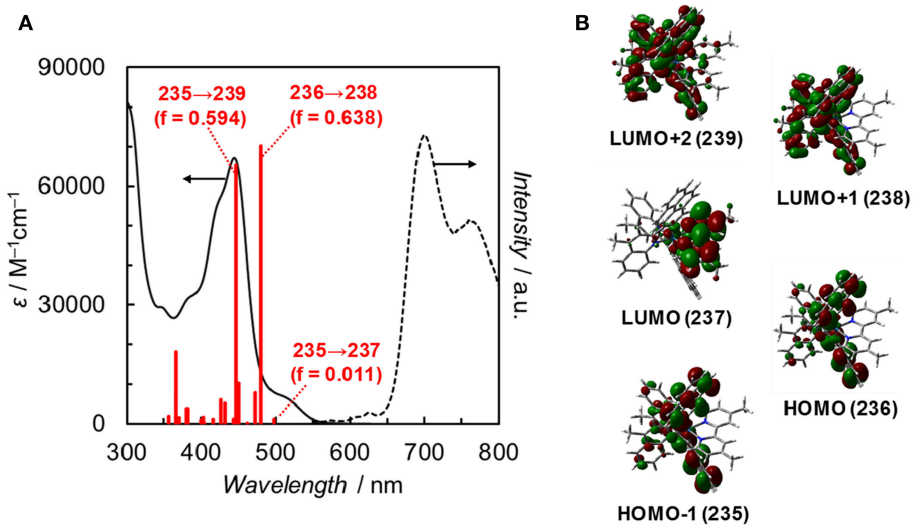

FIGURE 4 | (A) UV–vis absorption spectrum (solid line), TDDFT theoretical excitations (red bars, >350 nm, f: oscillator strength), and emission spectrum (dotted line) of **Ir(pyr)** in DMA at 298 K. **(B)** Frontier orbitals of **Ir(pyr)**. Calculation method: B3LYP/LANL2DZ(Ir)/6-31G(d,p) (H, C, N) levels by using polarizable continuum model (PCM) with the default for DMA, isovalue = 0.02.

TABLE 1 | Electrochemical data in DMA (dichloromethane or THF) at 298 K[a].

	$E_{1/2}^{ox}$/V[b]	$E_{1/2}^{red}$/V	$E(PS^{\cdot+}/PS^*)$/V[c]	$E(PS^*/PS^{\cdot-})$/V[c]
$[Ir(piq)_2(dmb)]^+$[d]	+0.92	−1.75, −2.07, −2.31	−1.18	+0.35
Ir(pyr)	+0.84	−1.68, −1.86, −2.15	−0.96	+0.12
	(+0.45)[e]	(−1.70, −1.89, −2.29)[e]	–	(+0.23)[e]
Ru	–	−1.66[f]	–	–

[a]*E vs. Ag/AgNO$_3$ (10 mM).* [b]*Estimated by DPV in acetonitrile.* [c]*Excited-state oxidation and reduction potentials of the photosensitizer were calculated from $E_{1/2}^{ox} - E_{00}$ and $E_{1/2}^{red} + E_{00}$, respectively.* [d]*Kuramochi and Ishitani (2016).* [e]*The values were correlated by using conversion factor (−0.631 V) from NHE to Ag/AgNO$_3$, see Fan et al. (2014) and Elgrishi et al. (2017).* [f]*Kuramochi et al. (2018b).*

contribution from the singlet–triplet transitions, as described in the literature (Fan et al., 2014). The emission spectrum of **Ir(pyr)** in DMA is shown in **Figure 4**, and the Franck–Condon line-shape analysis (**Figure S1**) gave a 0–0 band energy gap of 14,500 cm^{-1} for **Ir(pyr)**, which is lower than that for $[Ir(piq)_2(dmb)]^+$ (16,950 cm^{-1}) (Kuramochi and Ishitani, 2016).

The redox potentials of **Ir(pyr)** in DMA were obtained by cyclic voltammetry (CV; **Figure S2**) and differential pulse voltammetry (DPV) and are summarized in **Table 1** together with those of $[Ir(piq)_2(dmb)]^+$ and **Ru** (Kuramochi and Ishitani, 2016; Kuramochi et al., 2018b). The oxidation waves of the Ir complexes were measured in acetonitrile due to its wide-potential window. The CV showed three each of reversible cathodic and irreversible anodic waves, indicating that **Ir(pyr)** is stable against reduction but relatively unstable to oxidation on the CV timescale. According to the DFT calculation, the LUMO mainly distributes across the dmb ligand of **Ir(pyr)** (**Figure 4**). Thus, it is expected that the first electron is injected into the dmb ligand, which benefits the electron transfer from the one-electron reduced species of **Ir(pyr)** to the **Ru** moiety. This property has been previously observed in $[Ir(piq)_2(dmb)]^+$ (Kuramochi and Ishitani, 2016).

Emission Quenching by Electron Donors

The emission intensity of **Ir(pyr)–Ru** was similar to that of **Ir(pyr)**, suggesting that oxidative quenching of the excited state of the **Ir** unit by the **Ru** unit does not proceed in **Ir(pyr)–Ru**. This is reasonable because the oxidative quenching process is endothermic; the oxidation potential of the excited state of **Ir(pyr)** is much more positive (−0.96 V; **Table 1**) than the reduction potential of **Ru** (−1.66 V).

Emission quenching of **Ir(pyr)** by 1-benzyl-1,4-dihydronicotinamide (BNAH) was inefficient: Stern–Volmer constant (K_{SV}) = 13 M^{-1} in DMA. Assuming that the emission lifetime is 3.1 μs (Fan et al., 2014), the quenching rate constant (k_q) was estimated to be 4.2 × 10^6 M^{-1} s^{-1}. When a stronger electron donor, BI(OH)H (Hasegawa et al., 2006; Tamaki et al., 2015), was used, the emission of **Ir(pyr)** was more efficiently quenched (**Figure 5**); K_{SV} reached 3,000 M^{-1} in DMA/TEOA (5:1 v/v), and k_q was 9.7 × 10^8 M^{-1} s^{-1}, which is close to the diffusion-controlled rate constant (Tamaki et al., 2013). The K_{SV} of **Ir(pyr)–Ru** by BI(OH)H was 2,800 M^{-1}, which is similar to that of **Ir(pyr)**. In previous work by Fan et al. (2014), **Ir(pyr)** did not work as a PS for H_2 evolution because the emission from **Ir(pyr)** was not quenched by TEA. This emission is not quenched by TEOA as well because TEOA has a similar oxidation potential to TEA. Conversely,

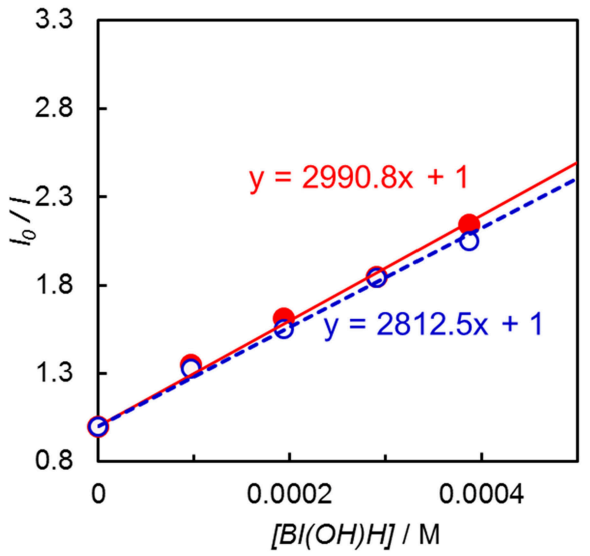

FIGURE 5 | Emission quenching of the excited **Ir(pyr)** (closed red circle) and **Ir(pyr)–Ru** (open blue circle) by BI(OH)H in DMA/TEOA (5:1 v/v) at 298 K.

BI(OH)H significantly quenches the emission from **Ir(pyr)**, indicating efficient electron transfer from BI(OH)H to the excited **Ir(pyr)**.

Photocatalytic CO_2 Reduction

DMA-TEOA (5:1 v/v) mixed solutions containing both **Ir(pyr)** and **Ru** or **Ir(pyr)–Ru** (0.05 mM) as the photocatalysts and BI(OH)H as the ED were irradiated at $\lambda_{ex} > 480$ nm under a CO_2 atmosphere. In both cases, HCOOH was mainly detected with small amounts of CO and H_2. **Figure 6** shows the time profiles of product formation during the photocatalytic reaction. Blank experiments in the absence of the **Ru** catalyst produced trace amounts of CO (3.9 μmol) and formate (7.6 μmol) after 24 h. From the Stern–Volmer constants, the quenching efficiencies of the excited states of **Ir(pyr)** and **Ir(pyr)–Ru** by 0.1 M BI(OH)H were estimated as $\eta_q > 99\%$, indicating that the excited states of **Ir(pyr)** and **Ir(pyr)–Ru** were almost completely quenched by BI(OH)H under these reaction conditions. **Figure 6** shows that **Ir(pyr)** does work as a PS for CO_2 reduction when using BI(OH)H. The time profiles for the mixture of **Ir(pyr)** and **Ru** showed a linear increase reaching a $TON_{HCOOH} = \sim 2{,}000$ during 24-h irradiation, indicating that **Ir(pyr)** has a high durability during photocatalytic CO_2 reduction. Although **Ir(pyr)–Ru** also worked as a photocatalyst for CO_2 reduction, it showed a lower activity compared to the mixture of **Ir(pyr)** and **Ru**. While the initial formation rates of the products were similar, the reaction stopped after just 5 h of irradiation in the case of **Ir(pyr)–Ru**. Because the reaction solution of **Ir(pyr)–Ru** was decolorized during the photocatalytic reaction, the low activity of **Ir(pyr)–Ru** would result from its low durability. The decoloration was also observed in irradiation experiments of $[Ir(piq)_2(dmb)]^+$ and ED without the CAT because of hydrogenation of the ligands in $[Ir(piq)_2(dmb)]^+$ (Kuramochi and Ishitani, 2016). Thus, it is also expected that the decoloration of **Ir(pyr)–Ru** is caused by hydrogenation of the Ir unit. In **Ir(pyr)–Ru**, the accumulated electron(s) might be stabilized because of electron hopping between the Ir and Ru units, which might be enhanced by the hydrogenation of the Ir unit.

Figure 7 illustrates the time profiles of the products during the irradiation of CO_2-saturated DMA/TEOA (5:1 v/v, 2.0 ml) solutions containing **Ir(pyr)** or $[Ru(dmb)_3]^{2+}$ as PS in the presence of *trans*-$Ru(bpy)(CO)_2Cl_2$ (bpy = 2,2-bipyridine) and BI(OH)H as CAT and ED, respectively. The initial formation rate of HCOOH in the system using **Ir(pyr)** (**Figure 7A**) is slower than that using $[Ru(dmb)_3]^{2+}$ (**Figure 7B**), although **Ir(pyr)** has more intense absorption band at >480 nm than $[Ru(dmb)_3]^{2+}$ (**Figure 3**). In **Figure 7**, *trans*-$Ru(bpy)(CO)_2Cl_2$ is used instead of **Ru**. Although *trans*-$Ru(bpy)(CO)_2Cl_2$ has a much less negative reduction potential (−1.51 V vs. $Ag/AgNO_3$; Kuramochi et al., 2015) than **Ru** (−1.66 V *vs.* $Ag/AgNO_3$), the initial formation rate of HCOOH in the system using *trans*-$Ru(bpy)(CO)_2Cl_2$ (**Figure 7A**) is similar to that using **Ru** (**Figure 6A**), suggesting that the electron transfer process from the one-electron reduced **Ir(pyr)** to CAT is not the rate-determining step and does not significantly affect the reaction rate. Considering that the emission of **Ir(pyr)** is almost completely quenched, the slow initial formation rate of HCOOH in **Ir(pyr)** would result from the competitive back-electron transfer process soon after the electron transfer from BI(OH)H to the excited state of **Ir(pyr)** in the solvent cage (Kavarnos, 1993; Nakada et al., 2015).

CONCLUSION

Photocatalytic CO_2 reduction using **Ir(pyr)** as PS, which has a strong absorption in the visible region, proceeded efficiently for more than 1 day when a suitable electron donor, BI(OH)H, and **Ru** were used as CAT. A new supramolecular photocatalyst, **Ir(pyr)–Ru**, was successfully synthesized, which exhibited a similar reaction rate during the initial stage of CO_2 reduction to that of the mixed system, but the durability of **Ir(pyr)–Ru** was lower than that of the mixed system. While Ir(pyr) showed high durability in the mixed system, the initial formation rate of HCOOH tended to be slower than that of the catalytic system using $[Ru(dmb)_3]^{2+}$ as PS, which is possibly due to the faster back-electron transfer from the reduced Ir(pyr) to the oxidized BI(OH)H.

EXPERIMENTAL SECTION

General Procedure

All chemicals and solvents were of commercial reagent quality and were used without further purification unless otherwise stated. DMA was dried over molecular sieves of size 4 Å and distilled under reduced pressure. TEOA was distilled under reduced pressure. Tetraethylammonium tetrafluoroborate was dried *in vacuo* at 100°C overnight before use. $[Ir(piq)_2(BL)](PF_6)$ (Kuramochi and Ishitani, 2016), BNAH (Mauzerall and Westheimer, 1955), BI(OH)H (Hasegawa et al.,

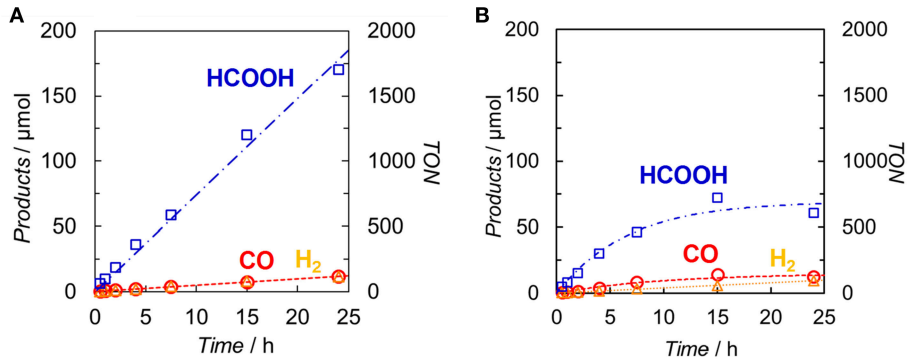

FIGURE 6 | Time dependences of the products during the photo-irradiation of CO_2-saturated DMA/TEOA (5:1 v/v, 2.0 ml) solutions containing **(A)** a mixed system of **Ir(pyr)** (0.05 mM) and **Ru** (0.05 mM) or **(B) Ir(pyr)–Ru** (0.05 mM) in the presence of BI(OH)H (0.1 M): CO (○), HCOOH (□) and H_2 (Δ). A 500-W high-pressure Hg lamp was used for the irradiation (λ > 480 nm).

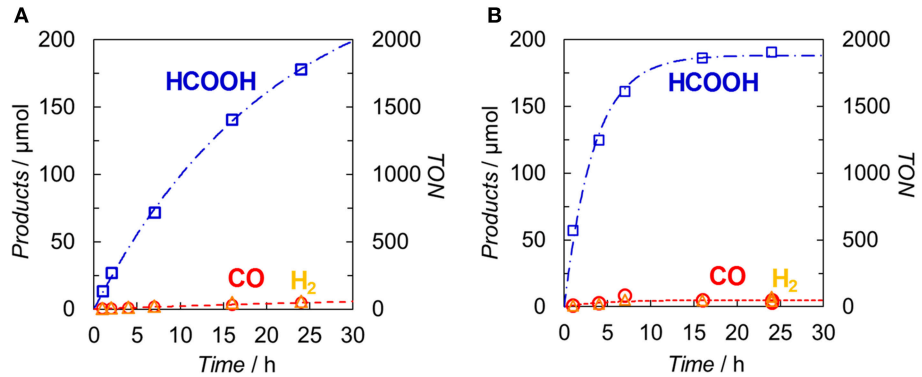

FIGURE 7 | Time dependences of the products during the photo-irradiation of CO_2-saturated DMA/TEOA (5:1 v/v, 2.0 ml) solutions containing **(A) Ir(pyr)** (0.05 mM) or **(B)** $[Ru(dmb)_3]^{2+}$ (0.05 mM) in the presence of *trans*-$Ru(bpy)(CO)_2Cl_2$ (0.05 mM) and BI(OH)H (0.1 M): CO (○), HCOOH (□) and H_2 (Δ). A 500-W high-pressure Hg lamp was used for the irradiation (λ > 480 nm).

2005; Zhu et al., 2008), **Ru** (Anderson et al., 1995), and BL (Sun et al., 1997) were synthesized according to literature procedures. ^{1}H NMR spectra were recorded on an AL400 NMR spectrometer. IR spectra were measured in dichloromethane on a JASCO FT/IR-610 spectrometer. Electrospray ionization–mass spectroscopy (ESI-MS) was undertaken using a SHIMADZU LCMS-2010A system with acetonitrile as a mobile phase. UV–vis absorption spectra were recorded with a JASCO V-670 instrument. Emission spectra were measured at 25°C under an Ar atmosphere using a JASCO FP-8600 spectrofluorometer with correlation for the detector sensitivity. Emission quenching experiments were performed in DMA or DMA/TEOA (5:1 v/v) solutions containing a complex and several different concentrations of BNAH or BI(OH)H.

Emission Spectral Fitting

Double-mode Franck–Condon band shape analysis was used to fit the emission spectra. The spectral fittings were carried out according to the following equation (Caspar et al., 1984) using the Wavemetrics Igor software.

$$I(\tilde{\nu}) = \sum_{n_1=0}^{5}\sum_{n_2=0}^{5}\left(\frac{E_{00}-n_1\tilde{\nu}_1-n_2\tilde{\nu}_2}{E_{00}}\right)^4\left(\frac{S_1^{n_1}}{n_1!}\right)\left(\frac{S_2^{n_2}}{n_2!}\right)\exp\left[-4log2\left(\frac{\tilde{\nu}-E_{00}+n_1\tilde{\nu}_1+n_2\tilde{\nu}_2}{\tilde{\nu}_{1/2}}\right)^2\right] \quad (1)$$

$I(\nu)$ is the relative emission intensity at frequency ν. E_{00} is the energy gap between the zeroth vibrational levels in the ground and excited states, n_1 and n_2 are the vibrational quantum numbers of the high- and low-frequency vibrational modes, respectively, S_1 and S_2 are the Huang–Rhys factors, and $\nu_{1/2}$ is the half-width at half-maximum (fwhm) of the individual vibronic band. The 0–0 band energy gaps between the lowest excited state and the ground state were obtained from the emission spectral fitting (**Figure S1**).

$[Ir(pyr\text{-}mq)_2(CH_3CN)_2](PF_6)$

$[(pyr\text{-}mq)_2Ir\text{-}\mu\text{-}Cl]_2$ (100 mg, 5.4×10^{-5} mol), $AgPF_4$ (31 mg, 1.2×10^{-4} mol), and acetonitrile (10 ml) were placed in a 50-ml flask. The mixture was stirred for 4 h at room temperature. The resulting suspension was filtered through Celite pad to remove AgCl. The filtrate was concentrated to *ca.* 1 ml, and the product was precipitated by the addition of diethyl ether (10 ml). After cooling the suspension for 30 min at 0°C, the product was collected by filtration, giving 96 mg (80%) of the titled compound as a dark orange solid: ^{1}H NMR ($CDCl_3$, 400 MHz) δ 9.18 (brs, 2H), 8.73 (d, $J = 8.8$ Hz, 2H), 8.56 (s, 2H), 8.23 (d, $J = 7.2$ Hz, 2H), 8.15–7.95 (m, 8H), 7.85–7.70 (m, 6H), 7.27 (m, 2H), 6.40 (brs, 2H), 3.23 (s, 6H), 2.22 (s, 6H, CH_3CN).

$[Ir(pyr\text{-}mq)_2(BL)](PF_6)$

The bridging ligand (BL, 80 mg, 2.2×10^{-4} mol), dichloromethane (40 ml), and methanol (20 ml) were placed in a 100-ml flask, and the system was purged with argon gas. A solution of $[Ir(pyr\text{-}mq)_2(CH_3CN)_2](PF_6)$ (80 mg, 7.3×10^{-5} mol) in dichloromethane (10 ml) and methanol (5 ml) was then added dropwise at room temperature. The reaction mixture was stirred at room temperature. The reaction progress was monitored with ESI-MS. After stirring for 48 h, the resulting solution was evaporated. The residue was purified with a silica gel column (1 to 2 vol% methanol in dichloromethane). The second red band eluted with 2 vol% methanol was collected and evaporated to dryness, giving 42 mg (43% based on the iridium precursor) of the titled complex as a dark red solid: ESI-MS *m/z*: 1,243 ($[M\text{–}PF_6^-]^+$). ^{1}H NMR ($CDCl_3$, 400 MHz) δ 8.94 (brs, 1H), 8.92 (brs, 1H), 8.60 (d, $J = 2.8$ Hz, 2H), 8.51 (d, $J = 5.2$ Hz, 1H), 8.45 (d, $J = 5.2$ Hz, 1H), 8.24–8.12 (m, 8H), 8.02 (s, 1H), 8.00 (s, 1H), 7.91–7.76 (m, 8H), 7.58 (s, 2H), 7.52–7.38 (m, 5H), 7.35 (m, 1H), 7.25–7.21 (m, 1H), 7.09 (d, $J = 4.4$ Hz, 1H), 6.99–6.88 (m, 3H), 6.77 (m, 1H), 3.13–3.00 (m, 4H), 2.97 (s, 3H), 2.95 (s, 3H), 2.45 (s, 3H), 2.42 (s, 3H).

Ir(pyr)–Ru

An acetone/ethenol (1:2 v/v) mixed solution (6 ml) containing $[Ru(CO)_2Cl_2]_n$ (9.9 mg, 4.3×10^{-5}/n mol) was refluxed for 1 h, and then $[Ir(pyr\text{-}mq)_2(BL)](PF_6)$ (30 mg, 2.2×10^{-5} mol) was added to it. The reaction mixture was heated to 60°C and stirred for 4.5 h under Ar atmosphere. As the reaction proceeded, the starting red solution became a red suspension. The resulting solid was filtered and washed with ethanol. The solid was dissolved in dichloromethane (*ca.* 2 ml) and filtered to remove insoluble materials. The solution was evaporated to afford 30 mg (87%) of the titiled compound as a dark red solid. ESI-MS *m/z*: 1,471 ($[M\text{–}PF_6^-]^+$). FT-IR ν_{CO}/cm^{-1}: 1,992, 2,058. Anal. calcd (%) for $C_{78}H_{54}Cl_2F_6IrN_6O_2PRu\cdot 3H_2O$: C, 56.08; N, 5.03; H, 3.62. Found (%): C, 55.88; N, 4.81; H, 3.21. ^{1}H NMR ($CDCl_3$, 400 MHz) δ 8.97–8.88 (m, 4H), 8.74 (brs, 1H), 8.65–8.62 (m, 3H), 8.42 (brs, 1H), 8.30 (brs, 1H), 8.25–8.21 (m, 2H), 8.18–8.15 (m, 2H), 8.03–8.01 (m, 2H), 7.96–7.79 (m, 8H), 7.61 (s, 1H), 7.56 (s, 1H), 7.53–7.49 (m, 2H), 7.45–7.40 (m, 4H), 7.36 (m, 1H), 7.28–7.24 (m, 1H), 7.09 (d, $J = 5.6$ Hz, 1H), 6.98–6.88 (m, 3H), 3.05–2.94 (m, 4H), 2.99 (s, 3H), 2.98 (s, 3H), 2.61 (s, 3H), 2.47 (s, 3H).

Photocatalytic CO_2 Reduction

DMA-TEOA (2 ml; 5:1 v/v) solutions containing a mixture of PS and CAT or the supramolecular **Ir(pyr)–Ru** complex and BI(OH)H were bubbled with CO_2 for 30 min. Photo-irradiations were carried out in 11-mL Pyrex tubes (i.d. = 8 mm) with light at $\lambda > 480$ nm using a 500-W high-pressure Hg lamp combined with a K_2CrO_4 solution filter (30% w/w, optical path length: 1 cm) using a merry-go-round apparatus. The reaction temperature was maintained at 25°C using an IWAKI constant-temperature system (CTS-134A). The gaseous reaction products (CO and H_2) were quantified with GC-TCD (GL Science GC323), and the product (formate) in the solutions was analyzed with a capillary electrophoresis system (Otuka Electronics Co.CAPI-3300I).

Computational Methods

DFT calculations were carried out using the Gaussian 09 package of programs (Frisch et al., 2009). Each structure was fully optimized using the B3LYP functional using the 6-31G(d,p) basis set for all atoms except Ir and the standard double-ζ type LANL2DZ basis set with the effective core potential of Hay–Wadt for Ir. The calculation was carried out by using the polarizable continuum model (PCM) with default parameter for DMA. The stationary points were verified using the vibrational analysis.

AUTHOR CONTRIBUTIONS

YK concieved the research and conducted experiments. OI directed the project and co-wrote the paper.

FUNDING

This work was supported by JST CREST (grant number JPMJCR13L1) and the Strategic International Collaborative Research Program (SICORP) of JST.

SUPPLEMENTARY MATERIAL

The Supplementary Material for this article can be found online at: https://www.frontiersin.org/articles/10.3389/fchem.2019.00259/full#supplementary-material

REFERENCES

Anderson, P. A., Deacon, G. B., Haarmann, K. H., Keene, F. R., Meyer, T. J., Reitsma, D. A., et al. (1995). Designed synthesis of mononuclear Tris(heteroleptic) ruthenium complexes containing bidentate polypyridyl ligands. *Inorg. Chem.* 34, 6145–6157. doi: 10.1021/ic00128a028

Bonin, J., Robert, M., and Routier, M. (2014). Selective and efficient photocatalytic CO_2 reduction to CO using visible light and an iron-based

homogeneous catalyst. *J. Am. Chem. Soc.* 136, 16768–16771. doi: 10.1021/ja510290t

Caspar, J. V., Westmoreland, T. D., Allen, G. H., Bradley, P. G., Meyer, T. J., and Woodruff, W. H. (1984). Molecular and electronic structure in the metal-to-ligand charge-transfer excited states of d6 transition-metal complexes in solution. *J. Am. Chem. Soc.* 106, 3492–3500. doi: 10.1021/ja00324a017

Chen, L., Guo, Z., Wei, X.-G., Gallenkamp, C., Bonin, J., Anxolabéhère-Mallart, E., et al. (2015). Molecular catalysis of the electrochemical and photochemical reduction of CO_2 with earth-abundant metal complexes. selective production of CO vs HCOOH by switching of the metal center. *J. Am. Chem. Soc.* 137, 10918–10921. doi: 10.1021/jacs.5b06535

Elgrishi, N., Chambers, M. B., Wang, X., and Fontecave, M. (2017). Molecular polypyridine-based metal complexes as catalysts for the reduction of CO_2. *Chem. Soc. Rev.* 46, 761–796. doi: 10.1039/C5CS00391A

Fan, S., Zong, X., Shaw, P. E., Wang, X., Geng, Y., Smith, A. R., et al. (2014). Energetic requirements of iridium(III) complex based photosensitisers in photocatalytic hydrogen generation. *Phys. Chem. Chem. Phys.* 16, 21577–21585. doi: 10.1039/C4CP02997F

Frisch, M. J., Trucks, G. W., Schlegel, H. B., Scuseria, G. E., Robb, M. A., Cheeseman, J. R., et al. (2009). *Gaussian 09, Revision D.01*. Wallingford, CT.

Goldsmith, J. I., Hudson, W. R., Lowry, M. S., Anderson, T. H., and Bernhard, S. (2005). Discovery and high-throughput screening of heteroleptic iridium complexes for photoinduced hydrogen production. *J. Am. Chem. Soc.* 127, 7502–7510. doi: 10.1021/ja0427101

Hasegawa, E., Seida, T., Chiba, N., Takahashi, T., and Ikeda, H. (2005). Contrastive photoreduction pathways of benzophenones governed by regiospecific deprotonation of imidazoline radical cations and additive effects. *J. Org. Chem.* 70, 9632–9635. doi: 10.1021/jo0514220

Hasegawa, E., Takizawa, S., Seida, T., Yamaguchi, A., Yamaguchi, N., Chiba, N., et al. (2006). Photoinduced electron-transfer systems consisting of electron-donating pyrenes or anthracenes and benzimidazolines for reductive transformation of carbonyl compounds. *Tetrahedron* 62, 6581–6588. doi: 10.1016/j.tet.2006.03.061

Kavarnos, G. J. (1993). *Fundamentals of Photoinduced Electron Transfer* (Weinheim: VCH).

Kumagai, H., Sahara, G., Maeda, K., Higashi, M., Abe, R., and Ishitani, O. (2017). Hybrid photocathode consisting of a $CuGaO_2$ p-type semiconductor and a Ru(II)–Re(I) supramolecular photocatalyst: non-biased visible-light-driven CO_2 reduction with water oxidation. *Chem. Sci.* 8, 4242–4249. doi: 10.1039/C7SC00940B

Kuramochi, Y., Fukaya, K., Yoshida, M., and Ishida, H. (2015). *trans*-(Cl)-[Ru(5,5′-diamide-2,2′-bipyridine)$(CO)_2Cl_2$]: synthesis, structure, and photocatalytic CO_2 reduction activity. *Chem. Eur. J.* 21, 10049–10060. doi: 10.1002/chem.201500782

Kuramochi, Y., and Ishitani, O. (2016). Iridium(III) 1-phenylisoquinoline complexes as a photosensitizer for photocatalytic CO_2 reduction: a mixed system with a Re(I) catalyst and a supramolecular photocatalyst. *Inorg. Chem.* 55, 5702–5709. doi: 10.1021/acs.inorgchem.6b00777

Kuramochi, Y., Ishitani, O., and Ishida, H. (2018a). Reaction mechanisms of catalytic photochemical CO_2 reduction using Re(I) and Ru(II) complexes. *Coord. Chem. Rev.* 373, 333–356. doi: 10.1016/j.ccr.2017.11.023

Kuramochi, Y., Itabashi, J., Toyama, M., and Ishida, H. (2018b). Photochemical CO2 reduction catalyzed by trans(Cl)-[Ru(2,2′-bipyridine)(CO)2Cl2] bearing two methyl groups at 4,4′-, 5,5′- or 6,6′-positions in the ligand. *ChemPhotoChem* 2, 314–322. doi: 10.1002/cptc.201700201

Kuramochi, Y., Kamiya, M., and Ishida, H. (2014). Photocatalytic CO_2 reduction in *N*,*N*-dimethylacetamide/water as an alternative solvent system. *Inorg. Chem.* 53, 3326–3332. doi: 10.1021/ic500050q

Kuriki, R., Matsunaga, H., Nakashima, T., Wada, K., Yamakata, A., Ishitani, O., et al. (2016). Nature-inspired, highly durable CO_2 reduction system consisting of a binuclear ruthenium(II) complex and an organic semiconductor using visible light. *J. Am. Chem. Soc.* 138, 5159–5170. doi: 10.1021/jacs.6b01997

Kuriki, R., Yamamoto, M., Higuchi, K., Yamamoto, Y., Akatsuka, M., Lu, D., et al. (2017). Robust binding between carbon nitride nanosheets and a binuclear ruthenium (II) complex enabling durable, selective CO_2 reduction under visible light in Aqueous solution. *Angew. Chem. Int. Ed.* 56, 4867–4871. doi: 10.1002/anie.201701627

Lehn, J.-M., and Ziessel, R. (1990). Photochemical reduction of carbon dioxide to formate catalyzed by 2,2t-bipyridine- or 1,10-phenanthroline-ruthenium(II) complexes. *J. Organomet. Chem.* 382, 157–173. doi: 10.1016/0022-328X(90)85224-M

Lowry, M. S., and Bernhard, S. (2006). Synthetically tailored excited states: phosphorescent, cyclometalated iridium(III) complexes and their applications. *Chem. Eur. J.* 12, 7970–7977. doi: 10.1002/chem.200600618

Mauzerall, D., and Westheimer, F. (1955). 1-benzyldihydronicotinamide—a model for reduced DPN. *J. Am. Chem. Soc.* 77, 2261–2264. doi: 10.1021/ja01613a070

Nakada, A., Koike, K., Nakashima, T., Morimoto, T., and Ishitani, O. (2015). Photocatalytic CO_2 reduction to formic acid using a Ru(II)–Re(I) supramolecular complex in an aqueous solution. *Inorg. Chem.* 54, 1800–1807. doi: 10.1021/ic502707t

Prier, C. K., Rankic, D. A., and MacMillan, D. W. C. (2013). Visible light photoredox catalysis with transition metal complexes: applications in organic synthesis. *Chem. Rev.* 113, 5322–5363. doi: 10.1021/cr300503r

Rao, H., Bonin, J., and Rober, M. (2018). Toward visible-light photochemical CO_2-to-CH_4 conversion in aqueous solutions using sensitized molecular catalysis. *J. Phys. Chem. C* 122, 13834–13839. doi: 10.1021/acs.jpcc.8b00950

Rao, H., Schmidt, L. C., Bonin, J., and Robert, M. (2017). Visible-light-driven methane formation from CO_2 with a molecular iron catalyst. *Nature* 548, 74–77. doi: 10.1038/nature23016

Sahara, G., Kumagai, H., Maeda, K., Kaeffer, N., Artero, V., Higashi, M., et al. (2016). Photoelectrochemical reduction of CO_2 coupled to water oxidation using a photocathode with a Ru(II)–Re(I) complex photocatalyst and a CoO_x/TaON photoanode. *J. Am. Chem. Soc.* 138, 14152–14158. doi: 10.1021/jacs.6b09212

Sato, S., Arai, T., Morikawa, T., Uemura, K., Suzuki, T. M., Tanaka, H., et al. (2011). Selective CO_2 conversion to formate conjugated with H_2O oxidation utilizing semiconductor/complex hybrid photocatalysts. *J. Am. Chem. Soc.* 133, 15240–15243. doi: 10.1021/ja204881d

Schultz, D. M., and Yoon, T. P. (2014). Solar synthesis: prospects in visible light photocatalysis. *Science* 343:1239176. doi: 10.1126/science.1239176

Sekizawa, K., Maeda, K., Domen, K., Koike, K., and Ishitani, O. (2013). Artificial Z-scheme constructed with a supramolecular metal complex and semiconductor for the photocatalytic reduction of CO_2. *J. Am. Chem. Soc.* 135, 4596–4599. doi: 10.1021/ja311541a

Shaw, M. H., Twilton, J., and MacMillan, D. W. (2016). Photoredox catalysis in organic chemistry. *J. Org. Chem.* 81, 6898–6926. doi: 10.1021/acs.joc.6b01449

Sun, L., Berglund, H., Davydov, R., Norrby, T., Hammarstroem, L., Korall, P., et al. (1997). Binuclear ruthenium–manganese complexes as simple artificial models for photosystem II in green plants. *J. Am. Chem. Soc.* 119, 6996–7004. doi: 10.1021/ja962511k

Takizawa, S., Kano, R., Ikuta, N., and Murata, S. (2018). An anionic iridium(III) complex as a visible-light absorbing photosensitizer. *Dalton Trans.* 47, 11041–11046. doi: 10.1039/C8DT02477D

Takizawa, S., Pérez-Bolívar, C., Anzenbacher, P. Jr., and Murata, S. (2012). Cationic iridium complexes coordinated with coumarin dyes – sensitizers for visible-light-driven hydrogen generation. *Eur. J. Inorg. Chem.* 2012, 3975–3979. doi: 10.1002/ejic.201200474

Takizawa, S., Shimada, K., Sato, Y., and Murata, S. (2014). Controlling the excited state and photosensitizing property of a 2-(2-Pyridyl)benzo[*b*]thiophene-based cationic iridium complex through simple chemical modification. *Inorg. Chem.* 53, 2983–2995. doi: 10.1021/ic402778x

Tamaki, Y., and Ishitani, O. (2017). Supramolecular photocatalysts for the reduction of CO_2. *ACS Catal.* 7, 3394–3409. doi: 10.1021/acscatal.7b00440

Tamaki, Y., Koike, K., and Ishitani, O. (2015). Highly efficient, selective, and durable photocatalytic system for CO_2 reduction to formic acid. *Chem. Sci.* 6, 7213–7221. doi: 10.1039/C5SC02018B

Tamaki, Y., Koike, K., Morimoto, T., and Ishitani, O. (2013). Substantial improvement in the efficiency and durability of a photocatalyst for carbon dioxide reduction using a benzoimidazole derivative as an electron donor. *J. Catal.* 304, 22–28. doi: 10.1016/j.jcat.2013.04.002

Thoi, V. S., Kornienko, N., Margarit, C. G., Yang, P., and Chang, C. J. (2013). Visible-light photoredox catalysis: selective reduction of carbon dioxide to carbon monoxide by a nickel N-heterocyclic carbene-isoquinoline complex. *J. Am. Chem. Soc.* 135, 14413–14424. doi: 10.1021/ja4074003

Yamazaki, Y., Takeda, H., and Ishitani, O. (2015). Photocatalytic reduction of CO_2 using metal complexes. *J. Photochem. Photobiol. C* 2015, 106–137. doi: 10.1016/j.jphotochemrev.2015.09.001

Zhu, X.-Q., Zhang, M.-T., Yu, A., Wang, C.-H., and Cheng, J.-P. (2008). Hydride, hydrogen atom, proton, and electron transfer driving forces of various five-membered heterocyclic organic hydrides and their reaction intermediates in acetonitrile. *J. Am. Chem. Soc.* 130, 2501–2516. doi: 10.1021/ja075523m

Conflict of Interest Statement: The authors declare that the research was conducted in the absence of any commercial or financial relationships that could be construed as a potential conflict of interest.

Copyright © 2019 Kuramochi and Ishitani. This is an open-access article distributed under the terms of the Creative Commons Attribution License (CC BY). The use, distribution or reproduction in other forums is permitted, provided the original author(s) and the copyright owner(s) are credited and that the original publication in this journal is cited, in accordance with accepted academic practice. No use, distribution or reproduction is permitted which does not comply with these terms.

frontiers in Chemistry

ORIGINAL RESEARCH
published: 14 May 2019
doi: 10.3389/fchem.2019.00327

Ruthenium Picolinate Complex as a Redox Photosensitizer With Wide-Band Absorption

*Yusuke Tamaki, Kazuma Tokuda, Yasuomi Yamazaki†, Daiki Saito, Yutaro Ueda and Osamu Ishitani**

Department of Chemistry, Tokyo Institute of Technology, Tokyo, Japan

Ruthenium(II) picolinate complex, $[Ru(dmb)_2(pic)]^+$ (**Ru(pic)**; dmb = 4,4′-dimethyl-2,2′-bipyridine; Hpic = picolinic acid) was newly synthesized as a potential redox photosensitizer with a wider wavelength range of visible-light absorption compared with $[Ru(N^\wedge N)_3]^{2+}$ (N^N = diimine ligand), which is the most widely used redox photosensitizer. Based on our investigation of its photophysical and electrochemical properties, **Ru(pic)** was found to display certain advantageous characteristics of wide-band absorption of visible light ($\lambda_{abs} < 670$ nm) and stronger reduction ability in a one-electron reduced state ($E^{red}_{1/2} = -1.86$ V vs. $Ag/AgNO_3$), which should function favorably in photon-absorption and electron transfer to the catalyst, respectively. Performing photocatalysis using **Ru(pic)** as a redox photosensitizer combined with a Re(I) catalyst reduced CO_2 to CO under red-light irradiation ($\lambda_{ex} > 600$ nm). TON_{CO} reached 235 and Φ_{CO} was 8.0%. Under these conditions, $[Ru(dmb)_3]^{2+}$ (**Ru(dmb)**) is not capable of working as a redox photosensitizer because it does not absorb light at $\lambda > 560$ nm. Even in irradiation conditions where both **Ru(pic)** and **Ru(dmb)** absorb light ($\lambda_{ex} > 500$ nm), using **Ru(pic)** demonstrated faster CO formation ($TOF_{CO} = 6.7$ min^{-1}) and larger TON_{CO} (2347) than **Ru(dmb)** ($TOF_{CO} = 3.6$ min^{-1}; $TON_{CO} = 2100$). These results indicate that **Ru(pic)** is a superior redox photosensitizer over a wider wavelength range of visible-light absorption.

Keywords: redox photosensitizer, CO_2 reduction, photocatalyst, Ruthenium(II) complex, wide-band absorption

OPEN ACCESS

Edited by:
Hitoshi Ishida, Kitasato University, Japan

Reviewed by:
Wee Han Ang, École Polytechnique Fédérale de Lausanne, Switzerland
Mahmut Özacar, Sakarya University, Turkey

***Correspondence:**
Osamu Ishitani
ishitani@chem.titech.ac.jp

†Present Address:
Department of Materials and Life Science, Seikei University, Tokyo, Japan

Specialty section:
This article was submitted to Inorganic Chemistry, a section of the journal Frontiers in Chemistry

Received: *30 January 2019*
Accepted: *24 April 2019*
Published: *14 May 2019*

Citation:
Tamaki Y, Tokuda K, Yamazaki Y, Saito D, Ueda Y and Ishitani O (2019) Ruthenium Picolinate Complex as a Redox Photosensitizer With Wide-Band Absorption. Front. Chem. 7:327. doi: 10.3389/fchem.2019.00327

INTRODUCTION

Redox photosensitizers, which absorb visible light and facilitate the electron transfer process, play a key role in various photochemical reactions, such as CO_2 reduction (Takeda et al., 2017; Tamaki and Ishitani, 2017), water oxidation (Fukuzumi et al., 2016), hydrogen evolution (Schulz et al., 2012), and organic synthesis (Prier et al., 2013). Effective photosensitizers should be endowed with three important properties, including (1) visible-light absorption, (2) a long lifetime in the excited state to initiate the electron transfer process, and (3) reducing and/or oxidizing power that is strong enough to donate electrons or holes to the catalyst. In particular, the utilization of visible-light over a wider range of wavelengths is important both to utilize sunlight efficiently and avoid the internal filter effect and side reactions that are commonly caused by the light-absorption of catalysts and/or electron donor/acceptor. Ru(II) complexes coordinated with three diimine ligands, $[Ru(N^\wedge N)_3]^{2+}$ (N^N = diimine ligand) are the most widely used redox photosensitizers in various photochemical

redox reactions because these types of complexes exhibit strong absorption in the visible-light region and have a long lifetime in their triplet metal-to-ligand charge-transfer (^{3}MLCT) excited states (Juris et al., 1988; Thompson et al., 2013).

However, one of the disadvantages of $[Ru(N^\wedge N)_3]^{2+}$-type photosensitizers is the limited access to the wavelength region of visible light, e.g., $\lambda_{abs} < 560$ nm in the cases of N^N = 2,2′-bipyridine (bpy) and 4,4′-dimethyl-2,2′-bipyridine (dmb), and these complexes cannot utilize visible light having lower energy ($\lambda > 560$ nm). To overcome this, ligand-modified Ru(II) photosensitizers have been reported. For example, Ru(II) complexes have an extended π-system for photodynamic therapy (Zhang et al., 2017) and multinuclear Ru(II) complexes by conjugated bridging ligand are used for hydrogen evolution (Tsuji et al., 2018). However, these modifications lower the reducing power of photosensitizers and limit the choice of catalyst especially for the reduction of CO_2. On the other hand, we have reported an osmium(II) analog, i.e., $[Os(N^\wedge N)_3]^{2+}$, which could function as a redox photosensitizer utilizing a much wider wavelength range of visible light ($\lambda_{abs} < 700$ nm) due to its singlet-to-triplet direct excitation (S-T absorption) and drive photocatalytic CO_2 reduction by red-light irradiation ($\lambda_{ex} > 620$ nm) in the combination with rhenium(I) catalyst unit (Tamaki et al., 2013b), whereas the high toxicity of $Os^{VIII}O_4$ inhibits the wider application of osmium complexes.

Therefore, we developed a novel ruthenium(II) redox photosensitizer that can utilize a wider wavelength range of visible light than $[Ru(N^\wedge N)_3]^{2+}$. In the photocatalytic system for CO_2 reduction, a photosensitizer mediates an electron from a sacrificial electron donor to a catalyst. Since the positive shift of the LUMO level of redox photosensitizer should limit the choice of a catalyst for reducing CO_2, for the expansion of the useable wavelength range, we try to decrease the energy-gap between HOMO and LUMO by the negative shift of the HOMO level, while maintaining the LUMO level. We introduced anionic electron-donating picolinate instead of a diimine ligand into a ruthenium complex (Norrby et al., 1997; Couchman et al., 1998). $[Ru(dmb)_2(pic)]^+$ (**Ru(pic)**; Hpic = picolinic acid) was synthesized, and we investigated its photophysical properties and functions as a redox photosensitizer using $[Ru(dmb)_3]^{2+}$ (**Ru(dmb)**) as a reference redox photosensitizer and $Re(dmb)(CO)_3Br$ (**Re**) as a catalyst for the reduction of CO_2 (Hawecker et al., 1983; Gholamkhass et al., 2005; Tamaki et al., 2016). **Chart 1** shows structures and abbreviations of the metal complexes used.

RESULTS AND DISCUSSION

Figure 1 displays UV-vis absorption spectra of **Ru(pic)**, **Ru(dmb)**, and **Re** measured in *N*,*N*-dimethylacetamide (DMA). **Ru(pic)** exhibited a broad singlet MLCT absorption band at $\lambda_{abs} = 450$–640 nm, with molar absorptivity at an absorption maximum ($\lambda_{max} = 498$ nm) of 1.04×10^4 $M^{-1}cm^{-1}$, which was red-shifted in wavelength compared to that of **Ru(dmb)** ($\lambda_{abs} = 420$–550 nm). The absorption band attributed to the π-π* transition of dmb ligands was observed at 294 nm. According to this result, **Ru(pic)** have the potential to utilize visible light over a wider range of wavelengths ($\lambda_{abs} < 670$ nm) than **Ru(dmb)** ($\lambda_{abs} < 560$ nm). This expected red-shift of the MLCT band should be induced by the stronger electron-donating ability of the picolinate ligand to negatively shift the energy level of HOMO.

Ru(pic) exhibited phosphorescence from its ^{3}MLCT excited state (**Figure 2**) with a quantum yield of $\Phi_{em} = 0.8\%$ and a lifetime of $\tau_{em} = 66$ ns. Emission spectrum of **Ru(pic)** ($\lambda_{em} = 734$ nm) was also red-shifted compared to that of **Ru(dmb)** ($\lambda_{em} = 638$ nm). The quantum yield and lifetime of **Ru(pic)** were smaller and shorter than those of **Ru(dmb)** ($\Phi_{em} = 9.1\%$, $\tau_{em} = 741$ ns) due to the 12-times faster non-radiative deactivation process (**Ru(pic)**: $k_{nr} = 1.5 \times 10^7$ s^{-1}; **Ru(dmb)**: $k_{nr} = 1.2 \times 10^6$ s^{-1}), which is a reasonable behavior from energy-gap law. **Table 1** summarizes photophysical properties of **Ru(pic)** along with those of **Ru(dmb)** and **Re**.

Figure 3 shows the cyclic voltammograms of **Ru(pic)** and **Ru(dmb)** and their redox potentials are summarized in **Table 2** along with that of **Re**. **Ru(pic)** displayed two reversible reduction waves and a reversible oxidation wave, which are attributable to the subsequent reduction of two dmb ligands and the oxidation couple of $Ru^{III/II}$, respectively. Both the first reduction ($E^{red}_{1/2} = -1.86$ V vs. $Ag/AgNO_3$) and oxidation ($E^{0x}_{1/2} = 0.41$ V) waves were observed at more negative potentials than those of **Ru(dmb)** ($E^{red}_{1/2} = -1.74$ V and $E^{0x}_{1/2} = 0.77$ V), which should be induced by the stronger electron-donating ability of the picolinate ligand. The stronger reducing power of one-electron reduced species

Chart 1 | Structures and abbreviations of complexes used.

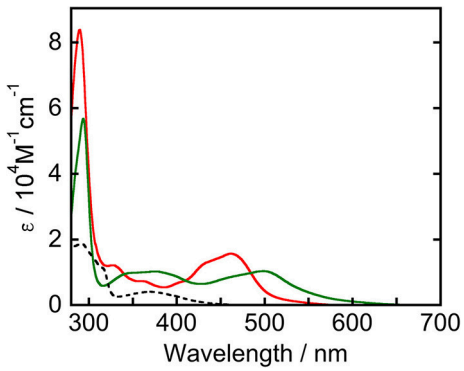

FIGURE 1 | UV-vis absorption spectra of **Ru(pic)** (green line), **Ru(dmb)** (red line), and **Re** (broken line) measured in a DMA solution.

(OERS) of **Ru(pic)** ($E^{red}_{1/2} = -1.86$ V) facilitates an increase in the number of choices of applicable catalyst because the electron transfer from OERS of **Ru(pic)** to a catalyst must occur during photocatalysis in the case of reductive quenching mechanisms. When using **Ru(pic)** as a photosensitizer and **Re** as a catalyst, the electron transfer process from OERS of **Ru(pic)** to **Re** ($E^{red}_{1/2} = -1.76$ V) occurs exothermically.

These results indicated that **Ru(pic)** had some advantages with respect to its function as a redox photosensitizer compared with **Ru(dmb)**, including its wider wavelength range of visible-light absorption and stronger reducing power of OERS, which is effective in the electron transfer to the catalyst. However, certain unfavorable properties were also observed, i.e., a shorter lifetime ($\tau_{em} = 66$ ns) and weaker oxidizing power in its excited state ($\Delta E = E(\mathbf{Ru(dmb)}^*/\mathbf{Ru(dmb)}^-)$–$E(\mathbf{Ru(pic)}^*/\mathbf{Ru(pic)}^-) = 0.28$–$(-0.11) = 0.39$ V). In the reductive quenching process, an excited photosensitizer accepts an electron from a sacrificial electron donor. Weaker oxidation power in the excited state of a photosensitizer should decrease the driving force of this electron transfer process. In addition, since this process competes with the radiative and non-radiative deactivation processes from the excited state of a photosensitizer by itself, the shorter lifetime results in less opportunity of the reductive quenching process to occur. To evaluate whether reductive quenching occurs, the emission intensity from **Ru(pic)** was compared in the presence of five different concentrations of a sacrificial electron donor, 1,3-dimethyl-2-phenyl-2,3-dihydro-1*H*-benzo[*d*]imidazole (BIH) (Tamaki et al., 2013a; Hasegawa et al., 2015) in DMA-triethanoamine (TEOA; 5:1 v/v). As shown in **Figure 4**, the emission intensities from the ^{3}MLCT excited state of **Ru(pic)** decreased at higher concentrations of BIH, which indicated that the excited **Ru(pic)** was quenched by BIH. The quenching rate constant was determined to be $k_q = 1.7 \times 10^8$ M^{-1}s^{-1} from the Stern-Volmer plot (**Figure S1**) and the lifetime of the emission ($\tau_{em} = 66$ ns), which was 8-times slower than that of **Ru(dmb)** ($k_q = 1.4 \times 10^9$ M^{-1}s^{-1}) as expected from the weaker oxidizing power in the ^{3}MLCT excited state of **Ru(pic)**. In the photocatalytic reaction condition, i.e., [BIH] = 0.2 M, 69% of the excited **Ru(pic)** was estimated to be quenched by BIH, which should be enough to initiate a photocatalytic reaction.

To clarify the produced species as a result of the quenching of excited **Ru(pic)** by BIH, UV-vis absorption spectral change was observed during photo-irradiation of **Ru(pic)** in the presence of BIH (**Figure 5**). Irradiation by light at $\lambda_{ex} = 480$ nm caused spectral changes and new absorption bands appeared at $\lambda_{abs} = 420$ and 547 nm. The shape of differential absorption spectra before and after irradiation (**Figure 5B**) were quite similar to that of OERS of **Ru(pic)** obtained by electrochemical spectroscopy (**Figure S2**). These results indicate that the reductive quenching

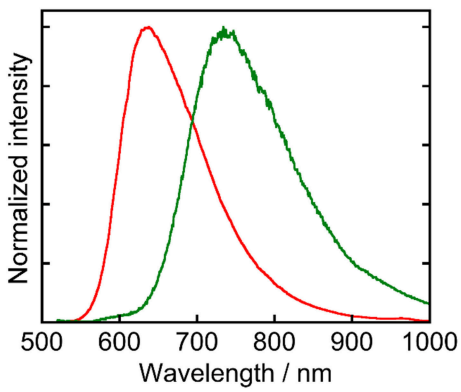

FIGURE 2 | Normalized emission spectra of **Ru(pic)** (green line) and **Ru(dmb)** (red line) measured in a DMA solution. The excitation wavelength was 480 nm.

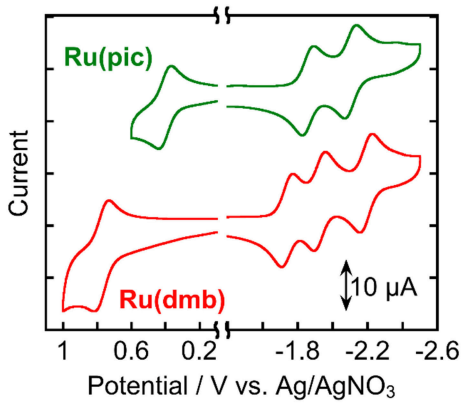

FIGURE 3 | Cyclic voltammograms of **Ru(pic)** and **Ru(dmb)** measured in a DMA solution containing Et_4NBF_4 (0.1 M) as a supporting electrolyte with a $Ag/AgNO_3$ (10 mM) reference electrode.

TABLE 1 | Photophysical properties of **Ru(pic)**, **Ru(dmb)**, and **Re**.[a].

Complex	λ_{abs}/nm (ε/10^{4}M^{-1}cm^{-1})		λ_{em}[b]/nm	Φ_{em}[b]	τ_{em}[c]/ns	k_r[d]/10^{5}s^{-1}	k_{nr}[e]/10^{6}s^{-1}	E_{00}[f]/eV
	π-π^*	^{1}MLCT						
Ru(pic)	294 (5.67)	498 (1.04)	734	0.008	66	1.2	15	1.75
Ru(dmb)	290 (8.38)	462 (1.57)	638	0.091	741	1.2	1.2	2.02
Re	292 (1.87)	370 (0.41)	–	–	–	–	–	–

[a]*Measured in DMA.* [b]*Excitation wavelength: 480 nm.* [c]*Excitation wavelength: 510 nm.* [d]*Rate constants for radiative deactivation calculated as* $k_r = \Phi_{em}/\tau_{em}$. [e]*Rate constants for non-radiative deactivation calculated as* $k_{nr} = (1-\Phi_{em})/\tau_{em}$. [f]*Energy for 0-0 transition obtained from Franck-Condon analyses of the emission spectra.*

TABLE 2 | Electrochemical properties of the metal complexes in DMA[a].

Complex	$E_{1/2}$/V vs. Ag/AgNO$_3$ (ΔE/mV)				$E(PS^+/PS^*)^b$ / V	$E(PS^*/PS^-)^b$ / V
	$Ru^{III/II}$	M(N^N/N^N·$^-$) (M = Ru or Re)				
Ru(pic)	+0.41 (72)	−1.86 (72)	−2.11 (69)	–	−1.34	−0.11
Ru(dmb)	+0.77 (68)	−1.74 (72)	−1.93 (70)	−2.19 (74)	−1.25	+0.28
Re	–	−1.76 (74)	–	–	–	–

[a]*Measured in a DMA solution containing the complex (0.5 mM) and Et_4NBF_4 (0.1 M) with a scan rate of 200 mV·s^{-1} under an Ar atmosphere.* [b]*Redox potentials of the photosensitizers (PS) in their excited states were calculated from $E^{0x}_{1/2}$-E_{00} and $E^{red}_{1/2} + E_{00}$, respectively.*

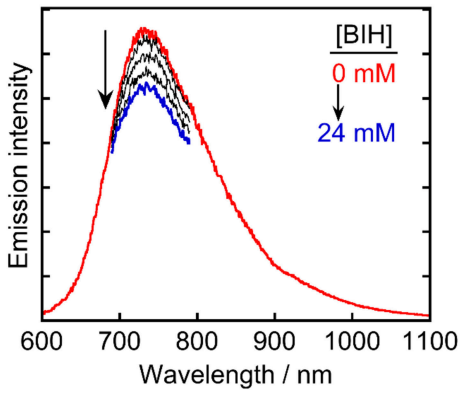

FIGURE 4 | Emission spectra of **Ru(pic)** in Ar-saturated DMA-TEOA (5:1 v/v) containing five different concentrations of BIH (0–24 mm).

of the ^{3}MLCT excited state of **Ru(pic)** by BIH proceeded successfully to give OERS of **Ru(pic)** (Equation 1) and **Ru(pic)** can be expected to function as a redox photosensitizer over the wide-range absorption of visible light.

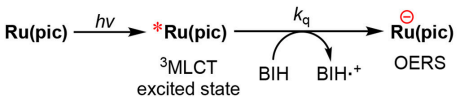

(1)

The results of photocatalytic reactions for the reduction of CO_2 are summarized in **Table 3**. In a typical run of photocatalytic reactions, a mixed solution of DMA-TEOA (5:1 v/v) containing **Ru(pic)** (50 μM), **Re** (50 μM), and BIH (0.2 M) as a sacrificial electron donor was irradiated under a CO_2 atmosphere using light at λ_{ex} > 620 nm. CO production proceeded linearly and selectively and the turnover number for CO production (TON_{CO}) was 235 after 36 h of irradiation (**Figure 6A**). The quantum yield for CO formation (Φ_{CO}) was determined to be Φ_{CO} = 8% using λ_{ex} = 600-nm light (light intensity: 6.0 × 10^{-9} einstein·s^{-1}). By contrast, when using **Ru(dmb)** as a redox photosensitizer instead of **Ru(pic)**, no photocatalysis proceeded (**Figure 6A**) because **Ru(dmb)** does not absorb lower-energy light at λ_{ex} > 620 nm (**Figure 1**). To compare the function as a redox photosensitizer, the photocatalytic reactions were also conducted under photo-irradiation condition, where both **Ru(pic)** and **Ru(dmb)** absorb incident light (λ_{ex} > 480 nm). In this condition, both systems photocatalytically produced CO with high selectivity. **Figure 6B** shows the time course of photocatalytic CO production using light at λ_{ex} > 500 nm, and the system using **Ru(pic)** formed CO faster (TOF_{CO} = 6.7 min^{-1}) than **Ru(dmb)** (TOF_{CO} = 3.6 min^{-1}) in the initial stage of photocatalysis. TON_{CO} reached 2347 and 2100 after 36 h of irradiation using **Ru(pic)** and **Ru(dmb)**, respectively. The values of Φ_{CO} using light at λ_{ex} = 480 nm (light intensity: 6.0 × 10^{-9} einstein·s^{-1}) were 10% and 44% in the cases using **Ru(pic)** and **Ru(dmb)**, respectively. The **Ru(pic)** system demonstrated similar Φ_{CO} values in both irradiation conditions (λ_{ex} = 600 and 480 nm). These results indicated that **Ru(pic)** has a clear advantage of a wider wavelength range of utilizable visible light compared to **Ru(dmb)**, even for the photocatalytic condition of λ_{ex} > 480 nm. Since **Ru(pic)** displays larger molar absorptivity in the λ_{abs} > 480-nm region and a wider wavelength range than **Ru(dmb)** (**Figure 1**), **Ru(pic)** absorbs a much larger number of photons at λ_{ex} > 480-nm, which leads to a faster TOF_{CO} and larger TON_{CO}, even though the quantum yields for CO production were lower.

The quantitative analyses of BIH and its oxidized compound during photocatalysis were conducted in the system using 0.1 M of BIH to simplify the HPLC analyses. As the only oxidized compound of BIH, two-electron oxidized and deprotonated BIH (BI^+) was observed (Equation 2).

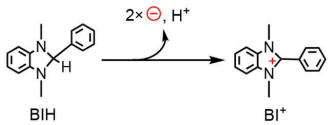

(2)

Figure 7 shows the change in the amounts of both BIH and BI^+ during photocatalytic reaction along with the amount of CO produced. The amount of produced BI^+ was fairly similar to that of CO. For example, after 20 h of irradiation, 205 μmol of BI^+ and 203 μmol of CO formed. CO is the two-electron reduced compound of CO_2, and BIH supplies two electrons per molecule to give BI^+ as a oxidized form. These results clearly indicate that BIH acted as a two-electron donor in the photocatalytic reactions using **Ru(pic)** as a redox photosensitizer (Equation 3).

$$CO_2 + BIH \xrightarrow[\text{DMA-TEOA}]{\textbf{Ru(pic)} + \textbf{Re} / hv} CO + BI^+ + [O^{2-}] + H^+ \quad (3)$$

The reaction mechanisms of the photocatalytic reactions using **Ru(pic)** and **Re** were investigated. Since **Re** does not absorb

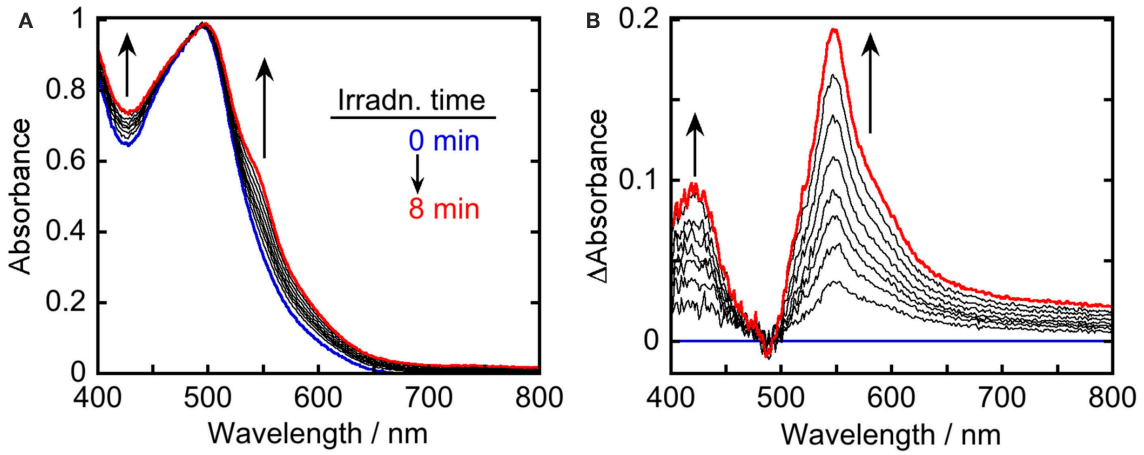

FIGURE 5 | UV-vis **(A)** absorption and **(B)** differential absorption spectral change of a DMA-TEOA (5:1 v/v, 4 mL) solution containing **Ru(pic)** (0.1 mM) and BIH (0.2 M) during irradiation using light at $\lambda_{ex} = 480$ nm (0–8 min at 1-min intervals). The incident light intensity was 5.0×10^{-9} einstein·s^{-1}. Blue and red lines represent spectra at 0 and 8-min irradiation, respectively.

TABLE 3 | Photocatalytic properties using the mixed system of the Ru(II) photosensitizer and **Re**[a].

Photosensitizer	Wavelength	TON[b]			Φ_{CO}[f]/%	k_q[i]	η_q[j]/%	Φ_{OERS}[k]/%
		CO	HCOOH	H_2		10^8 $M^{-1}s^{-1}$		
Ru(pic)	$\lambda_{ex} > 600$ nm	235[c]	4[c]	<1[c]	8.0[g]	1.7	69	–
Ru(dmb)		n.d.[c,e]	n.d.[c,e]	n.d.[c,e]	–	–	–	–
Ru(pic)	$\lambda_{ex} > 480$ nm	2347[d]	< 1[d]	< 1[d]	10[h]	1.7	69	8.3
Ru(dmb)		2100[d]	11[d]	< 1[d]	44[h]	14	99	66

[a]*A CO_2-saturated DMA-TEOA (5:1 v/v) mixed solution containing the photosensitizer (50 μM),* ***Re*** *(50 μM), and BIH (0.2 M) was irradiated.* [b]*Turnover number for the reaction products after 36 h of irradiation calculated as [product (mol)]/[added* ***Re*** *(mol)].* [c]*$\lambda_{ex} > 620$ nm.* [d]*$\lambda_{ex} > 500$ nm.* [e]*Irradiation for 12 h.* [f]*Quantum yield of CO production calculated as [CO (mol)]/[absorbed photon (einstein)].* [g]*$\lambda_{ex} = 600$ nm (light intensity: 6.0×10^{-9} einstein·s^{-1}).* [h]*$\lambda_{ex} = 480$ nm (light intensity: 6.0×10^{-9} einstein·s^{-1}).* [i]*Quenching rate constants for emission from Ru(II) photosensitizers by BIH obtained from the slopes of Stern-Volmer plots and lifetimes of excited states.* [j]*Quenching fractions of emission from Ru(II) photosensitizers by 0.2 M of BIH calculated as $0.2k_q\tau_{em}/(1 + 0.2k_q\tau_{em})$.* [k]*Quantum yield for one-electron reduction of the photosensitizer using light at $\lambda_{ex} = 480$ nm (light intensity: 5.0×10^{-9} einstein·s^{-1}).*

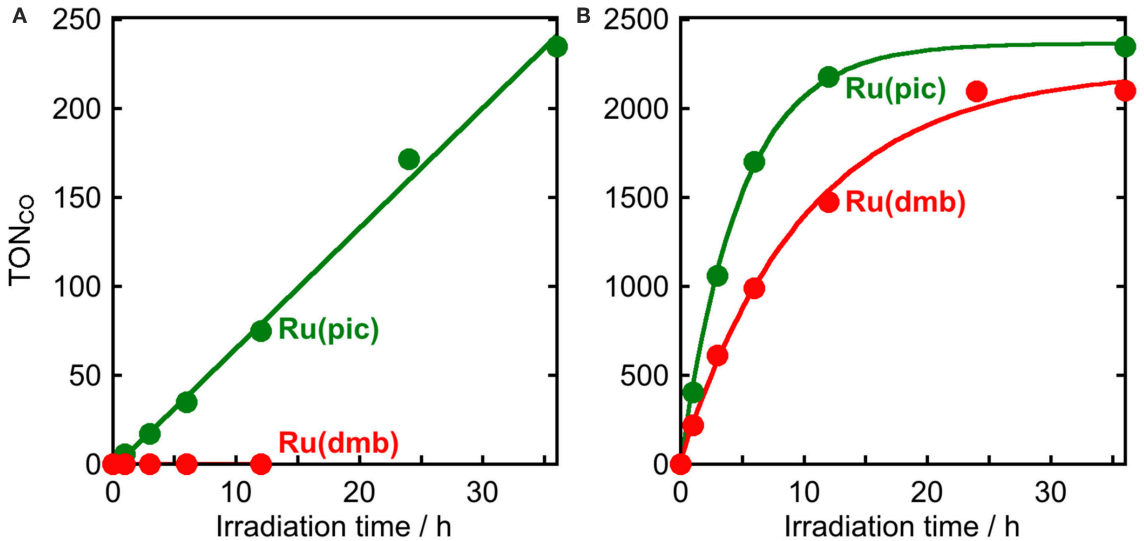

FIGURE 6 | Photocatalytic production of CO as a function of irradiation time using **Ru(pic)** (●) or **Ru(dmb)** (●) as a photosensitizer: CO_2-saturated DMA-TEOA (5:1 v/v, 2 mL) solutions containing Ru(II) photosensitizer (50 μM), **Re** (50 μM), and BIH (0.2 M) were irradiated at **(A)** $\lambda_{ex} > 620$ nm or **(B)** $\lambda_{ex} > 500$ nm.

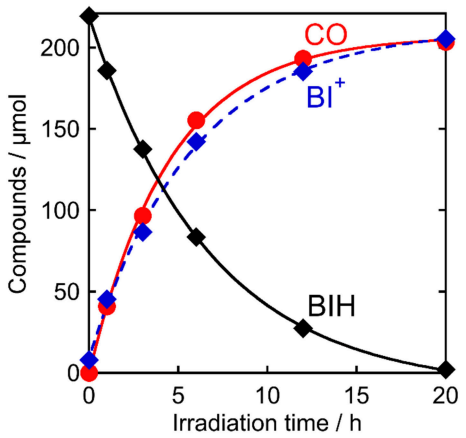

FIGURE 7 | Photocatalytic production of CO (●) and BI^+ (◆) and consumption of BIH (◆): CO_2-saturated DMA-TEOA (5:1 v/v) solutions containing **Ru(pic)** (50 μM), **Re** (50 μM), and BIH (0.1 M) were irradiated at λ_{ex} > 500 nm.

light at λ_{ex} > 460 nm, as shown in **Figure 1**, **Ru(pic)** should absorb the irradiated photon selectively under photocatalytic reaction conditions, i.e., λ_{ex} > 600 nm or > 480 nm. The photon absorption by **Ru(pic)** gives its OERS via the reductive quenching process of its ^{3}MLCT excited state by BIH, as described above (Equation 1). The reducing power of OERS of **Ru(pic)** ($E^{red}_{1/2}$ = −1.86 V) is strong enough to trigger electron transfer to **Re** ($E^{red}_{1/2}$ = −1.76 V), which functions as a catalyst for the reduction of CO_2. The process of two-electron supply using BIH has already been reported in the photocatalytic reaction system using a Ru(II)-Re(I) supramolecular photocatalyst (Tamaki et al., 2013a). The initial process of the photocatalysis is also a photoinduced electron transfer from BIH to the Ru(II) tris-diimine type photosensitizer unit, forming OERS of the photosensitizer unit and one-electron oxidized BIH ($BIH^{\bullet+}$). $BIH^{\bullet+}$ is rapidly deprotonated by TEOA to give BI•. TEOA functioned only as a base, but not as a sacrificial electron donor to quench the excited photosensitizer unit. BI• has a strong reducing power ($E^{red}_{1/2}$ = −1.95 V) (Zhu et al., 2008) enough to provide one more electron to the supramolecular photocatalyst to be converted to BI^+. In other words, BIH works as a two-electron donor by one-photon excitation of the photocatalyst via the ECE mechanism. Similar processes should also proceed in the photocatalytic system using **Ru(pic)** and **Re** because both **Ru(pic)** ($E^{red}_{1/2}$ = −1.86 V) and **Re** ($E^{red}_{1/2}$ = −1.76 V) have a lower reduction potential than BI• ($E^{red}_{1/2}$ = −1.95 V). Based on this investigation, the electron-supply processes of BIH are presumed, as depicted in Equation 4.

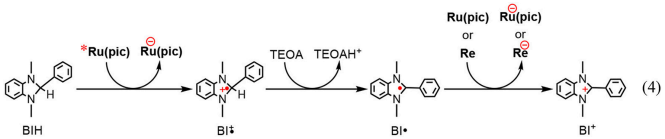

Photocatalysis using **Ru(pic)** displayed an advantages of a wider wavelength region of visible-light absorption, which achieved both red-light driven CO_2 reduction (λ_{ex} > 620 nm) and faster CO production than the system using **Ru(dmb)** (λ_{ex} > 500 nm), whereas the quantum yield for CO formation using **Ru(pic)** (Φ_{CO} = 10%) was 1/4 the value when **Ru(dmb)** (Φ_{CO} = 44%) was used. The main reason for smaller Φ_{CO} should be the smaller quantum yield of one-electron reduction (Φ_{OERS}) of **Ru(pic)**. Φ_{OERS} of **Ru(pic)** using light at λ_{ex} = 480 nm (light intensity: 5.0 × 10^{-9} einstein·s^{-1}) was determined to be 8.3%, which was 1/8 that of **Ru(dmb)** (Φ_{OERS} = 66%). The elementary processes of one-electron reduction of **Ru(pic)** is displayed in **Scheme 1**. The reductive quenching of the ^{3}MLCT excited state of **Ru(pic)** by BIH gives an ion pair, [**Ru(pic)**$^-$···$BIH^{\bullet+}$]. If the ion pair dissociate, free OERS and $BIH^{\bullet+}$ are obtained. The charge-recombination processes from the ion pair or by the re-collision of OERS of **Ru(pic)** and $BIH^{\bullet+}$ should form **Ru(pic)** and BIH. The differences in properties between **Ru(pic)** and **Ru(dmb)**, i.e., the cationic valence and the reducing power of OERS, should affect each elementary process and consequently the quantum yield for one-electron reduction. Since OERS of **Ru(dmb)** is a monovalent cation, the ion pair with $BIH^{\bullet+}$ involves cationic repulsion, which should accelerate the dissociation process. On the other hand, OERS of **Ru(pic)** is zero-valent, which provides no repulsion between $BIH^{\bullet+}$, and therefore, the dissociation process should become slower when using **Ru(pic)** (smaller k_{esc}). In addition, since the reducing power of OERS of **Ru(pic)** ($E^{red}_{1/2}$ = −1.86 V) is stronger than that of **Ru(dmb)** ($E^{red}_{1/2}$ = −1.74 V), the driving forces for the charge-recombination processes become larger when **Ru(pic)** is used (larger k_{rec1}, k_{rec2}). Consequently, the smaller Φ_{OERS} using **Ru(pic)** should be induced by the slower dissociation process of the ion pair and the faster charge-recombination processes. The quantitative analyses of the factors controlling Φ_{OERS} of photosensitizing complexes are in progress and will be reported elsewhere.

In the photocatalytic reaction conditions, the electron-consuming process for CO_2 reduction via the electron transfer to **Re** (the broken box in Scheme 1) will compete against the charge-recombination by the re-collision of OERS and $BIH^{\bullet+}$. Therefore, since Φ_{OERS}s were determined in the absence of **Re**, Φ_{CO} (10%) was larger than the expected value from half of Φ_{OERS} (8.3/2 = 4.2%), which was derived from the fact that the reduction of CO_2 to CO is a two-electron reduction process. Higher reduction potential of **Ru(pic)** should operate in favor of the electron transfer to **Re**. Therefore, the ratio of quantum yields for CO_2 reduction between using **Ru(pic)** and **Ru(dmb)**, i.e., Φ_{CO}(**Ru(pic)**)/Φ_{CO}(**Ru(dmb)**) = 10/44 = 0.23, became larger than that for one-electron reduction (Φ_{OERS}(**Ru(pic)**)/Φ_{OERS}(**Ru(dmb)**) = 8.3/66 = 0.13). In other words, **Ru(pic)** has another advantage of faster electron transfer to **Re** in the photocatalysis.

EXPERIMENTS

General Procedures

^{1}H NMR spectra were measured using a JEOL ECA400II (400 MHz) system in solutions of acetone-d_6. The residual

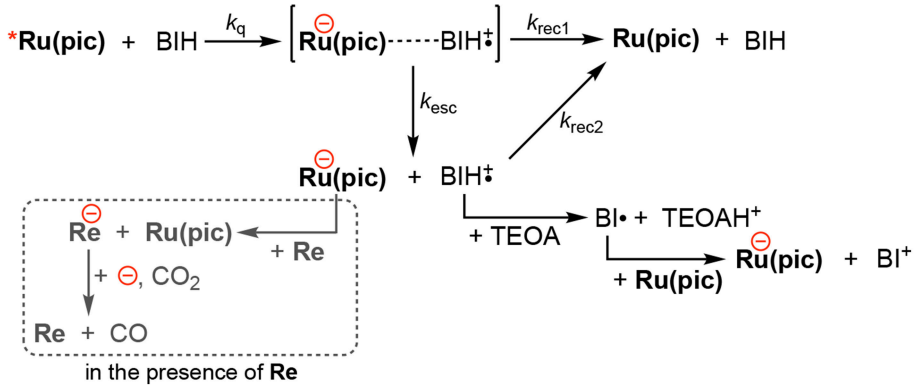

SCHEME 1 | The one-electron reduction processes of **Ru(pic)**.

protons of acetone-d_6 were used as an internal standard for measurements. Electrospray ionization-mass spectroscopy (ESI-MS) was performed using a Shimadzu LCMS-2010A system with acetonitrile as the mobile phase. UV-vis absorption spectra were measured with a JASCO V-565 spectrophotometer. Emission spectra were measured using a Horiba Fluorolog-3-21 spectrofluorometer equipped with a NIR-PMT R5509-43 near infrared detector. A Horiba FluoroCube time-correlated single-photon counting system was used to obtain emission lifetimes. The excitation light source was a NanoLED-515L pulse lamp (510 nm). A HAMAMATSU absolute PL quantum yield spectrometer C9920-02 was used to determine emission quantum yields. The samples were degassed by Ar-bubbling of solutions for 30 min prior to measuring emissions. Emission quenching experiments were performed on solutions containing the complexes and five different concentrations of BIH. The quenching rate constants k_q were calculated from linear Stern-Volmer plots for the emission from the ^{3}MLCT excited state of the photosensitizing complexes and their lifetimes. The redox potentials of the complexes were measured in an Ar-saturated DMA solution containing Et_4NBF_4 (0.1 M) as a supporting electrolyte using cyclic voltammetric techniques performed with an ALS CHI-720Dx electrochemical analyzer with a glassy carbon disk working electrode (3 mm diameter), a $Ag/AgNO_3$ (10 mM) reference electrode, and a Pt counter electrode. The supporting electrolyte was dried under vacuum at 100°C for 1 day prior to use. The scan rate was 200 $mV \cdot s^{-1}$.

Photocatalytic Reactions

Photocatalytic reactions were performed in DMA–TEOA (5:1 v/v) solutions containing the photosensitizer (50 μM), **Re** (50 μM), and BIH (0.2 M). After the solution was purged with CO_2 for 20 min, the solution was irradiated. For TON measurements, the mixed solution (2 mL) in an 11 mL test tube (i.d. 8 mm) was irradiated in a merry-go-round apparatus using $\lambda_{ex} > 620$ nm light from a halogen lamp equipped with a Rhodamin B (0.2% w/v, $d = 1$ cm) solution filter or $\lambda_{ex} > 500$ nm light from a high-pressure Hg lamp equipped with a uranyl glass and a K_2CrO_4 (30% w/w, $d = 1$ cm) solution filter. During irradiation, the temperature of the solution was maintained at 25°C using an EYELA CTP-1000 constant-temperature system. For quantum yield measurements, the mixed solution in a quartz cubic cell (11 mL, light pass length: 1 cm) was irradiated in a Shimadzu photoreaction quantum yield evaluation system QYM-01 using 600 nm or 480 nm light from a 300 W Xe lamp equipped with a 600 nm or 480 nm (FWHM: 10 nm) bandpass filters. The temperature of the solution was controlled during irradiation at 25 ± 0.1°C using an IWAKI CTS-134A constant-temperature system. The gaseous products of photocatalysis, i.e., CO and H_2, were analyzed by GC-TCD (GL science GC323). A capillary electrophoresis system (Agilent 7100) was used to analyze HCOOH. HPLC analyses for BIH and BI^+ were conducted using a JASCO 880-PU pump, a Develosil ODS-UG-5 column (250 × 4.6 mm), a JASCO 880–51 degasser, and a JASCO UV-2070 detector. The column temperature was maintained at 30°C using a JASCO 860-CO oven. The mobile phase was a 6:4 (v/v) mixture of acetonitrile and a NaOH–KH_2PO_4 buffer solution (50 mM, pH 7) with a flow rate of 0.5 $mL \cdot min^{-1}$.

Electrochemical Spectroscopy

Electrochemical spectroscopy to determine the molar absorptivity of OERS was performed using a JASCO PU-980 pump and an EC Frontier flow-type electrolysis cell VF-2 equipped with a carbon felt working electrode (18 mm diameter), a $Ag/AgNO_3$ (10 mM) reference electrode, and a Pt wire counter electrode in an Ar-saturated acetonitrile solution of **Ru(pic)** (0.5 mM) and Et_4NBF_4 (0.1 M) as a supporting electrolyte. Applied potential was controlled using an ALS CHI-720Dx electrochemical analyzer and UV-vis absorption spectra were measured using a Photal MCPD-9800 spectrometer (Otsuka Electronics) and a flow-type transmission cell (light pass length: 1.5 mm) (Ishitani et al., 1994).

Quantum Yields for One-Electron Reduction of Photosensitizers

A 4-mL DMA–TEOA (5:1 v/v) solution of the photosesnsitizer (0.1 mM) and BIH (0.2 M) in a quartz cubic cell (light pass

length: 1 cm) was purged with Ar for 20 min, and then irradiated with the 500-W Xe lamp combined with a 480-nm (FWHM = 10 nm) bandpass filter (Asahi Spectra Co.), ND filter, and a 5-cm-long H_2O solution filter. UV–vis absorption spectral changes during irradiation were measured using a Photal MCPD-9800 spectrometer (Otsuka Electronics). The light intensity was determined as 5.0×10^{-9} einstein·s^{-1} using a $K_3Fe(C_2O_4)_3$ actinometer.(Hatchard and Parker, 1956) The amount of OERS of **Ru(pic)** was calculated using the molar absorption coefficient of OERS (500–700 nm) obtained by electrochemical spectroscopy.

MATERIALS

DMA was dried over molecular sieves 4A, distilled under reduced pressure (∼10 mmHg) and used in a week. TEOA was distilled under reduced pressure (<1 mmHg) and used in a month. Both solvents were kept under Ar in the dark. All other reagents were of reagent-grade quality and used without further purification.

Synthesis

Ru(dmb) (Sullivan et al., 1978), **Re** (Morimoto et al., 2013), and BIH (Hasegawa et al., 2005; Zhu et al., 2008) were prepared according to the methods reported in the literatures. **Ru(pic)** was synthesized using a method similar to the synthesis of $[Ru(bpy)_2(pic)](PF_6)$ (bpy = 2,2′-bipyridine) (Norrby et al., 1997; Couchman et al., 1998), except for using dmb instead of bpy. $[Ru(dmb)_2(pic)](PF_6)$ (**Ru(pic)**): ^{1}H NMR (acetone-d_6) δ/ppm: 8.81 (d, J = 5.6 Hz, 1H), 8.65 (s, 1H), 8.63 (s, 1H) 8.60 (s, 1H), 8.55 (s, 1H), 8.14 (dd, J = 5.6, 0.8 Hz, 1H), 8.03 (dd, J = 6.4, 2.4 Hz, 1H), 7.94 (d, J = 5.6 Hz, 1H), 7.91 (d, J = 5.6 Hz, 1H), 7.77 (d, J = 5.6 Hz, 1H), 7.70 (dd, J = 5.6, 0.8 Hz, 1H), 7.64 (d, J = 5.6 Hz, 1H), 7.50 (dd, J = 6.4, 2.4 Hz, 1H), 7.43 (dd, J = 5.6, 1.2 Hz, 1H), 7.26 (dd, J = 5.6, 1.2 Hz, 1H), 7.21 (dd, J = 5.6, 1.2 Hz, 1H), 2.67 (s, 3H), 2.58 (s, 3H), 2.55 (s, 3H), 2.49 (s, 3H). ESI-MS (in acetonitrile) m/z: 592 ($[M–PF_6^-]^+$). Anal. calcd for $C_{30}H_{28}F_6N_5O_2PRu·H_2O$: C, 47.75; H, 4.01; N, 9.28. Found: C, 47.72; H, 3.75; N, 9.40.

CONCLUSION

Ruthenium(II) picolinate complex, **Ru(pic)**, successfully functioned as a redox photosensitizer with a much wider wavelength range of visible-light absorption (λ_{abs} < 670 nm) compared with a fairly typical **Ru(dmb)** (λ_{abs} < 560 nm). The system using **Ru(pic)** as a photosensitizer and **Re** as a catalyst photocatalyzed the reduction of CO_2 to CO by red-light irradiation (λ_{ex} > 620 nm). TON_{CO} reached 235 and Φ_{CO} was 8.0%. Even in the irradiation conditions where **Ru(dmb)** also absorbed light, i.e., λ_{ex} > 500 nm, the system using **Ru(pic)** demonstrated faster CO formation (TOF_{CO} = 6.7 min^{-1}) and larger TON_{CO} (2347) than that using **Ru(dmb)** (TOF_{CO} = 3.6 min^{-1}, TON_{CO} = 2100).

AUTHOR CONTRIBUTIONS

KT, DS, YY, and YT performed all experiments. YU and OI designed this project. YT wrote the manuscript.

FUNDING

This work was supported by JSPS KAKENHI Grant Numbers JP17H06440 in Scientific Research on Innovative Areas Innovations for Light-Energy Conversion (I4LEC), JP18K14238, JP17K14526.

SUPPLEMENTARY MATERIAL

The Supplementary Material for this article can be found online at: https://www.frontiersin.org/articles/10.3389/fchem.2019.00327/full#supplementary-material

REFERENCES

Couchman, S. M., Dominguez-Vera, J. M., Jeffery, J. C., McKee, C. A., Nevitt, S., Pohlman, M., et al. (1998). Structures, electrochemical and spectroscopic properties of ternary ruthenium(II)-polypyridyl complexes with additional carboxylate, biguanide or sulfonamide donors. *Polyhedron* 17, 3541–3550. doi: 10.1016/S0277-5387(98)00145-4

Fukuzumi, S., Jung, J., Yamada, Y., Kojima, T., and Nam, W. (2016). Homogeneous and heterogeneous photocatalytic water oxidation by persulfate. *Chemist. Asian J.* 11, 1138–1150. doi: 10.1002/asia.201501329

Gholamkhass, B., Mametsuka, H., Koike, K., Tanabe, T., Furue, M., and Ishitani, O. (2005). Architecture of supramolecular metal complexes for photocatalytic co2 reduction: ruthenium-rhenium bi- and tetranuclear complexes. *Inorg. Chem.* 44, 2326–2336. doi: 10.1021/ic048779r

Hasegawa, E., Ohta, T., Tsuji, S., Mori, K., Uchida, K., Miura, T., et al. (2015). Aryl-substituted dimethylbenzimidazolines as effective reductants of photoinduced electron transfer reactions. *Tetrahedron* 71, 5494–5505. doi: 10.1016/j.tet.2015.06.071

Hasegawa, E., Seida, T., Chiba, N., Takahashi, T., and Ikeda, H. (2005). Contrastive photoreduction pathways of benzophenones governed by regiospecific deprotonation of imidazoline radical cations and additive effects. *J. Org. Chem.* 70, 9632–9635. doi: 10.1021/jo0514220

Hatchard, C. G., and Parker, C. A. (1956). A new sensitive chemical actinometer. II. Potassium ferrioxalate as a standard chemical actinometer. *Proc. R. Soc. London Ser. A. Mathemat. Phys. Sci.* 235, 518–536. doi: 10.1098/rspa.1956.0102

Hawecker, J., Lehn, J.-M., and Ziessel, R. (1983). Efficient photochemical reduction of CO2 to CO by visible light irradiation of systems containing Re(bipy)(CO)3X or Ru(bipy)32+ -Co2+ combinations as homogeneous catalysts. *J.Chem. Soc. Chem. Commun.* 9, 536–538. doi: 10.1039/c39830000536

Ishitani, O., George, M. W., Ibusuki, T., Johnson, F. P. A., Koike, K., Nozaki, K., et al. (1994). Photophysical behavior of a new co2 reduction catalyst, Re(CO)2(bpy){P(OEt)3}2+. *Inorg. Chem.* 33, 4712–4717.

Juris, A., Balzani, V., Barigelletti, F., Campagna, S., Belser, P., and von Zelewsky, A. (1988). Ru(II) polypyridine complexes: photophysics, photochemistry, eletrochemistry, and chemiluminescence. *Coord. Chem. Rev.* 84, 85–277. doi: 10.1016/0010-8545(88)80032-8

Morimoto, T., Nakajima, T., Sawa, S., Nakanishi, R., Imori, D., and Ishitani, O. (2013). CO2 Capture by a rhenium(I) complex with the aid of triethanolamine. *J. Am. Chem. Soc.* 135, 16825–16828. doi: 10.1021/ja409271s

Norrby, T., Börje, A., Åkermark, B., Hammarström, L., Alsins, J., Lashgari, K., et al. (1997). Synthesis, structure, and photophysical properties of novel ruthenium(II) carboxypyridine type complexes. *Inorg. Chem.* 36, 5850–5858. doi: 10.1021/ic9705812

Prier, C. K., Rankic, D. A., and MacMillan, D. W. (2013). Visible light photoredox catalysis with transition metal complexes: applications in organic synthesis. *Chem. Rev.* 113, 5322–5363. doi: 10.1021/cr300503r

Schulz, M., Karnahl, M., Schwalbe, M., and Vos, J. G. (2012). The role of the bridging ligand in photocatalytic supramolecular assemblies for the reduction of protons and carbon dioxide. *Coordination Chemis. Rev.* 256, 1682–1705. doi: 10.1016/j.ccr.2012.02.016

Sullivan, B. P., Salmon, D. J., and Meyer, T. J. (1978). Mixed phosphine 2,2'-bipyridine complexes of ruthenium. *Inorg. Chem.* 17, 3334–3341. doi: 10.1021/ic50190a006

Takeda, H., Cometto, C., Ishitani, O., and Robert, M. (2017). Electrons, photons, protons and earth-abundant metal complexes for molecular catalysis of CO2 reduction. *ACS Catal.* 7, 70–88. doi: 10.1021/acscatal.6b02181

Tamaki, Y., Imori, D., Morimoto, T., Koike, K., and Ishitani, O. (2016). High catalytic abilities of binuclear rhenium(i) complexes in the photochemical reduction of CO2 with a ruthenium(ii) photosensitiser. *Dalton Trans.* 45, 14668–14677. doi: 10.1039/C6DT00996D

Tamaki, Y., and Ishitani, O. (2017). Supramolecular photocatalysts for the reduction of CO2. *ACS Catal.* 7, 3394–3409. doi: 10.1021/acscatal.7b00440

Tamaki, Y., Koike, K., Morimoto, T., and Ishitani, O. (2013a). Substantial improvement in the efficiency and durability of a photocatalyst for carbon dioxide reduction using a benzoimidazole derivative as an electron donor. *J. Catal.* 304, 22–28. doi: 10.1016/j.jcat.2013.04.002

Tamaki, Y., Koike, K., Morimoto, T., Yamazaki, Y., and Ishitani, O. (2013b). Red-light-driven photocatalytic reduction of CO2 using Os(II)–Re(I) supramolecular complexes. *Inorg. Chem.* 52, 11902–11909. doi: 10.1021/ic4015543

Thompson, D. W., Ito, A., and Meyer, T. J. (2013). [Ru(bpy)3]2+* and other remarkable metal-to-ligand charge transfer (MLCT) excited states. *Pure Applied Chemis.* 85, 1257–1305. doi: 10.1351/pac-con-13-03-04

Tsuji, Y., Yamamoto, K., Yamauchi, K., and Sakai, K. (2018). Near-infrared light-driven hydrogen evolution from water using a polypyridyl triruthenium photosensitizer. *Angew. Chem. Internat. Ed.* 57, 208–212. doi: 10.1002/anie.201708996

Zhang, Y., Zhou, Q., Tian, N., Li, C., and Wang, X. (2017). Ru(II)-Complex-based DNA photocleaver having intense absorption in the phototherapeutic window. *Inorg. Chem.* 56, 1865–1873. doi: 10.1021/acs.inorgchem.6b02459

Zhu, X. Q., Zhang, M. T., Yu, A., Wang, C. H., and Cheng, J. P. (2008). Hydride, hydrogen atom, proton, and electron transfer driving forces of various five-membered heterocyclic organic hydrides and their reaction intermediates in acetonitrile. *J. Am. Chem. Soc.* 130, 2501–2516. doi: 10.1021/ja075523m

Conflict of Interest Statement: The authors declare that the research was conducted in the absence of any commercial or financial relationships that could be construed as a potential conflict of interest.

Copyright © 2019 Tamaki, Tokuda, Yamazaki, Saito, Ueda and Ishitani. This is an open-access article distributed under the terms of the Creative Commons Attribution License (CC BY). The use, distribution or reproduction in other forums is permitted, provided the original author(s) and the copyright owner(s) are credited and that the original publication in this journal is cited, in accordance with accepted academic practice. No use, distribution or reproduction is permitted which does not comply with these terms.

frontiers in Chemistry

ORIGINAL RESEARCH
published: 21 May 2019
doi: 10.3389/fchem.2019.00330

Synthesis of a Redox-Active NNP-Type Pincer Ligand and Its Application to Electrocatalytic CO_2 Reduction With First-Row Transition Metal Complexes

*Kallol Talukdar, Asala Issa and Jonah W. Jurss**

Department of Chemistry and Biochemistry, University of Mississippi, University, MS, United States

We report the synthesis of a rigid phosphine-substituted, redox-active pincer ligand and its application to electrocatalytic CO_2 reduction with first-row transition metal complexes. The tridentate ligand was prepared by Stille coupling of 2,8-dibromoquinoline and 2-(tributylstannyl)pyridine, followed by a palladium-catalyzed cross-coupling with $HPPh_2$. Complexes were synthesized from a variety of metal precursors and characterized by NMR, high-resolution mass spectrometry, elemental analysis, and cyclic voltammetry. Formation of bis-chelated metal complexes, rather than mono-chelated complexes, was favored in all synthetic conditions explored. The complexes were assessed for their ability to mediate electrocatalytic CO_2 reduction, where the cobalt complex was found to have the best activity for CO_2-to-CO conversion in the presence of water as an added proton source.

Keywords: molecular catalyst, CO_2 reduction, electrocatalysis, pincer ligand, first-row metals

OPEN ACCESS

Edited by:
Hitoshi Ishida,
Kitasato University, Japan

Reviewed by:
Karthik Ramasamy,
Los Alamos National Laboratory (DOE), United States
Andrew Nattestad,
University of Wollongong, Australia

***Correspondence:**
Jonah W. Jurss
jwjurss@olemiss.edu

Specialty section:
This article was submitted to Inorganic Chemistry, a section of the journal Frontiers in Chemistry

Received: *30 January 2019*
Accepted: *24 April 2019*
Published: *21 May 2019*

Citation:
Talukdar K, Issa A and Jurss JW (2019) Synthesis of a Redox-Active NNP-Type Pincer Ligand and Its Application to Electrocatalytic CO_2 Reduction With First-Row Transition Metal Complexes Front. Chem. 7:330. doi: 10.3389/fchem.2019.00330

INTRODUCTION

Carbon dioxide (CO_2) is a greenhouse gas which is produced in large quantities from fossil fuel combustion. From the Industrial Revolution forward, anthropogenic CO_2 emissions have increased at an alarming rate, along with associated concerns including climate change, rising sea levels, and ocean acidification (Hansen et al., 2008; Jiang and Guan, 2016; Blunden and Arndt, 2017). These environmental issues can be mitigated by effective technologies capable of converting CO_2 into sustainable fuels (Lim et al., 2014). In this context, electrocatalytic CO_2 reduction to generate carbon-neutral fuels and value-added commodity chemicals is a promising strategy that allows CO_2 to serve as a cheap and abundant C_1 feedstock.

However, reducing CO_2 is an energetically uphill process, and more efficient and selective catalysts are needed to facilitate its conversion. Many homogeneous metal complexes have been developed for CO_2 reduction, but these systems often rely on precious metals and/or are limited to privileged supporting ligands such as tetraazamacrocycles and bipyridines (Qiao et al., 2013; Francke et al., 2018). Tridentate "pincer" ligands represent an underexplored class of ligands, which are of particular interest given their strong chelate effect, preorganized geometry, high tunability, and potential for ligand-based redox activity (van der Vlugt and Reek, 2009; Younus et al., 2014; Peris and Crabtree, 2018). Indeed, Earth-abundant first-row transition metals supported by well-designed pincer ligands have been successfully employed in a variety of catalytic applications

(Benito-Garagorri and Kirchner, 2008; van der Vlugt and Reek, 2009; van der Vlugt, 2012; Chakraborty et al., 2015; Bauer and Hu, 2016). Yet, only a limited number of pincer complexes have been reported for electrocatalytic CO_2 reduction (Arana et al., 1992; Chiericato et al., 2000; Elgrishi et al., 2014, 2015; Sheng et al., 2015; Rao et al., 2016; Cope et al., 2017; Liu et al., 2018; Therrien et al., 2018; Myren et al., 2019). Early examples from Arana et al. (1992) and Chiericato et al. (2000) were reported with redox-active terpyridine and bis(imino)pyridine-based ligands (**Figure 1**). The metal ions decorated with these NNN-type ligands showed catalytic activity under reducing potentials in CO_2-saturated solutions. Detailed product analysis was not reported, but formic acid was a notable reduced carbon product obtained with a cobalt bis(imino)pyridine complex. Recently, Liu et al. (2018) prepared a related pincer ligand, based in part on bis(imino)pyridine, in which steric bulk was added and one arm was replaced with pyridine to access a bipyridyl unit, producing a cobalt catalyst that is selective for CO_2 reduction to formate. Rao et al. (2016) reported a PNP-ligated manganese-tricarbonyl complex which can reduce CO_2 to CO without any added Brønsted acid. Mixed-donor *N*-heterocyclic carbene-based pincer ligands have also proven to be effective supporting frameworks for transition metal catalysts for CO_2 conversion (Sheng et al., 2015; Cope et al., 2017; Therrien et al., 2018; Myren et al., 2019).

Given these results, we sought to design a new redox-active mixed-donor ligand with extended conjugation for CO_2 reduction employing first-row transition metals. The ligand design aims to exploit the well-established redox activity of bipyridine at a lower overpotential by extending its conjugation. In addition, the triphenylphosphine donor fragment serves as a good π-acceptor to facilitate metal-based reductions at lower potentials. We note that closely-related NNP ligands have been recently reported (Basu et al., 2018; Kamitani et al., 2018) and applied to the synthesis of new Fe and Co complexes for catalytic hydrosilylation and dehydrogenative silylation. Herein, first-row metal complexes of a rigid NNP pincer ligand and their electrocatalytic activity toward CO_2 reduction are reported.

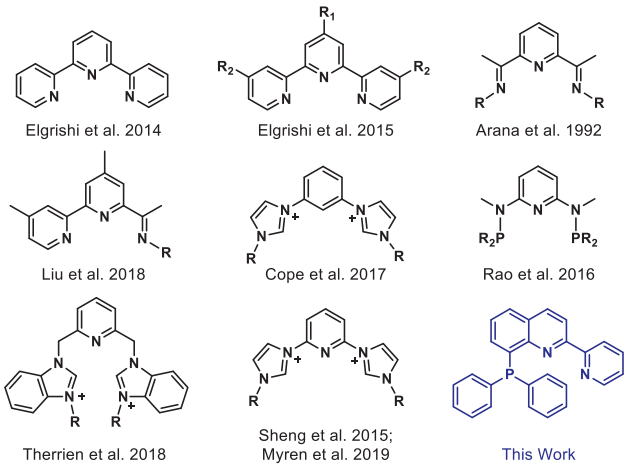

FIGURE 1 | Selected pincer ligands used with first-row transition metals for electrocatalytic CO_2 reduction.

EXPERIMENTAL

Materials and Methods

All synthetic manipulations were carried out using standard Schlenk techniques or in an MBraun glovebox under nitrogen atmosphere. Freshly distilled acetonitrile (CH_3CN) and *N,N*-dimethylformamide (DMF) were used in synthesis and electrochemistry. Tetrahydrofuran, toluene, and diethyl ether were dried with a Pure Process Technology solvent purification system. 1,1′-Bis(diisopropylphosphino)-ferrocene (DiPPF), diphenylphosphine, iron(II) trifluoromethanesulfonate, and copper(II) perchlorate hexahydrate were purchased from Strem Chemicals. Zinc(II) trifluoromethanesulfonate and sodium tert-butoxide were purchased from Acros Organics. Nickel perchlorate hexahydrate and palladium(II) acetate were purchased from Alfa Aesar and Chem-Impex International, respectively. All other chemicals were reagent or ACS grade, purchased from commercial vendors, and used without further purification. ^1H, ^{31}P, and ^{13}C NMR spectra were obtained using Bruker spectrometers operating at 500 MHz (^1H), 167 MHz (^{31}P), or 126 MHz (^{13}C). Spectra were calibrated vs. observed solvent peaks. Chemical shifts are reported in parts per million (ppm). Solution magnetic susceptibilities were determined by NMR using the Evans method. High-resolution electrospray ionization mass spectra (HR-ESI-MS) were obtained with a Waters SYNAPT HDMS Q-TOF mass spectrometer and elemental analyses of carbon, hydrogen, and nitrogen were conducted by Atlantic Microlab, Inc., Norcross, Georgia. Gas samples were analyzed by a custom Agilent 7890B Gas Chromatograph (Agilent PorapakQ column, 6 ft, 1/8 in. OD) with a dual detector system (TCD and FID). Calibration curves for the observed gases were prepared from commercial standards of known concentration obtained from buycalgas.com.

Electrochemical Measurements

Cyclic voltammetry was performed with a typical three-electrode setup using a CH Instruments 600E Series potentiostat. The electrochemical cell was equipped with a glassy carbon disk working electrode (3 mm diameter), a platinum wire counter electrode, and a silver wire quasi-reference electrode. Acetonitrile or DMF solutions containing 0.1 M Bu_4NPF_6 as the supporting electrolyte were used in all studies as specified. Ferrocene was added at the end of experiments and served as an internal standard to reference the potential. Electrolysis solutions and electrochemical cells were thoroughly degassed with nitrogen or carbon dioxide for 10–20 min prior to each experiment. Freshly made solutions were used for each experiment. Controlled potential electrolyses (CPE) were conducted in an airtight two-compartment cell with a glassy carbon rod working electrode (type 2, Alfa Aesar, 2 mm diameter), a silver wire quasi-reference electrode, and a high-surface area platinum mesh counter electrode. The platinum counter electrode was positioned inside a small isolation chamber with a fine frit. The isolation chamber contained the same solution, but without catalyst.

The electrolysis solution in the working electrode compartment was continuously stirred during the experiments. Evolved gases were quantified by taking aliquots (0.30 mL) from the headspace using a sealable gastight syringe for injection into the gas chromatograph for analysis.

X-Ray Crystallography

A single crystal coated with Paratone-N hydrocarbon oil was mounted on the tip of a MiTeGen micromount. The temperature was maintained at 200 K with an Oxford Cryostream 700 during data collection at the University of Mississippi, Department of Chemistry and Biochemistry, X-ray Crystallography Facility. Samples were irradiated with Mo-Kα radiation with λ = 0.71073 Å using a Bruker Smart APEX II diffractometer equipped with a fine-focus sealed tube source and APEX-II detector. The Bruker APEX2 v. 2009.1 software package was used to integrate raw data which were corrected for Lorentz and polarization effects (APEX2, 2009). A semi-empirical absorption correction (SADABS) was applied (Sheldrick, 2000). The space group was identified based on systematic absences, E-statistics, and successive refinement of the structure. The structure was solved using direct methods and refined by least-squares refinement on F2 and standard difference Fourier techniques using SHELXL (Sheldrick, 1990, 2008, 2014). Thermal parameters for all non-hydrogen atoms were refined anisotropically, and hydrogen atoms were included at ideal positions. Crystallographic data in CIF format was deposited into The Cambridge Crystallographic Data Center (CCDC); see deposition number CCDC 1909986 (**NiL_2^{2+}**) and **Table S1**.

Synthesis of the Ligand

Ligand precursor 8-bromo-2-(pyridin-2′-yl)quinoline (**2**) was synthesized as previously reported (Mao et al., 2005; Wickramasinghe et al., 2015). New ligand (8-(diphenylphosphaneyl)-2-(pyridin-2′-yl)quinoline) was prepared using a modified procedure (Murata and Buchwald, 2004; Zhang et al., 2017).

8-(diphenylphosphaneyl)-2-(pyridin-2′-yl)quinoline, *L*

Inside the glovebox, to an oven-dried pressure flask with a Teflon screw cap was added 8-bromo-2-(pyridin-2′-yl)quinoline, **2** (0.80 g, 2.81 mmol), $Pd(OAc)_2$ (0.032 g, 0.140 mmol), 1,1′-bis(diisopropylphosphino)ferrocene (0.071 g, 0.168 mmol), and NaO^tBu (0.324 g, 3.37 mmol). Then 5 mL anhydrous toluene was added and the mixture was stirred for 1 h. Diphenylphosphine (0.41 mL, 2.34 mmol) was added to the flask via a micropipette and the flask was re-sealed and heated at 120°C for 36 h. After cooling to room temperature, the reaction mixture was concentrated and purified by a deactivated silica column eluting with hexanes:ethyl acetate (5:1). The product was obtained as a light yellow solid, which is air stable in the solid phase (0.667 g, 73 %). ^{1}H NMR (CD_3CN, 500 MHz): δ 8.64 (dq, J = 0.7 Hz, J = 4.8 Hz, 1H), 8.54 (d, J = 8.6 Hz, 1H), 8.40 (d, J = 8.6 Hz, 1H), 8.04 (d, J = 8.0 Hz, 1H), 7.95 (d, J = 8.2 Hz, 1H), 7.75 (td, J = 1.7 Hz, J = 7.8 Hz, 1H), 7.50 (td, J = 0.8 Hz, J = 8.0 Hz, 1H), 7.43–7.34 (m, 11H), 7.13 (qd, J = 1.3 Hz, J = 3.8 Hz, 1H). $^{13}C\{^1H\}$ NMR ($CDCl_3$, 126 MHz): δ 156.18 (s), 154.94 (s), 148.86 (s), 148.63 (d), 139.26 (d), 137.62 (d), 137.13 (s), 136.98 (s), 134.54 (s), 134.38 (s), 134.06 (s), 128.74 (s), 128.56 - 128.43 (m), 127.93 (s), 126.96 (s), 124.11 (s), 122.37 (s), 119.00 (s). $^{31}P\{^1H\}$ NMR ($CDCl_3$, 167 MHz) δ−13.35. HR-ESI-MS (M^+) m/z calc. for $[L+Cs^+]^+$, 523.0340, Found, 523.0327.

Synthesis of the Metal Complexes

Common Synthetic Procedure

An acetonitrile or methanol solution (5 mL) of the NNP ligand **L** (0.050 g, 0.128 mmol) was prepared in a two-neck round bottom flask equipped with a reflux condenser before 0.5 equivalents of the corresponding metal precursor was added to the solution. The reaction mixture was refluxed for 6 h under nitrogen. After cooling to room temperature, the solvent was evaporated under reduced pressure and the residue was washed with Et_2O.

FeL_2^{2+}, *$[FeL_2](OTf)_2$*

The complex was prepared from $Fe(OTf)_2$ (0.023 g, 0.064 mmol) and 2 equivalents of **L** (0.050 g, 0.128 mmol) in acetonitrile. A short size-exclusion column (Sephadex® LH-20) was run, eluting with methanol, and a single dark band was collected and dried under vacuum. The complex was further purified by crystallization from a concentrated solution of methanol by slow diffusion of diethyl ether. Yield = 0.065 g (90%). ^{1}H NMR (CD_3CN, 500 MHz): δ 9.04 (d, J = 8.7 Hz, 2H). 8.79 (d, J = 8.0 Hz, 2H), 8.62 (d, J = 8.7 Hz, 2H), 8.33 (br t, 2H), 8.25 (t, J = 7.6 Hz, 2H), 8.14 (d, J = 8.0 Hz, 2H), 7.65 (t, J = 7.65 Hz, 2H), 7.11–7.06 (m, 6H), 6.91 (t, J = 6.35 Hz, 2H), 6.80 (t, J = 7.35 Hz, 4H), 6.67 (t, J = 7.3 Hz, 4H), 6.31 (br t, 4H), 6.11 (br t, 4H). $^{13}C\{^1H\}$ NMR (acetone-d_6, 126 MHz): δ 161.36 (s), 157.83 (t), 157.55 (s), 125.27 (s), 141.26 (s), 139.20 (s), 138.62 (s), 134.92 (s), 131.79 (t), 131.49 (t), 130.97–130.89 (m), 130.56–130.48 (m), 129.77 (t), 129.51–129.38 (m), 129.22 (s), 129.03 (s), 128.87 (s), 128.71 (s), 128.54 (s), 128.44 (s), 128.29 (s), 128.12 (d), 127.97 (s), 126.30 (s), 123.42 (s), 121.81 (s), 120.87 (s). $^{31}P\{^1H\}$ NMR ($CDCl_3$, 167 MHz) δ 58.94. HR-ESI-MS (M^+) m/z calc. for $[FeL_2(OTf)]^+$, 985.1441, Found, 985.1454.

$[FeL_2](Br)_2$

This complex was made in analogous fashion to $[FeL_2](OTf)_2$ as detailed above using $FeBr_2$ (0.014 g, 0.064 mmol). Yield = 0.058 g (91%). ^{1}H NMR (DMSO-d_6, 500 MHz): δ 9.29 (d, J = 8.8 Hz, 2 H), 9.03 (d, J = 8.85 Hz, 2H), 8.95 (d, J = 8.1 Hz, 2H), 8.54 (d, J = 8.05 Hz, 2H), 8.46 (br t, 2H), 8.32 (t, J = 7.6 Hz, 2H), 7.79 (t, J = 7.8 Hz, 2H), 7.26 (d, J = 5.55 Hz, 2H), 7.13 (t, J = 7.45 Hz, 2H), 7.08 (t, J = 7.35 Hz, 2H), 7.02 (t, J = 6.25 Hz, 2H), 6.85 (t, J = 7.55 Hz, 4H), 6.68 (t, J = 7.45 Hz, 4H), 6.27 (br t, 4H), 6.03 (br t, 4H). $^{13}C\{^1H\}$ NMR (DMSO-d_6, 126 MHz): δ 160.19 (s), 156.43 (t), 156.26 (s), 151.31 (s), 140.07 (s), 138.35 (s), 137.65 (s), 133.98 (s), 130.81 (s), 130.25 (t), 129.72–129.59 (m), 129.33 (s), 129.15 (t), 128.53 (t), 128.37 (t), 128.14 (s), 127.95 (s), 127.79 (s), 127.67–127.59 (m), 126.77 (s), 126.61 (s), 126.46 (s), 125.49 (s), 121.16 (s). $^{31}P\{^1H\}$ NMR (DMSO-d_6, 167 MHz) δ 59.07. HR-ESI-MS (M^+) m/z calc. for $[FeL_2Br]^+$, 915.1104, Found, 915.1077.

CoL_2^{2+}, *[CoL$_2$](OTf)$_2$]*

The complex was prepared from $Co(CH_3CN)_2(OTf)_2$ (0.028 g, 0.064 mmol) and 2 equivalents of **L** in acetonitrile. A short size-exclusion column (Sephadex® LH-20) was run, eluting with methanol, and a single dark band was collected and dried under vacuum. Yield = 0.067 g (92%). HR-ESI-MS (M^+) m/z calc. for $[CoL_2(OTf)]^+$, 988.1424, Found, 988.1389. The complex was fully characterized as a Co(III) complex, prepared by stirring a methanol solution of the Co(II) species overnight under air. Crystals of the Co(III) complex were grown from methanol by slow diffusion of diethyl ether. Elem. Anal. calc. for $C_{52}H_{38}CoN_4P_2(CF_3SO_3)_3\cdot(H_2O)$: C, 50.62; H, 3.09; N, 4.29. Found: C, 50.19; H, 3.05; N, 4.12. HR-ESI-MS (M^+) m/z calc. for $[CoL_2(OTf)_2]^+$, 1137.0944. Found, 1137.0947.

NiL_2^{2+}, *[NiL$_2$](ClO$_4$)$_2$*

The complex was synthesized by reacting $Ni(ClO_4)_2\cdot 6H_2O$ (0.023 g, 0.064 mmol) and **L** (0.050 g, 0.128 mmol) in methanol. The complex was purified by recrystallization from hot methanol. Yield = 0.057 g (86%). Elem. Anal. calc. for $C_{52}H_{38}Cl_2N_4NiO_8P_2\cdot(H_2O)_2$: C, 58.13; H, 3.94; N, 5.21. Found: C, 58.33; H, 3.86; N, 5.20. HR-ESI-MS (M^+) m/z calc. for $[NiL_2(ClO_4)]^+$, 937.1410. Found, 937.1398.

CuL_2^{2+}, *[CuL$_2$](ClO$_4$)$_2$*

The complex was prepared from $Cu(ClO_4)_2\cdot 6H_2O$ (0.024 g, 0.064 mmol) and two equivalents of **L** in acetonitrile. The complex was found to be unstable in solutions and could not be fully purified. Yield = 0.061 g (92%). ESI-MS (M^+) m/z calc. for $[CuL_2(ClO_4)]^+$, 942.14. Found, 942.13.

ZnL_2^{2+}, *[ZnL$_2$](OTf)$_2$*

Treatment of $Zn(OTf)_2$ (0.023 g, 0.064 mmol) with 2 equivalents of **L** in methanol gave the product as a light green powder. Yield = 0.065 g (89%). ^{1}H NMR (CD_3CN, 500 MHz): δ 9.13 (d, J = 8.75 Hz, 2H), 8.80 (d, J = 8.75 Hz, 2H), 8.56 (t, J = 8.55 Hz, 4H), 8.01–7.94 (m, 6H), 7.44 (br d, 2H), 7.22 (t, J = 7.35 Hz, 2H), 7.13 (t, J = 7.15 Hz, 2H), 6.94–6.89 (m, 10H), 6.70 (br m, 4H), 6.38 (br d, 4H). $^{13}C\{^1H\}$ NMR (acetone-d_6, 126 MHz): δ 152.88 (s), 148.71 (s), 148.56 (s), 148.07 (t), 144.93 (s), 142.76 (s), 142.35 (s), 141.95 (s), 134.96 (t), 134.49 (s), 132.37 (s), 132.18 (t), 131.02 (t), 130.67 (d), 130.11 (t), 129.92 (t), 128.92 (s), 128.30 (t), 127.41 (t), 125.63 (s), 122.07 (s). $^{31}P\{^1H\}$ NMR ($CDCl_3$, 167 MHz) δ −34.69. HR-ESI-MS (M^+) m/z calc. for $[ZnL_2(OTf)]^+$, 993.1383, Found, 993.1382.

RESULTS AND DISCUSSION

Synthesis of the Ligand and the Metal Complexes

Ligand precursor 2,8-dibromoquinoline **(1)** was prepared via a three-step synthetic route starting with 2-bromoaniline and cinnamoyl chloride (Wickramasinghe et al., 2015). A CombiFlash® Rf+ system was utilized to obtain high purity product from the crude reaction mixture. As shown in **Figure 2**, Stille coupling of 2-(tributylstannyl)pyridine and **1** afforded 8-bromo-2-(pyridin-2′-yl)quinoline **(2)** (Wickramasinghe et al., 2015). The final ligand, 8-(diphenylphosphaneyl)-2-(pyridin-2′-yl)quinoline **(L)**, was prepared from **2** and diphenylphosphine using a modified cross-coupling reaction (Murata and Buchwald, 2004; Zhang et al., 2017). A deactivated silica gel column allowed purification of the product, in which 2-(pyridin-2′-yl)quinoline was found to be the only major side-product.

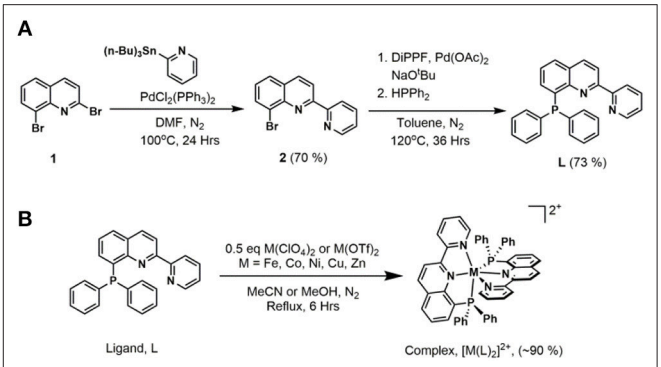

FIGURE 2 | (A) Synthesis of 8-(diphenylphosphaneyl)-2-(pyridin-2′-yl)quinoline, ***L***. **(B)** General synthetic route for the metal complexes.

The metal complexes were synthesized by refluxing the appropriate metal(II) salts with 2 equivalents of the ligand **L** in acetonitrile or methanol. Metal complexes in powder form were obtained after evaporation of the solvent and washing with diethyl ether. The Fe and Co complexes were initially purified by a Sephadex® column and obtained in high yields of ∼90%. Further purification of all complexes was done by recrystallization from concentrated methanol or acetonitrile solutions, generally at −20°C or by slow diffusion of diethyl ether into the solution. The complexes are stable in the solid state to ambient light, air, and moisture.

In all cases, formation of the bis-chelated complexes was favored in the reaction conditions employed here. For reactions involving Co(II), Ni(II), Cu(II), and Zn(II), treatment of the appropriate metal precursor with 1 equivalent of **L** in polar solvents initially led to the formation of a mixture of mono- and bis-chelated metal complexes. Stirring the reaction mixture for prolonged periods led to clean formation of the bis-chelated complexes. In the case of Fe(II), the reaction of **L** and $Fe(OTf)_2$ in a 1:1 ratio immediately formed bis-chelated complex as the only product. A similar result was observed when $FeBr_2$ was used instead of $Fe(OTf)_2$. This observation with iron complexes is analogous to the $[(Ph\text{-}PNN)_2Fe]^{2+}$ complexes reported by Zell et al. (2013). In their studies, DFT calculations indicated that formation of the bis-chelated complexes is thermodynamically favored relative to the mono-chelated compounds in all conditions. They could tune this coordination behavior by altering the substituents of the phosphine donor where bulky tert-butyl groups allowed formation of the mono-chelated complex only and isopropyl substituents gave access to both the mono- and bis-chelated complexes depending on the initial ratio of metal precursor and

ligand during metalation. Basu et al. (2018) followed the same principle to avoid bis-chelation in their report.

Synthesis of the mono-chelated Co(II) complex was attempted by treating a tetrahydrofuran solution of $CoCl_2$ with 1 equivalent of **L**. A green precipitate appeared immediately which was identified by mass spectroscopy to be mono-chelated **L**-$CoCl_2$ complex. However, due to limited solubility in traditional non-coordinating solvents, it could not be further characterized. Dissolving the complex in polar solvents such as acetonitrile, methanol, or DMF led to a gradual color change to a reddish-brown solution, indicating formation of the bis-chelated $\mathbf{CoL_2^{2+}}$ complex. This behavior is similar to the observation made by Harris et al. (1969) for Co(tpy) complexes.

Stirring 2:1 mixtures of the ligand and the appropriate metal precursors in methanol or acetonitrile for ∼12 h led to quantitative formation of the bis-chelated complexes, ML_2^{2+}. Elevated temperatures significantly reduced the reaction time. Each of the ML_2^{2+} complexes are stable in the solid state, and apart from the Cu(II) complex, they are also stable in solution. $\mathbf{CuL_2^{2+}}$ slowly decomposes in solution and could not be purified or fully characterized. We note that the cobalt(II) complex is easily oxidized to the cobalt(III) complex in solution when exposed to air.

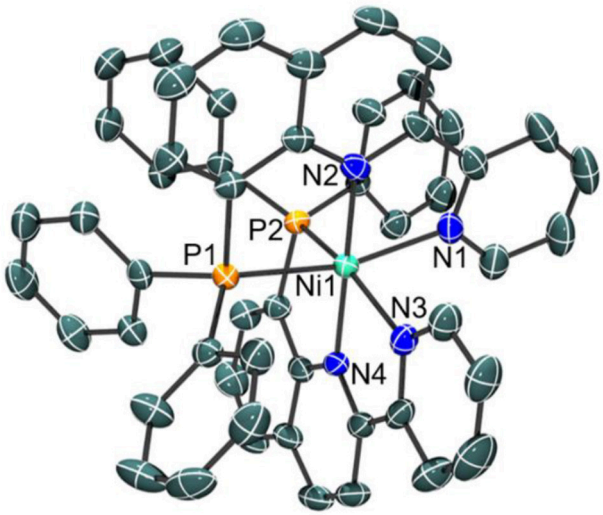

FIGURE 3 | Crystal structure of the cation of $\mathbf{[NiL_2](ClO_4)_2}$ with thermal ellipsoids shown at the 35% probability level. Hydrogen atoms have been omitted for clarity. Selected bond distances: Ni–N(1), 2.086(4); Ni–N(2), 2.062(4); Ni–N(3), 2.093(4); Ni–N(4), 2.054(4); Ni–P(1), 2.4323(13); Ni–P(2), 2.4183(13) Å.

Characterization of Metal Complexes

Elemental analyses and mass spectrometry of each ML_2^{2+} complex show the 2:1 ratio of ligand to metal. The Co(II), Ni(II), and Cu(II) complexes are paramagnetic. As expected of a d^{10} metal center, the Zn(II) complex is diamagnetic. The diamagnetic nature of the d^6 Fe(II) complex indicates a low-spin octahedral electronic state. Two distinct sets of ^{1}H signals were observed for the phenyl groups in these complexes, which suggests that no plane of symmetry passes through the metal center. Notably, only one peak is observed in the ^{31}P NMR spectra of $\mathbf{FeL_2^{2+}}$ and $\mathbf{ZnL_2^{2+}}$ signifying that the phosphorus atoms are chemically equivalent, consistent with κ^3 coordination modes for both NNP pincer ligands and octahedral complexes.

Indeed, a crystal structure of the octahedral nickel complex was obtained as shown in **Figure 3**. Single crystals of $\mathbf{NiL_2^{2+}}$ were grown from a concentrated solution of hot methanol that was allowed to cool to room temperature. The nickel-nitrogen bond distances range from 2.054(4) to 2.093(4) Å, with pyridine donors *trans* to the phosphine donor having an average Ni-N bond distance of 2.090 Å while those that are *trans* to another pyridine have an average Ni-N bond distance of 2.058 Å. Significantly longer bond distances are observed for the phosphine donors at 2.4323(13) for Ni-P(1) and 2.4183(13) for Ni-P(2) in the solid state.

For the three reported paramagnetic complexes, solution magnetic susceptibilities (μ_{eff}) were determined by the Evans method (Evans, 1959). At room temperature, the values are 2.6, 2.8, and 2.0 for $\mathbf{CoL_2^{2+}}$, $\mathbf{NiL_2^{2+}}$, and $\mathbf{CuL_2^{2+}}$, respectively. The experimental values are close to previously reported values of similar octahedral complexes and characteristic of 1, 2, and 1 unpaired electron(s) for the Co(II), Ni(II), and Cu(II) complexes, respectively. The relatively high μ_{eff} value for cobalt (2.6) is typical of cobalt polypyridyl complexes, and indicates significant orbital contribution (Chen et al., 2018).

Electrochemistry

Cyclic voltammetry was performed on the series of metal complexes to assess and compare the redox potentials in acetonitrile/0.1 M Bu_4NPF_6 solutions under inert atmosphere. The cyclic voltammograms are shown in **Figure 4** and $E_{1/2}$ values (peak potentials for the irreversible redox features) are summarized in **Table S2**. All potentials are reported against the ferrocenium/ferrocene couple (V vs. $Fc^{+/0}$).

The cyclic voltammogram (CV) of $\mathbf{ZnL_2^{2+}}$ shows four redox couples at −1.36, −1.54, −2.16, and −2.35 V. Since this complex has a redox-inactive metal center, these processes are assigned to ligand-based redox events. The zinc complex is helpful in identifying metal- and ligand-based redox processes in the remaining complexes. Notably, $\mathbf{ZnL_2^{2+}}$ is unstable under repeated scans. The redox couples at −2.16 and −2.35 V become irreversible and a visible change in peak intensities is observed presumably due to passivation of the working electrode.

The reduction waves at $E_{p,c} = -2.22$ and −2.36 V of $\mathbf{CuL_2^{2+}}$ can be safely assigned to ligand-based reductions. A sharp irreversible oxidation peak at −0.76 V is also observed, indicative of adsorption on the electrode surface. The redox features of the copper complex also lose their reversibility and peak shape under repeated scans.

Reversible metal-based $M^{III/II}$ redox couples occur at $E_{1/2}$ = 0.80, −0.46, and 0.66 V for $\mathbf{FeL_2^{2+}}$, $\mathbf{CoL_2^{2+}}$, and $\mathbf{NiL_2^{2+}}$, respectively. In addition, three reversible redox events are

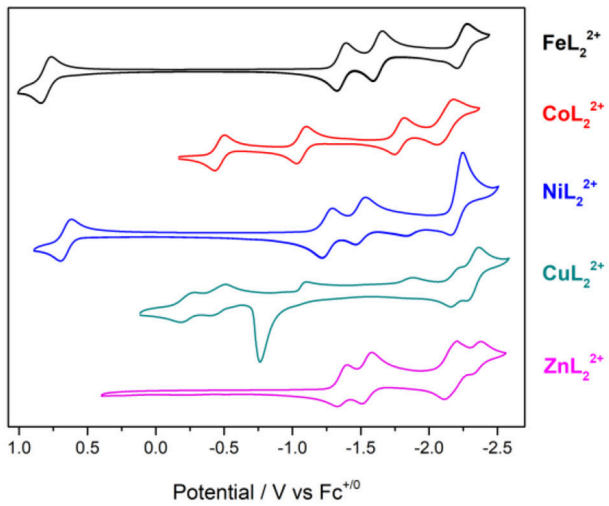

FIGURE 4 | Cyclic voltammograms of $[ML_2]^{2+}$ complexes of Fe, Co, Ni, Cu, and Zn at 1 mM concentrations in CH_3CN/0.1 M Bu_4NPF_6 under N_2. Scan rate: 100 mV/s; glassy carbon disk working electrode.

observed at negative potentials with the iron and cobalt complexes in the potential range studied here. The nickel complex shows slightly different behavior with two reversible reductions at −1.28 and −1.53 V, and a quasireversible reduction at −2.25 V. The quasireversible reduction has two small return oxidations at −2.15 and −1.83 V. The most negative features of these complexes are assigned to ligand-based reductions by comparison to the zinc analog.

Electrochemical Reduction of CO_2

Next, the complexes were analyzed by cyclic voltammetry to probe their reactivity toward CO_2 reduction. We focused on $\mathbf{FeL_2^{2+}}$, $\mathbf{CoL_2^{2+}}$, and $\mathbf{NiL_2^{2+}}$ as the copper and zinc complexes were not stable under electrochemical reduction. DMF solutions containing 0.1 M Bu_4NPF_6 were employed for electrocatalytic studies for two reasons. First, using acetonitrile resulted in a significant amount of precipitation during controlled potential electrolysis (CPE) experiments. This is consistent with previously reported observations with 3d transition metal terpyridine complexes and ruthenium polypyridyl complexes. It was concluded that the build-up of HCO_3^-/CO_3^{2-} during bulk electrolyses resulted in precipitation of the complexes as HCO_3^- or CO_3^{2-} salts (Chen et al., 2011; Elgrishi et al., 2014). We confirmed the formation of carbonate in CPE experiments with $\mathbf{CoL_2^{2+}}$ by barium triflate titration (Yang et al., 2018), consistent with the reductive disproportionation of CO_2 to CO and CO_3^{2-}. The use of DMF solved this solubility issue as no precipitate was observed during electrolyses over extended periods of time. Second, using DMF gave us the opportunity to directly compare the performance of these complexes with the previously reported terpyridine systems (Elgrishi et al., 2014, 2015).

Under N_2 atmosphere, CVs of $\mathbf{FeL_2^{2+}}$, $\mathbf{CoL_2^{2+}}$, $\mathbf{NiL_2^{2+}}$, and $\mathbf{ZnL_2^{2+}}$ in DMF (shown in **Figure S1**) exhibit similar behavior to that in acetonitrile, but with significantly lower stability for the nickel and zinc compounds. Redox potentials of the complexes in DMF are summarized in **Table 1**. Comparing the CV of the cobalt complex to its zinc counterpart, we assign the redox couples ($E_{1/2}$) at −1.06 and −1.74 V to a metal-based $Co^{II/I}$ process and to a ligand-based process, respectively. The open circuit potential of the $\mathbf{CoL_2^{2+}}$ was measured at −0.61 V, which is consistent with these assignments. A reversible ligand-based wave was also observed at $E_{1/2} = -2.07$ V. Adding free ligand to the solution increases the intensity of this peak (**Figure S2**), which further supports the assignment of this feature as a ligand-based reduction. Scanning past this ligand-based reduction gives rise to an irreversible ligand-based reduction at −2.65 V, which was found to be unstable under repeated scans (**Figure S3**).

TABLE 1 | Reductive peak potentials and diffusion coefficients (*D*) of 0.5 mM solutions of $\mathbf{FeL_2^{2+}}$, $\mathbf{CoL_2^{2+}}$, $\mathbf{NiL_2^{2+}}$, and $\mathbf{ZnL_2^{2+}}$ in DMF/0.1 M Bu_4NPF_6 under N_2.

Complex	$E_{p1,c}$	$E_{p2,c}$	$E_{p3,c}$	$E_{p4,c}$	D ($cm^2\ s^{-1}$)
$\mathbf{FeL_2^{2+}}$	−1.43	−1.67	−2.31	–	4.69×10^{-6}
$\mathbf{CoL_2^{2+}}$	−1.09	−1.77	−2.12	−2.65	1.02×10^{-6}
$\mathbf{NiL_2^{2+}}$	−1.32	−1.51	−1.83	−2.25	4.36×10^{-6}
$\mathbf{ZnL_2^{2+}}$	−1.61	−1.83	−2.24	−2.41	–

Glassy carbon working electrode, platinum wire counter electrode, and silver wire quasi-reference electrode.

For $\mathbf{FeL_2^{2+}}$, reversible waves with $E_{1/2}$ values at −1.40, −1.64, and −2.27 V are attributed to ligand-based reductions by comparison with $\mathbf{ZnL_2^{2+}}$. Different behavior was observed with $\mathbf{NiL_2^{2+}}$ relative to the Fe and Co complexes with one reversible redox feature at $E_{1/2} = -1.27$ V, followed by one irreversible reduction at $E_{p,c} = -1.51$ V and two quasireversible reductions at $E_{p,c} = -1.83$ and −2.25 V. The open circuit potential was determined to be −0.68 V. Thus, the reversible redox process at −1.27 V is expected to be a metal-centered $Ni^{II/I}$ couple, while the remaining waves are consistent with ligand-based redox events. Irreversible reductions are presumably due to dissociation of one of the tridentate ligands from the complex. This redox behavior is different from the related $Co(tpy)_2^{2+}$ and $Ni(tpy)_2^{2+}$ systems (Hamacher et al., 2009; Elgrishi et al., 2014). CVs of $\mathbf{FeL_2^{2+}}$, $\mathbf{CoL_2^{2+}}$, and $\mathbf{NiL_2^{2+}}$ at scan rates ranging from 10 to 1,000 mVs^{-1} show that the peak currents change linearly with the square root of the scan rate (**Figures S5–S7**), consistent with diffusion-controlled homogeneous species. The diffusion coefficients were calculated from the slopes of the linear fits of the first reduction peaks using the Randles-Sevcik equation (Bard and Faulkner, 2001) and are presented in **Table 1**.

Water was added as a proton source to investigate the proton-coupled reduction of CO_2 with these complexes. The concentration of added water was kept fixed at 5% in these studies. No significant current enhancement was observed in the CVs when water was introduced to the systems under N_2 (**Figure 5**). Likewise, there was little change to the CV of $\mathbf{CoL_2^{2+}}$ with added H_2O. The third (most negative) reduction peak of $\mathbf{FeL_2^{2+}}$ and $\mathbf{NiL_2^{2+}}$ becomes irreversible in the presence of H_2O.

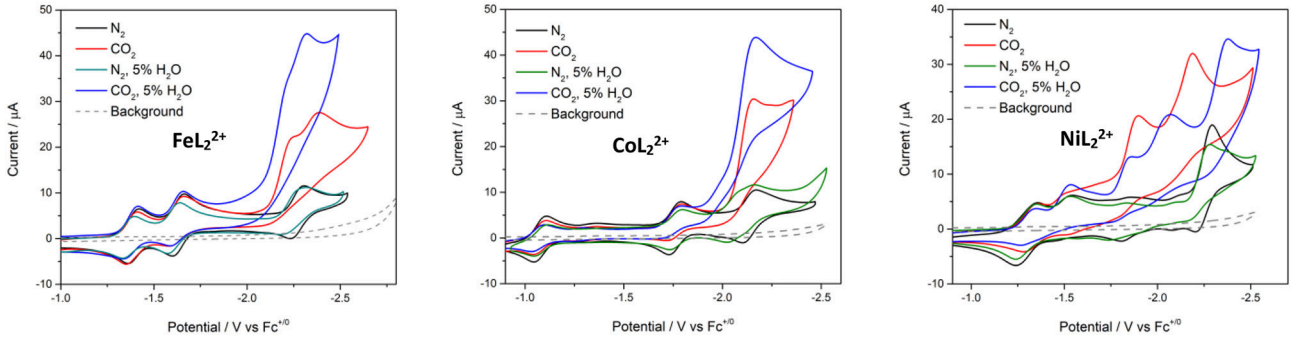

FIGURE 5 | Cyclic voltammograms of $\mathbf{FeL_2^{2+}}$, $\mathbf{CoL_2^{2+}}$, and $\mathbf{NiL_2^{2+}}$ at 0.5 mM concentrations in DMF/0.1 M Bu_4NPF_6 under N_2 (black), CO_2 (red), N_2 with 5% H_2O (green), and CO_2 with 5% H_2O (blue). Scan rate = 100 mV/s; glassy carbon disk working electrode.

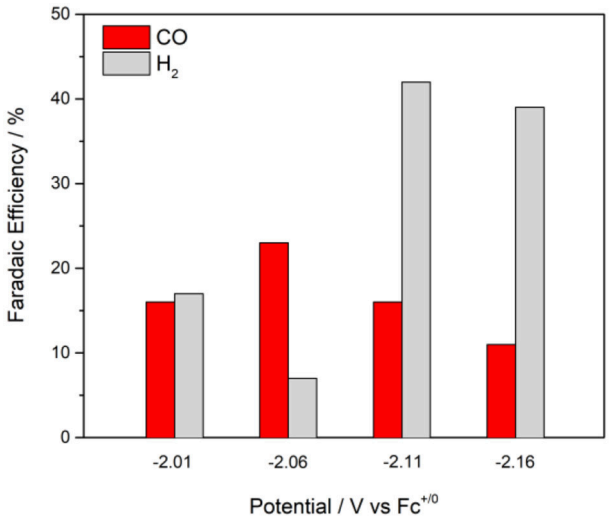

FIGURE 6 | Faradaic efficiencies and product distributions from control potential electrolyses at different applied potentials with 0.5 mM $\mathbf{CoL_2^{2+}}$ in CO_2-saturated DMF/0.1 M Bu_4NPF_6 solutions containing 5% H_2O, glassy carbon rod.

In CO_2-saturated anhydrous solutions, the third reduction of all three complexes loses reversibility and shows current enhancement, suggesting catalytic reactivity toward CO_2 (**Figure 5**). A 2.4-fold current increase was observed at the third reduction peak of $\mathbf{FeL_2^{2+}}$ with the appearance of a new peak at $E_{p,c} = -2.23$ V. The new peak showed current enhancement of 1.9-fold. In $\mathbf{CoL_2^{2+}}$, the most negative reduction peak was catalytically enhanced with an i_{cat}/i_p value of 2.9 (where i_{cat} is the limiting catalytic current obtained under CO_2 and i_p is the reductive peak current of the catalyst in the absence of substrate). CVs of $\mathbf{NiL_2^{2+}}$ showed current enhancement of 3.5- and 1.7-fold in the third and fourth reduction waves, respectively.

Additional current enhancement at the terminal reduction peaks of the $\mathbf{FeL_2^{2+}}$ and $\mathbf{CoL_2^{2+}}$ systems was observed when 5% water was added to CO_2-saturated solutions, indicating that the complexes are capable of catalyzing the proton–coupled reduction of CO_2 (**Figure S10**). The CV of $\mathbf{NiL_2^{2+}}$ under the same conditions showed a decrease in the initial catalytic waves, but an additional and larger catalytic wave appeared at $E_{p,c} = -2.40$ V (**Figure 5**).

To better understand the reactivity of the complexes and to quantify the products, a series of controlled potential electrolyses (CPEs) were performed at different applied potentials with and without added H_2O. Gaseous products were analyzed by periodic sampling of the headspace of the airtight electrochemical cell. **Table 2** summarizes the product distribution and Faradaic efficiencies (FE) of each complex over the first 2 h. Representative charge vs. time plots are provided in **Figures S11–S13**, **S16**. Carbon monoxide and hydrogen were the major products detected in all cases. A trace amount of methane was also found in the electrolyses of $\mathbf{CoL_2^{2+}}$ and $\mathbf{FeL_2^{2+}}$ but corresponds to <1% of the total charge passed.

The maximum overall FE was found to be 58% for $\mathbf{CoL_2^{2+}}$ at an applied potential of −2.11 V in the presence of 5% water (**Figure 6**). A maximum FE of 23% for evolved CO was recorded at $E_{appl} = -2.06$ V. The production of H_2 varied with the applied potential from 7 to 42%. When methanol—a more acidic proton source—was used, the overall FE decreased, but the ratio for H_2 production increased (**Table 2**). No evolved H_2 was observed when electrolyses were performed in anhydrous solutions. However, Faradaic efficiencies for CO were lower. Rinse tests were performed on the glassy carbon rod after CPEs to investigate possible adsorption or deposition of a heterogeneous catalyst on the electrode surface. There was no visible deposition and the glassy carbon rod did not exhibit any catalytic activity in fresh CO_2-saturated DMF/0.1 M Bu_4NPF_6 solution, which suggests catalysis is governed by a molecular cobalt species.

The turnover frequency (TOF) of $\mathbf{CoL_2^{2+}}$ was calculated as previously described (Narayanan et al., 2016; Yang et al., 2018) from scan rate-dependent linear sweep voltammograms performed in N_2- and CO_2-saturated solutions containing 5% H_2O. A plot of the i_{cat}/i_p current ratio at different scan rates as a function of potential is shown in **Figure S8**. Although a scan rate-independent TOF was not completely reached at scan rates up to 1 V/s, an estimated TOF of 12.4 s^{-1} was determined (**Figure S9**).

CPEs of the $\mathbf{NiL_2^{2+}}$ complex show that the complex is selective for CO_2 reduction over proton reduction, albeit with very low FEs. The maximum FE observed with the nickel complex was

TABLE 2 | Summary of 2 h CPEs with $\mathbf{FeL_2^{2+}}$, $\mathbf{CoL_2^{2+}}$, and $\mathbf{NiL_2^{2+}}$ (0.5 mM catalyst concentration) in CO_2-saturated DMF/0.1 Bu_4NPF_6 solutions (glassy carbon rod).

Complex	H^+ Source	E_{appl} (V)	Charge (C)	Total FE (%)	FE_{CO} (%)	FE_{H2} (%)
$\mathbf{CoL_2^{2+}}$	5% H_2O	−2.01	2.07	33	16	17
	5% H_2O	−2.06	2.94	30	23	7
	5% H_2O	−2.11	5.51	58	16	42
	5% H_2O	−2.16	6.77	50	11	39
	None	−2.11	2.92	6	6	–
	5% MeOH	−2.12	5.56	41	7	34
$\mathbf{NiL_2^{2+}}$	5% H_2O	−2.06	1.18	5	5	–
	5% H_2O	−2.28	1.37	8	8	–
$\mathbf{FeL_2^{2+}}$	5% H_2O	−2.15	5.21	27	1	26
	5% H_2O	−2.25	5.67	26	< 1	25
	None	−2.23	1.53	< 1	< 1	–
$\mathbf{ZnL_2^{2+}}$	5% H_2O	−2.20	0.81	< 1	< 1	–

For the CPE with $\mathbf{ZnL_2^{2+}}$, a 2 mM concentration of the complex was used. All values are the average of at least two runs.

8%. The total charge passed was also very low compared to its iron and cobalt counterparts. The $\mathbf{FeL_2^{2+}}$ complex primarily catalyzed proton reduction in the presence of H_2O. Indeed, the FE for CO production was ∼1% in anhydrous DMF solutions or with 5% added H_2O. Under anhydrous conditions, proton reduction was suppressed, but CO production remained low. Rinse tests were also performed following electrolyses of both the nickel and iron complexes. For $\mathbf{FeL_2^{2+}}$, the electrode did not show any sign of deposition. On the other hand, visible signs of deposition on the glassy carbon rod were observed with $\mathbf{NiL_2^{2+}}$ and the electrode showed catalytic activity in fresh solutions that signals decomposition of the complex occurs to form an active heterogeneous material.

DISCUSSION

In general, to be an effective catalyst for CO_2 or H^+ reduction, a metal complex should be able to activate the substrate molecule via an open coordination site at the metal center. Thus, molecular catalysts are typically designed with at least one open or labile coordination site (Chiericato et al., 2000; Benson et al., 2009; Thoi et al., 2013; Su et al., 2018). In contrast, the complexes investigated here form an active catalyst *in situ* by ligand loss or dissociation of a donor moiety during electrolysis. Given the rigidity of the ligand, we hypothesize that one of the ligands completely dissociates. Thus, the bis-chelated $\mathbf{ML_2^{2+}}$ complex acts as a precatalyst, which under reducing conditions loses a ligand to generate a mono-chelated, catalytically active species (bearing a single pincer ligand) with available coordination sites for substrate activation and conversion. Our attempts to isolate the mono-chelated active species were unsuccessful. However, controlled potential electrolysis of $\mathbf{CoL_2^{2+}}$ was performed under inert atmosphere at an applied voltage of −2.65 V, and the electrolysis solution was analyzed by mass spectrometry, which showed evidence of free ligand that was not present in pre-electrolysis solutions (**Figure S4**). In addition, CVs taken before and after electrolysis of $\mathbf{CoL_2^{2+}}$ show the formation of new redox features, indicating that a new electroactive species is formed under reducing conditions (**Figure S14**). Together, these experiments indicate that a mono-chelated complex is formed when the pre-catalyst is subjected to electrochemical reduction, and it is this species that is responsible for the catalytic activity observed in the presence of substrates (CO_2 and H^+).

Given the structural similarities, $\mathbf{CoL_2^{2+}}$ likely operates by the mechanism proposed by Elgrishi et al. (2014) and Elgrishi et al. (2015) for $Co(tpy)_2^{2+}$ complexes. The low Faradaic efficiencies are also consistent with their findings, which showed that the reduced mono-chelated active species can dimerize to give a deactivated species that does not reduce CO_2. Moreover, the redox-active ligand liberated during creation of the active catalyst can be reduced further, contributing to the low overall Faradaic efficiencies (**Table 2**). Proposed mechanisms for CO_2 reduction as well as the competing hydrogen evolution reaction are shown in **Figure S18** for the cobalt(II) complex.

The $\mathbf{FeL_2^{2+}}$ and $\mathbf{NiL_2^{2+}}$ complexes behave differently than the Fe and Ni bis(terpyridine) complexes reported by Elgrishi et al. (2014). In their studies, $Fe(tpy)_2^{2+}$ did not show any current enhancement in CO_2-saturated solutions containing a proton source. Conversely, the $Ni(tpy)_2^{2+}$ complex showed considerable catalytic activity under comparable conditions to those employed here and selectively produced CO in bulk electrolyses. The redox potentials of the bis(tpy) complexes and the present systems are also significantly different under N_2 atmosphere. It was concluded from CVs of $Fe(tpy)_2^{2+}$, $Ni(tpy)_2^{2+}$, and $Zn(tpy)_2^{2+}$ that they undergo ligand-based reductions exclusively in the potential window studied. The current enhancement observed in CVs of the complexes studied here under anhydrous conditions may be a result of CO_2 binding to the reduced active species to form a stable intermediate, which is not effective for catalysis and does not liberate a reduced carbon product. Related observations have been reported for molecular nickel complexes that have poor Faradaic efficiencies for CO_2 reduction despite encouraging results from cyclic voltammetry (Narayanan et al., 2016; Lieske et al., 2018). The irreversible reductions and dissimilarity between the anodic and cathodic scans of $\mathbf{NiL_2^{2+}}$ under N_2

indicates formation of a new species. Consistent with the rinse test, ligand dissociation likely occurs from the nickel complex during electrolysis, which is followed by formation of a heterogeneous material on the electrode surface. Decomposition of the molecular species following reduction may account for the low Faradaic efficiencies.

$\mathbf{ZnL_2^{2+}}$ was electrochemically and spectroscopically analyzed to better understand the underlying mechanism and stability of the catalysts. The zinc complex did not show any notable current increase in CO_2-saturated solutions by cyclic voltammetry (**Figure S15**). It also performed poorly in CPEs with an overall FE of <1%. However, the diamagnetic nature of $\mathbf{ZnL_2^{2+}}$ was used to obtain insight into the decomposition pathway of the reported complexes. We conducted an electrochemical experiment as described by Elgrishi et al. (2014) and Fuchs et al. (1981), in which $\mathbf{ZnL_2^{2+}}$ was subjected to bulk electrolysis and the electrolyzed product was studied by ^{1}H NMR. NMRs were taken of the solution before and after electrolysis, and after adding iodomethane as an alkylating agent (**Figure S17**). Free ligand peaks were visible in the ^{1}H NMR spectrum of the electrolyzed solution after a 3-h CPE, consistent with ligand dissociation. Changes in the aromatic region of the NMR spectrum and appearance of new peaks in the aliphatic region after alkylation suggest possible dearomatization and carboxylation of the ligand (Fuchs et al., 1981; Elgrishi et al., 2014).

While our cobalt system suffers from low overall Faradaic efficiency and poor selectivity, the ligand structure is amenable to electronic and steric modifications. Elgrishi et al. (2015) were able to tune the selectivity of $Co(tpy)_2^{2+}$ complexes by introducing different substituents on the tpy ligand. They improved selectivity toward CO production by disfavoring the hydrogen evolution reaction (HER), but overall Faradaic efficiencies remained low. The best derivative featuring bulky tert-butyl substituents on the tpy ligand led to the highest overall FE at 41%, presumably by reducing catalyst deactivation via dimerization. However, these results indicate that ligand modifications are largely ineffective for improving catalyst stability and thus they were not pursued with the NNP ligand investigated here.

An early example of electrochemical CO_2 reduction was reported by Arana et al. (1992) involving bis-chelated Fe, Co, and Ni complexes of redox-active NNN-type ligands. These complexes showed CO_2 reduction activity to various extents based on their current response in cyclic voltammetry studies. Among them, $Co(dapa)_2^{2+}$ and $Ni(dapa)_2^{2+}$ complexes (dapa = 2,6-bis-[1-(phenylimino)ethyl]pyridine) showed the best activity in CVs. Under inert atmosphere, both complexes showed one metal-based and two ligand-based reductions, similar to the complexes reported here. Catalytic current was observed at the second reduction for these systems, whereas catalysis begins in earnest at the third reduction with our system. However, the stability and substrate selectivity of the catalysts were not reported. Only a limited product analysis was done for the cobalt system, which had a ∼60% FE for formic acid production. This clearly suggests that this system follows a different catalytic mechanism than ours and the Fontecave systems where CO was the sole carbon-containing product.

As discussed previously, introducing steric bulk in pincer ligands can enforce mono-chelation, thereby avoiding the ligand dissociation step needed to access available coordination sites for substrate binding to the metal core. In addition, they can obstruct dimerization of reduced intermediates. Recently, electrocatalytic CO_2 reduction with cobalt and nickel complexes featuring modified dapa ligands were reported by Kang and Rochford, respectively. Mono-chelation was achieved by introducing diisopropyl groups in the ligand framework (Narayanan et al., 2016; Liu et al., 2018). The Co complex showed minimal reactivity toward CO_2 and was not studied further, whereas the Ni complex showed a good current response in CVs under CO_2. However, during bulk electrolysis, the Ni complex produced only a small amount of CO with nearly quantitative formation of H_2. Liu et al. (2018) hypothesized that catalysis could be improved by replacing one imino group with a pyridyl moiety. Their new NNN ligand has a redox-active bipyridine unit with extended π-conjugation and a sterically bulky imino group on one side. With this ligand, the corresponding cobalt complex shows metal- and ligand-based redox events under argon. Adding water to the system gave rise to new waves corresponding to a Co-hydride species, which was found to mediate formate production in CO_2-saturated solution. Consistent with DFT calculations, the reduced species in the presence of substrate can access two different pathways to generate both CO and formate, where formate is produced via a Co^{II}-H intermediate. Despite similarities between this ligand and the NNP ligand reported here, our $\mathbf{CoL_2^{2+}}$ complex has different product selectivity and CO was found to be the only $2e^-$ reduced C_1 product. This is likely due to a difference in hydricity of the Co^{II}-H intermediate formed in our case, in which CO_2 insertion into the metal-hydride to make a formato intermediate is not competitive with protonation to form H_2 (Thoi et al., 2013; Kang et al., 2015).

Examples of phosphine-based pincer-ligated 3d metal complexes are still scarce among CO_2 reduction electrocatalysts. Recently, a manganese tri-carbonyl complex with a symmetric PNP-pincer ligand was reported by the Richeson group. This complex shows an unusual coordination environment with a *mer*-$M(CO)_3$ motif rather than the usual *fac*-$M(CO)_3$ configuration (Rao et al., 2016). Moreover, this complex also triggers CO_2 reduction at its first reduction. Addition of H_2O as a weak proton source increased the current and lowered the catalytic overpotential, but also reduced substrate selectivity as HER activity was enhanced.

Pincer ligands with *N*-heterocylic carbene (NHC) donors have also been employed in CO_2 reduction. A nickel-based catalyst for CO_2 reduction supported by a mixed donor CNC-type ligand was reported by Sheng et al. (2015). This distorted square planner complex has a labile acetonitrile ligand at the fourth position and shows three irreversible reductions under N_2. Among them, the first reduction at −1.19 V (vs $Fc^{+/0}$) was assigned to the $Ni^{II/I}$ couple. Catalysis occurs at the most negative reduction in CO_2-saturated CH_3CN. Added water was found to enhance catalysis without compromising product selectivity. Myren et al. (2019) recently reported two manganese tricarbonyl complexes with similar CNC

pincer ligands which can reduce CO_2 to CO at the first reduction potential. Though the overpotential is large, these catalysts also exhibit high selectivity in the presence of a proton source.

Cope et al. (2017) replaced the pyridyl group of the Sun catalyst with an aryl donor to prepare a Ni complex ligated by an anionic CCC-pincer ligand. This more electron-rich ligand on nickel results in faster catalysis (30x TOF), at the expense of a higher overpotential, and produces a mixture of CO and formate. Electrocatalysis occurs at the first reduction with this catalyst and added water enhances CO_2 reduction and the rate of catalysis. Bulk electrolysis experiments confirmed that the catalyst is selective, producing CO and formate with an optimal FE of 81% for reduced carbon products. However, catalysis slows down after ∼1 h of electrolysis for unspecified reasons.

CONCLUSIONS

A rigid NNP-type pincer ligand and its mid-to-late first-row transition metal complexes have been synthesized. The ML_2^{2+} complexes reported here are the first examples of an asymmetric phosphine-substituted pincer ligand employed for electrocatalytic CO_2 reduction. Despite the steric bulk of the phenyl substituents on this ligand, the metal ions prefer to coordinate with two ligands to form pseudo-octahedral bis-chelated complexes. Electrochemical studies confirm that the cobalt complex is capable of catalyzing the electrochemical reduction of CO_2 to CO. However, catalytic activity is greatly limited by deleterious side reactions. We reason that the rigid NNP framework inhibits ligand dissociation from the reduced complex and, thus, impedes formation of the catalytically active species.

AUTHOR CONTRIBUTIONS

KT synthesized and characterized the catalysts, collected and analyzed data, and wrote the original draft. AI synthesized and characterized the catalysts and collected data. JJ conceptualized the experiments, analyzed data, supervised research activities, acquired funding, and revised the manuscript.

FUNDING

We thank the National Science Foundation for financial support through seed grant funding (OIA-1539035) and a CAREER Award (CHE-1848478). We are also grateful for start-up support from the University of Mississippi (UM).

ACKNOWLEDGMENTS

We thank Prof. Jared Delcamp (UM) for allowing us to use his gas chromatograph and automated flash chromatography system. We also thank Senthil Kumar Eswaramoorthy and Prof. Amala Dass (UM) for their support with high-resolution mass spectrometry.

SUPPLEMENTARY MATERIAL

The Supplementary Material for this article can be found online at: https://www.frontiersin.org/articles/10.3389/fchem.2019.00330/full#supplementary-material

REFERENCES

APEX2 (2009). *APEX2 (Version 2009.1)*. Madison, WI: Bruker Analytical X-ray Systems Inc.

Arana, C., Yan, S., Keshavarz,-K., M., Potts, K. T., and Abruna, H. D. (1992). Electrocatalytic reduction of carbon dioxide with iron, cobalt, and nickel complexes of terdentate ligands. *Inorganic Chem.* 31, 3680–3682. doi: 10.1021/ic00043a034

Bard, A. J., and Faulkner, L. R. (2001). *Electrochemical Methods: Fundamentals and Applications. 2nd Edn*. New York, NY: John Wiley and Sons.

Basu, D., Gilbert-Wilson, R., Gray, D. L., Rauchfuss, T. B., and Dash, A. K. (2018). Fe and Co complexes of rigidly planar phosphino-quinoline-pyridine ligands for catalytic hydrosilylation and dehydrogenative silylation. *Organometallics* 37, 2760–2768. doi: 10.1021/acs.organomet.8b00416

Bauer, G., and Hu, X. (2016). Recent developments of iron pincer complexes for catalytic applications. *Inorganic Chem. Front.* 3, 741–765. doi: 10.1039/C5QI00262A

Benito-Garagorri, D., and Kirchner, K. (2008). Modularly designed transition metal PNP and PCP pincer complexes based on aminophosphines: synthesis and catalytic applications. *Accounts Chem. Res.* 41, 201–213. doi: 10.1021/ar700129q

Benson, E., Kubiak, C. P., Sathrum, A. J., and Smieja, J. M. (2009). Electrocatalytic and homogeneous approaches to conversion of CO_2 to liquid fuels. *Chem. Soc. Rev.* 38, 89–99. doi: 10.1039/B804323J

Blunden, J., and Arndt, D. S. (2017). State of the climate in 2016. *Bull. Am. Meteorol. Soc.* 98, S1–S280. doi: 10.1175/2017BAMSStateoftheClimate.1

Chakraborty, S., Bhattacharya, P., Dai, H., and Guan, H. (2015). Nickel and iron pincer complexes as catalysts for the reduction of carbonyl compounds. *Accounts Chem. Res.* 48, 1995–2003. doi: 10.1021/acs.accounts.5b00055

Chen, L., Dulaney, H. A., Wilkins, B. O., Farmer, S., Zhang, Y., Fronczek, F. R., et al. (2018). High-spin enforcement in first-row metal complexes of a constrained polyaromatic ligand: synthesis, structure, and properties. *New J. Chem.* 42, 18667–18677. doi: 10.1039/C8NJ02072H

Chen, Z., Chen, C., Weinberg, D. R., Kang, P., Concepcion, J. J., Harrison, D. P., et al. (2011). Electrocatalytic reduction of CO_2 to CO by polypyridyl ruthenium complexes. *Chem. Commun.* 47, 12607–12609. doi: 10.1039/C1CC15071E

Chiericato, G., Arana, C. R., Casado, C., Cuadrado, I., and Abruña, H. D. (2000). Electrocatalytic reduction of carbon dioxide mediated by transition metal complexes with terdentate ligands derived from diacetylpyridine. *Inorganica Chim. Acta* 300–302, 32–42. doi: 10.1016/S0020-1693(99)00420-X

Cope, J. D., Liyanage, N. P., Kelley, P. J., Denny, J. A., Valente, E. J., Webster, C. E., et al. (2017). Electrocatalytic reduction of CO_2 with CCC-NHC pincer nickel complexes. *Chem. Commun.* 53, 9442–9445. doi: 10.1039/C6CC06537F

Elgrishi, N., Chambers, M. B., Artero, V., and Fontecave, M. (2014). Terpyridine complexes of first row transition metals and electrochemical reduction of CO_2 to CO. *Phys. Chem. Chem. Phys.* 16, 13635–13644. doi: 10.1039/C4CP00451E

Elgrishi, N., Chambers, M. B., and Fontecave, M. (2015). Turning it off! disfavouring hydrogen evolution to enhance selectivity for CO production during homogeneous CO_2 reduction by cobalt–terpyridine complexes. *Chem. Sci.* 6, 2522–2531. doi: 10.1039/C4SC03766A

Evans, D. F. (1959). 400. The determination of the paramagnetic susceptibility of substances in solution by nuclear magnetic resonance. *J. Chem. Soc.* 2003, 2003–2005. doi: 10.1039/JR9590002003

Francke, R., Schille, B., and Roemelt, M. (2018). Homogeneously catalyzed electroreduction of carbon dioxide—methods, mechanisms, and catalysts. *Chem. Rev.* 118, 4631–4701. doi: 10.1021/acs.chemrev.7b00459

Fuchs, P., Hess, U., Holst, H. H., and Lund, H. (1981). Electrochemical carboxylation of some heteroaromatic compounds. *Acta Chem. Scand. B* 35, 185–192.

Hamacher, C., Hurkes, N., Kaiser, A., Klein, A., and Schüren, A. (2009). Electrochemistry and spectroscopy of organometallic terpyridine nickel complexes. *Inorganic Chem.* 48, 9947–9951. doi: 10.1021/ic900753r

Hansen, J., Sato, M., Kharecha, P., Beerling, D., Berner, R., Masson-Delmotte, V., et al. (2008). Target atmospheric CO_2: where should humanity aim? *Open Atmos. Sci. J.* 2, 217–231. doi: 10.2174/1874282300802010217

Harris, C. M., Lockyer, T. N., Martin, R. L., Patil, H. R. H., and Sinn, E. (1969). Five- and six-coordinated complexes of cobalt(II) with 2,2′,2′-terpyridyl: unusual structure and magnetism. *Aust. J. Chem.* 22, 2105–2116. doi: 10.1071/ch9692105

Jiang, X., and Guan, D. (2016). Determinants of global CO_2 emissions growth. *Appl. Energy* 184, 1132–1141. doi: 10.1016/j.apenergy.2016.06.142

Kamitani, M., Kusaka, H., Toriyabe, T., and Yuge, H. (2018). Facile entry to iron complexes supported by quinoline-based PNN pincer ligand. *Bull. Chem. Soc. Jpn.* 91, 1429–1435. doi: 10.1246/bcsj.20180124

Kang, P., Chen, Z., Brookhart, M., and Meyer, T. J. (2015). Electrocatalytic reduction of carbon dioxide: let the molecules do the work. *Top. Catalysis* 58, 30–45. doi: 10.1007/s11244-014-0344-y

Lieske, L. E., Rheingold, A. L., and Machan, C. W. (2018). Electrochemical reduction of carbon dioxide with a molecular polypyridyl nickel complex. *Sustain. Energy Fuels* 2, 1269–1277. doi: 10.1039/c8se00027a

Lim, R. J., Xie, M., Sk, M. A., Lee, J.-M., Fisher, A., Wang, X., et al. (2014). A review on the electrochemical reduction of CO_2 in fuel cells, metal electrodes and molecular catalysts. *Catalysis Today* 233, 169–180. doi: 10.1016/j.cattod.2013.11.037

Liu, F. W., Bi, J., Sun, Y., Luo, S., and Kang, P. (2018). Cobalt Complex with redox-active imino bipyridyl ligand for electrocatalytic reduction of carbon dioxide to formate. *ChemSusChem* 11, 1656–1663. doi: 10.1002/cssc.201800136

Mao, L., Moriuchi, T., Sakurai, H., Fujii, H., and Hirao, T. (2005). New tridentate cyclometalated platinum(II) and palladium(II) complexes of N,2-diphenyl-8-quinolinamine: syntheses, crystal structures, and photophysical properties. *Tetrahedron Lett.* 46, 8419–8422. doi: 10.1016/j.tetlet.2005.09.120

Murata, M., and Buchwald, S. L. (2004). A general and efficient method for the palladium-catalyzed cross-coupling of thiols and secondary phosphines. *Tetrahedron* 60, 7397–7403. doi: 10.1016/j.tet.2004.05.044

Myren, T. H. T., Lilio, A. M., Huntzinger, C. G., Horstman, J. W., Stinson, T. A., Donadt, T. B., et al. (2019). Manganese N-heterocyclic carbene pincers for the electrocatalytic reduction of carbon dioxide. *Organometallics* 38, 1248–1253. doi: 10.1021/acs.organomet.8b00535

Narayanan, R., McKinnon, M., Reed, B. R., Ngo, K. T., Groysman, S., and Rochford, J. (2016). Ambiguous electrocatalytic CO_2 reduction behaviour of a nickel bis(aldimino)pyridine pincer complex. *Dalton Transac.* 45, 15285–15289. doi: 10.1039/C6DT01872F

Peris, E., and Crabtree, R. H. (2018). Key factors in pincer ligand design. *Chem. Soc. Rev.* 47, 1959–1968. doi: 10.1039/C7CS00693D

Qiao, J., Liu, Y., Hong, F., and Zhang, J. (2013). A review of catalysts for the electroreduction of carbon dioxide to produce low-carbon fuels. *Chem. Soc. Rev.* 43, 631–675. doi: 10.1039/C3CS60323G

Rao, G. K., Pell, W., Korobkov, I., and Richeson, D. (2016). Electrocatalytic reduction of CO_2 using Mn complexes with unconventional coordination environments. *Chem. Commun.* 52, 8010–8013. doi: 10.1039/C6CC03827A

Sheldrick, G. M. (1990). Phase annealing in SHELX-90: direct methods for larger structures. *Acta Crystallograph. Sect. A Foundations Crystallograph.* 46, 467–473. doi: 10.1107/S0108767390000277

Sheldrick, G. M. (2000). *SADABS (Version 2.03)*. Madison, WI: Bruker Analytical X-ray Systems Inc.

Sheldrick, G. M. (2008). A short history of SHELX. *Acta Crystallograph. Section A Foundations Crystallograph.* 64, 112–122. doi: 10.1107/S0108767307043930

Sheldrick, G. M. (2014). *SHELXL-2014/7: Program for Crystal Structure Determination*. Göttingen: University of Göttingen.

Sheng, M., Jiang, N., Gustafson, S., You, B., Ess, D. H., and Sun, Y. (2015). A nickel complex with a biscarbene pincer-type ligand shows high electrocatalytic reduction of CO_2 over H_2O. *Dalton Transac.* 44, 16247–16250. doi: 10.1039/C5DT02916C

Su, X., McCardle, K. M., Panetier, J. A., and Jurss, J. W. (2018). Electrocatalytic CO_2 reduction with Nickel complexes supported by tunable bipyridyl-N-heterocyclic carbene donors: understanding redox-active macrocycles. *Chem. Commun.* 54, 3351–3354. doi: 10.1039/C8CC00266E

Therrien, J. A., Wolf, M. O., and Patrick, B. O. (2018). Synthesis and comparison of nickel, palladium, and platinum bis(N-heterocyclic carbene) pincer complexes for electrocatalytic CO_2 reduction. *Dalton Transac.* 47, 1827–1840. doi: 10.1039/C7DT04089J

Thoi, V. S., Sun, Y., Long, J. R., and Chang, C. J. (2013). Complexes of earth-abundant metals for catalytic electrochemical hydrogen generation under aqueous conditions. *Chem. Soc. Rev.* 42, 2388–2400. doi: 10.1039/C2CS35272A

van der Vlugt, J. I. (2012). Cooperative catalysis with first-row late transition metals. *Eur. J. Inorganic Chem.* 2012, 363–375. doi: 10.1002/ejic.201100752

van der Vlugt, J. I., and Reek, J. N. (2009). Neutral tridentate PNP ligands and their hybrid analogues: versatile non-innocent scaffolds for homogeneous catalysis. *Angew. Chem. Int. Ed.* 48, 8832–8846. doi: 10.1002/anie.200903193

Wickramasinghe, L. D., Zhou, R., Zong, R., Vo, P., Gagnon, K. J., and Thummel, R. P. (2015). Iron complexes of square planar tetradentate polypyridyl-type ligands as catalysts for water oxidation. *J. Am. Chem. Soc.* 137, 13260–13263. doi: 10.1021/jacs.5b08856

Yang, W., Sinha Roy, S., Pitts, W. C., Nelson, R. L., Fronczek, F. R., and Jurss, J. W. (2018). Electrocatalytic CO_2 reduction with Cis and Trans conformers of a rigid dinuclear rhenium complex: comparing the monometallic and cooperative bimetallic pathways. *Inorganic Chem.* 57, 9564–9575. doi: 10.1021/acs.inorgchem.8b01775

Younus, H. A., Ahmad, N., Su, W., and Verpoort, F. (2014). Ruthenium pincer complexes: ligand design and complex synthesis. *Coordination Chem. Rev.* 276, 112–152. doi: 10.1016/j.ccr.2014.06.016

Zell, T., Langer, R., Iron, M. A., Konstantinovski, L., Shimon, L. J., Diskin-Posner, Y., et al. (2013). Synthesis, structures, and dearomatization by deprotonation of iron complexes featuring bipyridine-based PNN pincer ligands. *Inorganic Chem.* 52, 9636–9649. doi: 10.1021/ic401432m

Zhang, D., Zhang, Y., Hou, W., Guan, Z., and Huang, Z. (2017). Phosphine-iminoquinoline iron complexes for ethylene polymerization and copolymerization. *Organometallics* 36, 3758–3764. doi: 10.1021/acs.organomet.7b00537

Conflict of Interest Statement: The authors declare that the research was conducted in the absence of any commercial or financial relationships that could be construed as a potential conflict of interest.

Copyright © 2019 Talukdar, Issa and Jurss. This is an open-access article distributed under the terms of the Creative Commons Attribution License (CC BY). The use, distribution or reproduction in other forums is permitted, provided the original author(s) and the copyright owner(s) are credited and that the original publication in this journal is cited, in accordance with accepted academic practice. No use, distribution or reproduction is permitted which does not comply with these terms.

frontiers in Chemistry

ORIGINAL RESEARCH
published: 22 May 2019
doi: 10.3389/fchem.2019.00371

Improved Conditions for the Visible-Light Driven Hydrocarboxylation by Rh(I) and Photoredox Dual Catalysts Based on the Mechanistic Analyses

*Kei Murata†, Nobutsugu Numasawa, Katsuya Shimomaki, Jun Takaya and Nobuharu Iwasawa**

Department of Chemistry, Tokyo Institute of Technology, Tokyo, Japan

OPEN ACCESS

Edited by:
Soumyajit Roy,
Indian Institute of Science Education and Research Kolkata, India

Reviewed by:
Munetaka Akita,
Tokyo Institute of Technology, Japan
Yang Yang,
University of Central Florida, United States

***Correspondence:**
Nobuharu Iwasawa
niwasawa@chem.titech.ac.jp

†Present Address:
Kei Murata,
Institute of Industrial Science, The University of Tokyo, Tokyo, Japan

Specialty section:
This article was submitted to Inorganic Chemistry, a section of the journal Frontiers in Chemistry

Received: *07 March 2019*
Accepted: *06 May 2019*
Published: *22 May 2019*

Citation:
Murata K, Numasawa N, Shimomaki K, Takaya J and Iwasawa N (2019) Improved Conditions for the Visible-Light Driven Hydrocarboxylation by Rh(I) and Photoredox Dual Catalysts Based on the Mechanistic Analyses. Front. Chem. 7:371. doi: 10.3389/fchem.2019.00371

The improved catalytic conditions and detailed reaction mechanism of the visible-light driven hydrocarboxylation of alkenes with CO_2 by the Rh(I) and photoredox dual catalysts were investigated. The use of the benzimidazoline derivative, BI(OH)H, as a sacrificial electron donor was found to increase the yield of the hydrocarboxylated product by accelerating the reduction process. In addition, the incorporation of the cyclometalated Ir(III) complex as a second photosensitizer with $[Ru(bpy)_3]^{2+}$ photosensitizer also resulted in the promotion of the reduction process, supporting that the catalytic cycle includes two photochemical elementary processes: photoinduced electron and energy transfers.

Keywords: carboxylation, CO_2 fixation, photoredox catalyst, rhodium catalyst, visible light

INTRODUCTION

Catalytic hydrocarboxylation of unsaturated hydrocarbons with CO_2 is one of the promising methods for the CO_2 fixation (Luan and Ye, 2018; Yan et al., 2018; for recent reviews, see: Tortajada et al., 2018). The most common strategy to accomplish the hydrocarboxylation is to utilize a metal hydride complex as an active species. However, in these reactions, more than a stoichiometric amount of highly active, metallic reductants such as $ZnEt_2$, $AlEt_3$, or hydrosilanes are usually required to promote the reduction process in the catalytic cycle (Takaya and Iwasawa, 2008; Williams et al., 2008; Fujihara et al., 2011; Li et al., 2011; Hayashi et al., 2015; Wang et al., 2015; Zhu et al., 2015; Kawashima et al., 2016). In order to realize a more efficient and environmentally-friendly system, the reaction which necessitates just a catalytic amount of metallic reagents is highly desirable. Meanwhile, the photochemical reduction process has been widely employed in the field of artificial photosynthesis, such as photocatalytic hydrogen generations (for review, see Esswein and Nocera, 2007) and CO_2 reductions (for reviews, see Morris et al., 2009; Doherty et al., 2010; Takeda and Ishitani, 2010) in homogeneous systems. In these reactions, transition-metal catalysts are combined with redox photosensitizers and sacrificial electron donors to drive the multielectron transfer processes under visible-light irradiation. When the electron transfer is accompanied by the

Abbreviations: bpy, 2,2′-bipyridyl; dtbbpy, 4,4′-di-*tert*-butyl-2,2′-bipyridyl; bpz, 2,2′-bipyrazine; ppy, 2-phenylpyridiine; dF(CF_3)ppy, 3,5-difluoro-2-[5-(trifluoromethyl)-2-pyridinyl]phenyl; SCE, saturated calomel electrode; BIH, 1,3-dimethyl-2-phenyl-2,3-dihydro-1*H*-benzo[*d*]imidazole; BI(OH)H, 1,3-dimethyl-2-(*o*-hydroxyphenyl)-2,3-dihydro-1*H*-benzo[*d*]imidazole; SED, sacrificial electron donor; PC, photoredox catalyst; SCE, saturated calomel electrode; vt, virtual coupling. For the abbreviations of the rhodium complexes, see **Supplementary Table 1**.

proton transfer, metal hydrides can act as an active species in the catalytic cycle (for reviews, see Stoll et al., 2015; Adams et al., 2018). Although transition-metal/photoredox dual catalysis has been actively studied in the field of organic synthesis (for recent reviews, see Fabry and Rueping, 2016; Skubi et al., 2016; Twilton et al., 2017), few examples have been reported for catalytic organic transformations driven by photochemically-generated metal hydrides (Ghosh et al., 2015).

We recently developed the visible-light driven hydrocarboxylation of alkenes with CO_2 for the first time by means of the photochemical generation of Rh(I) hydride species (Murata et al., 2017). 4-Cyanostyrene was transformed to the branched hydrocarboxylated product by using a Rh(I) hydride or chloride complex as a carboxylation catalyst, $[Ru(bpy)_3]^{2+}$ as a photoredox catalyst, $^{i}Pr_2NEt$ as a sacrificial electron donor, with visible-light irradiation under CO_2 atmosphere at room temperature (**Figure 1**). The photoredox catalysis made it possible to take electrons from tertiary amines and drive the reduction process without using a metallic reductant. Since then, several photoredox-catalyzed hydrocarboxylation reactions of unsaturated hydrocarbons with CO_2 have been reported by other groups (Seo et al., 2017b; Hou et al., 2018b; Meng et al., 2018). Concomitantly, difunctionalizations of alkenes such as thiocarboxylation (Ye et al., 2017), carbocarboxylation and silylcarboxylation (Yatham et al., 2017; Hou et al., 2018a) have also been developed by incorporating an appropriate radical precursor with CO_2. Furthermore, in addition to unsaturated hydrocarbons, various substrates such as aryl and alkyl halides (Meng et al., 2017; Shimomaki et al., 2017), amines (Seo et al., 2017a), imines and enamides (Fan et al., 2018; Ju et al., 2018) have been carboxylated with CO_2 by photoredox catalysis so far (for review, see Yeung, 2019). These examples demonstrated wide applicability of the photoinduced electron transfer to carboxylation reactions.

On the basis of our previous experiments, the reaction mechanism of the hydrocarboxylation by Rh(I) and photoredox dual catalysts was proposed as shown in **Figure 2**. Initially, the hydrometallation of a styrene derivative by Rh(I) hydride species **A** gave the Rh(I) benzyl species **B** (i), and the visible-light promoted nucleophilic addition to CO_2 afforded the Rh(I) carboxylate species **C** (ii). Then, the reductive quenching cycle of $[Ru(bpy)_3]^{2+}$ with $^{i}Pr_2NEt$ mediated 2-electron, 2-proton transfers afforded the Rh(III) dihydride carboxylate species **D** (iii), followed by the base-promoted liberation of the carboxylated product to regenerate the active species **A** (iv). Although this reaction demonstrated fundamental aspects of the application of photochemical reduction processes to catalytic carboxylation reactions, there still has been room for improvement from the viewpoint of the applicability in organic synthesis: (i) The efficiency of the reaction was not very high. Good yield was obtained with 4-cyanostyrene and moderate yields were obtained with several other substrates. (ii) A large excess amount of a tertiary amine and long reaction time (>24 h) were necessary for completion of the reaction even for the reactive substrates, (iii) A significant amount of the hydrogenated product was produced as a byproduct. In order to resolve these problems, further screenings of the catalytic conditions were desired.

Herein, we explored the improved conditions of the visible-light driven hydrocarboxylation, and the catalytic efficiency was analyzed based on the detailed mechanistic study with a series of stoichiometric reactions of the rhodium intermediates. Through the investigation, the hydrocarboxylation was successfully improved by the alteration of the sacrificial electron donor or the incorporation of the second photosensitizer. The mechanistic study suggested that the promotion of the photochemical reduction process was crucial for the enhancement of the catalytic reaction.

RESULTS AND DISCUSSION

Screening of Reaction Conditions

On the basis of our previous experiments in terms of the screening of catalytic conditions and the observation of the reaction intermediates under the catalytic conditions, the followings were demonstrated: (i) As a carboxylation catalyst, Rh(I) hydride or chloro complexes with triarylphosphines were applicable. In particular, the μ-chloro bridged Rh(I) dimer $[Rh(P(4\text{-}CF_3C_6H_4)_3)_2Cl]_2$ (**4**) was the most effective catalyst. (ii) When **4** was employed under the catalytic conditions, the resting state was the corresponding Rh(I) carboxylate complex, indicating that the rate-determining step was its transformation to the Rh(I) hydride species. This result suggested that the promotion of the reduction process was crucial for the improvement of the catalytic reaction. According to these considerations, the reaction conditions were screened in terms of the photoredox catalyst and sacrificial electron donor,

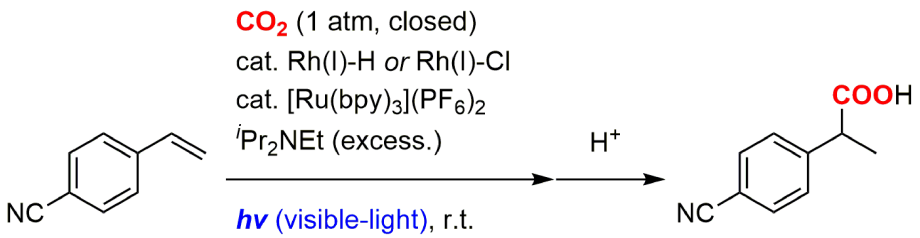

FIGURE 1 | The photocatalytic hydrocarboxylation of 4-cyanostyrene.

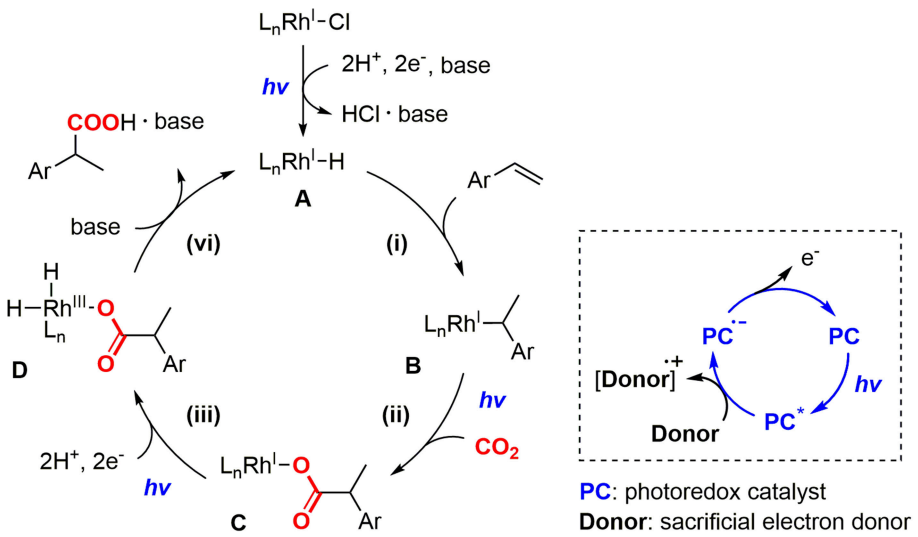

FIGURE 2 | The proposed reaction mechanism of the photocatalytic hydrocarboxylation with the schematic representation of the reductive quenching cycle of a photoredox catalyst.

which would have taken an important part in the reductive quenching cycle.

Photoredox Catalyst

Photoredox catalysts were initially screened by performing the reaction of 4-cyanostyrene (**1a**) in a mixture of 2.0 mol% of a photosensitizer, 3.5 mol% of **4** and 4.0 equiv. of $^{i}Pr_2NEt$ under a CO_2 atmosphere at room temperature (**Table 1**). In the case of $[Ru(bpy)_3](PF_6)_2$ ($E_{1/2}^{II^*/I} = +0.77$ V, $E_{1/2}^{II/I} = -1.33$ V vs. SCE) (Kalyanasundaram, 1982) as a photoredox catalyst, the hydrocarboxylated (**2a**) and hydrogenated (**3a**) products were obtained in 54 and 25% yields, respectively, after visible-light irradiation for 24 h (**Table 1**, entry 1). A small amount of polymerized product of **1a** was also produced as byproduct. Though no other photosensitizers overcame this activity, the yield of **2a** was found to be strongly dependent on the photoredox catalyst. For instance, when $[Ru(bpz)_3](PF_6)_2$ ($E_{1/2}^{II^*/I} = +1.45$ V, $E_{1/2}^{II/I} = -0.80$ V vs. SCE) (Crutchley and Lever, 1980) or *fac*-$Ir(ppy)_3$ ($E_{1/2}^{III^*/II} = +0.31$ V, $E_{1/2}^{III/II} = -2.19$ V vs. SCE) (Flamigni et al., 2007) was employed, the yields substantially decreased compared to $[Ru(bpy)_3](PF_6)_2$ (**Table 1**, entries 3, 6). On the other hand, when using $[Ir(dF(CF_3)ppy)_2(dtbbpy)](PF_6)$ ($E_{1/2}^{III^*/II} = +1.21$ V, $E_{1/2}^{III/II} = -1.37$ V vs. SCE) or $[Ir(ppy)_2(dtbbpy)](PF_6)$ ($E_{1/2}^{III^*/II} = +0.66$ V, $E_{1/2}^{III/II} = -1.51$ V vs. SCE) (Lowry et al., 2005), moderate yields were obtained (**Table 1**, entry 4, 5). These results indicated that both sufficient oxidizing ability of the excited state and reducing ability of the one-electron reduced species are at least necessary for the photosensitizer. However, the detailed dependency was not simple, as other factors such as absorption properties, excited-state energies and photochemical stability of the photosensitizer could also affect the catalytic performances. Meanwhile, the screenings of additives with $[Ru(bpy)_3]^{2+}$ photosensitizer demonstrated that the addition of Cs_2CO_3 as an inorganic base significantly improved the yield of the hydrocarboxylated product by suppressing the formation of the hydrogenated byproduct: the yield of **2a** increased to 67% while the yield of **3a** decreased to 1% (**Table 1**, entry 11).

Sacrificial Electron Donor and Additives

Sacrificial electron donors were then screened in the presence of an excess amount of Cs_2CO_3. In order to highlight the reactivity, a less reactive alkene, 3,5-bis(trifluoromethyl)styrene (**1b**), was used as a substrate. The reactions of **1b** were performed in a mixture of 2.0 mol% of $[Ru(bpy)_3](PF_6)_2$, 3.5 mol% of **4**, 4.0 equiv. of sacrificial electron donor and 1.2 equiv. of Cs_2CO_3 under a CO_2 atmosphere at room temperature (**Table 2**). When $^{i}Pr_2NEt$ was employed as a sacrificial electron donor, 32% yield of the hydrocarboxylated product (**2b**) and a trace amount of the hydrogenated product (**3b**) were obtained after visible-light irradiation for 12 h (**Table 2**, entry 1). Although the use of TEOA (triethanolamine) slightly increased the yield of **2b**, the formation of **3b** became pronounced probably due to the increase of proton concentration (**Table 2**, entry 3). On the other hand, the use of BI(OH)H (1,3-dimethyl-2-(*o*-hydroxyphenyl)-2,3-dihydro-1*H*-benzo[*d*]imidazole) successfully accelerated the hydrocarboxylation and increased the yield of **2b** considerably with maintaining the low yield of **3b** (**Table 2**, entry 5). Furthermore, the incorporation of BI(OH)H made it possible to reduce the amounts of the photoredox catalyst and the sacrificial electron donor: the use of only 1.0 mol% of $[Ru(bpy)_3](PF_6)_2$ and 2.0 equiv. of BI(OH)H gave 70% yield of **2b** (**Table 2**, entry 7). When the reaction was performed under an Ar atmosphere in the presence of Cs_2CO_3, no hydrocarboxylated product **2b** was obtained. This result confirmed that the carbonate did not work as a source of CO_2 in the present reaction (**Table 2**, entry 9). BI(OH)H has been known to work as a 2-electron, 2-proton

TABLE 1 | Optimization of the reaction conditions of the hydrocarboxylation of 4-cyanostyrene.

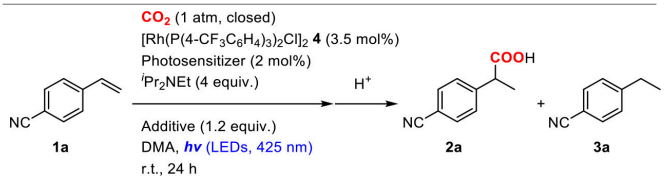

Entry	Photosensitizer	Additive	Conv. /%	Yield/%	
				2a[a]	3a[b]
1	$[Ru(bpy)_3](PF_6)_2$	–	95	54	25
2	$[Ru(dmbpy)_3](PF_6)_2$	–	92	37	14
3	$[Ru(bpz)_3](PF_6)_2$	–	24	n.d.	n.d.
4	$[Ir(dF(CF_3)ppy)_2(dtbpy)](PF_6)$	–	>99	44	8
5	$[Ir(ppy)_2(dtbbpy)](PF_6)$	–	>99	27	trace
6	*fac*-$Ir(ppy)_3$	–	98	17	2
7[c]	$[Ru(bpy)_3](PF_6)_2$	–	72	33	8
8[d]	$[Ru(bpy)_3](PF_6)_2$	–	95	46	23
9	$[Ru(bpy)_3](PF_6)_2$	Na_2CO_3	89	43	trace
10	$[Ru(bpy)_3](PF_6)_2$	K_2CO_3	87	46	trace
11	$[Ru(bpy)_3](PF_6)_2$	Cs_2CO_3	70	67	1

[a] *NMR yield.*
[b] *GC yield.*
[c] *1 mol% of $[Ru(bpy)3](PF_6)_2$.*
[d] *5 mol% of $[Ru(bpy)3](PF_6)_2$.*

TABLE 2 | Optimization of the reaction conditions of the hydrocarboxylation of 3,5-bis(trifluoromethyl)styrene.

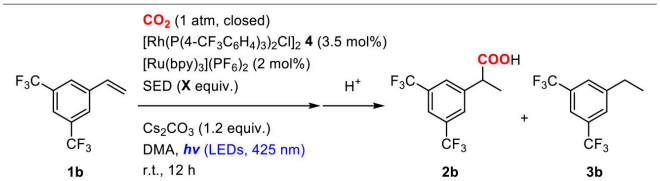

Entry	SED	X	Conv. /%	Yield/%	
				2b[a]	3b[b]
1	$^iPr_2NEt$	4.0	52	32	Trace
2	Et_3N	4.0	16	4	n.d.
3	TEOA	4.0	>99	42	26
4	BIH	4.0	47	27	5
5	BI(OH)H	4.0	>99	63	5
6	BI(OH)H	2.0	>99	67	9
7[c]	BI(OH)H	2.0	>99	70[e]	3
8[c]	BI(OH)H	1.2	79	63	Trace
9[d]	BI(OH)H	2.0	>99	n.d.	34

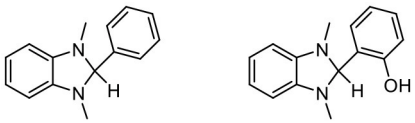

BIH BI(OH)H

[a] *NMR yield.*
[b] *GC yield.*
[c] *1 mol% of $[Ru(bpy)_3](PF_6)_2$ was used.*
[d] *Without CO_2, under an Ar atmosphere.*
[e] *Isolated yield was 63%.*

donor with high reducing ability in redox photosensitizing reactions (Hasegawa et al., 2005, 2006; Tamaki et al., 2015). Since a tertiary amine contributed to the reductive quenching cycle of $[Ru(bpy)_3]^{2+}$, the increase in the yield of **2b** was attributed to the promotion of the reduction process of the Rh(I) carboxylate species, which was the rate-determining step in the hydrocarboxylation. These results indicated that the redox property of a sacrificial electron donor is one of the crucial factors for the efficient promotion of the reaction.

Generality of the Hydrocarboxylation Under the Improved Conditions

Based on the improved conditions using **1b** as discussed above, the generality of the hydrocarboxylation was examined using various alkene substrates. 1.0 mol% of $[Ru(bpy)_3](PF_6)_2$, 3.5 mol% of **4**, 2.0 equiv. of BI(OH)H and 1.2 equiv. of Cs_2CO_3 were employed for the hydrocarboxylation (**Table 3**). In the cases of using styrenes with an electron-withdrawing group such as **1a** and 4-methoxycarbonyl styrene (**1d**), the reaction was almost completed after irradiation for 12 h, and the yields of the corresponding hydrocarboxylated products were significantly improved compared with those obtained in the previous conditions where 2.0 mol% of $[Ru(bpy)_3](PF_6)_2$ and 4.0 equiv. of $^iPr_2NEt$ were employed. Moreover, 4-trifluoromethyl styrene (**1c**) and non-substituted styrene (**1e**), which exhibited quite low reactivities in the previous conditions, did react to afford significant amounts of the corresponding hydrocarboxylated products though the yields were still not sufficiently high. The yields of the hydrocarboxylated products were also improved in the case of alkyl acrylates (**1f** and **1g**). Consequently, the introduction of BI(OH)H electron donor with Cs_2CO_3 base successfully resulted in the increase in the yields of the present hydrocarboxylation reaction.

Mechanistic Study

In order to reveal the reaction mechanism of the photocatalytic hydrocarboxylation, the stoichiometric reactions of the possible rhodium intermediates, which corresponded to each elementary step in the proposed catalytic cycle, were examined.

Rh Hydride Formation

Initially, the Rh(I) hydride formation step was investigated using $Rh(PPh_3)_2(OAc)$ (**5**) as a model complex of the Rh(I) carboxylate intermediate. The DMA solution of **5** was irradiated by visible-light in the presence of a catalytic amount of $[Ru(bpy)_3](PF_6)_2$, an excess amount of $^iPr_2NEt$ and 1.5 equivalent of PPh_3. After visible-light irradiation for 6 h, the Rh(I) monohydride complex, $Rh(PPh)_3H$ (**6**) was successfully obtained in 57% yield with the recovery of ca. 30% of **5**

TABLE 3 | Generality of the hydrocarboxylation of alkenes[a].

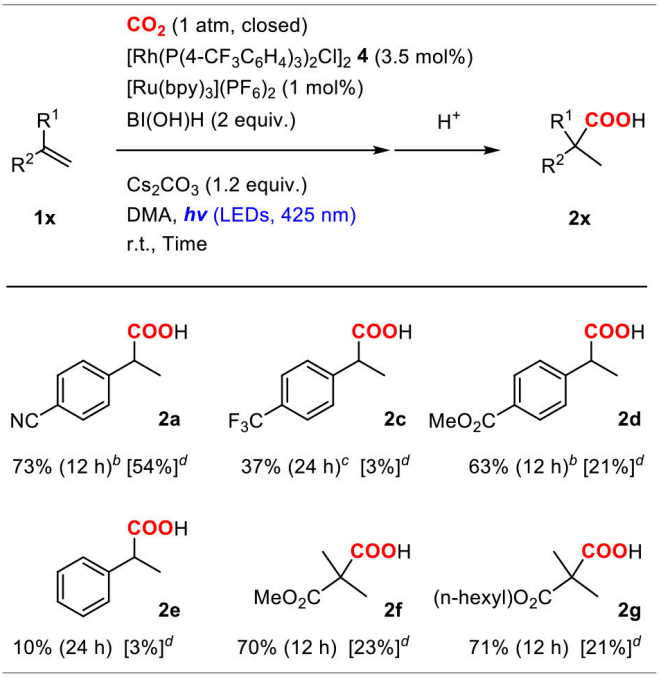

[a] *NMR yield.*
[b] *Isolated yield after methyl esterification: 57% (**2a**), 59% (**2d**).*
[c] *With 2 mol% of [Ru(bpy)3](PF6)2.*
[d] *Yield obtained by the previous conditions with [Ru(bpy)3](PF6)2 (2 mol%), **4** (3.5 mol%).*
[i] *$^iPr_2NEt$ (4 equiv.) and irradiation for 24 h.*

(based on ^{1}H NMR using an internal standard) (**Figure 3A**; **Supplementary Figure 1**). Control experiments demonstrated that $[Ru(bpy)_3](PF_6)_2$, $^iPr_2NEt$, and visible-light were all essential for the transformation. Since hydrogen evolution was not evident during the reaction, the contribution of gaseous hydrogen was excluded. Thus, this transformation was considered to proceed via (i) stepwise 2-electron, 2-proton transfers from the tertiary amine by the photoredox catalysis to give the Rh(III) dihydride carboxylate (**7**), and (ii) the base-assisted elimination of the carboxylic acid to give **6**. In terms of step (i), the similar mechanisms have been proposed in photocatalytic hydrogen generation systems by a Rh(I) catalyst (Stoll et al., 2015). The initial single electron transfer to the protonated form of **5** would give the Rh(II) carboxylate monohydride, and the following electron and proton transfers or disproportionation of the two Rh(II) hydride species would give **7** (**Figure 4**). The presence of the Rh(III) dihydride intermediate was also supported by the fact that $Rh(PCy_3)_2(OAc)$ (**5′**) was transformed to $Rh(PCy_3)_2(OAc)(H)_2$ (**7′**) almost quantitatively under the similar conditions although the reaction was relatively slow (**Figure 3B**; **Supplementary Figure 2**). In this case, PCy_3 ligands with strong σ-donation were considered to stabilize the Rh(III) dihydride intermediate to inhibit the following elimination reaction.

In order to confirm the carboxylic acid elimination step (ii), the reactivity of **7** was investigated in the presence of base. **7** was alternatively synthesized by the hydrogenation of **5** with H_2, and was treated with an excess amount of $^iPr_2NEt$ in the presence of PPh_3 in C_6D_6. The reaction readily gave a mixture of **7** and **6** with liberation of $[^iPr_2NHEt]^+[CH_3COO]^-$. Furthermore, addition of a small excess amount of $[^iPr_2NHEt]^+[CH_3COO]^-$ to the C_6D_6 solution of **6** resulted in the quantitative formation of **7**. These results demonstrated that **7** was in equilibrium with **6** in the presence of $^iPr_2NEt$ and PPh_3 (**Figure 5**). When the treatment of **7** with $^iPr_2NEt$ was similarly conducted in DMA, **6** was detected as a sole rhodium species in the reaction mixture, indicating that the equilibrium was almost completely shifted to the product side owing to the solvent effect of DMA.

The possible mechanisms for generation of the hydrogenated product were (i) 2-electron, 2-proton transfers to the Rh(I) benzyl intermediate by the photoredox catalysis to give Rh(III) benzyl dihydride intermediate, which would undergo reductive elimination of the hydrogenated product, and (ii) the alkene insertion to the Rh(III) dihydride intermediate and the successive reductive elimination. Both pathways could be inhibited by lowering proton concentrations, as proton transfers would become inefficient in the former, and the competing carboxylic acid elimination from the dihydride complex would be promoted in the latter. Therefore, the inhibition of the hydrogenated product formation by the addition of Cs_2CO_3 was attributed to the decrease of the proton concentration in the catalytic system.

The photochemical formation of Rh(I) monohydride species was also feasible by using Rh(I) chloride complex as a Rh(I) source. It was demonstrated by the fact that Wilkinson's type complex $Rh(PPh_3)_3Cl$ was converted to $Rh(PPh)_3H$ (**6**) by visible-light irradiation in the presence of a catalytic amount of $[Ru(bpy)_3](PF_6)_2$ and an excess amount of $^iPr_2NEt$. Therefore, the Rh(I) chloride complex was confirmed to work as a precursor of the Rh(I) hydride active species.

Hydrometalation and Carboxylation

Since the Rh(I) monohydride species was successfully generated from the Rh(I) carboxylate species by photoredox catalysis, the hydrometallation and subsequent carboxylation processes were then investigated to complete the catalytic cycle. Treatment of $Rh(PPh)_3H$ (**6**) with an excess amount of **1a** at room temperature readily formed the Rh(I) benzyl species, $Rh(PPh_3)_2(\eta^3\text{-}CHCH_3(4\text{-}CNC_6H_4))$ (**8**), almost quantitatively with the liberation of a PPh_3 ligand (**Figure 6**i). The benzyl ligand in **8** was found to possess η^3-coordination to the Rh(I) center based on NMR spectroscopic data (Werner et al., 1994). However, the attempt for isolation of **8** was not successful due to the presence of an equilibrium with **6**. Therefore, *in situ* generated **8** was directly used for the carboxylation step.

To investigate the carboxylation process with CO_2, a DMA solution of a 1:1 mixture of *in-situ* generated **8** and PPh_3 was exposed to the atmospheric pressure of CO_2 under various conditions. The carboxylation did not proceed under dark even by heating, which was against our expectations based on the general reactivity of organorhodium(I) complexes with CO_2 (Ukai et al., 2006; Mizuno et al., 2011; Suga et al., 2014; Kawashima et al., 2016). Quite interestingly, when the mixture was irradiated by visible-light for 30 min in the presence of 30 mol% of $[Ru(bpy)_3](PF_6)_2$, **8** was successfully converted to

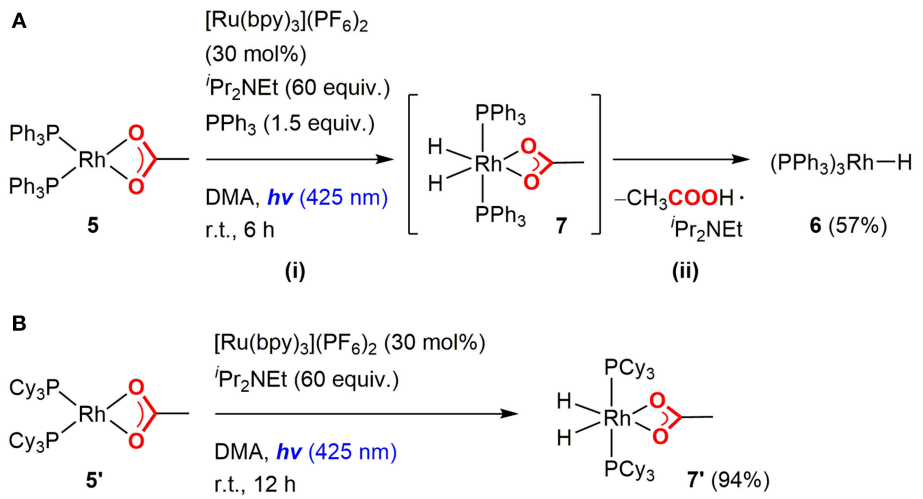

FIGURE 3 | Rh hydride formation from the Rh(I) acetate complexes with **(A)** triphenylphosphines and **(B)** tricyclohexylphosphines.

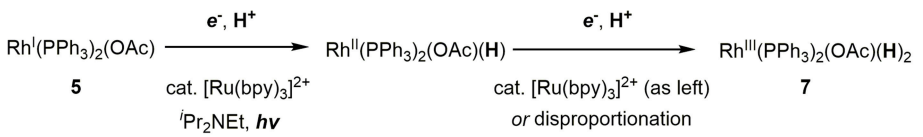

FIGURE 4 | Proposed mechanism for the formation of the Rh(III) dihydride complex.

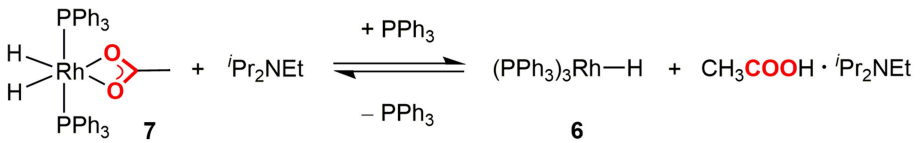

FIGURE 5 | Equilibrium between the Rh(III) dihydride and Rh(I) monohydride complexes.

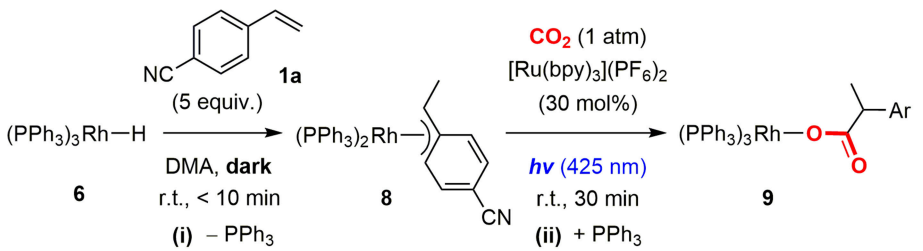

FIGURE 6 | Hydrometallation of Rh(I) hydride complex and successive carboxylation of the Rh(I) π-benzyl complex with CO_2.

the Rh(I) carboxylate complex, $Rh(PPh_3)_3(\eta^1\text{-}O_2CCHCH_3(4\text{-}CNC_6H_4))$ (**9**), almost quantitatively (**Figure 6**ii). $^{31}P\{^1H\}$ NMR spectroscopy confirmed the clean formation of **9**: a pair of the doublet of doublet signals attributed to **8** completely disappeared with the PPh_3 signal, and the doublet of doublet and doublet of triplet signals attributed to **9** appeared in 2: 1 ratio by visible-light irradiation (**Figure 7**). The control experiments demonstrated that CO_2, $[Ru(bpy)_3](PF_6)_2$ and visible-light were all essential for the carboxylation, suggesting that the nucleophilic addition of **8** to CO_2 was facilitated by the photosensitization of $[Ru(bpy)_3]^{2+}$. The luminescence quenching experiment demonstrated that the excited state of $[Ru(bpy)_3]^{2+}$ was effectively quenched by **8** (**Figure 8**). The quenching constant was determined to be $K_q = 2.07 \times 10^3$, which was much larger than that by $^iPr_2NEt$ ($K_q =$

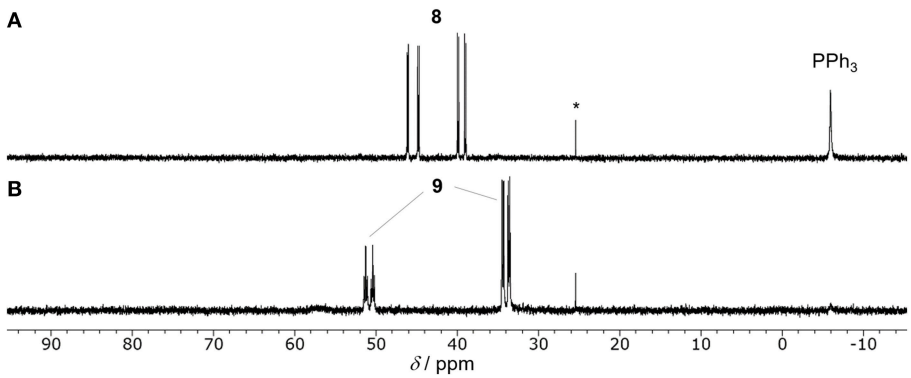

FIGURE 7 | $^{31}P\{^1H\}$ NMR spectra (202 MHz, DMA, −15°C) of the reactions of **8** under CO_2 atmosphere in the presence of $[Ru(bpy)_3](PF_6)_2$ (30 mol%) **(A)** after kept in dark, **(B)** after visible-light irradiation ($\lambda_{irr.}$ = 425 nm) for 30 min. *(O=)PPh_3.

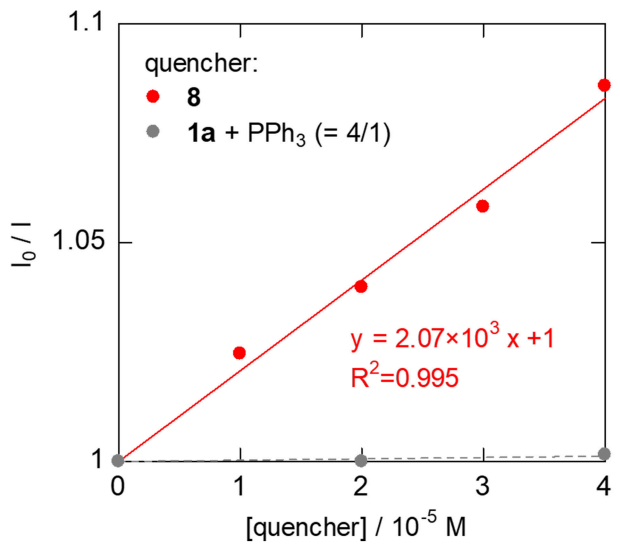

FIGURE 8 | Luminescent quenching experiments of $[Ru(bpy)_3]^{2+}$ (1.0×10^{-5} M, deaerated DMF, r.t., $\lambda_{ex.}$ = 450 nm). **8** was generated *in situ* by the addition of 5 equiv. of **1a** to the DMF solution of **6**.

1.56×10^2, **Supplementary Figure 3A**). This result indicates that either photoinduced electron transfer or triplet-triplet energy transfer to **8** contributed to the quenching (Campagna et al., 2007; Arias-Rotondo and McCusker, 2016; Strieth-Kalthoff et al., 2018). However, the photoinduced electron transfer mechanism was unlikely in this case since (i) the carboxylation of **8** proceeded with a catalytic amount of $[Ru(bpy)_3](PF_6)_2$ even in the absence of the sacrificial electron donor, and (ii) the cyclic voltammogram of **8** showed no significant redox peak within the window where the oxidative quenching of $[Ru(bpy)_3]^{2+}$ was possible. Therefore, the photoinduced triplet-triplet energy transfer from the excited $[Ru(bpy)_3]^{2+}$ to **8** was considered to be the most likely process in this carboxylation process. Although not very common, several examples on the photocatalytic organic transformations mediated by the triplet-triplet energy transfer were previously reported (Ikezawa et al., 1986; Osawa et al., 2001; Islangulov and Castellano, 2006; Lu and Yoon, 2012; Farney and Yoon, 2014).

In order to investigate the detailed effect of the photoinduced energy transfer, the electronic structure analyses were performed in terms of the ground (S_0) and the lowest excited triplet (T_1) states of **8** based on DFT/TD-DFT methods. The calculated energy level of the T_1 state of **8** (1.07 eV, based on the comparison between the S_0 and T_1 optimized geometries) was much lower than that of $[Ru(bpy)_3]^{2+}$ (2.17 eV), indicating that the triplet-triplet energy transfer from the excited $[Ru(bpy)_3]^{2+}$ to **8** was feasible. In terms of the optimized structures, a notable difference was found on the coordination manner of the benzyl ligand between the S_0 and T_1 geometries. In the S_0 optimized structure, the η^3-coodination of the benzyl ligand was represented by the similar three Rh-C distances, which coincided with the results of the ^{1}H NMR observation (**Figure 9A**; **Table 4**). On the other hand, in the T_1 optimized structure, while the Rh-C1 (benzyl carbon) distance remained unchanged, the Rh-C2/C3 distances significantly elongated compared with those of the S_0 structure. These results indicated that the benzyl ligand changed its coordination-mode from η^3-type (α-benzyl) to η^1-type (σ-benzyl) in the T_1 state. According to the analysis on the electronic transition characters, the T_1 state was mainly contributed by the transitions of HOMO→LUMO (88%) and HOMO→LUMO+16 (4%) (**Supplementary Table 2**). The molecular orbital distribution indicated that LUMO and LUMO+16 mainly localized on the Rh (dπ) and benzyl ligand (π*) while the HOMO localized on the Rh (dσ) center (**Figure 9B**). As these LUMOs partially possessed the antibonding character on the Rh-C2/C3 bonds, the photoexcitation induced the dissociation of these Rh-C bonds, which resulted in the isomerization to the σ-benzyl species.

Concerning the acceleration of the carboxylation step, one possibility is the generation of the coordination site by taking σ-benzyl structure in the T_1 state, which would promote the following carboxylation by facilitating coordination of CO_2 to Rh center. Indeed, a similar thermal process has been proposed as a plausible mechanism for the carboxylation of organorhodium(I)

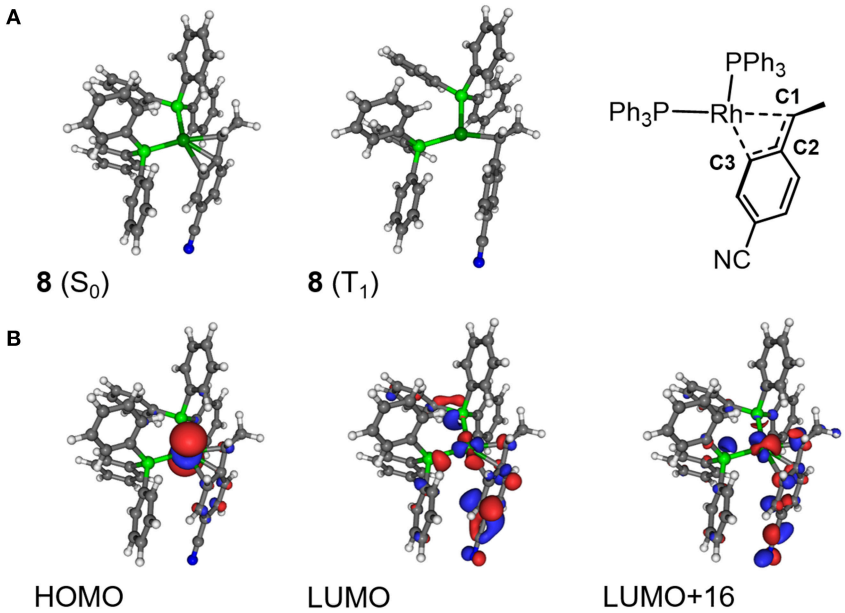

FIGURE 9 | (A) Optimized structures of **8** in the ground (S_0) state and lowest excited triplet (T_1) state, and **(B)** the selected molecular orbitals of **8** (S_0).

TABLE 4 | Selected bond lengths and NBO natural charges in the optimized geometries of **8**(S_0) and **8**(T_1).

State		S_0	T_1
l(Rh-C1)/Å		2.184	2.176 (−0.008)
l(Rh-C2)/Å		2.225	2.510 (+0.285)
l(Rh-C3)/Å		2.295	3.189 (+0.894)
NBO	Rh	−0.547	+0.158 (+0.705)
charge	C1	−0.287	−0.412 (−0.125)

complexes (Darensbourg et al., 1987). Another possibility is the direct nucleophilic addition of the benzyl carbon to CO_2 in the T_1 state. The NBO analysis demonstrated that the natural charge on the C1 atom significantly shifted to the negative side while that on the Rh atom shifted to the positive side in the T_1 state. The increase of the electron density on the C1 atom in the T_1 state would result in the acceleration of the nucleophilic addition to CO_2. Therefore, the structural and/or electronic factors associated with the transition to the T_1 state are thought to contribute to the carboxylation of **8**.

The effect of the photoactivation of the Rh(I) π-benzyl complex was also supported by the reactivity of the Rh(I) σ-alkyl complex with CO_2. When a mixture of **6** and an excess amount of methyl acrylate (**1f**) was subjected to a CO_2 atmosphere for 3 h even under dark, the quantitative formation of $Rh(PPh_3)_3(\eta^1\text{-}O_2CCHCH_3(CO_2CH_3))$ (**10**) was indicated by $^{31}P\{^1H\}$ NMR spectroscopy. The carboxylation of **1f** was confirmed by the fact that the corresponding hydrocarboxylated product (**2f**) was obtained from the reaction mixture. This result indicated that the photosensitization by $[Ru(bpy)_3]^{2+}$ was not essential in this case. Thus, the major role of the excitation was thought to be the transformation from π-benzyl to σ-benzyl complexes to generate a coordination site and to make them more nucleophilic.

Addition of the Second Photosensitizer

The above mechanistic study revealed that a photosensitizer played two key roles in the hydrocarboxylation cycle: one is a "photoredox catalyst" to reduce the Rh(I) carboxylate species, and the other is a "triplet photosensitizer" to promote carboxylation of the Rh(I) benzyl species. With a single photosensitizer, the excited state of the photosensitizer was quenched by either a tertiary amine for the electron transfer or a Rh(I) benzyl species for the energy transfer, and these two processes competed during the reaction. Since the former was related to the rate-determining step when using $^iPr_2NEt$ as a sacrificial electron donor, the incorporation of the second photosensitizer possessing suitable redox properties for the reductive quenching cycle was expected to facilitate the catalytic reaction.

On the basis of the idea, 2.0 mol% of a cyclometalated Ir(III) complex was added as a second photosensitizer to a mixture of **1b**, 3.5 mol% of **4**, 2.0 mol% of $[Ru(bpy)_3](PF_6)_2$ and 4.0 equiv. of $^iPr_2NEt$, and the solution was irradiated under CO_2 atmosphere at room temperature (**Table 5**). To excite both photosensitizers, a wide range of UV-visible-light (380–750 nm) was applied to the reactions. As expected, the addition of the second photosensitizer was found to be effective. For instance, when $[Ir(ppy)_2(dtbbpy)](PF_6)$ was added, the reaction was completed after irradiation for only 6 h, and the yield of **2b** was increased more than five-fold compared to that of the reaction without the second photosensitizer (**Table 5**, entry 2). According to the redox properties of $[Ir(ppy)_2(dtbbpy)](PF_6)$, the acceleration of the reaction was thought to be attributed mainly to the

TABLE 5 | Screening of the reaction conditions of the hydrocarboxylation of 3,5-bis(trifluoromethyl)styrene with a second photosensitizer.

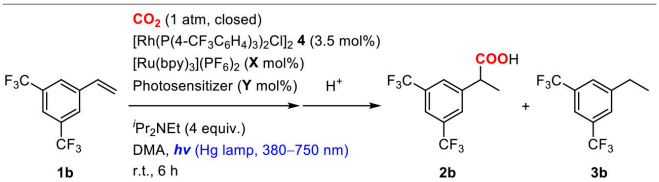

Entry	Photosensitizer	X/Y	Conv. /%	Yield /%	
				2b[a]	3b[b]
1	None	2/0	37	7	9
2	$[Ir(ppy)_2(dtbbpy)](PF_6)$	2/2	>99	40	25
3	$[Ir(dF(CF_3)ppy)_2(dtbbpy)](PF_6)$	2/2	>99	43	23
4	$[Ir(dF(CF_3)ppy)_2(dtbbpy)](PF_6)$	2/1	>99	43	29
5	$[Ir(dF(CF_3)ppy)_2(dtbbpy)](PF_6)$	1/2	90	24	16
6	*fac*-$Ir(ppy)_3$	2/2	71	22	33
7[c]	None	2/0	74	45	19
8[c]	$[Ir(dF(CF_3)ppy)_2(dtbbpy)](PF_6)$	2/2	53	23	7

[a]*NMR yield.*
[b]*GC yield.*
[c]*BI(OH)H (1.2 equiv.) was used instead of* $^{i}Pr_2NEt$ *(4.0 equiv.).*

high reducing ability of the one-electron reduced species to promote the reduction process. The yield of **2b** further increased when incorporating $[Ir(dF(CF_3)ppy)_2(dtbbpy)](PF_6)$ as a second photosensitizer (**Table 5**, entry 3), and its concentration could be reduced to 1.0 mol% without lowering the yield (**Table 5**, entry 4). This result was assumed to be due to the high oxidizing ability of the excited state in addition to the sufficient reducing ability of the one-electron reduced species. The excited state of $[Ir(dF(CF_3)ppy)_2(dtbbpy)](PF_6)$ was found to be able to work as an energy transfer agent of **8** based on the luminescence quenching experiment ($K_q = 2.76 \times 10^4$, **Supplementary Figure 3B**). However, it is considered to contribute to the reaction mainly as an electron transfer agent under the catalytic conditions owing to the efficient quenching by the sacrificial electron donor. On the other hand, the addition of *fac*-$Ir(ppy)_3$ resulted in only a small acceleration, which was probably attributable to the inferior oxidizing ability in the excited state (**Table 5**, entry 6). These results demonstrate that photosensitizers possessing both high oxidizing ability of the excited state and high reducing ability of the one-electron reduced species are advantageous as a second photosensitizer. The positive result on the addition of the two appropriate photosensitizers reflected the fact that the catalytic cycle was composed of the multiple photochemical processes, and the acceleration of the reduction process led to the enhancement of the catalytic activity when using $^{i}Pr_2NEt$ as a sacrificial electron donor.

Rate-Determining Step in the Hydrocarboxylation With BI(OH)H

The previous experiments demonstrated that the rate-determining step of the catalytic cycle was the reduction process of the Rh(I) carboxylate species **9** when employing $^{i}Pr_2NEt$ as a sacrificial electron donor. In order to investigate the contribution of BI(OH)H to the catalytic cycle, the similar examination was carried out using BI(OH)H as a sacrificial electron donor instead of $^{i}Pr_2NEt$. Interestingly, the resting-state was found to be Rh(I) π-benzyl intermediate **8** when a mixture of **1a**, catalytic amounts of **6** and $[Ru(bpy)_3](PF_6)_2$, and 1.2 equiv. of BI(OH)H was irradiated by visible-light under CO_2 atmosphere (**Supplementary Figure 4**). In that case, **9** was not detectable even after prolonged irradiation, indicating that the rate-determining step obviously altered from the reduction process to the carboxylation process by changing the sacrificial electron donor. This result was also supported by the fact that the acceleration of the reaction by the addition of a second photosensitizer was not observed in the case of the reaction using BI(OH)H as a sacrificial electron donor (**Table 5**, entry 8). These observations suggested that the use of BI(OH)H strongly accelerated the reductive quenching cycle of $[Ru(bpy)_3]^{2+}$ to promote the reduction process.

CONCLUSION

In this study, the improved catalytic conditions of the visible-light driven hydrocarboxylation by Rh(I) and $[Ru(bpy)_3]^{2+}$ catalysts were explored, and the detailed reaction mechanism was investigated. On the basis of the stoichiometric reactions of the possible rhodium intermediates, the proposed catalytic cycle was confirmed to be composed of (i) the hydrometallation of alkenes by Rh(I) monohydride species, (ii) the photochemical carboxylation of the Rh(I) benzyl species with CO_2, (iii) the photoinduced 2-electron, 2-proton transfers to the Rh(I) carboxylate species, and (iv) the base-assisted carboxylic acid elimination. One strategy for the enhancement of the catalytic reaction was to employ BI(OH)H possessing superior reducing ability as a sacrificial electron donor instead of $^{i}Pr_2NEt$. It successfully improved the efficiency of the reaction, which had been major challenges in the previous catalytic conditions. The alteration of the resting-state by changing the sacrificial electron donor indicated that the addition of BI(OH)H significantly promoted the reduction process of the Rh(I) carboxylate species through the enhancement of the reductive quenching efficiency of $[Ru(bpy)_3]^{2+}$. Another strategy for the enhancement of the efficiency was to add the second photosensitizer in charge of the reductive quenching cycle. The acceleration of the catalytic reaction by the addition of the appropriate cyclometalated Ir(III) complex together with $[Ru(bpy)_3]^{2+}$ supported this hypothesis. These two effective strategies suggested that the promotion of the reduction processes was a key to enhance the catalytic activity in the present system. In addition to expand the versatility of the present hydrocarboxylation, this study would provide fundamental insights into the catalytic organic transformations by transition-metal/photoredox dual catalysis.

EXPERIMENTAL

General

All operations were carried out under an argon atmosphere unless otherwise noted. ^{1}H, ^{13}C, and ^{31}P NMR spectra were recorded on Bruker DRX-500, JEOL ECZ-500, ECX-400, and

ECS-400 spectrometers. ^{31}P and ^{19}F NMR chemical shifts were calibrated using external 85% H_3PO_4 (δ: 0.0 ppm) and neat C_6F_6 (δ: −164.9 ppm), respectively. IR spectra were recorded on an SC-100-VIR with an ATR PRO450-S accessory (JASCO Co., Ltd.). Emission spectra were recorded on an FP-6500 spectrofluorometer (JASCO Co., Ltd.). FAB-MS and FD-MS spectra were recorded on a JEOL JMS-700 spectrometer and a JMS-T100 spectrometer, respectively. Gas chromatography (GC-FID / TCD) was recorded on a Shimadzu GC-2010 spectrometer. Analytical thin-layer chromatography (TLC) was performed with a glass plate coated with silica gel (Wakogel B-5F). Visible-light irradiation was performed with a Relyon Twin LED Light (3W × 2, $\lambda_{irr.} = 425 \pm 15$ nm), and UV-visible-light irradiation was performed with an USHIO Optical Modulex OPM2-502XQ (500 W Xe lamp) with a super cold filter ZSC0750 (ASAHI Spectra Inc.).

THF, toluene, pentane and diethyl ether were purified by a solvent purification system by Glass Contour. Dehydrated dimethylacetamide (DMA) and dimethylformamide (DMF) were purchased from Kanto Chemical Co., Inc., degassed by argon bubbling and stored in a glovebox. Tertiary amines were distilled, degassed three times by freeze-pump-thaw method and stored under N_2. Solvents for NMR measurements were dried over molecular sieves, degassed three times by freeze-pump-thaw method and stored under N_2. All other solvents were distilled, degassed by argon bubbling and stored in a glovebox. CO_2 and H_2 gases were purchased from Taiyo Nippon Sanso Corporation. $[Rh(coe)_2Cl]_2$ (Van der Ent et al., 1990), $P(4\text{-}CF_3C_6H_4)_3$ (Suomalainen et al., 2001), $Rh(PPh_3)_2(OAc)$ (**5**) (Grushin et al., 1995), $[Rh(cod)(OAc)]_2$ (Chatt and Venanzi, 1957), $Rh(PPh_3)_3H$ (**6**) (Annibale and Song, 2014), $[Ru(bpy)_3](PF_6)_2$ (Damrauer et al., 1997), $[Ru(dmbpy)_3](PF_6)_2$ (Damrauer et al., 1997), $[Ru(bpz)_3](PF_6)_2$ (Schultz et al., 2015), $Ir(ppy)_2(dtbbpy)(PF_6)$ (Tellis et al., 2014), $[Ir(dF(CF_3)ppy)_2(dtbbpy)](PF_6)$ (Slinker et al., 2004), *fac*-$Ir(ppy)_3$ (Tamayo et al., 2003), and diisopropylethylammonium acetate (Anouti et al., 2008) were prepared according to the published methods. 4-Cyanostyrene (**1a**) was prepared by Wittig reaction of 4-cyanobenzaldehyde (Falk et al., 2013). Other chemicals were purchased and used as received.

Photocatalytic Reactions

For screening conditions with alkenes (**1a**–**1g**), a DMA solution (0.6 mL) of an alkene (0.060 mmol), $[Rh(P(4\text{-}CF_3C_6H_4)_3)_2Cl]_2$ (**4**, 4.5 mg, 0.0021 mmol), photoredox catalyst(s), sacrificial electron donor and inorganic base (defined amounts) was prepared in a glass tube (φ 2.0 cm, 18 cm) under an argon atmosphere. Then the headspace gas was replaced by an atmospheric pressure of CO_2, and the reaction vessel was put in a water bath placed at a distance of 10 mm from light sources. The mixture was irradiated with visible-light from blue LED lamp ($\lambda_{irr.} = 425$ nm, two sockets) or UV-visible-light from Xe lamp ($\lambda_{irr.} = 380$–800 nm) for defined time in the closed system. The product mixture was analyzed by ^{1}H NMR and GC to determine the NMR yield of the hydrocarboxylated product (**2a**–**2g**) and the GC yield of the hydrogenated product (**3a**, **3b**), respectively (internal standard: 1,1,2,2-tetrachloroethane).

For isolation of the methyl esters of the hydrocarboxylated products (**2a**, **2b**, **2d**), a DMA solution (1.2 mL) of a styrene (0.12 mmol), **4** (9.0 mg, 0.0042 mmol), $[Ru(bpy)_3](PF_6)_2$ (1.0 mg, 0.0012 mmol), BI(OH)H (58 mg, 0.24 mmol), and Cs_2CO_3 (47 mg, 0.14 mmol) was prepared in a glass tube (φ 2.0 cm, 18 cm), and irradiated with visible-light from blue LED lamp ($\lambda_{irr.} = 425$ nm, three sockets) for defined time after replacement of the headspace gas by an atmospheric pressure of CO_2. After irradiation, the reaction mixture was diluted with diethyl ether and extracted with H_2O three times. The combined aqueous layer was acidified by 1N HCl aq., and then extracted with diethyl ether three times. The combined organic layer was dried over $MgSO_4$, filtered and evaporated under reduced pressure to give the hydrocarboxylated product. Then, the product was dissolved in Et_2O-MeOH, and $TMSCHN_2$ (excess) was added at 0°C. The mixture was stirred at 0°C for 30 min and the solvent was removed under reduced pressure. The crude product was purified by preparative TLC (AcOEt/*n*-hexane = 1/5) to give the corresponding methyl-esterified product.

Preparations of Rhodium Complexes and Their Stoichiometric Reactions

Preparation of $[Rh(P(4\text{-}CF_3C_6H_4)_3)_2Cl]_2$ (4)

A solution of $P(4\text{-}CF_3C_6H_4)_3$ (200 mg, 0.429 mmol) in toluene (2 mL) was added dropwise to a solution of $[Rh(coe)_2Cl]_2$ (77 mg, 0.107 mmol) in toluene (2 mL) and the mixture was stirred at room temperature overnight. After removal of solvent under reduced pressure, the crude product was dissolved in THF and then pentane was added to induce precipitation. The precipitates were collected to give the target product (218 mg, 0.102 mmol, 95% yield). ^{1}H NMR (500 MHz, THF-d_8, r.t., δ/ppm): δ 7.73–7.67 (m, 24 H, P*Ar*$_3$), 7.39 (d, J = 8 Hz, 24 H, P*Ar*$_3$). ^{13}C{^{1}H} NMR (125 MHz, r.t., THF-d_8, δ/ppm): δ 139.3 (vt, N = 22 Hz, P*Ar*$_3$), 135.7 (s, P*Ar*$_3$), 132.1 (q, J_{C-F} = 33 Hz, P*Ar*$_3$), 125.0 (s, P*Ar*$_3$), 124.6 (q, J_{C-F} = 272 Hz, -*C*F$_3$). ^{31}P{^{1}H} NMR (202 MHz, THF-d_8, r.t., δ/ppm): δ 53.4 (d, J = 194 Hz). ^{19}F NMR (471 MHz, THF-d_8, r.t., δ/ppm): δ −60.6 (s). ESI-MS: m/z = 1035 $[M/2 - Cl]^+$. Anal. Found (calcd for $C_{84}H_{48}Cl_2F_{36}P_4Rh_2$): C, 46.94 (47.11); H, 2.28 (2.26).

Preparation of $Rh(PCy_3)_2(OAc)$ (5′)

$[Rh(cod)(OAc)]_2$ (60 mg, 0.111 mmol) and PCy_3 (125 mg, 0.444 mmol) were suspended in DMA (4 mL), and the mixture was irradiated with UV-visible-light (500 W Xe lamp, $\lambda_{irr.}$ = 380–800 nm) at room temperature with vigorous stirring for 30 h. The precipitate was filtered, washed with DMA and cold pentane (−35°C), and then recrystallized from a minimum volume of pentane at −35°C to yield the target compound (98 mg, 0.135 mmol, 61%). IR (KBr): $\nu(OCO_{as})$ = 1,528, $\nu(OCO_{sym})$ = 1,445 cm^{-1}. ^{1}H NMR (500 MHz, C_6D_6, r.t., δ/ppm): δ 2.35 – 1.24 (m, 69 H, P*Cy*$_3$ and O_2CCH_3). ^{13}C{^{1}H} NMR (125 MHz, r.t., C_6D_6, δ/ppm): δ 188.2 (s, O_2CCH_3), 35.9 (vt, N = 10 Hz, P*Cy*$_3$), 31.1 (s, P*Cy*$_3$), 28.4 (vt, N = 5 Hz, P*Cy*$_3$), 27.3 (s, P*Cy*$_3$), 24.9 (s, O_2CCH_3). ^{31}P{^{1}H} NMR (202 MHz, C_6D_6, r.t., δ/ppm): δ 59.1 (d, J_{P-Rh} = 198 Hz). HR-MS (FAB): m/z = 722.3817 $[M]^+$ (calcd for $[C_{38}H_{69}O_2P_2Rh]^+$: 722.3828).

Preparation of an Authentic Sample of $Rh(PCy_3)_2(OAc)(H)_2$ (7′)

$[Rh(cod)(OAc)]_2$ (60 mg, 0.111 mmol) and PCy_3 (125 mg, 0.444 mmol) were dissolved in THF (3 mL), and the mixture was stirred under H_2 (1 atm) at room temperature overnight. After removal of solvent, the crude product was dissolved in toluene and filtered through Celite®. The resultant solid after evaporation was washed with cold diethyl ether (−35°C) to give the target compound (113 mg, 0.156 mmol, 70%). IR (KBr): ν(RhH) = 2,143, $\nu(OCO_{as})$ = 1,551, $\nu(OCO_{sym})$ = 1,436 cm^{-1}. ^1H NMR (500 MHz, C_6D_6, r.t., δ/ppm): δ 2.20 – 1.22 (m, 69 H, P*Cy*$_3$ and O_2CCH_3), −23.7 (dt, J_{H-Rh} = 24, J_{H-P} = 15 Hz, 2 H, Rh-*H*) $^{13}C\{^1H\}$ NMR (125 MHz, r.t., C_6D_6, δ/ppm): δ 180.2 (s, O_2CCH_3), 35.8 (vt, J_{C-P} = 10 Hz, P*Cy*$_3$), 30.5 (s, P*Cy*$_3$), 28.3 (vt, *N* = 5 Hz, P*Cy*$_3$), 27.1 (s, P*Cy*$_3$), 24.8 (s, O_2CCH_3). $^{31}P\{^1H\}$ NMR (202 MHz, C_6D_6, r.t., δ/ppm): δ 51.1 (d, J_{P-Rh} = 115 Hz). HR-MS (FD): *m/z* = 724.3975 (calcd for $[C_{38}H_{71}O_2P_2Rh]^+$: 724.3984).

Preparation of $Rh(PPh_3)_2(\eta^3\text{-}CHCH_3(4\text{-}CNC_6H_4))$ (8)

To a solution of $Rh(PPh_3)_3H$ (**6**) (5.4 mg, 0.0060 mmol) in THF-d_8 (0.6 mL) in a J. Young NMR tube was added 4-cyanostyrene (**1a**) (1.6 μL, 0.012 mmol) at room temperature. $Rh(PPh_3)_2(\eta^3\text{-}CHCH_3(4\text{-}CNC_6H_4))$ (**8**) formed almost quantitatively. ^1H NMR (500 MHz, THF-d_8, −10°C, δ/ppm): δ 7.47 – 7.00 (m, 30 H, P*Ph*$_3$), 6.81 (brd, *J* = 8 Hz, 1 H, *Ar*), 6.57 (brd, *J* = 7 Hz, 1 H, *Ar*), 6.10 (brd, *J* = 8 Hz, 1 H, *Ar*), 4.89 (brd, *J* = 7 Hz, 1 H, *Ar*), 2.47 – 2.40 (m, 1 H, -C*H*CH$_3$), 0.92 – 0.87 (m, 3 H, -CHC*H*$_3$). $^{31}P\{^1H\}$ NMR (202 MHz, THF-d_8, −10°C, δ/ppm): δ 46.2 (dd, J_{P-Rh} = 263 Hz, J_{P-P} = 31 Hz), 39.6 (dd, J_{P-Rh} = 178 Hz, J_{P-P} = 31 Hz). HR-MS (FAB): *m/z* = 757.1539 (calcd for $[C_{45}H_{38}NP_2Rh]^+$: 757.1535).

Preparation of $Rh(PPh_3)_3(\eta^1\text{-}O_2CCHCH_3(4\text{-}CNC_6H_4))$ (9)

To a solution of $Rh(PPh_3)_3H$ (**6**) (60 mg, 0.090 mmol) in toluene (3 mL) was added dropwise a solution 2-(4-cyanophenyl)propionic acid (16 mg, 0.090 mmol) in toluene (2 mL), and the mixture was stirred at room temperature for 4 h. After removal of solvent under reduced pressure, the crude product was dissolved in toluene and then pentane was added to induce precipitation. The precipitates were collected to give the target product as a 9: 1 mixture with $Rh(PPh_3)_2(\eta^2\text{-}O_2CCHCH_3(4\text{-}CNC_6H_4))$ which was formed by dissociation of PPh_3 from **9** (59 mg). **9** IR (KBr): ν(CN) = 2,224, $\nu(OCO_{as})$ = 1,604, $\nu(OCO_{sym})$ = 1,342 cm^{-1}. ^1H NMR (500 MHz, THF-d_8, −60°C, δ/ppm): δ 7.56 – 6.79 (m, 47 H, P*Ph*$_3$, O_2CCHCH_3*Ar*), 6.30 (brd, *J* = 8 Hz, 2 H, O_2CCHCH_3*Ar*), 1.65 (brq, *J* = 7 Hz, 1 H, O_2CC*H*CH_3Ar), 0.25 (brd, *J* = 7 Hz, 3 H, O_2CCHC*H*$_3$Ar). $^{13}C\{^1H\}$ NMR (125 MHz, r.t., THF-d_8, −30°C, δ/ppm): δ 176.6 (s, O_2*C*$CHCH_3$Ar), 150.8 (s, O_2CCHCH_3*Ar*), 135.7 (vt, *N* = 6 Hz, P*Ph*$_3$), 131.1 (s, O_2CCHCH_3*Ar*), 129.6 (s, O_2CCHCH_3*Ar*), 129.2 (s, P*Ph*$_3$), 127.8 (s, P*Ph*$_3$), 127.5 (s, P*Ph*$_3$), 127.4 (s, P*Ph*$_3$), 119.8 (s, -*C*N), 108.9 (s, O_2CCHCH_3*Ar*), 47.8 (s, O_2CCHCH_3Ar), 18.1 (s, O_2CCHCH_3Ar). $^{31}P\{^1H\}$ NMR (202 MHz, THF-d_8, −30°C, δ/ppm): δ 51.5 (dt, J_{P-Rh} = 174 Hz, J_{P-P} = 41 Hz), 34.9 (dd, J_{P-Rh} = 153 Hz, J_{P-P} = 41 Hz). HR-MS (FAB): *m/z* = 801.1453 $[M-(PPh_3)]^+$ (calcd for $[C_{46}H_{38}NO_2P_2Rh]^+$: 801.1433). $Rh(PPh_3)_2(\eta^2\text{-}O_2CCHCH_3(4\text{-}CNC_6H_4))$ $^{31}P\{^1H\}$ NMR (202 MHz, THF-d_8, −30°C, δ / ppm): δ 57.6 (brd, J_{P-Rh} = 210 Hz).

Redox-Photosensitized Reaction of $Rh(PPh_3)_2(OAc)$ (5)

$Rh(PPh_3)_2(OAc)$ (**5**) (2.7 mg, 0.0040 mmol), $[Ru(bpy)_3](PF_6)_2$ (1.0 mg, 0.0012 mmol), PPh_3 (1.5 mg, 0.0060 mmol), $^iPr_2NEt$ (41 μL, 0.24 mmol) and DMA (0.6 mL) were added in a glass tube with a magnetic stirrer. The mixture was irradiated with visible-light ($\lambda_{irr.}$ = 425 nm) at room temperature for 6 h. The solvent was removed under reduced pressure, and the resulting solid was analyzed by ^1H and ^{31}P NMR spectroscopies (THF-d_8, internal standard: mesitylene). The Rh(I) monohydride species corresponding to $Rh(PPh_3)_3H$ (**6**) formed in 57% yield (based on the Rh-hydride signal) and ca. 30% of the starting material **5** remained in the product mixture. **6** was highly fluxional in the reaction solution at room temperature in the presence of triphenylphosphine. ^1H NMR (500 MHz, THF-d_8, δ/ppm, r.t.): −8.45 (brd, J_{H-Rh} = 13 Hz, Rh-*H*). ^{31}P NMR (202 MHz, THF-d_8, δ/ppm, r.t.): 41 (br). The intensity of the Rh-hydride signal was significantly increased at room temperature when $Rh(PPh_3)_3H$ (**6**) synthesized alternatively was added to the reaction mixture, also supporting the formation of **6**. In addition, when the solution was cooled to −90°C, the signals attributed to $Rh(PPh_3)_4H$ were observed instead, indicating **6** was converted to $Rh(PPh_3)_4H$ at low temperature. ^1H NMR (500 MHz, THF-d_8, δ/ppm, −90°C): −13.5 (dq J_{H-Rh} = 118, J_{H-P} = 15 Hz, Rh-*H*). ^{31}P NMR (202 MHz, THF-d_8, δ/ppm, −90°C): 33.4 (dm, J_{P-Rh} = 112), 30.2 (dd, J_{P-Rh} = 162, J_{P-P} = 32 Hz). The spectrosopic data was analogous to the values reported previously (Dewhirst et al., 1968; Strauss and Shriver, 1978).

Redox-Photosensitized Reaction of $Rh(PCy_3)_2(OAc)$ (5′)

$Rh(PCy_3)_2(OAc)$ (**5′**) (2.9 mg, 0.0040 mmol), $[Ru(bpy)_3](PF_6)_2$ (1.0 mg, 0.0012 mmol), $^iPr_2NEt$ (41 μL, 0.24 mmol) and DMA (0.6 mL) were added in a glass tube with a magnetic stirrer. The mixture was irradiated with visible-light ($\lambda_{irr.}$ = 425 nm) at room temperature for 12 h. The solvent was removed under reduced pressure, and the resulting solid was analyzed by ^1H and ^{31}P NMR spectroscopies (C_6D_6, internal standard: mesitylene). $Rh(PCy_3)(OAc)(H)_2$ (**7′**) was formed in 94% yield (based on the rhodium hydride signal). The spectroscopic feature well agreed with the complex **7′** synthesized alternatively (*vide supra*). No other Rh hydride signal was observed even by addition of 1 equiv. of PCy_3 to the reaction mixture.

Reaction of $Rh(PPh_3)_2(OAc)(H)_2$ (7) and $^iPr_2NEt$

A solution of $Rh(PPh_3)_2(OAc)$ (**5**) (2.7 mg, 0.0040 mmol) in C_6D_6 (0.6 mL) was put in a J. Young NMR tube under hydrogen atmosphere at room temperature. After 2 h, $Rh(PPh_3)_2(OAc)(H)_2$ (**7**) formed *in situ*. ^1H NMR (500 MHz, C_6D_6, δ/ppm, r.t.): 7.86 – 7.00 (m, P*Ph*$_3$), −20.8 (dt, J_{H-Rh} = 22 Hz, J_{H-P} = 17 Hz, Rh-*H*). $^{31}P\{^1H\}$ NMR (202 MHz, C_6D_6, δ/ppm, r.t.): 41.4 (d, J_{P-Rh} = 121 Hz). Then, the reaction solution was degassed by freeze-pump-thaw method 3 times to remove the hydrogen gas. Addition of 1 equiv. of PPh_3 (1.5 mg, 0.0060 mmol)

and 80 equiv. of $^{i}Pr_2NEt$ (41 μL, 0.24 mmol) gave $Rh(PPh_3)_3H$ (**6**) in 58% yield (based on the rhodium hydride signal). Ca. 20% of **7** remained in the reaction mixture. The spectroscopic data of **6** was identical with that of the sample prepared by the photosensitizing reaction of $Rh(PPh_3)_2(OAc)$ (**5**). The same reaction was also performed in DMA. In this case, **7** converted fully after addition of PPh_3 and $^{i}Pr_2NEt$, and **6** was obtained as a major product.

Reaction of $Rh(PPh_3)_3H$ (6) and $[^{i}Pr_2NHEt]^{+}[CH_3COO]^{-}$

To a solution of $Rh(PPh_3)_3H$ (**6**) (3.6 mg, 0.0040 mmol) in C_6D_6 (0.6 mL) was added diisopropylethylammonium acetate (1.1 mg, 0.0060 mmol) and the mixture was stirred at room temperature for 10 min. $Rh(PPh_3)_2(OAc)(H)_2$ (**7**) formed quantitatively. The spectroscopic data of the product in C_6D_6 was identical with those of the sample prepared by the hydrogenation of $Rh(PPh_3)_2(OAc)$ (**5**).

Redox-Photosensitized Reaction of $Rh(PPh_3)_3Cl$

$Rh(PPh_3)_3Cl$ (3.7 mg, 0.0040 mmol), $[Ru(bpy)_3](PF_6)_2$ (1.0 mg, 0.0012 mmol), $^{i}Pr_2NEt$ (41 μL, 0.24 mmol) and DMF-d_7 (0.6 mL) were added in a J. Young NMR tube. The mixture was irradiated with visible-light ($\lambda_{irr.}$ = 425 nm) at room temperature for 6 h. $Rh(PPh_3)_3H$ (**6**) formed in 52% yield (based on the Rh-hydride signal) and ca. 40% of the starting material remained in the reaction mixture. ^{1}H NMR (500 MHz, δ/ppm, −50°C): −8.48 (ddt, J_{H-Rh} = 101 Hz, J_{H-P} = 18 Hz, J_{H-P} = 15 Hz, Rh-*H*). ^{31}P NMR (202 MHz, δ/ppm, −50°C): 43.7 (dd, J_{P-Rh} = 170 Hz, J_{P-P} = 25 Hz), 38.9 (dm, J_{P-Rh} = 149 Hz). The spectrosopic data was analogous to the values reported previously (Dewhirst et al., 1968; Strauss and Shriver, 1978).

Reaction of $Rh(PPh_3)_3H$ (6) With 4-Cyanostyrene (1a) and CO_2

To a solution of $Rh(PPh_3)_3H$ (**6**) (3.6 mg, 0.0040 mmol) in DMA (0.6 mL) was added 4-cyanostyrene (**1a**) (2.6 μL, 0.020 mmol) in a J. Young NMR tube at room temperature. $Rh(PPh_3)_2(\eta^3\text{-}CHCH_3(4\text{-}CNC_6H_4))$ (**8**) was generated *in situ* almost quantitatively. Then, $[Ru(bpy)_3](PF_6)_2$ (1.0 mg, 0.0012 mmol) was added, and the mixture was irradiated with visible-light ($\lambda_{irr.}$ = 425 nm) under a CO_2 atmosphere (1 atm) at room temperature for 30 min. $Rh(PPh_3)_3(\eta^1\text{-}O_2CCHCH_3(4\text{-}CNC_6H_4))$ (**9**) was formed almost quantitatively, as the spectroscopic data well agreed with the complex synthesized alternatively.

Reaction of $Rh(PPh_3)_3H$ (6) With Methyl Acrylate (1f) and CO_2

To a solution of $Rh(PPh_3)_3H$ (**6**) (3.6 mg, 0.0040 mmol) and $[Ru(bpy)_3](PF_6)_2$ (1.0 mg, 0.0012 mmol) in DMA (0.6 mL) was added methyl acrylate (**1f**) (1.8 μL, 0.020 mmol) in a J. Young NMR tube at room temperature. The mixture was exposed to a CO_2 atmosphere (1 atm) under dark at room temperature for 3 h. The observed $^{31}P\{^{1}H\}$ NMR spectral feature was analogous to that of **9**, indicating the formation of $Rh(PPh_3)_3(\eta^1\text{-}O_2CCHCH_3(CO_2CH_3))$ (**10**). $^{31}P\{^{1}H\}$ NMR (162 MHz, DMA, −15°C, δ/ppm): δ 50.6 (dt, J_{P-Rh} = 174 Hz, J_{P-P} = 44 Hz), 33.5 (dd, J_{P-Rh} = 153 Hz, J_{P-P} = 44 Hz). The reaction solution was treated with $NaHCO_3$ aq., and then acidified with 1N HCl aq. The organic layer was extracted with diethyl ether three times, dried over $MgSO_4$, filtered and evaporated under reduced pressure to give methyl methylmalonate in 54% yield (based on **6**).

Observation of the Reaction Intermediates Under Catalytic Conditions

$Rh(PPh_3)_3H$ (**6**) (3.6 mg, 0.0040 mmol), $[Ru(bpy)_3](PF_6)_2$ (1.0 mg, 0.0012 mmol), BI(OH)H (17.3 mg, 0.072 mmol), 4-cyanostyrene (**1a**) (7.7 μL, 0.060 mmol) and DMA (0.6 mL) were added in a J. Young NMR tube. The mixture was irradiated with visible-light ($\lambda_{irr.}$ = 425 nm) under CO_2 atmosphere (1 atm) at room temperature for 30 min. The $^{31}P\{^{1}H\}$ NMR spectra were observed at −15°C before and after irradiation, and only $Rh(PPh_3)_2(\eta^3\text{-}CHCH_3(4\text{-}CNC_6H_4))$ (**8**) was observed as a resting-state in both spectra.

Theoretical Study

Theoretical calculations were performed at the DFT level with the Gaussian 09 package. The geometry optimizations were performed using the mPW1PW91 functional (Adamo and Barone, 1998). The LanL2DZ basis set was used for all atoms and extended by a polarization function (except for H) (Dunning and Hay, 1976; Wadt and Hay, 1985a,b). To address solvation effects, the conductor-like polarizable continuum model (CPCM, N,N-Dimethylacetamide) (Tomasi et al., 2005) was used for the ground and excited states. For validation, vibrational frequencies were calculated for the ground and excited states. The orbital plots as well as the graphical representations were performed using Molekel (Varetto, 2009). Natural bond orbital (NBO) analysis was used to predict and interpret the computational results (Glendening et al., 2001). Total ZPE energies and cartesian coordinates of computed structures are given in **Supplementary Table 3**.

DATA AVAILABILITY

All datasets generated for this study are included in the manuscript and/or the **Supplementary Files**.

AUTHOR CONTRIBUTIONS

NN and KM performed the experiments. KS instructed the experiments of NN. KM performed the theoretical calculations. NI and JT supervised the project. KM and NI wrote the paper.

FUNDING

The authors are grateful for the financial supports by an ACT-C program JPMJCR12Y3 from JST and JSPS KAKENHI Grant no. 15H05800, 17H06143, and 24245019.

ACKNOWLEDGMENTS

The authors also thank Prof. Osamu Ishitani for valuable discussions on the use of photosensitizers and sacrificial electron donors.

SUPPLEMENTARY MATERIAL

The Supplementary Material for this article can be found online at: https://www.frontiersin.org/articles/10.3389/fchem.2019.00371/full#supplementary-material

REFERENCES

Adamo, C., and Barone, V. (1998). Exchange functionals with improved long-range behavior and adiabatic connection methods without adjustable parameters: the mPW and mPW1PW models. *J. Chem. Phys.* 108, 664–675. doi: 10.1063/1.475428

Adams, R. E., Grusenmeyer, T. A., Griffith, A. L., and Schmehl, R. H. (2018). Transition metal hydride complexes as mechanistic models for proton reduction catalysis. *Coord. Chem. Rev.* 362, 44–53. doi: 10.1016/j.ccr.2018.02.014

Annibale, V. T., and Song, D. (2014). Reaction of dinuclear rhodium 4,5-diazafluorenyl-9-carboxylate complexes with H_2 and CO_2. *Organometallics* 33, 2776–2783. doi: 10.1021/om500278a

Anouti, M., Caillon-Caravanier, M., Le Floch, C., and Lemordant, D. (2008). Alkylammonium-based protic ionic liquids part I: preparation and physicochemical characterization. *J. Phys. Chem. B* 112, 9406–9411. doi: 10.1021/jp803483f

Arias-Rotondo, D. M., and McCusker, J. K. (2016). The photophysics of photoredox catalysis: a roadmap for catalyst design. *Chem. Soc. Rev.* 45, 5803–5820. doi: 10.1039/c6cs00526h

Campagna, S., Puntoriero, F., Nastasi, F., Bergamini, G., and Balzani, V. (2007). Photochemistry and photophysics of coordination compounds: ruthenium. *Topp. Curr. Chem.* 280, 117–214. doi: 10.1007/128_2007_133

Chatt, J., and Venanzi, L. M. (1957). 955. Olefin co-ordination compounds. Part VI. Diene complexes of rhodium(I). *J. Chem. Soc.* 1957, 4735–4741. doi: 10.1039/JR9570004735

Crutchley, R. J., and Lever, A. B. P. (1980). Ruthenium(II) tris(bipyrazyl) dication - a new photocatalyst. *J. Am. Chem. Soc.* 102, 7128–7129. doi: 10.1021/ja00543a053

Damrauer, N. H., Boussie, T. R., Devenney, M., and McCusker, J. K. (1997). Effects of intraligand electron delocalization, steric tuning, and excited-state vibronic coupling on the photophysics of aryl-substituted bipyridyl complexes of Ru(II). *J. Am. Chem. Soc.* 119, 8253–8268. doi: 10.1021/ja971321m

Darensbourg, D. J., Grotsch, G., Wiegreffe, P., and Rheingold, A. L. (1987). Insertion reactions of carbon dioxide with square-planar rhodium alkyl and aryl complexes. *Inorg. Chem.* 26, 3827–3830. doi: 10.1021/ic00269a043

Dewhirst, K. C., Keim, W., and Reilly, C. A. (1968). Preparation and nuclear magnetic resonance spectra of hydridophosphine complexes of ruthenium and rhodium. *Inorg. Chem.* 7, 546–551. doi: 10.1021/ic50061a033

Doherty, M. D., and Grills, D. C., Muckerman, J. T., Polyansky, D. E., and Fujita, E. (2010). Toward more efficient photochemical CO_2 reduction: Use of $scCO_2$ or photogenerated hydrides. *Coord. Chem. Rev.* 254, 2472–2482. doi: 10.1016/j.ccr.2009.12.013

Dunning, T. H., and Hay, P. J. (1976). "Gaussian basis sets for molecular calculations in methods of electronic structure theory," in *Modern Theoretical Chemistry,* Vol. 3, ed H. F. Schaefer III (Plenum Press), 1–28.

Esswein, A. J., and Nocera, D. G. (2007). Hydrogen production by molecular photocatalysis. *Chem. Rev.* 107, 4022–4047. doi: 10.1021/cr050193e

Fabry, D. C., and Rueping, M. (2016). Merging visible light photoredox catalysis with metal catalyzed C–H activations: On the role of oxygen and superoxide ions as oxidants. *Acc. Chem. Res.* 49, 1969–1979. doi: 10.1021/acs.accounts.6b00275

Falk, A., Göderz, A.-L., and Schmalz, H.-G. (2013). Enantioselective nickel-catalyzed hydrocyanation of vinylarenes using chiral phosphine-phosphite ligands and TMS-CN as a source of HCN. *Angew. Chem. Int. Ed.* 52, 1576–1580. doi: 10.1002/anie.201208082

Fan, X., Gong, X., Ma, M., Wang, R., and Walsh, P. J. (2018). Visible light-promoted CO_2 fixation with imines to synthesize diaryl α-amino acids. *Nat. Chem.* 9:4936. doi: 10.1038/s41467-018-07351-2

Farney, E. P., and Yoon, T. P. (2014). Visible-light sensitization of vinyl azides by transition-metal photocatalysis. *Angew. Chem. Int. Ed.* 53, 793–797. doi: 10.1002/anie.201308820

Flamigni, L., Barbieri, A., Sabatini, C., Ventura, B., and Barigelletti, F. (2007). Photochemistry and photophysics of coordination compounds: iridium. *Top. Curr. Chem.* 281, 143–203. doi: 10.1007/128_2007_131

Fujihara, T., Xu, T., Semba, K., Terao, J., and Tsuji, Y. (2011). Copper-catalyzed hydrocarboxylation of alkynes using carbon dioxide and hydrosilanes. *Angew. Chem. Int. Ed.* 50, 523–527. doi: 10.1002/anie.201006292

Ghosh, T., Slanina, T., and Knig, B. (2015). Visible light photocatalytic reduction of aldehydes by Rh(III)–H: a detailed mechanistic study. *Chem. Sci.* 6, 2027–2034. doi: 10.1039/C4SC03709J

Glendening, E. D., Badenhoop, J. K., Reed, A. E., Carpenter, J. E., Bohmann, J. A., Morales, C. M., et al. (2001). *NBO 5.0, Theoretical Chemistry Institute.* Madison, WI: University of Wisconsin.

Grushin, V. V., Kuznetsov, V. F., Bensimon, C., and Alper, H. (1995). A simple and convenient preparation of $[(Ph_3P)_4Rh_2(\mu\text{-}OH)_2]$ and its reactions with C-H, O-H, and M-H acids. *Organometallics* 14, 3927–3932. doi: 10.1021/om00008a044

Hasegawa, E., Seida, T., Chiba, N., Takahashi, T., and Ikeda, H. (2005). Contrastive photoreduction pathways of benzophenones governed by regiospecific deprotonation of imidazoline radical cations and additive effects. *J. Org. Chem.* 70, 9632–9635. doi: 10.1021/jo0514220

Hasegawa, E., Takizawa, S., Seida, T., Yamaguchi, A., Yamaguchi, N., Chiba, N., et al. (2006). Photoinduced electron-transfer systems consisting of electron-donating pyrenes or anthracenes and benzimidazolines for reductive transformation of carbonyl compounds. *Tetrahedron* 62, 6581–6588. doi: 10.1016/j.tet.2006.03.061

Hayashi, C., Hayashi, T., and Yamada, T. (2015). Cobalt-catalyzed reductive carboxylation of α,β-unsaturated compounds with carbon dioxide. *Bull. Chem. Soc. Jpn.* 88, 862–870. doi: 10.1246/bcsj.20150043

Hou, J., Ee, A., Cao, H., Ong, H.-W., Xu, J.-H., and Wu, J. (2018a). Visible-light-mediated metal-free difunctionalization of alkenes with CO_2 and silanes or $C(sp^3)$-H alkanes. *Angew. Chem., Int. Ed.* 57, 17220–17224. doi: 10.1002/anie.201811266

Hou, J., Ee, A., Feng, W., Xu, J.-H., Zhao, Y., and Wu, J. (2018b). Visible-light-driven alkyne hydro-/carbocarboxylation using CO_2 via iridium/cobalt dual catalysis for divergent heterocycle synthesis. *J. Am. Chem. Soc.* 140, 5257–5263. doi: 10.1021/jacs.8b01561

Ikezawa, H., Kutal, C., Yasufuku, K., and Yamazaki, H. (1986). Direct and sensitized valence photoisomerization of a substituted norbornadiene. Examination of the disparity between singlet- and triplet-state reactivities. *J. Am. Chem. Soc.* 108, 1589–1594. doi: 10.1021/ja00267a032

Islangulov, R. R., and Castellano, F. N. (2006). Photochemical upconversion: anthracene dimerization sensitized to visible light by a Ru^{II} Chromophore. *Angew. Chem. Int. Ed.* 45, 5957–5959. doi: 10.1002/anie.200601615

Ju, T., Fu, Q., Ye, J.-H., Zhang, Z., Liao, L.-L., Yan, S.-S., et al. (2018). Selective and catalytic hydrocarboxylation of enamides and imines with CO_2 to generate α,α-disubstituted α-amino acids. *Angew. Chem. Int. Ed.* 57, 13897–13901. doi: 10.1002/anie.201806874

Kalyanasundaram, K. (1982). Photophysics, photochemistry and solar energy conversion with tris(bipyridyl)ruthenium(II) and its analogues. *Coord. Chem. Rev.* 46, 159–244. doi: 10.1016/0010-8545(82)85003-0

Kawashima, S., Aikawa, K., and Mikami, K. (2016). Rhodium-catalyzed hydrocarboxylation of olefins with carbon dioxide. *Eur. J. Org. Chem.* 2016, 3166–3170. doi: 10.1002/ejoc.201600338

Li, S., Yuan, W., and Ma, S. (2011). Highly regio- and stereoselective three-component nickel-catalyzed syn-hydrocarboxylation of alkynes with diethyl zinc and carbon dioxide. *Angew. Chem. Int. Ed.* 50, 2578–2582. doi: 10.1002/anie.201007128

Lowry, M. S., Goldsmith, J. I., Slinker, J. D., Rohl, R., Pascal, R. A., Malliaras, G. G., et al. (2005). Single-layer electroluminescent devices and photoinduced hydrogen production from an ionic iridium(III) complex. *Chem. Mater.* 17, 5712–5719. doi: 10.1021/cm051312+

Lu, Z., and Yoon, T. P. (2012). Visible light photocatalysis of [2+2] styrene cycloadditions by energy transfer. *Angew. Chem. Int. Ed.* 51, 10329–10332. doi: 10.1002/anie.201204835

Luan, Y.-X., and Ye, M. (2018). Transition metal-mediated or catalyzed hydrocarboxylation of olefins with CO_2. *Tetrahedron Lett.* 59, 853–861. doi: 10.1016/j.tetlet.2018.01.035

Meng, Q.-Y., Wang, S., Huff, G. S., and König, B. (2018). Ligand-controlled regioselective hydrocarboxylation of styrenes with CO_2 by combining visible light and nickel catalysis. *J. Am. Chem. Soc.* 140, 3198–3201. doi: 10.1021/jacs.7b13448

Meng, Q.-Y., Wang, S., and König, B. (2017). Carboxylation of aromatic and aliphatic bromides and triflates with CO_2 by dual visible-light–nickel catalysis. *Angew. Chem. Int. Ed.* 56, 13426–13430. doi: 10.1002/anie.201706724

Mizuno, H., Takaya, J., and Iwasawa, N. (2011). Rhodium(I)-catalyzed direct carboxylation of arenes with CO_2 via chelation-assisted C-H bond activation. *J. Am. Chem. Soc.* 133, 1251–1253. doi: 10.1021/ja109097z

Morris, A. J., Meyer, G. J., and Fujita, E. (2009). Molecular approaches to the photocatalytic reduction of carbon dioxide for solar fuels. *Acc. Chem. Res.* 42, 1983–1994. doi: 10.1021/ar9001679

Murata, K., Numasawa, N., Shimomaki, K., Takaya, J., and Iwasawa, N. (2017). Construction of a visible light-driven hydrocarboxylation cycle of alkenes by the combined use of Rh(I) and photoredox catalysts. *Chem. Commun.* 53, 3098–3101. doi: 10.1039/C7CC00678K

Osawa, M., Hoshino, M., and Wakatsuki, Y. (2001). A Light-harvesting *tert*-phosphane ligand bearing a ruthenium(II) polypyridyl complex as substituent. *Angew. Chem. Int. Ed.* 40, 3472–3474. doi: 10.1002/1521-3773(20010917)40:18<3472::AID-ANIE3472>3.0.CO;2-W

Schultz, D. M., Sawicki, J. M., and Yoon, T. P. (2015). An improved procedure for the preparation of $Ru(bpz)_3(PF_6)_2$ via a high-yielding synthesis of 2,2'-bipyrazine. *Beilstein J. Org. Chem.* 11, 61–65. doi: 10.3762/bjoc.11.9

Seo, H., Katcher, M. H., and Jamison, T. F. (2017a). Photoredox activation of carbon dioxide for amino acid synthesis in continuous flow. *Nat. Chem.* 9, 453–456. doi: 10.1038/nchem.2690

Seo, H., Liu, A., and Jamison, T. F. (2017b). Direct β-selective hydrocarboxylation of styrenes with CO_2 enabled by continuous flow photoredox catalysis. *J. Am. Chem. Soc.* 139, 13969–13972. doi: 10.1021/jacs.7b05942

Shimomaki, K., Murata, K., Martin, R., and Iwasawa, N. (2017). Visible-light-driven carboxylation of aryl halides by the combined use of palladium and photoredox catalysts. *J. Am. Chem. Soc.* 139, 9467–9470. doi: 10.1021/jacs.7b04838

Skubi, K. L., Blum, T. R., and Yoon, T. P. (2016). Dual catalysis strategies in photochemical synthesis. *Chem. Rev.* 116, 10035–10074. doi: 10.1021/acs.chemrev.6b00018

Slinker, J. D., Gorodetsky, A. A., Lowry, M. S., Wang, J., Parker, S., Rohl, R., et al. (2004). Efficient yellow electroluminescence from a single layer of a cyclometalated iridium complex. *J. Am. Chem. Soc.* 126, 2763–2767. doi: 10.1021/ja0345221

Stoll, T., Castillo, C. E., Kayanuma, M., Sandroni, M., Daniel, C., Odobel, F., et al. (2015). Photo-induced redox catalysis for proton reduction to hydrogen with homogeneous molecular systems using rhodium-based catalysts. *Coord. Chem. Rev.* 304, 20–37. doi: 10.1016/j.ccr.2015.02.002

Strauss, S. H., and Shriver, D. F. (1978). Lewis acid-influenced ethylene hydrogenation by rhodium(I) complexes. *Inorg. Chem.* 17, 3069–3074. doi: 10.1021/ic50189a020

Strieth-Kalthoff, F., James, M. J., Teders, M., Pitzer, L., and Glorius, F. (2018). Energy transfer catalysis mediated by visible light: principles, applications, directions. *Chem. Soc. Rev.* 47, 7190–7202. doi: 10.1039/c8cs00054a

Suga, T., Mizuno, H., Takaya, J., and Iwasawa, N. (2014). Direct carboxylation of simple arenes with CO_2 through a rhodium-catalyzed C–H bond activation. *Chem. Commun.* 50, 14360–14363. doi: 10.1039/C4CC06188H

Suomalainen, P., Reinius, H. K., Riihimäki, H., Laitinen, R. H., Jääskeläinen, S., Haukka, M., et al. (2001). Hydroformylation of 1-hexene and propene with *in situ* formed rhodium phosphine catalysts. *J. Mol. Catal. A. Chem.* 169, 67–78. doi: 10.1016/S1381-1169(01)00038-3

Takaya, J., and Iwasawa, N. (2008). Hydrocarboxylation of allenes with CO_2 catalyzed by silyl pincer-type palladium complex. *J. Am. Chem. Soc.* 130, 15254–15255. doi: 10.1021/ja806677w

Takeda, H., and Ishitani, O. (2010). Development of efficient photocatalytic systems for CO_2 reduction using mononuclear and multinuclear metal complexes based on mechanistic studies. *Coord. Chem. Rev.* 254, 346–354. doi: 10.1016/j.ccr.2009.09.030

Tamaki, Y., Koike, K., and Ishitani, O. (2015). Highly efficient, selective, and durable photocatalytic system for CO_2 reduction to formic acid. *Chem. Sci.* 6, 7213–7221. doi: 10.1039/C5SC02018B

Tamayo, A. B., Alleyne, B. D., Djurovich, P. I., Lamansky, S., Tsyba, I., Ho, N. N., et al. (2003). Synthesis and characterization of facial and meridional tris-cyclometalated iridium(III) complexes. *J. Am. Chem. Soc.* 125, 7377–7387. doi: 10.1021/ja034537z

Tellis, J. C., Primer, D. N., and Molander, G. A. (2014). Single-electron transmetalation in organoboron cross-coupling by photoredox/nickel dual catalysis. *Science* 345, 433–436. doi: 10.1126/science.1253647

Tomasi, J., Mennucci, B., and Cammi, R. (2005). Quantum mechanical continuum solvation models. *Chem. Rev.* 105, 2999–3094. doi: 10.1021/cr9904009

Tortajada, A., Juliá-Hernández, F., Börjesson, M., Moragas, T., and Martin, R. (2018). Transition-metal-catalyzed carboxylation reactions with carbon dioxide. *Angew. Chem. Int. Ed.* 57, 15948–15982. doi: 10.1002/anie.201803186

Twilton, J., Le, C., Zhang, P., Shaw, M. H., Evans, R. W., and MacMillan, D. W. C. (2017). The merger of transition metal and photocatalysis. *Nat. Rev. Chem.* 1:0052. doi: 10.1038/s41570-017-0052

Ukai, K., Aoki, M., Takaya, J., and Iwasawa, N. (2006). Rhodium(I)-catalyzed carboxylation of aryl- and alkenylboronic esters with CO_2. *J. Am. Chem. Soc.* 128, 8706–8707. doi: 10.1021/ja061232m

Van der Ent, A., Onderdelinden, A. L., and Schunn, R. A. (1990). Chlorobis(cyclooctene)rhodium(I) and –iridium(I) complexes. *Inorg. Synth.* 28, 90–92. doi: 10.1002/9780470132593.ch23

Varetto, U. (2009). *Molekel 5.4, Swiss National Supercomputing Centre.* Lugano.

Wadt, W. R., and Hay, P. J. (1985a). *Ab initio* effective core potentials for molecular calculations. Potentials for main group elements Na to Bi. *J. Chem. Phys.* 82, 284–298. doi: 10.1063/1.448800

Wadt, W. R., and Hay, P. J. (1985b). *Ab initio* effective core potentials for molecular calculations. Potentials for K to Au including the outermost core orbitals. *J. Chem. Phys.* 82, 299–310. doi: 10.1063/1.448975

Wang, X., Nakajima, M., and Martin, R. (2015). Ni-catalyzed regioselective hydrocarboxylation of alkynes with CO_2 by using simple alcohols as proton sources. *J. Am. Chem. Soc.* 137, 8924–8927. doi: 10.1021/jacs.5b05513

Werner, H., Schäfer, M., Nürnberg, O., and Wolf, J. (1994). η^3-Allyl and η^3-benzyl rhodium complexes: synthesis, structure dynamic, and reactions with carboxylic acids. *Chem. Ber.* 127, 27–38. doi: 10.1002/cber.19941270106

Williams, C. M., Johnson, J. B., and Rovis, T. (2008). Nickel-catalyzed reductive carboxylation of styrenes using CO_2. *J. Am. Chem. Soc.* 130, 14936–14937. doi: 10.1021/ja8062925

Yan, S.-S., Fu, Q., Liao, L.-L., Sun, G.-Q., Ye, J.-H., Gong, L., et al. (2018). Transition metal-catalyzed carboxylation of unsaturated substrates with CO_2. *Coord. Chem. Rev.* 374, 439–463. doi: 10.1016/j.ccr.2018.07.011

Yatham, V. R., Shen, Y., and Martin, R. (2017). Catalytic intermolecular dicarbofunctionalization of styrenes with CO_2 and radical precursors. *Angew. Chem. Int. Ed.* 56, 10915–10919. doi: 10.1002/anie.201706263

Ye, J.-H., Miao, M., Huang, H., Yan, S.-S., Yin, Z.-B., Zhou, W.-J., et al. (2017). Visible-light-driven iron-promoted thiocarboxylation of styrenes and acrylates with CO_2. *Angew. Chem. Int. Ed.* 56, 15416–15420. doi: 10.1002/anie.201707862

Yeung, C. S. (2019). Photoredox catalysis as a strategy for CO_2 incorporation: direct access to carboxylic acids from a renewable feedstock. *Angew. Chem. Int. Ed.* 58, 5492–5502. doi: 10.1002/anie.201806285

Zhu, C., Takaya, J., and Iwasawa, N. (2015). Use of formate salts as a hydride and a CO_2 source in PGeP-palladium complex-catalyzed hydrocarboxylation of allenes. *Org. Lett.* 17, 1814–1817. doi: 10.1021/acs.orglett.5b00692

Conflict of Interest Statement: The authors declare that the research was conducted in the absence of any commercial or financial relationships that could be construed as a potential conflict of interest.

The reviewer MA declared a shared affiliation, with no collaboration, with the authors NN, KS, JT, NI, to the handling editor at the time of review.

Copyright © 2019 Murata, Numasawa, Shimomaki, Takaya and Iwasawa. This is an open-access article distributed under the terms of the Creative Commons Attribution License (CC BY). The use, distribution or reproduction in other forums is permitted, provided the original author(s) and the copyright owner(s) are credited and that the original publication in this journal is cited, in accordance with accepted academic practice. No use, distribution or reproduction is permitted which does not comply with these terms.

frontiers in Chemistry

ORIGINAL RESEARCH
published: 05 June 2019
doi: 10.3389/fchem.2019.00417

Electronic Effects of Substituents on *fac*-M(bpy-R)$(CO)_3$ (M = Mn, Re) Complexes for Homogeneous CO_2 Electroreduction

Laura Rotundo[1,2,3], Emanuele Azzi[1], Annamaria Deagostino[1], Claudio Garino[1,2,3], Luca Nencini[1], Emanuele Priola[1,2], Pierluigi Quagliotto[1,2], Riccardo Rocca[1,2,3], Roberto Gobetto[1,2,3] and Carlo Nervi[1,2,3]**

[1] Department of Chemistry, Università degli Studi di Torino, Turin, Italy, [2] NIS Interdepartmental Centre, Università degli Studi di Torino, Turin, Italy, [3] Consorzio Interuniversitario Reattività Chimica e Catalisi (CIRCC), Bari, Italy

OPEN ACCESS

Edited by:
Hitoshi Ishida,
Kitasato University, Japan

Reviewed by:
Baojian Shen,
China University of Petroleum,
Beijing, China
Yusuke Tamaki,
Tokyo Institute of Technology, Japan

***Correspondence:**
Roberto Gobetto
roberto.gobetto@unito.it
Carlo Nervi
carlo.nervi@unito.it

Specialty section:
This article was submitted to
Inorganic Chemistry,
a section of the journal
Frontiers in Chemistry

Received: 29 January 2019
Accepted: 21 May 2019
Published: 05 June 2019

Citation:
Rotundo L, Azzi E, Deagostino A, Garino C, Nencini L, Priola E, Quagliotto P, Rocca R, Gobetto R and Nervi C (2019) Electronic Effects of Substituents on fac-M(bpy-R)$(CO)_3$ (M = Mn, Re) Complexes for Homogeneous CO_2 Electroreduction. Front. Chem. 7:417. doi: 10.3389/fchem.2019.00417

Synthesis and characterization of 14 new 2,2′-bipyridine metal complexes *fac*-M(bpy-R)$(CO)_3$X (where M = Mn, X = Br or M = Re, X = Cl and R = -CF_3, -CN, -Ph, -PhOH, -NMe_2) are reported. The complexes have been characterized by NMR, IR spectroscopy and elemental analysis. Single crystal X-Ray diffraction structures have been solved for Re(dpbpy)$(CO)_3$Cl (dpbpy = 4,6-diphenyl-2,2′-bipyridine) and Re(hpbpy)$(CO)_3$Cl (hpbpy = 4-(2-hydroxy-phenyl)-6-phenyl-2,2′-bipyridine). Electrochemical behaviors of the complexes in acetonitrile under Ar and their catalytic performances for CO_2 reduction with added water and MeOH have been investigated by cyclic voltammetry and controlled potential electrolysis. The role of the substituents on the electrochemical properties and the related over potentials required for CO_2 transformation have been analyzed. The complexes carrying only electron withdrawing groups like -CF_3, -CN totally lose their catalytic activities toward CO_2 reduction, whereas the symmetric -NMe_2 substituted and push-pull systems (containing both -NMe_2 and -CF_3) still display electrocatalytic current enhancement under CO_2 atmosphere. The complexes carrying a phenyl or a phenol group in position 4 show catalytic behaviors similar to those of simple M-bpy systems. The only detected reduction product by GC analysis is CO: for example, *fac*-Re (bpy-4,4′-NMe_2)$(CO)_3$Cl gives CO with high faradic efficiency and a TON of 18 and 31, in absence of external proton source and with 5% MeOH, respectively. DFT calculations were carried out to highlight the electronic properties of the complexes; results are in agreement with experimental electrochemical data.

Keywords: CO_2 electroreduction, Mn complexes, Re complexes, DFT calculations, bipy ligands, homogeneous catalysis, electron-withdrawing, electron-donating

INTRODUCTION

Nowadays the CO_2 concentration in the atmosphere is continuously increasing alongside with the overall world energy demand. Converting carbon dioxide via electrochemical reduction into useful chemicals and fuels for energy storage is an attractive and promising approach. CO_2 reduction is a competition between its thermodynamic and kinetic: the one electron reduction in water occurs at a very negative potential (−1.90 V vs. SCE at pH 7) (Hammouche et al., 1988; Saveant, 2008) because it requires a drastic change in the geometry, from the linear CO_2 molecule to the bent $CO_2^{-\bullet}$ radical anion. The reason of such high negative overpotential is due to the slow kinetics of the electron transfer, which is associated to the different geometries of the neutral and reduced species, respectively. However, the reduction reactions involving multiple electron transfers coupled with proton transfers provide a significant lowering of the thermodynamic barrier. To avoid the $CO_2^{-\bullet}$ as intermediate and to lower the energy cost of the reduction process, key catalytic strategies have been developed with the aim of obtaining the various products selectively. The best electrocatalysts currently studied work at a potential 100 mV negative with respect to E^0 CO_2/P (where P generically indicates the reduction products, CO, HCOOH, HCHO, CH_3OH, CH_4) (Francke et al., 2018; Franco et al., 2018). Despite the numerous advantages of heterogeneous electrocatalysis (Sun et al., 2016; Rotundo et al., 2019a), clever integration with the homogeneous counterpart allows a rational design of the catalysts, by tuning both the metal center and/or the ligand. One of the greatest challenge of the homogeneous approach lies in the search of stability, durability and improved turnover number (TON) efficiencies (Grice, 2017; Takeda et al., 2017; Wang et al., 2019). Bipyridine transition metal complexes represent one of the most studied classes of molecular electrocatalysts since the 1980s (Stanbury et al., 2018). Bipyridine has been extensively studied as ligand in the field of electro and photo-catalysis because of the capability to store electrons and subsequently delocalize electronic density on its π orbitals (Vlček, 2002; Elgrishi et al., 2017). Both *fac*-Re(bpy)$(CO)_3$Cl and *fac*-Mn(bpy)$(CO)_3$Br are capable of reducing CO_2 to CO with high faradaic efficiency (Hawecker et al., 1984; Bourrez et al., 2011). Comparing these two complexes, Mn exhibits a catalytic peak that is shifted more anodically (around 300 mV, $E_p = -1.51$ V vs. Ag/AgCl in MeCN) in comparison with the second reduction of Re analogous ($E_p = -1.8$ V vs. Ag/AgCl in MeCN). Another important difference is that usually the Mn-bpy complexes show their catalytic activities only in the presence of external proton sources. To better shed light on this uniqueness, our research group synthesized Mn(pdbpy)$(CO)_3$Br (Franco et al., 2014, 2017), in which two pendant phenolic groups act as local proton source (Costentin et al., 2012), capable of reducing CO_2 even in anhydrous acetonitrile. In this case a considerable amount of HCOOH was also detected. Conversely the analogous complex in which the OH groups were replaced by methoxy groups did not show any catalytic activity without the addition of Brønsted acid.

The electrochemical behavior of the two well-known Re and Mn-bpy complexes could be reasonably altered by varying the bipyridine moiety, i.e., introducing electron-withdrawing and electron-donating groups (Machan et al., 2014; Walsh et al., 2015; Stanbury et al., 2018). Kubiak and his group investigated the effect of 4,4′-di-tertbutyl-2,2′-bipyridine (tBu_2-bpy) firstly on rhenium carbonyl complexes, secondarily on manganese (Smieja and Kubiak, 2010; Smieja et al., 2013). In other works they studied the role of the modification in the 6,6′ position of the bipyridine (Sampson et al., 2014; Sampson and Kubiak, 2016). A similar approach has already been applied to Mo and W-bpy complexes (Franco et al., 2017; Rotundo et al., 2018), to both Mn and Re-bpy complexes by some of us (Franco et al., 2017; Rotundo et al., 2019b) and in the current work.

The target of the modification is the reduction potential of the catalyst, namely E^0_{cat}: usually a less negative E^0_{cat} corresponds to a decreased rate of CO_2 conversion (Francke et al., 2018). Electronic properties of organic groups are commonly described by the inductive (±I) and mesomeric (±M) effects. Substituents with electron withdrawing groups like -CF_3 (strong –I effect) and -CN (weaker –I effect) and with electron donating groups, like -$N(Me)_2$ (strong +M effect), -Ph and -PhOH (weaker +M effect), were placed in the 4,4′, 4,6, and 5,5′ positions of the bipyridine ligand coordinated to the metals. Combining both push and pull effects in the so called "push-pull" system, an electronic gradient is forced through the bipyridine. In this paper we explore the electrocatalytic properties of novel Mn and Re bpy-type complexes, bearing 7 differently substituted ligands (**Scheme 1**). More generally electron-donating groups are expected to convey greater nucleophilicity to the metal-center, although catalysis should require higher overpotentials. DFT calculations have been used as complementary tool to better correlate experimental electrochemical data, whereas Controlled Potential Electrolysis (CPE) experiments are useful to elucidate the stability and durability of the catalysts in acetonitrile solutions.

RESULTS

Synthesis and Structure

Fourteen new 2,2′-bipyridine metal complexes *fac*-M(bpy-R)$(CO)_3$X where M = Mn, X = Br or M = Re, X = Cl are reported, namely Mn(bpy-4,4′-CF_3)$(CO)_3$Br (**1a**), Mn(bpy-5,5′-CF_3)$(CO)_3$Br (**1b**), Mn(bpy-4,4′-CN)$(CO)_3$Br (**1c**), Mn(bpy-4,4′-CF_3-NMe_2)$(CO)_3$Br (**1d**), Mn(dpbpy)$(CO)_3$Br (**1e**), Mn(hpbpy)$CO)_3$Br (**1f**), Mn(bpy-4,4′-NMe_2)$(CO)_3$Br (**1g**), Re(bpy-4,4′-CF_3)$(CO)_3$Cl (**2a**), Re(bpy-5,5′-CF_3)$(CO)_3$Cl (**2b**), Re(bpy-4,4′-CN)$(CO)_3$Cl (**2c**), Re(bpy-4,4′-CF_3-NMe_2)$(CO)_3$Cl (**2d**), Re(dpbpy)$(CO)_3$Cl (**2e**), Re(hpbpy)$(CO)_3$Cl (**2f**), Re(bpy-4,4′-NMe_2)$(CO)_3$Cl (**2g**).

The ligands and the corresponding Mn and Re complexes have been synthesized according to the procedure reported in the experimental section. The complexes have been characterized by NMR, IR spectroscopy and elemental analysis. Single crystal X-Ray diffraction structures have been solved for **2e** and **2f** (for XRD data see **Tables S1–S6**).

The complex Re(dpbpy)$(CO)_3$Cl (**2e**) crystallized from both acetonitrile and benzene solutions by slow evaporation, forming prismatic orange platelets of a phase of the pure molecular product (structure A, **Figure S1a**) and a solvate with two benzene

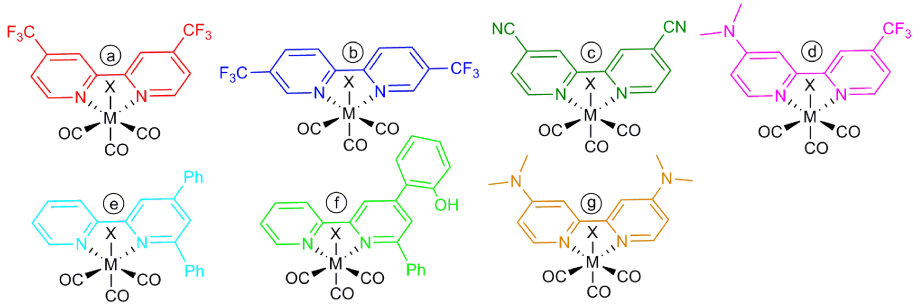

SCHEME 1 | Chemical sketches of the investigated complexes, where M = Mn, X = Br, or M = Re, X = Cl.

molecules (structure B, **Figure S1b**). The first presents the monoclinic centrosymmetric $P2_1/a$ space group (**Figure S1c**) while the second the monoclinic centrosymmetric P2/n space group (**Figure S1d**). The complex $Re(hpbpy)(CO)_3Cl$ (**2f**) crystallized in dark by slow evaporation of solutions of toluene and benzene as yellow platelets and from ethyl acetate as orange prisms, both stable to air (**Figure S2a**). The crystal structure has been obtained from a platelet obtained from toluene solution and has monoclinic $P2_1/n$ space group type (**Figure S2b**). The structures of both **2e** and **2f** present a quite distorted octahedral geometry around the rhenium center, as can be seen by the values in **Table 1**. The coordination bond of N1 is 0.1 Å longer than that of N2 (see **Figure 1** for numeration) and a similar asymmetry can be observed in the coordination of CO in trans position to the nitrogens. This asymmetric coordination, also present in other terpyridine derivatives (Anderson et al., 1990; Civitello et al., 1993; Wang et al., 2013; Klemens et al., 2016) is completely different from the very symmetrically bonded bpy derivatives (with N-Re average distances equal in the two coordinating pyridyl rings and long 2.17 Å). At the same time, while most of the 2,2′-bipyridine derivatives of *fac*-$Re(CO)_3Cl$ complex unit are almost planar respect to the basal OC–Re–CO plane (Kurz et al., 2006; Smieja and Kubiak, 2010; Bullock et al., 2012; Machan et al., 2014; Manbeck et al., 2015), in the case of **2e** and **2f**, the ligand is distorted outside this plane (see **Table 1**). This behavior can be detected in all the terpyridines, in which the third pyridine ring is not coordinated to the metal center and is equivalent to a phenyl ring, and in 6-phenyl substituted 2,2′-bipyridine derivatives. The reason of such distortion is clarified by considering the steric hindrance of the vicinal phenyl ring (the distance between the nearest CO group and the centroid of the phenyl ring in ortho to N1 is about 3.2 Å) that pushes up all the framework of the organic ligand, modifying the Re environment. This phenyl group is rotated to follow the shape of carbonyls with a torsion angle respect to the central pyridine ring of about 130°.

The distortion effects observed in the solid state are predicted also by molecular DFT calculations. Indeed, the optimized geometries of **2e** and **2f** perfectly overlap with the experimentally determined structures (**Figure 1D** and **Figure S3**), confirming that these anomalies originate from the coordination of 6-phenyl substituted 2,2′-bipyridine ligands to carbonyl complexes and are not induced by crystal packing contributions.

TABLE 1 | Selected X-ray bond lengths [Å] and angles [°] for **2e** and **2f**.

	2e (structure A)	2e (structure B)	2f
Re–C1	1.906 (5)	1.919 (5)	1.919 (5)
Re–C2	1.936 (5)	1.952 (5)	1.935 (5)
Re–C3	1.890 (5)	1.933 (5)	1.898 (5)
Re–N1	2.160 (5)	2.177 (5)	2.164 (5)
Re–N2	2.220 (5)	2.233 (5)	2.214 (5)
N2–C13–C14–C15	132.85 (5)	125.66 (4)	125.47 (4)
C2O2–ph	3.110 (5)	3.239 (3)	3.233 (5)
Re1–N2–C11	165.28 (6)	162.38 (6)	159.09 (6)

The crystal packing of **2e** (both structure A and structure B) and **2f** is dominated by weak C–H···Cl, C–H···O and π···π stacking interactions. In the case of **2f**, the presence of -OH group on the organic ligand interacting with the chloride induces the formation of hydrogen-bonded molecular chains (see **Figure 1C** and **Figure S2c**). For a more detailed analysis on the crystal packing consults the Supplementary Material (see **Figures S4–S9**).

Cyclic Voltammetry Under Ar

Cyclic Voltammetries (CVs) of all manganese complexes are reported in **Figure 2**. The CV of the $Mn(bpy)(CO)_3Br$ under our experimental conditions (in black) is included for comparison. This complex undergoes two successive irreversible reduction reactions and two reoxidation peaks (Bourrez et al., 2011). The first ($E_{p1} = -1.29$ V vs. Ag/AgCl) and the second ($E_{p2} = -1.51$ V vs. Ag/AgCl) reduction processes lead to the formation of the dimer and the mononuclear pentacoordinated anion species, respectively. Reoxidations of the pentacoordinated anion and of the dimer are located at −1.09 and −0.21 V vs. Ag/AgCl, respectively. The new synthesized complexes are supposed to display similar electrochemical behavior. **Table 2** reports the peak potentials of the first and second reductions. As expected, the presence of $-CF_3$ (**1a** and **1b**) and –CN (**1c**) shifts first and second potentials toward more positive values, when compared to $Mn(bpy)(CO)_3Br$. In a recent paper (Rawat et al., 2019) DFT calculations suggested that electron-withdrawing substituents like $-CF_3$ stabilize the radical anion. Furthermore,

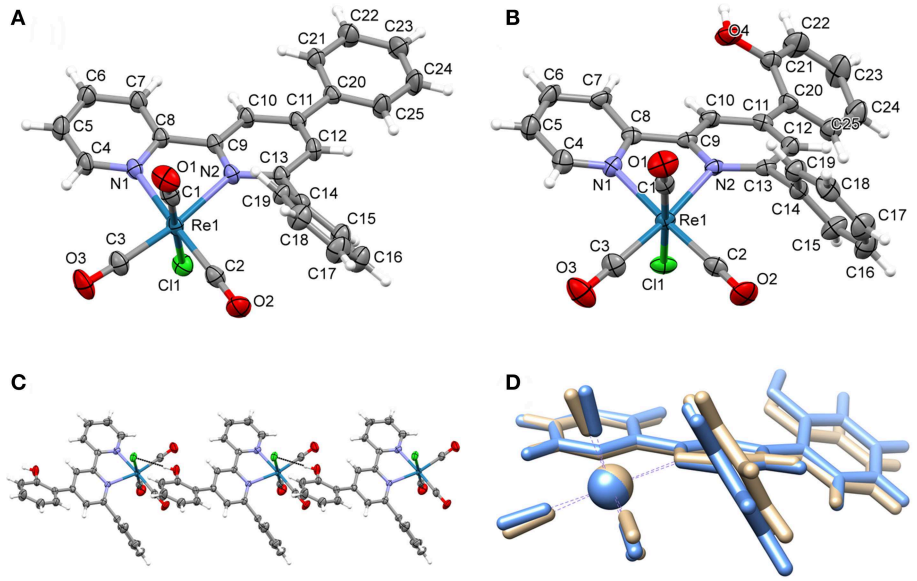

FIGURE 1 | (A) molecular structure of Re(dpbpy)(CO)$_3$Cl (**2e**, structure A), **(B)** molecular structure of Re(hpbpy)(CO)$_3$Cl (**2f**), **(C)** chain formed by O–H···Cl intermolecular contacts in the crystal structure of **2f,** and **(D)** comparison of DFT optimized (light blue) and X-ray (brown) structures of **2f**.

the formation of all Mn-Mn dimers was indicated as unfavorable. However, the electrochemical mechanism outlined above is commonly accepted, and the Mn dimer is strongly favored. We experimentally found that all complexes undergo a first and second chemically irreversible reductions. For example, **1a** shows two chemical irreversible processes followed by the reoxidations of the pentacoordinated radical anion and that of the dimer (**Figure S10**), even at high scan rates (1 V/s, **Figure S11**), thus confirming the general mechanism. CV of **1g** confirms that the strong electron-donating properties of dimethyl amino group result in more negative reduction potentials with respect to Mn(bpy)(CO)$_3$Br. The push-pull system **1d**, **1e** and **1f** display similar potential values to the unsubstituted bpy-complex. In some complexes decomposition processes occurring after reduction generate small peaks (i.e., for **1e** and **1f** $E_p = -1.65$ and -1.63 V vs. Ag/AgCl are observed, respectively). The very negative peak around -3V vs. Ag/AgCl, is commonly assigned to a ligand-centered reduction.

CVs of all rhenium complexes are reported in **Figure 3**. CV of the reference Re(bpy)(CO)$_3$Cl under our experimental conditions is included for comparison. This complex exhibits a first reversible reduction, due to the formation of the radical anion, which is more stable than the analogous with manganese, thus resulting in electrochemical reversibility and no presence of the reoxidation peak of the dimer (Hawecker et al., 1984). The second reduction leads to the pentacoordinated anion. Intrinsically, rhenium complexes require slightly higher overpotentials with respect to the corresponding manganese ones. The first reversible reduction of Re(bpy)(CO)$_3$Cl is located at $E_{1/2} = -1.35$ V vs. Ag/AgCl, whereas the second chemically irreversible reduction is at $E_{p2} = -1.80$ V vs. Ag/AgCl. Similarly to manganese, the new synthesized rhenium complexes show no significant difference in the electrochemical pathway under Ar when compared to the reference Re(bpy)(CO)$_3$Cl (**Table 2**). Electron withdrawing groups (**2a**, **2b,** and **2c**) shift the reduction processes toward less negative values; electron donating groups like in **2g** essentially merge the first and second reductions into a single peak. The push-pull system **2d**, in analogy with the case of **1d**, do not significantly alter the positioning of the reduction potentials. The third peak, around -2.5V, also for these complexes, is generally attributed to a bpy-centered reduction.

The reduction potentials estimated by DFT calculation are in excellent agreement with the experimental values obtained for the first reduction potential of all rhenium complexes (**Figure 4**). This confirms the reversible nature of the first reduction process, leading to stable radical anions characterized by a very small increase (about 0.05 Å) in the Re–Cl bond length (**Figure S12**). Conversely, in the case of manganese complexes, DFT calculations, which compute thermodynamic reduction potentials, are not suitable to estimate the irreversible electrochemical behavior of the compounds (**Figure S13**). Indeed, the high instability of the radical anion leads to the weakening of the Mn–Br bond, as clearly evidenced by the significant increase of the Mn–Br bond length in the anion structures (**Figure S14**). Our DFT calculations that include weak interactions, are in agreement with the chemically irreversibility of the first reduction and dimer production, even in the case of electron-withdrawing substituents. For example, the formation of the dimer [Mn(bpy)(CO)$_3$]$_2$ from its radical anion is favored by 143.5 kJ/mol, and in the case of **1a** is favored by 102.6 kJ/mol.

Cyclic Voltammetry Under CO_2

The electrochemical behavior of manganese complexes under CO_2 and with H_2O (5%v) is reported in **Figure 5** for **1d** to

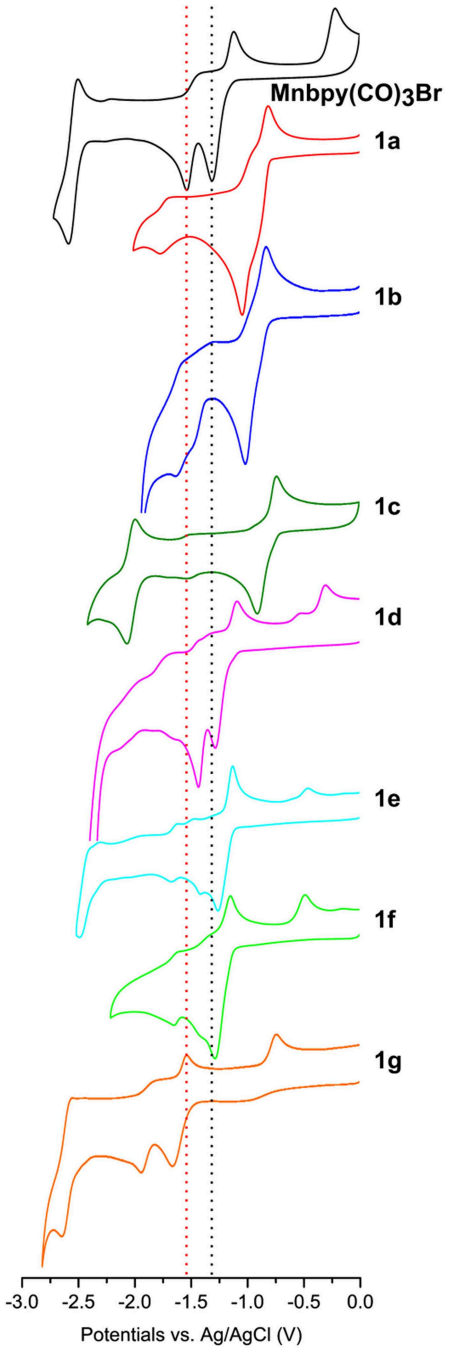

FIGURE 2 | CVs of 1 mM solutions of **1a–1g** Mn complexes in MeCN/0.1 M $TBAPF_6$ at GCE, scan rate 200 mVs^{-1} under Ar. CV of the reference *fac*-Mn(bpy)$(CO)_3$Br is in black.

TABLE 2 | Reduction peak potentials [V] from the CV of Mn and Re complexes.

Mn complexes	E_{p1}	E_{p2}
Mn(bpy)$(CO)_3$Br	−1.29	−1.51
1a	−0.92	−1.07
1b	−0.88	−0.99
1c	−0.89	−0.89
1d	−1.31	−1.42
1e	−1.26	−1.4
1f	−1.24	−1.39
1g	−1.64	−1.91
Re complexes	$E_{1/2}$ **(or** E_{p1}**)**	E_{p2}
Re(bpy)$(CO)_3$Cl	−1.35	−1.80
2a	−0.92	−1.45
2b	−0.83	−1.57
2c	−0.77	−1.85
2d	−1.29	−1.77
2e	−1.31	−1.68
2f	−1.37	−1.66
2g	−1.82 (1st + 2nd peak)	

1g and in **Figure S15** for **1a**, **1b,** and **1c**, (these complexes are catalytically inactive toward CO_2 reduction). CVs of **1a-1g** under CO_2 with 5%v MeOH are included for comparison in **Figure S15** too. All complexes do not show significant current increases switching from Ar to CO_2 atmosphere. While this is expected for manganese complexes, **1g** shows a current increase, though limited, even in absence of Brønsted acid addition.

The electrochemical behavior of rhenium complexes under CO_2 and with 5%v MeOH is reported in **Figure 6** for **2d** to **2g** and in **Figure S16** for **2a**, **2b,** and **2c**. CVs of **2a-2g** under CO_2 with 5%v H_2O are included for comparison in **Figure S16** too. All complexes exhibit catalytic current switching from Ar to CO_2 atmosphere, even in absence of Brønsted acid, as expected for rhenium complexes.

Controlled Potential Electrolysis Experiments of the Complexes

Bulk electrolysis experiments of all manganese and rhenium complexes series under CO_2 were performed upon setting the potential at values slightly negative to the second reductions, with and without external added Brønsted acids (water and methanol, 5%). A CO_2 flow of 50 mL min^{-1} was kept constant during the experiments, gaseous products were determined by gas chromatography, and formate, if present, was assessed by NMR spectroscopy at the end of the experiments. **Table 3** summarizes the results obtained during these CPE experiments. A general trend can be outlined: addition of water results in increased TONs for Mn complexes (**Table 3** and **Figure S17**), differently from methanol, which drops them to lower values (**Table S7**). On the other hand, for the case of Re complexes, addition of methanol (**Table 3** and **Figure S18**) seems to enhance the catalytic activity with respect to water, except for complex **2d**, which is catalytically inactive, despite the promising current increase in presence of MeOH under CO_2.

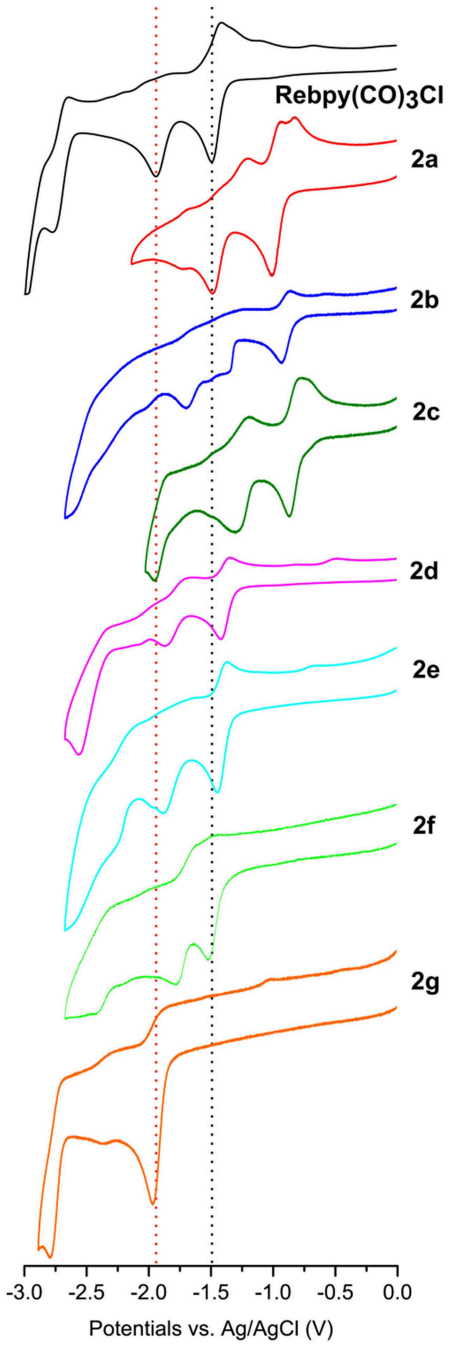

FIGURE 3 | CVs of 1 mM solutions of **2a–2g** Re complexes in MeCN/0.1 M $TBAPF_6$ at GCE, scan rate 200 mVs^{-1} under Ar. CV of the reference *fac*-Re(bpy)$(CO)_3$Cl is in black.

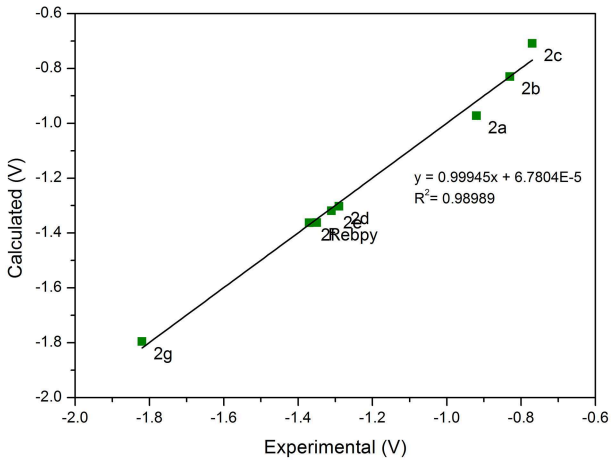

FIGURE 4 | Plot of the calculated vs. experimental standard reduction potentials for **2a–2g**.

CONCLUSIONS

In summary, a systematic study of the effect of the electronic properties of the substituents on 2,2′-bipyridine Mn and Re complexes was conducted. Electron-withdrawing substituents shift the reduction potentials to more positive values, and eventually inhibit the catalytic activities of the corresponding Mn and Re complexes toward CO_2 reduction. In the case of electron-donating substituents the opposite trend is observed. These observations are in agreement with the induced electron density localized on the metal, strongly influencing the change in the reactivity with the weak electrophile CO_2. Increasing or decreasing the electron density on the metal should facilitate or prevent the formation of intermediate in which the CO_2 is coordinated to the metal. Another interesting effect in varying the electron properties of the substituents is the merging of the first and second reduction processes, observed in some Re and Mn complexes. A judicious selection of bpy substituents provides an alternative way to the use of bulky substituents to prevent dimer formation (Sampson et al., 2014), with the aim of transforming two 1e reduction into a single **2e** reduction process (CO_2 to CO reduction requires **2e**).

It is interesting to note that in spite of the presence of a -OH group in **1f**, no formic acid is detected, probably because in contrast with Mn carrying local proton sources (Franco et al., 2014, 2017) the hydroxyl group is located far from the metal center, thus the generation of the metal-hydride, commonly considered catalyst for formate production, is no longer entropically favored. It is interesting to note how CVs under CO_2 of the push-pull systems **1d** and **2d** show enhanced catalytic currents; during CPE the Mn derivative **1d** displays the higher TON value, while the corresponding Re derivative **2d**, albeit from CV appears to be a potentially highly active catalyst, undergoes decomposition. While Mn catalysts suffer from the presence of MeOH, they appear to work better in water, which seems to react promptly with reduced Mn. In fact, even if the reduction potential of **1g** is rather negative (**Table 2**), no hydrogen is produced. This is in line with the high TON values observed for the CO_2 electrochemical reduction in pure water by Mn electrocatalysts supported on electrode surface (Walsh et al., 2015; Reuillard et al., 2017; Rotundo et al., 2019b). DFT calculations performed with dispersion correction agree with

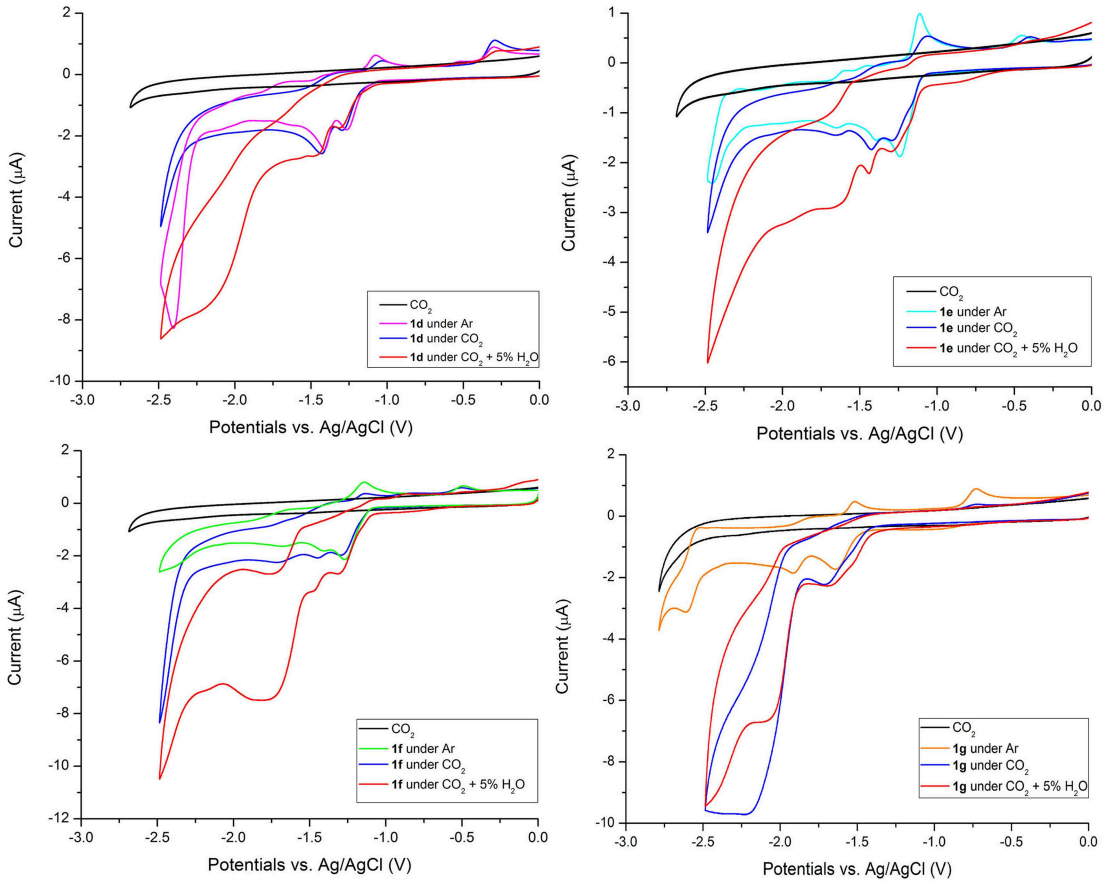

FIGURE 5 | CVs of 0.5 mM solutions of **1d–1g** Mn complexes in MeCN/0.1 M $TBAPF_6$ at GCE, scan rate 200 mVs^{-1} under Ar, under CO_2 and with H_2O (5%v). CV in black is the electrolyte saturated with CO_2.

the experimental data for both Mn and Re complexes. The Mn–Br bonds computed for the Mn radical anions undergo a significant elongation, around 0.2 Å, which indicate non-negligible weakening of the Mn–Br bonds. The release of halogen is also very probably favored by the polar and coordinating solvent MeCN; indeed Br substitution by MeCN has been experimentally observed not only in the radical anion, but also in neutral Mn species (Franco et al., 2017). We demonstrated here how the appropriate choice of the electron properties of the ligands is of critical importance in the design of more effective bipyridine Mn and Re electrocatalysts for CO_2 reduction.

MATERIALS AND METHODS

General Considerations

CV and CPE experiments were performed using a Metrohm Autolab 302n potentiostat. CO and H_2 as CO_2 reduction products were detected and quantified by an Agilent 490 Micro GC. NMR spectra were recorded on a JEOL ECP 400 FT-NMR spectrometer (^{1}H operating frequency 400 MHz) or on a JEOL ECZR 600 FT-NMR spectrometer (^{1}H operating frequency 600 MHz) at 298 K. ^{1}H and ^{13}C chemical shifts are reported relative to TMS ($\delta = 0$) and referenced against solvent residual peaks. IR-ATR spectra were collected on a Fourier transform Equinox 55 (Bruker) spectrophotometer equipped with an ATR device; resolution was set at 2 cm^{-1} for all spectra. A spectral range of 400–4,000 cm^{-1} was scanned, using KBr as a beam splitter. GC-MS spectra were obtained on a mass selective detector Agilent 5,970 B operating at an ionizing voltage of 70 eV connected to a HP 5,890 GC equipped with a HP-1 MS capillary column (25 m length, 0.25 mm I.D., 0.33 μm film thickness. Elemental analyses (C, H, N) were performed on a Fisons Instruments EA-1108 CHNS-O Elemental Analyzer. ESI-MS spectra were recorded with a Thermo Advantage Max Spectrometer equipped with an ion trap analyzer and an ESI ion source.

Synthesis and Characterization of Ligands

Flasks and all equipment used for the generation and reaction of moisture-sensitive compounds were dried by electric heat gun under N_2. All commercially obtained reagents and solvents were used as received. Anhydrous DMF was purchased by Sigma Aldrich. Products were purified by preparative column chromatography on Macherey Nagel silica-gel for flash chromatography, 0.04–0.063 mm/230–400 mesh. Reactions were monitored by TLC using silica-gel on TLC-PET foils Fluka, 2–25 μm, layer thickness 0.2 mm, medium pore diameter

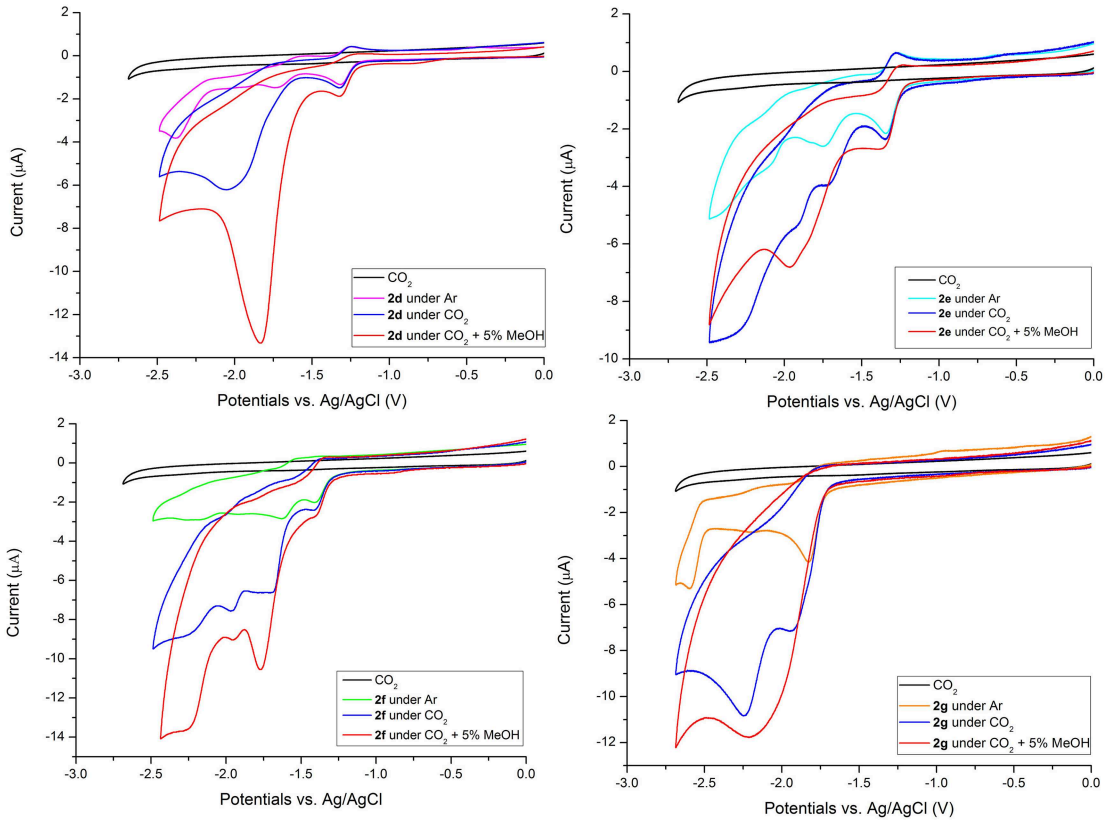

FIGURE 6 | CVs of 0.5 mM solutions of **2d–2g** Re complexes in MeCN/0.1 M $TBAPF_6$ at GCE, scan rate 200 mVs^{-1} under Ar, under CO_2 and with 5%v MeOH. CV in black is the electrolyte saturated with CO_2.

60 Å. hpbpy (4-(2-hydroxy-phenyl)-6-phenyl-2,2′-bipyridine) was synthesized by using the Kröhnke (1976) reaction and subsequently coupling the pyridinium iodide salt (**1**) with the corresponding hydroxy chalcone (**2**). dpbpy (4,6-diphenyl-2,2'-bipyridine) was synthesized according to reported procedure (Franco et al., 2015).

Synthesis of 4,4′-bis(trifluoromethyl)-2,2′-bipyridine: the method of O'Donnell et al. (2016) was slightly modified to synthesize 4,4′-bis(trifluoromethyl)-2,2′-bipyridine first reported by Furue et al. (1992). In a degassed 20 mL screw cap vial a solution of 2-bromo-4-(trifluoromethyl)pyridine (500 mg, 2.2 mmol) in 7.5 mL of anhydrous DMF was poured and degassed for 5 min. $Pd(OAc)_2$ (25 mg, 0.11 mmol) was added later and the mixture degassed for additional 5 min. TBAI (815 mg 2.2 mmol), anhydrous K_2CO_3 (460 mg, 3.3 mmol), and i-PrOH (0.35 mL, 4.4 mmol) were then added to the mixture, subsequently heated at 100°C for 20 h. The heating was suspended, and the reaction mixture was filtered through a pad of celite. The filtrate was diluted in 25 mL of DCM and was washed with deionized water (3 × 25 mL). The organic phase was collected, and the water layer further extracted with 10 mL of DCM. The collected organic phase was dried with anhydrous $MgSO_4$, filtered, and the solvent removed under reduced pressure to afford the crude solid that was purified by column chromatography on silica gel (eluent PE/AcOEt 10/1) to afford 220 mg of white solid as product. (Yield = 80%).

Synthesis of [2,2′-bipyridine]-4,4′-dicarbonitrile: the procedure reported by Losse et al. (2008) was followed with slight modifications. 4-Cyanopyridine (700 mg, 6.7 mmol) and 10% Pd/C (50 mg) were added into a 25 mL round-bottomed flask and five vacuum/nitrogen cycle were operated to minimize the amount of oxygen, then the flask was connected to a reflux condenser under nitrogen atmosphere. The mixture was heated to 230°C in a sand bath in order to reflux the 4-Cyanopyridine. After 24 h the mixture was cooled to room temperature, $CHCl_3$ (15 mL) was added and the black suspension filtered through a frit. Solvent was removed under reduced pressure from the pale-yellow solution obtained until the product started to crystallize. Pentane (15 mL) was then added, and the concentrated solution cooled at 4–6°C for 16 h. The precipitate was filtered on Buchner funnel and washed with cold EtOH and dried to yield 100 mg of the product as a yellow-orange solid. (Yield 15%).

General procedures for synthesis of 2-substitued N,N-dimethylpyridin-4-amine derivatives. The previously reported procedure of Cuperly et al. (2002) was adapted according to the used electrophile. 2-(dimethylamino)-ethanol (0.8 mL, 8.0 mmol) was added to a three-necked round bottomed flask and dissolved in hexane (10 mL) under a N_2 atmosphere. The

TABLE 3 | TON and faradic efficiencies (η) upon CPE (applied potential E in V vs. Ag/AgCl) of solutions of manganese and rhenium complexes (0.5 mM) in 0.1 M $TBAPF_6$/MeCN in the presence of Brønsted acids (5%v).

Complex	E [V]	T [min]	acid [5%]	TON_{CO}	η_{CO} [%]	TON_{H2}	η_{H2} [%]
$Mnbpy(CO)_3Br$	−1.6	240	H_2O	13	100	–	–
1d	−1.5	420	H_2O	26	84	1.7	16
1e	−1.5	300	H_2O	12	72	2.3	10
1f	−1.5	300	H_2O	13	64	3	20
1g	−1.95	120	–	3.5	85	–	–
1g	−1.95	300	H_2O	13	90	–	–
$Rebpy(CO)_3Cl$	−1.85	180	MeOH	15	80	–	–
2d	−1.8	180	MeOH	–	–	–	–
2e	−1.7	300	MeOH	5	56	–	–
2f	−1.7	240	–	5	64	–	–
2f	−1.7	300	MeOH	15	86	–	–
2g	−2	420	–	17.6	100	–	–
2g	−2	600	MeOH	31.5	100	–	–

solution was cooled at −5°C, BuLi (2.5 M, 6.4 mL, 16.0 mmol) was added dropwise for 10 min and the resulting mixture stirred for 40 min at −5°C. 4-DMAP (488 mg, 4.0 mmol) was then added and stirring continued for additional 60 min at 0°C, then the reaction medium was cooled at −78°C and the solution of the appropriate electrophile (10.0 mmol) was added dropwise by mean of a dropping funnel with pressure balance. Once the addition of the electrophile was completed the temperature was allowed to raise to 0°C (1.5 h) and the reaction quenched with deionized water at this temperature.

Synthesis of N,N-dimethyl-2-(tributylstannyl)pyridin-4-amine. 2-(dimethylamino)ethanol (0.8 mL, 8.0 mmol) in hexane (10 mL), BuLi (2.5 M, 6.4 mL, 16.0 mmol), and 4-DMAP (0.488 g, 4.0 mmol) were reacted as previously described then a solution of Bu_3SnCl (3.255 g, 10.0 mmol) in 15 mL of hexane was added dropwise for 20 min. The reaction was quenched with deionized water (15 mL) then the aqueous phase was extracted with DCM (2 × 20 mL) and AcOEt (2 × 20 mL). The collected organic phase was dried with anhydrous Na_2SO_4, filtered, and the solvent removed under reduced pressure to afford a crude orange oil, that was used without further purification in the cross-coupling reactions (NMR-calculated yield = 69%).

Synthesis of 2-iodo-N,N-dimethylpyridin-4-amine: 2-(dimethylamino)ethanol (1.6 mL, 16.0 mmol) in hexane (25 mL), BuLi (2.5 M, 12.8 mL, 32.0 mmol), and 4-DMAP (0.980 g, 8.0 mmol) were reacted as previously described, then a solution of resublimed I_2 (5.080 g, 20.0 mmol) in 50 mL of freshly distilled Et_2O was added dropwise for 35 min. The reaction was quenched with a saturated solution of $Na_2S_2O_3$ (25 mL) and stirred for additional 20 min at 0°C. The organic phase was separated and washed again with $Na_2S_2O_3$ solution (2×15 mL) and brine (2 × 15 mL). The collected organic phase was dried with anhydrous Na_2SO_4, filtered, and the solvent removed under reduced pressure to afford a crude brown solid that was purified by column chromatography on silica gel (eluent: PE/AcOEt 5/5) to afford 1.683 g of white solid as product (Yield = 86%).

General Procedure for Stille cross-coupling of N,N-dimethyl-2-(tributylstannyl)pyridin-4-amine with 2-halopyridine. In a degassed 50 ml screw cap vial freshly distilled toluene (25 mL) was added and degassed for 10 min then $Pd(OAc)_2$ (22 mg, 0.1 mmol) and PPh_3 (52 mg, 0.2 mmol) were added in one portion. The resulting mixture was stirred and degassed until toning of the solution to red. Subsequently, *N,N*-dimethyl-2-(tributylstannyl)pyridin-4-amine (370 mg, 0.9 mmol), LiI (40 mg, 0.3 mmol), and CuI (57 mg, 0.3 mmol) were added to the mixture, then degassed for additional 5 min. Finally, the appropriate 2-halopyridine (1.1 mmol) was poured in the reaction medium that was kept under N_2 atmosphere and heated to reflux for 16 h. After being cooled at room temperature, the resulting mixture was diluted with EtOAc (30 mL) and washed with a NH_4OH solution (10 M) until the water layer did not turn blue any more, indicating that all the copper had been extracted. The collected organic phase was filtered on a pad of celite, diluted with DCM (30 mL) and dried with anhydrous Na_2SO_4. Then the solvents were removed under reduced pressure to afford the crude solid subsequently purified to yield the desired product.

Synthesis of N^4,N^4,$N^{4'}$,$N^{4'}$-tetramethyl-[2,2′-bipyridine]-4,4′-diamine: Following the general procedure, *N,N*-dimethyl-2-(tributylstannyl)pyridin-4-amine (370 mg, 0.9 mmol) and 2-iodo-*N,N*-dimethylpyridin-4-amine (270 mg, 1.1 mmol) in 25 mL of freshly distilled toluene were reacted to afford a crude yellowish solid that was suspended in 25 mL of Et_2O and vigorously stirred for 30 min. The desired product was separated by filtration to yield 115 mg of a brown powder (Yield = 53 %).

Synthesis of N,N-dimethyl-4′-(trifluoromethyl)-[2,2′-bipyridin]-4-amine: following the general procedure, *N,N*-dimethyl-2-(tributylstannyl)pyridin-4-amine (370 mg, 0.9 mmol) and commercially available 2-bromo-4-(trifluoromethyl)pyridine (250 mg, 1.1 mmol) in 25 mL of freshly distilled toluene were reacted to afford a crude brown solid that was purified by column chromatography on silica

gel (eluent: MeOH/DCM 5/95) to yield 169 mg of the desired product as a brown powder (Yield = 70%).

*Synthesis of N-(2-pyridylacetyl)-pyridinium iodide (**1**):* in a three-necked flask 82.5 mmol of 2-acetylpyridine and 90.5 mmol of iodine are dissolved in 100 ml of pyridine. The solution is refluxed for 3 h. The shiny black precipitate is then filtered and washed with diethyl ether (20 ml). The solid is recrystallized in hot ethanol: fine-scaled golden crystals are obtained (overall yield: 54%).

*Synthesis of (E)-3-(2-hydroxyphenyl)-1-phenyl-2-propen-1-one (**2**):* is synthesized by Claisen-Schmidt condensation of salicylaldehyde (50 mmol) with acetophenone (40 mmol) dissolved in 50 mL of ethanol (Tatsuzaki et al., 2006; Yin et al., 2012). The solution is vigorously stirred and 10 mL of KOH 40% (w/w) is dropwise added. The mixture is then heated to 60°C for 2–4 h until the disappearance of the starting reagents, monitored by TLC (EtAc: hexane 1:4). Once the reaction is completed, the suspension is poured into cold distilled water and acidified with HCl 2 M (final pH 2–3). The resulting precipitate is collected and washed once with water and then with cyclohexane (yield: 70%).

Synthesis of 4-(2-hydroxy-phenyl)-6-phenyl-2,2′-bipyridine (hpbpy): precursors **1** (4.8 mmol) and **2** (4.8 mmol) are added to a three-necked flask with an excess of ammonium acetate (48 mmol) and glacial acetic acid (4 mL). The solution is refluxed for 3 h. The glacial acetic acid is removed, and the residue dissolved in methanol. The yellowish product crystallizes on cooling.

Synthesis of 4,6-diphenyl-2,2′-bipyridine (dpbpy): is already reported in literature; NMR data are in agreement with previously published data (Cave and Raston, 2001).

Synthesis of Mn Complexes

$[Mn(CO)_5Br]$ (0.100 mmol, 1 equiv) and the corresponding bipyridyl ligand (0.101 mmol, 1,01 equiv) were dissolved in sealed flasks containing 5 mL of diethyl ether (anhydrous for complex **1f**), and heated in a Biotage Initiator$^+$ microwave reactor. When the microwave vial has been inserted into the microwave cavity and the cavity lid has been closed, high-frequency microwaves (2.45 GHz), generated by the magnetron, heat the reaction mixture at a constant temperature of 75°C for 15 min. The reaction mixtures were cooled to room temperature and the products centrifuged and washed once with diethyl ether. Yields of reactions: (**1a:** 75%, **1b:** 84%, **1c:** 70%, **1d**: 81%, **1e:** 68%, **1f:** 65%, **1g:** 78%).

Synthesis of Re Complexes

$[Re(CO)_5Cl]$ (0.100 mmol, 1 equiv) and the corresponding bipyridyl ligand (0.101 mmol, 1.01 equiv) were dissolved in sealed flasks containing 5 mL of toluene (anhydrous for complex **2f**), and heated in the Biotage microwave reactor at a constant temperature of 130°C for an hour. After cooling of the reaction mixtures to room temperature, petroleum ether was added to precipitate the products, which were then centrifuged, filtered and washed once with cold diethyl ether. Yields of reactions: (**2a:** 70%, **2b:** 82%, **2c:** 67%, **2d**: 85%, **2e:** 65%, **2f:** 65%, **2g:** 75%).

Elemental Analysis of the Complexes

The samples for microanalyses were dried in vacuum to constant weight (20°C, ca. 0.1 Torr). Elemental analysis (C, H, N) was performed in-house with a Fisons Instruments 1108 CHNS-O Elemental Analyzer.

Anal. Calcd.(%) for **1a** ($C_{15}H_6BrF_6N_2O_3Mn$): C 35.25; H, 1.18; N, 5.48. Found: C 35.49, H 1.25, N, 5.36.

Anal. Calcd.(%) for **1b** ($C_{15}H_6BrF_6N_2O_3Mn$): C, 35.25; H, 1.18; N, 5.48. Found: C 35.55, H 1.09, N 5.57.

Anal. Calcd.(%) for **1c** ($C_{15}H_6BrN_4O_3Mn$): C, 42.38; H, 1.42; N, 13.18. Found: C 42.62, H, 1.50, N, 13.07.

Anal. Calcd.(%) for **1d** ($C_{16}H_{12}BrF_3N_3O_3Mn$): C, 39.53; H, 2.49; N, 8.64. Found: C, 39.41, H, 2.61, N, 8.75.

Anal. Calcd.(%) for **1e** ($C_{25}H_{16}BrN_2O_3Mn$): C, 56.95; H, 3.06; N, 5.31. Found: C, 57.13, H, 2.96, N, 5.45.

Anal. Calcd.(%) for **1f** ($C_{25}H_{16}BrN_2O_4Mn$): C, 55.27; H, 2.97; N, 5.16. Found: C, 55.15, H, 3.14, N, 4.95.

Anal. Calcd.(%) for **1g** ($C_{17}H_{17}BrN_4O_3Mn$): C, 44.37; H, 3.72; N, 12.17. Found: C, 44.51, H, 3.82, N, 12.04

Anal. Calcd.(%) for **2a** ($C_{15}H_6ClF_6N_2O_3Re$): C, 30.13; H, 1.01, N, 4.69. Found: C, 30.20, H, 1.12, N, 4.35.

Anal. Calcd.(%) for **2b** ($C_{15}H_6ClF_6N_2O_3Re$): C, 30.13; H, 1.01, N, 4.69. Found: C, 29.95, H, 1.16, N, 4.78.

Anal. Calcd.(%) for **2c** ($C_{15}H_6ClN_4O_3Re$): C, 35.20; H, 1.18; N, 10.95. Found: C, 35.34, H, 1.26, N, 10.77.

Anal. Calcd.(%) for **2d** ($C_{16}H_{12}ClF_3N_3O_3Re$): C, 33.54; H, 2.11; N, 7.33. Found: C, 33.43, H, 2.26, N, 7.48.

Anal. Calcd.(%) for **2e** ($C_{25}H_{16}ClN_2O_3Re$): C, 48.90; H, 2.63; N, 4.56. Found: C, 49.06, H, 2.75, N, 4.43.

Anal. Calcd.(%) for **2f** ($C_{25}H_{16}ClN_2O_4Re$): C, 47.66; H, 2.56; N, 4.45. Found: C, 47.53, H, 2.78, N, 4.36.

Anal. Calcd.(%) for **2g** ($C_{17}H_{17}ClN_4O_3Re$): C, 37.33; H, 3.13; N, 10.24. Found: C, 37.25, H, 3.22, N, 10.16.

Single-Crystal X-Ray Diffraction

The single-crystal data were collected with a Gemini R Ultra diffractometer with graphite-monochromated Mo-Kα radiation ($\lambda = 0.71073$) by the ω-scan method. The cell parameters were retrieved with the CrysAlisPro (Agilent, 2015) software, and the same program was used to perform data reduction with corrections for Lorenz and polarizing effects. Scaling and absorption corrections were applied through the CrysAlisPro1 multiscan technique. The structures of complex **2e** (both structure A and B) were solved with direct methods, while in the case of **2f** a meaningful initial guess for electron density was obtained only with Patterson Function by using SHELXS-14 (Sheldrick, 2008, 2015). All the structures were refined with full-matrix least-squares techniques on F^2 with SHELXL-14 (Macrae et al., 2006) using the program Olex2 (Dolomanov et al., 2009). All non-hydrogen atoms were refined anisotropically. Hydrogen atoms were calculated and riding on the corresponding bonded atoms. The graphic of the crystal structures was generated using Mercury 3.9 (Macrae et al., 2006). CCDC codes 1891407–1891409 contain the supplementary crystallographic data for **2e** (structure A), **2e** (structure B) and **2f**. These data can be obtained free of charge via https://www.ccdc.cam.ac.uk/conts/retrieving.html, or from the Cambridge Crystallographic Data Center, 12

Union Road, Cambridge CB2 1EZ, UK; fax: (+44) 1223-336-033; or e-mail: deposit@ccdc.cam.ac.uk.

CV and CPE Experiments

Acetonitrile used for the experiments was freshly distilled over calcium hydride and purged with Ar before use. 0.5–1 mM solutions of the complexes were prepared with tetrabutylammonium hexafluorophosphate ($TBAPF_6$, Sigma-Aldrich, 98%) as supporting electrolyte (0.1 M). A single-compartment cell was employed for CV measurements, equipped with working a glassy carbon electrode (GCE, Ø = 1 mm), alongside a Pt counter electrode and a Ag/AgCl (KCl 3 M) reference electrode. The Ar- and CO_2-saturated conditions were achieved by purging gases for 5 min before each potential sweep. A double-compartment H-type cell was used for CPE measurements, thus allowing to separate through a glass frit the anodic compartment from the cathodic one (a Pt wire is placed as counter electrode). A glassy carbon rod is employed as working electrode jointly with the Ag/AgCl reference electrode. A controlled and constant flow of CO_2 (50 mL min^{-1}) was maintained during the CPE measurements by means of a Smart Trak 100 (Sierra) flow controller. Under these experimental conditions, the redox couple (Fc^+/Fc) is located at $E_{1/2} = 0.35$ V.

Quantitative Analysis of CO_2 Reduction Products

μGC measurements were used to detect CO and H_2. Two modules equipped with CP-Molsieve 5 Å columns were kept at 105°C and at a pressure of 30 and 28 psi, with a thermal conductivity detector. The carrier gases were Ar for H_2 and He for CO detection, respectively. The backflush vent option time was set to 7 s. The gas inside the measurement cell was sampled for 30 s every 3 min to fill the Micro GC 10 μL sample loop, and eventually 500 nL was injected into the column for the analyses. Instrument calibration was carried out measuring two different certified standards of CO and H_2 in Ar matrix (Rivoira). Formate production was assessed by NMR spectroscopy.

Computational Details

All the calculations were performed by the Gaussian 16 Revision B.01 (G16) program package (Frisch et al., 2016), employing density functional theory (DFT). Calculations were run using the Becke three-parameter hybrid functional (Becke, 1993), and the Lee–Yang–Parr gradient-corrected correlation functional (B3LYP) (Lee et al., 1988). Dispersion effects were added as semiempirical corrections with Becke–Johnson damping approach (GD3BJ) (Grimme et al., 2010, 2011). The solvent effect was included using the conductor-like polarizable continuum model (CPCM) with acetonitrile as solvent (Miertus et al., 1981). The def2TZVP basis set and effective core potential were used for the Mn, Br, and Cl atoms and the def2-SVP basis set was used for all the other atoms (Weigend and Ahlrichs, 2005). Unrestricted open-shell calculations were performed on the radical anions. Geometry optimizations were carried out without any symmetry constraints. The nature of the stationary points in the potential energy hypersurface was characterized by using harmonic vibrational frequency calculations. No imaginary frequencies were found, thus indicating we had located the minima on the potential-energy surfaces. Molecular-graphic images were produced by using the UCSF Chimera package from the Resource for Biocomputing, Visualization, and Informatics at the University of California, San Francisco (Pettersen et al., 2004).

AUTHOR CONTRIBUTIONS

RG and CN as corresponding authors wrote and revised the manuscript. EP performed Crystal X-ray structures. EA, AD, and PQ made the synthesis of the ligands. LR, RR, and LN synthesized the organometallic catalysts and performed the electrochemical and GC measurements. CG and CN made the DFT calculations.

ACKNOWLEDGMENTS

We gratefully thank R. Buscaino (Department of Chemistry, Università degli studi di Torino) for the ESI-MS spectra of the complexes. CRT (Fondazione CRT, ref. 2017.0812) project is acknowledged.

SUPPLEMENTARY MATERIAL

The Supplementary Material for this article can be found online at: https://www.frontiersin.org/articles/10.3389/fchem.2019.00417/full#supplementary-material

REFERENCES

Agilent (2015). *CrysAlis PRO*. Yarnton: Agilent Technologies Ltd.

Anderson, P. A., Keene, F. R., Horn, E., and Tiekink, E. R. T. (1990). Ambidentate coordination of the tripyridyl ligands 2,2': 6',2"-terpyridyl, tris(2-pyridyl)-amine, tris(2-pyridyl)methane, and tris(2-pyridyl)phosphine to carbonylrhenium centres: structural and spectroscopic studies. *Appl. Organomet. Chem.* 4, 523–533. doi: 10.1002/aoc.590040514

Becke, A. D. (1993). Density-functional thermochemistry. III. The role of exact exchange. *J. Chem. Phys.* 98, 5648–5652. doi: 10.1063/1.464913

Bourrez, M., Molton, F., Chardon-Noblat, S., and Deronzier, A. (2011). [Mn(bipyridyl)$(CO)_3$Br]: an abundant metal carbonyl complex as efficient electrocatalyst for CO_2 reduction. *Angew. Chem. Int. Ed.* 50, 9903–9906. doi: 10.1002/anie.201103616

Bullock, S., Hallett, A. J., Harding, L. P., Higginson, J. J., Piela, S. A. F., Pope, S. J. A., et al. (2012). Luminescent rhenium fac-tricarbonyl-containing complexes of androgenic oxo-steroids. *Dalton Trans.* 41, 14690–14696. doi: 10.1039/c2dt31476b

Cave, G. W. V., and Raston, C. L. (2001). Efficient synthesis of pyridines via a sequential solventless aldol condensation and Michael addition. *J. Chem. Soc. Perkin* 1, 3258–3264. doi: 10.1039/B107302H

Civitello, E. R., Dragovich, P. S., Karpishin, T. B., Novick, S. G., Bierach, G., O'Connell, J. F., et al. (1993). Spectroscopic and crystallographic characterization of (σ2-terpyridyl)Re$(CO)_3$Cl. 2D-NMR evidence for a linkage isomerization reaction. *Inorg. Chem.* 32, 237–241. doi: 10.1021/ic00054a022

Costentin, C., Drouet, S., Robert, M., and Saveant, J.-M. (2012). A local proton source enhances CO_2 electroreduction to CO by a molecular Fe catalyst. *Science* 338, 90–94. doi: 10.1126/science.1224581

Cuperly, D., Gros, P., and Fort, Y. (2002). First Direct C-2-Lithiation of 4-DMAP. Convenient access to reactive functional derivatives and ligands. *J. Org. Chem.* 67, 238–241. doi: 10.1021/jo016064p

Dolomanov, O. V., Bourhis, L. J., Gildea, R. J., Howard, J., a,. K., and Puschmann, H. (2009). OLEX2: a complete structure solution, refinement and analysis program. *J. Appl. Crystallogr.* 42, 339–341. doi: 10.1107/S0021889808042726

Elgrishi, N., Chambers, M. B., Wang, X., and Fontecave, M. (2017). Molecular polypyridine-based metal complexes as catalysts for the reduction of CO_2. *Chem. Soc. Rev.* 46, 761–796. doi: 10.1039/C5CS00391A

Francke, R., Schille, B., and Roemelt, M. (2018). Homogeneously catalyzed electroreduction of carbon dioxide—methods, mechanisms, and catalysts. *Chem. Rev.* 118, 4631–4701. doi: 10.1021/acs.chemrev.7b00459

Franco, F., Cometto, C., Nencini, L., Barolo, C., Sordello, F., Minero, C., et al. (2017). Local proton source in electrocatalytic CO_2 reduction with [Mn(bpy-R)(CO) $_3$ Br] complexes. *Chem. - Eur. J.* 23, 4782–4793. doi: 10.1002/chem.201605546

Franco, F., Cometto, C., Sordello, F., Minero, C., Nencini, L., Fiedler, J., et al. (2015). Electrochemical reduction of CO_2 by $M(CO)_4$(diimine) complexes (M = Mo, W): catalytic activity improved by 2,2'-dipyridylamine. *ChemElectroChem* 2, 1372–1379. doi: 10.1002/celc.201500115

Franco, F., Cometto, C., Vallana, F. F., Sordello, F., Priola, E., Minero, C., et al. (2014). A local proton source in a [Mn(bpy-R)$(CO)_3$Br]-type redox catalyst enables CO_2 reduction even in the absence of Brønsted acids. *Chem. Commun.* 50, 14670–14673. doi: 10.1039/C4CC05563B

Franco, F., Pinto, M. F., Royo, B., and Lloret-Fillol, J. (2018). A highly active n-heterocyclic carbene manganese(I) complex for selective electrocatalytic CO_2 reduction to CO. *Angew. Chem. Int. Ed.* 57, 4603–4606. doi: 10.1002/anie.201800705

Frisch, M. J., Trucks, G. W., Schlegel, H. B., Scuseria, G. E., Robb, M. A., Cheeseman, J. R., et al. (2016). *Gaussian 16, Revision B.01.* Wallingford, CT: Gaussian, Inc.

Furue, M., Maruyama, K., Oguni, T., Naiki, M., and Kamachi, M. (1992). Trifluoromethyl-substituted 2,2'-bipyridine ligands. Synthetic control of excited-state properties of ruthenium(II) tris-chelate complexes. *Inorg. Chem.* 31, 3792–3795. doi: 10.1021/ic00044a022

Grice, K. A. (2017). Carbon dioxide reduction with homogenous early transition metal complexes: opportunities and challenges for developing CO_2 catalysis. *Coord. Chem. Rev.* 336, 78–95. doi: 10.1016/j.ccr.2017.01.007

Grimme, S., Antony, J., Ehrlich, S., and Krieg, H. (2010). A consistent and accurate ab initio parametrization of density functional dispersion correction (DFT-D) for the 94 elements H-Pu. *J. Chem. Phys.* 132:154104. doi: 10.1063/1.3382344

Grimme, S., Ehrlich, S., and Goerigk, L. (2011). Effect of the damping function in dispersion corrected density functional theory. *J. Comput. Chem.* 32, 1456–1465. doi: 10.1002/jcc.21759

Hammouche, M., Lexa, D., Saveant, J., and Momenteau, M. (1988). Catalysis of the electrochemical reduction of carbon-dioxide by iron(0) porphyrins. *J. Electroanal. Chem.* 249, 347–351. doi: 10.1016/0022-0728(88)80372-3

Hawecker, J., Lehn, J.-M., and Ziessel, R. (1984). Electrocatalytic reduction of carbon dioxide mediated by Re(bipy)$(CO)_3$Cl (bipy = 2,2'-bipyridine). *J. Chem. Soc. Chem. Commun.* 0, 328–330. doi: 10.1039/C39840000328

Klemens, T., Switlicka-Olszewska, A., Machura, B., Grucela, M., Schab-Balcerzak, E., Smolarek, K., et al. (2016). Rhenium(I) terpyridine complexes - synthesis, photophysical properties and application in organic light emitting devices. *Dalton Trans. Camb. Engl.* 45, 1746–1762. doi: 10.1039/C5DT04093K

Kröhnke, F. (1976). The specific synthesis of pyridines and oligopyridines. *Synthesis* 1976, 1–24. doi: 10.1055/s-1976-23941

Kurz, P., Probst, B., Spingler, B., and Alberto, R. (2006). Ligand Variations in [ReX(diimine)$(CO)_3$] complexes: effects on photocatalytic CO_2 reduction. *Eur. J. Inorg. Chem.* 2006, 2966–2974. doi: 10.1002/ejic.200600166

Lee, C. T., Yang, W. T., and Parr, R. G. (1988). Development of the colle-salvetti correlation-energy formula into a functional of the electron-density. *Phys. Rev. B* 37, 785–789. doi: 10.1103/PhysRevB.37.785

Losse, S., Görls, H., Groarke, R., Vos, J. G., and Rau, S. (2008). One-step synthesis of 4,4'-dicyano-2,2'-bipyridine and its bis(4,4'-di-tert-butyl-2,2'-bipyridine)ruthenium(II) Complex. *Eur. J. Inorg. Chem.* 2008, 4448–4452. doi: 10.1002/ejic.200701304

Machan, C. W., Chabolla, S. A., Yin, J., Gilson, M. K., Tezcan, F. A., and Kubiak, C. P. (2014). Supramolecular assembly promotes the electrocatalytic reduction of carbon dioxide by Re(I) bipyridine catalysts at a lower overpotential. *J. Am. Chem. Soc.* 136, 14598–14607. doi: 10.1021/ja5085282

Macrae, C. F., Edgington, P. R., McCabe, P., Pidcock, E., Shields, G. P., Taylor, R., et al. (2006). Mercury: visualization and analysis of crystal structures. *J. Appl. Crystallogr.* 39, 453–457. doi: 10.1107/S002188980600731X

Manbeck, G. F., Muckerman, J. T., Szalda, D. J., Himeda, Y., and Fujita, E. (2015). Push or pull? proton responsive ligand effects in rhenium tricarbonyl CO_2 reduction catalysts. *J. Phys. Chem. B* 119, 7457–7466. doi: 10.1021/jp511131x

Miertus, S., Scrocco, E., and Tomasi, J. (1981). Electrostatic interaction of a solute with a continuum. A direct utilizaion of AB initio molecular potentials for the prevision of solvent effects. *Chem. Phys.* 55, 117–129. doi: 10.1016/0301-0104(81)85090-2

O'Donnell, R. M., Sampaio, R. N., Li, G., Johansson, P. G., Ward, C. L., and Meyer, G. J. (2016). Photoacidic and photobasic behavior of transition metal compounds with carboxylic acid group(s). *J. Am. Chem. Soc.* 138, 3891–3903. doi: 10.1021/jacs.6b00454

Pettersen, E. F., Goddard, T. D., Huang, C. C., Couch, G. S., Greenblatt, D. M., Meng, E. C., et al. (2004). UCSF chimera - a visualization system for exploratory research and analysis. *J. Comput. Chem.* 25, 1605–1612. doi: 10.1002/jcc.20084

Rawat, K. S., Mandal, S. C., and Pathak, B. (2019). A computational study of electrocatalytic CO_2 reduction by Mn(I) complexes: role of bipyridine substituents. *Electrochimica Acta* 297, 606–612. doi: 10.1016/j.electacta.2018.11.210

Reuillard, B., Ly, K. H., Rosser, T. E., Kuehnel, M. F., Zebger, I., and Reisner, E. (2017). Tuning product selectivity for aqueous CO_2 reduction with a Mn(bipyridine)-pyrene catalyst immobilized on a carbon nanotube electrode. *J. Am. Chem. Soc.* 139, 14425–14435. doi: 10.1021/jacs.7b06269

Rotundo, L., Filippi, J., Gobetto, R., Miller, H. A., Rocca, R., Nervi, C., et al. (2019a). Electrochemical CO_2 reduction in water at carbon cloth electrodes functionalized with a fac-Mn(apbpy)$(CO)_3$Br complex. *Chem. Commun.* 55, 775–777. doi: 10.1039/C8CC08385A

Rotundo, L., Garino, C., Gobetto, R., and Nervi, C. (2018). Computational study of the electrochemical reduction of $W(CO)_4$(2,2'-dipyridylamine). *Inorganica Chim. Acta* 470, 373–378. doi: 10.1016/j.ica.2017.05.061

Rotundo, L., Garino, C., Priola, E., Sassone, D., Rao, H., Ma, B., et al. (2019b). Electrochemical and photochemical reduction of Co_2catalyzed by Re(I) complexes carrying local proton sources. *Organometallics*. 38, 1351–1360. doi: 10.1021/acs.organomet.8b00588

Sampson, M. D., and Kubiak, C. P. (2016). Manganese electrocatalysts with bulky bipyridine ligands: utilizing lewis acids to promote carbon dioxide reduction at low overpotentials. *J. Am. Chem. Soc.* 138, 1386–1393. doi: 10.1021/jacs.5b12215

Sampson, M. D., Nguyen, A. D., Grice, K. A., Moore, C. E., Rheingold, A. L., and Kubiak, C. P. (2014). Manganese catalysts with bulky bipyridine ligands for the electrocatalytic reduction of carbon dioxide: eliminating dimerization and altering catalysis. *J. Am. Chem. Soc.* 136, 5460–5471. doi: 10.1021/ja501252f

Saveant, J.-M. (2008). Evidence for concerted pathways in ion-pairing coupled electron transfers. *J. Am. Chem. Soc.* 130, 4732–4741. doi: 10.1021/ja077480f

Sheldrick, G. M. (2008). A short history of SHELX. *Acta Crystallogr. A* 64, 112–122. doi: 10.1107/S0108767307043930

Sheldrick, G. M. (2015). Crystal structure refinement with SHELXL. *Acta Crystallogr. Sect. C Struct. Chem.* 71, 3–8. doi: 10.1107/S2053229614024218

Smieja, J. M., and Kubiak, C. P. (2010). Re(bipy-tBu)$(CO)_3$Cl-improved catalytic activity for reduction of carbon dioxide: IR-spectroelectrochemical and mechanistic studies. *Inorg. Chem.* 49, 9283–9289. doi: 10.1021/ic1008363

Smieja, J. M., Sampson, M. D., Grice, K. A., Benson, E. E., Froehlich, J. D., and Kubiak, C. P. (2013). Manganese as a substitute for rhenium in CO_2 reduction catalysts: the importance of acids. *Inorg. Chem.* 52, 2484–2491. doi: 10.1021/ic302391u

Stanbury, M., Compain, J.-D., and Chardon-Noblat, S. (2018). Electro and photoreduction of CO_2 driven by manganese-carbonyl molecular catalysts. *Coord. Chem. Rev.* 361, 120–137. doi: 10.1016/j.ccr.2018.01.014

Sun, C., Gobetto, R., and Nervi, C. (2016). Recent advances in catalytic CO_2 reduction by organometal complexes anchored on modified electrodes. *New J. Chem.* 40, 5656–5661. doi: 10.1039/C5NJ03426D

Takeda, H., Cometto, C., Ishitani, O., and Robert, M. (2017). Electrons, photons, protons and earth-abundant metal complexes for molecular catalysis of CO_2 reduction. *ACS Catal.* 7, 70–88. doi: 10.1021/acscatal.6b02181

Tatsuzaki, J., Bastow, K. F., Nakagawa-Goto, K., Nakamura, S., Itokawa, H., and Lee, K.-H. (2006). Dehydrozingerone, chalcone, and isoeugenol analogues as *in vitro* anticancer agents [#]. *J. Nat. Prod.* 69, 1445–1449. doi: 10.1021/np060252z

Vlček, A. (2002). Highlights of the spectroscopy, photochemistry and electrochemistry of $[M(CO)_4(\alpha\text{-diimine})]$ complexes, M = Cr, Mo, W. *Coord. Chem. Rev.* 230, 225–242. doi: 10.1016/S0010-8545(02)00047-4

Walsh, J. J., Smith, C. L., Neri, G., Whitehead, G. F. S., Robertson, C. M., and Cowan, A. J. (2015). Improving the efficiency of electrochemical CO_2 reduction using immobilized manganese complexes. *Faraday Discuss.* 183, 147–160. doi: 10.1039/C5FD00071H

Wang, D., Xu, Q. L., Zhang, S., Li, H. Y., Wang, C. C., Li, T. Y., et al. (2013). Synthesis and photoluminescence properties of rhenium(I) complexes based on 2,2':6',2"-terpyridine derivatives with hole-transporting units. *Dalton Trans. Camb. Engl.* 2003 42, 2716–2723. doi: 10.1039/C2DT32154H

Wang, J.-W., Liu, W.-J., Zhong, D.-C., and Lu, T.-B. (2019). Nickel complexes as molecular catalysts for water splitting and CO_2 reduction. *Coord. Chem. Rev.* 378, 237–261. doi: 10.1016/j.ccr.2017.12.009

Weigend, F., and Ahlrichs, R. (2005). Balanced basis sets of split valence, triple zeta valence and quadruple zeta valence quality for H to Rn: design and assessment of accuracy. *Phys. Chem. Chem. Phys.* 7, 3297–3305. doi: 10.1039/b508541a

Yin, G., Fan, L., Ren, T., Zheng, C., Tao, Q., Wu, A., et al. (2012). Synthesis of functionalized 2-aryl-4-(indol-3-yl)-4H-chromenes via iodine-catalyzed domino Michael addition–intramolecular cyclization reaction. *Org. Biomol. Chem.* 10:8877. doi: 10.1039/c2ob26642c

Conflict of Interest Statement: The authors declare that the research was conducted in the absence of any commercial or financial relationships that could be construed as a potential conflict of interest.

Copyright © 2019 Rotundo, Azzi, Deagostino, Garino, Nencini, Priola, Quagliotto, Rocca, Gobetto and Nervi. This is an open-access article distributed under the terms of the Creative Commons Attribution License (CC BY). The use, distribution or reproduction in other forums is permitted, provided the original author(s) and the copyright owner(s) are credited and that the original publication in this journal is cited, in accordance with accepted academic practice. No use, distribution or reproduction is permitted which does not comply with these terms.

frontiers in Chemistry

ORIGINAL RESEARCH
published: 06 June 2019
doi: 10.3389/fchem.2019.00418

Development of Visible-Light Driven Cu(I) Complex Photosensitizers for Photocatalytic CO_2 Reduction

Hiroyuki Takeda†, Yu Monma, Haruki Sugiyama†, Hidehiro Uekusa and Osamu Ishitani*

Department of Chemistry, School of Science, Tokyo Institute of Technology, Tokyo, Japan

OPEN ACCESS

Edited by:
Hitoshi Ishida,
Kitasato University, Japan

Reviewed by:
Helene Serier-Brault,
UMR6502 Institut des Matériaux Jean Rouxel (IMN), France
Yang Yang,
University of Central Florida, United States

***Correspondence:**
Hiroyuki Takeda
takedah@chem.titech.ac.jp;
takedah@recap.osaka-cu.ac.jp

†Present Address:
Hiroyuki Takeda,
Research Center for Artificial Photosynthesis, Osaka City University, Osaka, Japan
Haruki Sugiyama,
Research and Education Center for Natural Sciences, Keio University, Yokohama, Japan

Specialty section:
This article was submitted to Inorganic Chemistry, a section of the journal Frontiers in Chemistry

Received: 08 March 2019
Accepted: 21 May 2019
Published: 06 June 2019

Citation:
Takeda H, Monma Y, Sugiyama H, Uekusa H and Ishitani O (2019) Development of Visible-Light Driven Cu(I) Complex Photosensitizers for Photocatalytic CO_2 Reduction. Front. Chem. 7:418. doi: 10.3389/fchem.2019.00418

The visible-light responsive Cu(I)-complex photosensitizers were developed by introducing various aromatic substituents at the 4,7-positions of a 2,9-dimethyl-1,10-phenanthroline (dmp) ligand in a heteroleptic Cu^{I}(dmp)(DPEphos)$^{+}$-type complexes (DPEphos = [2-(diphenylphosphino)phenyl]ether) for photocatalytic CO_2 reduction. Introducing biphenyl groups (Bp-) on the dmp ligand enhanced the molar extinction coefficient (ε) of the metal-to-ligand charge transfer (MLCT) band in the visible region (ε = 7,500 $M^{-1}cm^{-1}$) compared to that of the phenyl (Ph-)-containing analog (ε = 5,700 $M^{-1}cm^{-1}$ at λ_{max} = 388 nm). However, introducing 4-R-Ph- groups (R = the electron-withdrawing groups NC-, or NO_2-) led to a red shift in the band to λ_{max} = 390, 400, and 401 nm, respectively. Single-crystal X-ray analysis showed the Ph- groups were twisted because of the steric repulsion between the 2,6-protons of the Ph- groups and 5,6-protons of the dmp ligand. The result strongly indicated that the π-conjugation effect of the 4-R-Ph- groups is so weak that the lowering of the energy of the dmp π* orbitals is small. However, when 4-R-ph- was substituted by a 5-membered heterorings, there was a larger red shift, leading to an increase in the ε value of the MLCT absorption band. Thus, the substitution to 2-benzofuranyl- groups resulted in visible-light absorption up to 500 nm and a shoulder peak at around 420 nm (ε = 12,300 $M^{-1}cm^{-1}$) due to the expansion of π-conjugation over the substituted dmp ligand. The photocatalytic reaction for CO_2 reduction was tested using the obtained Cu^{I} complexes as photosensitizers in the presence of a $Fe(dmp)_2(NCS)_2$ catalyst and 1,3-dimethyl-2-phenyl-2,3-dihydro-1*H*-benzo[d]imidazole as a sacrificial reductant, which showed improved CO generation.

Keywords: Cu(I) diimine complex, CO_2 reduction photocatalyst, redox photosensitizer, visible-light absorption, emission

INTRODUCTION

As one of the most important components of artificial photosynthesis, photocatalytic CO_2 reduction is attracting much attention. Although metal complexes are key players in CO_2 reduction due to their promising photosensitizing and/or catalytic ability, the metals used are often limited to low abundance ones, such as Ru, Re, Os, or Ir (Yamazaki et al., 2015). Thus, substituting these metals with more abundant elements is now being widely focused on in many groups, using the first row transition metals such as Mn, Fe, Co, and Ni to produce a multi-electron catalyst for CO_2 reduction (Takeda et al., 2017). However, such the attempts, especially to produce a redox

photosensitizer (which functions as a light absorber to transfer an excited electron in its excited state to the catalyst), are limited; the excited state deactivates quickly because of low lying d-d excited state.

Thus, the heteroleptic Cu^I phenanthroline complexes, such as $[Cu^I(dmp)(P)_2]^+$ (dmp = 2,9-dimethyl-1,10-phenanthroline, P = phosphine ligand), are gaining popularity, because of their long lifetimes, showing strong metal-to-ligand (MLCT) excited-state emission even in a solution at room temperature due to the Cu^I center's d^{10} configuration (Ruthkosky et al., 1998). Although homoleptic-type $[Cu^I(dmp)_2]^+$ has the advantage as a photosensitizer in terms of visible-light utilization because it can absorb longer wavelength light (Khnayzer et al., 2013), in the excited state, its oxidation power is less and lifetime shorter than those of a heteroleptic complex. Thus, heteroleptic-type of Cu complexes are now being used as redox photosensitizers to construct many photocatalytic systems (Lazorski and Castellano, 2014). Since these Cu complexes had previously been reported to have excellent emissive properties by McMillin et al. (Breddels et al., 1982), recent developments by Beller et al. on the catalytic H_2 evolution reaction using such complexes (Luo et al., 2013; Mejía et al., 2013; Rosas-Hernández et al., 2017) have opened up the way in this area.

However, when using heteroleptic Cu complexes as redox photosensitizers in photocatalytic reactions, some issues remain, such as their stability and light-absorption in the visible region. The first issue, stability, has previously been tackled by our group, where the stability of the Cu^I complex photosensitizer was improved by connecting phenanthroline phosphine ligands together using $-C_4H_8-$ alkyl groups (Takeda et al., 2016). Because the tetrahedral coordination around the Cu^I center was maintained in this molecule, the complex has a long lifetime in the excited state, exhibiting strong emission. Thus, the resulting Cu^I dimer complexes were much more stable, not only against thermal ligand exchanges in the ground state (Kaeser et al., 2013; Lennox et al., 2016) but also against "exciplex" deactivation of the excited state, even when CH_3CN was used as a coordinating solvent (McMillin et al., 1985) and a Cu^0 metal particle formed via ligand dissociation in the one-electron reduced state (Eggleston et al., 1997). Thus, utilizing this Cu^I complex as a redox photosensitizer in the photocatalytic CO_2 reduction, we could obtain the best photocatalytic performances for CO_2 reduction and clarified the photosensitizing scheme, which forms the corresponding one-electron reduced species through reductive quenching by a reductant such as BIH (1,3-dimethyl-2-phenyl-2,3-dihydro-1*H*-benzo[d]imidazole) in the excited state, donating the added electrons to CO_2 reduction catalyst (Takeda et al., 2018).

So far, many groups have attempted to red shift the ^{1}MLCT absorption band by expanding the dmp ligand's π-conjugation. These attempts are reasonable because the lowest excited state of the Cu^I complexes can be mainly attributed to the MLCT state, in which a charge on the Cu^I center transfers to the phenanthroline ligand's low-lying π* orbitals. Tsubomura et al. introduced phenyl groups at the 4,7-positions of dmp, which is known *neocuproine*, to produce a ligand called *bathocuproine* (bcp), enhancing the molar extinction coefficient of the resulting Cu^I complex, thus causing a red shift in the absorption maximum of the MLCT band (Tsubomura et al., 2015). The Cu^I complexes having a pyrazine- or phenazine-fused dmp ligand have been also reported. However, the resulting Cu complexes showed absorption maxima at around 380 nm (Xu et al., 2015; Heberle et al., 2017). The same group also reported introducing (thiophen-2-yl)vinyl groups at the 2,9-positions of the phenanthroline, but the MLCT absorption band maximum of the Cu complex was still only observed at 388 nm (Chen et al., 2017). Although introducing 4-benzoic acid or thiophene-3-carboxylic acid at the 4,7-positions shifts the absorption band to a longer wavelength, the absorption maxima are limited to 394 and 392 nm, respectively (Chen et al., 2017). Introducing sulfonate groups at the 5,6-positions of bcp also limits the absorption maximum to 390 nm (Rockstroh et al., 2014). Recently, Giereth et al. reported a Cu complex having anthracene-fused dmp, which shows absorption at a longer wavelength at around 430 nm (Giereth et al., 2019). McCullough et al. also reported a unique Cu complex incorporating 2,2′-biquinoline as an α-diimine and applied it as a photocatalytic system for H_2 evolution (McCullough et al., 2018). This type of complex showed a surprising red shift in its maximum to 455 nm (Zhang et al., 2007). However, the first-reduction potential of these Cu complexes underwent a positive shift from −2 V for the dmp complex to −1.19 V vs. Fc^+/Fc in CH_3CN for the anthracene-fused dmp complex and −1.69 V vs. Fc^+/Fc in CH_2Cl_2 for the biquinoline complex, that are more positive than that of the common redox-photosensitizer $Ru(dmb)_3^{2+}$ (dmb = 4,4′-dimethyl-2,2′-bipyridine). Thus, further study of these types of Cu^I complexes is required so that they can be used as visible-light absorbing redox-photosensitizers.

In this study, Cu^I complexes are synthesized with new bcp-based phenanthroline ligands, with electron-withdrawing groups on the phenyl groups, or various different aromatic groups such as heterorings, instead of the phenyl groups of the bcp ligand. The aim is improving these systems' visible-light absorption. The Cu^I complexes' UV-Vis absorption spectra, photophysical properties, and electrochemical properties were examined, providing evidence for a significant red shift in the MLCT absorption band. The redox-photosensitizing ability for photocatalytic CO_2 reduction of these Cu^I complexes was also tested using $Fe(dmp)_2(NCS)_2$ as a catalyst in the presence of a reductant.

RESULTS AND DISCUSSION

The structures of newly synthesized Cu^I complexes' structures are shown in **Figure 1** alongside the reported Cu^I complexes **Cu(H)** (Cuttell et al., 2002) and **Cu(ph)** (Luo et al., 2013). Two types of substituents were introduced at the 4,7-positions of the dmp ligand, (a) 4-substituted phenyl groups (**Figure 1A**) and (b) heteroring aryl groups (**Figure 1B**). In the type (a) substituents, **Cu(Bph)** is an expanded form of **Cu(ph)** with an increased number of the phenyl groups, while **Cu(NCph)** and **Cu(NO_2ph)** have π-electron withdrawing cyano and nitro substituents on the phenyl groups, respectively. In the (b) substituents, the

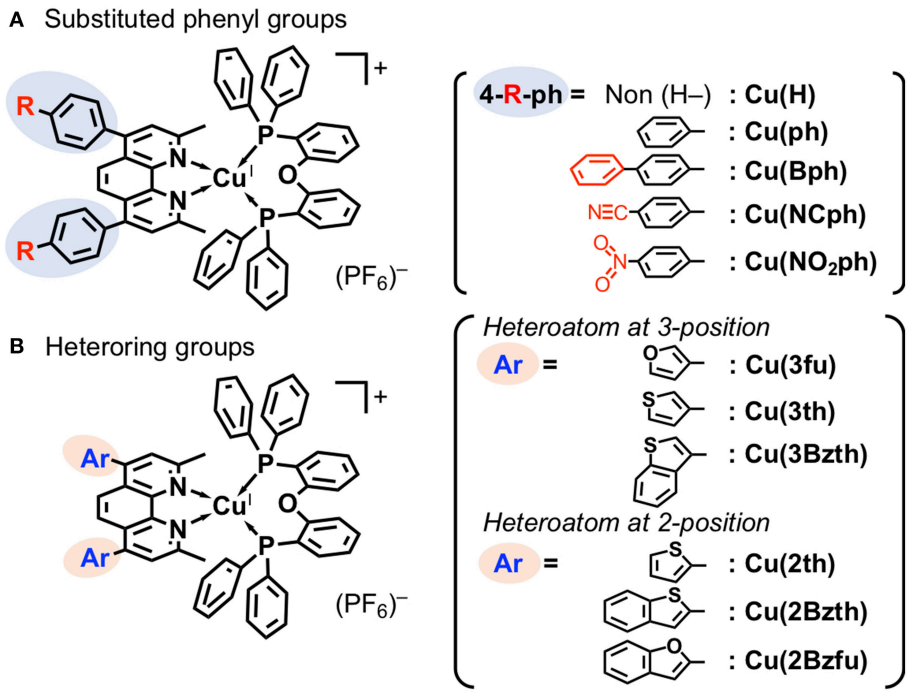

FIGURE 1 | Cu^I complexes with an aryl-substituted dmp [aryl = substituted phenyl **(A)** and heteroring **(B)** groups] and a DPEphos ligands.

ligands have aryl groups that are smaller in size, i.e., 5-membered heterorings containing O or S atoms at 2- or 3-position, than the phenyl groups adjacent to the dmp ligand. Because S and O atoms have different electronegativities of 3.44 and 2.58, respectively, and van der Waals radii (Bondi, 1964) of 1.52 and 1.80 Å, respectively, the electronic properties of the Cu^I complexes should be different.

The Cu^I complexes' UV-Vis absorption spectra in a non-coordinating solvent, such as CH_2Cl_2, are shown in **Figure 2**, and the data are summarized in **Table 1**. As a representative system, **Cu(ph)** exhibited a ^{1}MLCT transition band at 350–500 nm that was moderate in intensity (molar extinction coefficient (ε) ~ 6000 $M^{-1}s^{-1}$) and an intraligand π-π* transition band in the shorter-wavelength range with stronger intensity (ε ~50000 $M^{-1}s^{-1}$), as shown in **Figures 2A–C** (dotted line). Because the ^{1}MLCT transition is the lowest in energy from the spectrum, the lowest excited state of this complex is strongly indicated to be the MLCT state. Although the π-π* excited state which is higher in energy can proceed thermal relaxation to populate the lowest state, direct excitation of the lowest MLCT transition in the visible region can be assumed to be the most significant in a redox-photosensitizing reaction. Thus, we focused ^{1}MLCT band of the Cu^I complexes, referring the π-π* band as an indicator of π-system expansion over the aryl-substituted diimine ligands.

In the case of **Cu(Bph)** (**Figure 2A**, red), the intensities of both the ^{1}MLCT and π-π* bands were enhanced to 7500 and ~70000 $M^{-1}cm^{-1}$, respectively, with no shift observed for the ^{1}MLCT band and a red-shift observed for the π-π* band. Reports indicate that, for the similar types of heteroleptic Cu^I complexes, adding phenyl groups at the 4,7-positions of the dmp ligand, as in **Cu(ph)**, enhances the ^{1}MLCT absorption band intensity. This enhancement results in a red shifts of the band to λ_{abs} = 388 nm (ε = 5700 $M^{-1}cm^{-1}$) from that of **Cu(H)** (λ_{abs} = 380 nm, ε = 2700 $M^{-1}cm^{-1}$) due to the enhancement in the corresponding transition dipole moment and stabilization of the π* orbitals in the dmp ligand (Tsubomura et al., 2015). In our case, **Cu(Bph)** also retained this tendency, where the phenyl groups were modified from those in **Cu(ph)**, but to a much lesser degree.

Introducing NC- groups or NO_2- groups at the 4-position of the two phenyl groups, as in **Cu(NCph)** and **Cu(NO$_2$ph)** (**Figure 2A**, blue and purple), respectively, resulted in significant red shift in the ^{1}MLCT absorption bands to 400 and 401 nm, with almost no changes observed in their intensities. Because these substituents are known as π-electron-withdrawing substituents, these red shifts indicate that the π*-orbitals on the dmp ligand were stabilized by these substituents through the π-systems containing the phenyl groups.

Such the red shifts of the ^{1}MLCT bands were also observed for the Cu^I complexes featuring aryl substituents (**Figure 2B**). In the case of **Cu(3fu)** and **Cu(3th)** (**Figure 2B**, black and red, respectively), both ^{1}MLCT bands underwent slight red shifts to 390 and 391 nm, respectively, while retaining their intensities, compared to **Cu(ph)**. This result indicates the different electronegativities of the O and S atoms made only negligible effect on the absorption spectra. **Cu(3Bzth)** also underwent a further red shift of the ^{1}MLCT band than the other complexes in the form of a shoulder at 395 nm (**Figure 2B**,

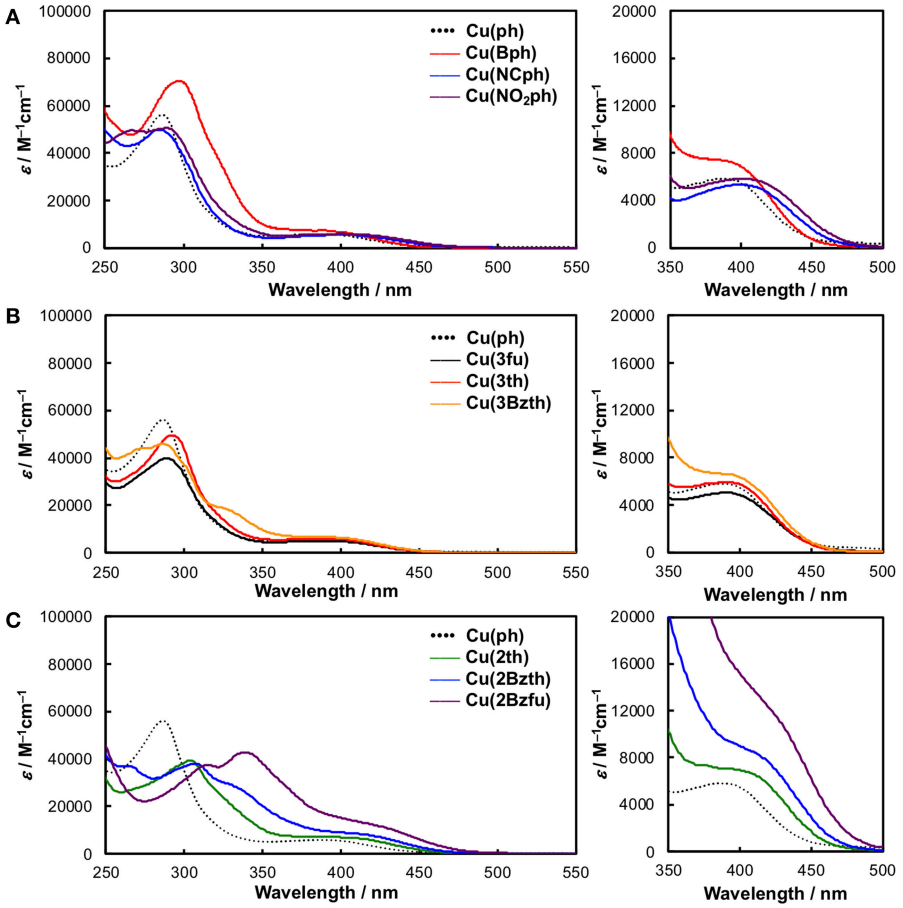

FIGURE 2 | UV-Vis absorption spectra of the Cu^{I} complexes in CH_2Cl_2 alongside the spectrum of **Cu(ph)** (dotted black line) as a reference. **(A) Cu(ph)** (dotted black line), **Cu(Bph)** (red), **Cu(NCph)** (blue), and **Cu(NO$_2$ph)** (purple). **(B) Cu(3fu)** (solid black line), **Cu(3th)** (red), and **Cu(3Bzth)** (yellow). **(C) Cu(2th)** (green), **Cu(2Bzth)** (blue), and **Cu(2Bzfu)** (purple). Right panels on each spectrum show magnified section of the spectra, zoomed in on the ^{1}MLCT absorption.

yellow). In this case, the π-π* absorption band was also red shifted to 330 nm, indicating destabilized π orbitals over the substituted dmp ligand due to the expansion of the π-systems.

Compared to these aryl groups, substituting the 2-positions of the 5-membered rings with heteroatoms resulted in much larger red shifts in both the ^{1}MLCT and π-π* absorption bands. For **Cu(2th)** (**Figure 2C**, green), **Cu(2Bzth)**, and **Cu(Bz2fu)** (**Figure 2C**, blue and purple, respectively) gradual shifts in the ^{1}MLCT bands of these complexes to longer wavelengths (400, 410, and 420 nm, respectively) occurred alongside an increase in the ε values to 6800, 8200, and 12300 $M^{-1}cm^{-1}$, respectively. Additionally, the π-π* bands were also red shifted largely up to 350 nm. Thus, the π-conjugation over the substituted dmp ligand was effectively observed, especially for the complex featuring 2-benzofuryl substituents [**Cu(Bzfu)**]. These trends were almost similar in CH_3CN solutions (**Figure S1** and **Table 2**), although undesired generation of the corresponding homoleptic-type Cu^{I} complexes with ^{1}MLCT absorption bands at over 450 nm obscured the original heteroleptic complexes.

Then, the single-crystal structures of these Cu^{I} complexes were determined to obtain information about the planarity of the substituted dmp ligand, which determines the overlap of the π* orbitals between the aryl substituents and dmp. Here, we could obtain four types of single crystals of Cu^{I} complexes, **Cu(ph)**, **Cu(NCph)**, **Cu(2Bzth)**, and **Cu(2Bzfu)**. The structures of these are shown in **Figure 3** and full analytical details are in the **Supplementary Information** (**Figures S44–47** and **Tables S2–6**). All of these complexes have tetrahedral Cu^{I} center with an almost right angle between NCuN and PCuP planes (88.6, 89.0, 88.6, and 86.8°, respectively), a configuration required for these types of Cu^{I} complexes to exhibit strong emission. There are no remarkable differences in the complexes' residual parts, other than in the substituted dmp ligand, as follows.

The twisted angles between the phen and ph planes in the **Cu(ph)** crystal were found to be 60.2 and 53.9°. Because the H atoms at the 5,6-positions of the phen ligand and the 2,6-positions of the ph groups are in close contact, these ph groups cannot lie in the same plane as that of the phen ligand. Actually, the shortest distances between these H atoms were measured as 2.49 and 2.54 Å. These values are closing to the limitation of van der Waals radius of the H atom, at 1.2 Å (Bondi, 1964).

TABLE 1 | Photophysical Properties of the Cu^I Complexes in CH_2Cl_2.

Complex	λ^a_{abs}/nm (ε^b/$M^{-1}cm^{-1}$)	$\lambda_{em}{}^c$/nm	$\Phi_{em}{}^d$	$\tau_{em}{}^e/\mu s$
Cu(H)	380 (2,700)	562	0.43	15.5
Cu(ph)	388 (5,700)	575	0.52	19.4
Cu(Bph)	388sh (7,500)	577	0.60	22.5
Cu(NCph)	400 (5,300)	609	0.16	5.6
Cu(NO_2ph)	401 (5,800)	640	0.00	0.01
Cu(3fu)	390 (5,000)	580	0.24	0.06, 0.69, 8.3, 23.6
Cu(3th)	391 (5,900)	579	0.35	22.6
Cu(3Bzth)	395sh (6,600)	580	0.45	0.03, 16.5
Cu(2th)	400 (6,800)	601	0.20	0.02, 93.3
Cu(2Bzth)	410sh (8,200)	614	0.06	0.02, 0.5, ∼130[f]
Cu(2Bzfu)	420sh (12,300)	611, 650sh	0.07	0.02, ∼240[f]

[a] λ_{abs}, ^{1}MLCT absorption maxima;
[b] ε, molar extinction coefficients;
[c] λ_{em}, emission maxima;
[d] Φ_{em}, emission quantum yield;
[e] τ_{em}, emission lifetimes;
[f] out of range for accurate determination;
[c–e] samples degassed using the freeze–pump–thaw method.

TABLE 2 | Photophysical Properties of the Cu^I Complexes in CH_3CN.

Complex	λ^a_{abs}/nm (ε^b/M^{-1} cm^{-1})	$\lambda_{em}{}^c$/nm	$\Phi_{em}{}^d$	$\tau_{em}{}^e/\mu s$
Cu(H)	375 (∼2,300[f])	575	0.021	0.96
Cu(ph)	384 (∼6,000[f])	590	0.027	0.99
Cu(Bph)	388sh (∼7,200[f])	596	0.028	1.2
Cu(NCph)	392 (∼5,200[f])	624	0.0073	0.19, 0.74
Cu(NO_2ph)	390 (∼6,300[f])	620	0.0009	0.004, 0.89
Cu(3fu)	387 (∼4,900[f])	593	0.026	0.0015, 0.0075, 0.054, 1.37
Cu(3th)	386 (∼6,000[f])	596	0.041	1.26
Cu(3Bzth)	385sh (∼6,100[f])	600	0.042	0.98
Cu(2th)	390sh (∼6,600[f])	618	0.021	0.001, 0.006, 8.29
Cu(2Bzth)	400sh (∼8,700[f])	631	0.0093	0.005, 1.2, 14.1
Cu(2Bzfu)	410sh (∼11,600[f])	620sh, 650	0.0081	0.004, 32.2

[a] λ_{abs}, ^{1}MLCT absorption maxima;
[b] ε, molar extinction coefficients;
[c] λ_{em}, emission maxima;
[d] Φ_{em}, emission quantum yield;
[e] τ_{em}, emission lifetimes; [f] minimum values considering partial decomposition to the corresponding homoleptic-type Cu^I complexes (see the spectra in ***Figure S1***);
[c–e] samples degassed using the freeze–pump–thaw method.

Thus, the steric repulsion between these H atoms hinders the planarity of the ph-phen plane, resulting in a small expansion of the π-conjugation over the substituted dmp ligand. Even when π-electron withdrawing NC- groups were introduced at the 4-position of ph as for **Cu(NCph)**, the twist angles and shortest distances between the H atoms were 49.4 and 53.9°, and 2.50 and 2.41 Å, respectively. Thus, the steric hindrance of the H atoms should still play a role in hindering the NCph-phen bonds' planarity.

Complexes with 5-membered, heteroring substituents exhibited decreased twist angles. In the case of **Cu(2Bzth)**, the angles were 51.1 and 46.3°, maintaining the distances between the H atoms of 2.45 and 2.32 Å. However, the angles in **Cu(2Bzfu)** drastically decreased to 32.2 and 7.1°, shortening the H–H distance to 2.13 Å and changing the direction of O atom in another 2-benzofuryl substituent to neighbor to the 5-H atom of phen with the shorter distance of 2.17 Å. This means the substituents were able to lie in the same plane as the phen moiety. Because the van der Waals radius of the O atom is 1.52 Å, which is smaller than the 1.80 Å radius of the S atom (Bondi, 1964), the steric hindrance of the planarity over the substituted dmp ligand is not strong enough to result in a planner structure. Thus, the π-systems over the substituted dmp should be the strongest for **Cu(2Bzfu)** among the Cu^I complexes in this work. This structural accessibility of a planner structure should lower the π* orbitals over the substituted dmp ligand, resulting in a red shift in the ^{1}MLCT absorption band (**Figure 2C**, purple).

Figure 4 shows the emission spectra and time-dependences of the emission intensity, and the data are summarized in **Table 1**. All of the Cu^I complexes showed strong emission, apart from **Cu(NO_2ph)**. In the case of **Cu(Bph)** (**Figures 4A,B**, red), the spectrum was almost the same as that of **Cu(ph)**, with a maximum (λ_{em}) at 577 nm; however, its quantum yield (Φ_r) of 0.60 was greater than that of **Cu(ph)**, which was 0.52. This is reasonable when considering the increased oscillator strength for the MLCT transition, as observed in the increased ε value of the ^{1}MLCT absorption band in the UV-Vis spectrum. Thus, the radiative transition rate (k_r) of the excited state should be enhanced, increasing the Φ_r because this value is defined in the context of k_r in all of the deactivation paths of the excited state ($k_r + k_{nr}$ in this case). The increased, excited-state lifetime [$\tau_{em} = 1/(k_r + k_{nr})$] for **Cu(Bph)** of 22.5 μs from that of **Cu(ph)** (19.4 μs) indicates that the k_{nr} value of **Cu(Bph)** is lower than that of **Cu(ph)**. This should be due to the increased mixing of the π-π* excited state in the lowest MLCT state, which is indicated by a red shift in the intraligand ^{1}π-π* absorption band close to the ^{1}MLCT band. Because these Cu^I complexes exhibit delayed fluorescence, the actual deactivation rates of k_r and k_{nr} could not be obtained in these measurements.

In the cases of **Cu(NCph)** and **Cu(NO_2ph)** (**Figures 4A,B**, blue and purple, respectively), the emission maxima were red shifted to 609 and 640 nm, respectively, manifesting as red shifts in the corresponding ^{1}MLCT absorption bands. In both cases, the Φ_r and τ_{em} values were significantly decreased [$\Phi_r = 0.16$ and $\tau_{em} = 5.6$ μs for **Cu(NCph)**], and **Cu(NO_2ph)** showed almost no emission ($\Phi_r < 0.00$, $\tau_{em} = 0.01$ μs). These can be reasonably explained by the energy-gap law similarly to the substituent effects on the emission behaviors of α-diimine complexes of Ru and Re (Cook et al., 1984; Worl et al., 1991). The lowered energy of the MLCT transition resulted in a lower energy gap

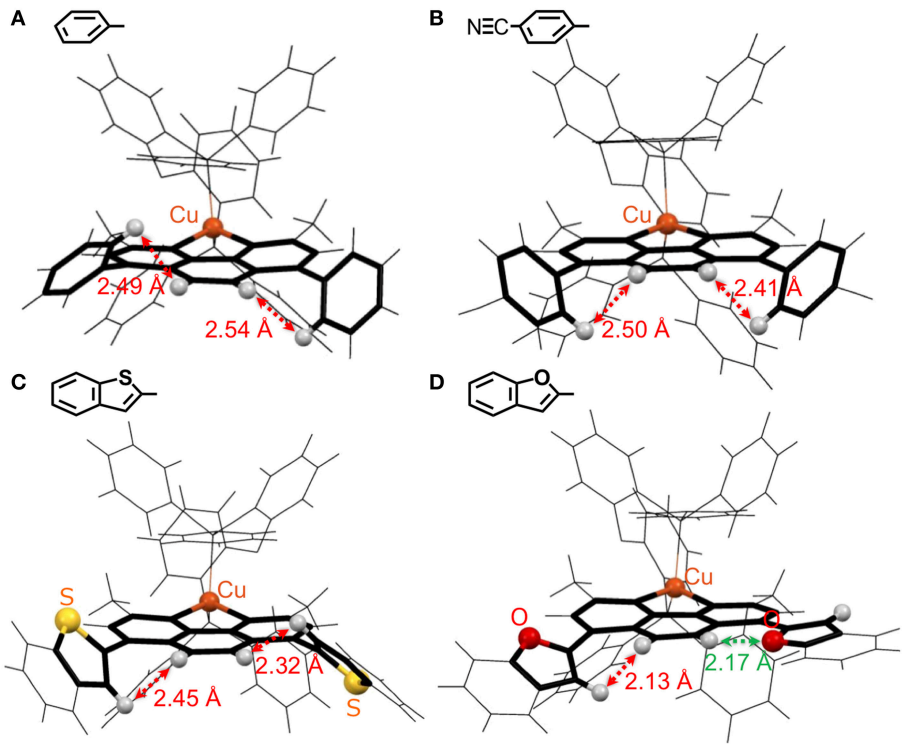

FIGURE 3 | Wire model representations of the single-crystal Cu^I-complexes: **(A) Cu(ph)**, **(B) Cu(NCph)**, **(C) Cu(2Bzth)**, and **(D) Cu(2Bzfu)**: the phen ligand and adjacent aryl substituents at the 4,7-positions are highlighted. The gray, yellow, red, and orange balls represent H atoms on the phen ligand and on the adjacent positions in the aryl rings, and the S, and O atoms on the aryl substituents, and Cu atoms, respectively.

between the excited state and the ground state, thus leading to an increased k_{nr} value. **Cu(NO_2ph)** exhibited almost no emissions, which can be attributed to charge localization on the strong, electron-withdrawing NO_2 groups in the excited state, leading to a charge-separated radical-like state (Prei et al., 2015). This, in turn, should lead to an increase in the k_{nr} value.

The Cu^I complexes, substituted with smaller aryl groups, showed two different sets of behavior. The emission spectra of the **Cu(3fu)**, **Cu(3th)**, and **Cu(3Bzth)** complexes containing 5-membered ring systems with heteroatoms at 3-position (**Figures 4C,D**, black, red, and yellow, respectively), showed almost the same features as those found in the **Cu(ph)** spectrum. All of these complexes showed strong emissions with Φ_r values of 0.24–0.45 and τ_{em} values of ca. 20 μs, values that are almost the same as those of **Cu(ph)**. In these cases, changing the heteroatoms from O to S in the aryl rings appeared to have no great effect on the complexes' transition energies, but Φ_r value increased from 0.24 for **Cu(3fu)** to 0.35 for **Cu(3th)**, which further increased in **Cu(3Bzth)** ($\Phi_r = 0.45$).

However, in systems where the heteroatoms featured at the 2-position of the rings, as in **Cu(2th)**, **Cu(2Bzth)**, and **Cu(2Bzfu)** (**Figures 4E,F**, green, blue, and purple for **Cu(2th)**, **Cu(2Bzth)**, and **Cu(2Bzfu)**, respectively), the emissions were drastically different from those of the other complexes. The emission spectra were observed to gradually red shift in the complexes in the aforementioned order and their shapes changed to vibronic shapes, particularly for **Cu(2Bzfu)**. Because the excitation spectrum from which this emission was monitored was in accordance with the UV-Vis absorption spectrum of **Cu(2Bzfu)** (**Figure S3A**), this emission could be confirmed to arise from the excited state of **Cu(2Bzfu)**.

This emission of **Cu(2Bzfu)** was found to be strongly air sensitive. If the emission spectrum was recorded for a sample prepared under an Ar atmosphere instead of a vacuum-degassed sample, the spectrum was observed to drastically change, resulting in a mismatch between the excitation and absorption spectra of **Cu(2Bzfu)** in CH_2Cl_2 (**Figure S3B**). However, this was not the case for the data recorded in a CH_3CN solution, which showed no remarkable changes in the spectral features, even for a sample prepared under an Ar atmosphere (**Figure S12C**) compared to under vacuum conditions (**Figure S3C**).

Interestingly, these Cu^I complexes' τ_{em} values increased to over 100 μs, with a corresponding decrease in the Φ_r values. These results strongly indicate that the emissive lowest excited state changed from the MLCT state to another state, possibly the intraligand π-π* excited state. This is a reasonable assumption, considering the red shift in the π-π* transition band, as observed in the UV-Vis absorption spectra, from the π-expansion of the dmp ligand. Thus, in these complexes, the emission from the

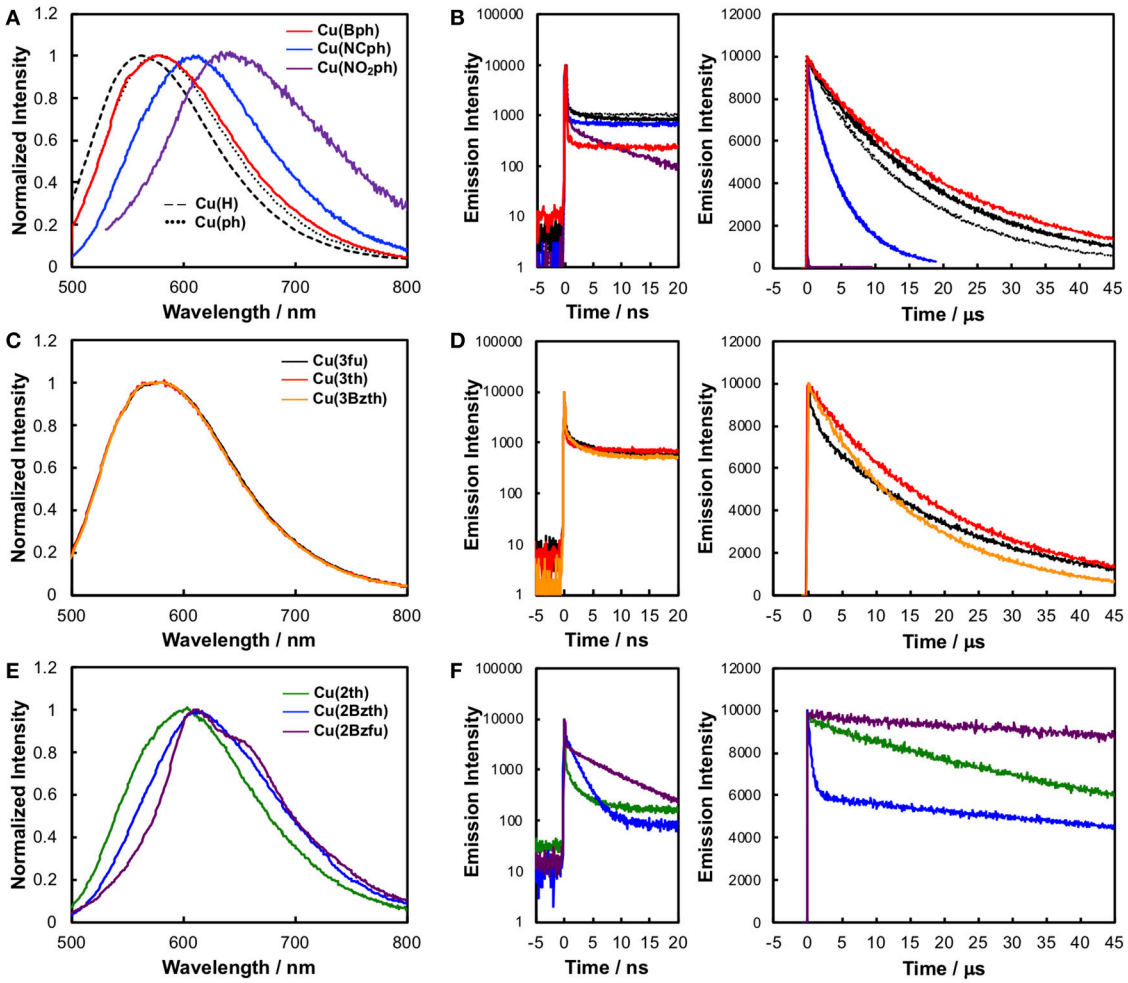

FIGURE 4 | The corrected emission spectra **(A, C,** and **E)** and time-dependence data of the emission intensity **(B, D,** and **F)** of the Cu^I complexes in CH_2Cl_2 at RT. **(A)** Emission spectra and **(B)** time-dependence data of the intensity of **Cu(H)** (broken black line), **Cu(ph)** (dotted black line), **Cu(Bph)** (red), **Cu(NCph)** (blue), and **Cu(NO_2ph)** (purple). **(C)** Emission spectra and **(D)** time-dependence data of the intensity of **Cu(3fu)** (black line), **Cu(3th)** (red), and **Cu(3Bzth)** (yellow). **(E)** Emission spectra and **(F)** time-dependence data of the intensity of **Cu(2th)** (green), **Cu(2Bzth)** (blue), and **Cu(2Bzfu)** (purple). Left panels on **(B, D,** and **F)** were observed from a shorter range of each right panel. The samples were degassed using the freeze–pump–thaw method. **Table S1** summarizes the excitation and monitored wavelengths.

lowest excited state should arise from the delayed fluorescence of the intraligand $^3\pi$-π^* state.

The spectral feature depended strongly on the heteroatoms on the 2-positions of the aryl substituents. In the case of **Cu(2th)** and **Cu(2Bzth)**, the emission spectra were much broadened than that of **Cu(2Bzfu)**, although the lifetimes were still long. These results strongly indicate that the accessibility of the planar structure over the aryl substituted dmp enhances the π-conjugation over the dmp ligand. The similar phenomena about the long excited-state lifetime caused by the planarity between aryl substituents and α-diimine ligand has been discussed for emissive Ru complexes, in which the delocalization of negative charge over the substituted bpy (bpy = 2,2′-bipyridine) in the ^{3}MLCT excited state lowers their structural changes from the ground state, leading to decreasing k_{nr} (Damrauer et al., 1997; Majewski et al., 2016). It is also reported that the Cu^I(dmp) complex has the close-lying $^3\pi$-π^* state near the lowest ^{3}MLCT excited state as for $Cu^I(dmp)(PPh_3)_2^+$, which showed the vibronic emission spectrum at 77 K as a long-lifetime component as $\tau_{em} \sim 10$ ms (Rader et al., 1981). Therefore, the long lifetime emission of **Cu(2th)**, **Cu(2Bzth)**, and **Cu(2Bzfu)** can be reasonably attributed to the participation of $^3\pi$-π^* excited state.

All of these tendencies were also valid even in CH_3CN as a photocatalytic reaction solvent, except that the emission was significantly quenched compared to that observed in CH_2Cl_2 solutions due to "exciplex" formation, in which a solvent molecule coordinates to the Cu center as a fifth ligand in the excited-state Cu^I complexes (**Figure S2** and **Table 2**). This type of quenching is characteristic of tetrahedral Cu^I complexes as the d^{10} Cu^I center decreases its charges upon closing to a d^9 configuration in the MLCT excited state, changing

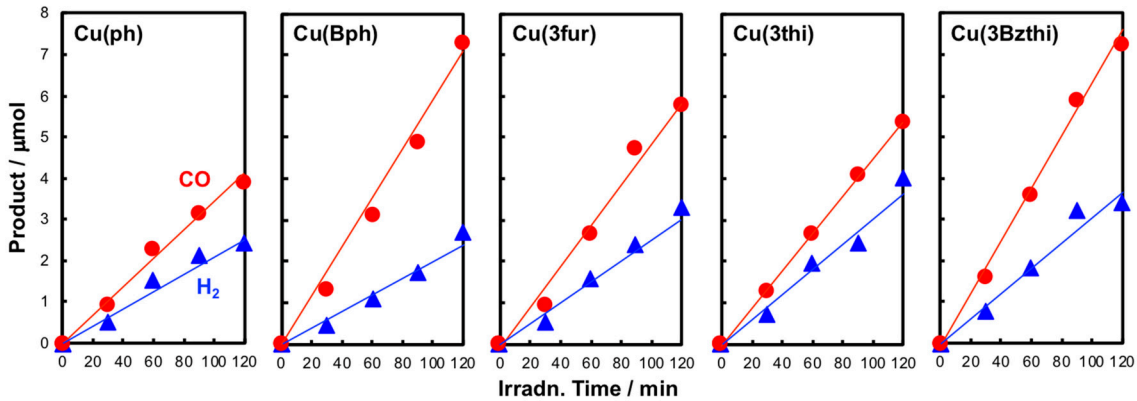

FIGURE 5 | Time-course data of CO (red) and H_2 (blue) evolution during the photocatalytic reactions using the Cu^I complexes as redox photosensitizers. A 4 ml CH_3CN-TEOA (5:1 v/v) solution containing a Cu^I complex (0.5 mM), $Fe(dmp)_2(NCS)_2$ (0.05 mM), and BIH (10 mM) was irradiated using the 436 nm monochromatic light (intensity: 3×10^{-8} einstein s^{-1}) of a Xe lamp under a CO_2 atmosphere at 25°C.

the structure to planer one because of the Jahn-Teller effect (McMillin et al., 1985).

Thus, the quenching all of the Cu^I complexes studied in CH_3CN indicates that they have MLCT character in their excited state to some extent, even for **Cu(2th)**, **Cu(2Bzth)**, and **Cu(2Bzfu)**, in which the excited state was mainly the π-π* state. The extents of the MLCT character should increase especially in CH_3CN because this state has CT in character, that are stabilized in a polarized solvent such as CH_3CN more strongly than the intraligand π-π* excited state. Actually, such the stabilizations were seen as red-shift of emission maxima in CH_3CN compared to those in CH_2Cl_2. In the case of **Cu(NO$_2$ph)**, the emission behavior completely changed in CH_3CN, possibly as a result of photodecomposition, manifesting in a different excitation spectrum than **Cu(NO$_2$ph)**'s original absorption spectrum.

Photocatalytic CO_2 reduction reactions were performed using these newly designed Cu^I complexes as redox photosensitizers mixed with $Fe^{II}(dmp)_2(NCS)_2$ (0.05 mM) as a catalyst and BIH (10 mM) as a reductant under a 436 nm monochromic light in a mixed solution of CH_3CN–triethanolamine [TEOA, 5:1 (v/v)]. The Cu photosensitizer's concentration was fixed at 0.5 mM, showing almost no transparency at 436 nm in reaction cells with a 1-cm optical path length. **Figure 5** shows the photocatalytic reaction results. The products were found to be only CO and H_2, without the formation of any HCOOH as reported in a previous study performed under similar conditions (Takeda et al., 2016), and these compounds were linearly generated against the photoirradiation time for up to 2 h.

The photocatalytic properties were highly dependent on the Cu complex photosensitizer used (**Table 3**). When **Cu(Bph)** was used, the efficiencies were enhanced to Φ_r = 3.9 with H_2 formation (Φ_r = 1.4). Take into account the low results for **Cu(H)** [Φ_r = 1.1 (Takeda et al., 2016)] and **Cu(ph)** (Φ_r = 2.3), increasing the number of the ph groups at the 4,7-positions of dmp tended to enhance the photosensitizing ability of these complexes for CO_2 reduction.

Such the enhancement in the photosensitizing ability was also confirmed in the cases of complexes featuring 5-membered ring systems with heteroatoms at the 3-position, such as **Cu(3fu)**, **Cu(3th)**, and **Cu(3Bzth)**. The most efficient case was **Cu(3Bzth)**, which showed Φ_r values of 4.1 and 2.0 for CO and H_2 evolution, respectively. Even in the cases of **Cu(3fu)** and **Cu(3th)**, the efficiencies for the CO_2 reduction were improved to Φ_r (CO) = 3.5 and 2.9, respectively, over those of **Cu(ph)**.

However, the Cu^I complexes containing 5-membered ring systems with heteroatoms at 2-position, such as **Cu(2th)**, **Cu(2Bzth)**, and **Cu(2Bzfu)**, showed no any photosensitizing ability in this reaction system. These complexes may have lower oxidative power in their excited state because their highest occupied molecular orbital (HOMO) energies should now increase since the π orbitals in the substituted dmp, as well as the *d* orbitals on the Cu^I center, are destabilized. Actually, the first oxidation wave in the cyclic voltammetry (CV) measurements, an indicator of the HOMO energy, showed positive shifts for **Cu(2th)**, **Cu(2Bzth)**, and **Cu(2Bzfu)** (shoulder waves around 0.9 V *vs.* Ag/$AgNO_3$) compared to that of **Cu(ph)** (E_p = 0.92 V vs. Ag/$AgNO_3$) (**Figure S4**).

The excited states of these Cu^I complexes were effectively quenched in the presence of BIH, except for that of **Cu(NO$_2$ph)**, which means that all of these complexes might generate the corresponding one-electron reduced state through the reductive quenching of their excited states by BIH during photoirradiation (Tamaki et al., 2013; Takeda et al., 2018). The quenching rate constants (k_q) were estimated to be $\sim 10^{10}$ $M^{-1}s^{-1}$, corresponding to quantitative quenching (η_q) under photocatalytic conditions with 10 mM of BIH (**Table 3**). Because the quenching behavior in terms of the emission lifetimes was in good agreement with the emission intensity changes, and no changes were observed in the UV-vis and emission spectra of the Cu^I complexes, even in the presence of BIH (**Figures S5–S12**). These quenching reactions can be attributed to a dynamic quenching process, in which the excited state reacts with BIH bimolecularly.

TABLE 3 | Quantum Yields of the Photocatalytic CO_2 Reduction (Φ_r) Using the Cu^I Complexes as Redox-Photosensitizer,[a] Reduction Potentials ($E_{1/2}$), and Excited-State Quenching Rate (k_q) by BIH of the Cu^I Complexes.

Complex	Φ_r		$E_{1/2}$/V[b]	k_q /10^{-9} $M^{-1}s^{-1}$	η_q/%[c]
	CO	H_2			
Cu(H)	1.1[d]	0.6 [d]	−2.03[d]	4.4[d]	96[d]
Cu(ph)	2.3	1.5	−1.96[d]	5.6[d]	95[d]
Cu(Bph)	3.9	1.4	−1.92	7.6	99
Cu(NCph)	n.d.[e]	n.d.[e]	−1.75	9.9	95
Cu(NO_2ph)	n.d.[e]	n.d.[e]	−1.31	– [f]	– [f]
Cu(3fu)	3.5	1.9	−1.96	10.6	99
Cu(3th)	2.9	2.1	−1.94	7.8	99
Cu(3Bzth)	4.1	2.0	−1.93	7.4	99
Cu(2th)	n.d.[e]	n.d.[e]	−1.83	9.0	100
Cu(2Bzth)	n.d.[e]	n.d.[e]	−1.74	7.9	100
Cu(2Bzfu)	n.d.[e]	n.d.[e]	−1.70	7.7	100

[a]*photocatalytic system consisting of $Fe(dmp)_2(NCS)_2$ (0.05 mM) as a catalyst and BIH (10 mM) as a reductant in CH_3CN–TEOA (5:1 v/v) (see **Figure 4**);*
[b]*Potentials [V] vs. Ag/$AgNO_3$ (0.01 M);*
[c]*η_q, quenching fraction of the excited-state Cu^I complexes by BIH (10 mM), estimated by $\eta_q = K_{SV}[BIH]/(1 + K_{SV}[BIH])$, in which the K_{SV} [M^{-1}] values are the slopes of the Stern-Volmer plots in **Figures S5–S12**;*
[d]*from Takeda et al. (2016);*
[e]*not determined due to the low product amount;*
[f]*not detected due to weak emission.*

Then, *in situ* UV-Vis absorption spectral changes in the reaction solutions during the photocatalytic reactions were investigated and compared to those of the complexes recorded under an Ar atmosphere for up to 1 h of photoirradiation. In the cases of **Cu(3fu)**, **Cu(3th)**, and **Cu(3Bzth)** (**Figures S15–17**), which were good photosensitizers for photocatalytic CO_2 reduction, almost no changes occurred in their spectra. This indicates that there was almost no decomposition of the Cu complexes in the photosensitizing cycles, donating electrons to the Fe catalyst, for the oxidation of BIH and CO_2 reduction. Under an Ar atmosphere, the MLCT absorption bands of the original Cu^I complexes decreased just after the photoirradiation caused broad absorption up to 950 nm. These changes clearly indicate the original Cu^I complexes' photodecomposition. Because the one-electron reduced state produced by the reductive quenching of the excited state cannot donate to the CO_2 reduction cycle of the Fe catalyst, the reduced species of the Cu^I complexes accumulate in the reaction solutions, decomposing due to their anionic radical character if CO_2 is not present.

On the other hand, non-photosensitizing Cu^I complexes, such as **Cu(NCph)**, **Cu(2th)**, **Cu(2Bzth)**, and **Cu(2Bzfu)** (**Figures S13**, **S18–20**, respectively) showed signs of drastic decomposition even in the presence of CO_2. This means that the Cu complexes cannot donate their electrons generated through the reductive quenching by BIH in the excited state for the CO_2 reduction. Thus, these complexes showed no photocatalytic CO_2 reduction properties. However, the lack of the photosensitizing ability of **Cu(NO_2ph)** should be due to its unstable excited state because no changes were observed, neither under a CO_2 nor an Ar atmosphere, meaning that no any redox cycles occurred under photoirradiation.

The Cu^I complexes' electrochemical properties were then examined, and the results are shown in **Figure 6**. All of the Cu^I complexes, apart from **Cu(H)**, showed a reversible redox couple in the CV as the first reduction wave, indicating that the corresponding one-electron reduced species was stabilized *via* the introduction of the aryl substituents on the dmp ligand, as observed for **Cu(ph)**. This is quite reasonable considering that the first reduction occurs in the dmp ligand's low-lying π^* orbital. However, for the CV of **Cu(NO_2ph)**, the redox couple current was much higher without any sharpening. Thus, the first reduction wave in the CV of **Cu(NO_2ph)** arises as a result of two sequential local electron reductions in the two NO_2ph parts of one **Cu(NO_2ph)**. The redox potentials ($E_{1/2}$) of these first reduction waves are summarized in **Table 3**. Apparently, introducing electron-withdrawing groups, such as NCph and NO_2ph, resulted in positive shifts in the $E_{1/2}$ values up to −1.75 and −1.31 V vs. Ag/$AgNO_3$ for **Cu(NCph)** and **Cu(NO_2ph)**, respectively, indicating that the electron-donating ability of the corresponding reduced species was lowered. Those of the **Cu(Bph)**, **Cu(3fu)**, **Cu(3th)**, and **Cu(3Bzth)** complexes that have photosensitizing ability in this photocatalytic system maintained values more negative than −1.9 V, although these $E_{1/2}$ values were positively shifted from those of **Cu(H)** and **Cu(ph)** ($E_{1/2}$ = −2.03 and −1.96 V vs. Ag/$AgNO_3$, respectively). For **Cu(2th)**, **Cu(2Bzth)**, and **Cu(2Bzfu)**, in which the π-system largely extends to the aryl substituents, exhibited more positive first reduction potentials of −1.83, −1.74, and −1.70 V, respectively, due to the stabilization of the π^* orbital over the substituted dmp ligand. Thus, the lowering energy of the π^* orbital on the dmp ligand *via* the introduction of phenyl rings with π-electron-withdrawing groups or 5-membered aryl groups was clearly confirmed.

Compared to the first reduction wave potential of $Fe(dmp)_2(NCS)_2$ in CH_3CN–TEOA (5:1 v/v) solution (−1.61 V vs. Ag/$AgNO_3$) under a CO_2 atmosphere (Takeda et al., 2016), the reducing power of these Cu complexes is enough for them to donate their first single electron on the corresponding reduced species to the Fe catalyst. However, the decomposition behavior during the photoirradiation process indicates that the electron transfer to the Fe catalyst is inefficient, resulting in an accumulation of the reduced species of the Cu complexes and decomposition over longer time scales than those of the CV measurements. We are now continuing the photocatalytic reaction using the other catalysts for the CO_2 reduction that function at a more positive potential.

CONCLUSION

This study found the heteroleptic Cu^I complexes' visible-light absorption properties could be improved via expanding the dmp ligand's π-systems. Simple expansion using biphenyl substitution at the 4,7-popsitions of dmp enhanced ε without red shift

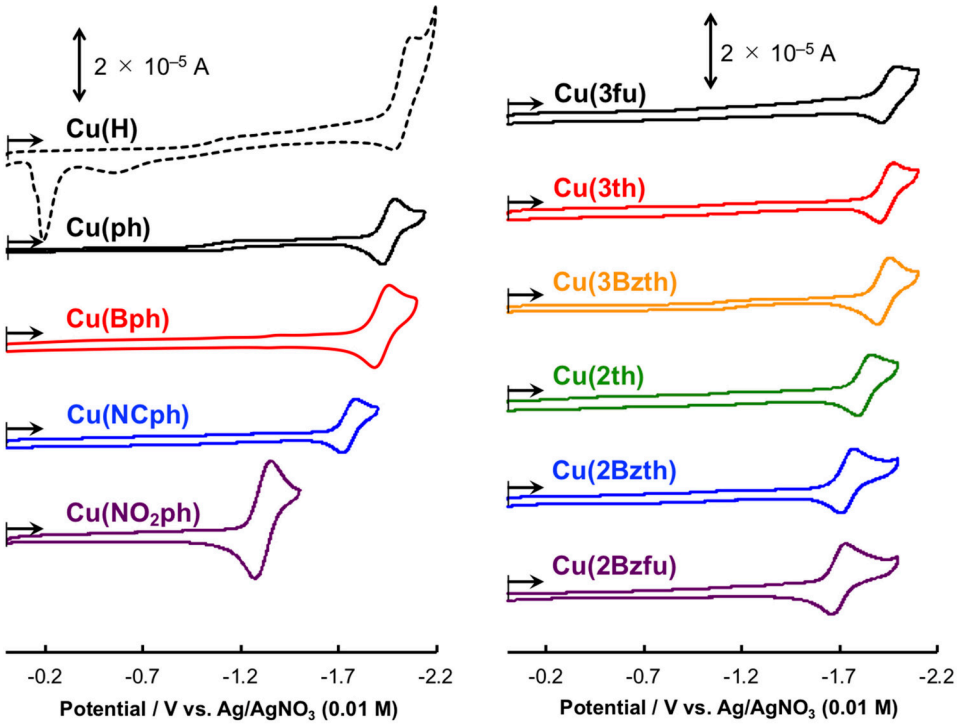

FIGURE 6 | Cyclic voltammograms of the Cu^I complexes (0.5 mM) in CH_3CN containing 0.1 M Et_4NBF_4 as a supporting electrolyte at a scan rate of 0.1 V s^{-1}. WE: glassy carbon (Φ 3 mm); CE: Pt wire; RE: $Ag/AgNO_3$ (0.01 M). The **Cu(H)** and **Cu(ph)** voltammograms are reproduced from ref. (Takeda et al., 2016) for comparison.

of the ^{1}MLCT band compared to that of the ph substituted one. Although π-electron accepting substituents such as 4-NCph or 4-NO_2ph shifted the band, the λ_{max} values were still around 400 nm. The X-ray single crystal analysis showed the presence of protons at the 2,6-positions of the ph substituents slows the π-conjugation between the ph groups and dmp due to the steric hindrance of the 5,6-protons in the dmp ligand. Thus, substitution with 5-membered heterorings, with heteroatoms and no protons at the 2-positions, was enough to make improvements to the properties of the complexes. Thus, the complexes containing 2-benzofuryl groups having an O atom which size is smaller than a S atom at each 2-position showed a planner structure over the substituted dmp ligand, resulting in a red shift in the ^{1}MLCT absorption bands up to 500 nm. Because the 3-thienyl and 3-furyl substitutions showed almost no effect on the light absorbing property, this red shift in **Cu(2Bzfu)** was not from a difference of electronegativities of the S and O atoms. Photocatalytic CO_2 reduction reactions were carried out with the complexes in the presence of a Fe catalyst, showing quantum yields of up to 4% for the maximum amount of CO generated. The knowledge obtained in this study should help not only for further expansion of visible-light absorbing but also for designing the efficient redox-photosensitizer using the Cu^I complex to construct efficient earth-abundant system for the photocatalytic CO_2 reduction.

EXPERIMENTAL

General Measurements

^{1}H NMR spectra were recorded on a JEOL ECA-400II NMR spectrometer. The chemical shifts and coupling values arising from the second order effects of the protons in the phenanthroline derivatives were assigned by analyzing the obtained ^{1}H NMR spectra using the iNMR (ver. 6.1.8) and WINDNMR (ver. 7.1.14) software (Reich, 1995). UV-vis absorption spectra were recorded on a JASCO V-565 or V-670 spectrometers. To measure the molar extinction coefficiencies (ε [$M^{-1}cm^{-1}$]), a 10 mL solution containing quantitatively weighted each Cu^I complexes (∼2 mg) was prepared by dissolving in CH_2Cl_2 or CH_3CN as a stock solution. An 1 mL of the stock solution was further diluted to 5 mL by each solvent and UV-vis absorption spectra of these two solutions were recorded using a cuvette cell having an 1-cm path length. After confirmation of no concentration effect on the spectral features indicating no dimer formation by comparison these two spectra, the absorbance was divided by each concentration to obtain ε value. The spectrum of the stock solution was used for assessment of the ^{1}MLCT band and the latter was used for π-π* absorption band because the detection range of absorbance (0.1−1.0) is suitable. Emission and excitation spectra were recorded on a JASCO FP8600 fluorescence spectrometer. Emission quantum yields of the Cu^I complexes in CH_3CN were determined by

a relative method, using an air-saturated CH_3CN solution containing $Ru(bpy)_3(PF_6)$ as a standard ($\Phi = 0.018$) (Suzuki et al., 2009; Ishida and Beeby, 2016). Emission quantum yields in CH_2Cl_2 were collected using a Hamamatsu Photonics C9920–02G absolute photoluminescence quantum yield measurement system, consisting of a calibrated integrating sphere and a multi-channel spectrometer. Excited-state lifetimes were recorded on a HORIBA FluoroCube 1000U-S single-photon counting system. The sample solutions were degassed, *via* freeze–pump–thaw cycles, before the emission and lifetime measurements. For the quenching experiments, changes in the emission intensities and excited-state lifetimes of the Cu^I complexes in CH_3CN, with or without various concentrations of BIH, were monitored under an Ar atmosphere. CVs were measured using Et_4NBF_4 (0.1 M) as a supporting electrolyte under an Ar atmosphere using a BAS CHI620EX or CHI760Es electrochemical analyzer with a glassy carbon working electrode (diameter, 3 mm), an $Ag/AgNO_3$ (0.01 M) as a reference electrode, and a Pt counter electrode.

Photocatalytic Reactions

A 4-mL CH_3CN–TEOA (5:1 v/v) solution containing $Fe(dmp)_2(NCS)_2$ (0.05 mM), and the Cu photosensitizer (0.5 mM), and BIH (10 mM) as a reductant in a quartz cubic cell (1 cm path length; 11.0 mL volume) was bubbled with CO_2 for 20 min. For the quantum yield determinations, a SHIMADZU QYM-01 photoreaction, quantum yield, evaluation system was adopted. The sample solution was irradiated using an Asahi Spectra Co. MAX-303 300-W Xe lamp with a 436 nm band-pass filter (FWHM: 10 nm), with the irradiated light intensity set at 3×10^{-8} einstein s^{-1} and the temperature of the reaction solution was maintained at 25 ± 0.1 °C using an IWAKI CTS-134A cooling thermo pump during the irradiation. The gaseous products, i.e., CO and H_2, were analyzed using GC-TCD (GL science GC323) with an active carbon column. The amount of formic acid in the reaction solution with diluted water was analyzed using a capillary electrophoresis system (Otsuka Electronics Co. 7100L) with a buffer solution (pH 5.9) consisting of quinolinic acid, hexadecyltrimethylammonium hydroxide, and 2-amino-2-hydroxymethyl-1,3-propanediol as the electrolyte. To observe *in situ* UV-Vis spectral changes of the photocatalytic-reaction solution, the solution was irradiated, using an Ushio Optical Module high-pressure Hg lamp (BA-H500), with a 436 nm band-pass filter (FWHM = 10 nm), purchased from Asahi Spectra Co., and a $CuSO_4$ solution (250 g L^{-1}, 5 cm path length) filter with a 436 nm band-pass filter (FWHM: 10 nm) purchased from Asahi Spectra Co. Neutral density glass filters reduced the light intensity. The spectral changes were recorded on a Photal MCPD-6800 photodiode array detector equipped with a MC-2530 light source.

DATA AVAILABILITY

All datasets generated for this study are included in the manuscript and/or the **Supplementary Files**.

AUTHOR CONTRIBUTIONS

HT and OI planned the all experiments. HT and YM synthesized the samples and performed the photophysical, electrochemical, and photocatalytic measurements. HT, HS, and HU analyzed the single crystal structures. HT wrote the manuscript and all authors have read and approved it.

FUNDING

This work was supported by JST CREST (Grant Number JPMJCR13L1). HT has received funding from JSPS KAKENHI (Grant Number JP16K17876). HU has received funding from JSPS KAKENHI (Grant Number JP17K05745 and JP18H04504).

SUPPLEMENTARY MATERIAL

The Supplementary Material for this article can be found online at: https://www.frontiersin.org/articles/10.3389/fchem.2019.00418/full#supplementary-material

Data Sheet 1 | The Cu^I complexes' photophysical properties in CH_3CN, emission and excitation spectra of **Cu(2Bzfu)** in CH_2Cl_2 under Ar or degassed atmospheres, positive scans of the cyclic voltammograms of the Cu^I complexes, quenching experiments of the excited state of the Cu^I complexes by BIH, *in situ* UV-Vis spectral changes during the photoirradiation reactions, experimental details such as materials, synthesis, ^1H NMR spectra, peak analysis of the ^1H NMR spectra of the newly synthesized ligands, and details of the single-crystal X-ray crystallography of **Cu(ph)**, **Cu(NCph)**, **Cu(2Bzth)**, and **Cu(2Bzfu)**.

Data Sheet 2 | Crystallographic data for **Cu(ph)**, **Cu(NCph)**, **Cu(2Bzth)**, and **Cu(2Bzfu)** (CCDC numbers: 1895526-1895529) embedding RES and structure factors.

REFERENCES

Bondi, A. (1964). van der Waals Volumes and Radii. *J. Phys. Chem.* 68, 441–451. doi: 10.1021/j100785a001

Breddels, P. A., Berdowski, P. A. M., Blasse, G., and McMillin, D. R. (1982). Luminescence of Some Cu^I Complexes. *J. Chem. Soc. Faraday Trans.* 278, 595–601. doi: 10.1039/f29827800595

Chen, N.-Y., Xia, L., Lennox, A. J. J., Sun, Y., Chen, H., Jin, H.-M., et al. (2017). Structure-Activated copper photosensitisers for photocatalytic water reduction. *Chem. A Eur. J.* 23, 3631–3636. doi: 10.1002/chem.201602598

Cook, M. J., Lewis, A. P., McAuliffe, G. S. G., Skarda, V., Thomson, A. J., Glasper, J. L., et al. (1984). Luminescent metal complexes. part 2. a model for the luminescence properties of the tris-chelates of substituted 2,2'-Bipyridyls with Ruthenium(II). *J. Chem. Soc. Perkin Trans.* 2, 1303–1307. doi: 10.1039/P29840001303

Cuttell, D. G., Kuang, S.-M., Fanwick, P. E., McMillin, D. R., and Walton, R. A. (2002). Simple Cu(I) complexes with unprecedented excited-state lifetimes. *J. Am. Chem. Soc.* 124, 6–7. doi: 10.1021/ja012247h

Damrauer, N. H., Boussie, T. R., Devenney, M., Mccusker, J. K., and April, R. V. (1997). Effects of intraligand electron delocalization, steric tuning, and excited-state vibronic coupling on the Photophysics of Aryl-Substituted Bipyridyl Complexes of Ru(II). *J. Am. Chem. Soc.* 119, 8253–8268. doi: 10.1021/ja971321m

Eggleston, M. K., McMillin, D. R., Koenig, K. S., and Pallenberg, A. J. (1997). Steric effects in the ground and excited states of $Cu(NN)_2^+$ systems. *Inorg. Chem.* 36, 172–176. doi: 10.1021/ic960698a

Giereth, R., Reim, I., Frey, W., Junge, H., Tschierlei, S., and Karnahl, M. (2019). Remarkably long-lived excited states of copper photosensitizers containing an extended π-system based on an anthracene moiety. *Sustain. Energ. Fuels* 3, 692–700. doi: 10.1039/C8SE00521D

Heberle, M., Tschierlei, S., Rockstroh, N., Ringenberg, M., Frey, W., Junge, H., et al. (2017). Heteroleptic copper photosensitizers: why an extended π-system does not automatically lead to enhanced hydrogen production. *Chem. A Eur. J.* 23, 312–319. doi: 10.1002/chem.201604005

Ishida, H., and Beeby, A. (2016). Guidelines for measurement of luminescence spectra and quantum yields of inorganic and organometallic compounds in solution and solid State (IUPAC Technical Report). *Pure Appl. Chem.* 88, 701–711. doi: 10.1515/pac-2014-0706

Kaeser, A., Mohankumar, M., Mohanraj, J., Monti, F., Holler, M., Cid, J.-J., et al. (2013). Heteroleptic Copper(I) Complexes prepared from phenanthroline and bis-phosphine ligands. *Inorg. Chem.* 52, 12140–12151. doi: 10.1021/ic4020042

Khnayzer, R. S., McCusker, C. E., Olaiya, B. S., and Castellano, F. N. (2013). Robust Cuprous Phenanthroline Sensitizer for Solar Hydrogen Photocatalysis. *J. Am. Chem. Soc.* 135, 14068–14070. doi: 10.1021/ja407816f

Lazorski, M. S., and Castellano, F. N. (2014). Advances in the Light Conversion Properties of Cu(I)-Based Photosensitizers. *Polyhedron* 82, 57–70. doi: 10.1016/j.poly.2014.04.060

Lennox, A. J. J., Fischer, S., Jurrat, M., Luo, S.-P. P., Rockstroh, N., Junge, H., et al. (2016). Copper-Based photosensitisers in water reduction: a more efficient in situ formed system and improved mechanistic understanding. *Chem. A Eur. J.* 22, 1233–1238. doi: 10.1002/chem.201503812

Luo, S. P., Esteban, M., Friedrich, A., Pazidis, A., Junge, H., Surkus, A. E., et al. (2013). Photocatalytic water reduction with copper-based photosensitizers: a noble-metal-free system. *Angew. Chem. Int. Ed.* 52, 419–423. doi: 10.1002/anie.201205915

Majewski, M. B., Smith, J. G., Wolf, M. O., and Patrick, B. O. (2016). Long-lived, emissive excited states in direct and amide-linked thienyl-Substituted Ru^{II} Complexes. *Eur. J. Inorg. Chem.* 1470–1479. doi: 10.1002/ejic.201501436

McCullough, B. J., Neyhouse, B. J., Schrage, B. R., Reed, D. T., Osinski, A. J., Ziegler, C. J., et al. (2018). Visible-light-driven photosystems using heteroleptic Cu(I) photosensitizers and Rh(III) catalysts to produce H_2. *Inorg. Chem.* 57, 2865–2875. doi: 10.1021/acs.inorgchem.7b03273

McMillin, D. R., Kirchhoff, J. R., and Goodwin, K. V. (1985). Exciplex Quenching of photo-excited copper complexes. *Coord. Chem. Rev.* 64, 83–92. doi: 10.1016/0010-8545(85)80043-6

Mejía, E., Luo, S.-P., Karnahl, M., Friedrich, A., Tschierlei, S., Surkus, A., et al. (2013). A noble-metal-free system for photocatalytic hydrogen production from water. *Chem. A Eur. J.* 19, 15972–15978. doi: 10.1002/chem.201302091

Preiß, J., Jäger, M., Rau, S., Dietzek, B., Popp, J., Martínez, T., et al. (2015). how does peripheral functionalization of ruthenium(II)-Terpyridine complexes affect spatial charge redistribution after photoexcitation at the franck-condon point? *ChemPhysChem* 16, 1395–1404. doi: 10.1002/cphc.201500223

Rader, R. A., McMillin, D. R., Buckner, M. T., Matthews, T. G., Casadonte, D. J., Lengel, R. K., et al. (1981). Photostudies of 2,2'-bipyridine bis(triphenylphosphine)copper(1+), 1,10-phenanthroline bis(triphenylphosphine)copper(1+), and 2,9-dimethyl-1,10-phenanthroline bis(triphenylphosphine)copper(1+) in solution and in rigid, low-temperature glasses. simultaneous multiple emissions from intraligand and charge-transfer states. *J. Am. Chem. Soc.* 103, 5906–5912. doi: 10.1021/ja00409a048

Reich, H. J. (1995). WinDNMR: Dynamic NMR spectra for windows. *J. Chem. Edu.* 72:1086. doi: 10.1021/ed072p1086.1

Rockstroh, N., Lochbrunner, S., Tschierlei, S., Junge, H., Karnahl, M., Beller, M., et al. (2014). Substitution-controlled excited state processes in heteroleptic copper(I) photosensitizers used in hydrogen evolving systems. *ChemPhysChem* 15, 3709–3713. doi: 10.1002/cphc.201402585

Rosas-Hernández, A., Steinlechner, C., Junge, H., and Beller, M. (2017). Earth-abundant photocatalytic systems for the visible-light-driven reduction of CO_2 to CO. *Green Chem.* 19, 2356–2360. doi: 10.1039/C6GC03527B

Ruthkosky, M., Kelly, C. A., Castellano, F. N., and Meyer, G. J. (1998). Electron and energy transfer from Cu^{I} MLCT excited states. *Coord. Chem. Rev.* 171, 309–322. doi: 10.1016/S0010-8545(98)90045-5

Suzuki, K., Kobayashi, A., Kaneko, S., Takehira, K., Yoshihara, T., Ishida, H., et al. (2009). Reevaluation of absolute luminescence quantum yields of standard solutions using a spectrometer with an integrating sphere and a back-thinned CCD Detector. *Phys. Chem. Chem. Phys.* 11, 9850–9860. doi: 10.1039/B912178A

Takeda, H., Cometto, C., Ishitani, O., and Robert, M. (2017). Electrons, photons, protons and earth-abundant metal complexes for molecular catalysis of CO_2 reduction. *ACS Catal.* 7, 70–88. doi: 10.1021/acscatal.6b02181

Takeda, H., Kamiyama, H., Okamoto, K., Irimajiri, M., Mizutani, T., Koike, K., et al. (2018). Highly efficient and robust photocatalytic systems for CO_2 reduction consisting of a Cu(I) photosensitizer and Mn(I) catalysts. *J. Am. Chem. Soc.* 140, 17241–17254. doi: 10.1021/jacs.8b10619

Takeda, H., Ohashi, K., Sekine, A., and Ishitani, O. (2016). Photocatalytic CO_2 reduction using Cu(I) photosensitizers with a Fe(II) catalyst. *J. Am. Chem. Soc.* 138, 4354–4357. doi: 10.1021/jacs.6b01970

Tamaki, Y., Koike, K., Morimoto, T., and Ishitani, O. (2013). Substantial Improvement in the efficiency and durability of a photocatalyst for carbon dioxide reduction using a benzoimidazole derivative as an electron donor. *J. Catal.* 304, 22–28. doi: 10.1016/j.jcat.2013.04.002

Tsubomura, T., Kimura, K., Nishikawa, M., and Tsukuda, T. (2015). Structures and Photophysical Properties of Copper(I) Complexes Bearing Diphenylphenanthroline and Bis(Diphenylphosphino)Alkane: the effect of phenyl groups on the phenanthroline ligand. *Dalton Trans.* 44, 7554–7562. doi: 10.1039/C5DT00835B

Worl, L. A., Duesing, R., Chen, P., Ciana, L. D., and Meyer, T. J. (1991). Photophysical properties of polypyridyl carbonyl complexes of rhenium(I). *J. Chem. Soc. Dalton Trans.* 849–858. doi: 10.1039/DT9910000849

Xu, S., Wang, J., Zhao, F., Xia, H., and Wang, Y. (2015). Photophysical properties of copper(I) complexes containing pyrazine-fused phenanthroline ligands: a joint experimental and theoretical investigation. *J. Mol. Model.* 21:313. doi: 10.1007/s00894-015-2857-0

Yamazaki, Y., Takeda, H., and Ishitani, O. (2015). Photocatalytic reduction of CO_2 using metal complexes. *J. Photochem. Photobiol. C.* 25, 106–137. doi: 10.1016/j.jphotochemrev.2015.09.001

Zhang, Q., Ding, J., Cheng, Y., Wang, L., Xie, Z., Jing, X., et al. (2007). Novel Heteroleptic Cu^{I} complexes with tunable emission color for efficient phosphorescent light-emitting diodes. *Adv. Funct. Mater.* 17, 2983–2990. doi: 10.1002/adfm.200601053

Conflict of Interest Statement: The authors declare that the research was conducted in the absence of any commercial or financial relationships that could be construed as a potential conflict of interest.

Copyright © 2019 Takeda, Monma, Sugiyama, Uekusa and Ishitani. This is an open-access article distributed under the terms of the Creative Commons Attribution License (CC BY). The use, distribution or reproduction in other forums is permitted, provided the original author(s) and the copyright owner(s) are credited and that the original publication in this journal is cited, in accordance with accepted academic practice. No use, distribution or reproduction is permitted which does not comply with these terms.

frontiers in Chemistry

REVIEW
published: 13 June 2019
doi: 10.3389/fchem.2019.00397

Secondary-Sphere Effects in Molecular Electrocatalytic CO_2 Reduction

*Asa W. Nichols and Charles W. Machan**

Department of Chemistry, University of Virginia, Charlottesville, VA, United States

The generation of fuels and value-added chemicals from carbon dioxide (CO_2) using electrocatalysis is a promising approach to the eventual large-scale utilization of intermittent renewable energy sources. To mediate kinetically and thermodynamically challenging transformations of CO_2, early reports of molecular catalysts focused primarily on precious metal centers. However, through careful ligand design, earth-abundant first-row transition metals have also demonstrated activity and selectivity for electrocatalytic CO_2 reduction. A particularly effective and promising approach for enhancement of reaction rates and efficiencies of molecular electrocatalysts for CO_2 reduction is the modulation of the secondary coordination sphere of the active site. In practice, this has been achieved through the mimicry of enzyme structures: incorporating pendent Brønsted acid/base sites, charged residues, sterically hindered environments, and bimetallic active sites have all proved to be valid strategies for iterative optimization. Herein, the development of secondary-sphere strategies to facilitate rapid and selective CO_2 reduction is reviewed with an in-depth examination of the classic $[Fe(tetraphenylporphyrin)]^+$, $[Ni(cyclam)]^{2+}$, $Mn(bpy)(CO)_3X$, and $Re(bpy)(CO)_3X$ (X = solvent or halide) systems, including relevant highlights from other recently developed ligand platforms.

Keywords: inorganic, electrocatalysis, CO_2, secondary-sphere, molecular

OPEN ACCESS

Edited by:
Soumyajit Roy,
Indian Institute of Science Education and Research Kolkata, India

Reviewed by:
Zhong Jin,
Nanjing University, China
Kyle Grice,
DePaul University, United States

Correspondence:
Charles W. Machan
machan@virginia.edu
orcid.org/0000-0002-5182-1138

Specialty section:
This article was submitted to Inorganic Chemistry, a section of the journal Frontiers in Chemistry

Received: *30 January 2019*
Accepted: *17 May 2019*
Published: *13 June 2019*

Citation:
Nichols AW and Machan CW (2019) Secondary-Sphere Effects in Molecular Electrocatalytic CO_2 Reduction. Front. Chem. 7:397. doi: 10.3389/fchem.2019.00397

INTRODUCTION

The development of scalable and cost-effective processes to store electrical energy in chemical bonds using CO_2 as a primary feedstock remains a significant challenge for energy research (Centi and Perathoner, 2009; Senftle and Carter, 2017). Of particular interest are homogeneous catalysts for CO_2 reduction, as their well-defined structures give chemists an opportunity to effectively characterize intermediates relevant to the operating mechanism and further optimize active catalyst families through iterative ligand design (Benson et al., 2009; Rountree et al., 2014). While the influence of different ligand types in the primary coordination sphere can be observed in the catalytic activity and selectivity of transition metals across the *d*-block towards CO_2 reduction, more subtle effects—including rate enhancement and lowered overpotentials—can be obtained through modulation of the secondary coordination sphere within specific classes of metal complexes (Jiang et al., 2019). This has been particularly successful in the design of highly active and selective catalysts for CO_2 reduction, directing a paradigmatic shift in the general understanding of "design principles" (Costentin et al., 2012a, 2014a,b; Sampson et al., 2014; Azcarate et al., 2016; Ngo et al., 2017).

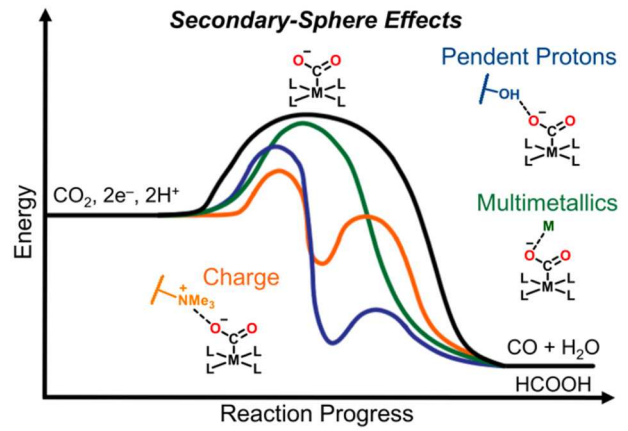

GRAPHICAL ABSTRACT | Secondary-sphere strategies known to improve catalytic selectivity and activity include pendent proton donors/shuttles in the form of Brønsted sites, charged moieties, sterically demanding functional groups, bimetallic active species, and stoichiometric participation of alkali and alkaline earth metal cations.

While this review focuses on molecular catalysts which were specifically examined for electrochemical CO_2 reduction, secondary-sphere effects have been successfully harnessed in related catalytic processes, including thermal CO_2 hydrogenation (Himeda et al., 2004, 2005, 2007; Hull et al., 2012; Wang et al., 2012, 2013, 2014; Manaka et al., 2014; Suna et al., 2014; Cammarota et al., 2017), hydrogen evolution (Curtis et al., 2003; Henry et al., 2005, 2006; Wilson et al., 2006; Fraze et al., 2007; Jacobsen et al., 2007a,b; DuBois and DuBois, 2009; Gloaguen and Rauchfuss, 2009; Helm et al., 2011; Reback et al., 2013; Ginovska-Pangovska et al., 2014), hydrogen oxidation (Curtis et al., 2003; Henry et al., 2005, 2006; Wilson et al., 2006; Fraze et al., 2007; Jacobsen et al., 2007a,b; Dutta et al., 2013, 2014; Ginovska-Pangovska et al., 2014), formate oxidation (Galan et al., 2011, 2013; Seu et al., 2012), and oxygen reduction (Collman, 1977; Collman et al., 2004; Lewis and Tolman, 2004; Mirica et al., 2004; Fukuzumi, 2013; Ray et al., 2014; Fukuzumi et al., 2015; Nam, 2015; Sahu and Goldberg, 2016; Elwell et al., 2017; Hong et al., 2017; Sinha et al., 2019) reactions. In this review, we focus on how the mechanism of CO_2 reduction relates to the type of secondary-sphere effects employed in molecular systems. Strategies discussed here which have been shown to increase catalytic activity and selectivity include pendent proton donors/shuttles in the form of Brønsted sites, charged moieties, sterically demanding functional groups, bimetallic active species, and stoichiometric participation of alkali and alkaline earth metal cations (**Graphical Abstract**).

To contextualize the motivation and principles, examples of secondary-sphere effects in enzymes which catalyze the interconversion of CO_2 with either CO or formic acid are discussed. This overview is followed by a careful examination of secondary-sphere effects in several abiotic molecular electrocatalyst examples, beginning with the $[Fe(tetraphenylporphyrin)]^+$ $[Fe(TPP)]^+$ systems pioneered by Savéant, Robert, and Constentin, including a discussion of the effects of pendent proton source placement and the distance dependence of through-space effects induced by charged residues (Costentin et al., 2014a,b; Manbeck et al., 2015; Mohamed et al., 2015; Azcarate et al., 2016; Zahran et al., 2016; Margarit et al., 2018; Nichols et al., 2018b; Sinha and Warren, 2018). Next, $M(bpy)(CO)_3X$ catalysts (M = Mn or Re; X = solvent molecule or halide) (Wong et al., 1998; Bourrez et al., 2011; Smieja et al., 2013; Chabolla et al., 2014, 2017; Franco et al., 2014; Machan et al., 2014a, 2015, 2016; Riplinger et al., 2014; Agarwal et al., 2015; Manbeck et al., 2015; Riplinger and Carter, 2015; Machan and Kubiak, 2016; Ngo et al., 2017; Sahu et al., 2017; Sinha et al., 2019) in which steric parameters, pendent Lewis acid effects, and charged residues have been shown to be effective will be discussed. Finally, $[Ni(cyclam)]^{2+}$ (cyclam = 1,4,8,11-tetraazacyclotetradecane), which contains pendent proton donors on the coordinating N atoms of the macrocycle, is discussed (Beley et al., 1984; Barefield et al., 1986; Balazs and Anson, 1993; Kelly et al., 1999; Froehlich and Kubiak, 2012; Song et al., 2014; Nichols and Chang, 2018). These systems are among the most highly studied in the field and representative of the progress that has been made in understanding how secondary-sphere coordination effects enhance molecular electrocatalysis. Additional discussions on emerging systems for CO_2 reduction which utilize secondary-sphere effects are included to summarize some of the current work in the field.

ENZYMES FOR THE INTERCONVERSION OF CO_2 AND CO OR FORMIC ACID

Cu,Mo-Containing Carbon Monoxide Dehydrogenase (Cu,Mo-CODH)

The structure and function of Cu,Mo-CODH enzymes have been previously reviewed in great detail (Appel et al., 2013; Kroneck and Torres, 2014). Of this class of enzyme, the Cu,Mo-CODH in *O. carboxydovorans* has been the most extensively studied (**Figure 1A**) (Dobbek et al., 2001a, 2002; Hille, 2013). The active site of this enzyme contains Mo and Cu ions, which are bridged by a μ_2-sulfido ligand. Mo is coordinated in a distorted square pyramidal fashion by an enedithiolate moiety (from the pyran ring found in the pyranopterin cofactor), a μ_2-sulfido ligand, and an oxo/hydroxo ligand in the equatorial plane. The apical ligand is an oxo, with a glutamine residue within hydrogen-bonding distance and a glutamate residue in a *trans* position. A unique structural feature of Cu,Mo-CODH in comparison to other Mo-containing hydrogenases is its covalent linkage through a cysteine residue to the Cu ion, connecting the heterobimetallic active site to the large subunit of the CODH enzyme.

In the catalytic cycle for transformation of CO to CO_2 by Cu,Mo-CODH, CO is proposed to initially bind to the Cu(I) ion **2**, followed by nucleophilic attack by the equatorial oxo ligand to generate the bridging μ_2-η^2-CO_2 adduct **3** (**Figure 1B**) (Dobbek et al., 2002). This five membered metallacycle results from a redox-neutral reaction which maintains the Mo(VI) state (**Figure 1B**). Following rearrangement and net oxidation of CO, CO_2 release occurs with hydroxide binding to produce the Mo(IV) species **4**. Subsequent $2e^-$ oxidation returns the Mo active site to the initial Mo(VI) oxidation state. Notably, the glutamine residue, which is in contact with the equatorial

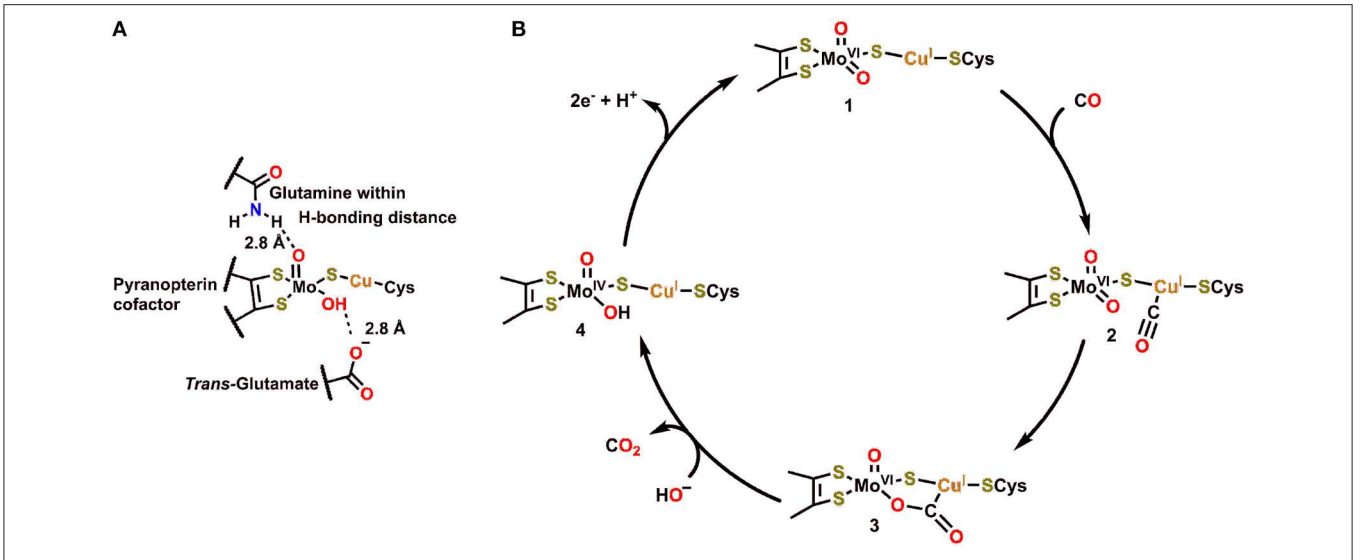

FIGURE 1 | (A) Active site of Cu,Mo-CODH. **(B)** Proposed catalytic cycle for oxidation of CO by Cu,Mo-CODH (Dobbek et al., 2002; Kroneck and Torres, 2014).

oxo ligand (**Figure 1B**), can act as a Brønsted base (proton acceptor) to regenerate the more nucleophilic oxo ligand when transitioning from **4** to **1**. If the reverse of this catalytic cycle is imagined, it is clear that a proton-donating residue would be beneficial for CO_2 reduction and C–O bond cleavage to produce CO.

Monofunctional Ni,Fe-Containing CODHs

The active site of Ni,Fe-containing CODHs, known as cluster C, is proposed to cycle between three separate redox states during catalytic CO oxidation (C_{red1}, C_{int}, and C_{red2}; **Figure 2**) (Jeoung and Dobbek, 2007). The behavior and activity of cluster C from *Carboxydothermus hydrogenoformans* have been experimentally interrogated in these three different redox states utilizing chemical-reducing agents (Jeoung and Dobbek, 2007). The cofactor contains an Fe_4Ni cluster bridged by sulfide ligands with a single Fe and Ni atom in the active site, which also contains histidine and lysine residues in close proximity to interact with active site-bound substrate molecules. In C_{red1}, the active site contains Fe^{2+} and Ni^{2+} ions with an Fe-bound hydroxo ligand that is within hydrogen-bonding distance of the proximal lysine residue. Upon exposure to CO, the Fe-bound hydroxide is deprotonated, and the resultant oxo species can form a new C–O bond to generate the μ_2-η^2-CO_2 adduct C_{red2}-CO_2, where CO_2 is bound through C by Ni and O by Fe (**Figure 2**) (Jeoung and Dobbek, 2007). This μ_2-η^2-CO_2 binding mode is stabilized by hydrogen-bonding interactions with the pendent histidine and lysine residues (Jeoung and Dobbek, 2007). A $2e^-$ oxidation with concomitant binding of an aquo ligand reduces the Ni^{2+} to Ni^0 in C_{red1}, triggering release of CO_2. Oxidation of the reduced cofactor by $2e^-$ regenerates the C_{red1} catalytic resting state.

Formic Acid Dehydrogenase

Formic acid dehydrogenase (FADH) enzymes catalyze the reversible $2e^-/1H^+$ interconversion of CO_2 and formate, another reaction of interest to CO_2 utilization (Sawers, 1994). The active site of the FADH enzyme in *Escherichia coli* contains a single Mo(VI) atom coordinated to four S atoms from two *cis*-dithiolene moieties originating from the bis(molybdopterin guanine dinucleotide) cofactor, a hydroxyl ligand, and a SeCysteine (Boyington et al., 1997). The active site also contains histidine and arginine residues in a position to interact with activated Mo-bound intermediates (**Figure 2B**). The catalytic oxidation of formate begins by displacement of the hydroxyl ligand with an equivalent of formate, which binds as an η^1-OCHO ligand; the η^1-*O* binding mode is stabilized through hydrogen-bonding interactions between the arginine and histidine residues and the unbound H and O atoms of formate (**Figure 2B**). Subsequent oxidation and transfer of $2e^-$ from formate to the Mo center occurs with the release of CO_2 and proton transfer to the SeCysteine residue. The Mo(IV) center can then be returned to the resting state through the loss of $2e^-$ as the histidine deprotonates the Mo-bound SeCysteine. Abiotic structural motifs similar to these three examples are discussed in the subsequent sections where either a) bimetallic active sites or b) secondary-sphere moieties are used to mediate electrochemical CO_2 reduction.

Benchmarking Molecular Electrocatalysts for CO_2 Reduction

Electrochemical techniques can facilitate the determination of kinetic and thermodynamic parameters for both Faradaic and catalytic reactions. Cyclic voltammetry (CV), a nondestructive potentiostatic technique, is particularly informative. Indeed, the breadth and importance of rigorous CV analysis have been reviewed in great detail (Savéant, 2008, 2018; Costentin et al., 2012b; Costentin and Savéant, 2014, 2018a; Rountree et al., 2014). Experimental determination of fundamental reaction parameters

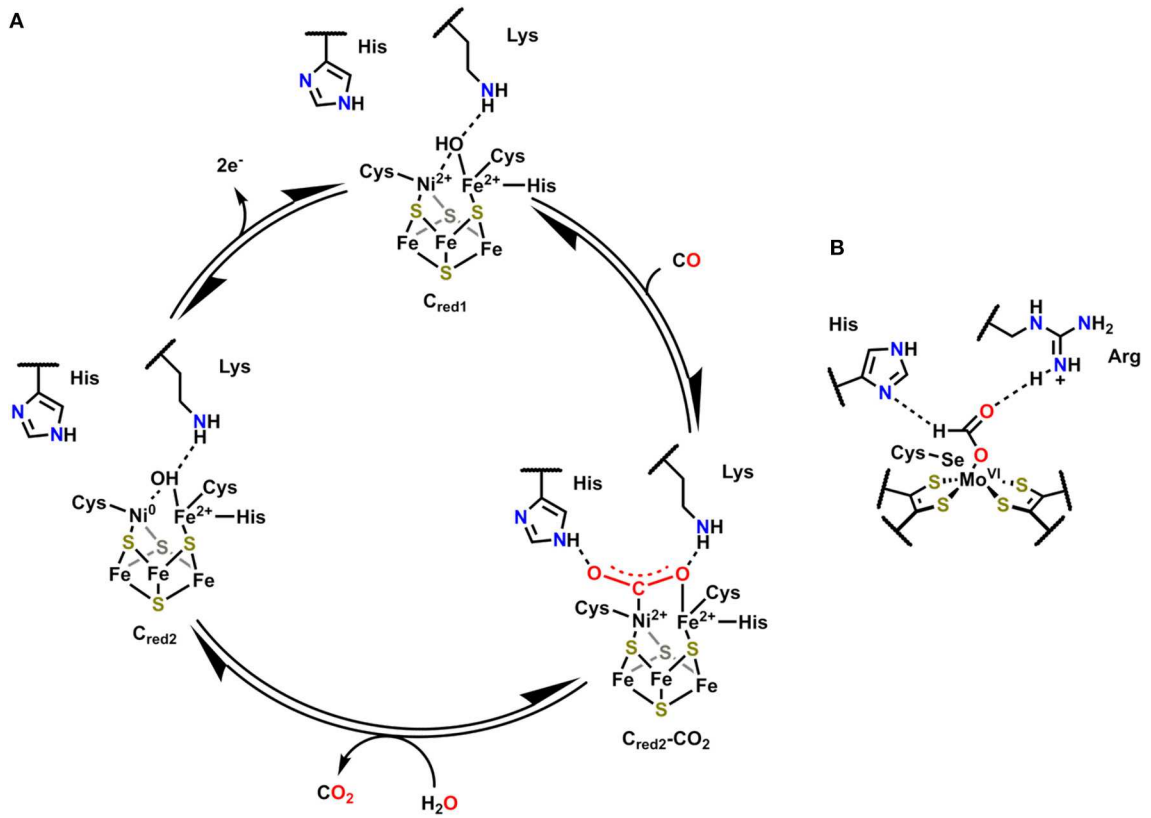

FIGURE 2 | (A) Proposed mechanism for CO oxidation by Ni,Fe CODH (Jeoung and Dobbek, 2007). **(B)** Active site of FADH in *Escherichia coli* with bound formate substrate (Boyington et al., 1997).

is essential for comparing the effects of pendent functional groups on the activity of electrocatalysts.

The effective catalytic overpotential (η) is the difference between the standard potential of CO_2 reduction ($E^0_{CO2/CO}$) and the potential at half catalytic current height ($E_{cat/2}$) as described in Equation (1) and describes a thermodynamic quantity: the electrochemical energy beyond the standard potential which is required to drive a reaction of interest at an appreciable rate. We note that some prefer to define the overpotential term as $E_{CO2} - E_{1/2}$. We distinguish between these through the use of "effective catalytic overpotential" to describe the overpotential calculated utilizing $E_{cat/2}$ (Appel and Helm, 2014).

$$\eta = E^0_{CO2/CO} - E_{cat/2} \tag{1}$$

Another reaction parameter commonly measured through CV is the maximal turnover frequency (TOF_{max}), which can also be described as the observed catalytic rate constant (k_{obs}) with units of s^{-1} (Costentin and Savéant, 2014). In a Nernstian electrocatalytic reaction, TOF is related to overpotential by the catalytic Tafel equation, Equation (2). TOF is the turnover frequency at the applied potential, F is Faraday's constant, R is the ideal gas constant, T is the temperature, $E_{1/2}$ is the catalyst standard reduction potential, and η_{app} is the difference between $E^0_{CO2/CO}$ and the applied potential. It is worth noting, however, that the limitations of the molecular catalytic reactions, including diffusion and side phenomena, can cause 'peaks' in catalytic CV waves and truncate the region where the Tafel relationship results in increased activity as the applied potential becomes more negative.

$$TOF = \frac{TOF_{max}}{1 + \exp[\frac{F}{RT}\left(E^0_{CO2/CO} - E_{1/2} - \eta_{app}\right)]} \tag{2}$$

To benchmark the kinetic and thermodynamic parameters of different electrocatalysts, Equation (2) can be used to generate catalytic Tafel plots (*nota bene*, these explicitly include the limitations imposed on molecular Tafel behavior mentioned above and enable comparison across different experimental conditions). **Figure 3** shows an example of a catalytic Tafel plot for a generic molecular catalyst: "better" catalysts are located at the top left of catalytic Tafel plots, where overpotential is low and TOF_{max} is large and "worse" catalysts are located at the bottom right of a catalytic Tafel plot where the trends in overpotential and TOF_{max} are reversed. **Figure 4** shows a Tafel plot comparing reported catalysts.

Finally, simple plots of $\log(TOF_{max})$ vs. $E_{cat/2}$ can be used to compare catalysts in the same family to look for secondary-sphere effects (Pegis et al., 2017; Costentin and Savéant, 2018b; Nichols et al., 2018b). If there is no secondary-sphere effect, then

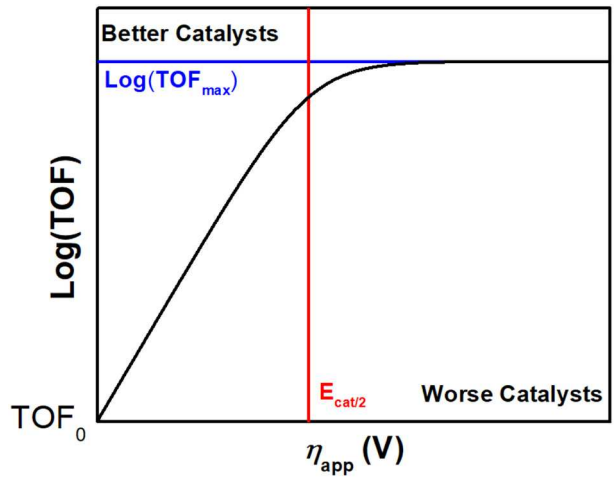

FIGURE 3 | Example of a catalytic Tafel plot of a generic molecular species with regions where better and worse catalysts are located explicitly labeled, along with the position of important benchmarking parameters.

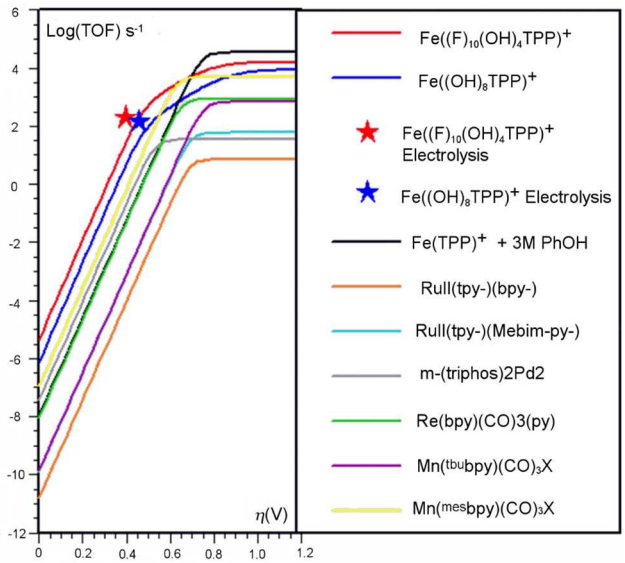

FIGURE 4 | Catalytic Tafel plot showing enhancements from the inclusion of a secondary coordination sphere in the $[Fe(TPP)]^+$ system (Costentin et al., 2014b).

a linear scaling relationship based on electrochemical driving force should occur; however, if a secondary-sphere effect is present, a deviation from the linearity achieved by comparing inductive substitution effects can be observed. One should utilize caution using this method for comparing catalysts, however, as changes to the reaction mechanism that alter cosubstrate identity, concentration dependence, solvent, and cosolvent effects can greatly impact the catalytic activity of a series of complexes through scaling relationships that are unrelated to the secondary-sphere interactions of interest. Likewise, the effects of Nernstian changes in the experimentally observed potential based on changes in the reaction equilibrium, K_{eq}, can obscure details if not properly accounted for (Costentin and Savéant, 2018b).

Secondary-Sphere Effects in $[Fe(TPP)]^+$

For $[Fe(TPP)]^+$ complexes, increased activity for the electrocatalytic reduction of CO_2 to CO is observed with the addition of both Lewis and Brønsted acids (Bhugun et al., 1994, 1996; Gennaro et al., 1996). As a result, $[Fe(TPP)]^+$ complexes bearing secondary-sphere functionalities exploiting classical Brønsted acid/base push–pull reactions have been the subject of extensive studies (Costentin et al., 2012a, 2014a,b; Sinha and Warren, 2018). In particular, iron 5, 10, 15, 20-*tetrakis*-(2,6-dihydroxyphenyl)-porphyrin ($[Fe((OH)_8TPP)]^+$) was identified as a promising candidate for electrochemical CO_2 reduction because it positioned proton donors oriented toward the active site in close enough proximity to interact with bound substrate. Experimentally, the pendent –OH moieties were observed to cause a large catalytic current enhancement and a decrease in overpotential (Costentin et al., 2012a). Control experiments using $[Fe((OMe)_8TPP)]^+$, where the –OH groups were converted to –OMe ether moieties, also showed an increased TOF_{max} relative to $[Fe(TPP)]^+$; however, the overpotential was much larger than both $[Fe(TPP)]^+$ and $[Fe((OH)_8TPP)]^+$. These differences relate to the mechanism of CO_2 reduction by $[Fe(TPP)]^+$ and how key steps are affected by the presence of the pendent –OH moieties (Bonin et al., 2017).

The proposed mechanism for the reduction of CO_2 by $[Fe(TPP)]^+$ requires the electrochemical generation of $[Fe(0)TPP]^{2-}$ at the electrode surface, followed by CO_2 binding and activation to generate $[Fe(I)(TPP)(\eta^1\text{-}CO_2^{\bullet-})]^{2-}$. The sacrificial proton donor, AH, stabilizes the binding of the $CO_2^{\bullet-}$ radical anion through hydrogen bonding. Concerted protonation and electron transfer from the metal center cause C–O bond cleavage, leading to the formation of $[Fe(II)(TPP)(CO)]^0$. Release of CO is facilitated by a comproportionation reaction with a second equivalent of $[Fe(0)TPP]^{2-}$ to generate two equivalents of $[Fe(I)TPP]^-$ and one equivalent of CO. We note that a second mechanism has been proposed for Fe(TPP), wherein upon CO_2 binding, the metal center is oxidized by $2e^-$ from Fe(0) to Fe(II) in the η^1-CO_2 adduct before interaction with the proton donor, rather than generating an Fe(I) species (Fukuzumi et al., 2018).

The introduction of a pendent proton source minimally alters the mechanism for CO_2 reduction but causes catalytic rate increases by favoring several steps of the reaction. Upon the generation of $[Fe(0)((OH)_8TPP)]^{2-}$, CO_2 also binds in η^1 fashion and is activated to the $CO_2^{\bullet-}$ radical anion, but stabilization occurs through hydrogen-bonding interactions with the pendent proton donors (Costentin et al., 2012a). Experimentally, this is observed as a prewave to the catalytic feature in CV experiments, which can be more easily examined through additional modulation of electron density at the metal center with the related partially fluorinated derivative $[Fe((F)_{10}(OH)_8TPP)]^+$ (Costentin et al., 2014a,b). Subsequent intramolecular protonation balanced by the exogenous proton source can occur, generating η^1-$^{\bullet}CO_2H$ at an Fe(I) center (Costentin et al., 2014a). The cleavage of the C–OH bond is induced upon further reduction and a concerted intramolecular

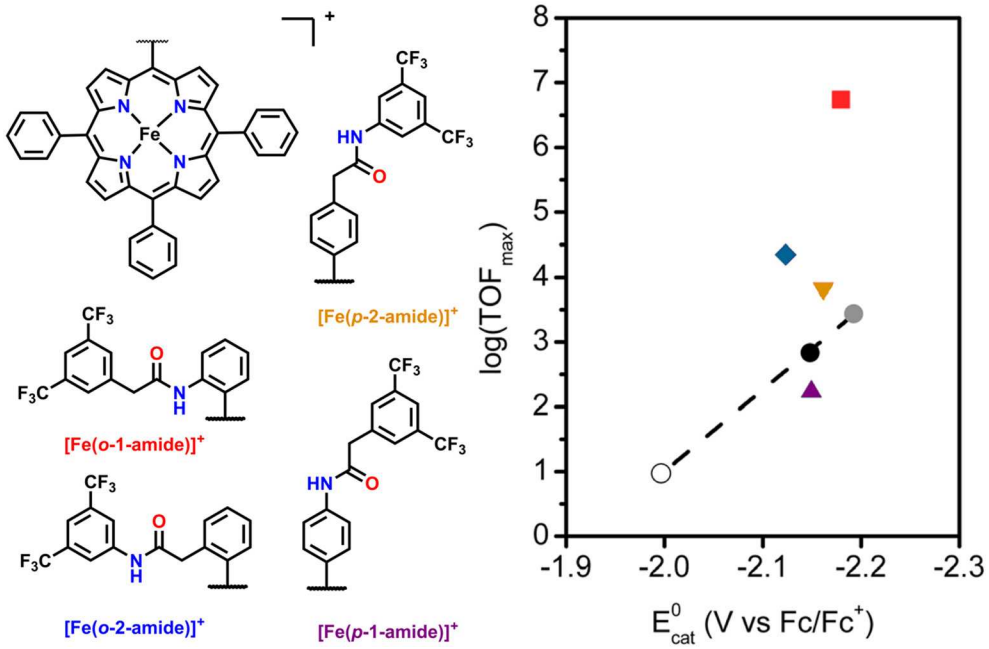

FIGURE 5 | Plot of log(TOF_{max}) vs. E^0_{cat} for mono-functionalized porphyrins used to study positional dependence of catalytic enhancement for this system. Circles are $[Fe(TPP)]^+$ derivatives which utilize electronic substitution of the phenyl rings for modulation of the redox potential of the $Fe^{I/0}$ couple. The upward purple triangle is $[Fe(p\text{-1-amide-TPP})]^+$, the downward orange triangle is $[Fe(p\text{-2-amide-TPP})]^+$, the blue diamond is $[Fe(o\text{-1–amide-TPP})]^+$, and the red square is $[Fe(o\text{-2-amide-TPP})]^+$. Reprinted with permission from Nichols et al. (2018b)—published by the Royal Society of Chemistry.

protonation reaction (again balanced by proton transfer from the sacrificial donor) to regenerate the resting state, Fe(I), of the electrocatalytic cycle and CO product. The enhanced catalytic activity at more negative potentials of the ether-containing control complex may also be explained through an enhancement of this mechanism (the ether groups function as a Brønsted base to orient and enhance the proton activity of the exogeneous proton donor), but this has a relatively lower enhancement effect on the CO_2 reduction reaction. A comparison of the catalytic activity increases from these effects can be seen through the catalytic Tafel analysis shown in **Figure 4**.

Another area of study for secondary-sphere effects focuses on mono-functionalized porphyrins, which also orient functional groups toward the metal active site. Both the positioning of these functional groups relative to the active site and the pK_a of the pendent proton source are of importance to the electrocatalytic activity for CO_2 reduction. In a study by Chang and co-workers the positional effects of pendent amide groups were investigated. It was found that orientation toward the active site and positioning above the active site were both important for catalytic enhancement, as these stabilized catalytic intermediates through hydrogen bonding and facilitated efficient proton transfer (Nichols et al., 2018b). This was quantified experimentally through equilibrium binding constants for CO_2 determined by rapid-scan CV techniques. When a pendent amide group was attached to the *meso*-phenyl of the porphyrin in the ortho position, $[(Fe(o\text{-2-amide-TPP})]^+$, the highest catalytic activity was observed. In comparison with the other reported derivatives, a "Goldilocks" relationship was observed, where positioning the amide group either closer or farther did not result in comparable catalytic current enhancement (**Figure 5**).

Nocera and co-workers found the pK_a of the pendent proton source was important for the stabilization of CO_2 binding in the active site of related "hangman-type" porphyrin architectures (**Figure 6**) (Margarit et al., 2018). Pendent phenol- and guanidinium-based hangman functional groups were predicted by DFT to cause a 2.1–6.6 kcal/mol stabilization of bound CO_2 within the hangman pocket. Conversely, a sulfonic acid derivative was found to function as a proton donor under the experimental conditions in the absence of applied potential, which was attributed to an estimated pK_a of ~3 under experimental conditions. The resultant anionic sulfonate derivative showed diminished catalytic activity relative to the porphyrins functionalized with phenol and guanidinium. The anionic charge of the conjugate base, combined with the overall steric bulk of the sulfonate, was proposed to prevent CO_2 binding within the hangman cleft and contribute minimally to the stabilization of the CO_2 adduct (Margarit et al., 2018). The pendent phenol-based "hangman-type" architecture was predicted to have the greatest stabilization of CO_2 binding by DFT calculations and was observed to have the fastest catalytic rate constant by CV methods.

Others have examined the relationship between electrocatalytic activity and the H-bonding ability of pendent residues on triazole-based picket-fence-type $[Fe(TPP)]^+$ derivatives with pendent amide functional groups (Sen et al.,

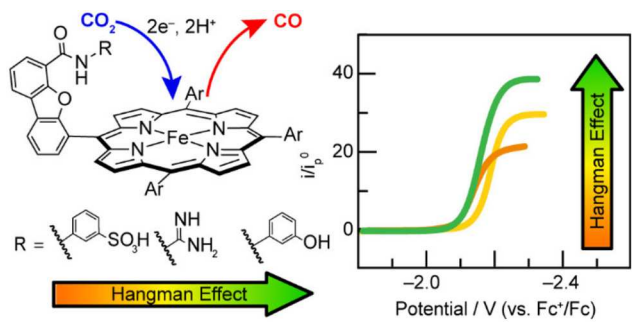

FIGURE 6 | Figure showing effect of pK_a of the hanging group on CO_2 reduction activity in hangman $[Fe(TPP)]^+$. Reprinted with permission from Margarit et al. (2018). Copyright 2018 American Chemical Society.

2019). In this report, a correlation between $\log(TOF_{max})$ and the pK_a of pendent proton donors was established for a picket fence amide with an encapsulated water molecule in comparison to previously reported $[Fe(TPP)]^+$ derivatives. The pendent groups are proposed to contribute to the stabilization of the Fe-bound CO_2 molecule through hydrogen-bonding interactions and facilitate proton transfer to mediate the rate-determining C–O bond cleavage step.

The studies discussed above have shown that pendent protons can be beneficial for $[Fe(TPP)]^+$-based electrocatalysts, but also that careful consideration of steric constraints and the pK_a of the chosen pendent proton donor under experimental conditions is necessary. Installation of pendent proton groups in porphyrin ligands can have a detrimental effect if their pK_a and spatial orientation are not chosen carefully (e.g., sulfonic acid, *vide supra*). A recent study has also shown that the choice of solvent can largely alter the catalytic response of $[Fe(TPP)]^+$ with an asymmetrically substituted pendent proton moiety (Sinha and Warren, 2018). Using a porphyrin containing a single pendent hydroxy functionality in the 2-position of a single *meso*-phenyl ring, it was demonstrated that the electrocatalytic activity of this system can be greatly hindered by utilizing solvents with strong hydrogen-bonding properties through a comparison of activity in MeCN, DMF, and DMSO. Strong hydrogen bond acceptor solvents like DMF and DMSO lead to a decrease in activity of the catalyst, while in MeCN, the activity approached that reported for $[Fe((ortho\text{-TMA})TPP)]^{5+}$, which is the fastest molecular electrocatalyst for CO_2 reduction reported to date. The authors postulated that the interference of competitive hydrogen bonding between solvent molecules leads to slowed electrochemical kinetic parameters (Sinha and Warren, 2018). This suggests that more rigorous interrogations of functional group cooperativity (specifically the number and type of functional groups) and the interactions of functional groups with solvent and proton donors will offer additional insight into these mechanisms. Indeed, Costentin and Savéant described the origin of catalytic enhancement by pendent proton relays (Costentin and Savéant, 2018b). Boosting of electrocatalytic activity by pendent proton donors occurs when the forward rate constant of proton transfer from the pendent group to the active site is competitive with that of exogeneous proton donor directly to the active site (under the assumption that reprotonation of the pendent donor is extremely rapid). Should these forward rate constants not be well-matched, inefficiency in the proton relay mechanism will limit the ultimate catalytic current enhancement.

Further studies on this class of catalysts have modulated the potential of the $Fe^{I/0}$ reduction where the catalytic response occurs by examining electron-withdrawing perfluorophenyl-substituted tetraphenylporphyrins ($[Fe(F_5TPP)]^+$, $[Fe(F_{10}TPP)]^+$, and $[Fe(F_{20}TPP)]^+$, where F_5 corresponds to a single perfluorinated phenyl ring, etc.) (Azcarate et al., 2016). This is a purely electronic effect, perturbing the continuum of electronic distribution in the ligand–metal manifold. The inclusion of proximal ionic charges has also been explored with trimethylanilinium- ($[Fe(\text{-}ortho\text{-TMA-TPP})]^{5+}$ and $[Fe(\text{-}para\text{-TMA-TPP})]^{5+}$) and sulfonato-functionalized porphyrins ($[Fe(\text{-}para\text{-sulfonato-TPP})]^{3-}$) to understand the role of through-space electrostatic interactions (Azcarate et al., 2016). The perfluorinated derivatives demonstrated a relationship between the catalytic response and the $Fe^{I/0}$ potential: as the potential of that redox couple becomes more positive, $\log(TOF_{max})$ decreases in a linear fashion, corresponding to a relative decrease in added electron density at the metal center upon electrochemical reduction (Azcarate et al., 2016; Costentin et al., 2018). However, for $[Fe(TPP)]^+$ substituted with a charged functional group (*para*–SO_3^{2-}, *para*–NMe_3^+, and *ortho*–NMe_3^+), $\log(TOF_{max})$ increases linearly as the redox potential of the $Fe^{I/0}$ couple shifts to more positive potentials. $[Fe\text{-}ortho\text{-TMA-TPP}]^{5+}$ has the most positive $Fe^{I/0}$ redox potential of any $[Fe(TPP)]^+$-based electrocatalyst reported to date, as well as largest $\log(TOF_{max})$ value. To understand this, one can once again imagine the CO_2 binding mode wherein a single electron generates radical $CO_2^{\bullet-}$ anion, which is stabilized by the charged groups close to the active site. It is compelling that such dramatic enhancements should be observed, but this could suggest that the reaction pathway might also be significantly altered from other $[Fe(TPP)]^+$ derivatives, as the effect is an inverse scaling relationship to that predicted for purely inductive reasons (Azcarate et al., 2016).

The data points from charge-based functionalization are relatively limited; the proposal of design principles for new systems for molecular CO_2 reduction systems requires additional information on these effects. For instance, the synthesis of further positional isomers of charged systems could give more evidence that a scaling relationship exists based on the distance between the charged moiety and the active site. Ultimately, it is clear that the inclusion of charge should seek to explore deliberate manipulation of the known mechanism to achieve the greatest enhancement effect.

$Re(bpy)(CO)_3X$

$Re(bpy)(CO)_3X$ (where bpy is a 2,2′-bipyridine, often additionally functionalized in a symmetric fashion, and X is a halide anion or solvent molecule) is active for the electrocatalytic reduction of CO_2 to CO in near quantitative fashion (Hawecker et al., 1984; Grice and Kubiak, 2013). Under Faradaic conditions, this complex is proposed to undergo reduction according

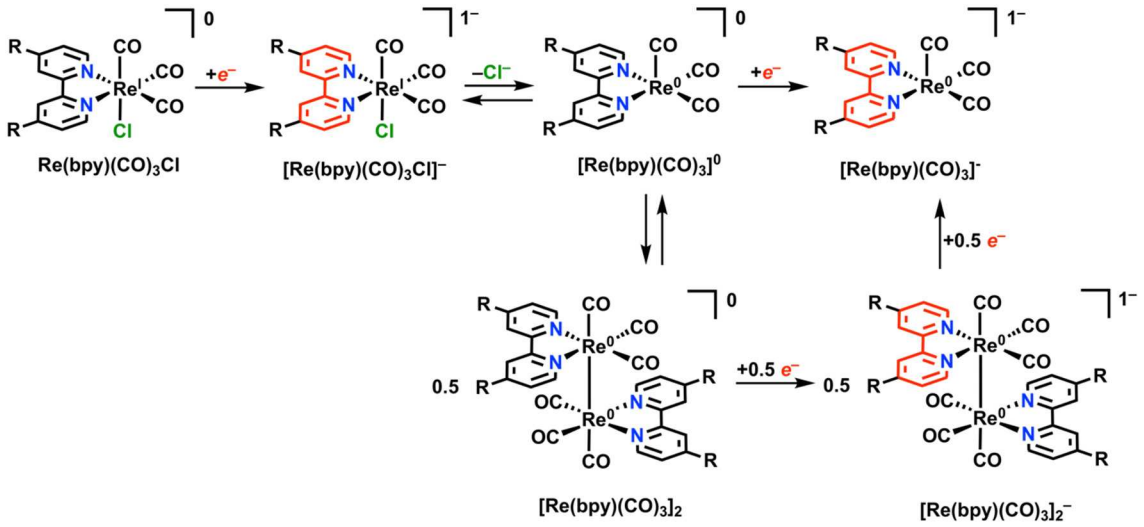

FIGURE 7 | Faradaic reduction of Re(bpy)(CO)$_3$X. Adapted with permission from Machan et al. (2014b). Copyright 2014 American Chemical Society.

to **Figure 7**. Initial reduction is localized at the bpy ligand, followed by loss of Cl^- from $[Re(bpy)(CO)_3Cl]^-$ *via* an overall EC mechanism to generate the neutral five-coordinate species $[Re(bpy)(CO)_3]^0$. At this stage, two separate mechanisms for reduction can occur: 1) a single reduction assigned to the ligand framework can occur, generating the catalytically active monoanionic species $[Re(bpy)(CO)_3]^-$. Commonly, the $[Re(bpy)(CO)_3Cl]^-$ species is stable long enough on the CV timescale that $[Re(bpy)(CO)_3]^-$ forms instead at the second reduction with Cl^- loss. 2) Following initial single-electron reduction and Cl^- loss, a Re–Re bond between two equivalents of $[Re(bpy)(CO)_3]^0$ can form to generate $Re(bpy)(CO)_3]_2$. Dimer formation requires two sequential reductions to cleave the Re–Re bond and form the $[Re(bpy)(CO)_3]^-$ active species. The formation of the metal–metal bond is slow under most conditions because of the persistence of $[Re(bpy)(CO)_3Cl]^-$ on the CV timescale and is most often outcompeted by the unimolecular pathway to $[Re(bpy)(CO)_3]^-$ (Grills et al., 2014).

There are also two possible mechanisms for CO_2 reduction under electrocatalytic conditions. First, a relatively slower bimolecular process involving two equivalents of $[Re(bpy)(CO)_3]^0$ can occur, resulting in a net reductive disproportionation of two equivalents of CO_2 into one each of CO and CO_3^{2-} (Sullivan et al., 1985). Second, a unimolecular catalytic process with $[Re(bpy)(CO)_3]^-$ as the resting state, where the two-electron reduction of CO_2 occurs at a single Re center (Sullivan et al., 1985; Keith et al., 2013). As is observed with the $[Fe(TPP)]^+$-based electrocatalysts above, there are observable enhancements in TOF_{max} and catalyst stability for CO_2 reduction upon the addition of a sacrificial proton donor (Wong et al., 1998).

In the proposed mechanism for electrocatalytic CO_2 reduction, a monoanionic five-coordinate species $[Re(bpy)(CO)_3]^-$ is invoked as the active species which binds CO_2 (**Figure 8**) (Keith et al., 2013). This has been validated experimentally through direct synthesis of $[Re(bpy)(CO)_3]^-$ using chemical-reducing agents, with subsequent spectrochemical studies demonstrating a kinetic preference for CO_2 over H^+ (Smieja et al., 2012; Sampson et al., 2013). $Re(bpy)(CO)_3(\eta^1\text{-}CO_2H)$ is initially formed upon the binding and activation of CO_2 by $[Re(bpy)(CO)_3]^-$ with a proton donor present. Further reduction generates an anionic species, $[Re(bpy)(CO)_3(\eta^1\text{-}CO_2H)]^-$, at which point C–O bond cleavage is facilitated by an exogenous proton source to generate water and the neutral species, $[Re(bpy)(CO)_4]^0$. CO release from the 19e$^-$ complex $[Re(bpy)(CO)_4]^0$ is facile, and additional reduction regenerates the resting $[Re(bpy)(CO)_3]^-$ state. In the $Re(bpy)(CO)_3X$ catalyst family, most work has focused on modulating the steric and electronic properties of the bipyridine ligand in attempts to modulate the reducing power and activity of Re. Generally, the use of electron-rich bpy ligands like 4,4′-di-*tert*-butylbpy enhances the activity of the catalyst by creating a more nucleophilic Re center upon reduction, albeit at larger overpotentials (Clark et al., 2018).

Kubiak and co-workers have demonstrated, however, that steric considerations can supersede electronic effects in this class of catalysts. $Re(bpy)(CO)_3X$-type complexes were synthesized with 3,3′- and 5,5′-dimethyl bpy (Chabolla et al., 2014). The methyl groups in those ring positions have identical Hammett parameters, so for purely electronic reasons, their respective electrocatalytic activities with a $[Re(CO)_3]^+$ core would be expected to be similar. When compared to the unsubstituted parent compound, however, the 5,5′-dimethyl bpy complex shows increased catalytic current at slightly more negative potentials, while the 3,3′-dimethyl bpy shows decreased catalytic current at nearly the same potential. This is rationalized through the steric hindrance from the methyl groups at the 3,3′-positions, which is observed in the non-planarity of the bpy ligand in the crystal structure of the precatalyst. Previous experimental and computational studies have postulated that a key mechanistic

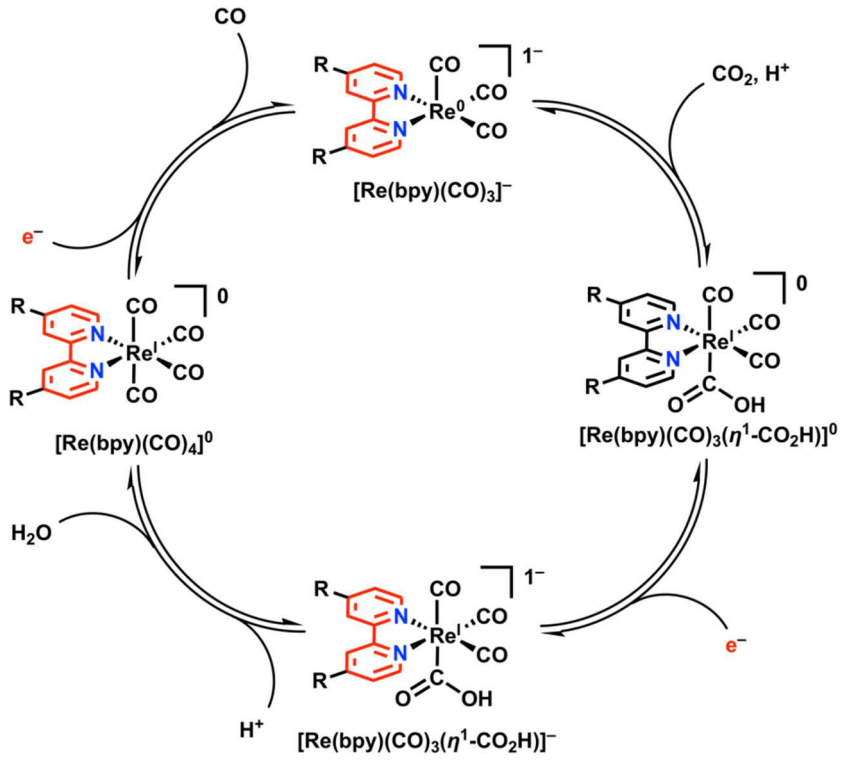

FIGURE 8 | $2e^-/2H^+$-dependent catalytic cycle for $Re(bpy)(CO)_3X$ in the reduction of CO_2 to CO. Adapted with permission from Machan et al. (2014b). Copyright 2014 American Chemical Society.

component is the participation of π^* orbitals in the bpy ligand in the redox mechanism, suggesting that an inability to achieve a higher degree of planarity upon reduction diminishes catalytic activity for 3,3′-dimethyl bpy-based Re catalysts (Smieja et al., 2012; Benson et al., 2013; Keith et al., 2013; Chabolla et al., 2014). Since the distribution of added electron density between the bpy ligand and the Re metal center has been identified as important to the selectivity for CO_2 over H^+ as the electrophile of choice; it is noteworthy that an steric perturbation of the HOMO of the active species should have this effect.

The effect of secondary-sphere modifications on the $Re(bpy)CO_3X$ system was explored through the incorporation of –OH groups at the 4,4′- and 6,6′-positions of the bpy, with the goal of using them both as a pendent proton source and to contribute electron density to the bpy ligand (Manbeck et al., 2015). In this case, the authors found atypical behavior during electrocatalysis: the O–H bonds of the bipyridine ligand are cleaved by stepwise electrochemical reduction, which they propose leads to dearomatization of the doubly reduced bpy ligand. By isolating the deprotonated species in a chemical fashion, the authors were able to give both UV-vis and IR spectroscopic evidence—which aligned well with infrared spectroelectrochemistry (IR-SEC), UV-vis spectroelectrochemistry (UV-vis-SEC), and DFT calculations—supporting this hypothesis. Interestingly, only the 4,4′-dihydroxybpy complex is active as an electrocatalyst for CO_2 reduction, while the 6,6′-dihydroxybpy complex completes only ∼1 TON for CO, despite having nearly identical electrochemical properties under Faradaic conditions by CV. This result suggests slow CO release and decomposition of intermediates at applied potentials limit activity for the 6,6′-dihydroxybpy derivative.

Further work with monomeric $Re(bpy)(CO)_3X$ electrocatalysts showed promising results with the incorporation of peptide linkages of varying lengths containing proton relays and hydrogen-bonding groups on the bpy backbone (Chabolla et al., 2017). Through electrochemical experiments, 2D NMR spectroscopy, and molecular dynamics modeling, the study showed that an optimal chain length of five peptides allows for the peptide backbone to adopt conformations which allow for intramolecular interactions on the NMR timescale. Importantly, this study showed the $Re(bpy)(CO)_3X$ system to be stable under peptide synthesis conditions, allowing for insertion of the complex into peptide linkages at any desired point (Chabolla et al., 2017).

The asymmetric incorporation of a thiourea tether into $Re(bpy)(CO)_3X$ systems has been shown to be a successful strategy for enhancing the CO_2 reduction activity (Haviv et al., 2018). Interestingly, the sulfur atom of the thiourea tether was shown to bind CO_2 prior to reduction of the Re catalyst, which is expected to lower the reorganization energy penalty expected for the reduction of the linear CO_2 molecule. This interaction was shown to work synergistically with the reduced Re state, as the

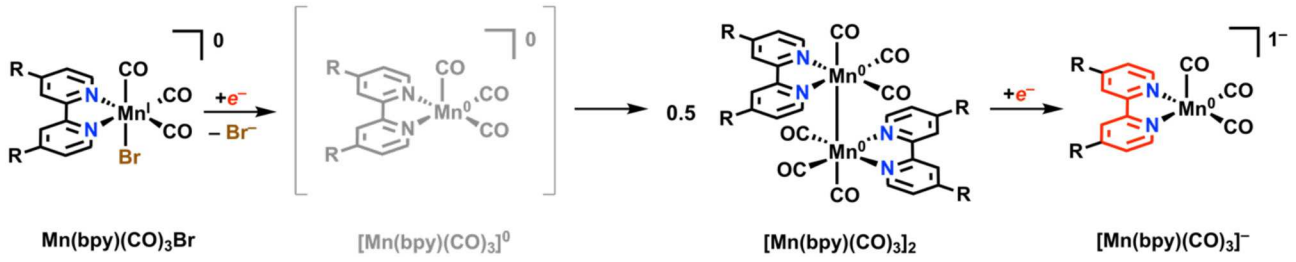

FIGURE 9 | Faradaic reduction mechanism of $Mn(bpy)(CO)_3X$. Adapted with permission from Machan et al. (2014b). Copyright 2014 American Chemical Society.

thiourea moiety also enhanced the catalytic response by acting as a pendent proton donor capable of beneficial hydrogen-bonding interactions and facilitating C–O bond cleavage. Added Brønsted acids inhibited catalytic activity, likely the result of competitive interactions with the pendent thiourea tether. In a separate study on the asymmetric incorporation of phenolic pendent proton sources to $Re(bpy)(CO)_3X$, catalysis was 'turned on' at lower overpotentials, specifically the first reduction potential by CV in the two complexes studied (Rotundo et al., 2019). These complexes did, however, suffer from low Faradaic efficiencies for CO when no external proton source was present. Each of these catalysts also had issues with electrode absorption phenomena, a deleterious reaction with inhibitory consequences for nominally molecular electrocatalysts.

A Re(bpy)-based CO_2 reduction catalyst which features an imidazolium group as a charged residue in the secondary sphere reported by Nippe and co-workers was observed to cause changes in redox properties and mechanism compared to unfunctionalized $Re(bpy)(CO)_3X$ (Sung et al., 2017). It was proposed that the C_2-H carbon of the imidazolium moiety was important for the catalytic enhancement through an alteration of mechanism: theoretical methods suggested that hydrogen bond-like or electrostatic C_2-H—X (X = Cl^-, CO_2^-, or H_2O) interactions change the ground state energies of intermediates relevant to the catalytic cycle. These assignments were supported experimentally through testing of a control complex where the imidazolium C_2-H was replaced by C_2-CH_3, and the non-linear dependence of the catalytic activity of each complex on [H_2O], which is anomalous to the archetypal electrocatalytic response of $Re(bpy)(CO)_3X$. It was postulated that a reduction-first mechanism for CO_2 reduction was occurring, where reduction of the Re(I)(η^1-CO_2H) adduct preceded protonation and C–O bond cleavage, as is classically seen in the unfunctionalized complex (**Figure 8**).

The effects of charge on the electrocatalytic activity of $Re(bpy)(CO)_3X$ were studied in a series of polymeric frameworks using a series of charged monomers (Sahu et al., 2017). Three norbornenyl-based polymers containing either positively charged quaternary ammonium, neutral phenyl, or negatively charged trifluoroborate moieties were generated through ROMP and covalently end-labeled with a $Re(bpy)(CO)_3X$-based terminating reagent. Electrochemical studies in acetonitrile indicated that the polymers containing quaternary ammonium salts exhibited catalytic behavior at a significantly more positive potential (∼300 mV) than the neutral polymer, which behaved consistently with unfunctionalized $Re(bpy)(CO)_3X$. The incorporation of negatively charged groups caused a shift to more reducing potentials, and catalytic activity was not observed in the solvent window. The incorporation of known catalysts onto a polymeric framework with the ability to tune reduction potential is a possible precursor to highly ordered structures such as thin films, abiotic metalloproteins, porous catalytic membranes, and cationic nanoparticles for use in devices.

$Mn(bpy)(CO)_3X$

Unpublished results referenced by Johnson et al. in 1996 stated that $Mn(bpy)(CO)_3X$, unlike its third-row congener Re, was inactive for electrocatalytic CO_2 reduction under aprotic conditions (Johnson et al., 1996). A more recent examination by Deronzier and co-workers in 2011 repeated this result, but also showed that the addition of a weak proton donor facilitated a significant and selective electrocatalytic response for CO_2 reduction to CO (Bourrez et al., 2011). One important mechanistic detail about the $Mn(bpy)(CO)_3X$ system is that upon reduction by a single electron and subsequent loss of X, a Mn–Mn dimer $[Mn(bpy)(CO)_3]_2$ can rapidly form with rates approaching the diffusion limit (**Figure 9**) (Grills et al., 2014). The formation of this dimer has two detrimental effects: (1) it increases the electrochemical driving force required to generate the catalytically active monoanionic five-coordinate $[Mn(bpy)(CO)_3]^-$ species required for CO_2 reduction (the Mn–Mn bond requires more reducing potentials to cleave), and (2) it reduces the activity of the complex toward CO_2 reduction as a non-catalytic competing pathway (Grice and Kubiak, 2013; Smieja et al., 2013).

In attempts to combat these detrimental effects from dimerization, a bulky bpy analog was designed (6,6′-dimesitylbpy) (Sampson et al., 2014; Sampson and Kubiak, 2016). This ligand framework proved to be effective in eliminating the dimerization reaction. Rather than two irreversible $1e^-$ waves on the reductive sweep as seen in $Mn(bpy)(CO)_3X$, a single reversible $2e^-$ wave was observed (Sampson et al., 2014). This leads to the formation of monomeric, anionic $[Mn(mesbpy)(CO)_3]^-$ at 300 mV more positive potentials than in the case of the original $Mn(bpy)(CO)_3X$ complexes (Sampson et al., 2014). In the presence of CO_2 and a proton source, the $2e^-$ reversible feature becomes irreversible and shifts toward positive potentials, which is indicative of CO_2

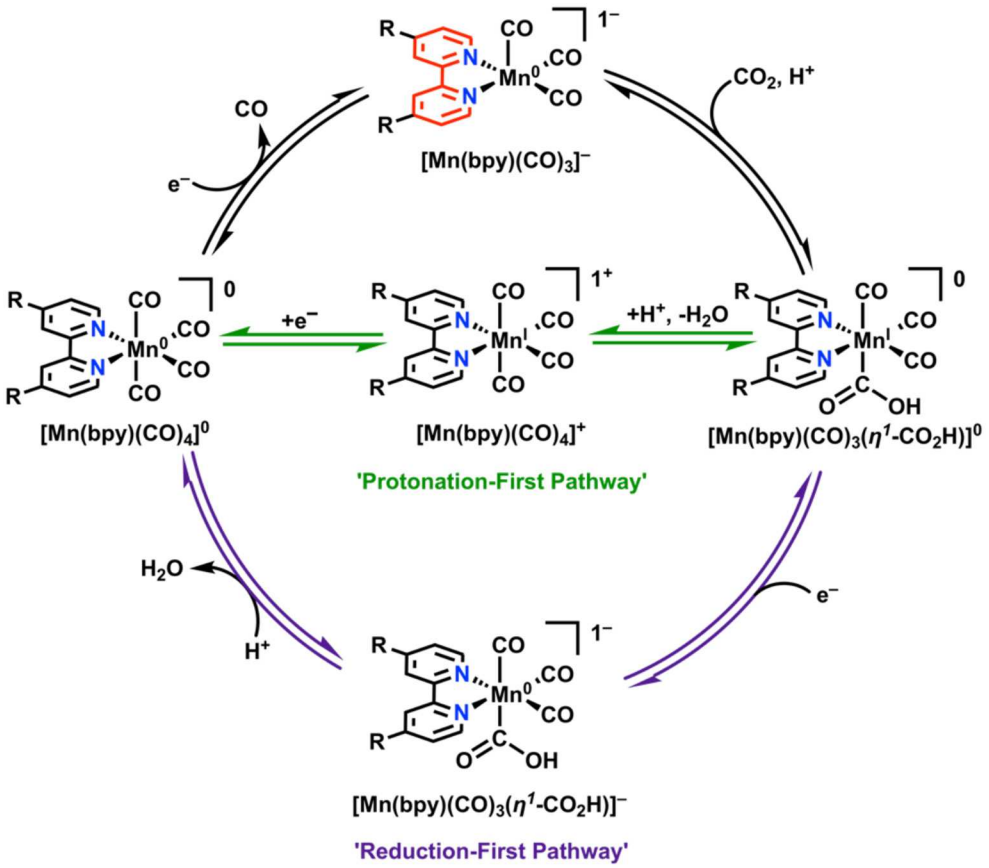

FIGURE 10 | "Protonation-first" and "reduction-first" pathways for CO_2 reduction by $Mn(bpy)(CO)_3X$ (Riplinger et al., 2014).

binding (Sampson et al., 2014). This mechanistic difference was confirmed through control experiments, IR-SEC (Ashley and Pons, 1988; Zavarine and Kubiak, 2001; Best et al., 2008; Kaim and Fiedler, 2009; Machan et al., 2014b), and the direct synthesis of the active species. A significant catalytic response does not occur in the presence of Brønsted acids until potentials are similar to those that are catalytic for the unfunctionalized parent complex (Sampson et al., 2014). Rapid C–O bond cleavage in the hydroxycarbonyl intermediate $[Mn(mesbpy)(CO)_3(\eta^1\text{-}CO_2H)]$ does not occur until "overreduction" to generate $[Mn(mesbpy)(CO)_3(\eta^1\text{-}CO_2H)]^-$ at potentials 400 mV more negative than the $2e^-$ reversible feature (**Figure 10**) (Riplinger et al., 2014). To take advantage of the initial CO_2 binding event by $[Mn(mesbpy)(CO)_3]^-$ at more positive potentials, a subsequent report used Lewis acid additives (Sampson and Kubiak, 2016). This strategy proved successful, as the addition of Mg^{2+} ions as cosubstrate to solution aided in C–O bond cleavage at the potential where CO_2 binding occurs, greatly reducing the overpotential required for the generation of CO from CO_2 (Sampson and Kubiak, 2016).

Initial attempts to incorporate pendent proton relays into the $Mn(bpy)(CO)_3X$ framework involved asymmetric attachment of phenol moieties onto the bpy ligand (Franco et al., 2014; Agarwal et al., 2015). This led to enhanced activity in comparison to the parent $Mn(bpy)(CO)_3X$ complex, including activity in the absence of a proton source; however, the competitive dimerization reaction was still apparent in each case (Franco et al., 2014; Agarwal et al., 2015). Converting the pendent –OH groups to ethers with methoxy groups showed insignificant or no catalytic activity in control studies for these derivatives.

To extend these studies to symmetrically functionalized systems, Rochford and co-workers synthesized a methoxy ether-containing analog of the bulky bpy ligand, 6,6′-(2,6-dimethoxyphenyl)bpy $[(MeO)_2Ph]_2bpy$ (Ngo et al., 2017). A combined experimental and theoretical analysis showed that through the introduction of sufficiently acidic exogeneous proton sources, the slower "protonation-first" pathway seen in the original bulky bpy study could be "turned on" at lower overpotentials in comparison to the "reduction-first" pathway at more negative potentials (Ngo et al., 2017). In the protonation-first pathway, a bound hydroxycarbonyl is formed, and further protonation by a sufficiently strong acid can lead to the facilitation of C–O bond cleavage prior to reduction and release of CO at more positive potentials than the reduction-first pathway (**Figure 10**). In the reduction-first pathway, a bound hydroxycarbonyl is again formed; however, without a sufficiently

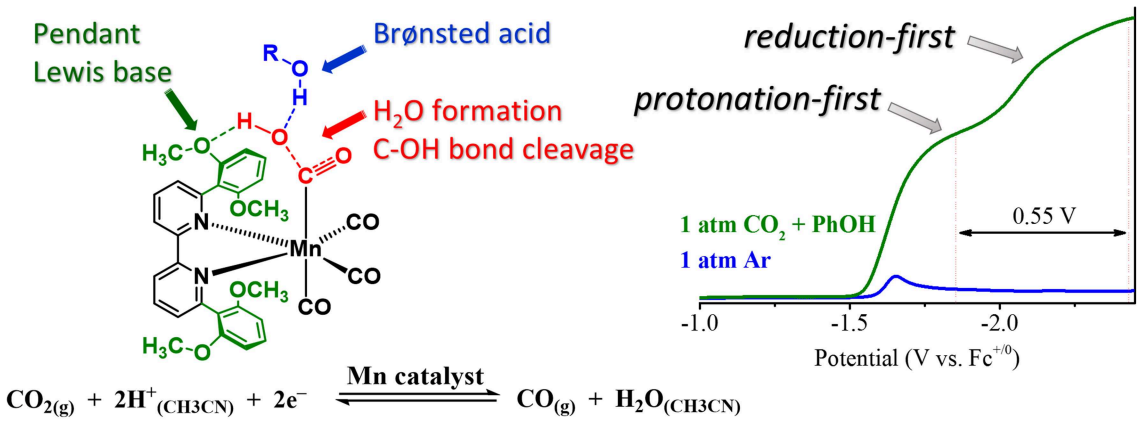

FIGURE 11 | Figure showing proposed transition state which occurs to turn on a low-overpotential, secondary-sphere-promoted mechanism for CO_2 reduction with $Mn((OMe)_2bpy)(CO)_3X$. Adapted with permission from Ngo et al. (2017). Copyright American Chemical Society 2017.

strong acid present, reduction of the hydroxycarbonyl must occur at more negative potentials prior to protonation and C–O bond cleavage.

The acid dependence of the "protonation-first" and "reduction-first" pathways for $Mn([(MeO)_2Ph]_2bpy)(CO)_3X$ was rationalized through a hydrogen-bonding interaction between the Mn-bound η^1-CO_2H hydroxycarbonyl species and the pendent Lewis base groups located on the ligand (**Figure 11**). This hydrogen bond donor–acceptor interaction was also proposed to facilitate the subsequent transfer of a second equivalent of a sufficiently strong Brønsted acid additive to protonate and facilitate C–O bond cleavage, ultimately producing H_2O and Mn-bound CO (Ngo et al., 2017). In the presence of a proton source of insufficient acidity, the reduction of the bound η^1-CO_2H hydroxycarbonyl species is instead required before protonation and C–O bond cleavage can occur, as is observed with the "overreduction" of the Mn catalyst with the "bulky" bpy ligand (Ngo et al., 2017). Importantly, no metal–metal dimerization reaction was observed for this ligand.

Recently, a charged imidazolium functionality was also introduced asymmetrically into the $Mn(bpy)(CO)_3X$ system (Sung et al., 2019). A series of derivatives examining hydrogen-bonding effects showed activity for CO_2 reduction at potentials of only −1.4 V vs. Fc^+/Fc in the presence of water. This was postulated to originate from a synergistic effect between the pendent imidazolium functionality and a network of water molecules in the solvation shell that facilitated CO_2 reduction. The combined use of charge and hydrogen-bonding donors shows promise for lowering the catalytic overpotential, but further work is needed to enhance Faradaic efficiencies to match other catalyst platforms in this family.

Ni(cyclam)]$^{2+}$

The electrocatalytic activity of a $[Ni(cyclam)]^{2+}$ (cyclam = 1,4,8,11-tetraazacyclotetradecane) derivative was first reported in 1980 by Fisher and Eisenberg (1980). It has been the subject of continuous study because of its tolerance for a wide range of acid strengths and solvent systems without a loss of catalytic activity (Beley et al., 1984; Barefield et al., 1986; Balazs and Anson, 1993; Kelly et al., 1999; Schneider et al., 2012). The activity of Ni(cyclam)]$^{2+}$ for electrocatalytic reduction of CO_2 to CO in the presence of water as a Brønsted acid source was attributed specifically to the *Trans I* isomer (one of six possible isomers based on the orientation of the H atoms on the four metal-coordinated secondary amines in the macrocycle; all four H atoms are cofacial). This isomer is the most favorable for high CO_2 reduction activity due to the hydrogen bond donor–acceptor interactions between the ligand NH groups and a Ni-bound CO_2 molecule (Froehlich and Kubiak, 2012). Furthermore, DFT calculations have indicated that the *trans I* isomer has a more stable CO_2 adduct than the *trans III* isomer (two H atoms are cofacial) by approximately 3 kcal/mol (Song et al., 2014).

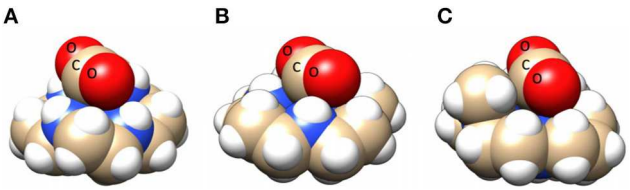

FIGURE 12 | Space-filling models of *trans I* $[Ni(cyclam)(CO_2)]^+$ **(A)**, *trans III* $[Ni(cyclam)(CO_2)]^+$ **(B)**, and $[Ni(DMC)(CO_2)]^+$ **(C)**. Structures indicate that enhanced CO_2 reduction in the case of *trans I* $[Ni(cyclam)(CO_2)]^+$ may be due to increased stabilization of the CO_2 adduct through increased hydrogen bond donors oriented toward the hydrogen bond accepting O atoms on the CO_2 adduct. Used with permission from Song et al. (2014). Copyright American Chemical Society 2014.

Further evidence for the importance of the amine protons and these hydrogen-bonding interactions is found through a comparison with the *N*-alkylated derivatives $[Ni(dimethylcyclam)]^{2+}$ and $[Ni(tetramethylcyclam)]^{2+}$, where greatly diminished activity for electrocatalytic CO_2 reduction is observed (Froehlich and Kubiak, 2012). The absence of hydrogen bond-induced stabilization effects and

increased steric parameters make CO_2 binding less facile in the *N*-alkylated derivatives (**Figure 12**). Pendent proton donor effects have been shown with other functional groups as well: the introduction of a carboxylic acid on the carbon backbone of Ni(cyclam)]$^{2+}$ improves its activity by making it stable and selective for CO_2 reduction down to pH 2 at similar overpotentials to other reported water-soluble CO_2 reduction catalysts (Neri et al., 2016).

The use of an exogenous urea additive with Ni(cyclam)]$^{2+}$ was shown to improve catalytic activity for CO_2 reduction for similar reasons (Nichols and Chang, 2018). This study demonstrated that the urea additive acted as a cocatalyst for the system, and it was proposed that its unique structure allows for it to promote CO_2 reduction through the formation of multipoint hydrogen bonds with the bound CO_2 adduct [Ni(cyclam)(η^1-CO_2)]$^+$ (Nichols and Chang, 2018). This conclusion was supported through the introduction of multiple cationic and neutral additives with similar pK_as. In each case, the cocatalytic response observed with urea was not present (Nichols and Chang, 2018). Although the urea additive was not tethered to cyclam, it is conspicuous that it should have a cocatalytic role with both Ni(cyclam)]$^{2+}$- and Re(bpy)-based catalysts for CO_2 reduction, *vide supra*.

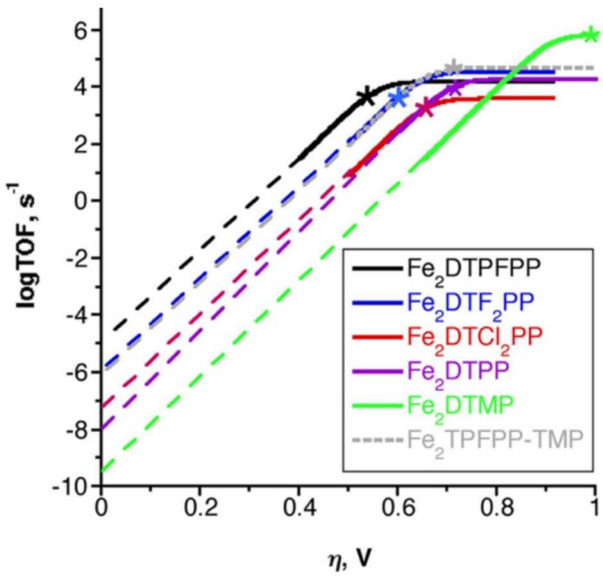

FIGURE 13 | Catalytic Tafel plot showing overpotential tuning in cofacial Fe(TTP) through the introduction of electron with drawing substituents on the phenyl groups of the porphyrin system. Adapted from Zahran et al. (2016).

Multimetallic Systems

Multimetallic systems are important examples of secondary-sphere interactions, because they are common to the enzymes which catalyze CO_2 reduction chemistry (Dobbek et al., 2001b, 2002). In many cases, these multimetallic systems work cooperatively to both store excess charge and to activate the molecule of interest using "push–pull" donor–acceptor effects. Homobimetallic cofacial [Fe(TPP)]$^+$ systems connected by a phenylene bridge were synthesized to generate a bimetallic species from the well-known [Fe(TPP)]$^+$ system discussed above (Mohamed et al., 2015). By tuning the Fe–Fe distance through synthetic modification, CO_2 binding could be induced at the $Fe^{3+/2+}$ wave rather than the $Fe^{1+/0}$ as observed in most [Fe(TPP)]$^+$ systems (Mohamed et al., 2015; Bonin et al., 2017). This was rationalized through the expected Fe–Fe distance of 3.2–4.0 Å in the *ortho*-bridged system, which would be suitable for binding the linear CO_2 molecule. In contrast, the *meta*-bridged system was expected to have a significantly shorter separation and showed diminished activity similar to monomeric [Fe(TPP)]$^+$ (Mohamed et al., 2015). The *ortho*-bridged system has significant catalytic activity (TOF_{max} = 4300 s^{-1}) and high Faradaic efficiency for CO (95%) at an overpotential of ∼0.7 V in the presence of 10% H_2O in DMF, which is a significant improvement over monomeric [Fe(TPP)]$^+$. The overpotential for this class of homobimetallic catalyst could be further tuned using electron-withdrawing and -donating substituents on the phenyl rings of each [Fe(TPP)]$^+$ unit (**Figure 13**) (Zahran et al., 2016). When the overpotential was synthetically tuned to ∼0.4 V with electron-withdrawing groups, a ∼3-fold decrease in activity in comparison to the parent phenyl-functionalized dimer was observed (Zahran et al., 2016). Chang and co-workers have recently demonstrated that these beneficial multimetallic effects extend beyond bimetallic systems using a porous organic cage containing six [Fe(TPP)]$^+$ units, which was active for CO_2 reduction in aqueous solutions (Smith et al., 2018).

A multimetallic Fe carbonyl cluster system with an interstitial main group element [$Fe_4X(CO)_{12-n}L_n$]$^-$ (X = N or C, L = another ligand, n = 1 or O) has been developed by the Berben group for the reduction of CO_2 to formate under both aqueous and non-aqueous conditions (Rail and Berben, 2011; Taheri et al., 2015; Taheri and Berben, 2016; Loewen et al., 2017). This cluster is proposed to generate formate *via* an intermediate bridging hydride. The bridging hydride on the cluster motif has the ideal hydricity and pK_a to selectively generate formate in the presence of CO_2, preventing the competitive formation of H_2 (Loewen et al., 2017). Pendent proton groups in this system alter the selectivity of this catalyst family from nearly quantitative generation of formate to the generation of H_2, which highlights the importance of controlling the kinetics of substrate delivery in determining selectivity for competitive CO_2 and H^+ reduction reactions (Loewen et al., 2016).

The development of bimetallic Re complexes based on Re(bpy)$(CO)_3$X and its derivatives has been of recent interest for both photocatalytic (Bruckmeier et al., 2012) and electrocatalytic processes due to the concentration-dependent formation of binuclear intermediates as part of the catalytic cycle (Machan et al., 2014a, 2016; Wilting et al., 2017; Yang et al., 2018). In electrocatalytic systems, the first bimolecular Re system studied utilized acetoamidomethyl modified bpy to generate a supramolecular catalyst system *in situ*. This system operated at more positive potentials (∼250 mV) in MeCN than the 4,4′-dimethylbpy-based control complex as the result of a hydrogen-bonded dimer active state, albeit with a lower TOF and FE than the unimolecular process (Machan et al., 2014a). To further probe this hydrogen bond-based dimer system, a subsequent

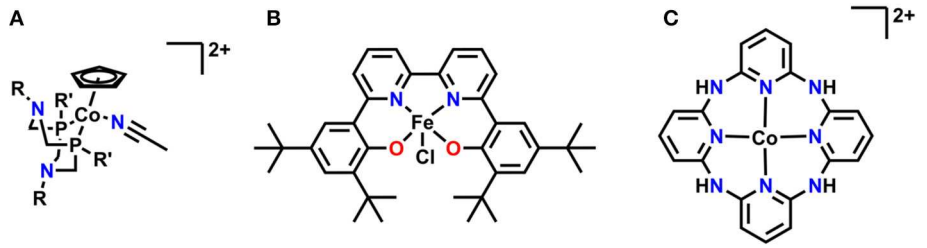

FIGURE 14 | (A) Co(Cp)(P_2N_2) utilizing pendent tertiary amines for reduction of CO_2 to formate. **(B)** Fe(^{tbu}dhbpy)Cl is protonated at the Fe-coordinating O atoms upon reduction and reduces CO_2 to formate. **(C)** Macrocyclic–aminopyridyl complex which reduces CO_2 to CO.

report focused on a heterobimetallic Re–Mn construct using a 1:1 mixture of acetoamidomethyl-modified Re(bpy)$(CO)_3$X with acetoamidomethyl-modified Mn(bpy)$(CO)_3$X (Machan and Kubiak, 2016). Results from this study indicated a cooperative heterobimetallic pathway was operative, and it was proposed that the Mn center was activating CO_2 followed by protonation to generate a Mn-bound hydroxycarbonyl species within the heterobimetallic dimer. Enhanced reduction-first pathway kinetics were initiated in this case by electron transfer from the reduced Re species present in the dimer.

Further modifications to this supramolecular system replaced the acetoamidomethyl unit with an amide-linked PhOH-containing tyrosine functional group (Machan et al., 2016). This modification led to an increased TOF_{max} in comparison to the initial complex and near quantitative Faradaic efficiency; mechanistic studies where the PhOH unit was substituted for a phenyl ring showed the pendent –OH functionality was essential for improving catalytic activity in the bimetallic mechanism (Machan et al., 2016). The "soft" non-covalent linkages used in this strategy are reminiscent of biological active sites: the catalytic system can adopt a variety of conformations on the potential energy surface facilitated by weaker interactions instead of more rigid systems reliant on distance or conformational tuning through purely synthetic means. The success of this approach is dependent on how well the weak interactions overcome the added diffusional component of the bimolecular reaction mechanism.

Work to generate rigid homobimetallic Re(bpy)$(CO)_3$X systems where the metal centers are in close proximity has been achieved using an anthracene linker by Jurss and co-workers (Yang et al., 2018). This complex can be isolated as *cis* or *trans* isomers through chromatography, which alters the relative positioning of the Re centers (Yang et al., 2018). The *cis* isomer, in which the Re centers are in close proximity to one another, outperformed both a monometallic anthracene control complex and the *trans* isomer of the homobimetallic species in catalytic studies. Another covalently linked homobimetallic system with an imidazole–pyridine bridge was examined by Siewert and co-workers (Wilting et al., 2017). The observed catalytic activity of the homobimetallic species outperformed the mononuclear control complex, which was inactive for CO_2 reduction (Sinha et al., 2017). The introduction of the phenol linker between the two imidazole–pyridine arms to generate a proton relay in close proximity to the active site of the two metal centers was also examined (Wilting et al., 2017). The pendent proton source enhanced the activity of the bimetallic Re complex, with Faradaic efficiencies for CO of ∼60% (Wilting et al., 2017).

EMERGING SYSTEMS

Several relatively new systems have also been reported where pendent functional group interactions are essential to the overall mechanism (**Figure 14**). A recent report on a series of cobalt(cyclopentadienyl)(P_2N_2) complexes by Artero and co-workers showed that pendent tertiary amines enabled selective formate generation from CO_2 (Roy et al., 2017). DFT calculations suggest that a reaction-defining transition state occurs where one of the pendent amines forms a hydrogen-bonding interaction with water to align it with CO_2 as simultaneous hydride transfer occurs from the Co center, lowering the overall transition state energy and enhancing activity (Roy et al., 2017). Work in our own group has identified a Schiff base-type ligand based on bpy as a promising new direction: the Fe(III) derivative is active for the reduction of CO_2 to formate with PhOH as a proton source. Mechanistic investigations suggest the Fe-bound oxygen atoms act as a site for protonation upon initial reduction of the complex, generating a pendent proton source for the reaction at applied potential (Nichols et al., 2018a). A macrocyclic, aminopolypyridyl Co complex from Marinescu and co-workers generated CO in a near quantitative fashion in the presence of MeOH as a proton source (Chapovetsky et al., 2016, 2018). Upon alkylation of the pendent amine functionalities, a two-fold decrease in activity occurred, suggesting that the pendent protons on the amines linking the pyridyl groups play an important role as hydrogen bond donors during CO_2 reduction (Chapovetsky et al., 2016, 2018). The activity and selectivity of all these platforms are promising for future studies on optimizing secondary-sphere effects.

CONCLUSIONS AND OUTLOOK

Molecular electrocatalysts for CO_2 reduction are of continuing interest for their possible utility in storing renewable energy in chemical bonds. Through careful mechanistic observations and design principles inspired by nature, researchers have managed to improve many of the known catalyst systems for CO_2 reduction. This iterative optimization of catalysts

has demonstrated that the incorporation of pendent Brønsted acids/bases, charged groups, sterically bulky groups, Lewis basic sites, and the use of multimetallic sites with careful solvent choice can lead to improved catalytic activity and even new mechanisms through secondary-sphere effects reminiscent of biological systems.

With these successes in mind, it is useful to acknowledge that there is still much work to do: CODHs can *reversibly* interconvert CO_2/CO in aqueous systems with a TOF_{max} of 0.5 s^{-1} (CO_2 to CO) and 31,000 s^{-1} (CO to CO_2) with minimal overpotentials (Maynard and Lindahl, 2001). However, the use of secondary-sphere effects in abiotic molecular electrocatalysts has already been shown to be important for enhancing selectivity and activity. Further development in this area may lead to the development of catalysts capable of reducing products beyond CO and HCO_2H, which are a burgeoning area for molecular electrocatalysts. The study of immobilized molecular Cu(TPP) systems has shown to be a successful strategy in generating higher ordered products like methane and ethylene in an electrocatalytic fashion (Weng et al., 2016), which is interesting, since crystalline copper electrodes are known to do this chemistry as heterogenous electrode materials (Kuhl et al., 2012). Bringing molecular design principles to materials seems to be another viable strategy for using secondary-sphere effects in electrocatalysis: Gong et al. (2017) immobilized porphyrin cages on Cu electrodes to tune activity and selectivity for carbon–carbon coupling products from CO_2 reduction through supramolecular effects. Recent reports have also described photocatalysts which convert CO_2 to methane from molecular catalysts related to those described here, which is promising for developing eventual electrocatalytic behavior (Rao et al., 2017; Shirley et al., 2019).

Running CO_2 reduction reactions reversibly with abiotic systems could close the "loop" on the energy cycle, enabling the development of new fuel cell technologies beyond H_2 (Matsumoto et al., 2011, 2013; Kadirov et al., 2018). New catalyst systems which approach these biological efficiencies are unlikely to be rapidly found through purely synthetic routes due to the inherent depth and synthetic difficulty of the parameter space. Rather, the most efficient approach to future catalyst development should utilize a multidisciplinary approach which combines statistical, computational, and experimental methods to assist in the search for new CO_2 reduction catalysts unique from the current catalytic systems by improving predictive power.

AUTHOR CONTRIBUTIONS

The manuscript was written through contributions of all the authors. All authors have given approval to the final version of the manuscript.

FUNDING

Funding was obtained from the University of Virginia.

ACKNOWLEDGMENTS

The authors thank the University of Virginia for the generous funding.

REFERENCES

Agarwal, J., Shaw, T. W., Schaefer, H. F., and Bocarsly, A. B. (2015). Design of a catalytic active site for electrochemical CO_2 reduction with Mn(I)-tricarbonyl species. *Inorg. Chem.* 54, 5285–5294. doi: 10.1021/acs.inorgchem.5b00233

Appel, A. M., Bercaw, J. E., Bocarsly, A. B., Dobbek, H., DuBois, D. L., Dupuis, M., et al. (2013). Frontiers, opportunities, and challenges in biochemical and chemical catalysis of CO_2 fixation. *Chem. Rev.* 113, 6621–6658. doi: 10.1021/cr300463y

Appel, A. M., and Helm, M. L. (2014). Determining the overpotential for a molecular electrocatalyst. *ACS Catal.* 4, 630–633. doi: 10.1021/cs401013v

Ashley, K., and Pons, S. (1988). Infrared spectroelectrochemistry. *Chem. Rev.* 88, 673–695. doi: 10.1021/cr00086a006

Azcarate, I., Costentin, C., Robert, M., and Saveant, J.-M. (2016). Through-space charge interaction substituent effects in molecular catalysis leading to the design of the most efficient catalyst of CO_2-to-CO electrochemical conversion. *J. Am. Chem. Soc.* 138, 16639–16644. doi: 10.1021/jacs.6b07014

Balazs, G. B., and Anson, F. C. (1993). Effects of CO on the electrocatalytic activity of Ni (cyclam)$^{2+}$ toward the reduction of CO_2. *J. Electroanal. Chem.* 361, 149–157. doi: 10.1016/0022-0728(93)87049-2

Barefield, E. K., Freeman, G. M., and Van Derveer, D. G. (1986). Electrochemical and structural studies of nickel (II) complexes of *N*-alkylated cyclam ligands: x-ray structures of trans-[Ni (C14H32N4)(OH2) 2] Cl2. 2H2O and [Ni (C14H32N4)](O3SCF3)2. *Inorg. Chem.* 25, 552–558. doi: 10.1021/ic00224a033

Beley, M., Collin, J.-P., Ruppert, R., and Sauvage, J.-P. (1984). Nickel (II)-cyclam: an extremely selective electrocatalyst for reduction of CO_2 in water. *J. Chem. Soc. Chem. Commun.* 1315–1316. doi: 10.1039/c39840001315

Benson, E. E., Kubiak, C. P., Sathrum, A. J., and Smieja, J. M. (2009). Electrocatalytic and homogeneous approaches to conversion of CO_2 to liquid fuels. *Chem. Soc. Rev* 38, 89–99. doi: 10.1039/B804323J

Benson, E. E., Sampson, M. D., Grice, K. A., Smieja, J. M., Froehlich, J. D., Friebel, D., et al. (2013). The electronic states of rhenium bipyridyl electrocatalysts for CO_2 reduction as revealed by x-ray absorption spectroscopy and computational quantum chemistry. *Angew. Chem. Int.* 52, 4841–4844. doi: 10.1002/anie.201209911

Best, S., Crumbliss, A., Dunsch, L., Haga, M.-A., Hartl, F., Kubiak, C., et al. (2008). *Spectroelectrochemistry*. Cambridge, UK: Royal Society of Chemistry.

Bhugun, I., Lexa, D., and Saveant, J.-M. (1994). Ultraefficient selective homogeneous catalysis of the electrochemical reduction of carbon dioxide by an iron (0) porphyrin associated with a weak Broensted acid cocatalyst. *J. Am. Chem. Soc.* 116, 5015–5016. doi: 10.1021/ja00090a068

Bhugun, I., Lexa, D., and Savéant, J.-M. (1996). Catalysis of the electrochemical reduction of carbon dioxide by iron (0) porphyrins: synergystic effect of weak Brönsted acids. *J. Am. Chem. Soc.* 118, 1769–1776. doi: 10.1021/ja9534462

Bonin, J., Maurin, A., and Robert, M. (2017). Molecular catalysis of the electrochemical and photochemical reduction of CO_2 with Fe and Co metal based complexes. Recent advances. *Coord Chem. Rev.* 334, 184–198. doi: 10.1016/j.ccr.2016.09.005

Bourrez, M., Molton, F., Chardon-Noblat, S., and Deronzier, A. (2011). [Mn (bipyridyl)(CO) 3Br]: an abundant metal carbonyl complex as efficient electrocatalyst for CO_2 reduction. *Angew. Chem. Int.* 123, 10077–10080. doi: 10.1002/ange.201103616

Boyington, J. C., Gladyshev, V. N., Khangulov, S. V., Stadtman, T. C., and Sun, P. D. (1997). Crystal structure of formate dehydrogenase H: catalysis involving Mo, molybdopterin, selenocysteine, and an Fe_4S_4 cluster. *Science* 275, 1305–1308. doi: 10.1126/science.275.5304.1305

Bruckmeier, C., Lehenmeier, M. W., Reithmeier, R., Rieger, B., Herranz, J., and Kavakli, C. (2012). Binuclear rhenium (I) complexes for the photocatalytic reduction of CO_2. *Dalton Trans.* 41, 5026–5037. doi: 10.1039/c2dt30273j

Cammarota, R. C., Vollmer, M. V., Xie, J., Ye, J., Linehan, J. C., Burgess, S. A., et al. (2017). A bimetallic nickel–gallium complex catalyzes CO_2 hydrogenation *via the* intermediacy of an anionic d10 nickel hydride. *J. Am. Chem. Soc.* 139, 14244–14250. doi: 10.1021/jacs.7b07911

Centi, G., and Perathoner, S. (2009). Opportunities and prospects in the chemical recycling of carbon dioxide to fuels. *Catal Today* 148, 191–205. doi: 10.1016/j.cattod.2009.07.075

Chabolla, S. A., Dellamary, E. A., Machan, C. W., Tezcan, F. A., and Kubiak, C. P. (2014). Combined steric and electronic effects of positional substitution on dimethyl-bipyridine rhenium (I) tricarbonyl electrocatalysts for the reduction of CO_2. *Inorganica Chim. Acta* 422, 109–113. doi: 10.1016/j.ica.2014.07.007

Chabolla, S. A., Machan, C. W., Yin, J., Dellamary, E. A., Sahu, S., Gianneschi, N. C., et al. (2017). Bio-inspired CO_2 reduction by a rhenium tricarbonyl bipyridine-based catalyst appended to amino acids and peptidic platforms: incorporating proton relays and hydrogen-bonding functional groups. *Faraday Discuss.* 198, 279–300. doi: 10.1039/C7FD00003K

Chapovetsky, A., Do, T. H., Haiges, R., Takase, M. K., and Marinescu, S. C. (2016). Proton-assisted reduction of CO_2 by cobalt aminopyridine macrocycles. *J. Am. Chem. Soc.* 138, 5765–5768. doi: 10.1021/jacs.6b01980

Chapovetsky, A., Welborn, M., Luna, J. M., Haiges, R., Miller, T. F., and Marinescu, S. C. (2018). Pendant hydrogen-bond donors in cobalt catalysts independently enhance CO_2 reduction. *ACS Cent. Sci.* 4, 397–404. doi: 10.1021/acscentsci.7b00607

Clark, M. L., Cheung, P. L., Lessio, M., Carter, E. A., and Kubiak, C. P. (2018). Kinetic and mechanistic effects of bipyridine (bpy) substituent, labile ligand, and Brønsted acid on electrocatalytic CO_2 reduction by Re(bpy) complexes. *ACS Catal.* 8, 2021–2029. doi: 10.1021/acscatal.7b03971

Collman, J. P. (1977). Synthetic models for the oxygen-binding hemoproteins. *Acc. Chem. Res.* 10, 265–272. doi: 10.1021/ar50115a006

Collman, J. P., Boulatov, R., Sunderland, C. J., and Fu, L. (2004). Functional analogues of cytochrome c oxidase, myoglobin, and hemoglobin. *Chem. Rev.* 104, 561–588. doi: 10.1021/cr0206059

Costentin, C., Drouet, S., Robert, M., and Savéant, J.-M. (2012a). A local proton source enhances CO_2 Electroreduction to CO by a Molecular Fe Catalyst. *Science* 338:90. doi: 10.1126/science.1224581

Costentin, C., Drouet, S., Robert, M., and Savéant, J.-M. (2012b). Turnover numbers, turnover frequencies, and overpotential in molecular catalysis of electrochemical reactions. Cyclic voltammetry and preparative-scale electrolysis. *J. Am. Chem. Soc.* 134, 11235–11242. doi: 10.1021/ja303560c

Costentin, C., Passard, G., Robert, M., and Savéant, J.-M. (2014a). Pendant acid–base groups in molecular catalysts: H-bond promoters or proton relays? Mechanisms of the conversion of CO_2 to CO by electrogenerated iron(0)porphyrins bearing prepositioned phenol functionalities. *J. Am. Chem. Soc.* 136, 11821–11829. doi: 10.1021/ja506193v

Costentin, C., Passard, G., Robert, M., and Savéant, J.-M. (2014b). Ultraefficient homogeneous catalyst for the CO2-to-CO electrochemical conversion. *Proc. Natl. Acad. Sci. U.S.A.* 111, 14990–14994. doi: 10.1073/pnas.1416697111

Costentin, C., and Savéant, J.-M. (2018a). Homogeneous catalysis of electrochemical reactions: the steady-state and nonsteady-state statuses of intermediates. *ACS Catal.* 8, 5286–5297. doi: 10.1021/acscatal.8b01195

Costentin, C., and Savéant, J.-M. (2018b). Homogeneous molecular catalysis of electrochemical reactions: manipulating intrinsic and operational factors for catalyst improvement. *J. Am. Chem. Soc.* 140, 16669–16675. doi: 10.1021/jacs.8b09154

Costentin, C., Savéant, J.-M., and Tard, C. (2018). Ligand "noninnocence" in coordination complexes vs. kinetic, mechanistic, and selectivity issues in electrochemical catalysis. *Proc. Natl. Acad. Sci. U.S.A.* 115, 9104–9109. doi: 10.1073/pnas.1810255115

Costentin, C., and Savéant, J. M. (2014). Multielectron, multistep molecular catalysis of electrochemical reactions: benchmarking of homogeneous catalysts. *ChemElectroChem* 1, 1226–1236. doi: 10.1002/celc.201300263

Curtis, C. J., Miedaner, A., Ciancanelli, R., Ellis, W. W., Noll, B. C., Rakowski DuBois, M., et al. (2003). [Ni (Et2PCH2NMeCH2PEt2) 2] 2+ as a functional model for hydrogenases. *Inorg. Chem.* 42, 216–227. doi: 10.1021/ic020610v

Dobbek, H., Gremer, L., Kiefersauer, R., Huber, R., and Meyer, O. (2002). Catalysis at a dinuclear [CuSMo (O) OH] cluster in a CO dehydrogenase resolved at 1.1-Å resolution. *Proc. Natl. Acad. Sci. U.S.A.* 99, 15971–15976. doi: 10.1073/pnas.212640899

Dobbek, H., Gremer, L., Meyer, O., and Huber, R. (2001a). *Handbook of Metalloproteins*. Chichester: John Wiley & Sons Ltd.

Dobbek, H., Svetlitchnyi, V., Gremer, L., Huber, R., and Meyer, O. (2001b). Crystal structure of a carbon monoxide dehydrogenase reveals a [Ni-4Fe-5S] cluster. *Science* 293, 1281–1285. doi: 10.1126/science.1061500

DuBois, M. R., and DuBois, D. L. (2009). The roles of the first and second coordination spheres in the design of molecular catalysts for H_2 production and oxidation. *Chem. Soc. Rev.* 38, 62–72. doi: 10.1039/B801197B

Dutta, A., Lense, S., Hou, J., Engelhard, M. H., Roberts, J. A., and Shaw, W. J. (2013). Minimal proton channel enables H_2 oxidation and production with a water-soluble nickel-based catalyst. *J. Am. Chem. Soc.* 135, 18490–18496. doi: 10.1021/ja407826d

Dutta, A., Roberts, J. A., and Shaw, W. J. (2014). Arginine-containing ligands enhance H_2 oxidation catalyst performance. *Angew. Chem. Int.* 53, 6487–6491. doi: 10.1002/anie.201402304

Elwell, C. E., Gagnon, N. L., Neisen, B. D., Dhar, D., Spaeth, A. D., Yee, G. M., et al. (2017). Copper–oxygen complexes revisited: structures, spectroscopy, and reactivity. *Chem. Rev.* 117, 2059–2107. doi: 10.1021/acs.chemrev.6b00636

Fisher, B. J., and Eisenberg, R. (1980). Electrocatalytic reduction of carbon dioxide by using macrocycles of nickel and cobalt. *J. Am. Chem. Soc.* 102, 7361–7363. doi: 10.1021/ja00544a035

Franco, F., Cometto, C., Vallana, F. F., Sordello, F., Priola, E., Minero, C., et al. (2014). A local proton source in a [Mn(bpy-R)(CO)3 Br]-type redox catalyst enables CO_2 reduction even in the absence of Brønsted acids. *Chem. Commun.* 50, 14670–14673. doi: 10.1039/C4CC05563B

Fraze, K., Wilson, A. D., Appel, A. M., Rakowski DuBois, M., and DuBois, D. L. (2007). Thermodynamic properties of the Ni–H bond in complexes of the type [HNi (P2RN2R')2](BF4) and evaluation of factors that control catalytic activity for hydrogen oxidation/production. *Organometallics* 26, 3918–3924. doi: 10.1021/om070143v

Froehlich, J. D., and Kubiak, C. P. (2012). Homogeneous CO_2 reduction by Ni(cyclam) at a glassy carbon electrode. *Inorg. Chem.* 51, 3932–3934. doi: 10.1021/ic3001619

Fukuzumi, S. (2013). Electron-transfer properties of high-valent metal-oxo complexes. *Coord Chem Rev* 257, 1564–1575. doi: 10.1016/j.ccr.2012.07.021

Fukuzumi, S., Lee, Y.-M., Ahn, H. S., and Nam, W. (2018). Mechanisms of catalytic reduction of $CO_2$with heme and nonheme metal complexes. *Chem. Sci* 9, 6017–6034. doi: 10.1039/C8SC02220H

Fukuzumi, S., Ohkubo, K., Lee, Y. M., and Nam, W. (2015). Lewis acid coupled electron transfer of metal–oxygen intermediates. *Chem. Eur. J.* 21, 17548–17559. doi: 10.1002/chem.201502693

Galan, B. R., Reback, M. L., Jain, A., Appel, A. M., and Shaw, W. J. (2013). Electrocatalytic oxidation of formate with nickel diphosphine dipeptide complexes: effect of ligands modified with amino acids. *Eur. J. Inorg. Chem.* 2013, 5366–5371. doi: 10.1002/ejic.201300751

Galan, B. R., Schöffel, J., Linehan, J. C., Seu, C., Appel, A. M., and, Roberts, J. A., et al. (2011). Electrocatalytic oxidation of formate by [Ni (PR2NR′ 2) 2 (CH3CN)] 2+ complexes. *J. Am. Chem. Soc.* 133, 12767–12779. doi: 10.1021/ja204489e

Gennaro, A., Isse, A. A., Severin, M.-G., Vianello, E., Bhugun, I., and Saveant, J.-M. (1996). Mechanism of the electrochemical reduction of carbon dioxide at inert electrodes in media of low proton availability. *J. Chem. Soc. Faraday Trans.* 92, 3963–3968. doi: 10.1039/FT9969203963

Ginovska-Pangovska, B., Dutta, A., Reback, M. L., Linehan, J. C., and Shaw, W. J. (2014). Beyond the active site: the impact of the outer coordination sphere on electrocatalysts for hydrogen production and oxidation. *Acc. Chem. Res.* 47, 2621–2630. doi: 10.1021/ar5001742

Gloaguen, F., and Rauchfuss, T. B. (2009). Small molecule mimics of hydrogenases: hydrides and redox. *Chem. Soc. Rev.* 38, 100–108. doi: 10.1039/B801796B

Gong, M., Cao, Z., Liu, W., Nichols, E. M., Smith, P. T., Derrick, J. S., et al. (2017). Supramolecular porphyrin cages assembled at molecular–materials

interfaces for electrocatalytic CO reduction. *ACS Cent. Sci.* 3, 1032–1040. doi: 10.1021/acscentsci.7b00316

Grice, K., and Kubiak, C. (2013). Chapter five—recent studies of rhenium and manganese bipyridine carbonyl catalysts for the electrochemical reduction of CO_2. *Adv. Inorg. Chem.* 66, 163–188. doi: 10.1016/B978-0-12-420221-4.00005-6

Grills, D. C., Farrington, J. A., Layne, B. H., Lymar, S. V., Mello, B. A., Preses, J. M., et al. (2014). Mechanism of the formation of a Mn-based CO_2 reduction catalyst revealed by pulse radiolysis with time-resolved infrared detection. *J. Am. Chem. Soc.* 136, 5563–5566. doi: 10.1021/ja501051s

Haviv, E., Azaiza-Dabbah, D., Carmieli, R., Avram, L., Martin, J. M. L., and Neumann, R. (2018). A thiourea tether in the second coordination sphere as a binding site for CO_2 and a proton donor promotes the electrochemical reduction of CO_2 to CO catalyzed by a rhenium bipyridine-type complex. *J. Am. Chem. Soc.* 140, 12451–12456. doi: 10.1021/jacs.8b05658

Hawecker, J., Lehn, J.-M., and Ziessel, R. (1984). Electrocatalytic reduction of carbon dioxide mediated by Re(bipy)(CO)3Cl (bipy = 2,2′-bipyridine). *J. Am. Chem. Soc. Chem. Commun.* 6, 328–330. doi: 10.1039/C39840000328

Helm, M. L., Stewart, M. P., Bullock, R. M., DuBois, M. R., and DuBois, D. L. (2011). A synthetic nickel electrocatalyst with a turnover frequency above $100{,}000^{s-1}$ for H^2 production. *Science* 333, 863. doi: 10.1126/science.1205864

Henry, R. M., Shoemaker, R. K., DuBois, D. L., and DuBois, M. R. (2006). Pendant bases as proton relays in iron hydride and dihydrogen complexes. *J. Am. Chem. Soc.* 128, 3002–3010. doi: 10.1021/ja057242p

Henry, R. M., Shoemaker, R. K., Newell, R. H., Jacobsen, G. M., DuBois, D. L., and Rakowski DuBois, M. (2005). Stereochemical control of iron (II) complexes containing a diphosphine ligand with a pendant nitrogen base. *Organometallics* 24, 2481–2491. doi: 10.1021/om050071c

Hille, R. (2013). The molybdenum oxotransferases and related enzymes. *Dalton Trans.* 42, 3029–3042. doi: 10.1039/c2dt32376a

Himeda, Y., Onozawa-Komatsuzaki, N., Sugihara, H., Arakawa, H., and Kasuga, K. (2004). Half-sandwich complexes with 4,7-dihydroxy-1,10-phenanthroline: water-soluble, highly efficient catalysts for hydrogenation of bicarbonate attributable to the generation of an oxyanion on the catalyst ligand. *Organometallics* 23, 1480–1483. doi: 10.1021/om030382s

Himeda, Y., Onozawa-Komatsuzaki, N., Sugihara, H., and Kasuga, K. (2005). Recyclable catalyst for conversion of carbon dioxide into formate attributable to an oxyanion on the catalyst ligand. *J. Am. Chem. Soc.* 127, 13118–13119. doi: 10.1021/ja054236k

Himeda, Y., Onozawa-Komatsuzaki, N., Sugihara, H., and Kasuga, K. (2007). Simultaneous tuning of activity and water solubility of complex catalysts by acid–base equilibrium of ligands for conversion of carbon dioxide. *Organometallics* 26, 702–712. doi: 10.1021/om060899e

Hong, S., Lee, Y.-M., Ray, K., and Nam, W. (2017). Dioxygen activation chemistry by synthetic mononuclear nonheme iron, copper and chromium complexes. *Coord Chem Rev* 334, 25–42. doi: 10.1016/j.ccr.2016.07.006

Hull, J. F., Himeda, Y., Wang, W. H., Hashiguchi, B., Periana, R., Szalda, D. J., et al. (2012). Reversible hydrogen storage using CO_2 and a proton-switchable iridium catalyst in aqueous media under mild temperatures and pressures. *Nat. Chem.* 4, 383–388. doi: 10.1038/nchem.1295

Jacobsen, G. M., Shoemaker, R., Rakowski DuBois, M., and DuBois, D. L. (2007a). Syntheses and reactions of iron (II) complexes containing diphosphine ligands with pendant nitrogen bases. *Organometallics* 26, 4964–4971. doi: 10.1021/om700510b

Jacobsen, G. M., Shoemaker, R. K., McNevin, M. J., Rakowski DuBois, M., and DuBois, D. L. (2007b). Syntheses and structural characterizations of iron (II) complexes containing cyclic diphosphine ligands with positioned pendant nitrogen bases. *Organometallics* 26, 5003–5009. doi: 10.1021/om700601h

Jeoung, J.-H., and Dobbek, H. (2007). Carbon Dioxide Activation at the Ni,Fe-cluster of anaerobic carbon monoxide dehydrogenase. *Science* 318, 1461–1464. doi: 10.1126/science.1148481

Jiang, C., Nichols, A. W., and Machan, C. W. (2019). A look at periodic trends in *d*-block molecular electrocatalysts for CO_2 reduction. *Dalton Trans.* doi: 10.1039/C9DT00491B. [Epub ahead of print].

Johnson, F. P., George, M. W., Hartl, F., and Turner, J. J. (1996). Electrocatalytic reduction of CO_2 using the complexes $[Re(bpy)(CO)_3L]^n$ ($n = +1$, L = P $(OEt)_3$, CH_3CN; $n = 0$, L = Cl^-, Otf^-; bpy = 2,2′-bipyridine; Otf^- = CF_3SO_3) as catalyst precursors: infrared spectroelectrochemical investigation. *Organometallics* 15, 3374–3387. doi: 10.1021/om960044+

Kadirov, M. K., Karasik, A. A., Nizameev, I. R., Strelnik, I. D., Kholin, K. V., Kadirov, D. M., et al. (2018). Organometallic polymer electrolyte membrane fuel cell bis-ligand nickel(Ii) complex of 1,5-di-*P*-tolyl-3,7-dipyridine-1,5,3,7-diazadiphosphacyclo-octane catalyst. *Energy Technol.* 6, 1088–1095. doi: 10.1002/ente.201700711

Kaim, W., and Fiedler, J. (2009). Spectroelectrochemistry: the best of two worlds. *Chem. Soc. Rev.* 38, 3373–3382. doi: 10.1039/b504286k

Keith, J. A., Grice, K. A., Kubiak, C. P., and Carter, E. A. (2013). Elucidation of the selectivity of proton-dependent electrocatalytic CO_2 reduction by fac-Re(bpy)(CO)3Cl. *J. Am. Chem. Soc.* 135, 15823–15829. doi: 10.1021/ja406456g

Kelly, C. A., Blinn, E. L., Camaioni, N., D'Angelantonio, M., and Mulazzani, Q. G. (1999). Mechanism of CO_2 and H^+ reduction by ni (cyclam)+ in aqueous solution. A pulse and continuous radiolysis study. *Inorg. Chem.* 38, 1579–1584. doi: 10.1021/ic980902p

Kroneck, P. M., and Torres, M. E. S. (2014). *The Metal-driven Biogeochemistry of Gaseous Compounds in the Environment*. Dordrecht: Springer. doi: 10.1007/978-94-017-9269-1

Kuhl, K. P., Cave, E. R., Abram, D. N., and Jaramillo, T. F. (2012). New insights into the electrochemical reduction of carbon dioxide on metallic copper surfaces. *Energy Environ. Sci.* 5, 7050–7059. doi: 10.1039/c2ee21234j

Lewis, E. A., and Tolman, W. B. (2004). Reactivity of dioxygen–copper systems. *Chem. Rev.* 104, 1047–1076. doi: 10.1021/cr020633r

Loewen, N. D., Neelakantan, T. V., and Berben, L. A. (2017). Renewable formate from C–H bond formation with CO_2: using iron carbonyl clusters as electrocatalysts. *Acc. Chem. Res.* 50, 2362–2370. doi: 10.1021/acs.accounts.7b00302

Loewen, N. D., Thompson, E. J., Kagan, M., Banales, C. L., Myers, T. W., Fettinger, J. C., et al. (2016). A pendant proton shuttle on [Fe4N(CO)12]– alters product selectivity in formate vs. H_2 production *via the* hydride $[H–Fe4N(CO)12]^-$. *Chem. Sci.* 7, 2728–2735. doi: 10.1039/C5SC03169A

Machan, C. W., Chabolla, S. A., and Kubiak, C. P. (2015). Reductive disproportionation of carbon dioxide by an alkyl-functionalized pyridine monoimine Re(I) fac-tricarbonyl electrocatalyst. *Organometallics* 34, 4678–4683. doi: 10.1021/acs.organomet.5b00406

Machan, C. W., Chabolla, S. A., Yin, J., Gilson, M. K., Tezcan, F. A., and Kubiak, C. P. (2014a). Supramolecular assembly promotes the electrocatalytic reduction of carbon dioxide by Re(I) bipyridine catalysts at a lower overpotential. *J. Am. Chem. Soc.* 136, 14598–14607. doi: 10.1021/ja5085282

Machan, C. W., and Kubiak, C. P. (2016). Interrogating heterobimetallic co-catalytic responses for the electrocatalytic reduction of CO_2 using supramolecular assembly. *Dalton Trans.* 45, 15942–15950. doi: 10.1039/C6DT01956K

Machan, C. W., Sampson, M. D., Chabolla, S. A., Dang, T., and Kubiak, C. P. (2014b). Developing a mechanistic understanding of molecular electrocatalysts for CO_2 reduction using infrared spectroelectrochemistry. *Organometallics* 33, 4550–4559. doi: 10.1021/om500044a

Machan, C. W., Yin, J., Chabolla, S. A., Gilson, M. K., and Kubiak, C. P. (2016). Improving the efficiency and activity of electrocatalysts for the reduction of CO_2 through supramolecular assembly with amino acid-modified ligands. *J. Am. Chem. Soc.* 138, 8184–8193. doi: 10.1021/jacs.6b03774

Manaka, Y., Wang, W.-H., Suna, Y., Kambayashi, H., Muckerman, J. T., Fujita, E., et al. (2014). Efficient H_2 generation from formic acid using azole complexes in water. *Catal. Sci. Technol.* 4, 34–37. doi: 10.1039/C3CY 00830D

Manbeck, G. F., Muckerman, J. T., Szalda, D. J., Himeda, Y., and Fujita, E. (2015). Push or pull? Proton responsive ligand effects in rhenium tricarbonyl CO_2 reduction catalysts. *J. Phys. Chem.* 119, 7457–7466. doi: 10.1021/jp511131x

Margarit, C. G., Schnedermann, C., Asimow, N. G., and Nocera, D. G. (2018). Carbon dioxide reduction by iron hangman porphyrins. *Organometallics* 38, 1219–1223. doi: 10.1021/acs.organomet.8b00334

Matsumoto, T., Kim, K., Nakai, H., Hibino, T., and Ogo, S. (2013). Organometallic catalysts for use in a fuel cell. *ChemCatChem* 5, 1368–1373. doi: 10.1002/cctc.201200595

Matsumoto, T., Kim, K., and Ogo, S. (2011). Molecular catalysis in a fuel cell. *Angew. Chem. Int.* 123, 11398–11401. doi: 10.1002/ange.201104498

Maynard, E. L., and Lindahl, P. A. (2001). Catalytic coupling of the active sites in acetyl-CoA synthase, a bifunctional CO-channeling enzyme. *Biochemistry* 40, 13262–13267. doi: 10.1021/bi015604+

Mirica, L. M., Ottenwaelder, X., and Stack, T. D. P. (2004). Structure and spectroscopy of copper–dioxygen complexes. *Chem. Rev.* 104, 1013–1046. doi: 10.1021/cr020632z

Mohamed, E. A., Zahran, Z. N., and Naruta, Y. (2015). Efficient electrocatalytic CO_2 reduction with a molecular cofacial iron porphyrin dimer. *Chem. Commun.* 51, 16900–16903. doi: 10.1039/C5CC04273A

Nam, W. (2015). Synthetic mononuclear nonheme iron–oxygen intermediates. *Acc. Chem. Res.* 48, 2415–2423. doi: 10.1021/acs.accounts.5b00218

Neri, G., Aldous, I. M., Walsh, J. J., Hardwick, L. J., and Cowan, A. J. (2016). A highly active nickel electrocatalyst shows excellent selectivity for CO_2 reduction in acidic media. *Chem. Sci* 7, 1521–1526. doi: 10.1039/C5SC03225C

Ngo, K. T., McKinnon, M., Mahanti, B., Narayanan, R., Grills, D. C., Ertem, M. Z., et al. (2017). Turning on the protonation-first pathway for electrocatalytic CO_2 reduction by manganese bipyridyl tricarbonyl complexes. *J. Am. Chem. Soc.* 139, 2604–2618. doi: 10.1021/jacs.6b08776

Nichols, A. W., Chatterjee, S., Sabat, M., and Machan, C. W. (2018a). Electrocatalytic reduction of CO_2 to formate by an iron Schiff base complex. *Inorg. Chem.* 57, 2111–2121. doi: 10.1021/acs.inorgchem.7b02955

Nichols, E. M., and Chang, C. J. (2018). Urea-based multipoint hydrogen-bond donor additive promotes electrochemical CO_2 reduction catalyzed by nickel cyclam. *Organometallics* 38, 1213–1218. doi: 10.1021/acs.organomet.8b00308

Nichols, E. M., Derrick, J. S., Nistanaki, S. K., Smith, P. T., and Chang, C. J. (2018b). Positional effects of second-sphere amide pendants on electrochemical CO_2 reduction catalyzed by iron porphyrins. *Chem. Sci.* 9, 2952–2960. doi: 10.1039/C7SC04682K

Pegis, M. L., Wise, C. F., Koronkiewicz, B., and Mayer, J. M. (2017). Identifying and breaking scaling relations in molecular catalysis of electrochemical reactions. *J. Am. Chem. Soc.* 139, 11000–11003. doi: 10.1021/jacs.7b05642

Rail, M. D., and Berben, L. A. (2011). Directing the reactivity of $[HFe4N(CO)12]^-$ toward H^+ or CO_2 reduction by understanding the electrocatalytic mechanism. *J. Am. Chem. Soc.* 133, 18577–18579. doi: 10.1021/ja208312t

Rao, H., Schmidt, L. C., Bonin, J., and Robert, M. (2017). Visible-light-driven methane formation from CO_2 with a molecular iron catalyst. *Nature* 548:74. doi: 10.1038/nature23016

Ray, K., Pfaff, F. F., Wang, B., and Nam, W. (2014). Status of reactive non-heme metal–oxygen intermediates in chemical and enzymatic reactions. *J. Am. Chem. Soc.* 136, 13942–13958. doi: 10.1021/ja507807v

Reback, M. L., Ginovska-Pangovska, B., Ho, M. H., Jain, A., Squier, T. C., Raugei, S., et al. (2013). The role of a dipeptide outer-coordination sphere on H2-production catalysts: influence on catalytic rates and electron transfer. *Chem. Eur. J.* 19, 1928–1941. doi: 10.1002/chem.201202849

Riplinger, C., and Carter, E. A. (2015). Influence of weak Brønsted acids on electrocatalytic CO_2 reduction by manganese and rhenium bipyridine catalysts. *ACS Catal.* 5, 900–908. doi: 10.1021/cs501687n

Riplinger, C., Sampson, M. D., Ritzmann, A. M., Kubiak, C. P., and Carter, E. A. (2014). Mechanistic contrasts between manganese and rhenium bipyridine electrocatalysts for the reduction of carbon dioxide. *J. Am. Chem. Soc.* 136, 16285–16298. doi: 10.1021/ja508192y

Rotundo, L., Garino, C., Priola, E., Sassone, D., Rao, H., Ma, B., et al. (2019). Electrochemical and photochemical reduction of CO_2 catalyzed by Re(I) complexes carrying local proton sources. *Organometallics* 38, 1351–1360. doi: 10.1021/acs.organomet.8b00588

Rountree, E. S., McCarthy, B. D., Eisenhart, T. T., and Dempsey, J. L. (2014). Evaluation of homogeneous electrocatalysts by cyclic voltammetry. *Inorg. Chem.* 53, 9983–10002. doi: 10.1021/ic500658x

Roy, S., Sharma, B., Pécaut, J., Simon, P., Fontecave, M., Tran, P. D., et al. (2017). Molecular cobalt complexes with pendant amines for selective electrocatalytic reduction of carbon dioxide to formic acid. *J. Am. Chem. Soc.* 139, 3685–3696. doi: 10.1021/jacs.6b11474

Sahu, S., Cheung, P. L., Machan, C. W., Chabolla, S. A., Kubiak, C. P., and Gianneschi, N. C. (2017). Charged macromolecular rhenium bipyridine catalysts with tunable CO_2 reduction potentials. *Chem. Eur. J.* 23, 8619–8622. doi: 10.1002/chem.201701901

Sahu, S., and Goldberg, D. P. (2016). Activation of dioxygen by iron and manganese complexes: a heme and nonheme perspective. *J. Am. Chem. Soc.* 138, 11410–11428. doi: 10.1021/jacs.6b05251

Sampson, M. D., Froehlich, J. D., Smieja, J. M., Benson, E. E., Sharp, I. D., and Kubiak, C. P. (2013). Direct observation of the reduction of carbon dioxide by rhenium bipyridine catalysts. *Energy Environ. Sci.* 6, 3748–3755. doi: 10.1039/c3ee42186d

Sampson, M. D., and Kubiak, C. P. (2016). Manganese electrocatalysts with bulky bipyridine ligands: utilizing lewis acids to promote carbon dioxide reduction at low overpotentials. *J. Am. Chem. Soc.* 138, 1386–1393. doi: 10.1021/jacs.5b12215

Sampson, M. D., Nguyen, A. D., Grice, K. A., Moore, C. E., Rheingold, A. L., and Kubiak, C. P. (2014). Manganese catalysts with bulky bipyridine ligands for the electrocatalytic reduction of carbon dioxide: eliminating dimerization and altering catalysis. *J. Am. Chem. Soc.* 136, 5460–5471. doi: 10.1021/ja501252f

Savéant, J.-M. (2008). Molecular catalysis of electrochemical reactions. Mechanistic aspects. *Chem. Rev.* 108, 2348–2378. doi: 10.1021/cr068079z

Savéant, J.-M. (2018). Molecular catalysis of electrochemical reactions. Cyclic voltammetry of systems approaching reversibility. *ACS Catal.* 8, 7608–7611. doi: 10.1021/acscatal.8b02007

Sawers, G. (1994). The hydrogenases and formate dehydrogenases of *Escherichia coli*. *Antonie Van Leeuwenhoek* 66, 57–88. doi: 10.1007/BF00871633

Schneider, J., Jia, H., Kobiro, K., Cabelli, D. E., Muckerman, J. T., and Fujita, E. (2012). Nickel (II) macrocycles: highly efficient electrocatalysts for the selective reduction of CO_2 to CO. *Energy Environ. Sci.* 5, 9502–9510. doi: 10.1039/c2ee22528j

Sen, P., Mondal, B., Saha, D., Rana, A., and Dey, A. (2019). Role of 2nd sphere H-bonding residues in tuning the kinetics of CO_2 reduction to CO by iron porphyrin complexes. *Dalton Trans.* 48, 5965–5977. doi: 10.1039/C8DT03850C

Senftle, T. P., and Carter, E. A. (2017). The holy grail: chemistry enabling an economically viable CO_2 capture, utilization, and storage strategy. *Acc. Chem. Res.* 50, 472–475. doi: 10.1021/acs.accounts.6b00479

Seu, C. S., Appel, A. M., Doud, M. D., DuBois, D. L., and Kubiak, C. P. (2012). Formate oxidation *via* β-deprotonation in $[Ni(PR2NR'2)2(CH3CN)]^{2+}$ complexes. *Energy Environ. Sci.* 5, 6480–6490. doi: 10.1039/c2ee03341k

Shirley, H., Su, X., Sanjanwala, H., Talukdar, K., Jurss, J. W., and Delcamp, J. H. (2019). Durable solar-powered systems with Ni-catalysts for conversion of CO_2 or CO to CH_4. *J. Am. Chem. Soc.* 141, 6617–6622. doi: 10.1021/jacs.9b00937

Sinha, S., Berdichevsky, E. K., and Warren, J. J. (2017). Electrocatalytic CO_2 reduction using rhenium(I) complexes with modified 2-(2′-pyridyl)imidazole ligands. *Inorganica Chim. Acta* 460, 63–68. doi: 10.1016/j.ica.2016.09.019

Sinha, S., Ghosh, M., and Warren, J. J. (2019). Changing the selectivity of O2 reduction catalysis with one ligand heteroatom. *ACS Catal.* 9, 2685–2691. doi: 10.1021/acscatal.8b04757

Sinha, S., and Warren, J. J. (2018). Unexpected solvent effect in electrocatalytic CO_2 to CO conversion revealed using asymmetric metalloporphyrins. *Inorg. Chem.* 57, 12650–12656. doi: 10.1021/acs.inorgchem.8b01814

Smieja, J. M., Benson, E. E., Kumar, B., Grice, K. A., Seu, C. S., Miller, A. J. M., et al. (2012). Kinetic and structural studies, origins of selectivity, and interfacial charge transfer in the artificial photosynthesis of CO. *Proc. Natl. Acad. Sci. U.S.A.* 109, 15646–15650. doi: 10.1073/pnas.1119863109

Smieja, J. M., Sampson, M. D., Grice, K. A., Benson, E. E., Froehlich, J. D., and Kubiak, C. P. (2013). Manganese as a substitute for rhenium in CO_2 reduction catalysts: the importance of acids. *Inorg. Chem.* 52, 2484–2491. doi: 10.1021/ic302391u

Smith, P. T., Benke, B. P., Cao, Z., Kim, Y., Nichols, E. M., Kim, K., et al. (2018). Iron porphyrins embedded into a supramolecular porous organic cage for electrochemical CO_2 reduction in water. *Angew. Chem. Int.* 57, 9684–9688. doi: 10.1002/anie.201803873

Song, J., Klein, E. L., Neese, F., and Ye, S. (2014). The mechanism of homogeneous CO_2 reduction by Ni(cyclam): product selectivity, concerted proton–electron transfer and C–O bond cleavage. *Inorg. Chem.* 53, 7500–7507. doi: 10.1021/ic500829p

Sullivan, B. P., Bolinger, C. M., Conrad, D., Vining, W. J., and Meyer, T. J. (1985). One-and two-electron pathways in the electrocatalytic reduction of CO_2 by fac-Re(bpy)(CO)3Cl (bpy = 2,2′-bipyridine). *J. Am. Chem. Soc. Chem. Commun.* 20, 1414–1416. doi: 10.1039/C39850001414

Suna, Y., Ertem, M. Z., Wang, W.-H., Kambayashi, H., Manaka, Y., Muckerman, J. T., et al. (2014). Positional effects of hydroxy groups on catalytic activity of proton-responsive half-sandwich Cp* Iridium (III) complexes. *Organometallics* 33, 6519–6530. doi: 10.1021/om500832d

Sung, S., Kumar, D., Gil-Sepulcre, M., and Nippe, M. (2017). Electrocatalytic CO_2 reduction by imidazolium-functionalized molecular catalysts. *J. Am. Chem. Soc.* 139, 13993–13996. doi: 10.1021/jacs.7b07709

Sung, S., Li, X., Wolf, L. M., Meeder, J. R., Bhuvanesh, N. S., Grice, K. A., et al. (2019). Synergistic effects of imidazolium-functionalization on fac-Mn(CO)3 bipyridine catalyst platforms for electrocatalytic carbon dioxide reduction. *J. Am. Chem. Soc.* 141, 6569–6582. doi: 10.1021/jacs.8b13657

Taheri, A., and Berben, L. A. (2016). Tailoring electrocatalysts for selective CO_2 or H^+ reduction: iron carbonyl clusters as a case study. *Inorg. Chem.* 55, 378–385. doi: 10.1021/acs.inorgchem.5b02293

Taheri, A., Thompson, E. J., Fettinger, J. C., and Berben, L. A. (2015). An iron electrocatalyst for selective reduction of CO_2 to formate in water: including thermochemical insights. *ACS Catal.* 5, 7140–7151. doi: 10.1021/acscatal.5b01708

Wang, W.-H., Muckerman, J. T., Fujita, E., and Himeda, Y. (2013). Mechanistic insight through factors controlling effective hydrogenation of CO_2 catalyzed by bioinspired proton-responsive iridium (III) complexes. *ACS Catal.* 3, 856–860. doi: 10.1021/cs400172j

Wang, W. H., Hull, J., Muckerman, J. T., Fujita, E., and Himeda, Y. (2012). Second-coordination-sphere and electronic effects enhance iridium(III)-catalyzed homogeneous hydrogenation of carbon dioxide in water near ambient temperature and pressure. *Energy Environ. Sci.* 5, 7923–7926. doi: 10.1039/C2EE21888G

Wang, W. H., Xu, S., Manaka, Y., Suna, Y., Kambayashi, H., Muckerman, J. T., et al. (2014). Formic acid dehydrogenation with bioinspired iridium complexes: a kinetic isotope effect study and mechanistic insight. *ChemSusChem* 7, 1976–1983. doi: 10.1002/cssc.201301414

Weng, Z., Jiang, J., Wu, Y., Wu, Z., Guo, X., Materna, K. L., et al. (2016). Electrochemical CO_2 reduction to hydrocarbons on a heterogeneous molecular Cu catalyst in aqueous solution. *J. Am. Chem. Soc.* 138, 8076–8079. doi: 10.1021/jacs.6b04746

Wilson, A. D., Newell, R. H., McNevin, M. J., Muckerman, J. T., Rakowski DuBois, M., and DuBois, D. L. (2006). Hydrogen oxidation and production using nickel-based molecular catalysts with positioned proton relays. *J. Am. Chem. Soc.* 128, 358–366. doi: 10.1021/ja056442y

Wilting, A., Stolper, T., Mata, R. A., and Siewert, I. (2017). Dinuclear rhenium complex with a proton responsive ligand as a redox catalyst for the electrochemical CO_2 reduction. *Inorg. Chem.* 56, 4176–4185. doi: 10.1021/acs.inorgchem.7b00178

Wong, K.-Y., Chung, W.-H., and Lau, C.-P. (1998). The effect of weak Brönsted acids on the electrocatalytic reduction of carbon dioxide by a rhenium tricarbonyl bipyridyl complex. *J. Electroanal. Chem.* 453, 161–170. doi: 10.1016/S0022-0728(98)00116-8

Yang, W., Sinha Roy, S., Pitts, W. C., Nelson, R. L., Fronczek, F. R., and Jurss, J. W. (2018). Electrocatalytic CO_2 reduction with cis and trans conformers of a rigid dinuclear rhenium complex: comparing the monometallic and cooperative bimetallic pathways. *Inorg. Chem.* 57, 9564–9575. doi: 10.1021/acs.inorgchem.8b01775

Zahran, Z. N., Mohamed, E. A., and Naruta, Y. (2016). Bio-inspired cofacial Fe porphyrin dimers for efficient electrocatalytic $CO_2$to CO conversion: overpotential tuning by substituents at the porphyrin rings. *Sci. Rep.* 6:24533. doi: 10.1038/srep24533

Zavarine, I. S., and Kubiak, C. P. (2001). A versatile variable temperature thin layer reflectance spectroelectrochemical cell. *J. Electroanal. Chem.* 495, 106–109. doi: 10.1016/S0022-0728(00)00394-6

Conflict of Interest Statement: The authors declare that the research was conducted in the absence of any commercial or financial relationships that could be construed as a potential conflict of interest.

Copyright © 2019 Nichols and Machan. This is an open-access article distributed under the terms of the Creative Commons Attribution License (CC BY). The use, distribution or reproduction in other forums is permitted, provided the original author(s) and the copyright owner(s) are credited and that the original publication in this journal is cited, in accordance with accepted academic practice. No use, distribution or reproduction is permitted which does not comply with these terms.

frontiers in Chemistry

REVIEW
published: 27 June 2019
doi: 10.3389/fchem.2019.00430

Carboxylation Reactions Using Carbon Dioxide as the C1 Source via Catalytically Generated Allyl Metal Intermediates

Tetsuaki Fujihara and Yasushi Tsuji*

Department of Energy and Hydrocarbon Chemistry, Graduate School of Engineering, Kyoto University, Kyoto, Japan

The use of carbon dioxide (CO_2) is an important issue with regard to current climate research and the Earth's environment. Transition metal-catalyzed carboxylation reactions using CO_2 are highly attractive. This review summarizes the transition metal-catalyzed carboxylation reactions of organic substrates with CO_2 via allyl metal intermediates. First, carboxylation reactions via transmetalation are reviewed. Second, catalytic carboxylation reactions using allyl electrophiles and suitable reducing agents are summarized. The last section discusses the catalytic carboxylation reactions via addition reactions, affording allyl metal intermediates.

Keywords: carbon dioxide, carboxylic acids, allyl metals, transmetalation, oxidative addition, addition reactions

OPEN ACCESS

Edited by:
Hitoshi Ishida, Kitasato University, Japan

Reviewed by:
Annaluisa Mariconda, University of Basilicata, Italy
Tian-Sheng Mei, Shanghai Institute of Organic Chemistry (CAS), China

****Correspondence:***
Tetsuaki Fujihara
tfuji@scl.kyoto-u.ac.jp

Specialty section:
This article was submitted to Inorganic Chemistry, a section of the journal Frontiers in Chemistry

Received: *05 February 2019*
Accepted: *27 May 2019*
Published: *27 June 2019*

Citation:
Fujihara T and Tsuji Y (2019) Carboxylation Reactions Using Carbon Dioxide as the C1 Source via Catalytically Generated Allyl Metal Intermediates. Front. Chem. 7:430. doi: 10.3389/fchem.2019.00430

INTRODUCTION

The development of fixation methods of carbon dioxide (CO_2) is an important task for chemists (Aresta et al., 2014; Artz et al., 2018). However, CO_2 is a kinetically and thermodynamically stable material. Therefore, using CO_2 as a substrate poses several difficulties such as high-pressure or high-temperature reaction conditions. Transition metal-catalyzed carboxylation reactions of organic substrates with CO_2 can allow the diverse production of carboxylic acids and their derivatives under mild reaction conditions via carbon-carbon bond formation. During the last decade, diverse transition metal-catalyzed carboxylation reactions have been reported and good reviews have also been published (Huang et al., 2011; Tsuji and Fujihara, 2012; Cai and Xie, 2013; Zhang and Hou, 2013; Liu et al., 2015; Yu et al., 2015; Borjesson et al., 2016; Sekine and Yamada, 2016; Wang et al., 2016; Hazari and Heimann, 2017; Chen et al., 2018; Luan and Ye, 2018; Tortajada et al., 2018).

Allyl metal reagents are known for being excellent reagents during organic synthesis. The characteristic feature of allyl metal species is its isomerization via π-σ-π intermediates. σ-Allyl metal reagents act as nucleophiles, whereas π-allyl metals serve as electrophiles. When CO_2 is used as electrophiles for transition metal-catalyzed reactions, a method to generate a catalytically active nucleophilic allyl metal intermediate is highly reliable. **Scheme 1** shows three methods to access these allyl metal species from several organic substrates. The first method involves the transmetalation between allyl metal precursors such as allyl boranes or allylstannanes and transition metals (**Scheme 1A**). The second method involves the oxidative addition of allyl halides or allyl acetates using low-valent transition metals (**Scheme 1B**). In this case, suitable reducing agents must be used to regenerate low-valent active species. The third method involves the addition of metal species to conjugated dienes (**Scheme 1C**). In this reaction, the key is a regioselective addition that yields an ally metal intermediate selectively.

This paper overviews the transition metal-catalyzed carboxylation reactions of organic substrates with CO_2 via allyl metal intermediates. First, Pd- and Cu-catalyzed carboxylation reactions via transmetalation are summarized. Second, Pd- and Ni-catalyzed carboxylation reactions using ally electrophiles such as allyl acetates are reviewed. Finally, the catalytic carboxylation reactions via addition reactions are discussed.

RESULTS AND DISCUSSION

Transmetalation

Transmetalation is a straightforward method that allows accessing catalytically active allyl metal intermediates during a carboxylation event. A pioneering work has been done by Nicholas who carried out the reaction of allylstannane using $Pd(PPh_3)_4$ as the catalyst in tetrahydrofurane (THF) at 70°C under 33 atm of CO_2 (**Scheme 2A**, Shi and Nicholas, 1997). The reaction proceeds via allylstannane transmetalation, followed by a carboxylation reaction with CO_2. Wendt observed an allyl Pd complex bearing a pincer ligand reacted with CO_2 under mild reaction conditions (**Scheme 2B**, Johansson and Wendt, 2007). In 2011, Hazari reported the Pd-catalyzed carboxylation of allylstannanes and allyl boranes, which were used as substrates (**Scheme 3**, Wu and Hazari, 2011). The reactions proceeded using a Pd complex with an N-heterocyclic (NHC) ligand as the catalyst under 1 atm of CO_2. Under the same reaction conditions, several allylboronates were also converted to the corresponding carboxylated products in good yields.

Duong reported the Cu-catalyzed carboxylation of allylboronic esters with CO_2 (**Scheme 4**, Duong et al., 2013). The desired reactions proceeded in the presence of a Cu catalyst with IPr as the ligand in THF under 1 atm of CO_2. Various allylboronic esters were subjected to the reaction, which generated corresponding products in moderate-to-high yields.

Oxidative Addition

Known as an elemental reaction during a Tsuji–Trost reaction, the oxidative addition of ally halides or allyl esters with low-valent metal species yields an ally metal intermediate (Trost and van Vranken, 1996; Trost and Crawley, 2003). Torii et al.

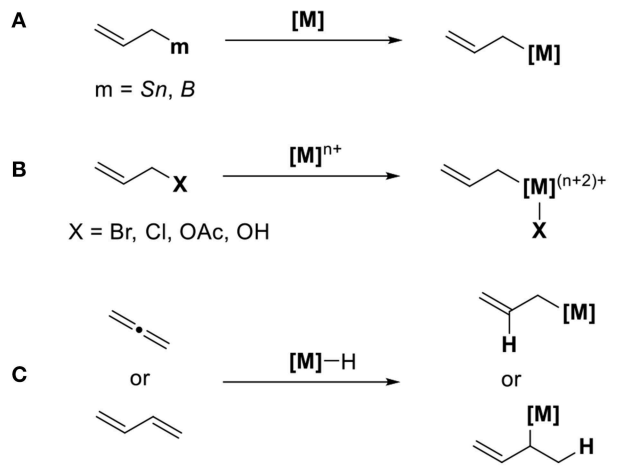

SCHEME 1 | Generation of allyl metal intermediates: **(A)** transmetalation, **(B)** oxidative addition, and **(C)** addition reaction.

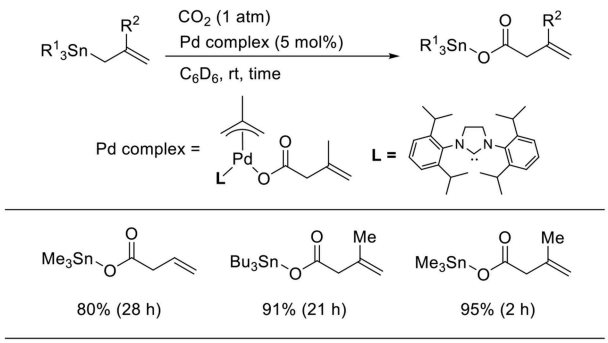

SCHEME 3 | Catalytic carboxylation of allylstannane with CO_2 using a Pd complex.

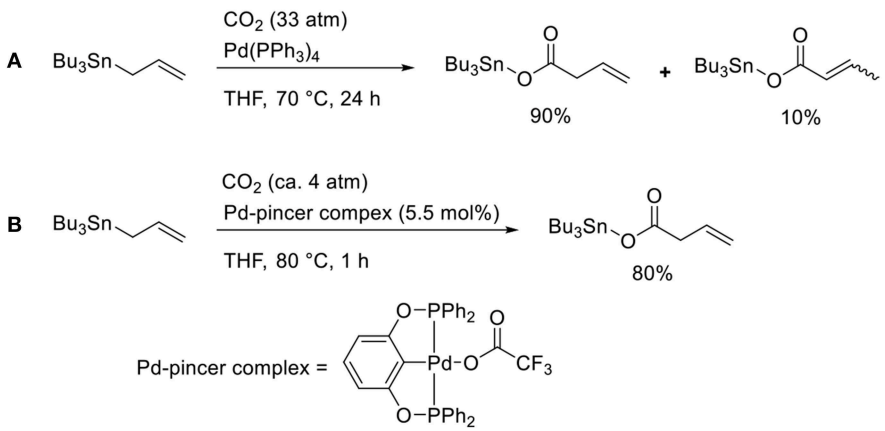

SCHEME 2 | Catalytic carboxylation of allylstannane with CO_2 using a Pd complex: **(A)** the reaction reported by Shi and Nicholas (1997) **(B)** the reaction reported by Johansson and Wendt (2007).

reported the Pd-catalyzed carboxylation of allyl acetates when exposed to electroreductive reductions (**Scheme 5**, Torii et al., 1986). The reaction of cinnamyl acetate with CO_2 in the presence of $PdCl_2(PPh_3)_2$ and PPh_3 afforded a mixture of regioisomers in 76% total yield. A branched substrate also afforded a mixture of regioisomers, indicating that the reaction proceeded via a π-allyl Pd intermediate. Dunach et al. found the Ni-catalyzed electrochemical carboxylation of allyl acetate with CO_2. In the reaction, a mixture of two regioisomers was obtained (Medeiros et al., 2011). Mei et al. also found the Pd-catalyzed electrochemical carboxylation of allyl acetate, giving branched product selectively (Jiao et al., 2018).

Martin et al. reported the Ni-catalyzed ligand-controlled regiodivergent carboxylation of allyl acetates using manganese as the reducing agent (**Scheme 6**, Moragas et al., 2014). When **L1** was used as the ligand, the linear carboxylated products were obtained. In contrast, the reactions using **L2** produced branched carboxylated products in good-to-high yields. The oxidative addition of a low-valent Ni species affords an allylic Ni intermediate. The reaction with CO_2 yields Ni carboxylate intermediates; this is a regio-determining step for carboxylation.

Allyl alcohols are excellent reagents that allow the generation of allyl metal intermediates. However, in general, the hydroxyl group must be converted to the corresponding halides or esters before their use. Thus, the direct use of alcohols as the substrate for carboxylation reactions is important for both atom- and step-economical points. Mita and Sato found the Pd-catalyzed carboxylation of allyl alcohols in the presence of Et_2Zn (**Scheme 7**, Mita et al., 2015). This reaction proceeded in the presence of a Pd catalyst with a PPh_3 ligand in a THF/hexane solution at room temperature under 1 atm of CO_2. Diverse allyl alcohols were converted to the corresponding branched

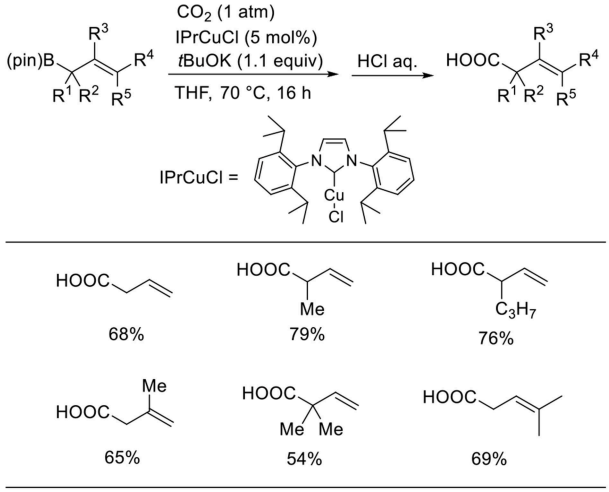

SCHEME 4 | Cu-catalyzed carboxylation of allylboronates with CO_2.

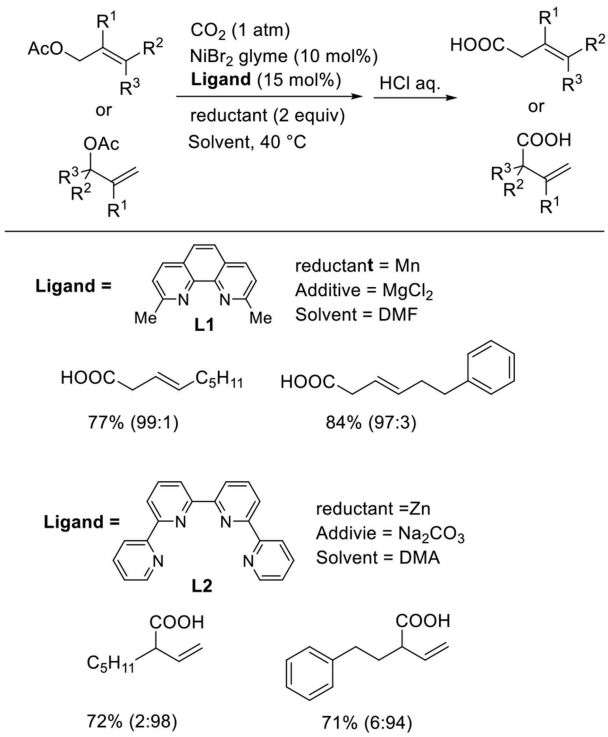

SCHEME 6 | Ni-catalyzed ligand-controlled regiodivergent carboxylation of allyl acetates with CO_2.

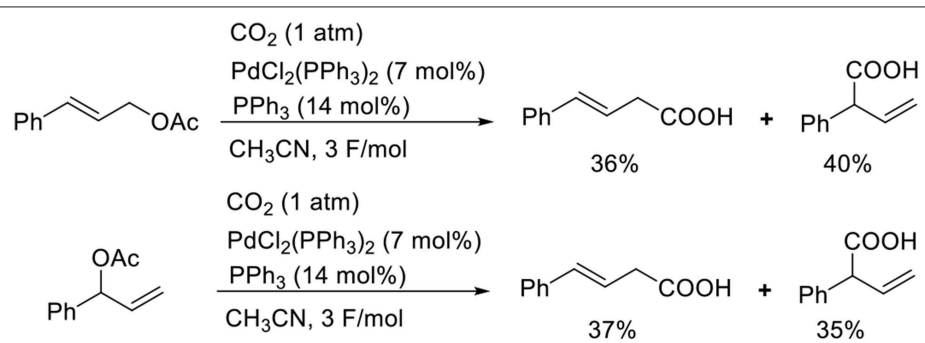

SCHEME 5 | Pd-catalyzed carboxylation of cinnamyl acetate with CO_2 under electrolysis.

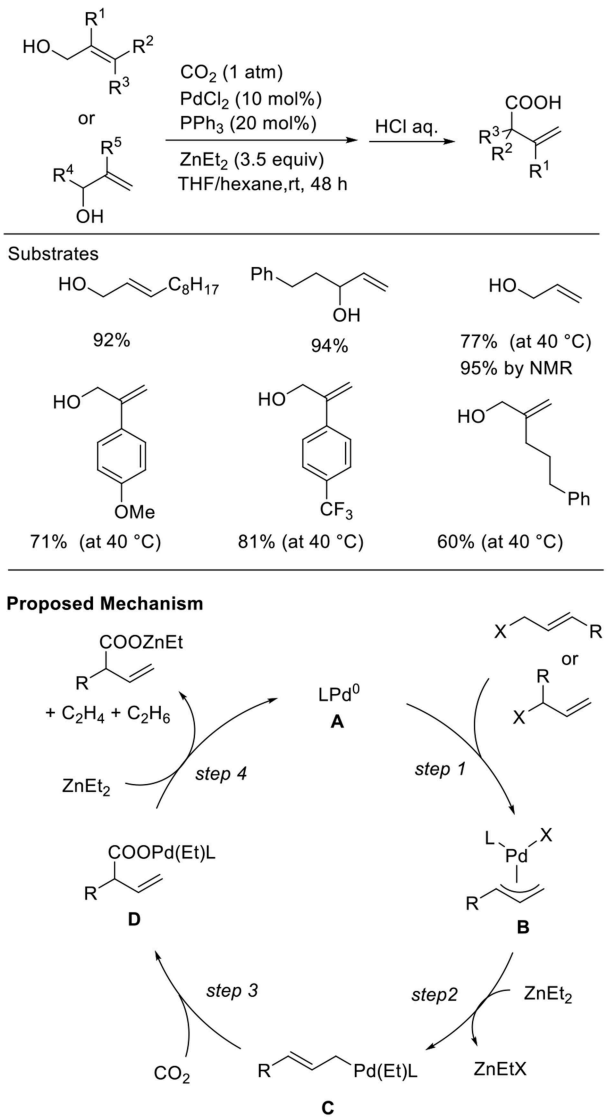

SCHEME 7 | Pd-catalyzed carboxylation of allyl alcohols with CO_2 using Et_2Zn.

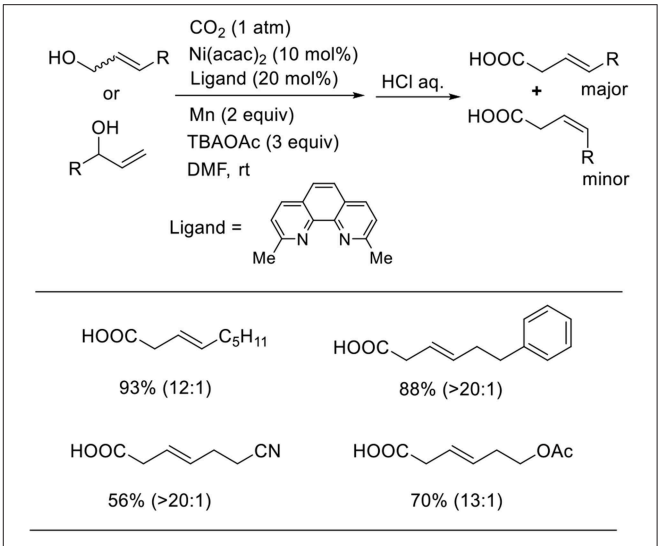

SCHEME 8 | Ni-catalyzed carboxylation of allyl alcohols with CO_2 using a manganese as reducing agent.

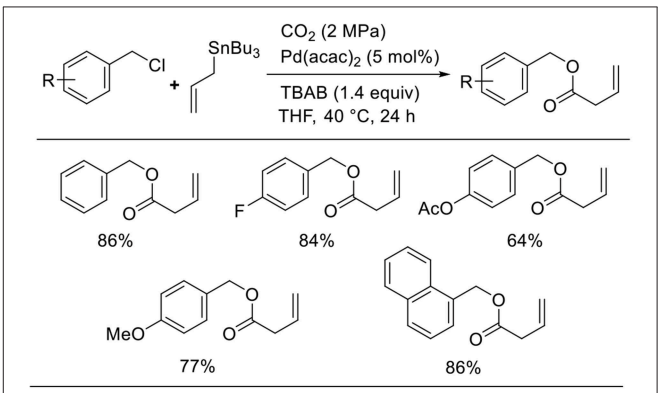

SCHEME 9 | Pd-catalyzed carboxylative coupling of benzyl chlorides and an allylstannane under CO_2.

carboxylic acids in good to high yields with high regioselectivity. Noteworthy is that a wide range of functional groups such as an ester and a free hydroxyl group was tolerated in the reactions. Regarding a reaction mechanism, allylic alcohols would be activated by $ZnEt_2$ followed by oxidative addition, leading to a π-allylpalladium intermediate (step 1). Then, nucleophilic σ-allylpalladium can capture CO_2 to generate a carboxylato Pd intermediate (step 3). Finally, transmetalation followed by reduction can regenerate Pd(0) active species (step 4).

Mei also reported that a Ni complex catalyzed the carboxylation of allyl alcohols using manganese as a reducing agent (**Scheme 8**, Chen et al., 2017). This reaction proceeded in the presence of an Ni complex with a neocuproine ligand in N.N-dimethylformamide (DMF) at room temperature under 1 atm of CO_2. In this reaction, tetrabutylammonium acetate (TBAOAc) was essential; without the additive, the desired product could not be obtained at all. The reactions using both linear and branched allyl alcohols produced linear carboxylic acids in good-to-high yields with high regioselectivity. The reactions tolerated several functionality such as cyano and ester groups.

Bao found the Pd-catalyzed carboxylative coupling of benzyl chlorides and an allylstannane under CO_2 atmosphere (**Scheme 9**, Feng et al., 2013). Diverse benzyl chloride derivatives took part in the reactions, which produced the corresponding carboxylative coupling products in good-to-high yields. A key intermediate, the π-benzyl-π-allyl Pd complex, can be obtained by the oxidative addition of Pd(0) to benzyl chloride followed by transmetalation.

Transition metal-catalyzed carboxylation reaction via direct carbon-hydrogen (C-H) activation is a central research issue. Thus, the development of less reactive C-H carboxylation

reactions is important. Mita and Sato observed a unique C-H carboxylation reaction with allylbenzene derivatives (**Scheme 10**, Michigami et al., 2017). The reaction of 4-phenyl allylbenzene was carried out in the presence of $AlMe_3$ (3 equivalent) using $Co(acac)_2$ and xantphos as the ligand in DMA at 60°C under 1 atm of CO_2 in the presence of CsF as an additive. With these reaction conditions, a carboxylated product was obtained in 68% yield. Reactions were performed with diverse substrates, which produced corresponding carboxylated products in good-to-high yields. Notably, the reactions tolerated substrates having ester and ketone moieties, which are generally more reactive with nucleophiles than CO_2. The reaction starts by generating a low-valent CH_3-Co(I) species (**A**). The C-C double bond of the substrate coordinates to the cobalt center, and subsequent cleavage of the adjacent allylic C–H bond affords η^3-allyl-Co(III) species **B** (step 1). Then, the reductive elimination of CH_4 from **B** affords a low-valent allyl-Co(I) species **C** (step 2). Next, C–C bond formation at the γ-position occurs via a reaction with CO_2, giving a carboxylato Co species **D** (step 3). Finally, a linear carboxylated product is obtained by the transmetalation between **D** and $Al(CH_3)_3$, with the concomitant regeneration of **A** (step 4).

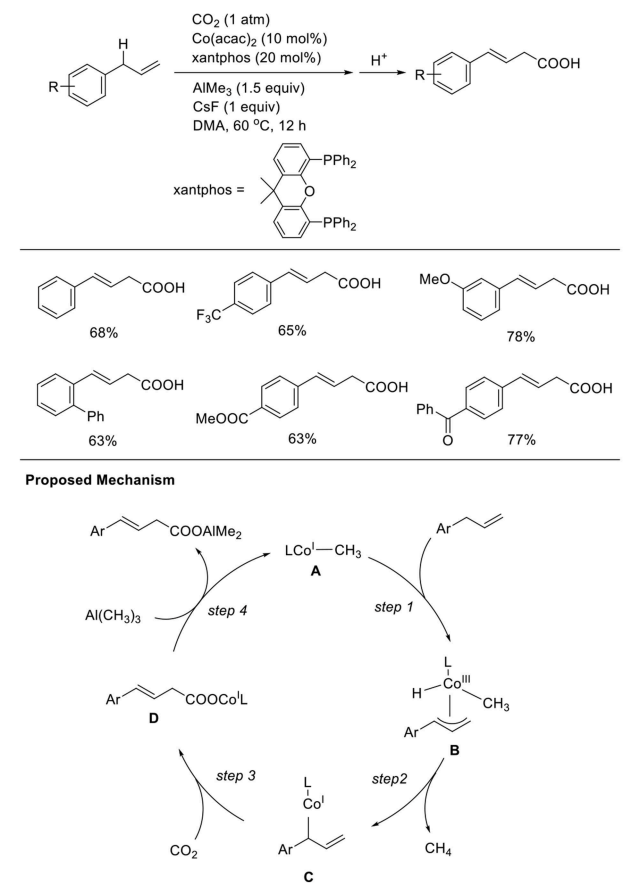

SCHEME 10 | Co-catalyzed allylic C-H carboxylation of allylarenes and a proposed mechanism.

Addition Reactions

Addition reactions are an important method to generate nucleophilic metal intermediates using unsaturated hydrocarbons. Among them, 1,2-dienes as well as 1,3-dienes are candidates accessing allyl metal intermediates. However, the regioselectivity of addition reactions must be controlled. Iwasawa et al. found hydrocarboxylation of 1,2-dienes (**Scheme 11**, Takaya and Iwasawa, 2008). These reactions proceeded via the hydropalladation of Pd–H to 1,2-dienes (step 1) followed by carboxylation (step 2). A P–Si–P coordinated pincer ligand was crucial for the reaction and $AlEt_3$ was employed as a reducing agent. With a similar Pd catalyst system, one-to-one coupling between 1,3-dienes and CO_2 also occurred (Takaya et al., 2011). The reaction between a Pd precursor and triethylaluminum reagents followed by β-hydrogen elimination produces a Pd–H intermediate. Then, hydropalladation of conjugated dienes yields allyl palladium intermediates, which can regioselectively react with CO_2.

For Cu catalysts, we reported Cu-catalyzed hydrohydroxymethylation using 1,2-dienes as the substrate (**Scheme 12**, Tani et al., 2015). The reaction of 1,2-dienes with CO_2 (1 atm) and a hydrosilane was examined in the presence of a copper catalyst bearing xantphos derivatives as the ligand. Using 1.5 mmol of hydrosilane, which corresponds

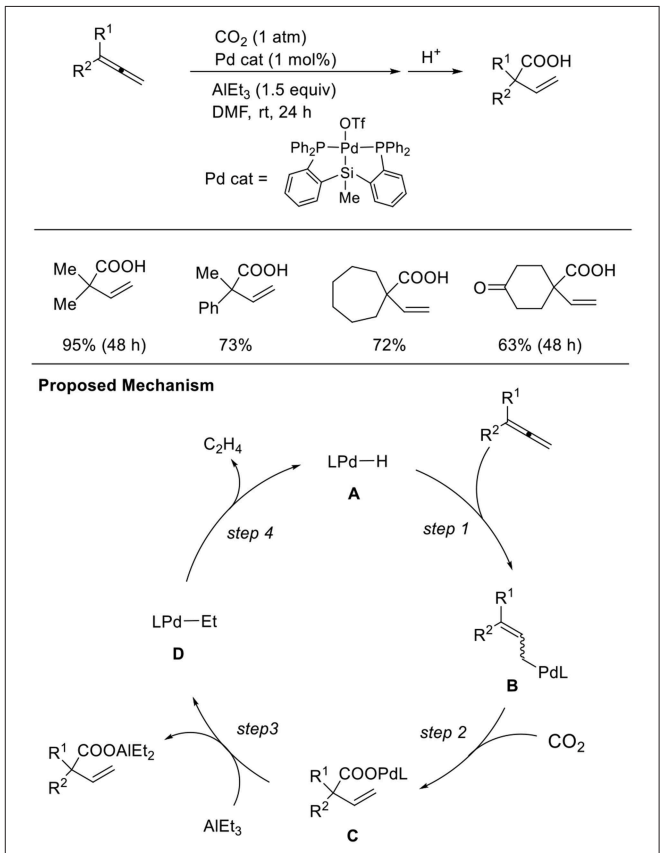

SCHEME 11 | Pd-catalyzed hydrocarboxylation of 1,2-dienes and a proposed mechanism.

to 2.0 equivalent for the required amount to yield the homoallyl alcohols, three H atoms were incorporated into the product. The corresponding homoallyl alcohols were obtained regioselectively, and the resulting terminal olefin moieties were preserved without hydrosilylation in the presence of an excess amount of hydrosilane. Various ester functionalities on the 1,2-dienes remained intact without reducing to their corresponding diols. Addition of a copper hydride **A** across a terminal double bond of allene **6** with the Cu atom at the less hindered site generates allylcopper intermediate **B** (step 1), which reacts with CO_2 regioselectively at the γ-position via a six-membered transition state to afford a copper carboxylate **C** (step 2). Then, carboxylate **C** could be further reduced by the hydrosilane to copper alkoxide **E** via a silyl copper ketal derivative **D** (steps 3 and 4). Finally, σ-bond metathesis between **E** and the hydrosilane provides silyl ether and **A** regenerates (step 5).

Using a stoichiometric amount of base and ^{Cl}IPr as the ligand, the product completely switched from homoallyl alcohols to β,γ-unsaturated carboxylic acids (**Scheme 13**, Tani et al., 2015). A stoichiometric amount of base is essential to induce selective carboxylic acid formation. Thus, products at two different oxidation levels (alcohols and carboxylic acids) were selectively prepared by simply adjusting the base equivalence and ligands in the Cu-catalyzed reactions.

Yu reported enantioselective hydrohydroxymethylation of 1,3-dienes using a copper catalyst (**Scheme 14**, Gui et al., 2017). The reaction was carried out using 1-aryl-1,3-butadiens as the substrates and a hydrosilane as the reducing agent in cyclohexane

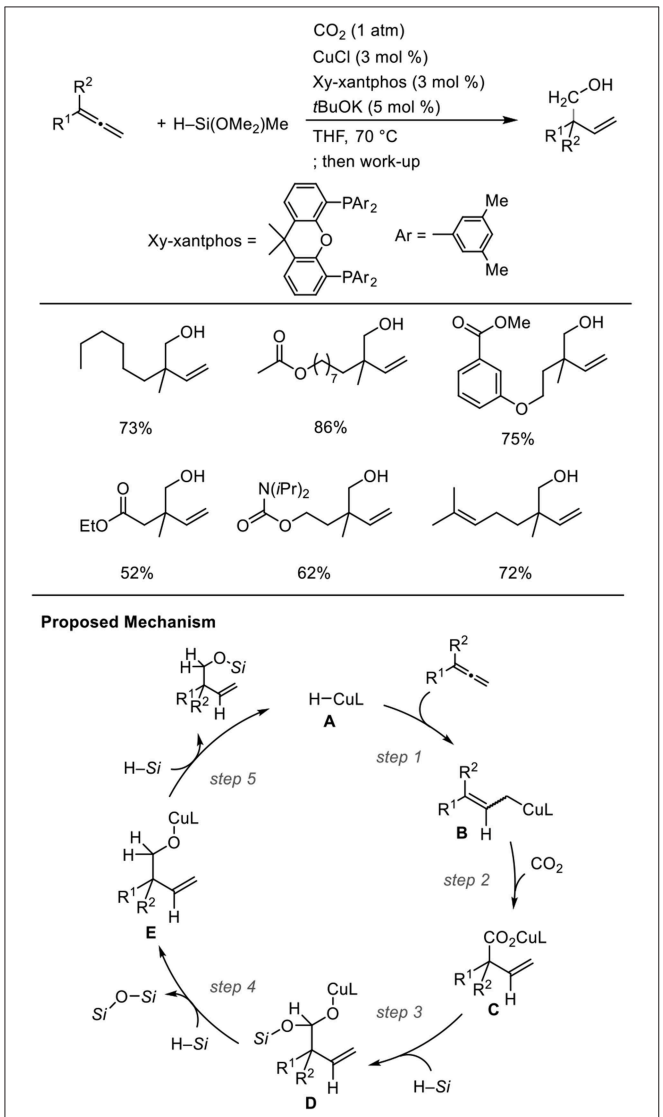

SCHEME 12 | Cu-catalyzed enantioselective hydrohydroxymethylation of 1,2-dienes using a hydrosilane and CO_2 and a proposed mechanism.

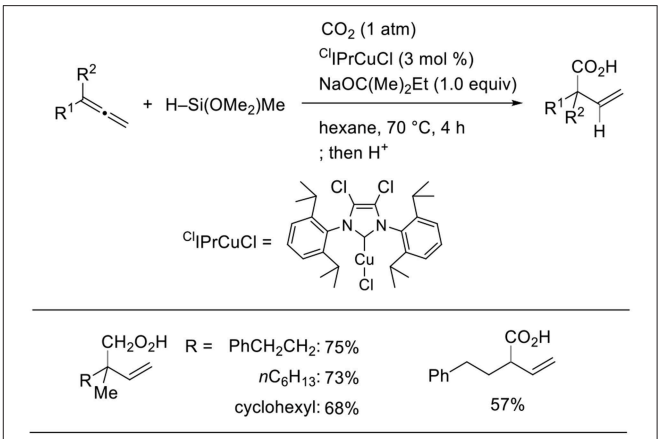

SCHEME 13 | Cu-catalyzed hydrocarboxylation of 1,2-dienes.

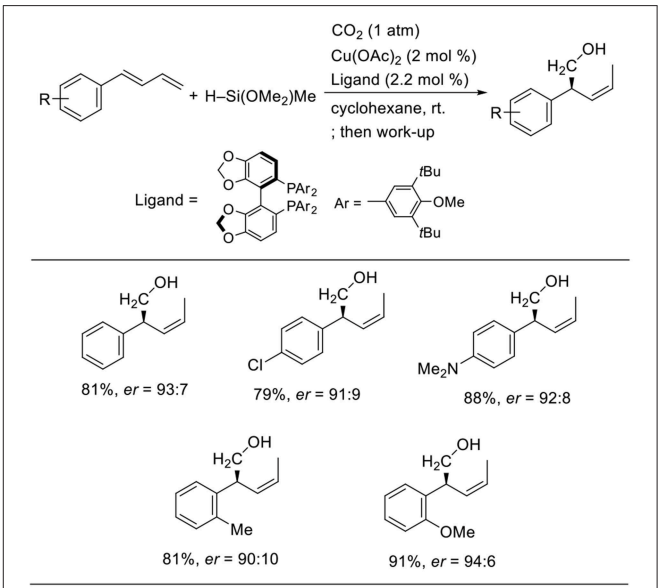

SCHEME 14 | Cu-catalyzed enantioselective hydrohydroxymethylation of 1,3-dienes using a hydrosilane and CO_2.

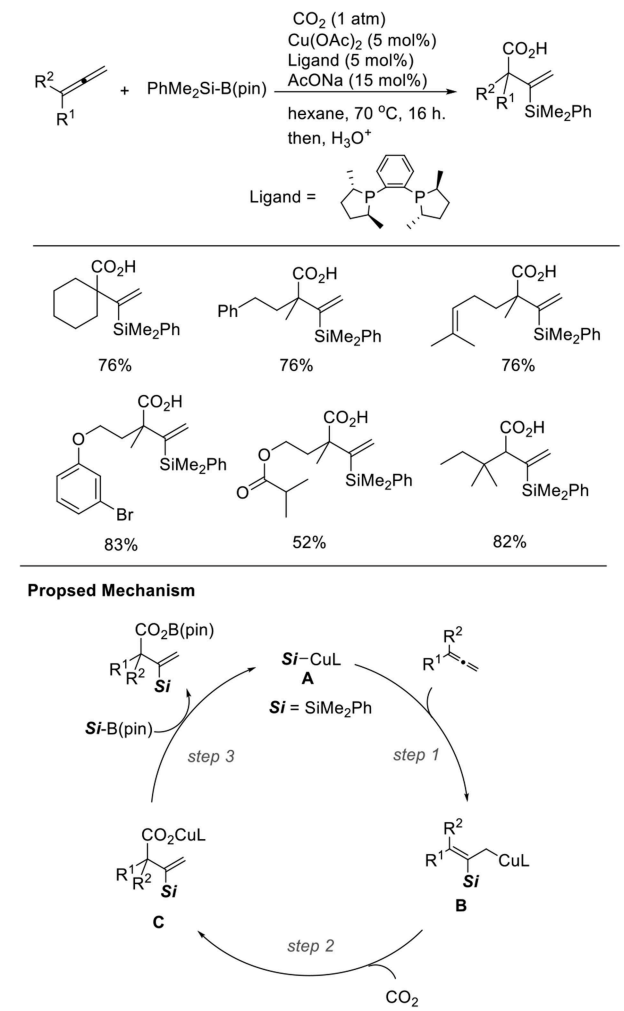

SCHEME 15 | Cu-catalyzed silacarboxylation of 1,2-dienes and a proposed mechanism.

at room temperature in the presence of a copper catalyst bearing 3,5-di-tert-butyl-4-methoxyphenyl (DTBM)-segphos as the ligand. Diverse 1-aryl-1,3-butadienes were used in the reactions, yielding the corresponding products in good-to-high yields with high enantioselectivity. The reactions tolerated several functional groups such as the chloro and amino groups.

Silylcupration to carbon–carbon multiple bonds is a reliable and powerful process, which produces both C–Si and C–Cu bonds. We found the Cu-catalyzed silacarboxylation of 1,2-dienes (**Scheme 15**, Tani et al., 2014). The reaction was carried out by using 1,2-dienes and $PhMe_2Si$–B(pin) under CO_2 (1 atm) with a catalytic amount of $Cu(OAc)_2{\cdot}H_2O$ and *rac*-Me-DuPhos as the ligand. With these reaction conditions, diverse carboxylated vinylsilanes were regioselectively obtained in good yields. The functionalities, such as alkenyl and ester groups were tolerated under the reaction conditions. In the reactions, a β-silyl allyl copper intermediate (**B**) that was generated by the addition of silylcopper (**A**) across an allene (step 1) captured CO_2 (step 2). Then, a carboxylate copper (**C**) reacts with a silylborane to afford **A** (step 3). The choice of an appropriate ligand can efficiently control the regioselectivity. Carboxylated allylsilanes were also obtained using CuCl/AcONa and PCy_3 as the catalyst system.

Conclusions

In conclusion, this short review summarized transition metal-catalyzed carboxylation reactions via allyl metal intermediates. Allylstannanes and allylboronates act as good reagents for Pd- or Cu-catalyzed carboxylation reactions via transmetalation. Transition metal-catalyzed allyl electrophiles via oxidative addition are disclosed herein. Ni complexes successfully produce ligand-controlled regiodivergent carboxylation. Allyl alcohols are possible substrates for Pd- and Ni-catalyzed carboxylation. Substrates, such as 1,2-dienes or 1,3-dienes, are usable for the generation of allyl metal intermediates via the addition of metal reagents. These processes involve hydrocarboxylation, hydrohydroxymethylation, and silacarboxylation. These methods allow efficient syntheses of unsaturated carboxylic acids using CO_2 as the C1 source. In the future, these methodologies will be applied to synthesizing numerous valuable molecules in shorter steps using CO_2.

AUTHOR CONTRIBUTIONS

TF arranged and wrote the manuscript. YT discussed the contents and commented on the manuscript.

REFERENCES

Aresta, M., Dibenedetto, A., and Angelini, A. (2014). Catalysis for the valorization of exhaust carbon: from CO_2 to chemicals, materials, and fuels. Technological use of CO_2. *Chem. Rev.* 114, 1709–1742. doi: 10.1021/cr4002758

Artz, J., Mueller, T. E., Thenert, K., Kleinekorte, J., Meys, R. L., Sternberg, A., et al. (2018). Sustainable conversion of carbon dioxide: an integrated review of catalysis and life cycle assessment. *Chem. Rev.* 118, 434–504. doi: 10.1021/acs.chemrev.7b00435

Borjesson, M., Moragas, T., Gallego, D., and Martin, R. (2016). Metal-catalyzed carboxylation of organic (Pseudo)halides with CO_2. *ACS Catal.* 6, 6739–6749. doi: 10.1021/acscatal.6b02124

Cai, X., and Xie, B. (2013). Carboxylative reactions for the transformation of carbon dioxide into carboxylic acids and derivatives. *Synthesis* 45, 3305–3324. doi: 10.1055/s-0033-1340061

Chen, X.-G., Xu, X.-T., Zhang, K., Li, Y.-Q., Zhang, L.-P., Fang, P., et al. (2018). Transition-metal-catalyzed carboxylation of organic halides andtheir surrogates with carbon dioxide. *Synthesis* 50, 35–48. doi: 10.1055/s-0036-1590908

Chen, Y.-G., Shuai, B., Zhang, X.-J., Fang, P., and Mei, T.-S. (2017). Regioselective Ni-catalyzed carboxylation of allylic and propargylic alcohols with carbon dioxide. *Org. Lett.* 19, 2969–2972, doi: 10.1021/acs.orglett.7b01208

Duong, H. A., Huleatt, P. B., Tan, Q.-W., and Shuying, E. L. (2013). Regioselective copper-catalyzed carboxylation of allylboronates with carbon dioxide. *Org. Lett.* 15, 4034–4037. doi: 10.1021/ol4019375

Feng, X., Sun, A., Zhang, S., Yu, X., and Bao, M. (2013). Palladium-catalyzed carboxylative coupling of benzyl chlorides with allyltributylstannane: remarkable effect of palladium nanoparticles. *Org. Lett.* 15, 108–111, doi: 10.1021/ol303135e

Gui,. Y.-Y., Hu, N., Chen, X.-W., Liao, L.-L., Ju, T., Ye, J.-H., et al. (2017). Highly regio- and enantioselective copper-catalyzed reductive hydroxymethylation of styrenes and 1,3-dienes with CO_2. *J. Am. Chem. Soc.* 139, 17011–17014. doi: 10.1021/jacs.7b10149

Hazari, N., and Heimann, J. E. (2017). Carbon dioxide insertion into group 9 and 10 metal–element σ bonds. *Inorg. Chem.* 56, 13655–13678. doi: 10.1021/acs.inorgchem.7b02315

Huang, K., Sum, C.-L., and Shi, Z.-J. (2011). Transition-metal-catalyzed C–C bond formation through the fixation of carbon dioxide. *Chem. Soc.Rev.* 40, 2435–2452. doi: 10.1039/c0cs00129e

Jiao, K.-J., Li, Z.-M., Xu, X.-T., Zhang, L.-P., Li, Y.-Q., Zhang, K., et al. (2018). Palladium-catalyzed reductive electrocarboxylation of allyl esters with carbon dioxide. *Org. Chem. Front.* 5, 2244–2248. doi: 10.1039/C8QO00507A

Johansson, R., and Wendt, O. F. (2007). Insertion of CO_2 into a palladium allyl bond and a Pd(II) catalyzed carboxylation of allyl stannanes. *Dalton Trans.* 488–492. doi: 10.1039/B614037H

Liu, Q., Wu, L., Jackstell, R., and Beller, M. (2015). Using carbon dioxide as a building block in organic synthesis. *Nat. Commun.* 6:5933. doi: 10.1038/ncomms6933

Luan, Y.-X., and Ye, M. (2018). Transition metal-mediated or catalyzed hydrocarboxylation of olefins with CO_2. *Tetrahedron Lett.* 59, 853–861. doi: 10.1016/j.tetlet.2018.01.035

Medeiros, M. J., Pintaric, C., Olivero, S., and Dunach, E. (2011). Nickel-catalysed electrochemical carboxylation of allylic acetates and carbonates. *Electrochim. Acta*, 56, 4384–4389. doi: 10.1016/j.electacta.2010.12.066

Michigami, K., Mita, T., and Sato, Y. (2017). Cobalt-catalyzed allylic C(sp^3)–H carboxylation with CO_2. *J. Am. Chem. Soc.* 139, 6094–6097. doi: 10.1021/ jacs.7b02775

Mita, T., Higuchi, Y., and Sato, Y. (2015). Highly regioselective palladium-catalyzed carboxylation of allylic alcohols with CO_2. *Chem. Eur. J.* 21, 16391–16394. doi: 10.1002/chem.201503359.

Moragas, T., Cornella, J., and Martin, R. (2014). Ligand-controlled regiodivergent Ni-catalyzed reductive carboxylation of allyl esters with CO_2. *J. Am. Chem. Soc.* 136, 17702–17705. doi: 10.1021/ja509077a

Sekine, K., and Yamada, T. (2016). Silver-catalyzed carboxylation. *Chem. Soc. Rev.* 45, 4524–4532. doi: 10.1039/C5CS00895F

Shi, M., and Nicholas, K. M. (1997). Palladium-catalyzed carboxylation of allyl stannanes. *J. Am. Chem. Soc.* 119, 5057–5058. doi: 10.1021/ja9639832

Takaya, J., and Iwasawa, N. (2008). Hydrocarboxylation of allenes with CO2 catalyzed by silyl pincer-type palladium complex. *J. Am. Chem. Soc.* 130, 15254–15255. doi: 10.1021/ja806677w

Takaya, J., Sasano, K., and Iwasawa, N. (2011). Efficient one-to-one coupling of easily available 1,3-dienes with carbon dioxide. *Org. Lett.* 13, 1698–1701. doi: 10.1021/ol2002094

Tani, Y., Fujihara, T., Terao, J., and Tsuji, Y. (2014). Copper-catalyzed regiodivergent silacarboxylation of allenes with carbon dioxide and a silylborane. *J. Am. Chem. Soc.* 136, 17706–17709. doi: 10.1021/ja512040c

Tani, Y., Kuga, K., Fujihara, T., Terao, J., and Tsuji, Y. (2015). Copper-catalyzed C-C bond-forming transformation of CO_2 to the alcohol oxidation level: selective synthesis of homoallylic alcohols from allenes, CO_2, and hydrosilanes. *Chem. Commun.* 51, 13020–13023. doi: 10.1039/C5CC03932K

Torii, S., Tanaka, H., Hamatani, T., Morisaki, K., Jutand, A., Pfluger, F., et al. (1986). Pd(0)-catalyzed electroreductive carboxylation of aryl halides, β-bromostyrene, and allyl acetates with CO_2. *Chem. Lett.* 1986, 169–172. doi: 10.1246/cl.1986.169

Tortajada, A., Julia-Hernandez, F., Boerjesson, M., Moragas, T., and Martin, R. (2018). Transition-metal-catalyzed carboxylation reactions with carbon dioxide. *Angew. Chem. Int. Ed.* 57, 15948–15982. doi: 10.1002/anie.201803186

Trost, B. M., and Crawley, M. L. (2003). Asymmetric transition metal-catalyzed allylic alkylations: application in total synthesis. *Chem. Rev.* 103, 2921–2944. doi: 10.1021/cr020027w

Trost, B. M., and van Vranken, D. (1996). Asymmetric transition metal-catalyzed allylic alkylations. *Chem. Rev.* 96, 395–422. doi: 10.1021/cr9409804

Tsuji, Y., and Fujihara, T. (2012). Carbon dioxide as a carbon source in organic transformation: carbon–carbon bond forming reactions by transition-metal catalysts. *Chem. Commun.* 48, 9956–9964. doi: 10.1039/C2CC33848C

Wang, S., Du, G., and Xi, C. (2016). Copper-catalyzed carboxylation reactions using carbon dioxide. *Org. Biomol. Chem.* 14, 3666–3676. doi: 10.1039/C6OB00199H

Wu, J., and Hazari, N. (2011). Palladium catalyzed carboxylation of allylstannanes and boranes using CO_2. *Chem. Commun.* 47, 1069–1071. doi: 10.1039 /c0cc03191g

Yu, D., Teong, S. P., and Zhang, Y. (2015). Transition metal complex catalyzed carboxylation reactions with CO_2. *Coord. Chem. Rev.* 293–294, 279–291. doi: 10.1016/j.ccr.2014.09.002

Zhang, L., and Hou, Z. (2013). *N*-Heterocyclic carbene (NHC)–copper-catalysed transformations of carbon dioxide. *Chem. Sci.* 4, 3395–3403. doi: 10.1039/C3SC51070K

Conflict of Interest Statement: The authors declare that the research was conducted in the absence of any commercial or financial relationships that could be construed as a potential conflict of interest.

Copyright © 2019 Fujihara and Tsuji. This is an open-access article distributed under the terms of the Creative Commons Attribution License (CC BY). The use, distribution or reproduction in other forums is permitted, provided the original author(s) and the copyright owner(s) are credited and that the original publication in this journal is cited, in accordance with accepted academic practice. No use, distribution or reproduction is permitted which does not comply with these terms.

frontiers in Chemistry

REVIEW
published: 24 July 2019
doi: 10.3389/fchem.2019.00525

CO_2 Capture and *in situ* Catalytic Transformation

Hong-Chen Fu[1,2], Fei You[2], Hong-Ru Li[1,2] and Liang-Nian He[2]**

[1] College of Pharmacy, Nankai University, Tianjin, China, [2] State Key Laboratory and Institute of Elemento-Organic Chemistry, College of Chemistry, Nankai University, Tianjin, China

The escalating rate of fossil fuel combustion contributes to excessive CO_2 emission and the resulting global climate change has drawn considerable attention. Therefore, tremendous efforts have been devoted to mitigate the CO_2 accumulation in the atmosphere. Carbon capture and storage (CCS) strategy has been regarded as one of the promising options for controlling CO_2 build-up. However, desorption and compression of CO_2 need extra energy input. To circumvent this energy issue, carbon capture and utilization (CCU) strategy has been proposed whereby CO_2 can be captured and *in situ* activated simultaneously to participate in the subsequent conversion under mild conditions, offering valuable compounds. As an alternative to CCS, the CCU has attracted much concern. Although various absorbents have been developed for the CCU strategy, the direct, *in situ* chemical conversion of the captured CO_2 into valuable chemicals remains in its infancies compared with the gaseous CO_2 conversion. This review summarizes the recent progress on CO_2 capture and *in situ* catalytic transformation. The contents are introduced according to the absorbent types, in which different reaction type is involved and the transformation mechanism of the captured CO_2 and the role of the absorbent in the conversion are especially elucidated. We hope this review can shed light on the transformation of the captured CO_2 and arouse broad concern on the CCU strategy.

Keywords: CO_2 capture, activation, conversion, *in situ* catalysis, green chemistry

OPEN ACCESS

Edited by:
Hitoshi Ishida,
Kitasato University, Japan

Reviewed by:
Salah S. Massoud,
University of Louisiana at Lafayette,
United States
Marc Robert,
Paris Diderot University, France
Jinquan Wang,
Institute of Bioengineering and
*Nanotechnology (A*STAR), Singapore*

***Correspondence:**
Hong-Ru Li
lihongru@nankai.edu.cn
Liang-Nian He
heln@nankai.edu.cn

Specialty section:
This article was submitted to
Inorganic Chemistry,
a section of the journal
Frontiers in Chemistry

Received: *11 January 2019*
Accepted: *09 July 2019*
Published: *24 July 2019*

Citation:
Fu H-C, You F, Li H-R and He L-N (2019) CO_2 Capture and in situ Catalytic Transformation. Front. Chem. 7:525. doi: 10.3389/fchem.2019.00525

INTRODUCTION

The demand for energy of the rapid industrialization results in large-scale combustion of fossil fuel, which causes excessive emissions of carbon dioxide. As the detrimental environmental impacts of CO_2 have drawn considerable attention, various strategies have been developed to mitigate CO_2 accumulation in the atmosphere, among which carbon capture and storage/sequestration (CCS) is considered as a promising CO_2 reducing option (Alexander et al., 2015). Nowadays, a plethora of CO_2 absorbents have been developed to facilitate CO_2 capture and desorption. Nevertheless, the extensive energy needed in the absorbent regeneration and CO_2 separation is not conducive to the implementation of CCS strategy.

In contrast to carbon sequestration, converting CO_2 into valuable chemicals could be a sustainable option, which has been proposed by Ciamician as early as 1912 (Ciamician, 1912). In recent decades, CO_2 conversion has attracted considerable concern and been intensively investigated (Rahman et al., 2017). However, in most processes for CO_2 conversion, pure or high pressure CO_2 is needed, implying that the CO_2 from the atmosphere or industrial exhaust cannot be used as C_1 source directly and thus the energy issue in CO_2 capture and separation still remains.

To address the energy penalties associated with CCS strategy and realize the direct fixation of CO_2 from the atmosphere or industrial exhaust, the CO_2 capture and utilization (CCU) strategy, whereby the captured CO_2 is used as a non-toxic, abundant, and sustainable feedstock to produce valuable organic compounds via chemical, electrochemical or photochemical reactions, was proposed and now is flourishing (**Scheme 1**). By now, both organic compounds and functional materials containing the bridging-carbonato metal complexes can be obtained from atmospheric CO_2 using the CCU strategy (Yang et al., 2011; Liu et al., 2012; Massoud et al., 2015). Although realizing the attractive prospect of the CO_2 capture and *in situ* conversion in the industry scale remains a challenge (Zhang and Lim, 2015), the emergence of efficient absorbents and the development of CO_2 transformation will cast light on it. In continuation of our work on the conversion of the captured CO_2 into value-added organic chemicals, this review summarized the recent progress on CO_2 capture and *in situ* conversion into organic products.

To realize the carbon capture and *in situ* conversion strategy, effective absorbents are always necessary. Ideally, the absorbents for CCU strategy should not only capture CO_2, but also activate CO_2 and even the substrate. Thus, the chemical transformation can proceed under mild conditions. Up to now, organic and inorganic bases, *N*-heterocyclic carbenes (NHCs) and *N*-heterocyclic olefins (NHOs), ionic liquids (ILs) and frustrated Lewis pairs (FLPs) have already been applied to CO_2 capture and *in situ* conversion. A plethora of valuable organic chemicals have been obtained through the CCU strategy as shown in **Scheme 2**.

INORGANIC/ORGANIC BASES

Due to the electrophilicity of carbon atom in CO_2, the organic and inorganic bases containing strong nucleophilic atom have been widely used in CO_2 trapping, where the base can interact with CO_2 directly or function as a proton acceptor. The resulting CO_2 capture products i.e., CO_2 adducts have been employed for subsequent synthesis of various valuable chemicals.

Considering the transformations of the captured CO_2 derived from primary and secondary amines and amino alcohols to isocyanates, carbamates, ureas, and oxazolidinones have been concerned by several excellent review papers (Hampe and Rudkevich, 2003; Chaturvedi and Ray, 2006; Yang et al., 2012; Tamura et al., 2014; Wang et al., 2017a,b), here we focus on the transcarboxylation effect and other transformations of the captured CO_2, namely CO_2 derivatives.

Synthesis of Carbamates and Ureas

In the synthesis of carbamates, the aprotic organic bases can function as CO_2 absorbents and transcarboxylation agents. The initial attempt was made by Rossi group, in which CO_2 is trapped by a methanol solution of commercially available tetraethylammonium hydroxide. The resulting tetraethylammonium hydrogen carbonate can be used as a surrogate of CO_2 in the synthesis of carbamate. Meanwhile, the presence of tetraethylammonium ion as counterion increases the nucleophilicity of carbamate anion (Inesi et al., 1998).

Soon after, Franco group has successfully identified the DBU-CO_2 complex via reacting CO_2 with DBU (1,8-Diazabicyclo[5.4.0]undec-7-ene) in anhydrous acetonitrile, implying that DBU can be used as CO_2 trap reagent (Pérez et al., 2002). Moreover, the resulting reactive DBU-CO_2 adduct can be utilized as transcarboxylating reagent for synthesis of *N*-alkyl carbamates. Later, the same group revealed the activation capacity of CO_2 by other bicyclic amidines and observed the inverse relation between the thermal stability and the transcarboxylating activity for the amidine-CO_2 adducts (**Scheme 3**) (Pérez et al., 2004), which is the first time to investigate the activation ability of organic bases to CO_2.

The combination of organic base and alcohol is an efficient CO_2 capture system and the absorbed CO_2 can be *in situ* transformed. The prototypical example is the polyethylene glycol (PEG)/superbase system developed by our group in 2011 (Yang et al., 2011). In the capture step, the superbase is used as a proton acceptor and almost equimolar CO_2 per mole superbase can be absorbed (**Scheme 4**). The resulting liquid amidinium carbonate can directly react with *n*-butylamine at 110°C to afford dibutyl urea in almost quantitative yield (96%) without any other additives. This protocol can be used in the synthesis of other symmetrical urea derivatives.

In the above examples, the captured CO_2 in the transcarboxylating agents can be regarded as the activated CO_2 because the linear structure of CO_2 is converted to bent structure, which is more liable to nucleophilic attack.

Synthesis of Oxazolidinones

The "CO_2 absorption and subsequent transcarboxylation" triggers the research on CO_2 capture and *in situ* transformation. Several years later, M. Yoshida and coworkers use DBU to enrich and activate CO_2 in air and perform the first example of directly transforming atmospheric CO_2 into the substituted 5-vinylideneoxazolidin-2-ones using propargylic substrate 4-(benzylamino)-2-butynyl carbonates or benzoates as a substrate (**Scheme 4**) (Yoshida et al., 2008). In their follow-up work, they further improve the reaction efficiency by utilizing $AgNO_3$ as catalyst and propargylic amines as substrates (**Scheme 4**) (Yoshida et al., 2012).

Inspired by these works, our group designs a series of novel CO_2 capture and activation systems. For example, by employing ammonium iodide as catalyst, the cycloaddition reaction of various aziridines with the captured CO_2 by $NH_2PEG_{150}NH_2$ gives rise to oxazolidinones at 40°C in >94% yield and selectivity (**Scheme 4**) (Yang et al., 2011).

Soon after, we report the first example of steric-hindrance-controlled CO_2 absorption, where the sodium *N*-alkylglycinates and *N*-alkylalaninates dissolved in PEG_{150} are used to capture CO_2, generating the carbamic acid rather than the ammonium carbamate (Liu et al., 2012). *N*-isopropylglycinate is found to be the best absorbent for the rapid and reversible capture of almost equimolar CO_2. Crucially, the captured CO_2 can be activated simultaneously and the resulting carbamic acid can react with either aziridine or propargyl amine to afford oxazolidinones in the presence of NH_4I and AgOAc as a catalyst, respectively (**Scheme 4**).

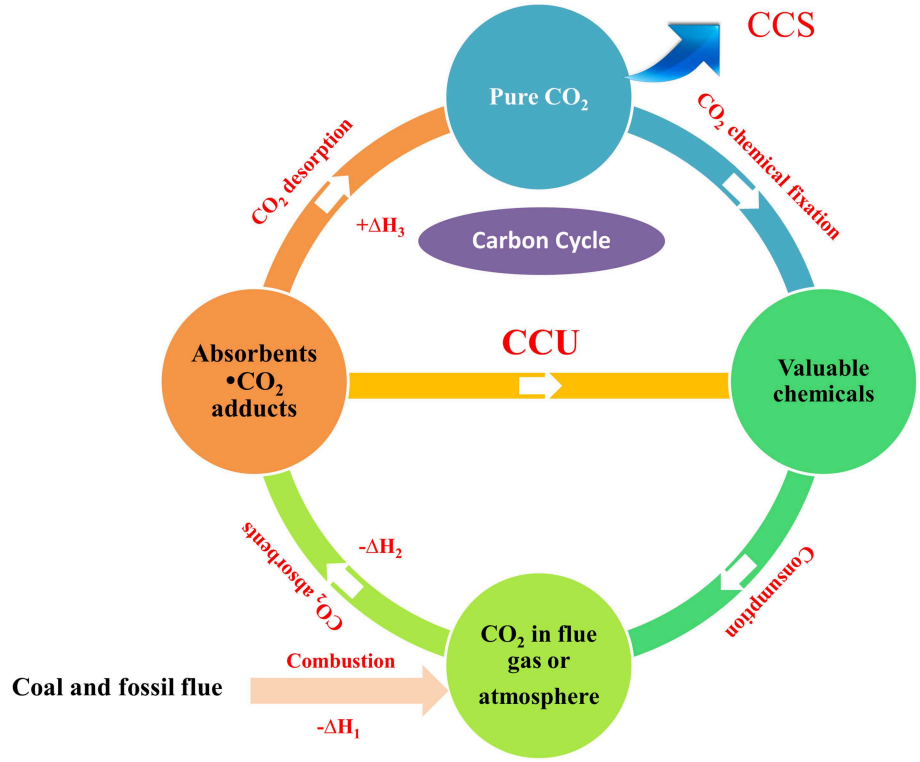

SCHEME 1 | CCU strategy and its importance in carbon cycle.

Motivated by these results, we further develop potassium phthalimide as absorbent to realize equimolar CO_2 capture in PEG_{150}. Moreover, the obtained product can be used as *in situ* transcarboxylating reagent to synthesize oxazolidinone derivatives (**Scheme 4**) (Zhang et al., 2014).

Recently, Hu group subtly designs a CCU example (Yu et al., 2016), in which carbamate salts generated from CO_2 and primary amines are used as substrates. The captured CO_2 not only acts as a reactant but also acts as a protecting reagent for the amine to avoid poisoning of the copper catalyst. By using 5 mol% of CuI as catalyst, carbamate salts can react with aromatic aldehydes and aromatic terminal alkynes, affording the important oxazolidin-2-ones (**Scheme 4**).

Synthesis of β-Oxopropylcarbamates

Based on these inspiring results, our group uses ammonium carbamates as surrogates of carbon dioxide and secondary amines in the three-component synthesis of β-oxopropylcarbamates from propargylic alcohols, secondary amines, and CO_2. Catalyzed by silver (I) catalyst, ammonium carbamates can react with propargylic alcohols to generate β-oxopropylcarbamates under atmospheric pressure (**Scheme 5**) (Song et al., 2015). In this example, the substitution of pure CO_2 with the captured CO_2 can facilitate the reaction running at atmospheric pressures with a broad substrate and reaction application scope. Furthermore, the solid ammonium carbamates are easier to handle and quantify than the volatile amines and gaseous CO_2.

The transcarboxylation is an important transformation strategy for the CO_2 adducts to valuable chemicals. However, for the CO_2 adducts formed by base and CO_2, the transcarboxylation is still limited to the substrates including amines, propargylamines and aziridines. Therefore, novel CO_2 absorbents and extended substrates are expected to facilitate the application of CO_2 adducts as transcarboxylation reagent in CCU strategy. Besides transcarboxylation, the integral transformation of CO_2 capture products is another attractive option in CCU strategy, wherein the ammonium carbamates derived from CO_2 and amines is a promising raw material. Nevertheless, the integral transformation of ammonium carbamates to valuable chemicals remains sporadic and underexplored. Hopefully, more conversion protocols of ammonium carbamates can be designed based on the reactivity of amine and CO_2.

CO_2 Capture and *in situ* Hydrogenation

CO_2 hydrogenation is widely investigated in the CCU strategy because the basic absorbent can react with the resulting formic acid to form formate, thus overcomes the thermodynamic limitation in the hydrogenation of CO_2. In the researches on CO_2 capture and *in situ* hydrogenation, both metal-based homogeneous catalysts (containing Rh-, Ru-, and Fe-based catalysts) and heterogeneous catalysts have been investigated.

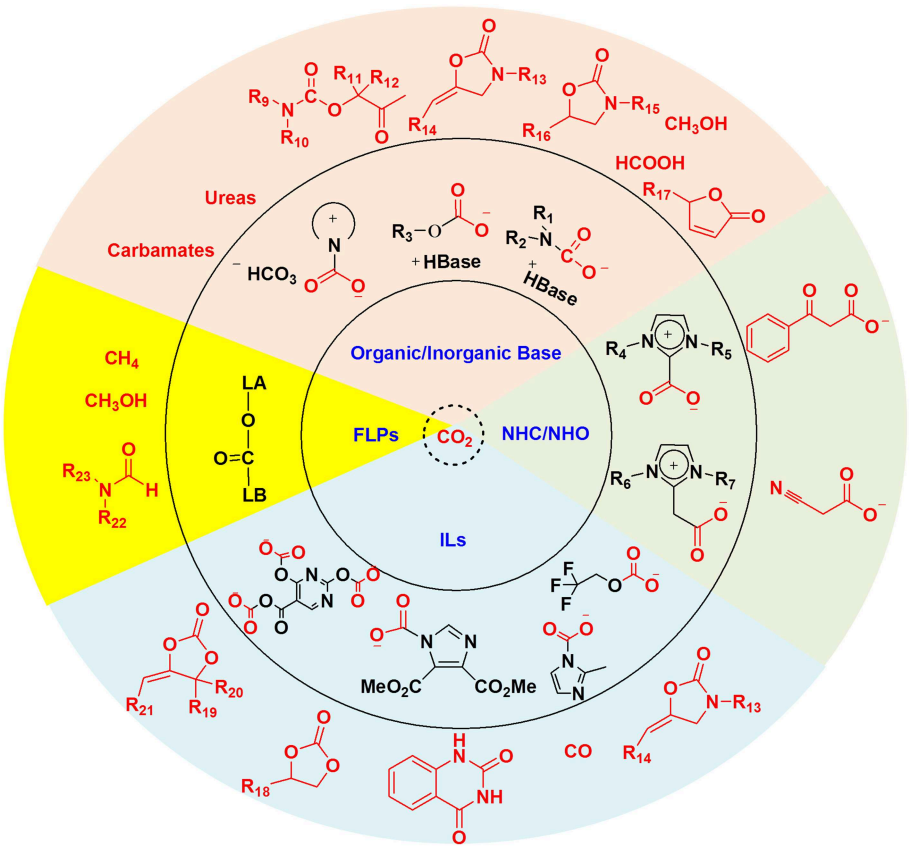

SCHEME 2 | Absorbents, CO_2 adducts, and the resulting valuable chemicals.

Hydrogenation Using Rh-Based Catalysts

The first example of CO_2 capture and *in situ* hydrogenation is reported by our group in 2013, in which polyethyleneimine 600 (PEI_{600}) or the combination of PEI_{600} and ethylene glycol is developed to absorb gaseous CO_2, affording the PEI-CO_2 or ethylene glycol-CO_2 adducts. With $RhCl_3{\cdot}3H_2O/CyPPh_2$ as catalyst, the captured CO_2 can be *in situ* transformed to formate (**Scheme 6**) (Li et al., 2013). Furthermore, direct hydrogenation of ammonium carbamate derived from CO_2, e.g., $DETA^+CO_2^-$ (DETA = diethylenetriamine), ammonium carbonates such as [DBNH] $[OCO_2(C_2H_4O)_3H]$, [DBNH] $[OCO_2CH_2OH]$ (DBN=1,5-diaza bicycle[4.3.0]non-5-ene), is also successfully performed facilitated by this Rh-based catalyst. Notably, a higher reaction rate and better results can be achieved when using the captured CO_2 in the form of ammonium carbonates as feedstock than using equivalent free gaseous CO_2 or ammonium carbamate, implying CO_2 activation upon capture with DBN/PEI and glycol.

After that, we further design a tunable ethoxyl-functionalized amidine to absorb CO_2 in order to avoid the use of volatile proton donor (Li et al., 2014). As an activated form of CO_2, the captured CO_2 in the form of zwitterionic amidinium carbonate is further hydrogenated to formate employing $RhCl_3$/DPEphos as the catalyst (**Scheme 6**). In the same time, we find that the CO_2 capture product of potassium phthalimide in PEG_{150}, can also be *in situ* hydrogenated to formic acid catalyzed by $RhCl_3{\cdot}3H_2O/CyPPh_2$ (**Scheme 6**) (Zhang et al., 2014).

Hydrogenation Using Ru- and Fe-Based Catalysts

Ru-based catalysts are also promising candidates for the hydrogenation of captured CO_2. In the study of Yadav et al., CO_2 is captured by DBU and an alcohol to form the alkyl carbonate ionic liquid and the resulting alkyl carbonate is hydrogenated into $[DBUH^+]$ formate and methyl formate facilitated by $RuCl_2(PPh_3)_3$ (**Scheme 7**) (Yadav et al., 2014). Although the reactive species (i.e., alkyl carbonates or CO_2) cannot be identified at this stage, this result indicates that alkyl carbonates may be a substrate for hydrogenation, in addition to free CO_2.

In 2015, Sanford group combined CO_2 capture to form a carbamate salt with hydrogenation to generate CH_3OH (Rezayee et al., 2015). In their study, $NHMe_2$ is used to capture CO_2 and a homogeneous Ru-based catalyst is used to facilitate the hydrogenation of the captured CO_2 to a mixture of DMF and CH_3OH (**Scheme 7**). Although the formation of carbamate salt can decrease the eletrophilicity of CO_2, causing the captured CO_2 difficult to hydrogenate, the existence of the equilibrium between DMC (Dimethylammonium dimethylcarbamate) and

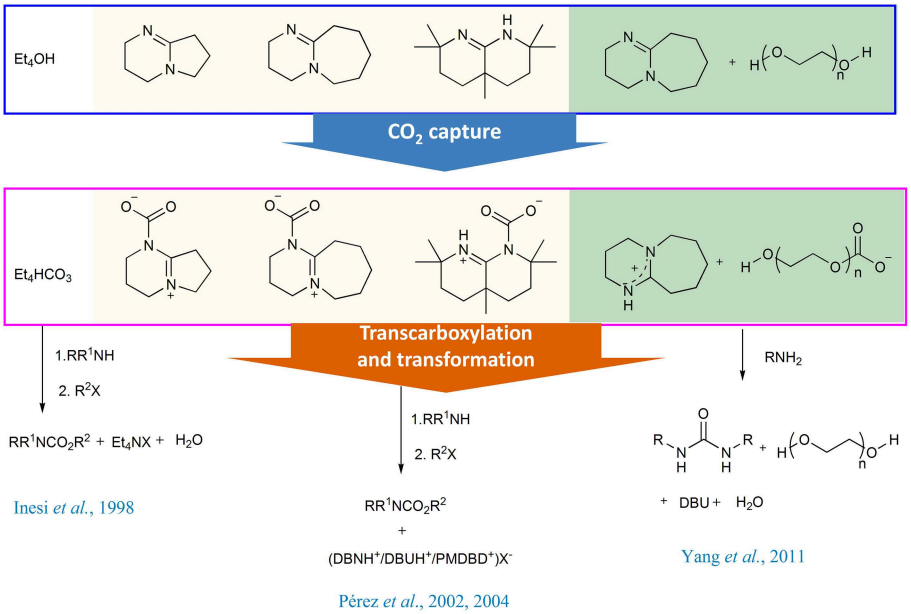

SCHEME 3 | CO_2 capture and transcarboxylation in the synthesis of carbamates and ureas.

CO_2 allows the release of CO_2 possible, thus promoting the CO_2 hydrogenation.

By employing pentaethylenehexamine (PEHA) as CO_2 absorbent and Ru-based complexes as catalyst, Olah and Surya Prakash group develops a process that combines CO_2 capture and the following hydrogenation in an ethereal solvent for the production of MeOH (Kothandaraman et al., 2016a). CO_2 from air can be captured by an aqueous solution of PEHA and up to 61% yield of MeOH can be obtained in the triglyme/H_2O mixtures at 155°C in the following hydrogenation (**Scheme 7**). The resulting MeOH can be easily separated by simple distillation from the reaction mixture.

Later, the same group captures CO_2 with aqueous amine solution and then *in situ* hydrogenates the resulting ammonium bicarbonate/carbonate utilizing Ru- and Fe-based pincer complexes in a biphasic solvent system (water/Me-THF) (Kothandaraman et al., 2016b). The superbases (DABCO, TMG, and DBU) shows to be efficient for both CO_2 capture and hydrogenation with more than 90% yield of formate under moderate reaction conditions (50 bar H_2 at 55°C) (**Scheme 7**). The biphasic system features easy separation of product and catalyst and the catalyst can be reused for at least five cycles.

Hydrogenation Using Heterogeneous Catalysts

Besides homogeneous catalysts, the heterogeneous catalysts were also used in the hydrogenation of CO_2 capture products. For example, H. Lin group applies Pd/AC catalyst to the hydrogenation of CO_2 capture products originated from ammonia. In the hydrogenation step, the dependence of the activity of CO_2 capture products on the solvent is observed (Su et al., 2015a,b). For example, the ammonium bicarbonate in water and ammonium carbamate in 70 wt% ethanol-water solution can offer more than 90% yield of formate under high H_2 pressure (5.52 and 2.75 MPa, respectively) at 20°C. The ammonium carbonate presents similar activity with ammonium carbamate. Identification of the species in the reactant solutions suggests the bicarbonate ion and ethyl carbonate ion, instead of the carbamate ion, are the activation forms of CO_2 in the hydrogenation (**Scheme 8**). Coincidently, Enthaler finds that sodium bicarbonate in methanol can be hydrogenated to sodium formate catalyzed by the nickel hydride complex while CO_2 cannot be hydrogenated in the identical conditions, which further confirms the activity of the captured CO_2 in hydrogenation (Enthaler et al., 2015).

Mertens and coworkers report the *in situ* hydrogenation of the captured CO_2 using Cu/ZnO-Al_2O_3 as catalyst under retrieval of the CO_2 capture reagent N,N-diethylethanolamine (DEEA) (Reller et al., 2014). In the reaction, DEEA can also function as a trapping reagent for the resulting formic acid and drives the hydrogenation forward. The authors find that the generation of the products 2-diethylaminoethylformate and methanol can be regulated by the reaction temperature (**Scheme 9**). The combination of CO_2 capture and hydrogenation realizes the energy integration by using the reaction heat of CO_2 hydrogenation in the energy demanding CO_2 stripping process.

In addition to the liquid absorption system, the alkali metal and alkali earth metal based solid CO_2 adsorbents are also developed (Li et al., 2010, 2011; Lee et al., 2011) and applied in the CCU strategy recently. Duyar et al. design a series of novel dual function materials (DFM) consisting of the catalyst and adsorbent components to couple the endothermic CO_2 desorption step with the exothermic hydrogenation of CO_2 (Duyara et al., 2016). The results show that DFM with the composition of 5% Ru 10% K_2CO_3/Al_2O_3 and 5% Ru

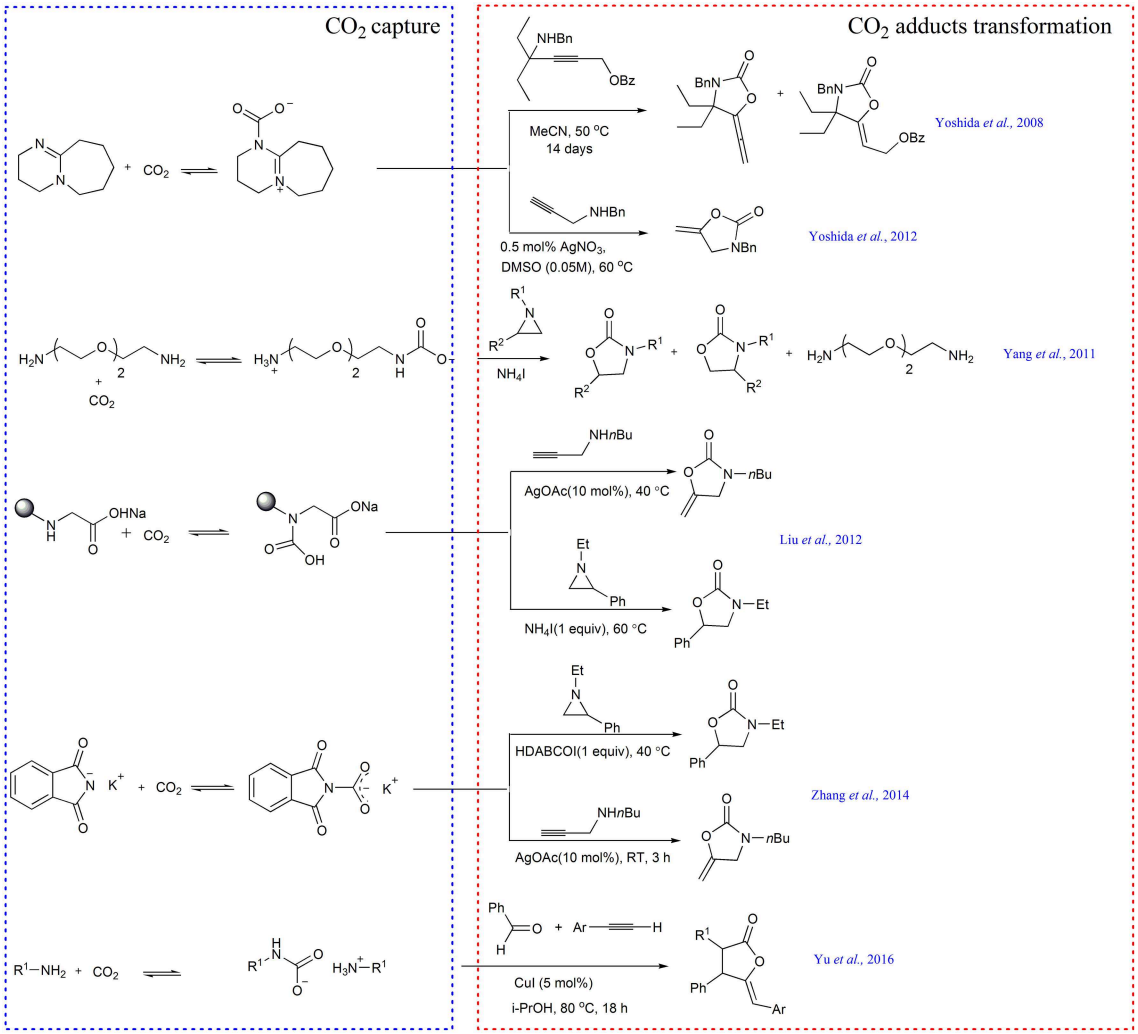

SCHEME 4 | CO_2 capture and transformation to oxazolidinones.

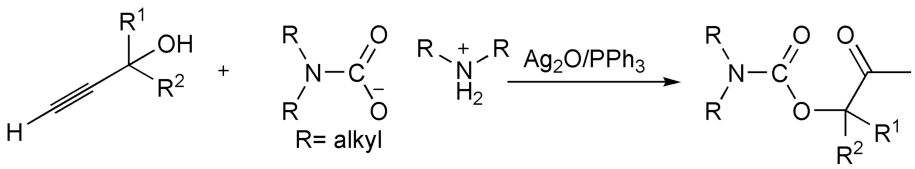

SCHEME 5 | Synthesis of β-oxopropylcarbamates from propargylic alcohols and ammonium carbamates.

10% Na_2CO_3/Al_2O_3 have a methanation capacity of 0.91 and 1.05 g-mol/kg DFM, respectively. Similarly, A. Urakawa group develops the catalyst consisting of earth-abundant chemical elements ($FeCrCu/K/MgO–Al_2O_3$), which can trap CO_2 from fuel gas in the form of surface carbonates and subsequently hydrogenated the adsorbed CO_2 to CO (Bobadilla et al., 2016). Accordingly, these DFMs are identified as promising candidates for CO_2 capture and direct utilizations.

Hydrogenation of captured CO_2 to energy chemicals can facilitate turning hydrogen gas to liquid fuel as well as realize carbon cycling. Albeit the hydrogenation of captured CO_2 has been extensively investigated and various capture reagents and catalysts have been developed, the identification of CO_2 activation forms is still controversial. For example, the CO_2 capture products alkyl carbonate ammonium salts are considered as the activated CO_2 species (Li et al., 2013, 2014; Su et al.,

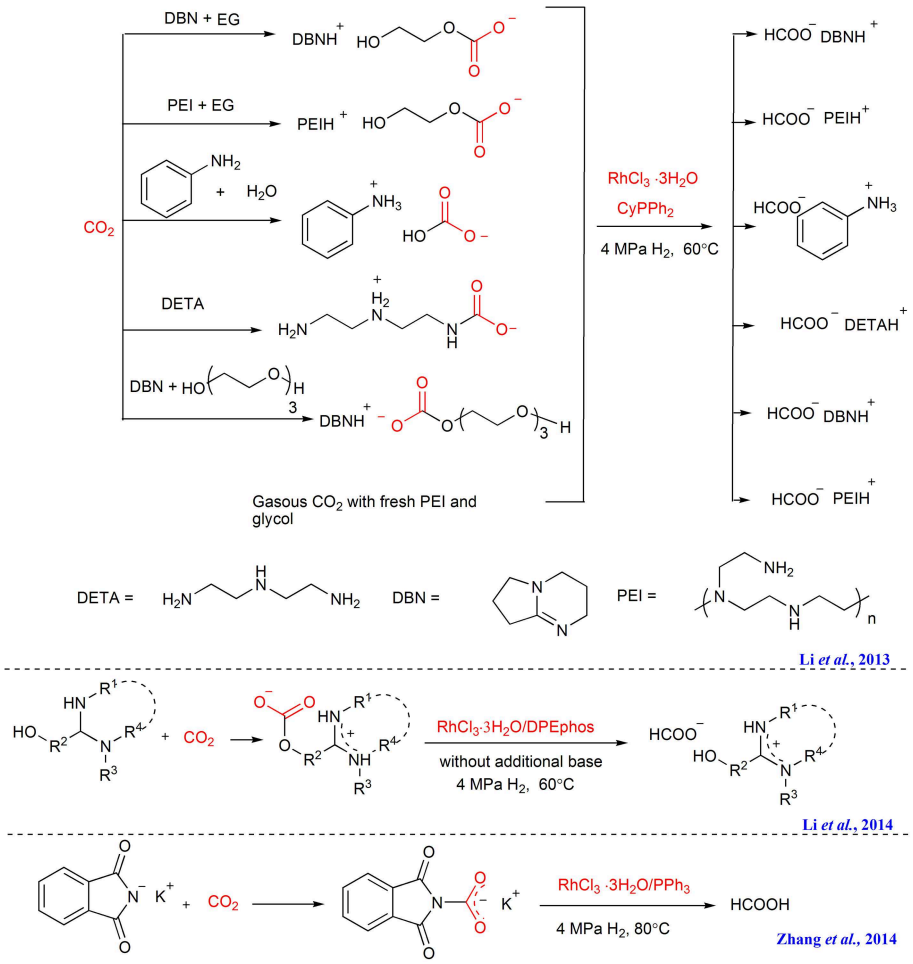

SCHEME 6 | CO_2 capture and Rh promoted CO_2 adducts hydrogenation.

2015a,b). However, the results of Jessop group show that [DBUH][OC(O)OMe] salt is less active than free CO_2 when using $RuCl(O_2CMe)(PMe_3)_4$ as catalyst in MeOH solution (Munshi et al., 2002). Thus, the relationship between the activity of CO_2 capture products and the catalyst is still underdeveloped.

N-HETEROCYCLIC CARBENES AND *N*-HETEROCYCLIC OLEFINS

It has been verified that *N*-heterocyclic carbenes and *N*-heterocyclic olefins can react with CO_2, forming the CO_2 adduct which can be used as "all-in-one" carboxylating agent (Zhou et al., 2008; Kelemen et al., 2014; Dong et al., 2015; Talapaneni et al., 2015; Finger et al., 2016; Saptal and Bhanage, 2016). For example, Tommasi group shows the CO_2 adduct 1-butyl-3-methylimidazolium-2-carboxylate and 1,3-dimethylimidazolium-2-carboxylate behaves as active CO_2-carriers and reacted with CH_3OH and acetophenone for the synthesis of methylcarbonate and benzoylacetate. The other organic compounds with active hydrogen (acetone, cyclohexanone, benzylcyanide, and propargyl alcohols) can also be carboxylated with these CO_2-transfer agents for the synthesis of carboxylates of pharmaceutical interest (Tommasi and Sorrentino, 2005, 2006, 2009) (**Scheme 10**). Similarly, the transcarboxylation of $IPrCO_2$ (1,3-bis(2,6-diisopropylphenyl)-imidazolum-2-carboxylate) to acetophenone with $NaBPh_4$ to yield sodium benzoylacetate and direct dicarboxylation of MeCN using I^tBuCO_2 (1,3-bis(tert-butyl)-imidazolium-2-carboxylate) are also reported (Van Ausdall et al., 2011) (**Scheme 10**).

The transcarboxylation capacity of NHOs-CO_2 adducts has also been verified by 1-ethyl-3-methyl-imidazolium-2-methylenecarboxylate through realizing the C-C coupling of CO_2 and MeCN (**Scheme 10**) (Finger et al., 2016). In this transcarboxylation process, the basicity of NHOs should be strong enough to abstract proton from the CH acid.

As highly efficient carboxylating agents, the NHC-CO_2 and NHO-CO_2 complexes can be easily obtained by reacting NHCs or NHOs with atmospheric CO_2. However, instead of serving as absorbent, NHCs and NHOs are usually used as catalysts to promote the conversion of pure CO_2 by forming transient NHC-CO_2 and NHO-CO_2 complexes (Kayaki et al., 2009; Zhou

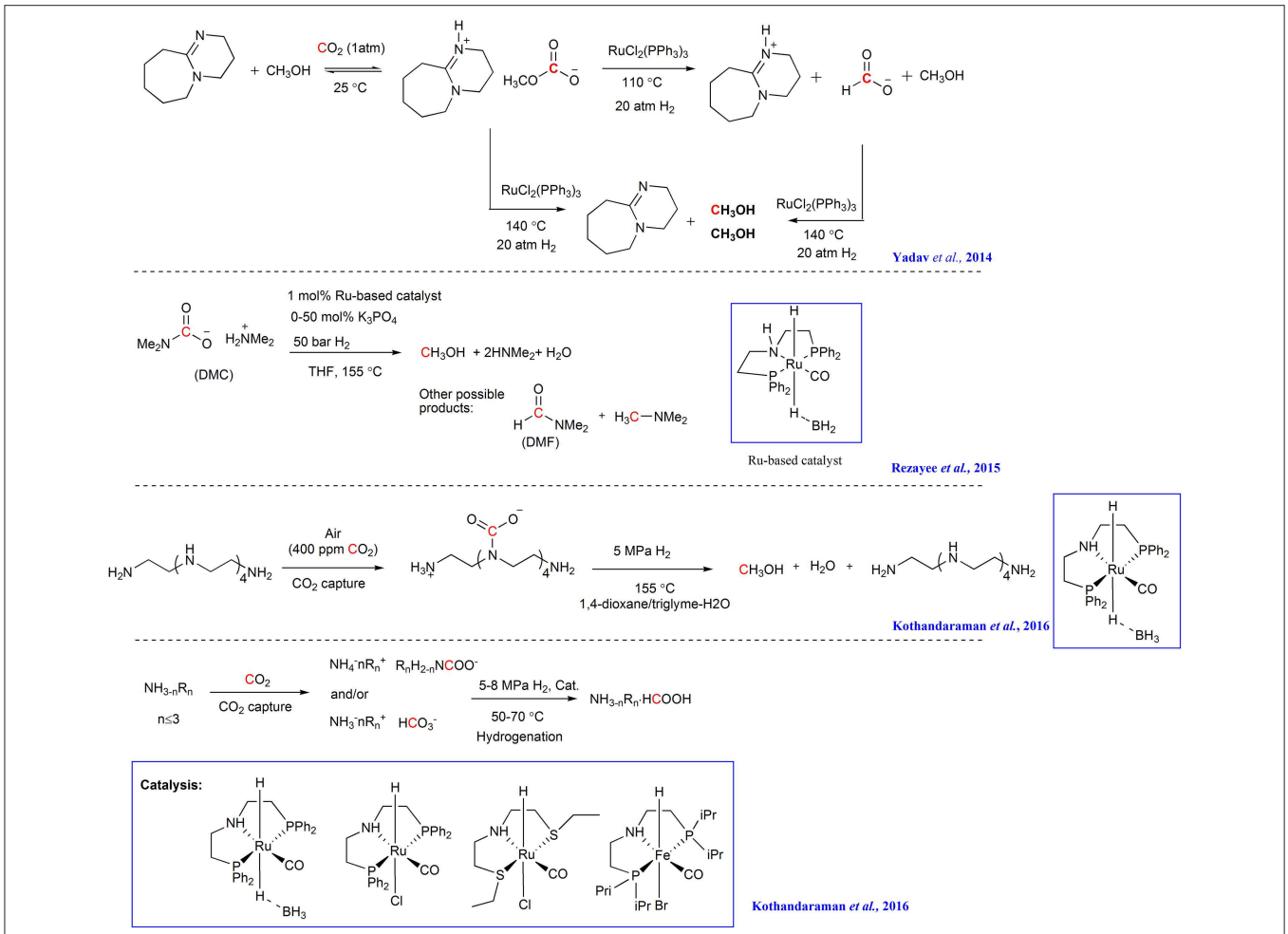

SCHEME 7 | CO_2 capture and Ru promoted CO_2 adducts hydrogenation.

et al., 2017). The reason is that NHCs and NHOs are sensitive to air and moisture thus they cannot be used as absorbents for CO_2 in air and industry exhaust. Nowadays, it is found that the imidazolium ionic liquids containing basic anion can absorb CO_2, producing imidazolium carboxylates (Gurau et al., 2011; Wang and Wang, 2016). Considering the imidazolium ionic liquids are stable to air and moisture, it opens a new way for the utilization of NHC-CO_2 and NHO-CO_2 complexes in CCU strategy.

IONIC LIQUIDS (ILS)

Ionic liquids (ILs) offer a new opportunity for developing novel CO_2 capture reagents (Huang and Rüther, 2009; Gurkan et al., 2010; Wang et al., 2011; Yang and He, 2014). Especially, the active site-containing ionic liquids can trap and activate CO_2 through chemical absorption. Besides, IL can also function as catalyst in CO_2 transformation (Lang et al., 2016; Zhang et al., 2017; Xia et al., 2018). Therefore, it is promising to combine the multiple roles of ILs in CCU strategy. Up to now, cyclocarbonates, oxazolidinones and quinazoline-2,4-(1H,3H)-diones have been synthesized using ILs as CO_2 absorbents and catalysts.

Wang group performs a series of investigation on ILs-based CO_2 capture and conversion. For example, they design bifunctionalized ionic liquids to capture and simultaneously fix CO_2 in the simulation of fuel gas to cyclic carbonates (**Scheme 11**) (Luo et al., 2016). The cation can capture CO_2 and the anion I^- can activate the substrate to facilitate CO_2 insertion. In the presence of a small amount of water, the yield of product can be improved, making this reaction more applicable to industrial exhaust.

Later, the same group finds that the basicity of anion of ILs is very important for CO_2 capture and transformation. A hydroxyl functionalized aprotic ionic liquid shows high efficiency in synthesis of quinazoline-2,4(1H,3H) -diones from atmospheric CO_2. The captured CO_2 instead of atmospheric CO_2 is also used and only 13% yield is obtained, being ascribed to the strong interaction between $[Im]^-$ and CO_2 (**Scheme 11**) (Shi et al., 2018). They also demonstrates the feasibility of using captured CO_2 as starting material in their another report, where the CO_2 captured by azole-type anion $[DEIm]^-$ renders a high

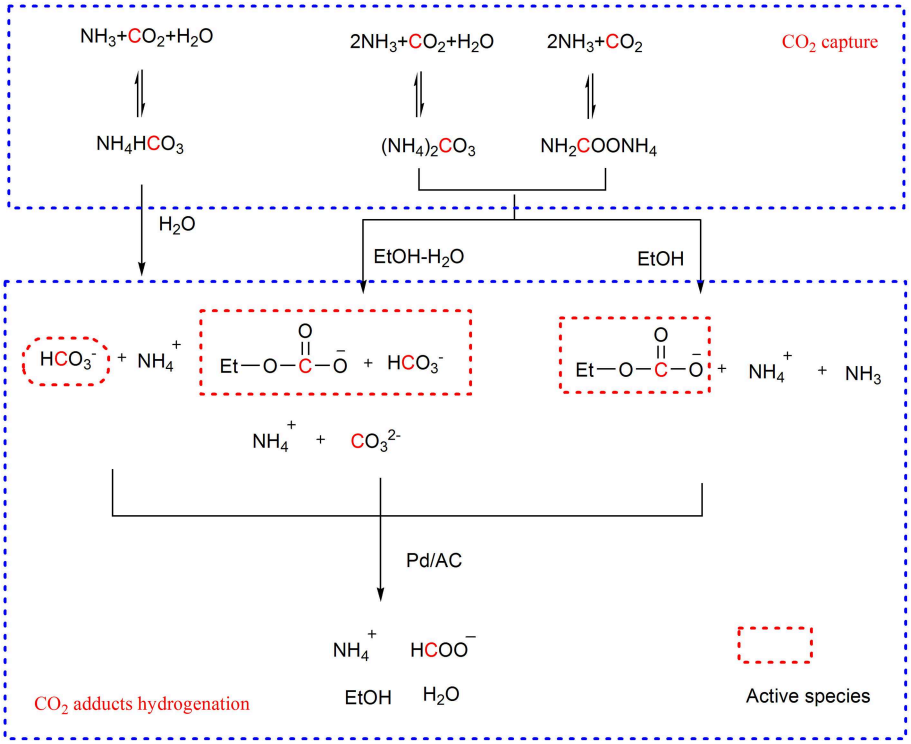

SCHEME 8 | CO_2 capture and Pd/AC facilitated CO_2 adducts hydrogenation.

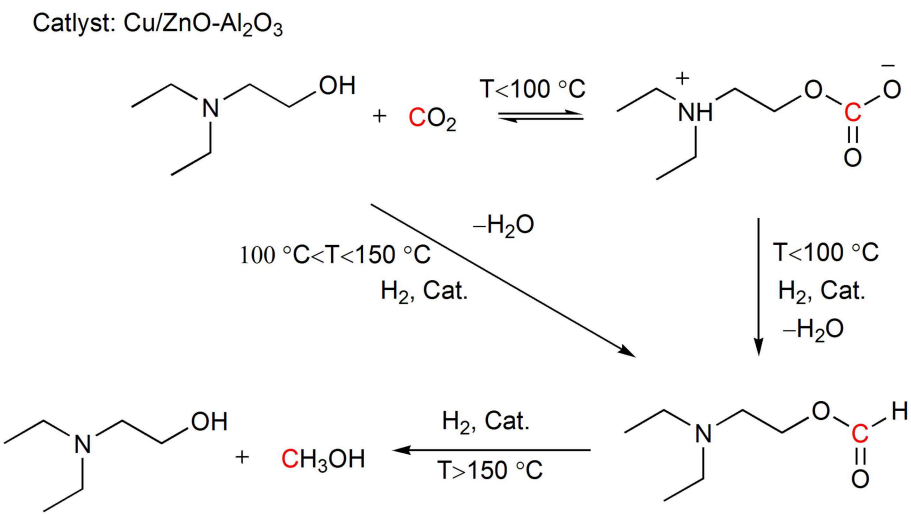

SCHEME 9 | Cu/ZnO-Al_2O_3 promoted CO_2 adducts hydrogenation.

yield of alkylidene carbonates in the carboxylative cyclization of propargyl alcohol due to the weak interaction between CO_2 and the anion (**Scheme 11**) (Chen et al., 2016).

Liu group reports that azole-anion-based ILs with the $[Bu_4P]^+$ cation can capture CO_2. With appropriate substrates, the forming carbamate intermediates can be transformed into the α-alkylidenecyclic carbonate, quinazoline-2,4(1H,3H)-diones and benzimidazolone without other catalysts (**Scheme 11**) (Zhao et al., 2016). Later, the same group reveals that a series of tetrabutylphosphonium ($[Bu_4P]^+$)-based ILs with multiple-site for CO_2 capture and activation in their anions can be used in CO_2 capture and conversion, wherein the IL $[Bu_4P]_3$[2,4-OPym-5-Ac] shows the optimal performance in preparation of α-alkylidene cyclic carbonates from propargylic alcohol substrate

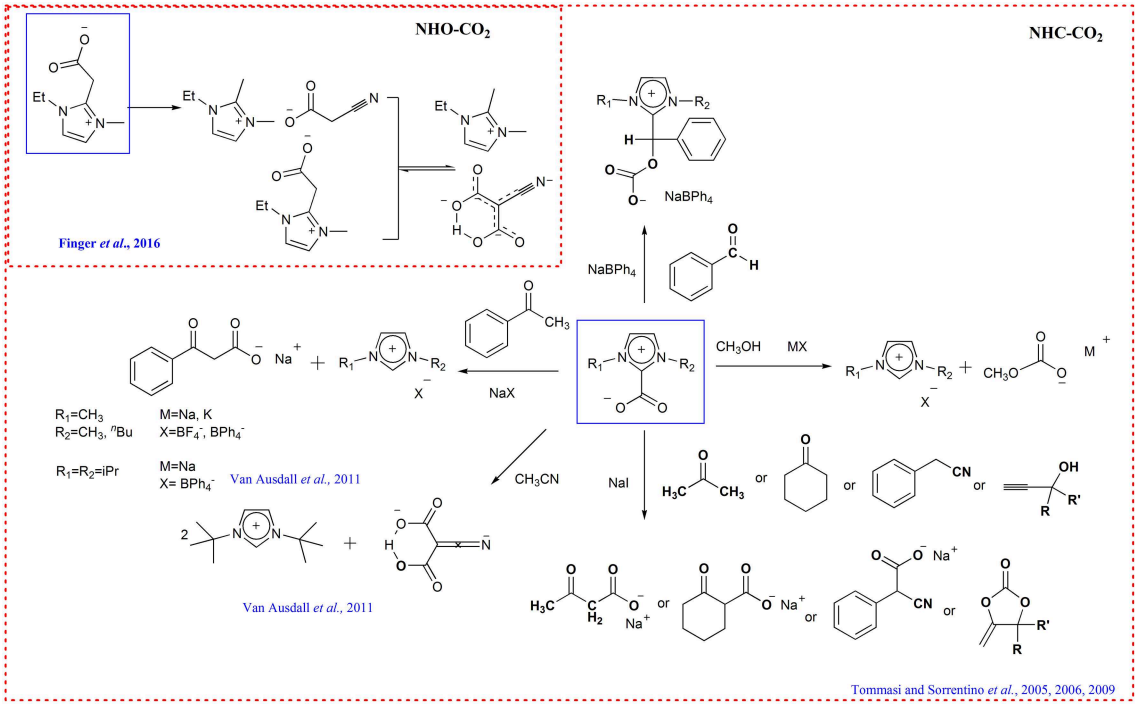

SCHEME 10 | Transcarboxylation of NHC-CO_2 and NHO-CO_2 adducts.

(Wu et al., 2017). The resulting polycarbonates derived from CO_2 and the anion is proved to be the key intermediate in this reaction (**Scheme 11**).

The ILs [HDBU][MIm] and [HDBU][TFE] can capture CO_2 and also show catalytic activity to the reaction of CO_2 and propargylic amines for the synthesis of 2-oxazolidinones and the reaction of CO_2 with 2-aminobenzonitrile derivatives to synthesis quinazoline-2,4-(1H,3H)-diones. By enhancing the mass transfer with gas-liquid laminar flow continuous-flow microreactor, the simultaneous capture and fixation CO_2 to 2-oxazolidinones and quinazoline-2,4-(1H,3H)-diones is realized (**Scheme 11**) (Vishwakarma et al., 2017).

Due to the dual function as CO_2 absorbents and conversion catalysts, ionic liquids can realize the transformation of captured CO_2 with several kinds of substrates. Furthermore, the non-volatility characteristic of ionic liquids can facilitate product separation. Thus, the ionic liquids are considered as promising absorbents for the CCU process.

FRUSTRATED LEWIS PAIRS (FLPS)

The CO_2 capture capacity of FLPs has been reported soon after the FLPs concept was in 2006 proposed (Welch et al., 2006; Momming et al., 2009; Travis et al., 2013; Weicker and Stephan, 2015; Wolff et al., 2016). As early as 2010, Stephan group revealed that 1:2 mixtures of $PMes_3/AlX_3$ (X = Cl or Br) in bromobenzene can react with CO_2, forming CO_2 adduct which can be converted to CH_3OH with ammonia borane as reductant (**Scheme 12**) (Ménard and Stephan, 2010). In the same year, Piers group found that CO_2 captured by FLP consisting of 2,2,6,6-tetramethylpiperidine (TMP) and $B(C_6F_5)_3$ can be reduced to methane with triethylsilane (**Scheme 12**) (Berkefeld et al., 2010). Soon, it is found that the FLP composed by bis-borane 1,2-$C_6H_4(BCl_2)_2$ and P*t*Bu_3 can capture CO_2 and the forming capture product can be reduced to methanol by reductant such as amine-borane Me_2NHBH_3 or $[C_5H_6Me_4NH_2][HB(C_6F_5)_2(C_7H_{11})]$ (**Scheme 12**) (Sgro et al., 2012). Wang group reports the FLP comprising of bis(2,4,6-tris(trifluoromethyl)phenyl)borane and a secondary amine (such as HN*i*Pr_2 or $HNEt_2$) readily reacts with CO_2 at 80°C, affording carbamate boryl esters which can function as an intramolecular FLP to activate H_2, affording ammonium borylformate salt and formamide adducts (**Scheme 12**) (Lu et al., 2013).

Recently, Yan group incorporates FLP acceptor and donor into the styrene-based monomers, respectively to prepare two diblock copolymers consisting of the complementary FLP blocks and common polystyrene block. These two diblock copolymers can bind CO_2, forming nanoparticle. The nanoparticle is then used as CO_2 reservoir and catalyst to facilitate the formylation of amines with phenylsilane (**Scheme 12**) (Chen et al., 2018).

The CO_2 capture and H_2 activation capacity makes FLPs attractive for CCU strategy, especially for the hydrogenation of captured CO_2. However, in the current study, the FLPs promoted CO_2 hydrogenation encounters difficulty in FLPs regeneration (Ashley et al., 2009). By now, the FLPs are merely used as CO_2 capture reagents and reductants are still needed. Thus, the hydrogen activation ability of FLPs hasn't

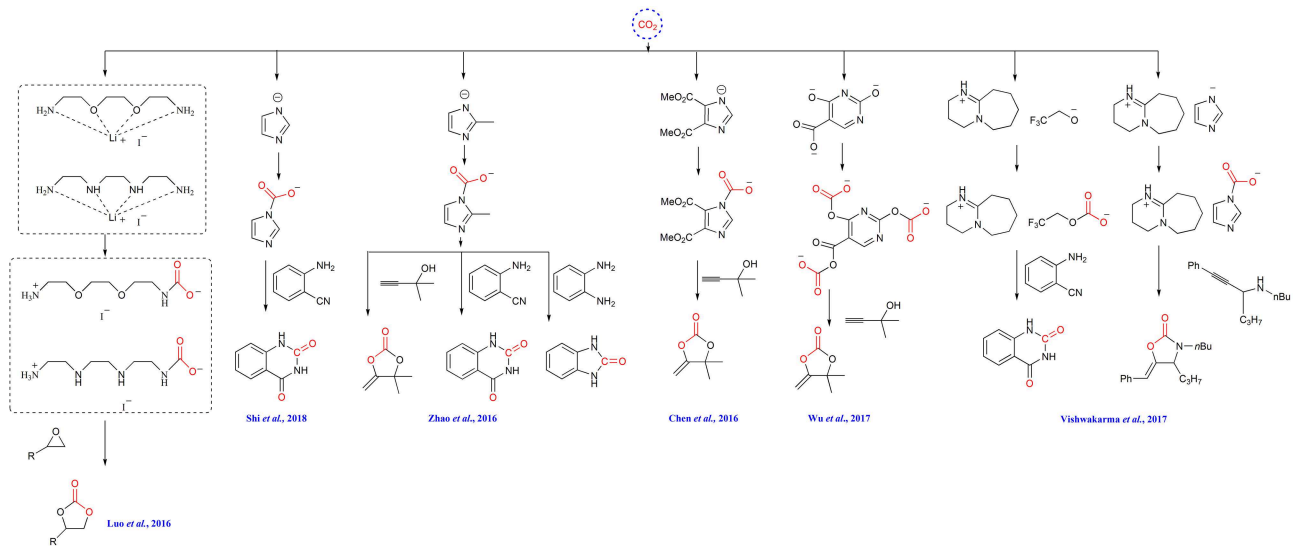

SCHEME 11 | ILs used in CO_2 capture and conversion.

been utilized. Recently, the breakthrough is made by Jazzar and Bertrand group. By combining the copper catalyst and Lewis pair, hydrogenation of carbon dioxide into formate is realized (Romero et al., 2018). Latter, X. Hu and Y. Wu group reports the first catalytic hydrogenation process of CO_2 to formate using transition metal free catalyst ($B(C_6F_5)_3/M_2CO_3$, M = Na, K, and Cs) (Zhao et al., 2019). These results open new vistas in the field of FLPs facilitated CO_2 capture and hydrogenation.

CATALYST DESIGN FOR DIRECT CONVERSION OF DILUTED CO_2

In addition to the CO_2 capture and transformation strategy, there are also examples that the CO_2 from waste streams can be directly converted by designing catalysts that tolerate to the contaminants in the waste streams such as exogenous water, nitrogen, SO_2, amine etc. For example, Williams et al. reports the synthesis of poly(cyclohexylene carbonate) using the power station generated CO_2 facilitated by the homogeneous dinuclear Zn or Mg catalysts, which is stable in the presence of contaminants from gas streams (Chapman et al., 2015) (**Scheme 13**). D'Elia and Basset group develops the combination of early transition metal halides (Y, Sc, Zr) and TBAB to quantitatively convert CO_2 from diluted streams and produce cyclic organic carbonates (Barthel et al., 2016). The features of metal-organic frameworks (MOFs) to selectively capture and catalyze CO_2 conversion make them a new type of platform for diluted CO_2 transformation. Recently, Hong group design and synthesize an acid-base resistant Cu(II)-MOF which can convert CO_2 from simulated post-combustion flue gas into corresponding cyclic carbonates (Liang et al., 2017). In direct conversion of diluted CO_2, the stability of the catalysts to the contaminants in the gas streams is crucial to the success of the process.

CONCLUSION AND OUTLOOK

The past 10 years have witnessed great advances in CO_2 capture and *in situ* conversion. Different CO_2 absorbents including inorganic and organic bases, NHCs, and NHOs, ILs, FLPs and polymeric functional materials have been employed in this field. As an emerging field, much effort is still desired to explore the potential conversion of the captured CO_2.

Considering amines and CO_2 can be involved in diverse reactions, it is hoped that the conversion of ammonia carbamate can be further extended to other valuable products besides isocyanates, carbamates and ureas.

On the other hand, although the hydrogenation of CO_2 captured by inorganic/organic bases and the combination of base and alcohol has been investigated, the hydrogenation of CO_2 captured by ILs and/or FLPs remains sporadic and underexplored. In light of the successful electrochemical reduction of IL-captured CO_2 and hydrogenation of CO_2 in ILs (Zhang et al., 2008, 2009; Wesselbaum et al., 2012; Scott et al., 2017), it is reasonable to conclude that the captured CO_2 by IL can be hydrogenated by designing appropriate catalyst. Besides, the breakthrough in FLP-mediated CO_2 hydrogenation opens new possibilities for FLP-based CO_2 capture and transformation (Romero et al., 2018; Zhao et al., 2019).

Another important transformation pathway for CO_2 adducts derived from reacting with amines, NHCs, NHOs and ILs is transcarboxylation reaction in the synthesis of cyclocarbonates, oxazolidinones and quinazoline-2,4-(1H,3H)-diones. It is foreseeable that the application of these transcarboxylating reagents will be investigated continuously with the emergence of new CO_2 conversion reactions.

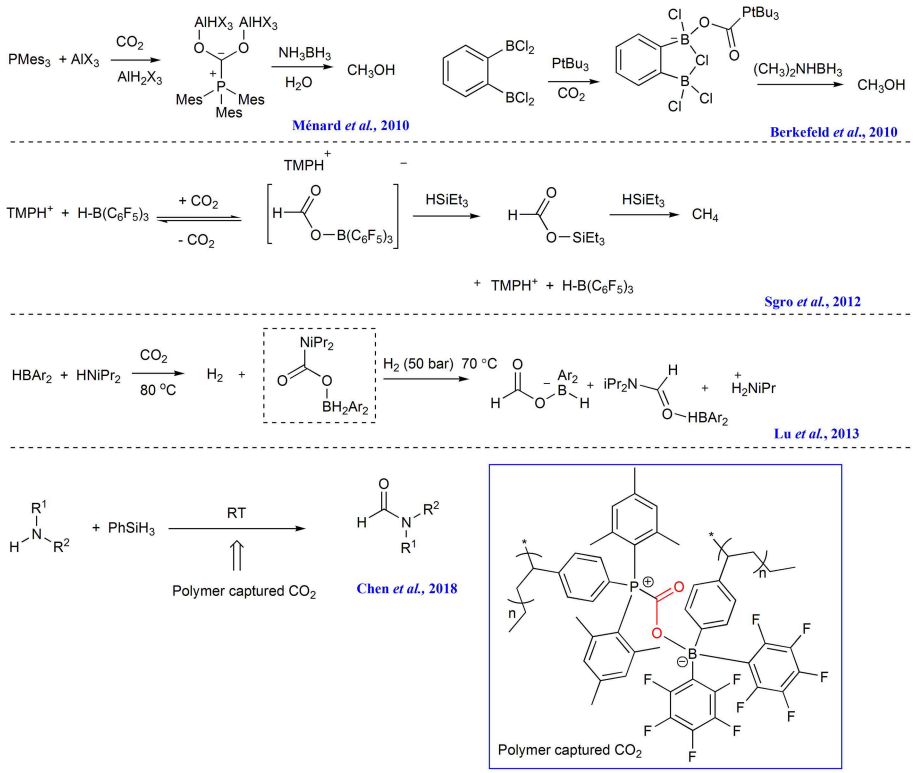

SCHEME 12 | FLPs employed in CO_2 capture and transformation.

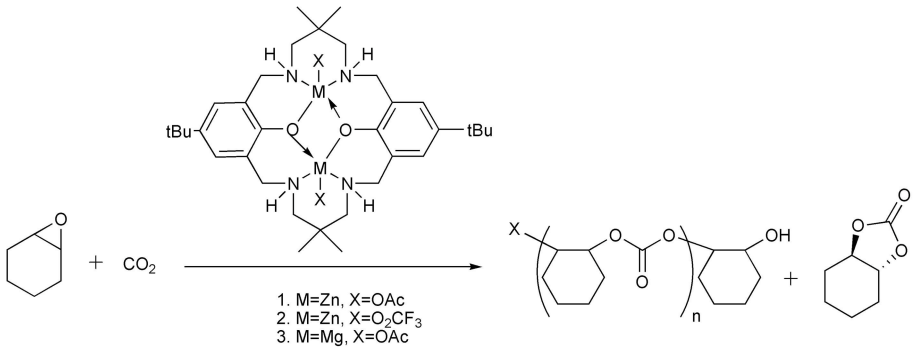

SCHEME 13 | Homogeneous dinuclear Zn or Mg catalysts used for the production of poly(cyclohexene carbonate).

Although a plethora of CO_2 absorbents has been developed and valuable products can be obtained from the resulting CO_2 adducts by different strategy, however, the cost and feasibility must be considered from the viewpoint of industrial application. With this in mind, amines and ionic liquids are considered as promising absorbents for the CCU strategy. For amine absorbents, their features of high absorbing capacity and comerical availability are attractive for industrial application. Besides, the CO_2 adducts derived from amines and CO_2 are non-volatile liquids or solids, which can be used as starting materials instead of the volatile amines and CO_2 gas to develop the gas free progress. For ionic liquid- based CO_2 absorbents, the acceptable cost, tunable structure as well as their high CO_2 capture capacity make them competent to the commercial CCU process. Moreover, the ionic liquids are nonvolatile and the corrosion of equipment can be avoided by subtly design the structure of ionic liquids, all of which can facilitate the industry operability.

In summary, the CO_2 capture and *in situ* catalytic transformation is still in its infancy. We hope this review can inspire the extensive research on CO_2 capture and *in situ* transformation, which will benefit for the design of efficient CO_2 capture and utilization system (CCU) and realize the

valorization of diluted CO_2 in waste gas streams or directly from the atmosphere.

AUTHOR CONTRIBUTIONS

All authors contributed for the writing of the manuscript. L-NH designed this proposal and determined the contents. H-RL wrote the Abstract, Introduction, Conclusion, and Outlook parts. H-CF wrote the Inorganic/organic bases and Ionic liquids parts. FY wrote *N*-heterocyclic carbenes and *N*-heterocyclic olefins and frustrated lewis pairs parts. H-RL and L-NH revised the manuscript.

FUNDING

This research was funded by National Key Research and Development Program (2016YFA0602900), the National Natural Science Foundation of China (21672119).

ACKNOWLEDGMENTS

We thank the Ministry of Science and Technology of China (National Key Research and Development Program) and the National Natural Science Foundation of China.

REFERENCES

Alexander, O., Grube, T., Schiebahn, S., and Stolten, D. (2015). Closing the loop: captured CO_2 as a feedstock in the chemical industry. *Energy Environ. Sci.* 8, 3283–3297. doi: 10.1039/c5ee02591e

Ashley, A. E., Thompson, A. L., and O'Hare, D. (2009). Non-metal-mediated homogeneous hydrogenation of CO_2 to CH_3OH. *Angew. Chem. Int. Ed.* 48, 9839–9843. doi: 10.1002/anie.200905466

Barthel, A., Saih, Y., Gimenez, M., Pelletier, J. D. A., Kühn, F. E., D'Elia, V., et al. (2016). Highly integrated CO_2 capture and conversion: direct synthesis of cyclic carbonates from industrial flue gas. *Green Chem.* 18, 3116–3123. doi: 10.1039/c5gc03007b

Berkefeld, A., Piers, W. E., and Parvez, M. (2010). Tandem frustrated lewis pair/tris(pentafluorophenyl)borane-catalyzed deoxygenative hydrosilylation of carbon dioxide. *J. Am. Chem. Soc.* 132, 10660–10661. doi: 10.1021/ja105320c

Bobadilla, L. F., Riesco-García, J. M., Penelás-Pérez, G., and Urakawa, A. (2016). Enabling continuous capture and catalytic conversion of flue gas CO 2 to syngas in one process. *J. CO_2 Util.* 14, 106–111. doi: 10.1016/j.jcou.2016.04.003

Chapman, A. M., Keyworth, C., Kember, M. R., Lennox, A. J. J., and Williams, C. K. (2015). Adding value to power station captured CO_2: tolerant Zn and Mg homogeneous catalysts for polycarbonate polyol production. *ACS Catal.* 5, 1581–1588. doi: 10.1021/cs501798s

Chaturvedi, D., and Ray, S. (2006). Versatile use of carbon dioxide in the synthesis of carbamates. *Monatsh. Chem.* 137, 127–145. doi: 10.1007/s00706-005-0423-7

Chen, K. H., Shi, G. L., Dao, R. N., Mei, K., Zhou, X. Y., Li, H. R, et al. (2016). Tuning the basicity of ionic liquids for efficient synthesis of alkylidene carbonates from CO_2 at atmospheric pressure. *Chem. Commun.* 52, 7830–7833. doi: 10.1039/c6cc02853e

Chen, L., Liu, R. J., and Yan, Q. (2018). Polymer meets frustrated lewis pair: second-generation CO_2 -responsive nanosystem for sustainable CO_2 conversion. *Angew. Chem. Int. Ed.* 57, 9336–9340. doi: 10.1002/anie.201804034

Ciamician, G. (1912). The Photochemistry of the future. *Science* 36, 385–394.

Dong, L., Wen, J., and Li, W. Y. (2015). A theoretical investigation of substituent effects on the stability and reactivity of *N*-heterocyclic olefin carboxylates. *Org. Biomol. Chem.* 13, 8533–8544. doi: 10.1039/c5ob01021g

Duyara, M. S., Wang, S., Arellano-Treviño, M. A., and Farrauto, R. J. (2016). CO_2 utilization with a novel dual function material (DFM) for capture and catalytic conversion to synthetic natural gas: an update. *J. CO_2 Util.* 15, 65–71. doi: 10.1016/j.jcou.2016.05.003

Enthaler, S., Brück, A., Kammer, A., Junge, H., Irran, E., and Gülak, S. (2015). Exploring the reactivity of nickel pincer complexes in the decomposition of formic acid to CO_2/H_2 and the hydrogenation of $NaHCO_3$ to HCOONa. *ChemCatChem* 7, 65–69. doi: 10.1002/cctc.201402716

Finger, L. H., Guschlbauer, J., Harms, K., and Sundermeyer, J. (2016). *N*-heterocyclic olefin-carbon dioxide and -sulfur dioxide adducts: structures and interesting reactivity patterns. *Chem. Eur. J.* 22, 16292–16303. doi: 10.1002/chem.201602973

Gurau, G., Rodríguez, H., Kelley, S. P., Janiczek, P., Kalb, R. S., and Rogers, R. D. (2011). Demonstration of chemisorption of carbon dioxide in 1,3-dialkylimidazolium acetate ionic liquids. *Angew. Chem. Int. Ed.* 50, 12024–12026. doi: 10.1002/anie.201105198

Gurkan, B. E., de la Fuente, J. C., Mindrup, E. M., Ficke, L. E., Goodrich, B. F., Price, E. A., et al. (2010). Equimolar CO_2 absorption by anion-functionalized ionic liquids. *J. Am. Chem. Soc.* 132, 2116–2117. doi: 10.1021/ja909305t

Hampe, E. M., and Rudkevich, D. M. (2003). Exploring reversible reactions between CO_2 and amines. *Tetrahedron* 59, 9619–9625. doi: 10.1016/j.tet.2003.09.096

Huang, J. H., and Rüther, T. (2009). Why are ionic liquids attractive for CO_2 absorption? An overview. *Aust. J. Chem.* 62, 298–308. doi: 10.1071/CH08559

Inesi, A., Mucciante, V., and Rossi, L. (1998). A convenient method for the synthesis of carbamate esters from amines and tetraethylammonium hydrogen carbonate. *J. Org. Chem.* 63, 1337–1338. doi: 10.1021/jo971695y

Kayaki, Y., Yamamoto, M., and Ikariya, T. (2009). N-Heterocyclic carbenes as efficient organocatalysts for CO_2 fixation reactions. *Angew. Chem. Int. Ed.* 48, 4194–4197. doi: 10.1002/anie.200901399

Kelemen, Z., Peter-Szabo, B., Szekely, E., Holloczki, O., Firaha, D. S., Kirchner, B., et al. (2014). An abnormal *N*-heterocyclic carbene-carbon dioxide adduct from imidazolium acetate ionic liquids: the importance of basicity. *Chem. Eur. J.* 20, 13002–13008. doi: 10.1002/chem.201402912

Kothandaraman, J., Goeppert, A., Czaun, M., Olah, G. A., and Prakash, G. K. (2016a). Conversion of CO_2 from air into methanol using a polyamine and a homogeneous ruthenium catalyst. *J. Am. Chem. Soc.* 138, 778–781. doi: 10.1021/jacs.5b12354

Kothandaraman, J., Goeppert, A., Czaun, M., Olah, G. A., and Surya Prakash, G. K. (2016b). CO_2 capture by amines in aqueous media and its subsequent conversion to formate with reusable ruthenium and iron catalysts. *Green Chem.* 18, 5831–5838. doi: 10.1039/c6gc01165a

Lang, X. D., Yu, Y. C., Li, Z. M., and He, L. N. (2016). Protic ionic liquids-promoted efficient synthesis of quinazolines from 2-aminobenzonitriles and CO_2 at ambient conditions. *J. CO_2 Util.* 15, 115–122. doi: 10.1016/j.jcou.2016.03.002

Lee, J. B., Eom, T. H., Oh, B. S., Baek, J. I., Ryu, J., Jeon, W. S., et al. (2011). CO_2 capture from flue gas using potassium-based dry regenerable sorbents. *Energy Procedia.* 4, 1494–1499. doi: 10.1016/j.egypro.2011.02.016

Li, L., Li, Y., Wen, X., Wang,F., Zhao, N., Xiao, F., et al. (2011). CO_2 Capture over $K_2CO_3/MgO/Al_2O_3$ dry sorbent in a fluidized bed. *Energy Fuels* 25, 3835–3842. doi: 10.1021/ef200499b

Li, L., Wen, X., Fu, X., Wang, F., Zhao, N., Xiao, F., et al. (2010). MgO/Al_2O_3 sorbent for CO_2 capture. *Energy Fuels* 24, 5773–5780. doi: 10.1021/ef100817f

Li, Y. N., He, L. N., Lang, X. D., Liu, X. F., and Zhang, S. (2014). An integrated process of CO_2 capture and *in situ* hydrogenation to formate using a tunable ethoxyl-functionalized amidine and Rh/bisphosphine system. *RSC Adv.* 4, 49995–50002. doi: 10.1039/c4ra08740b

Li, Y. N., He, L. N., Liu, A. H., Lang, X. D., Yang, Z. Z., Yu, B., et al. (2013). *In situ* hydrogenation of captured CO_2 to formate with polyethyleneimine and Rh/monophosphine system. *Green Chem.* 15, 2825–2829. doi: 10.1039/C3GC41265B

Liang, L., Liu, C., Jiang, F., Chen, Q., Zhang, L., Xue, H., et al. (2017). Carbon dioxide capture and conversion by an acid-base resistant metal-organic framework. *Nat. Commun.* 8:1233. doi: 10.1038/s41467-017-01166-3

Liu, A. H., Ma, R., Song, C., Yang, Z. Z., Yu, A., Cai, Y., et al. (2012). Equimolar CO_2 capture by N-substituted amino acid salts and subsequent conversion. *Angew. Chem. Int. Ed.* 51, 11306–11310. doi: 10.1002/anie.201205362

Lu, Z., Wang, Y., Liu, J., Lin, Y. J., Li, Z. H., and Wang, H. (2013). Synthesis and reactivity of the CO_2 adducts of amine/bis(2,4,6-tris(trifluoromethyl)phenyl)borane pairs. *Organometallics* 32, 6753–6758. doi: 10.1021/om4007246

Luo, X., Chen, K., Li, H., and Wang, C. (2016). The capture and simultaneous fixation of CO_2 in the simulation of fuel gas by bifunctionalized ionic liquids. *Int. J. Hydrogen Energy* 41, 9175–9182. doi: 10.1016/j.ijhydene.2015.12.223

Massoud, S. S, Louka,F. R., Al-Hasan, M. A., Vicenteb, R., and Mautner, F. A. (2015). Magneto-structural properties of carbonato-bridged copper(II) complexes: fixation of atmospheric CO2. *N. J. Chem.* 39, 5944–5952. doi: 10.1039/c5nj00285k

Ménard, G., and Stephan, D. W. (2010). Room temperature reduction of CO_2 to methanol by Al-based frustrated lewis pairs and ammonia borane. *J. Am. Chem. Soc.* 132, 1796–1797. doi: 10.1021/ja9104792

Momming, C. M., Otten, E., Kehr, G., Frohlich, R., Grimme, S., Stephan, D. W., et al. (2009). Reversible metal-free carbon dioxide binding by frustrated lewis pairs. *Angew. Chem. Int. Ed.* 48, 6643–6646. doi: 10.1002/anie.200901636

Munshi, P., Main, A. D., Linehan, J. C., Tai, C. C., and Jessop, P. G. (2002). Hydrogenation of carbon dioxide catalyzed by ruthenium trimethylphosphine complexes: the accelerating effect of certain alcohols and amines. *J. Am. Chem. Soc.* 124, 7963–7971. doi: 10.1021/ja0167856

Pérez, E. R., Santos, R. H. A., Gambardella, M. T. P., Macedo, L. G. M., de Rodrigues-Filho, U. P., Launay, J., et al. (2004). Activation of carbon dioxide by bicyclic amidines. *J. Org. Chem.* 69, 8005–8011. doi: 10.1021/jo049243q

Pérez, E. R., Silva, M. O., da Costa, V. C., Rodrigues-Filho, U. P., and Franco, D. W. (2002). Efficient and clean synthesis of *N*-alkyl carbamates by transcarboxylation and O-alkylation coupled reactions using a DBU–CO_2 zwitterionic carbamic complex in aprotic polar media. *Tetrahedron Lett.* 43, 4091–4093. doi: 10.1016/S0040-4039(02)00697-4

Rahman, F. A., Aziz, M. M. A., Saidur, R., Bakar, W. A. W. A., Hainin, M. R., Putrajaya, R., et al. (2017). Pollution to solution: capture and sequestration of carbon dioxide (CO_2) and its utilization as a renewable energy source for a sustainable future. *Renew. Sust. Energ. Rev.* 71, 112–126. doi: 10.1016/j.rser.2017.01.011

Reller, C., Pöge, M., Lißner, A., and Mertens, F. O. R. L. (2014). CO_2 capture and hydrogenation in one process step. *Environ. Sci. Technol.* 48, 14799–14804. doi: 10.1021/es503914d

Rezayee, N. M., Huff, C. A., and Sanford, M. S. (2015). Tandem amine and ruthenium-catalyzed hydrogenation of CO_2 to methanol. *J. Am. Chem. Soc.* 137, 1028–1031. doi: 10.1021/ja511329m

Romero, E. A., Zhao, T., Nakano, R., Hu, X. B., Wu, Y. T., Jazzar, R., et al. (2018). Tandem copper hydride–lewis pair catalysed reduction of carbon dioxide into formate with dihydrogen. *Nat. Catal.* 1, 743–747. doi: 10.1038/s41929-018-0140-3

Saptal, V. B., and Bhanage, B. M. (2016). *N*-Heterocyclic olefins as robust organocatalyst for the chemical conversion of carbon dioxide to value-added chemicals. *ChemSusChem* 9, 1980–1985. doi: 10.1002/cssc.201600467

Scott, M., Molinos, B. B., Westhues, C, Francik, G., and Leitner, W. (2017). Aqueous biphasic systems for the synthesis of formates by catalytic CO_2 hydrogenation: integrated reaction and catalyst separation for CO_2-scrubbing solutions. *ChemSusChem* 10, 1085–1093. doi: 10.1002/cssc.201601814

Sgro, M. J., Domer, J., and Stephan, D. W. (2012). Stoichiometric CO_2 reductions using a bis-borane-based frustrated lewis pair. *Chem. Commun.* 48, 7253–7255. doi: 10.1039/c2cc33301e

Shi, G. L., Chen, K. H., Wang, Y. T., Li, H. R., and Wang, C. M. (2018). Highly efficient synthesis of quinazoline-2,4(1H,3H)-diones from CO_2 by hydroxyl functionalized aprotic Ionic Liquids. *ACS Sustain. Chem. Eng.* 6, 5760–5765. doi: 10.1021/acssuschemeng.8b01109

Song, Q. W., Zhou, Z. H., Yin, H., and He, L. N. (2015). Silver(I)-catalyzed synthesis of β-oxopropylcarbamates from propargylic alcohols and CO_2 surrogate: a gas-free process. *ChemSusChem* 8, 3967–3972. doi: 10.1002/cssc.201501176

Su, J., Lu, M., and Lin, H. F. (2015a). High yield production of formate by hydrogenating CO_2 derived ammonium carbamate/carbonate at room temperature. *Green Chem.* 17, 2769–2773. doi: 10.1039/c5gc00397k

Su, J., Yang, L. S., Lu, M., and Lin, H. F. (2015b). Highly efficient hydrogen storage system based on ammonium bicarbonate/formate redox equilibrium over palladium nanocatalysts. *ChemSusChem* 8, 813–816. doi: 10.1002/cssc.201403251

Talapaneni, S. N., Buyukcakir, O., Je, S. H., Srinivasan, S., Seo, Y., Polychronopoulou, K., et al. (2015). Nanoporous polymers incorporating sterically confined N-heterocyclic carbenes for simultaneous CO_2 capture and conversion at ambient pressure. *Chem. Mater.* 27, 6818–6826. doi: 10.1021/acs.chemmater.5b03104

Tamura, M., Honda, M., Nakagawa, Y., and Tomishige, K. (2014). Direct conversion of CO_2 with diols, aminoalcohols and diamines to cyclic carbonates, cyclic carbamates and cyclic ureas using heterogeneous catalysts. *J. Chem. Technol. Biotechnol.* 89, 19–33. doi: 10.1002/jctb.4209

Tommasi, I., and Sorrentino, F. (2005). Utilisation of 1,3-dialkylimidazolium-2-carboxylates as CO_2-carriers in the presence of Na^+ and K^+: application in the synthesis of carboxylates, monomethylcarbonate anions and halogen-free ionic liquids. *Tetrahedron Lett.* 46, 2141–2145. doi: 10.1016/j.tetlet.2005.01.106

Tommasi, I., and Sorrentino, F. (2006). Synthesis of 1,3-dialkylimidazolium-2-carboxylates by direct carboxylation of 1,3-dialkylimidazolium chlorides with CO_2. *Tetrahedron Lett.* 47, 6453–6456. doi: 10.1016/j.tetlet.2006.06.106

Tommasi, I., and Sorrentino, F. (2009). 1,3-dialkylimidazolium-2-carboxylates as versatile *N*-heterocyclic carbene–CO_2 adducts employed in the synthesis of carboxylates and α-alkylidene cyclic carbonates. *Tetrahedron Lett.* 50, 104–107. doi: 10.1016/j.tetlet.2008.10.107

Travis, A. L., Binding, S. C., Zaher, H., Arnold, T. A. Q., Buffet, J. C., and O'Hare, D. (2013). Small molecule activation by frustrated lewis pairs. *Dalton Trans.* 42, 2431–2437. doi: 10.1039/c2dt32525j

Van Ausdall, B. R., Poth, N. F., Kincaid, V. A., Arif, A. M., and Louie, J. (2011). Imidazolidene carboxylate bound $MBPh_4$ complexes (M = Li, Na) and their relevance in transcarboxylation reactions. *J. Org. Chem.* 76, 8413–8420. doi: 10.1021/jo201647b

Vishwakarma, N. K., Singh, A. K., Hwang, Y. H., Ko, D. H., Kim, J. O., Babu, A. G., et al. (2017). Integrated CO_2 capture-fixation chemistry via interfacial ionic liquid catalyst in laminar gas/liquid flow. *Nat. Commun.* 8:14676. doi: 10.1038/ncomms14676

Wang, C. M., Luo, X. Y., Luo, H. M., Jiang, D. E., Li, H. R., and Dai, S. (2011). Tuning the basicity of ionic liquids for equimolar CO_2 capture. *Angew. Chem. Int. Ed.* 50, 4918–4922. doi: 10.1002/ange.201008151

Wang, H., Xin, Z., and Li, Y. H. (2017b). Synthesis of ureas from CO_2. *Top. Curr. Chem.* 375:49. doi: 10.1007/s41061-017-0137-4

Wang, P. X., Liu, S., and Deng, Y. Q. (2017a). Important green chemistry and catalysis: non-phosgene syntheses of isocyanates – thermal cracking way. *Chin. J. Chem.* 35, 821–835. doi: 10.1002/cjoc.201600745

Wang, S., and Wang, X. (2016). Imidazolium ionic liquids, imidazolylidene heterocyclic carbenes, and zeolitic imidazolate frameworks for CO2 capture and photochemical reduction. *Angew. Chem. Int. Ed.* 55, 2308–2320. doi: 10.1002/anie.201507145

Weicker, S. A., and Stephan, D. W. (2015). Activation of carbon dioxide by silyl triflate-based frustrated lewis pairs. *Chem. Eur. J.* 21, 13027–13034. doi: 10.1002/chem.201501904

Welch, G. C., Juan, R. R. S., Masuda, J. D., and Stephan, D. W. (2006). Reversible, metal-free hydrogen activation. *Science* 314, 1124–1126. doi: 10.1126/science.1134230

Wesselbaum, S., Hintermair, U., and Leitner, W. (2012). Continuous-flow hydrogenation of carbon dioxide to pure formic acid using an integrated $scCO_2$ process with immobilized catalyst and base. *Angew. Chem. Int. Ed.* 51, 8585–8588. doi: 10.1002/ange.201203185

Wolff, N., von, Lefèvre, G., Berthet, J. C., Thuèry, P., and Cantat, T. (2016). Implications of CO_2 activation by frustrated lewis pairs in the catalytic hydroboration of CO_2: a view using N/Si^+ frustrated lewis pairs. *ACS Catal.* 5, 4526–4535. doi: 10.1021/acscatal.6b00421

Wu, Y. Y., Zhao, Y. F., Li, R. P., Yu, B., Chen, Y., Liu, X. W., et al. (2017). Tetrabutylphosphonium-based ionic liquid catalyzed CO_2 transformation at ambient conditions: a case of synthesis of α-alkylidene cyclic carbonates. *ACS Catal.* 7, 6251–6255. doi: 10.1021/acscatal.7b01422

Xia, S. M., Chen, K. H., Fu, H. C., and He, L. N. (2018). Ionic liquids catalysis for carbon dioxide conversion with nucleophiles. *Front. Chem.* 6:462. doi: 10.3389/fchem.2018.00462

Yadav, M., Linehan, J. C., Karkamkar, A. J., van der Eide, E., and Heldebrant, D. J. (2014). Homogeneous hydrogenation of CO_2 to methyl formate utilizing switchable ionic liquids. *Inorg. Chem.* 53, 9849–9854. doi: 10.1021/ic501378w

Yang, Z. Z., and He, L. N. (2014). Efficient CO_2 capture by tertiary amine-functionalized ionic liquids through Li^+-stabilized zwitterionic adduct formation. *Beilstein J. Org. Chem.* 10, 1959–1966. doi: 10.3762/bjoc.10.204

Yang, Z. Z., He, L. N., Gao, J., Liu, A. H., and Yu, B. (2012). Carbon dioxide utilization with C–N bond formation: carbon dioxide capture and subsequent conversion. *Energy Environ. Sci.* 5, 6602–6639. doi: 10.1039/c2ee02774g

Yang, Z. Z., He, L. N., Zhao, Y. N., Li, B., and Yu, B. (2011). CO_2 capture and activation by superbase/polyethylene glycol and its subsequent conversion. *Energy Environ. Sci.* 4, 3971–3975. doi: 10.1039/c1ee02156g

Yoshida, M., Komatsuzaki, Y., and Ihara, M. (2008). Synthesis of 5-vinylideneoxazolidin-2-ones by DBU-mediated CO_2-fixation reaction of 4-(benzylamino)-2-butynyl carbonates and benzoates. *Org. Lett.* 10, 2083–2086. doi: 10.1021/ol800663v

Yoshida, M., Mizuguchi, T., and Shishido, K. (2012). Synthesis of oxazolidinones by efficient fixation of atmospheric CO_2 with propargylic amines by using a silver/1,8-diazabicyclo[5.4.0]undec-7-ene (DBU) Dual-catalyst system. *Chem. Eur. J.* 18, 15578–15581. doi: 10.1002/chem.201203366

Yu, B., Cheng, B. B., Liu, W. Q., Li, W., Wang, S. S., Cao, J., et al. (2016). Atmospheric pressure of CO_2 as protecting reagent and reactant: efficient synthesis of oxazolidin-2-ones with carbamate salts, aldehydes and alkynes. *Adv. Synth. Catal.* 358, 90–97. doi: 10.1002/adsc.201500921

Zhang, S., Li, Y. N., Zhang, Y. W., He, L. N., Yu, B., Song, Q. W., et al. (2014). Equimolar carbon absorption by potassium phthalimide and *in situ* catalytic conversion under mild conditions. *ChemSusChem* 7, 1484–1489. doi: 10.1002/cssc.201400133

Zhang, Y. G., and Lim, D. S. W. (2015). Synergistic carbon dioxide capture and conversion in porous materials. *ChemSusChem* 8, 2606–2608. doi: 10.1002/cssc.201500745

Zhang, Z. F., Hu, S. Q., Song, J. L., Li, W. J., Yang, G. Y., and Han, B. X. (2009). Hydrogenation of CO_2 to formic acid promoted by a diamine-functionalized ionic liquid. *ChemSusChem* 2, 234–238. doi: 10.1002/cssc.200800252

Zhang, Z. F., Xie, Y., Li, W. J., Hu, S. Q., Song, J. L., Jiang, T., et al. (2008). Hydrogenation of carbon dioxide is promoted by a task-specific ionic liquid. *Angew. Chem. Int. Ed.* 47, 1127–1129. doi: 10.1002/ange.200704487

Zhang, Z. G., Fan, F. J., Xing, H. B., Yang, Q. W., Bao, Z. B., and Ren, Q. L. (2017). Efficient synthesis of cyclic carbonates from atmospheric CO_2 using a positive charge delocalized ionic liquid catalyst. *ACS Sustain. Chem. Eng.* 5, 2841–2846. doi: 10.1021/acssuschemeng.7b00513

Zhao, T., Hu, X., Wu, Y., and Zhang, Z. (2019). Hydrogenation of CO_2 to formate with H_2: transition metal free catalyst based on a lewis pair. *Angew. Chem. Int. Ed.* 58, 722–726. doi: 10.1002/anie.201809634

Zhao, Y. F., Wu, Y. Y., Yuan, G. F., Hao, L. D., Gao, X., Yang, Z. Z., et al. (2016). Azole-anion-based aprotic ionic liquids: functional solvents for atmospheric CO_2 transformation into various heterocyclic compounds. *Chem. Asian J.* 11, 2735–2740. doi: 10.1002/asia.201600281

Zhou, H., Wang, G. X., and Lu, X. B. (2017). CO_2 Adducts of a-Carbon Alkylated N-Heterocyclic olefins:highly active organocatalysts for CO_2 chemical transformation. *Asian J. Org. Chem.* 6, 1264–1269. doi: 10.1002/ajoc.201700152

Zhou, H., Zhang, W. Z., Liu, C. H., Qu, J. P., and Lu, X. B. (2008). CO_2 adducts of *N*-heterocyclic carbenes: thermal stability and catalytic activity toward the coupling of CO_2 with epoxides. *J. Org. Chem.* 73, 8039–8044. doi: 10.1021/jo801457r

Conflict of Interest Statement: The authors declare that the research was conducted in the absence of any commercial or financial relationships that could be construed as a potential conflict of interest.

Copyright © 2019 Fu, You, Li and He. This is an open-access article distributed under the terms of the Creative Commons Attribution License (CC BY). The use, distribution or reproduction in other forums is permitted, provided the original author(s) and the copyright owner(s) are credited and that the original publication in this journal is cited, in accordance with accepted academic practice. No use, distribution or reproduction is permitted which does not comply with these terms.

frontiers in Chemistry

ORIGINAL RESEARCH
published: 20 August 2019
doi: 10.3389/fchem.2019.00580

A Novel Photo-Driven Hydrogenation Reaction of an NAD^+-Type Complex Toward Artificial Photosynthesis

Hideki Ohtsu, Tsubasa Saito and Kiyoshi Tsuge*

Graduate School of Science and Engineering, University of Toyama, Toyama, Japan

The photocatalytic reduction of carbon dioxide (CO_2) to value-added chemicals is an attractive strategy to utilize CO_2 as a feedstock for storing renewable energy, such as solar energy, in chemical bonds. Inspired by the biological function of the nicotinamide adenine dinucleotide redox couple (NAD^+/NADH), we have been developing transition-metal complexes containing NAD^+/NADH-functionalized ligands to create electro- and/or photochemically renewable hydride donors for the conversion of CO_2 into value-added chemicals. Our previous findings have provided insights for the development of photocatalytic organic hydride reduction reactions for CO_2, however, further examples, as well as investigation, of these photo-driven NAD^+/NADH-type hydrogenation and organic hydride transfer reactions are required not only to explore the mechanism in detail but also to develop a highly efficient catalyst for artificial photosynthesis. In this paper, we report the synthesis, characterization, and photo-induced NAD^+/NADH conversion properties of a new ruthenium(II) complex, $[Ru(bpy)_2(Me\text{-}pn)](PF_6)_2$ (**1**), which contains a new NAD^+-type ligand, Me-pn (2-methyl-6-(pyridin-2-yl)-1,5-naphthyridine). In addition, we have succeeded in the isolation of the corresponding two-electron reduced ruthenium(II) complex containing the NADH-type ligand Me-pnHH (2-methyl-6-(pyridin-2-yl)-1,4-dihydro-1,5-naphthyridine), i.e., $[Ru(bpy)_2(Me\text{-}pnHH)](PF_6)_2$ (**1HH**), by the photo-induced hydrogenation reaction of **1**. Thus, in this study, a new photo-driven NAD^+/NADH-type hydrogenation reaction for possible CO_2 reduction using the NAD^+/NADH redox function has been constructed.

Keywords: CO_2 reduction, photo-induced hydrogenation, NAD^+, NADH, organic hydride, ruthenium complex

OPEN ACCESS

Edited by:
Hitoshi Ishida,
Kitasato University, Japan

Reviewed by:
M. Jasim Uddin,
University of Texas Rio Grande Valley
Edinburg, United States
Koji Tanaka,
Kyoto University, Japan

****Correspondence:***
Hideki Ohtsu
ohtsu@sci.u-toyama.ac.jp

Specialty section:
This article was submitted to Inorganic Chemistry, a section of the journal Frontiers in Chemistry

Received: *21 February 2019*
Accepted: *02 August 2019*
Published: *20 August 2019*

Citation:
Ohtsu H, Saito T and Tsuge K (2019) A Novel Photo-Driven Hydrogenation Reaction of an NAD^+-Type Complex Toward Artificial Photosynthesis. Front. Chem. 7:580. doi: 10.3389/fchem.2019.00580

INTRODUCTION

Currently, the design and development of novel visible-light photoredox catalysts for carbon dioxide (CO_2) reduction are considered to be crucial challenges. In particular, it is vital not only to clarify how to employ solar energy, which is a sustainable clean energy source, but also to develop methods to convert CO_2, which is a major greenhouse gas and is harmful for the environment, into chemical fuels and feedstocks in the viewpoint of the current global energy and environmental crisis (Fox and Dulay, 1993; Kisch, 2013). Many research efforts have so far been devoted to the search for new and efficient catalysts for CO_2 conversion into value-added chemicals such as carbon monoxide (CO), formic acid (HCO_2H), and methanol (CH_3OH) (Meyer, 1989; Alstrum-Acevedo et al., 2005; Wang et al., 2015).

However, there are several problems facing photochemical CO_2 conversion, particularly related to the side reactions and low selectivity toward specific reduction products, as well as poor energy efficiency (Leitner, 1995; Jones et al., 2014). To solve these problems, the use of transition-metal coordination compounds as photocatalysts for CO_2 reduction has drawn significant attention because some of these compounds exhibit significant photocatalytic activity for CO_2 reduction (Morris et al., 2009; Berardi et al., 2014), and they play an essential role in artificial photosynthesis (Fukuzumi et al., 2018), as well as natural photosynthesis (Silva et al., 2015).

In particular, ruthenium complexes are promising candidates for photocatalysts because most Ru complexes show excellent photophysical properties with relatively long excited-state lifetimes and visible light absorption bands originating from metal-to-ligand charge transfer (MLCT) (Medlycott and Hanan, 2005; Sun et al., 2015; Dongare et al., 2017). In the past several decades, a number of Ru complexes having photocatalytic ability toward CO_2 reduction have been reported (Jessop et al., 1995; Tanaka and Ooyama, 2002; Kuramochi et al., 2018). In this context, we have focused on Ru complexes having NAD^+/NADH-functionalized ligands because the biological function of the NAD^+/NADH redox couple is as a generator and reservoir of hydride ions (H^-), which are equivalent to two electrons and one proton (Eisner and Kuthan, 1972; Walsh, 1980; Stout and Meyers, 1982; Gebicki et al., 2004; Bilan et al., 2015), and is of great interest for the development of photorenewable hydride reagents.

Previously, we have successfully demonstrated that a ruthenium(II) complex containing an NADH-type ligand, pbnHH $[Ru(bpy)_2(pbnHH)]^{2+}$ (bpy = 2,2′-bipyridine, pbnHH = 2-(pyridin-2-yl)-5,10-dihydrobenzo[*b*][1,5]naphthyridine), which is photochemically converted from the corresponding NAD^+-type complex $[Ru(bpy)_2(pbn)]^{2+}$ (pbn = 2-(pyridin-2-yl)benzo[*b*][1,5]naphthyridine) (Koizumi and Tanaka, 2005; Polyansky et al., 2007; Fukushima et al., 2009, 2010; Ohtsu and Tanaka, 2012a), can reduce CO_2 to HCO_2^- via organic hydride transfer involving C–H bond dissociation of the NADH-type ligand in $[Ru(bpy)_2(pbnHH)]^{2+}$ driven by the association of the bases (Ohtsu and Tanaka, 2012b; Ohtsu et al., 2015). These findings stimulated us to explore a new type of NAD^+/NADH-functionalized complex, and the expansion of the scope of our previous work on NAD^+/NADH model chemistry potentially opens new perspectives for the design of more efficient molecular photocatalysts for CO_2 reduction. As part of our ongoing research into Ru NAD^+/NADH-functionalized complexes, we have synthesized and characterized the photo-induced NAD^+/NADH-type hydrogenation reaction properties of a ruthenium(II) complex bearing a new NAD^+-type ligand, Me-pn (Me-pn = 2-methyl-6-(pyridin-2-yl)-1,5-naphthyridine), i.e., $[Ru(bpy)_2(Me\text{-}pn)](PF_6)_2$ (**1**). In addition, we have also successfully isolated a ruthenium(II) complex having the corresponding NADH-type ligand, Me-pnHH (Me-pnHH = 2-methyl-6-(pyridin-2-yl)-1,4-dihydro-1,5-naphthyridine), i.e., $[Ru(bpy)_2(Me\text{-}pnHH)](PF_6)_2$ (**1HH**), by the photochemical reduction of **1** under light irradiation ($\lambda > 420$ nm) in the presence of a sacrificial reagent.

MATERIALS AND METHODS

Materials

All chemicals used for the synthesis of the ligands and complexes were commercial products of the highest available purity and were used without further purification unless otherwise indicated. Solvents were purified by standard methods before use (Armarego and Chai, 2009).

Synthesis

All ligands and complexes used in this study were prepared according to the following procedures and the structures of the products were confirmed from analytical data (*vide infra*).

2-Methyl-6-(pyridin-2-yl)-1,5-naphthyridine (Me-pn)

This ligand was prepared in the same manner as that for the synthesis of 2-(pyridin-2-yl)-1,5-naphthyridine (Singh and Thummel, 2009) using 2-chloro-6-methyl-1,5-naphthyridine (Gellibert et al., 2004) instead of 2-chloro-1,5-naphthyridine. Anal. Calcd for $C_{14}H_{11}N_3$: C, 76.00; H, 5.01; N, 18.99. Found: C, 75.84; H, 4.88; N, 18.81. ^{1}H NMR (300 MHz, $CDCl_3$): δ 8.73 ∼ 8.79 (m, 2H), 8.60 (dt, $J = 8.0$, 1.1 Hz, 1H), 8.44 (d, $J = 8.8$ Hz, 1H), 8.35 (d, $J = 8.6$ Hz, 1H), 7.88 (td, $J = 7.8$, 2.0 Hz, 1H), 7.54 (d, $J = 8.6$ Hz, 1H), 7.38 (ddd, $J = 7.4$, 4.8, 1.3 Hz, 1H), 2.81 (s, 3H).

$[Ru(bpy)_2(Me\text{-}pn)](PF_6)_2$ (1)

To a 2-methoxyethanol solution (20 mL) of $[Ru(bpy)_2Cl_2]$ (363 mg, 0.75 mmol) was added $AgPF_6$ (381 mg, 1.5 mmol) in 2-methoxyethanol, and the mixture was stirred for 12 h at 70°C. The resulting mixture was cooled to room temperature, and insoluble material was removed by filtration through celite. After the addition of the ligand Me-pn (754 mg, 0.75 mmol) to the filtrate, the reaction mixture was stirred for 24 h at 70°C. The solution was concentrated to ca. 1 mL and poured into aqueous NH_4PF_6 solution. The solid formed was collected and dried in vacuo. Recrystallization from acetonitrile/diethylether gave **1** as reddish purple crystals (389 mg, 56.1%). ESI-MS: $m/z = 780$ $[M–PF_6]^+$. Anal. Calcd for $C_{34}F_{12}H_{29}N_7OP_2Ru$: C, 43.32; H, 3.10; N, 10.40. Found: C, 43.48; H, 3.25; N, 10.30. ^{1}H NMR(300 MHz, CD_3CN): δ 8.73 (d, $J = 9.1$ Hz, 1H), 8.72 (d, $J = 8.2$ Hz, 1H), 8.51 ∼ 8.61 (m, 3H), 8.38 (d, $J = 8.2$ Hz, 1H), 8.30 (d, $J = 8.1$ Hz, 1H), 8.18 ∼ 8.32 (m, 5H), 7.89 ∼ 7.99 (m, 2H),7.67 (d, $J = 5.6$ Hz, 1H), 7.58 (d, $J = 5.7$ Hz, 1H), 7.38 ∼ 7.53 (m, 4H), 7.27 ∼ 7.38 (m, 3H), 7.11 (d, $J = 9.1$ Hz, 1H), 2.62 (s, 3H).

$[Ru(bpy)_2(Me\text{-}pnHH)](PF_6)_2$ (1HH)

The NADH-type two-electron reduced complex was prepared photochemically: An anaerobic CH_3CN solution (2.35 mL) of **1** (30.7 mg, 0.033 mmol) containing TEOA (0.208 g, 1.4 mmol) was irradiated with light through a longpass filter (HOYA W-Y455) and a super cold filter (ASAHI SPECTRA SC0751) using a 150 W Xenon lamp for 0.5 h. The resulting solution was added to aqueous NH_4PF_6 solution, and the orange solid formed was collected by filtration and dried in vacuo. Yield: 24.2 mg (78.5%). ESI-MS: $m/z = 782$ $[M–PF_6]^+$. Anal. Calcd for $C_{34}F_{12}H_{29}N_7P_2Ru$: C, 44.07; H, 3.15; N, 10.58. Found: C, 43.95;

H, 3.21; N, 10.36. ^{1}H NMR(300 MHz, CD_3CN): δ 8.52 (d, J = 8.3 Hz, 2H), 8.44 (t, J = 7.1 Hz, 2H), 8.18 ∼ 8.26 (m, 2H), 8.06 ∼ 8.15 (m, 3H), 7.89 ∼ 8.05 (m, 3H), 7.64 ∼ 7.72 (m, 2H), 7.52 (td, J = 6.4, 1.4 Hz, 1H), 7.42 ∼ 7.48 (m, 2H), 7.24 ∼ 7.37 (m, 3H), 7.16 (td, J = 6.6, 1.3 Hz, 1H), 7.10 (d, J = 8.7 Hz, 1H), 6.68 (br, s, 1H), 3.85 (br, m, 1H), 3.36 (ddd, J = 21.5, 3.9, 1.6, Hz, 1H), 2.35 (ddd, J = 21.5, 3.4, 1.8 Hz, 1H), 1.62 (br, m, 3H).

Physical Measurements

All manipulations were carried out under an argon atmosphere using standard Schlenk techniques or in a glovebox. The absorption spectra were obtained using a Hewlett–Packard 8453 diode array spectrophotometer or a Shimadzu UV-3100PC scanning spectrophotometer. The emission spectra were recorded on a JASCO FP-8500 spectrofluorometer. The emission lifetimes were performed with a UNISOKU LSP-1000N-PX spectrometer. The electrospray (ESI)-mass spectrometry (MS) data were obtained with a Shimadzu LCMS-2020. Elemental analyses were performed using a Yanaco CHN Corder MT-5 (A Rabbit Science Japan Co., Ltd.). NMR measurements were measured with a JEOL JMN-ECX 300 (300 MHz) NMR spectrometer. Electron spin resonance (ESR) spectra were taken with a JEOL JES-X310 equipped with a variable temperature (VT) apparatus and were recorded under non-saturating microwave power conditions. The magnitude of the modulation was chosen to optimize the resolution and the signal-to-noise ratio of the observed spectra. The g values were calibrated with a Mn(II) marker used as a reference. Cyclic voltammetry measurements were performed on an ALS/Chi model 733D electrochemical analyzer in a deaerated solvent containing 0.1 M tetra-n-butylammonium hexafluorophosphate ($TBAPF_6$) as a supporting electrolyte. A conventional three-electrode cell was used with a glassy-carbon working electrode and a platinum wire as the counter electrode. The glassy-carbon working electrode was routinely polished with a BAS polishing alumina suspension and rinsed with acetone before use. The reversibility of the electrochemical processes was evaluated by standard procedures, and all potentials were recorded against an Ag/AgCl reference electrode. All electrochemical measurements were carried out under an argon atmosphere.

X-ray Crystal Structure Determination

The single crystal X-ray diffraction data of **1**•CH_3CN•Et_2O were collected on a Rigaku VariMax RAPID-DW/NAT with Mo-$K\alpha$ radiation (λ = 0.71075 Å) at 173 K and processed using RapidAuto program (Rigaku). An empirical absorption correction resulted in acceptable transmission factors. The data were corrected for Lorentz and polarization factors. The structure was solved by direct methods using SHELXT-2018/2 (Sheldrick, 2015) and refined by full-matrix least-squares techniques on F^2 using SHELXL-2018/3 (Sheldrick, 2015). All non-hydrogen atoms were refined anisotropically and all hydrogen atoms were included in the refinement process as per the riding model. CCDC-1894384 contains the supplementary crystallographic data for this paper. These data can be obtained free of charge via www.ccdc.cam.ac.uk/conts/retrieving.html (or from the Cambridge Crystallographic Data Center, 12, Union Road, Cambridge CB21EZ, UK; fax: (+44)1223-336-033; or deposit@ccdc.cam.ac.uk).

RESULTS AND DISCUSSION

The ruthenium(II) complex, $[Ru(bpy)_2(Me\text{-}pn)](PF_6)_2$ (**1**), which bears our newly designed NAD^+-type ligand, 2-methyl-6-(pyridin-2-yl)-1,5-naphthyridine (Me-pn), was successfully

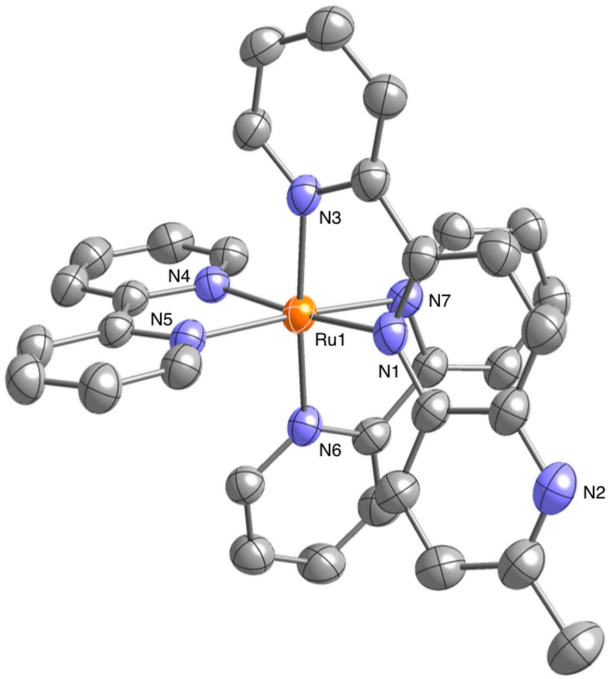

FIGURE 1 | Crystal structure of the ruthenium(II) NAD^+-type complex $[Ru(bpy)_2(Me\text{-}pn)](PF_6)_2$•$CH_3CN$•$Et_2O$ (**1**•CH_3CN•Et_2O) (50% probability ellipsoids. orange: ruthenium, blue: nitrogen, gray: carbon). The counter anion (PF_6^-), hydrogen atoms, and CH_3CN and Et_2O molecules are omitted for clarity.

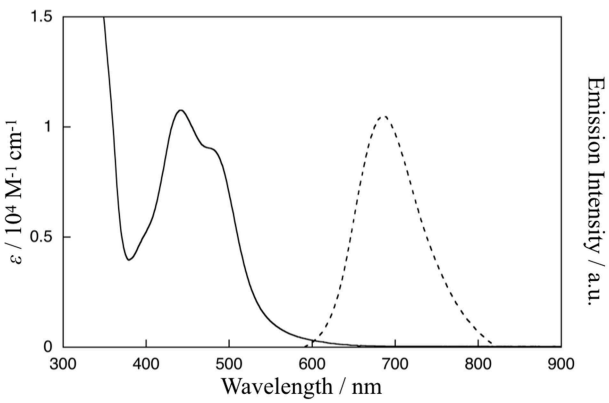

FIGURE 2 | Absorption spectrum (solid line) of **1** in CH_3CN at 298 K and emission spectrum (dotted line) of **1** in CH_3CN at 298 K upon excitation at 480 nm.

prepared by mixing $[Ru(bpy)_2Cl_2]$ and $AgPF_6$ in a 1:2 ratio in 2-methoxyethanol, followed by the addition of 1 equivalent of Me-pn at 343 K, and the composition of **1** was determined by elemental analysis, ESI-MS, and ^{1}H-NMR (see Material and Methods).

Well-shaped single crystals of **1** suitable for X-ray structure determination were obtained by recrystallization from an acetonitrile (CH_3CN) solution using the slow vapor diffusion of diethylether (Et_2O). This compound crystallizes in the monoclinic $P2_1/n$ space group with four molecules in the unit cell. The structure also contains solvated CH_3CN and Et_2O for each complex. The molecular structure of **1** is shown in **Figure 1**. The ruthenium(II) ion in **1** has a hexacoordinate octahedral structure formed of four N atoms of the two bpy ligands and two N atoms of the Me-pn ligand. The coordination environment of **1** is almost the same as that of a previously reported ruthenium(II) NAD^+-type complex $[Ru(bpy)_2(pbn)](PF_6)_2$ (Koizumi and Tanaka, 2005), and the bond lengths between the ruthenium(II) ion and the six N atoms of the ligands for **1** (2.046(4) to 2.119(4) Å) are not only the same as those of $[Ru(bpy)_2(pbn)](PF_6)_2$ (2.038(5) to 2.116(5) Å) (Koizumi and Tanaka, 2005) but also within the typical range of those of reported ruthenium(II) complexes having a similar coordination environment (Fukushima et al., 2009, 2010; Ohtsu and Tanaka, 2012a; Kobayashi et al., 2016). The ESI-MS results for **1** in CH_3CN show a dominant signal at $m/z = 780$, as shown in **Figure S1**, and the observed mass value, as well as the isotopic pattern, agree well with those of the simulated pattern of $[Ru(bpy)_2(pbn)](PF_6)]^+$. In addition, the ^{1}H-NMR spectrum of **1** in CD_3CN (**Figure S2**) displays a spectral pattern reflecting the *Cs* symmetry of **1**, including 24 aromatic proton signals between 7.11 and 8.73 ppm and three proton singlet signal assigned to the methyl group at 2.62 ppm. These results are in complete agreement with the single-crystal X-ray diffraction analysis described above.

The absorption and emission spectra of **1** in CH_3CN at 298 K are shown in **Figure 2**. Characteristic absorption bands centered around 440 and 480 nm can be assigned to MLCT transitions from the ruthenium(II) centers to the bpy ligand (Caspar and Meyer, 1983) and the Me-pn ligand, respectively. Complex **1** also exhibits a ^{3}MLCT emission band around 685 nm upon excitation at 480 nm, as shown in **Figure 2**. Additionally, the emission lifetime has been evaluated from the resulting single exponential emission decay (368 ns, see **Figure S3**), and this emission lifetime is larger than that of a previously reported ruthenium(II) NAD^+-type complex $[Ru(bpy)_2(pbn)](PF_6)_2$ (140 ns) (Polyansky et al., 2007). Furthermore, the emission quantum yield ($\lambda_{ex} = 480$ nm) was estimated at $\varnothing = 0.37\%$ using a relative method (Eaton, 1988) with $[Ru(bpy)_3](PF_6)_2$ as a reference (0.095) (Suzuki et al., 2009; Ishida et al., 2010). This value is more than 500 times larger than that of $[Ru(bpy)_2(pbn)](PF_6)_2$ (0.00071%) (Ohtsu and Tanaka, 2012a) reported previously.

Figure 3A shows the cyclic voltammogram (CV) of **1** (1 mM) in dimethylformamide (DMF) at 298 K. The CV shows one reversible redox wave at $E_{1/2(a)} = 1.42$ V (vs. Ag/AgCl) in the range above the rest potential ($E_{rest} = 0.00$ V) and three reversible redox waves at $E_{1/2(b)} = -0.88$ V, $E_{1/2(c)} = -1.31$ V, and $E_{1/2(d)} = -1.55$ V in the range below $E_{rest} = 0.00$ V. The $E_{1/2(a)}$ redox wave can be assigned to the Ru(II)/Ru(III) couple on the basis of the rest potential. To clarify the assignment of the other three redox waves, the CV of **1** upon the addition of an excess amount of a proton source such as acetic acid (AcOH) was measured in accordance with the previously reported procedure (Kobayashi et al., 2016). The CV changes observed upon the addition of 10 equivalents of AcOH into a solution of **1** in DMF are shown in **Figure 3B**. As shown, the reversibility of the $E_{1/2(b)}$ redox wave changes drastically to an irreversible cathodic peak at $E'_{pc(b)} = -0.92$ V, and a new anodic peak at $E'_{pa(b)} = 0.49$ V coupled with an irreversible $E'_{pc(b)}$ peak appears, whereas the other two $E_{1/2(c)}$ and $E_{1/2(d)}$ redox waves are barely changed from the redox waves at $E'_{1/2(c)} = -1.19$ V and $E'_{1/2(d)} = -1.41$ V, respectively, maintaining redox reversibility. The lack of reversibility of the $E_{1/2(b)}$ redox wave in the presence of the proton source is most likely caused by the protonation of the non-bonded N atom of the reduced Me-pn ligand; thus, the redox wave at $E_{1/2(b)} = -0.88$ V can be assigned to the Me-pn/Me-pn$^{\bullet-}$ couple. The large separation between the cathodic and anodic peak potentials of the Me-pn localized redox reaction under protic conditions may result from significant structural changes, such as the hydrogenation of the NAD^+-type Me-pn ligand to form the NADH-type Me-pnHH ligand through a two electron and two proton process. In the case of the other two redox waves ($E_{1/2(c)} = -1.31$ V and $E_{1/2(d)} = -1.55$ V), it is safe to conclude that the $E_{1/2(c)}$ and $E_{1/2(d)}$ redox waves

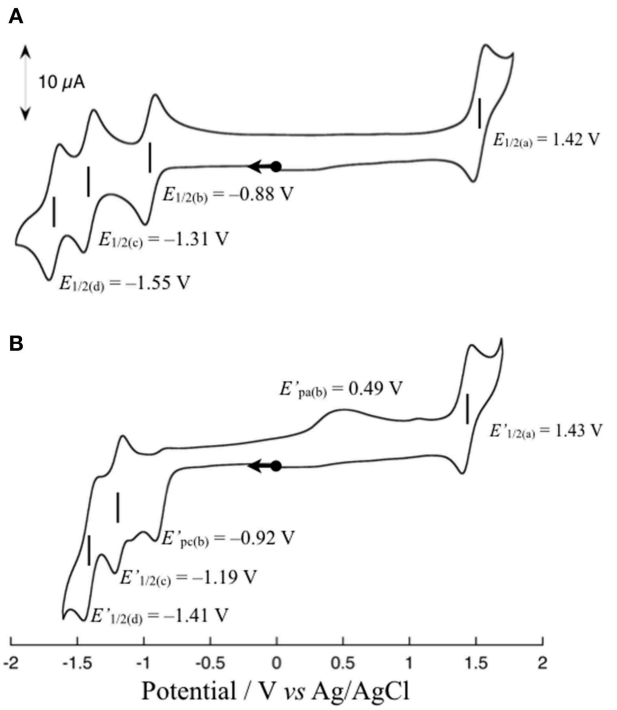

FIGURE 3 | Cyclic voltammograms of **1** in the absence **(A)** and presence **(B)** of 10 equivalents of AcOH in DMF containing 0.1 M $TBAPF_6$ at a scan rate 50 mV s^{-1}. All scans are started from the rest potential.

correspond to the redox couples of the two bpy ligands since almost no changes in the reversibility and the position of these redox waves are observed upon the addition of 10 equivalents of AcOH on the basis of CV measurements described above. In addition, the pK_a of the Me-pn ligand in **1** has been determined by spectrophotometric acid–base titration from pH 0.29 to pH 4.65, as shown in **Figure S4**. The estimated pK_a value of the protonated species $[Ru(bpy)_2(Me\text{-}pnH)]^{3+}$ is 1.6, the value of which is almost the same as previously reported in the case of $[Ru(bpy)_2(pbn)](PF_6)_2$ (pK_a = 1.7) (Polyansky et al., 2007).

To estimate the potential photochemical reactivity of **1**, the excited state reduction potential must be known. The excited state reduction potential of **1** ($E^\circ([Ru(bpy)_2(Me\text{-}pn)]^{2+*/+})$) is correlated with $E_{1/2}(Me\text{-}pn/Me\text{-}pn^{\bullet-})$ and $E_{em}(0\text{–}0)$ and is calculated to be 1.00 V using equation (1), where $E_{1/2}(Me\text{-}pn/Me\text{-}pn^{\bullet-}) = -0.88$ V and $E_{em}(0\text{–}0) = 1.88$ eV, which was estimated from the ^{3}MLCT emission band (λ_{ex} = 658 nm at 77 K in *n*-butyronitrile). The fact that the excited state reduction potential ($E^\circ([Ru(bpy)_2(Me\text{-}pn)]^{2+*/+})$ = 1.00 V) is located at a more positive potential than the oxidation potential of triethanolamine (TEOA, E_{ox} = 0.80 V vs. SCE) (Kalyanasundaram, 1986) stimulated us to research the photochemical reactivity of **1**, such as the photo-driven NAD^+/NADH-type hydrogenation reaction reported previously (Polyansky et al., 2007) in the presence of TEOA as a sacrificial reagent.

$$E^\circ([Ru(bpy)_2(Me\text{-}pn)]^{2+*/+}) = E_{1/2}(Me\text{-}pn/Me\text{-}pn^{\bullet-}) + E_{em}(0-0) \quad (1)$$

In the absence of TEOA, complex **1** in CH_3CN was quite stable even when exposed to visible light (150-W Xe lamp, λ > 420 nm) (see **Figure S5**). However, absorption spectral changes were observed upon the irradiation with visible light to a solution of **1** in the presence of TEOA (CH_3CN:TEOA = 4:1 v/v) at 293 K as shown in **Figure 4**. This reaction consists of two distinct steps. First, the characteristic absorption band located at 480 nm arising from **1** (red line) rapidly changes, and a spectrum (purple line) exhibiting a new broad band around 1,000 nm with an accompanying isosbestic point at 448 nm from 0 to 20 s is obtained; in addition, the intensity of the spectrum

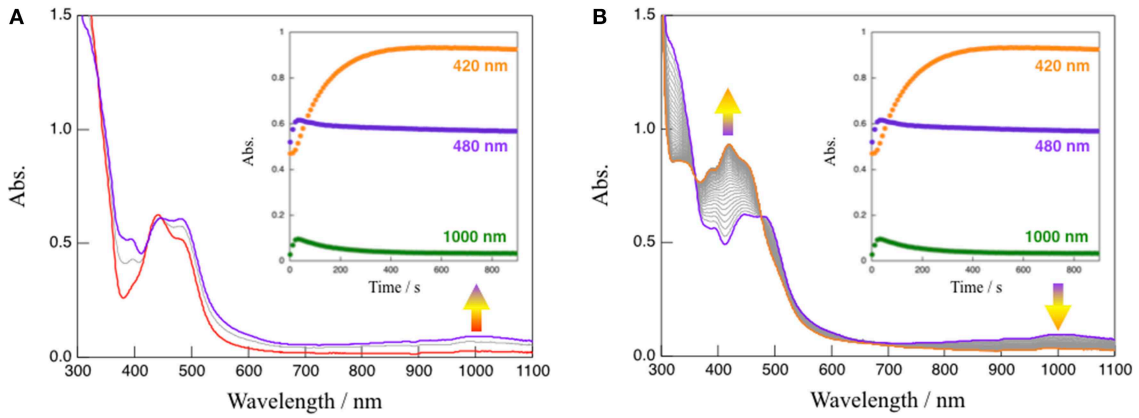

FIGURE 4 | Absorption spectral changes observed upon the irradiation with visible light (λ > 420 nm) to a solution (CH_3CN:TEOA = 4:1 v/v) of **1** at 293 K from 0 to 20 s **(A)** and from 20 to 900 s **(B)**, respectively. Inset: time course of the absorption changes at 420, 480, and 1,000 nm.

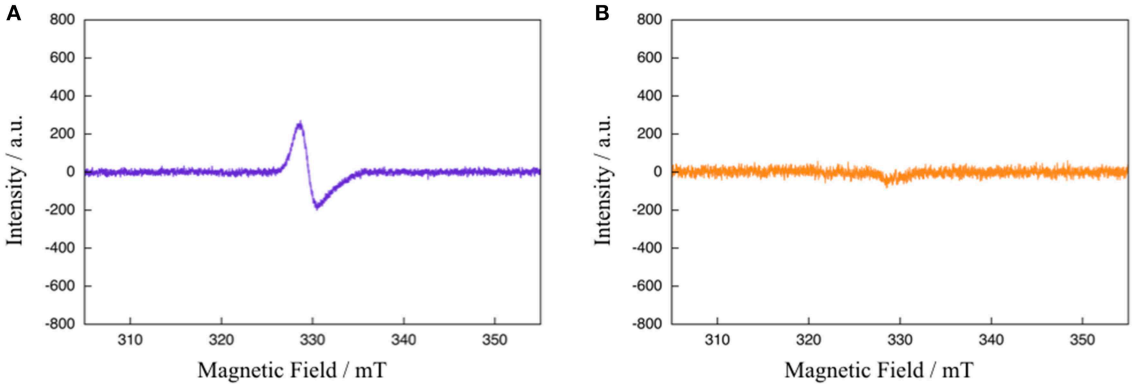

FIGURE 5 | ESR spectra of **1** in CH_3CN:TEOA = 4:1 v/v solution after photoirradiation (λ > 420 nm) for 20 s **(A)** and 900 s **(B)** at 173 K.

around 1,000 nm subsequently decreased. This is accompanied by an increase in the absorption band located at 420 nm (orange line) with an isosbestic point at 477 nm from 20 to 900 s. When triethylamine (TEA, $E_{ox} = 0.66$ V vs. SCE) (Yanagida et al., 1997), which is also a sacrificial reagent, was used instead of TEOA, almost the same absorption spectral changes indicating a two-step process have been observed (**Figure S6**), and a dominant signal ($m/z = 782$), which agrees well with the simulated pattern corresponding to the NADH-type complex, $[Ru(bpy)_2(Me\text{-}pnHH)](PF_6)]^+$, has been detected by ESI-MS measurements of the final reaction mixture, as shown in **Figure S7**. Furthermore, attempts to isolate the NADH-type complex $[Ru(bpy)_2(Me\text{-}pnHH)](PF_6)_2$ (**1HH**) by photochemical reduction using TEOA were successful based on the ESI-MS at $m/z = 782$ and the observed mass value, as well as the isotopic pattern, which agrees well with the simulated pattern of $[Ru(bpy)_2(Me\text{-}pnHH)](PF_6)]^+$. In addition, 22 characteristic proton signals in the aromatic region, a proton N–H signal at 6.68 ppm, and two proton signals at 3.36 and 2.35 ppm, which can be assigned to the methylene protons of the 1,4-dihydropyridine frameworks in the Me-pnHH ligand (see Material and Methods and **Figure S8**), were observed. As reported for the previous ruthenium(II) NAD^+-type complex $[Ru(bpy)_2(pbn)]^{2+}$, $[Ru(bpy)_2(pbn)]^{2+}$ is efficiently reduced to the corresponding NADH-type complex ($[Ru(bpy)_2(pbnHH)]^{2+}$) by photochemical reduction in CH_3CN in the presence of a sacrificial electron donor such as TEOA or TEA. The absorption spectral changes for the photo-driven NAD^+/NADH-type hydrogenation reaction in $[Ru(bpy)_2(pbn)]^{2+}$ system were observed in a one-step process (Ohtsu and Tanaka, 2012a) despite the use of the same experimental conditions as those of **1** (150-W Xe lamp($\lambda >$ 420 nm), CH_3CN:TEOA = 4:1 v/v, 293 K). Such a difference in the reactivity may be ascribed to the steric effects of the methyl group of the Me-pn ligand in **1**, which result in weaker π-π interactions between two $[Ru(bpy)_2(Me\text{-}pnH^\bullet)]^{2+}$ (**1$^{\bullet-}$H**) radical intermediate species compared to the case of the non-substituted pbn ligand in $[Ru(bpy)_2(pbn)]^{2+}$; this is based on a possible mechanism for the photo-driven NAD^+/NADH-type hydrogenation reaction discussed later.

To gain further mechanistic insight into the photo-induced NAD^+/NADH-type hydrogenation reaction of **1**, ESR measurements after photoirradiation for 20 and 900 s under the same conditions as those used to observe the absorption spectral changes shown in **Figure 4** were carried out (**Figure 5**). The ESR spectrum of **1** in CH_3CN:TEOA = 4:1 v/v solution after photoirradiation for 20 s at 173 K displays a pseudo-isotropic signal at $g = 2.000$ with a line width of $\Delta H = 19$ G, as shown in **Figure 5A**. In contrast to the case of photoirradiation for 900 s, no ESR signal is observed (**Figure 5B**). The observed ESR signal in the case of photoirradiation for 20 s (**Figure 5A**) is similar to that of a one electron reduced $[Ru(bpy)_3]^{2+}$ complex, namely $[Ru(bpy)_2(bpy^{\bullet-})]^+$ ($g = 1.996$ and $\Delta H =$ 26 G at 173 K) (Motten et al., 1981), which can be assigned to a ligand-centered radical species $[Ru(bpy)_2(Me\text{-}pnH^\bullet)]^{2+}$ (**1$^{\bullet-}$H**) based on a previous mechanistic study of the conversion of $[Ru(bpy)_2(pbn)]^{2+}$ into $[Ru(bpy)_2(pbnHH)]^{2+}$ (Polyansky et al., 2008). Complex **1HH**, which is the photoreduction product of **1** in the presence of a sacrificial reagent, is diamagnetic, which is consistent with the results of the ESR measurements in the case of photoirradiation for 900 s.

Based on the various experimental results described above and the previously reported mechanism for the photo-driven NAD^+/NADH-type hydrogenation reaction using $[Ru(bpy)_2(pbn)]^{2+}$ (Polyansky et al., 2008), a photo-driven hydrogenation reaction pathway of **1** into **1HH** in the presence of a sacrificial reagent under photoirradiation can be proposed,

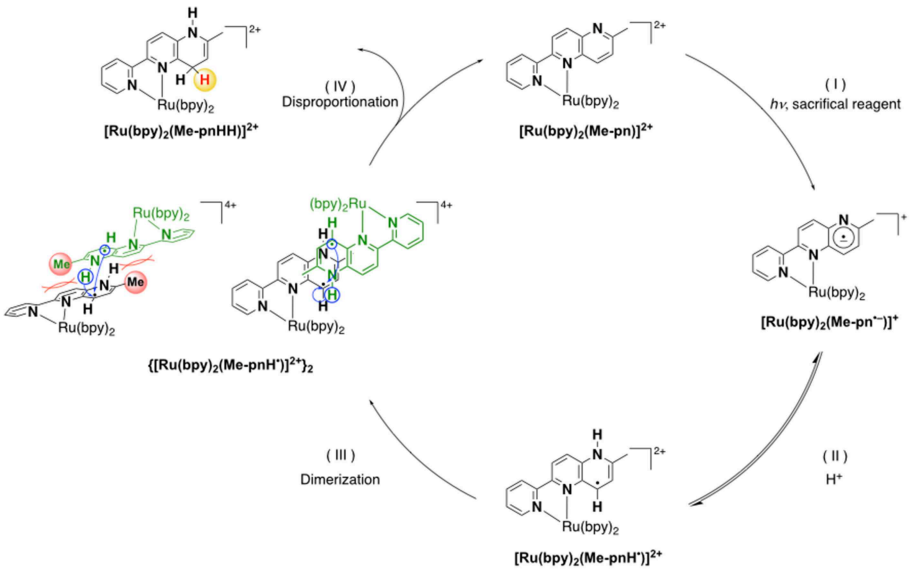

SCHEME 1 | A possible reaction mechanism for the photo-driven NAD^+/NADH-type hydrogenation reaction from **1** to **1HH**.

as shown in **Scheme 1**. First, the NAD^+-type complex **1** is photochemically reduced to the Me-pn radical anion species $[Ru(bpy)_2(Me\text{-}pn^{\bullet-})]^+$ ($\mathbf{1^{\bullet-}}$) by the reductive quenching of the photoexcited $\mathbf{1}^*$ by a sacrificial donor such as TEOA or TEA (step I). Secondly, the protonation of the non-coordinating N atom of the $Me\text{-}pn^{\bullet-}$ in $\mathbf{1^{\bullet-}}$ produces $[Ru(bpy)_2(Me\text{-}pnH^{\bullet})]^{2+}$ ($\mathbf{1^{\bullet-}H}$) radical species (step II). Then, each $\mathbf{1^{\bullet-}H}$ dimerizes via the π-π stacking of the neutral $Me\text{-}pnH^{\bullet}$ moieties to afford $\{[Ru(bpy)_2(Me\text{-}pnH^{\bullet})]^{2+}\}_2$ ($(\mathbf{1^{\bullet-}H})_2$) (step III). Finally, intramolecular proton-coupled electron transfer from one $Me\text{-}pnH^{\bullet}$ in $(\mathbf{1^{\bullet-}H})_2$ to another leads to disproportionation, thus generating the **1HH** NADH-type complex and regenerating the **1** NAD^+-type complex. At present, we have yet to clarify the reason why there is a significant difference in the photo-driven NAD^+/NADH-type hydrogenation reaction between **1** and the previously reported $[Ru(bpy)_2(pbn)]^{2+}$ system. However, the steric hindrance of the methyl groups in Me-pn complex may be the reason why we can see the radical intermediate species such as $\mathbf{1^{\bullet-}H}$ in the ESR measurements more easily than for the previously reported $[Ru(bpy)_2(pbn)]^{2+}$.

CONCLUSIONS

In conclusion, the present study has demonstrated the synthesis, characterization, and photoinduced NAD^+/NADH conversion properties of a new ruthenium(II) complex, $[Ru(bpy)_2(Me\text{-}pn)](PF_6)_2$ (**1**), as well as the isolated NADH-type complex $[Ru(bpy)_2(Me\text{-}pnHH)](PF_6)_2$ (**1HH**) under photochemical reduction conditions. The findings of the present study suggest a new type of photo-driven NAD^+/NADH-type hydrogenation reaction that makes possible the development of photoinduced CO_2 reduction reactions utilizing the NAD^+/NADH redox function. These results provide valuable information for the further development of functional transition-metal NAD^+/NADH-type complexes and shed new light on the applications of the NADH-type complexes for future catalysts and energy storage materials in the area of artificial photosynthesis. Further investigations concerning photochemical reduction of CO_2 and other substrates by using the NAD^+/NADH-functionalized complexes are now in progress.

DATA AVAILABILITY

The datasets generated for this study can be found in Cambridge Crystallographic Data Center, CCDC 1894384.

AUTHOR CONTRIBUTIONS

HO directed the project, conceived and designed the experiments, supervised the progress of this work, and wrote the manuscript. TS carried out the syntheses of ligands and complexes and performed most of the experiments. KT contributed X-ray structural analyses. All authors listed have discussed the results, drawn conclusions, and given the approval to the final version of the manuscript.

FUNDING

This work was supported by the Ministry of Education, Culture, Sports, Science, and Technology of Japan (MEXT) and the Japan Society for the Promotion of Science (JSPS) through Grants-in-Aid for Scientific Research C (JP17K05806, HO). HO also appreciates the financial support from Yashima Environment Technology Foundation and Yamaguchi Educational and Scholarship Foundation. TS gratefully acknowledges the financial support from The Japan Science Society by the Sasakawa Scientific Research Grant.

SUPPLEMENTARY MATERIAL

The Supplementary Material for this article can be found online at: https://www.frontiersin.org/articles/10.3389/fchem.2019.00580/full#supplementary-material

REFERENCES

Alstrum-Acevedo, J. H., Brennaman, M. K., and Meyer, T. J. (2005). Chemical approaches to artificial photosynthesis. 2. *Inorg. Chem*. 44, 6802–6827. doi: 10.1021/ic050904r

Armarego, W. L. F., and Chai, C. L. L. (2009). *Purification of Laboratory Chemicals, 6th ed.* Oxford: Pergamon Press.

Berardi, S., Drouet, S., Francàs, L., Gimbert-Suriñach, C., Guttentag, M., Richmond, C., et al. (2014). Molecular artificial photosynthesis. *Chem. Soc. Rev*. 43, 7501–7519. doi: 10.1039/C3CS60405E

Bilan, D. S., Shokhina, A. G., Lukyanov, S. A., and Belousov, V. V. (2015). Main cellular redox couples. *Russ. J. Bioorg. Chem*. 41, 341–356. doi: 10.1134/S1068162015040044

Caspar, J. V., and Meyer, T. J. (1983). Photochemistry of $Ru(bpy)_3^{2+}$. solvent effects. *J. Am. Chem. Soc*. 105, 5583–5590. doi: 10.1021/ja00355a009

Dongare, P., Myron, B. D. B., Wang, L., Thompson, D. W., and Thomas, J., Meyer, T. J. (2017). $[Ru(bpy)_3]^{2+*}$ revisited. Is it localized or delocalized? How does it decay? *Coord. Chem. Rev*. 345, 86–107. doi: 10.1016/j.ccr.2017.03.009

Eaton, D. F. (1988). Reference materials for fluorescence measurement. *Pure Appl. Chem*. 60, 1107–1114. doi: 10.1351/pac198860071107

Eisner, U., and Kuthan, J. (1972). Chemistry of dihydropyridines. *Chem. Rev*. 72, 1–42. doi: 10.1021/cr60275a001

Fox, M. A., and Dulay, M. T. (1993). Heterogeneous photocatalysis *Chem. Rev*. 93, 341–357. doi: 10.1021/cr00017a016

Fukushima, T., Fujita, E., Muckerman, J. T., Polyansky, D. E., Wada, T., and Tanaka, K. (2009). Photochemical stereospecific hydrogenation of a Ru complex with an NAD^+/NADH-type ligand. *Inorg. Chem*. 48, 11510–11512. doi: 10.1021/ic901935u

Fukushima, T., Wada, T., Ohtsu, H., and Tanaka, K. (2010). Photoinduced four- and six-electron reduction of mononuclear ruthenium complexes having NAD^+ analogous ligands. *Dalton Trans*. 39, 11526–11534. doi: 10.1039/c0dt00504e

Fukuzumi, S., Lee, Y. -M., and Nam, W. (2018). Artificial photosynthesis for production of ATP, NAD(P)H, and hydrogen peroxide. *Chem. Photo Chem*. 2, 121–135. doi: 10.1002/cptc.201700146

Gebicki, J., Marcinek, A., and Zielonka, J. (2004). Transient species in the stepwise interconversion of NADH and NAD^+. *Acc. Chem. Res*. 7, 379–386. doi: 10.1021/ar030171j

Gellibert, F., Woolven, J., Fouchet, M. -H., Mathews, N., V.,Goodland, H., and Lovegrove, V., et al. (2004). Identification of 1,5-naphthyridine derivatives as

a novel series of potent and selective TGF-ß type I receptor inhibitors. *J. Med. Chem*. 47, 4494–4506. doi: 10.1021/jm0400247

Ishida, H., Tobita, S., Hasegawa, Y., Katoh, R., and Nozaki, K. (2010). Recent advances in instrumentation for absolute emission quantum yield measurements. *Coord. Chem. Rev*. 254, 2449–2458. doi: 10.1016/j.ccr.2010.04.006

Jessop, P. G., Ikariya, T., and Noyori, R. (1995). Homogeneous hydrogenation of carbon dioxide. *Chem. Rev*. 95, 259–272. doi: 10.1021/cr00034a001

Jones, J. P., Prakash, G. K. S., and Olah, G. A. (2014). Electrochemical CO_2 reduction: recent advances and current trends. *Isr. J. Chem*. 54, 1451–1466. doi: 10.1002/ijch.201400081

Kalyanasundaram, K. (1986). Luminescence and redox reactions of the metal-to-ligand charge-transfer excited state of tricarbonylchloro(polypyridyl)rhenium(I) complexes. *J. Chem. Soc. Faraday Trans.* 2, 2401–2415. doi: 10.1039/F29868202401

Kisch, H. (2013). Semiconductor photocatalysis—mechanistic and synthetic aspects. *Angew. Chem. Int. Ed*. 52, 812–847. doi: 10.1002/anie.201201200

Kobayashi, K., Ohtsu, H., Nozaki, K., Kitagawa, S., and Tanaka, K. (2016). Photochemical properties and reactivity of a Ru compound containing an NAD/NADH-functionalized 1,10-phenanthroline ligand. *Inorg. Chem*. 55, 2076–2084. doi: 10.1021/acs.inorgchem.5b02390

Koizumi, T. -,a., and Tanaka, K. (2005). Reversible hydride generation and release from the ligand of $[Ru(pbn)(bpy)_2](PF_6)_2$ driven by a pbn-localized redox reaction *Angew. Chem. Int. Ed*. 44, 5891–5894. doi: 10.1002/anie.200500760

Kuramochi, Y., Ishitani, O., and Ishida, H. (2018). Reaction mechanisms of catalytic photochemical CO_2 reduction using Re(I) and Ru(II) complexes. *Coord. Chem. Rev*. 373, 333–356. doi: 10.1016/j.ccr.2017.11.023

Leitner, W. (1995). Carbon-dioxide as a raw-material: the synthesis of formic-acid and its derivatives from CO_2. *Angew. Chem. Int. Ed. Engl*. 34, 2207–2221. doi: 10.1002/anie.199522071

Medlycott, E. A., and Hanan, G. S. (2005). Designing tridentate ligands for ruthenium(II) complexes with prolonged room temperature luminescence lifetimes. *Chem. Soc. Rev*. 34, 133–142. doi: 10.1039/b316486c

Meyer, T. J. (1989). Chemical approaches to artificial photosynthesis. *Acc. Chem. Res*. 22, 163–170. doi: 10.1021/ar00161a001

Morris, A. J., Meyer, G. J., and Fujita, E. (2009). Molecular approaches to the photocatalytic reduction of carbon dioxide for solar fuels. *Acc. Chem. Res*. 42, 1983–1994. doi: 10.1021/ar9001679

Motten, A. G., Hanck, K., and DeArmond, M. K. (1981). ESR of the reduction products of $[Fe(bpy)_3]^{2+}$ and $[Ru(bpy)_3]^{2+}$. *Chem. Phys. Lett.*, 79, 541–546. doi: 10.1016/0009-2614(81)85032-4

Ohtsu, H., and Tanaka, K. (2012a). Drastic difference in the photo-driven hydrogenation reactions of ruthenium complexes containing NAD model ligands. *Chem. Commun*. 48, 1796–1798. doi: 10.1039/c2cc15886h

Ohtsu, H., and Tanaka, K. (2012b). An organic hydride transfer reaction of a ruthenium NAD model complex leading to carbon dioxide reduction. *Angew. Chem. Int. Ed*. 51, 9792–9795. doi: 10.1002/anie.201204348

Ohtsu, H., Tsuge, K., and Tanaka, K. (2015). Remarkable accelerating and decelerating effects of the bases on CO_2 reduction using a ruthenium NADH model complex. *J. Photochem. Photobiol. A* 313, 163–167. doi: 10.1016/j.jphotochem.2015.05.011

Polyansky, D., Cabelli, D., Muckerman, J. T., Fujita, E., Koizumi, T. A., Fukushima, T., et al. (2007). Photochemical and radiolytic production of an organic hydride donor with a Ru^{II} complex containing an NAD^+ model ligand. *Angew. Chem. Int. Ed*. 46, 4169–4172. doi: 10.1002/anie.200700304

Polyansky, D. E., Cabelli, D., Muckerman, J. T., Fukushima, T., Tanaka, K., and Fujita, E. (2008). Mechanism of hydride donor generation using a Ru(II) complex containing an NAD^+ model ligand: pulse and steady-state radiolysis studies. *Inorg. Chem*. 47, 3958–3968. doi: 10.1021/ic702139n

Sheldrick, G. M. (2015). Crystal structure refinement with SHELXL. *Acta Crystallograph. Sect. C* 71, 3–8. doi: 10.1107/S2053229614024218

Silva, C. S., Seider, W. D., and Lior, N. (2015). Exergy efficiency of plant photosynthesis. *Chem. Eng. Sci*. 130, 151–171. doi: 10.1016/j.ces.2015.02.011

Singh, A. N., and Thummel, R. P. (2009). 1,5-Naphthyridine as a new linker for the construction of bridging ligands and their corresponding Ru(II) complexes. *Inorg. Chem*. 48, 6459–6470. doi: 10.1021/ic900400t

Stout, D. M., and Meyers, A. I. (1982). Recent advances in the chemistry of dihydropyridines. *Chem. Rev*. 82, 223–243. doi: 10.1021/cr00048a004

Sun, Q., Mosquera-Vazquez, S., Suffren, Y., Hankache, J., Amstutz, N., Daku, L. M. L., et al. (2015). On the role of ligand-field states for the photophysical properties of ruthenium(II) polypyridyl complexes. *Coord. Chem. Rev*. 282–283, 87–99. doi: 10.1016/j.ccr.2014.07.004

Suzuki, K., Kobayashi, A., Kaneko, S., Takehira, K., Yoshihara, T., Ishida, H., et al. (2009). Reevaluation of absolute luminescence quantum yields of standard solutions using a spectrometer with an integrating sphere and a back-thinned CCD detector. *Phys. Chem. Chem. Phys*. 11, 9850–9860. doi: 10.1039/b912178a

Tanaka, K., and Ooyama, D. (2002). Multi-electron reduction of CO_2 via Ru–CO_2, –C(O)OH, –CO, –CHO, and –CH_2OH species. *Coord. Chem. Rev*. 226, 211–218. doi: 10.1016/S0010-8545(01)00434-9

Walsh, C. (1980). Flavin coenzymes: at the crossroads of biological redox chemistry. *Acc. Chem. Res*. 13, 148–155. doi: 10.1021/ar50149a004

Wang, W. H., Himeda, Y., Muckerman, J. T., Manbeck, G. F., and Fujita, E. (2015). CO_2 hydrogenation to formate and methanol as an alternative to photo- and electrochemical CO_2 reduction. *Chem. Rev*. 115, 12936–12973. doi: 10.1021/acs.chemrev.5b00197

Yanagida, S., Kanemoto, M., Ishihara, K., Wada, Y., Sakata, T., and Mori, H. (1997). Semiconductor photocatalysis. Part 22. Visible-light induced photoreduction of CO_2 with CdS nanocrystallites – Importance of the morphology and surface structures controlled through solvation by *N*, *N*-dimethylformamide. *Bull. Chem. Soc. Jpn*. 70, 2063–2070. doi: 10.1246/bcsj.70.2063

Conflict of Interest Statement: The authors declare that the research was conducted in the absence of any commercial or financial relationships that could be construed as a potential conflict of interest.

Copyright © 2019 Ohtsu, Saito and Tsuge. This is an open-access article distributed under the terms of the Creative Commons Attribution License (CC BY). The use, distribution or reproduction in other forums is permitted, provided the original author(s) and the copyright owner(s) are credited and that the original publication in this journal is cited, in accordance with accepted academic practice. No use, distribution or reproduction is permitted which does not comply with these terms.

frontiers in Chemistry

ORIGINAL RESEARCH
published: 24 September 2019
doi: 10.3389/fchem.2019.00628

An Investigation of Electrocatalytic CO_2 Reduction Using a Manganese Tricarbonyl Biquinoline Complex

Meaghan McKinnon[1], Veronika Belkina[1], Ken T. Ngo[1†], Mehmed Z. Ertem[2], David C. Grills[2*] and Jonathan Rochford[1*]*

[1] Department of Chemistry, University of Massachusetts Boston, Boston, MA, United States, [2] Chemistry Division, Brookhaven National Laboratory, Upton, NY, United States

The subject of this study [*fac*-Mn(bqn)$(CO)_3(CH_3CN)]^+$ (bqn = 2,2′-biquinoline), is of particular interest because the bqn ligand exhibits both steric and electronic influence over the fundamental redox properties of the complex and, consequently, its related catalytic properties with respect to the activation of CO_2. While not a particularly efficient catalyst for CO_2 to CO conversion, *in-situ* generation and activity measurements of the [*fac*-Mn(bqn)$(CO)_3]^-$ active catalyst allows for a better understanding of ligand design at the Mn center. By making direct comparisons to the related 2,2′-bipyridyl (bpy), 1,10-phenanthroline (phen), and 2,9-dimethyl-1,10-phenanthroline (dmphen) ligands via a combination of voltammetry, infrared spectroelectrochemistry, controlled potential electrolysis and computational analysis, the role of steric vs. electronic influences on the nucleophilicity of Mn-based CO_2 reduction electrocatalysts is discussed.

Keywords: carbon dioxide reduction, electrocatalysis, manganese, carbon monoxide, hydrogen evolution, computational modeling

OPEN ACCESS

Edited by:
Federico Cesano, University of Turin, Italy

Reviewed by:
Julio Lloret-Fillol, Institut Català d'Investigació Química, Spain
Charles Machan, University of Virginia, United States

****Correspondence:***
Mehmed Z. Ertem
mzertem@bnl.gov
David C. Grills
dcgrills@bnl.gov
Jonathan Rochford
jonathan.rochford@umb.edu

†Present address:
Ken T. Ngo, National Renewable Energy Laboratory (DOE), Golden, CO, United States

Specialty section:
This article was submitted to Inorganic Chemistry, a section of the journal Frontiers in Chemistry

Received: *01 March 2019*
Accepted: *02 September 2019*
Published: *24 September 2019*

Citation:
McKinnon M, Belkina V, Ngo KT, Ertem MZ, Grills DC and Rochford J (2019) An Investigation of Electrocatalytic CO_2 Reduction Using a Manganese Tricarbonyl Biquinoline Complex. Front. Chem. 7:628. doi: 10.3389/fchem.2019.00628

INTRODUCTION

The catalytic reduction of CO_2 into useful C-1 chemical feedstocks offers one potential strategy to develop a carbon-neutral alternative to our current dependence on fossil fuels. A major challenge for the catalysis community is to develop molecular catalysts capable of coupling electrochemical reduction with protonation of the CO_2 substrate toward useful C-1 products. One such example is the proton-coupled two-electron reduction of CO_2 to CO, which comes at a cost of just −0.52 V vs. SHE in water at pH 7 (Equation 1) (Arakawa et al., 2001), while in dry acetonitrile at pH 0 (Equation 2), the standard electrode potential for this reaction has been estimated, using two different thermodynamic cycles, as −0.13 V vs. $Fc^{+/0}$ (Matsubara et al., 2015) or −0.12 V vs. $Fc^{+/0}$ (Pegis et al., 2015).

$$CO_{2(g)} + 2H^+_{(aq)} + 2e^- \leftrightharpoons CO_{(g)} + H_2O_{(l)} \quad E^0 = -0.52\,\text{V vs. SHE (pH 7)} \tag{1}$$

$$CO_{2(g)} + 2H^+_{(CH3CN)} + 2e^- \leftrightharpoons CO_{(g)} + H_2O_{(CH3CN)} \quad E^0 = -0.13\,\text{V vs. } Fc^{+/0}\text{ (pH 0)} \tag{2}$$

This seemingly simple reaction is limited by slow kinetic parameters, however, which demands an appropriate catalyst to access a kinetically efficient pathway for CO_2 utilization – albeit at the cost of an electrochemical overpotential (η) (Appel and Helm, 2014). Of the homogeneous transition metal-based molecular catalysts used in this field (Francke et al., 2018; Sinopoli et al., 2018; Stanbury et al., 2018), manganese(I) polypyridyl tricarbonyl catalysts of the type [*fac*-Mn^I(N^N)$(CO)_3X]^n$ (where N^N = polypyridyl ligand, X = Br^- (n = 0) or CH_3CN (n = +1)), and their analogs, have been of keen interest due to their high selectivity, low

cost, and low overpotential (Grills et al., 2018). Recently we have reported on tuning both the inner coordination sphere (McKinnon et al., 2019) and second coordination sphere (Ngo et al., 2017) of the ligand to optimize catalytic efficiency and selectivity for CO formation, notably against the competitive two-electron two-proton coupled redox transformations of CO_2 to HCO_2H and H^+ to H_2. More subtle modification on the periphery of the bpy ligand is also known to strongly influence the reduction potentials observed for these catalysts. This is evident, for example, with the inductive electron donating influence of the dtbpy (dtbpy = 4,4′-^{t}Bu$_2$-bpy) ligand, which shifts the reduction potential 0.11 V more negative relative to the simple bpy analog (Smieja et al., 2013). Similarly, while maintaining the same inner coordination sphere of [*fac*-Mn(N^N)(CO)$_3$L]^n catalysts but introducing redox non-innocence on the ligand backbone, a recent report on [*fac*-MnBr(phen-dione)(CO)$_3$] (phen-dione = 1,10-phenanthroline-5,6-dione) demonstrated vastly different electrochemistry, maintaining a high selectivity for CO evolution, compared to the analogous bpy and phen (phen = 1,10-phenanthroline) complexes, notwithstanding significant ligand-based redox activity at the dione functional group to generate a bis-carboxylate phenanthroline intermediate species (Stanbury et al., 2017).

In the current study we have focused on a rather simple modification of the polypyridyl ligand, but one which allows us to directly investigate both steric and electronic influences in the [*fac*-Mn(bqn)(CO)$_3$(CH$_3$CN)]$^+$(**[4-CH$_3$CN]$^+$**) pre-catalyst, where bqn = 2,2′-biquinoline (**Figure 1**). While fundamental in approach, a simple systematic extension of the π-conjugated system of the polypyridyl ligand has not yet been reported for Mn(I) CO_2 reduction electrocatalysts. Four pre-catalysts of the general structure [*fac*-Mn(N^N)(CO)$_3$(CH$_3$CN)]$^+$ are here investigated using the benchmark 2,2′-bipyridyl (bpy) ligand (**[1-CH$_3$CN]$^+$**) alongside the 1,10-phenanthroline (phen) (**[2-CH$_3$CN]$^+$**), 2,9-dimethyl-1,10-phenanthroline (dmphen) (**[3-CH$_3$CN]$^+$**), and aforementioned bqn ligands. Although the phen ligand does not have as extensive a π-conjugation as the bqn ligand, it serves a critical role in this study by bridging the gap between the sterically related dmphen and bqn ligands. Indeed, a direct comparison of the sterically and electronically expanded bqn ligand to the sterically related dmphen ligand probes the question of whether steric or electronic effects dominate in determining the redox, and ultimately catalytic, properties of this class of CO_2 reduction electrocatalyst. As demonstrated below using a combination of IR-SEC and computational studies, the combined electronic and steric influences of the π-extended bqn ligand hinder formation of a **[4–4]^0** dimer, facilitating a concerted two-electron *ECE* mechanism for the generation of **[4]$^-$**. However, this comes at the cost of a change in product selectivity for the **[4-CH$_3$CN]$^+$** pre-catalyst to favor H_2 evolution in the presence of excess TFE. Selective CO_2 activation is observed for all catalysts here studied upon *in-situ* generation of a three-electron reduced [*fac*-Mn$^{(-1)}$(N^N$^{\bullet-}$)(CO)$_3$]$^{2-}$ active catalyst.

RESULTS AND DISCUSSION

Synthesis and Structural Characterization

Initial metathesis of [MnBr(CO)$_5$] with silver triflate was completed as a first step to produce the [Mn(CO)$_5$(OTf)] intermediate (Scheiring et al., 2000), allowing for the subsequent straightforward isolation of pure [*fac*-Mn^I(N^N)(CO)$_3$(OTf)] products. Microwave reflux of [Mn(CO)$_5$(OTf)] with one equivalent of the appropriate ligand in tetrahydrofuran afforded the pale yellow [*fac*-Mn(bpy)(CO)$_3$(OTf)] (**1-OTf**), [*fac*-Mn(phen)(CO)$_3$(OTf)] (**2-OTf**), and [*fac*-Mn(dmphen)(CO)$_3$(OTf)] (**3-OTf**) products, and the red-orange [*fac*-Mn(bqn)(CO)$_3$(OTf)] (**4-OTf**) solid, in quantitative yield following precipitation in excess diethyl ether. Each product was satisfactorily characterized by ^{1}H NMR and FTIR spectroscopies as well as elemental analysis. The *facial (fac)* arrangement of the Mn(CO)$_3$ core structure in each complex was confirmed by FTIR spectroscopy, where characteristic ν(CO) vibrational stretching modes for each of the solvated **[1-CH$_3$CN]$^+$**, **[2-CH$_3$CN]$^+$**, **[3-CH$_3$CN]$^+$** and **[4-CH$_3$CN]$^+$** complexes in neat acetonitrile provides a very useful comparison of structural and electronic properties of all four complexes using a basic knowledge of point-group symmetry and Mn(dπ)-CO(π*) back-bonding, respectively (**Table 2**). The bpy and phen complexes, **[1-CH$_3$CN]$^+$** and **[2-CH$_3$CN]$^+$**, each exhibit *pseudo-C*$_{3v}$ point group symmetry with identical FTIR spectra composed of a sharp, symmetric ν(CO) stretching mode at 2,050 cm^{-1} and a second broad, lower frequency asymmetric stretching mode at 1,958 cm^{-1}. Consistent with voltammetry and computational analysis presented below, the identical ν(CO) stretching modes illustrates the negligible electronic influence of the π-extended phen ligand in comparison to the bpy system. This observation is consistent with related reports of the analogous bromide complexes (Kurtz et al., 2015; Stanbury et al., 2017; Tignor et al., 2018). In contrast, the dmphen complex **[3-CH$_3$CN]$^+$** exhibits a descent in symmetry to *pseudo-C*$_s$, evident in a breaking of degeneracy for its lower frequency asymmetric ν(CO) stretching modes, which occur at 1,959 and 1,944(sh) cm^{-1}. This suggests a sterically induced distortion of the *fac*-Mn(CO)$_3$ core, likely by the 2,10-dimethyl substituents of the dmphen ligand. Furthermore, the higher frequency symmetric ν(CO) stretching mode of **[3-CH$_3$CN]$^+$** exhibits a 4 cm^{-1} shift to lower frequency at 2,046 cm^{-1}, consistent with an inductive electron-donating influence of the two methyl substituents at dmphen, likely due to increased Mn(dπ)→CO(π*) back-bonding. Interestingly, the bqn complex, **[4-CH$_3$CN]$^+$** exhibits an FTIR spectral profile with ν(CO) = 2,047 and 1,959 cm^{-1}, indicative again of *pseudo-C*$_{3v}$ symmetry, similar to **[1-CH$_3$CN]$^+$** and **[2-CH$_3$CN]$^+$**. However, with the high frequency symmetric ν(CO) stretching mode occurring at 2,047 cm^{-1}, this suggests that the inductive electron-donating influence of the bqn ligand is similar to that of the dmphen ligand in **[3-CH$_3$CN]$^+$**. Experimental FTIR spectral profiles are consistent with calculated spectra, as illustrated in **Figure 2**.

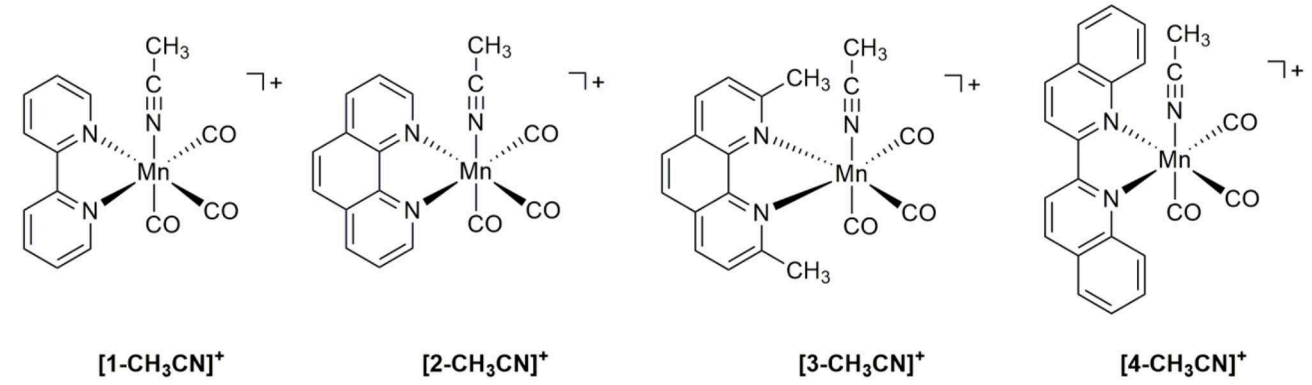

FIGURE 1 | Molecular structures of complexes investigated.

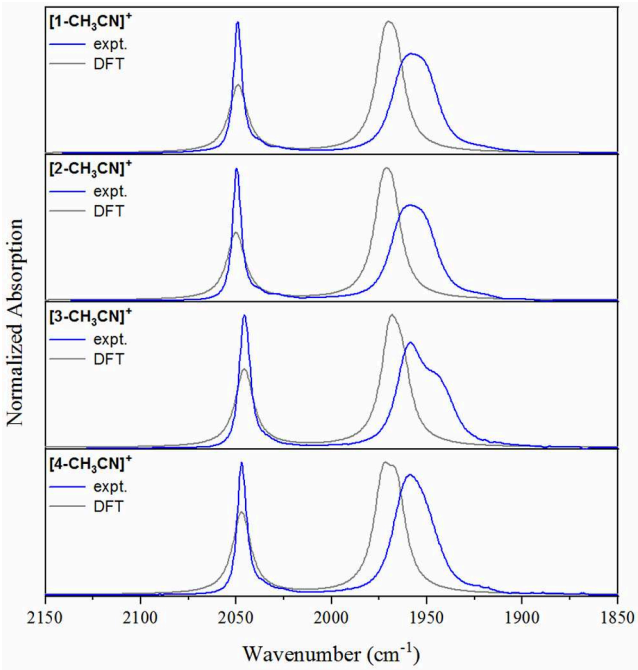

FIGURE 2 | Experimental FTIR spectra (blue) of **[1-CH_3CN]$^+$**, **[2-CH_3CN]$^+$**, **[3-CH_3CN]$^+$**, and **[4-CH_3CN]$^+$** recorded in acetonitrile displaying characteristic ν(CO) stretching modes. Density functional theory-computed IR spectra (gray) are included for comparison (empirically-derived frequency scaling factor = 0.9633, FWHM = 12 cm^{-1}).

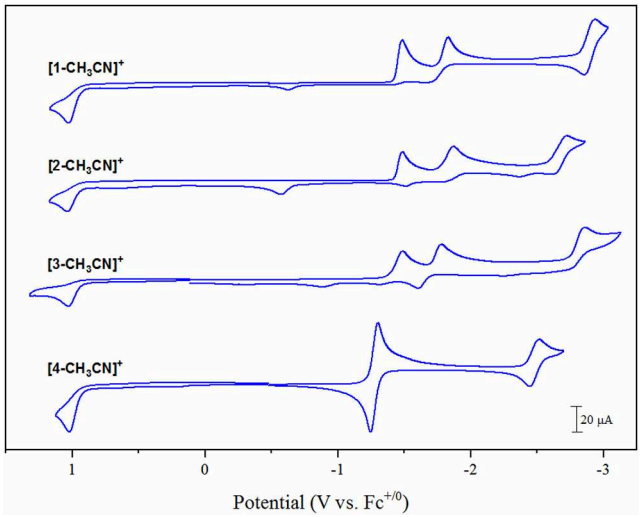

FIGURE 3 | Cyclic voltammograms of **[1-CH_3CN]$^+$**, **[2-CH_3CN]$^+$**, **[3-CH_3CN]$^+$** and **[4-CH_3CN]$^+$** recorded in 0.1 M $[Bu_4N][PF_6]$ acetonitrile supporting electrolyte at a glassy carbon working electrode with a scan rate of $\upsilon = 0.1$ V s^{-1} under 1 atmosphere of argon.

Cyclic Voltammetry Under Non-catalytic Conditions

Electrochemical characterization of each complex was carried out under inert conditions (1 atmosphere of argon), in the absence of auxiliary Brønsted acid, prior to screening for catalytic activity. Each complex displays an irreversible Mn(II/I) oxidation event within 20 mV of each other in the range of +1.02 to +1.04 V vs. the ferricenium/ferrocene ($Fc^{+/0}$) pseudo-reference (**Figure 3**, **Table 1**). This suggests that there is little difference in electron density between each Mn-center upon varying the polypyridyl ligand across the four complexes. The very subtle differences observed in the ν(CO) stretching modes by FTIR spectroscopy are unlikely to be reproduced by cyclic voltammetry. Furthermore, voltammetry data is more complex due to the *in-situ* generation of the Mn(II) oxidation state. We will focus on the reduction properties of these complexes forthwith due to their greater relevance toward our subsequent catalytic studies. The electrochemical properties of **[1-CH_3CN]$^+$** have been recently reported (Grills et al., 2018; McKinnon et al., 2019). Three sequential one-electron cathodic peaks are observed at $E_{pc} = -1.48$ V, -1.83 V and -2.94 V with only the third reduction exhibiting quasi-reversible behavior ($E_{1/2} = -2.90$ V, $\Delta E_p = 81$ mV at $\upsilon = 0.1$ V s^{-1}) vs. $Fc^{+/0}$. The phen complex, **[2-CH_3CN]$^+$** exhibits a first one-electron irreversible reduction at $E_{pc} = -1.48$ V vs. $Fc^{+/0}$, identical to that observed for

TABLE 1 | Redox potentials recorded by cyclic voltammetry for **[1-CH$_3$CN]$^+$**, **[2-CH$_3$CN]$^+$**, **[3-CH$_3$CN]$^+$**, and **[4-CH$_3$CN]$^+$** reported vs. the ferricenium/ferrocene ($Fc^{+/0}$) pseudo reference.

	Oxidation		Reduction		
[1-CH$_3$CN]$^+$	+1.03[a]	−0.61[b]	−1.48[c]	−1.83[c]	−2.90[d]
[2-CH$_3$CN]$^+$	+1.04[a]	−0.58[b]	−1.48[c]	−1.86[c]	−2.66[d]
[3-CH$_3$CN]$^+$	+1.03[a]	−0.65[b]	−1.49[c]	−1.78[c]	−2.86[c]
[4-CH$_3$CN]$^+$	+1.02[a]		−1.28[e]	−2.48[d]	

[a] *E_{pa}, irreversible one-electron oxidation.*
[b] *E_{pa}, Mn^0-Mn^0 dimer oxidation.*
[c] *E_{pc}, irreversible one-electron reduction.*
[d] *$E_{1/2}$, quasi-reversible one-electron reduction.*
[e] *$E_{1/2}$, reversible concerted two-electron reduction.*
Conditions: 1 mM sample concentration; 0.1 M $[Bu_4N][PF_6]$ acetonitrile supporting electrolyte; 3 mm diameter glassy carbon working electrode; Pt wire counter electrode; $Ag/AgPF_6$ acetonitrile non-aqueous reference electrode; $\upsilon = 0.1$ V s^{-1}.

[1-CH$_3$CN]$^+$, further supporting the electronic similarity of bpy and phen at least in the [*fac*-Mn(N^N)(CO)$_3$L]^n class of complexes (Tignor et al., 2018). This first reduction has been previously established (Grills et al., 2018) as ligand-based according to an electrochemical-chemical (*EC*) reaction scheme whereby, upon one-electron reduction of the bpy π* orbital, rapid CH_3CN dissociation occurs with a concurrent shift in radical character from the ligand to form the neutral five-coordinate 17-valence electron intermediate, [*fac*-Mn^0(bpy)(CO)$_3$] (**[1]^0**). This metastable Mn(0) complex, in the absence of any steric hindrance (Sampson et al., 2014), rapidly forms the Mn^0-Mn^0 bound 18-valence electron [*fac*-Mn^0(bpy)(CO)$_3$]$_2$ dimer, **[1–1]^0**. While unequivocal evidence of [*fac*-Mn^0(N^N)(CO)$_3$] dimer formation is presented below via infrared spectroelectrochemical (IR-SEC) studies, its oxidation is often evident in the reverse anodic scan in cyclic voltammetry, observed here at −0.61 V and −0.58 V for **[1–1]^0** and **[2–2]^0**, respectively. Thus, the second reduction event for [*fac*-Mn(N^N)(CO)$_3$L]^n complexes is often attributed to an irreversible two-electron *EC* event whereby the dimer is reductively cleaved to generate two equivalents of the two-electron reduced [*fac*-Mn^0(N^N$^{\bullet-}$)(CO)$_3$]$^-$ anion, now established as the principal active catalyst for CO_2 activation by this class of complex via the most common *reduction-first* pathway (Riplinger et al., 2014). Reduction of the phen based dimer, **[2–2]^0** is observed at $E_{pc} = -1.86$ V, suggesting that **[2]$^-$** is more nucleophilic than the benchmark bpy analog, **[1]$^-$** generated at the slightly more positive potential of $E_{pc} = -1.83$ V. Similar to its bpy analog, the native **[2-CH$_3$CN]$^+$** precursor exhibits a quasi-reversible third reduction event at $E_{pc} = -2.72$ V ($E_{1/2} = -2.66$ V, $\Delta E_p = 114$ mV at $\upsilon = 0.1$ V s^{-1}). This third quasi-reversible reduction has rarely been discussed in the literature but computational analysis here suggests that it is a predominantly ligand based reduction giving rise to a 19-electron [*fac*-Mn^0(N^N^{2-})(CO)$_3$]$^{2-}$ dianion. The related dmphen complex, **[3-CH$_3$CN]$^+$** exhibits unexceptionally similar voltammetry in comparison to both its bpy and phen analogs. Its first reduction again involves a ligand based *EC* pathway leading to formation of the **[3–3]^0** dimer. This *EC* reaction is shifted negatively by 10 mV to $E_{pc} = -1.49$ V, relative to formation of both **[1–1]^0** and **[2–2]^0**, consistent with the inductive donating character of the 2,9-dimethyl substituents observed by FTIR studies. Although there is weak evidence of dimer oxidation in the full scan voltammogram presented in **Figure 3**, reversing the scan after just one-electron reduction clearly demonstrates a significant dimer oxidation peak at $E_{pa} = -0.65$ V (**Figure S5**). Reductive cleavage of the **[3–3]^0** dimer to form the two-electron reduced five-coordinate [*fac*-Mn^0(dmbpy$^{\bullet-}$)(CO)$_3$]$^-$ anion (**[3]$^-$**), however, occurs at a more positive potential of −1.78 V. This observation suggests that the steric influence of dmphen slightly hinders electronic coupling between the Mn(0) and dmphen$^{\bullet-}$ radical centers in **[3]$^-$**, rendering it slightly less nucleophilic as a result. The third reduction wave for **[3]$^{-/2-}$** is observed at −2.86 V and, in contrast to its bpy and phen analogs, is completely irreversible.

Noticeably in **Figure 3**, the bqn complex, **[4-CH$_3$CN]$^+$** exhibits a single, reversible, concerted two-electron reduction event at $E_{pc} = -1.30$ V ($E_{1/2} = -1.28$ V, $\Delta E_p = 53$ mV at $\upsilon = 0.1$ V s^{-1}) followed by a single additional quasi-reversible one-electron reduction event at $E_{pc} = -2.51$ V ($E_{1/2} = -2.48$ V, $\Delta E_p = 71$ mV at $\upsilon = 0.1$ V s^{-1}) vs. $Fc^{+/0}$. Equally important here is the lack of any evidence for dimer oxidation in the reverse anodic scan of **[4-CH$_3$CN]$^+$**. This electrochemical behavior, at least in its peak profile, is uncannily similar to previously reported bulky 6,6′-substituted bpy ligands investigated at the identical [*fac*-Mn^0(N^N)(CO)$_3$(CH$_3$CN)]$^+$ center (Sampson et al., 2014; Ngo et al., 2017). Mn^0-Mn^0 formation is known to favor a staggered structure of both bpy ligands in **[1–1]^0** (Machan et al., 2014), and thus far only the inclusion of steric bulk orthogonal to the plane of the polypyridyl ligand has been demonstrated to prevent dimer formation (Sampson et al., 2014; Ngo et al., 2017). Thus, it is appropriate here to question whether the redox behavior exhibited by **[4-CH$_3$CN]$^+$** is in fact due to an electronic influence of this relatively electron deficient ligand, or rather, alternatively is the result of a steric influence of the bqn ligand. The bqn ligand is, after all, π-extended from the same 6,6′-positions as previously reported 6,6′-orthoganol-sterically bulky bpy stystems, albeit here non-orthogonal to, but in the same plane as, the core bpy structure. This question is addressed explicitly via computational analysis presented below.

Infrared Spectroelectrochemistry (IR-SEC)

To gain structural insight into electrochemical activation of these pre-catalysts, IR-SEC was carried out in 0.1 M $[Bu_4N][PF_6]$ acetonitrile supporting electrolyte under 1 atmosphere of argon (**Table 2**). IR-SEC is a powerful investigative tool that takes advantage of the structural specificity of IR spectroscopy for transition metal carbonyl complexes and the ability to prepare *in-situ* catalytic intermediates simply by gradually stepping the potential of the working electrode (Kaim and Fiedler, 2009; Machan et al., 2014). At open-circuit potential, i.e., resting potential of the native pre-catalyst, **[1-CH$_3$CN]$^+$** and **[2-CH$_3$CN]$^+$** both display identical ν(CO) stretching modes as presented earlier (**Figure 2**), confirming negligible influence of the 0.1 M $[Bu_4N][PF_6]$ electrolyte on their FTIR spectra. When the potential was biased beyond the first-reduction at −1.60 V

TABLE 2 | ν(CO) infrared stretches for **[1-CH$_3$CN]$^+$**, **[2-CH$_3$CN]$^+$**, **[3-CH$_3$CN]$^+$**, and **[4-CH$_3$CN]$^+$** precatalysts, and their one-electron reduced, dimeric, and two-electron reduced derivatives, obtained by solution phase FTIR and IR-SEC spectroscopy.

	ν(CO), cm^{-1}
[1-CH$_3$CN]$^+$ [a]	1,958; 2,050
[1–1]^0 [b]	1,857; 1,879; 1,933; 1,976
[1]$^-$ [b]	1,811; 1,911
[2-CH$_3$CN]$^+$ [a]	1,958; 2,050
[2–2]^0 [b]	1,857; 1,880; 1,935; 1,977
[2]$^-$ [b]	1,813; 1,923
[3-CH$_3$CN]$^+$ [a]	1,944(sh); 1,959; 2,046
[3–3]^0 [b]	1,849(sh); 1,860; 1,923; 1,968
[3]$^-$ [b]	1,799; 1,897
[4-CH$_3$CN]$^+$ [a]	1,959; 2,047
[4]$^-$ [b]	1,828; 1,925

[a] *Recorded in neat CH_3CN.*
[b] *Recorded in 0.1 M $[Bu_4N][PF_6]$ acetonitrile electrolyte.*

vs. $Fc^{+/0}$ for both **[1-CH$_3$CN]$^+$** and **[2-CH$_3$CN]$^+$**, a progression was observed where the native ν(CO) stretching modes diminished while four unique but related ν(CO) stretching modes grew in concurrently at 1,857, 1,879, 1,933, and 1,976 cm^{-1} from **[1-CH$_3$CN]$^+$** (**Figure S10**) and at 1,857, 1,880, 1,935, and 1,977 cm^{-1} from **[2-CH$_3$CN]$^+$** (**Figure S11**). These data are consistent with an earlier report of the **[1–1]^0** dimer (Hartl et al., 1995), and the peak profile associated with related Mn^0-Mn^0 dimers previously observed via IR-SEC (Grills et al., 2018), and they are also consistent with our computational frequency analysis. A similar assignment is made for **[2–2]^0** which exhibits almost identical ν(CO) stretching frequencies (vide supra). Upon biasing the working electrode potential further negative (−2.00 V vs. $Fc^{+/0}$) beyond the second Mn^0-Mn^0/Mn^- based reduction for both **[1-CH$_3$CN]$^+$** and **[2-CH$_3$CN]$^+$**, loss of the four dimer stretches was observed (**Figures S10, S11**) with concurrent growth of two new ν(CO) stretching modes at lower wavenumber, corresponding to the five-coordinate two-electron reduced [*fac*-Mn^0(N^N$^{\bullet-}$)(CO)$_3$]$^-$ active catalysts, **[1]$^-$** [ν(CO) = 1,811 and 1,911 cm^{-1}] and **[2]$^-$** [ν(CO) = 1,813 and 1,923 cm^{-1}]. Consistent with its comparable voltammetry behavior, the dmphen based complex, **[3-CH$_3$CN]$^+$** exhibits a similar IR-SEC transition to the two-electron reduced active catalyst, **[3]$^-$** [ν(CO) = 1,799 and 1,897 cm^{-1}] via the **[3–3]^0** dimer intermediate [ν(CO) = 1,849(sh), 1,860, 1,923, and 1,968 cm^{-1}] as illustrated in **Figure 4**. Although clean transformation of **[3-CH$_3$CN]$^+$** to **[3]$^-$** was observed upon direct electrolysis at −2.00 V, it is worth noting that selective electrolysis to the intermediate **[3–3]^0** dimer species did exhibit evidence of minor decomposition to an unidentified side-product [ν(CO) = 1,919 and 2,026 cm^{-1}] with concurrent growth of a broad weak infrared absorption consistent with free CO (**Figure S13**). This is consistent with an earlier report of poor stability of the simpler phen-based dimer, **[2–2]^0** (Stanbury et al., 2017).

As a concerted two-electron reduction event occurs for **[4-CH$_3$CN]$^+$**, the potential was set at −1.65 V vs. $Fc^{+/0}$ for quantitative *in-situ* formation of the two-electron reduced product. Indeed, no evidence for an intermediate one-electron reduced monomer or the Mn^0-Mn^0 dimer was observed. Instead, consistent with the observed voltammetry (vide supra) only a transition to two lower-frequency stretching modes at ν(CO) = 1,828 and 1,925 cm^{-1} was observed, which are attributed to the two-electron reduced [*fac*-Mn^0(bqn$^{\bullet-}$)(CO)$_3$]$^-$ species, **[4]$^-$** (**Figure 5**).

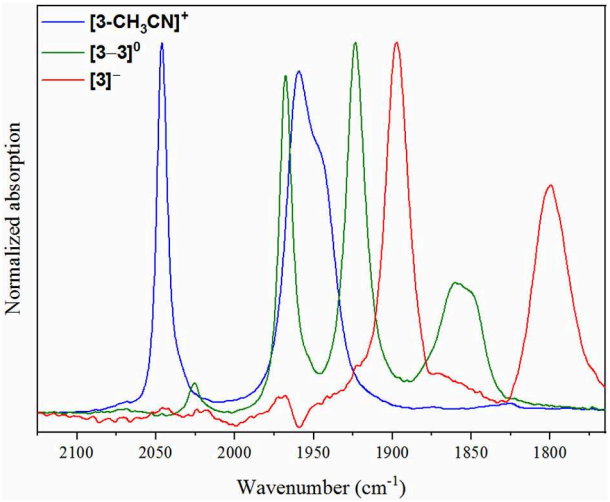

FIGURE 4 | IR-SEC spectra recorded on **[3-CH$_3$CN]$^+$** at the resting potential (blue), upon one-electron reduction (green) and upon two-electron reduction (red).

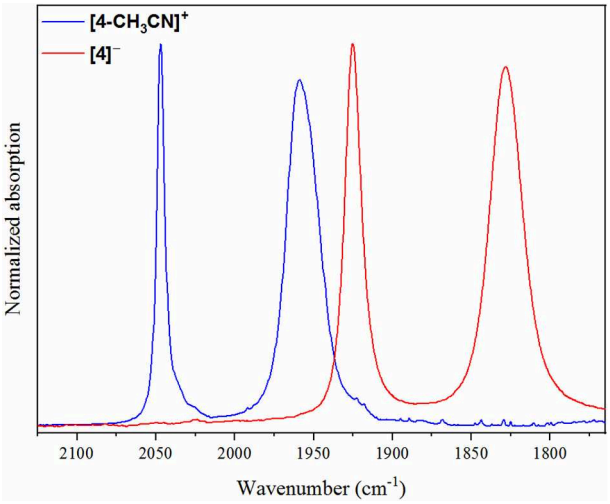

FIGURE 5 | IR-SEC spectra recorded on **[4-CH$_3$CN]$^+$** at the resting potential (blue) and upon two-electron reduction (red).

Voltammetry Under 1 Atm CO_2 in the Presence of 0.3 % H_2O

Prior studies of Mn(I) polypyridyl based electrocatalysts for CO_2 reduction have only reported catalytic current upon addition of excess weak Brønsted acid with, for example, 2.71 M (5%)

addition of H_2O (Bourrez et al., 2011). In contrast to their Re counterparts, which have been established for some time to promote CO_2 reduction in the absence of a proton donor, Mn(I) polypyridyl based electrocatalysts typically require the presence of a proton donor to promote intermediate metallocarboxylic acid formation due to the poorer nucleophilicity of Mn vs. Re catalysts (Riplinger and Carter, 2015). Cyclic voltammograms for pre-catalysts **[1-CH$_3$CN]$^+$**, **[2-CH$_3$CN]$^+$**, **[3-CH$_3$CN]$^+$** and **[4-CH$_3$CN]$^+$** recorded under 1 atm CO_2 at 0.1 V s^{-1} in 0.1 M $[Bu_4N][PF_6]$ acetonitrile electrolyte exhibit clear evidence of catalytic behavior for each complex (**Figure 6**). Although excess Brønsted acid was not added in these experiments, the reagent grade acetonitrile that was used still contains 0.17 M (0.3 %) residual H_2O, which was recently demonstrated to be sufficient to facilitate proton-coupled CO_2 reduction to form CO (McKinnon et al., 2019). This observation is logical due to the relatively larger overpotential applied, especially as the active catalyst under these experimental conditions is predicted by computation (vide infra) to be the more nucleophilic three-electron reduced dianion.

Without knowledge of the *in-situ* pH of the electrolyte solution, the half-wave potential of the catalytic wave ($E_{cat/2}$) can be used to make a relative comparison of overpotentials under these experimental conditions. As expected, π-extension with the bqn ligand in pre-catalyst **[4-CH$_3$CN]$^+$** gives rise to a significant positive shift of catalytic current with $E_{cat/2} = -2.42$ V, whereas the bpy, phen and dmphen pre-catalysts exhibit $E_{cat/2} = -2.85$, -2.64, and -2.74 V, respectively. One difficulty encountered under these experimental conditions was in attempting to establish steady-state catalytic conditions with respect to the rate-limiting consumption of CO_2 within the electrochemical double-layer. As discussed later, this became less problematic once excess Brønsted acid was added. As such, TOF_{max} could not be satisfactorily determined under these experimental conditions. Thus, the TOF value is reported for each catalyst in **Table 3** using Equation 3 and the i_{cat}/i_p ratio determined at a scan rate of 0.1 V s^{-1}, to aid their side-by-side comparison,

$$\mathrm{TOF} = 0.1992\left(\frac{F\upsilon}{RT}\right)\left(\frac{n_p^3}{n_{cat}^2}\right)\left(\frac{i_{cat}}{i_p}\right)^2 \quad (3)$$

where F is the Faraday constant (96,485 s A mol^{-1}), υ is the scan rate (V s^{-1}), R is the universal gas constant (8.3145 V A s K^{-1} mol^{-1}), T is the temperature (K), n_p is the number of electrons involved in the non-catalytic Faradaic current response (responsible for the non-catalytic Faradaic current, i_p, as described by the Randles-Sevcik equation (Bard and Faulkner, 2001), and n_{cat} is the number of electrons required for catalysis (two electrons for the reduction of CO_2 to CO as shown in Equations 1 and 2). In our calculations of TOF, the first one-electron reduction wave ($n_p = 1$) was used for reference to determine the non-catalytic Faradaic current (i_p) for **[1-CH$_3$CN]$^+$**, **[2-CH$_3$CN]$^+$** and **[3-CH$_3$CN]$^+$**. In contrast, the first reduction wave of **[4-CH$_3$CN]$^+$** exhibits a concerted two-electron event under non-catalytic conditions such that $n_p = 2$ at $E_{pc} = -1.30$ V. The significance of this distinction is important when determining TOF from cyclic voltammetry analysis using

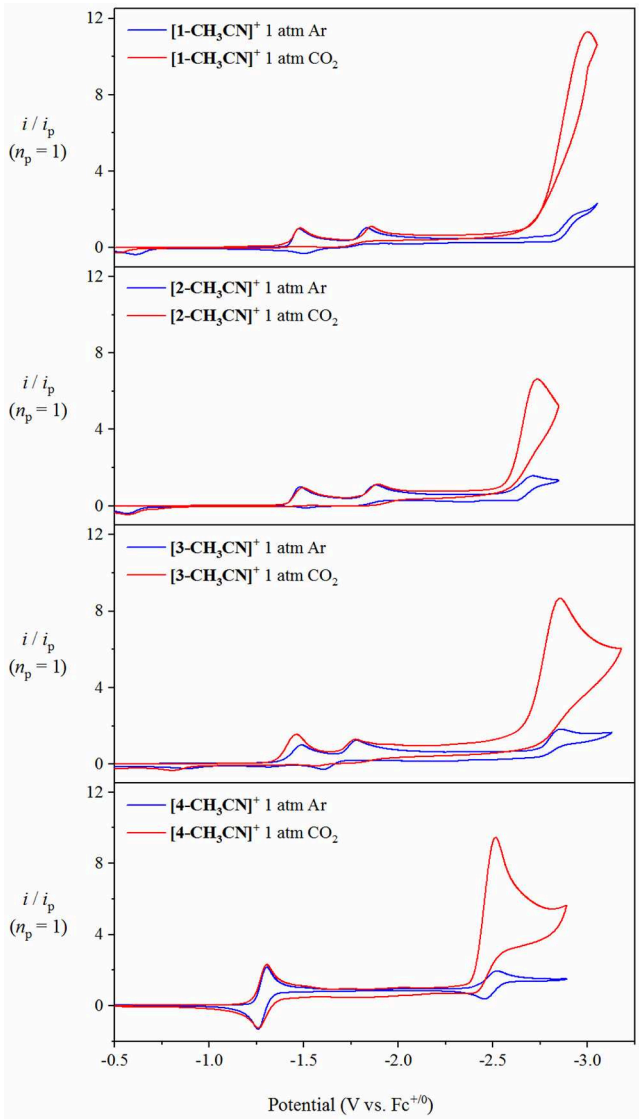

FIGURE 6 | Cyclic voltammograms demonstrating catalytic activity of **[1-CH$_3$CN]$^+$**, **[2-CH$_3$CN]$^+$**, **[3-CH$_3$CN]$^+$** and **[4-CH$_3$CN]$^+$** under 1 atm CO_2 (red) at $\upsilon = 0.1$ V s^{-1} with 0.1 M $[Bu_4N][PF_6]$ acetonitrile supporting electrolyte containing residual 0.17 M (0.3%) H_2O as a Brønsted acid source. Cyclic voltammograms recorded under 1 atm of argon are also shown (blue). The current (y-axis) data are normalized with respect to the non-catalytic Faradaic response (i_p).

Equation 3 as the ratio of $\frac{n_p^3}{n_{cat}^2}$ can differ by a factor of 8 (1/4 vs. 8/4 for $n_p = 1$ or 2, respectively). However, this should, with ideal Randles-Sevcik behavior ($i_p \propto n_p^{3/2}$) of the two-electron reduction event, be completely offset by the 8× smaller $(i_{cat}/i_p)^2$ ratio when $n_p = 2$. Thus, in theory, kinetic analysis of **[4-CH$_3$CN]$^+$** can be conducted using either the concerted two-electron reduction event at $E_{pc} = -1.30$ V ($n_p = 2$) or the subsequent one-electron reduction event at $E_{pc} = -2.51$ V ($n_p = 1$) for reference in determining i_{cat}/i_p. Using data recorded at $\upsilon = 0.1$ V s^{-1}, Equation 3 results in different TOF values

TABLE 3 | Summary of electrocatalysis data derived from voltammetry experiments, in the absence of TFE and at optimum TFE concentrations.

	[1-CH$_3$CN]$^+$		**[2-CH$_3$CN]$^+$**		**[3-CH$_3$CN]$^+$**		**[4-CH$_3$CN]$^+$**	
[TFE] (M)	0	2.0	0	2.0	0	2.5	0	1.5
$E_{cat/2}$ (V)[a]	−2.85	−1.94	−2.64	−1.97	−2.74	−1.97	−2.42	
i_{cat}/i_p[b]	11.3	20.2	7.4	17.1	10.7	18.5	8.5	11.6
TOF (s^{-1})	25[c,d]	75 ± 3[c,e]	11[c,d]	75 ± 6[c,e]	22[c,d]	67[c,d]	14[c,d]	26[c,d]

[a]*All potentials reported vs. the ferricenium/ferrocene pseudo reference recorded at* $\upsilon = 0.1$ *V* s^{-1}.
[b]*Calculated at* $\upsilon = 0.1$ *V* s^{-1}.
[c]*TOF calculated using* $n_p = 1$ *electron.*
[d]*Steady-state conditions not achieved, calculated at* $\upsilon = 0.1$ *V* s^{-1}.
[e]*Average* TOF_{max} *determined over a range of scan rates at steady-state conditions (see* ***Supporting Information****).*

of 25 s^{-1} ($i_{cat}/i_p = 4.0$, $n_p = 2$) or 14 s^{-1} ($i_{cat}/i_p = 8.5$, $n_p = 1$), indicating non-ideal behavior of the concerted two-electron reduction event, which is unsurprising considering this is an *ECE* mechanism and not a pure two-electron concerted *EE* mechanism. Scan rate analysis of this two-electron reduction event for **[4-CH$_3$CN]$^+$** clearly demonstrates an increase in peak separation between its cathodic and anodic waves (**Figure S9**). More importantly, the 2.83-fold increase in current for a two-electron event, predicted by the Randles-Sevcik equation ($i_p \propto n_p^{3/2}$) assuming similar diffusion coefficients for each redox state, is in fact found to be significantly smaller (2.13-fold) when we compare the i_p values of **[4-CH$_3$CN]$^+$** at $E_{pc} = -1.30$ ($n_p = 2$) and $E_{pc} = -2.51$ V ($n_p = 1$). The TOF value of 25 s^{-1} ($i_{cat}/i_p = 4.0$, $n_p = 2$) is therefore an overestimate of this catalyst's efficiency, and the value of TOF = 14 s^{-1} is henceforth quoted for **[4-CH$_3$CN]$^+$** ($i_{cat}/i_p = 8.5$, $n_p = 1$) recorded at $\upsilon = 0.1$ V s^{-1}. In summary, the benchmark bpy-based pre-catalyst, **[1-CH$_3$CN]$^+$** ($i_{cat}/i_p = 11.3$) exhibits the highest TOF in this study of 25 s^{-1} at $\upsilon = 0.1$ V s^{-1}, followed closely by **[3-CH$_3$CN]$^+$** at 22 s^{-1} ($i_{cat}/i_p = 10.7$), the bqn-based system **[4-CH$_3$CN]$^+$** at 14 s^{-1} ($i_{cat}/i_p = 8.5$) and finally **[2-CH$_3$CN]$^+$** at just 11 s^{-1} ($i_{cat}/i_p = 7.4$).

Voltammetry Under 1 Atm CO_2 in the Presence of Trifluoroethanol

To further probe the catalytic activity of **[1-CH$_3$CN]$^+$**, **[2-CH$_3$CN]$^+$**, **[3-CH$_3$CN]$^+$** and **[4-CH$_3$CN]$^+$**, the voltammetry conditions were altered by adding incremental amounts of a non-aqueous proton source. For the purpose of this study, 2,2,2-trifluoroethanol (TFE, $pK_{a(CH3CN)} = 35.4$(est.) Lam et al., 2015) was added as a Brønsted acid to observe and optimize proton-coupled catalytic CO_2 reduction. The addition of at least 1.5 M TFE results in a plateau of catalytic current for **[1-CH$_3$CN]$^+$**, **[2-CH$_3$CN]$^+$** and **[3-CH$_3$CN]$^+$** when monitored at $\upsilon = 0.1$ V s^{-1} (**Figure 7**, **Figures S16–S19**). Notably, each of their catalytic waves exhibit a significant positive shift compared to experiments in the absence of excess Brønsted acid, with $E_{cat/2} = -1.94$ V for **[1-CH$_3$CN]$^+$** and $E_{cat/2} = -1.97$ V for both **[2-CH$_3$CN]$^+$** and **[3-CH$_3$CN]$^+$**. The predominant catalytic peak observed for **[1-CH$_3$CN]$^+$**, **[2-CH$_3$CN]$^+$**, and **[3-CH$_3$CN]$^+$** is assigned, with the aid of computations, to the *reduction-first* pathway with the five-coordinate, two-electron reduced [*fac*-$Mn^0(N^\wedge N^{\bullet-})(CO)_3]^-$ monoanion being the active catalyst.

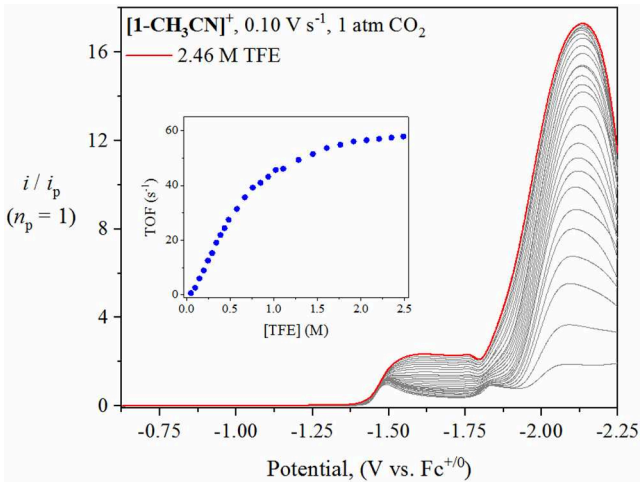

FIGURE 7 | Linear sweep voltammetry of **[1-CH$_3$CN]$^+$** recorded at $\upsilon = 0.1$ V s^{-1} under 1 atm CO_2 with increasing TFE concentration (0–2.46 M). The current (y-axis) data are normalized with respect to the non-catalytic Faradaic response (i_p). The inset plot of 'TOF vs. TFE concentration' demonstrates that zero-order conditions with respect to TFE concentration were achieved at 2.0 M TFE.

Interestingly, a weak grow-in of catalytic current can also be observed at $E_{cat/2} = -1.48$ V for both **[1-CH$_3$CN]$^+$** and **[2-CH$_3$CN]$^+$** (a similar maximum is less discernable for **[3-CH$_3$CN]$^+$**). This lower overpotential weak catalytic current occurs directly from the one-electron reduced species and is thus attributed to catalytic activity of the Mn^0-Mn^0 dimer intermediate. Indirect support of this hypothesis is the fact that such weak catalytic current is not observed with the bqn pre-catalyst, **[4-CH$_3$CN]$^+$** which we have already established, via IR-SEC studies, does not form a Mn^0-Mn^0 dimer intermediate. While appearance of this lower energy catalytic pathway is promising, the very weak current observed, and thus the minimal TOF (<1 s^{-1}) prompted us to focus on the more efficient *reduction-first* pathway for these complexes. Furthermore, this mechanism has already been the focus of other independent studies (Bourrez et al., 2014; Neri et al., 2019).

In contrast to the above mentioned studies in the absence of excess Brønsted acid, the presence of optimal TFE concentrations benefitted the pursuit of steady-state catalytic conditions, thus allowing for an estimation of a maximum turnover frequency (TOF_{max}), at least in the case of **[1-CH$_3$CN]$^+$** and **[2-CH$_3$CN]$^+$**. A collection of scan-rate dependent voltammetry data is provided in the **Supporting Information** for all pre-catalysts (**Figures S20–S23**) with kinetic analysis summarized in **Table 3**. Pre-catalysts **[1-CH$_3$CN]$^+$** and **[2-CH$_3$CN]$^+$** perform comparably with TOF_{max} values estimated at 75 s^{-1} under steady-state catalytic conditions. Pre-catalyst **[3-CH$_3$CN]$^+$** still exhibits a scan-rate dependent current upon increasing scan rate >0.1 V s^{-1}, thus preventing pure kinetic steady-state conditions, and hence TOF_{max}, to be obtained. Thus, an estimated TOF value of 67 s^{-1} is reported for **[3-CH$_3$CN]$^+$** recorded at a scan

rate of $\upsilon = 0.1$ V s^{-1} (**Figure S22**). Results from the addition of TFE to **[4-CH$_3$CN]$^+$** were rather complicated due to the grow-in of an additional pre-wave at approx. −2.42 V which prevented accurate determination of $E_{cat/2}$ or TOF_{max} (**Figure S23**). At least from a qualitative perspective, it can be stated that TFE addition does give rise to a modest increase in the observed catalytic current maximum (**Figure 8**). Unfortunately, this phenomenon of multiple catalytic waves raises concerns about product selectivity and competitive side reactions, which are borne true following controlled potential electrolysis experiments, discussed below, which conclusively confirm hydrogen evolution as not just a competitive but a dominant process under these experimental conditions with **[4-CH$_3$CN]$^+$**. Mechanistic details of competitive hydrogen evolution vs. CO_2 reduction are discussed in more detail below via computational analysis.

Controlled Potential Electrolysis

Product selectivity of all four pre-catalysts in the absence and presence of TFE under 1 atmosphere of CO_2 was investigated by controlled potential electrolysis (CPE) with *in-situ* gas chromatography analysis used for CO and H_2 quantification over a time period of 4 h. The potential bias applied in each case corresponded to $E_{cat/2}$ for specific experimental conditions as summarized in **Table 3** for each catalyst. The tabulated Faradaic efficiency (FE) data in **Table 4** represent the peak CO selectivity observed at a single time interval over the duration of the experiment, whereas the turnover number (TON) tabulated for both CO and H_2 represents the total TON over the entire course of the experiment. Plots summarizing all electrolysis data are provided in **Figures S28–S35**. Ultimately, all pre-catalysts yielded CO product regardless of the conditions employed. Each of the pre-catalysts, **[1-CH$_3$CN]$^+$**, **[2-CH$_3$CN]$^+$**, and **[3-CH$_3$CN]$^+$** exhibited a clear selectivity for CO production in the absence or presence of TFE with only **[4-CH$_3$CN]$^+$** yielding significant H_2 in the presence of 1.5 M TFE. Unfortunately, however, in most cases there is FE that is unaccounted for. This is especially true for pre-catalysts **[2-CH$_3$CN]$^+$** and **[3-CH$_3$CN]$^+$** which is likely due to rapid decomposition, consistent with their poor TONs for CO or H_2 evolution. Pre-catalyst **[1-CH$_3$CN]$^+$** performed significantly better, exhibiting percentage FE's of 62:2 CO:H_2 in the absence of TFE, which increased to 84:2 in the presence of 2.0 M TFE. Efforts to quantify any formate (HCO_2^-) production to account for the full FE of all catalysts were in vain. This is likely due to the low turnover numbers of these catalysts, which as a whole performed quite poorly under the experimental conditions employed; a recognized problem for the [*fac*-Mn(N^N)(CO)$_3$]$^-$ class of electrocatalysts under homogeneous conditions (Grills et al., 2018). Indeed, two prior CPE studies of the [*fac*-MnBr(phen)(CO)$_3$] pre-catalyst have each highlighted the poor performance of this system with the FE_{CO} ranging from 18 to 57% (Stanbury et al., 2017; Tignor et al., 2018). Interestingly, the bqn-derived pre-catalyst, **[4-CH$_3$CN]$^+$** exhibited the greatest FE_{CO} of 98% in the absence of TFE, albeit with a very low TON of just 3. However, with such a low TON we cannot rule out catalyst decomposition as a contributing factor. As anticipated from its irregular voltammetry behavior,

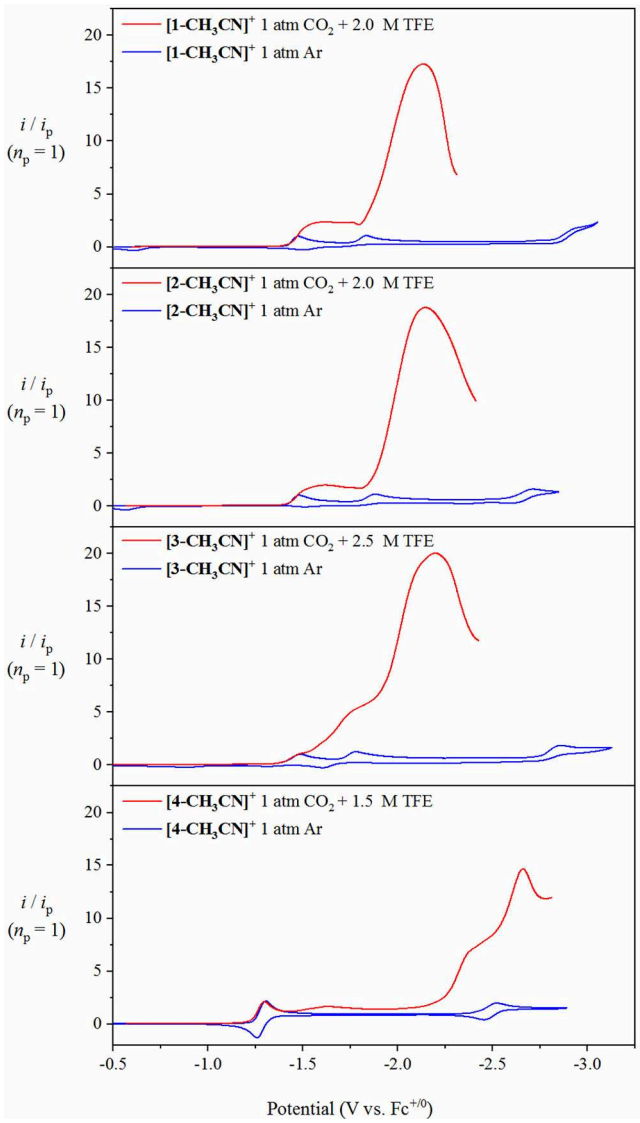

FIGURE 8 | Overlay of cyclic voltammograms for **[1-CH$_3$CN]$^+$**, **[2-CH$_3$CN]$^+$**, **[3-CH$_3$CN]$^+$** and **[4-CH$_3$CN]$^+$** recorded under 1 atm of Ar (blue), with respective linear sweep voltammetry recorded under 1 atm CO_2 in the presence of optimum TFE (red) at $\upsilon = 0.1$ V s^{-1} with 0.1 M [Bu_4N][PF_6] acetonitrile supporting electrolyte. The current (y-axis) data are normalized with respect to the non-catalytic Faradaic response (i_p).

at least in comparison to **[1-CH$_3$CN]$^+$**, **[2-CH$_3$CN]$^+$**, and **[3-CH$_3$CN]$^+$**, upon the introduction of TFE, a dramatic shift in product selectivity was observed, with FE's of 14:69 CO:H_2. As discussed below in the computational section, this shift in product selectivity is possibly a consequence of the reduced nucleophilicity of the two-electron reduced **[4]$^-$** active catalyst, in large part due to the lower lying π* orbitals of the bqn ligand.

Computational Analysis

Density functional theory (DFT) calculations at the M06 level of theory (Zhao and Truhlar, 2008a,b, 2010) in conjunction with the SMD continuum solvation model (Marenich et al.,

2009) for acetonitrile were performed to examine the catalyst activation and electrocatalytic CO_2 reduction mechanisms of **[1-CH$_3$CN]**$^+$, **[2-CH$_3$CN]**$^+$, and **[4-CH$_3$CN]**$^+$. Mechanistic calculations on **[3-CH$_3$CN]**$^+$ were omitted for the sake of brevity due to its similarity in behavior to **[2-CH$_3$CN]**$^+$. The results are summarized in **Schemes 1** and **2** along with tabulated energetics (**Tables 5**, **6**). Further details on the electronic structures of selected reaction intermediates are provided in **Supporting Information**.

Catalyst Activation and Dimer Formation

The activation of each catalyst starts with one-electron reduction of the solvent-coordinated **[Mn-CH$_3$CN]**$^+$ species. For all considered pathways in the present study, **[1-CH$_3$CN]**$^+$ and **[2-CH$_3$CN]**$^+$ exhibit similar energetics (**Scheme 1**), so henceforth we will focus on the activation of **[1-CH$_3$CN]**$^+$ to highlight the distinct behavior of **[4-CH$_3$CN]**$^+$. The one-electron reduction of **[Mn-CH$_3$CN]**$^+$ (E_1) results in the formation of a ligand-based radical anion for all of the complexes investigated (**Figure S36**).

TABLE 4 | Summary of controlled potential electrolysis data in the absence of TFE and at optimum TFE concentrations[a].

	[1-CH$_3$CN]$^+$		[2-CH$_3$CN]$^+$		[3-CH$_3$CN]$^+$		[4-CH$_3$CN]$^+$	
[TFE] (M)	0	2.0	0	2.0	0	2.5	0	1.5
FE_{CO} (%)[b]	62	80	47	64	31	15	98	14
FE_{H2} (%)[b]	6	2	7	1	1	1	1	69
TON (CO:H_2)[c]	17:9	18:12	6:2	3:2	4:1	4:2	3:1	2:10

[a] *Applied potential was equal to $E_{cat/2}$ as summarized in **Table 3** for each catalyst.*
[b] *Peak CO:H_2 FE ratio observed over a 4 h duration.*
[c] *Totaled over a 4 h duration.*

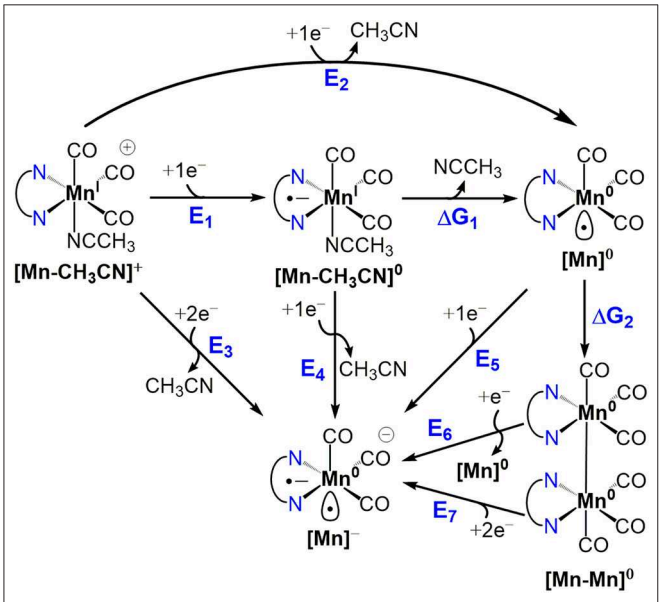

SCHEME 1 | Catalyst activation and dimerization pathways for Mn^I polypyridyl complexes **[1-CH$_3$CN]**$^+$, **[2-CH$_3$CN]**$^+$ and **[4-CH$_3$CN]**$^+$.

Typically observed as an *EC* mechanism in voltammetry ($E_1\,\Delta G_1$ in **Scheme 1**), subsequent dissociation of the acetonitrile ligand (ΔG_1) leads to localization of the unpaired spin on the Mn center, generating a formally Mn^0 species (**[Mn]^0**) (**Figure S36**). The extensive π-conjugation of **[4-CH$_3$CN]**$^+$ introduces an ∼+0.5 V anodic shift ($E_1 = -1.23$ V) compared to that of **[1-CH$_3$CN]**$^+$ ($E_1 = -1.74$ V), in line with the assumption of an initial ligand-based reduction. The computed energetics indicate that acetonitrile dissociation is very favorable upon reduction of **[1-CH$_3$CN]**$^+$ ($\Delta G_1 = -6.6$ kcal/mol) to generate pentacoordinate **[1]^0**, further reduction of which ($E_5 = -1.79$ V) will form **[1]**$^-$. In contrast, theory predicts that **[4-CH$_3$CN]^0** and **[4]^0** will coexist based on acetonitrile dissociation being nearly isoergic ($\Delta G_1 = -0.4$ kcal/mol). This distinct behavior is responsible for the experimentally observed concerted two-electron reduction of **[4-CH$_3$CN]**$^+$ to **[4]**$^-$ ($E_3 = -1.36$ V), which requires a lower potential than the sequential one-electron reduction pathway, i.e., **[4-CH$_3$CN]^0** to **[4]**$^-$ conversion ($E_4 = -1.48$ V) in contrast to **[1-CH$_3$CN]**$^+$ ($E_3 = -1.62$ V and $E_4 = -1.50$ V).

Another intriguing difference is in the energetics of dimerization of **[Mn]^0** to **[Mn-Mn]^0**, which is quite favorable for **[1]^0** ($\Delta G_2 = -11.5$ kcal/mol), in contrast to a nearly isoergic driving force in the case of **[4]^0** ($\Delta G_2 = -1.2$ kcal/mol). Closer inspection of the dimer geometries indicates that staggered conformations are more favorable and Mn–Mn distances are predicted as 2.96 Å and 3.16 Å for **[1–1]^0** and **[4–4]^0**, respectively (**Figure S37**). This difference is partly attributed to ligand-induced steric effects that lead the Mn center to be out-of-plane with respect to the ligand in the case of **[4]^0** (for **[4]^0**, C_{bridge}-N-Mn-N is 23.2°, compared to 1.1° for **[1]^0**). It should be noted that dimerization of **[4]^0** is even further suppressed due to the predicted equilibrium between hexacoordinate **[4-CH$_3$CN]^0** and pentacoordinate **[4]^0**, even if the latter forms during electrocatalysis. As a result of the computational analysis described above, **[1-CH$_3$CN]**$^+$ and **[2-CH$_3$CN]**$^+$ are predicted to form **[1]^0** and **[2]^0**, respectively, via an *EC* process followed by fast dimerization to form **[1–1]^0** and **[2–2]^0**, respectively, which can then be reduced via sequential one-electron processes, or a concerted two-electron reduction process, to generate

TABLE 5 | Computed reduction potentials (V vs. Fc$^{+/0}$) and free energy changes (ΔG, kcal/mol) of catalyst activation and dimerization pathways for Mn^I polypyridyl complexes **[1-CH$_3$CN]**$^+$, **[2-CH$_3$CN]**$^+$, and **[4-CH$_3$CN]**$^+$.

	[1-CH$_3$CN]$^+$	[2-CH$_3$CN]$^+$	[4-CH$_3$CN]$^+$
E_1	−1.74 V	−1.77 V	−1.23 V
ΔG_1	−6.6 kcal/mol	−6.6 kcal/mol	−0.4 kcal/mol
E_2	−1.45 V	−1.49 V	−1.21 V
E_3	−1.62 V	−1.66 V	−1.36 V
E_4	−1.50 V	−1.54 V	−1.48 V
E_5	−1.79 V	−1.83 V	−1.50 V
ΔG_2	−11.5 kcal/mol	−13.4 kcal/mol	−1.2 kcal/mol
E_6	−2.29 V	−2.41 V	−1.55 V
E_7	−2.04 V	−2.12 V	−1.52 V

the catalytically active $[\mathbf{1}]^-$ and $[\mathbf{2}]^-$ species. We should note that two-electron reduction of the $[\mathbf{Mn\text{-}Mn}]^{\mathbf{0}}$ dimer practically proceeds via two sequential one-electron reduction steps as the dimer is expected to decompose into $[\mathbf{Mn}]^{\mathbf{0}}$ and $[\mathbf{Mn}]^-$ upon the first reduction, and the computed reduction potential of $[\mathbf{Mn}]^{\mathbf{0}}$ is more anodic than that of $[\mathbf{Mn\text{-}Mn}]^{\mathbf{0}}$ (e.g., $E_5 = -1.79$ V for $[\mathbf{1}]^{\mathbf{0}}$ vs. $E_6 = -2.29$ V for $[\mathbf{1\text{–}1}]^{\mathbf{0}}$).

CO_2 Binding and CO Evolution

Next, we turn our attention to CO_2 binding to the two-electron reduced $[\mathbf{Mn}]^-$ catalyst and subsequent steps of electrocatalytic CO_2 reduction (**Scheme 2**). Similar to earlier reports (Riplinger et al., 2014), CO_2 binding to $[\mathbf{1}]^-$ is computed to be uphill ($\Delta G_3 = 8.6$ kcal/mol) and is driven by proton transfer from a Brønsted acid to generate $[\mathbf{1\text{-}CO_2H}]^{\mathbf{0}}$ ($pK_{a1} = 24.8$). Interestingly, we could not locate an optimized structure of CO_2-bound $[\mathbf{4\text{-}CO_2}]^-$, indicating that since the potential to generate $[\mathbf{4}]^-$ is nearly +0.5 V more positive compared to that of $[\mathbf{1}]^-$, the pentacoordinate $[\mathbf{4}]^-$ does not possess enough reducing power to activate CO_2. On the other hand, further reduction to $[\mathbf{4}]^{\mathbf{2-}}$ (**Figure S38**), results in increased reactivity toward CO_2 to generate $[\mathbf{4\text{-}CO_2}]^{\mathbf{2-}}$ ($\Delta G_4 = 10.8$ kcal/mol), and subsequent protonation yields $[\mathbf{4\text{-}CO_2H}]^-$ ($pK_{a3} = 29.4$) (**Scheme 2**). It should be noted that the spin density (**Figure S38**) and total electron density difference (**Figure S39**) plots indicate that the third reduction is predominantly ligand centered in $[\mathbf{4}]^{\mathbf{2-}}$ and best characterized as $[Mn^0\text{-bqn}^{2-}]^{2-}$, although the additional negative charge is shared between the metal center and the ligand in the case of $[\mathbf{1}]^{\mathbf{2-}}$ and $[\mathbf{2}]^{\mathbf{2-}}$ such that the electronic structure exhibits a resonance between $[Mn^-\text{-}(N\hat{}N)^{\bullet-}]^{2-}$ and $[Mn^0\text{-}(N\hat{}N)^{2-}]^{2-}$. $[\mathbf{Mn\text{-}CO_2H}]^-$ is predicted to be the common intermediate for both $[\mathbf{1\text{-}CH_3CN}]^+$ and $[\mathbf{4\text{-}CH_3CN}]^+$ electrocatalysts, as C–OH bond cleavage is expected to proceed predominantly via the *reduction-first* pathway (**Scheme 2**). Scission of the C–OH bond in $[\mathbf{Mn\text{-}CO_2H}]^-$ assisted by TFE leads to $[\mathbf{Mn\text{-}CO}]^{\mathbf{0}}$. CO evolution may occur spontaneously from $[\mathbf{Mn\text{-}CO}]^{\mathbf{0}}$ prior to one-electron reduction (Grice et al., 2013) and generation of $[\mathbf{Mn}]^-$. However, this mechanism is yet to be experimentally verified for this class of Mn catalyst. In contrast to $[\mathbf{1\text{-}CH_3CN}]^+$, $[\mathbf{4\text{-}CH_3CN}]^+$ produces H_2 as the dominant product in the presence of TFE as a Brønsted acid, which is attributed to less favorable interaction of $[\mathbf{4}]^-$

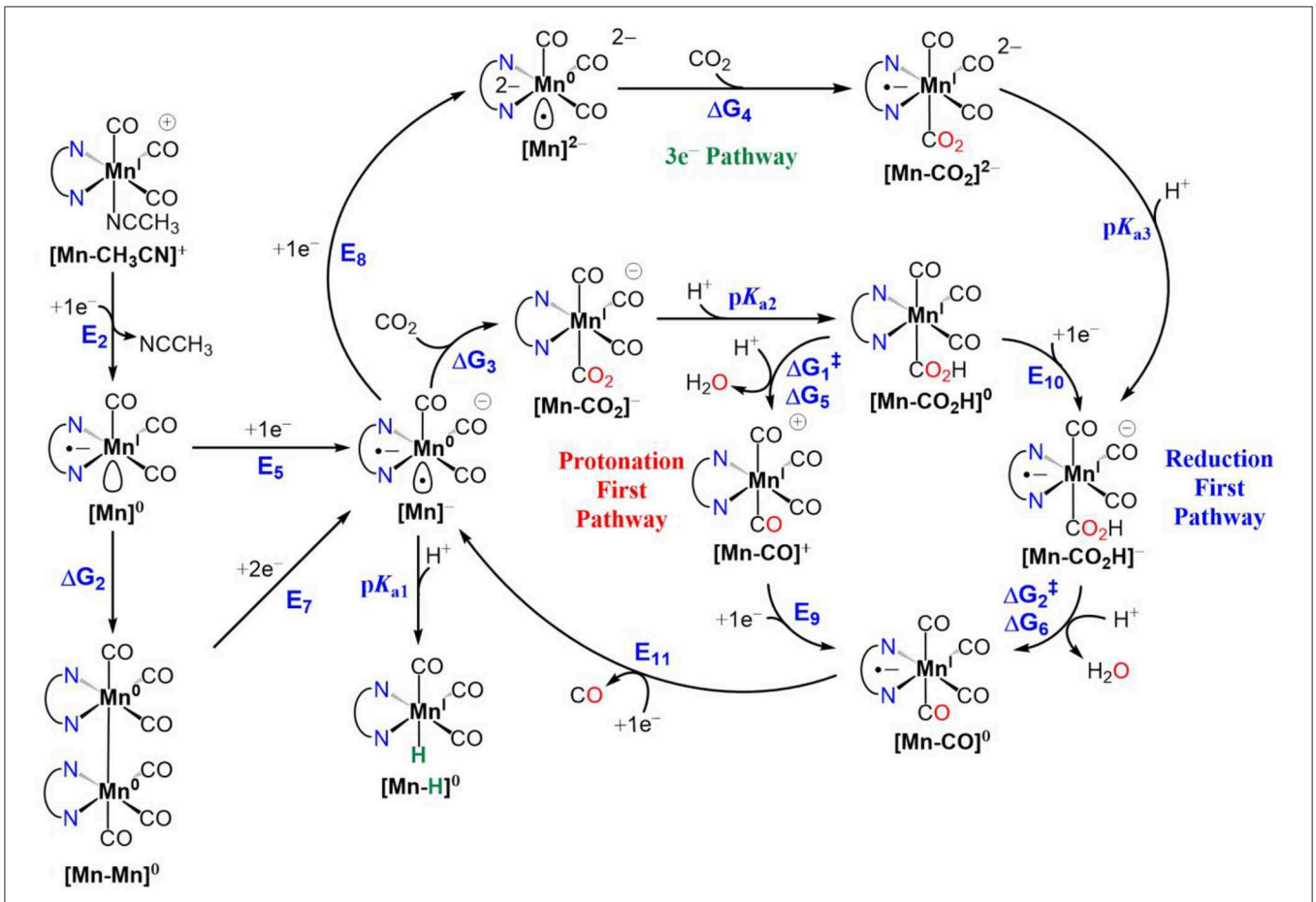

SCHEME 2 | Electrocatalytic reduction of CO_2 to CO for Mn^I polypyridyl complexes of $[\mathbf{1\text{-}CH_3CN}]^+$, $[\mathbf{2\text{-}CH_3CN}]^+$ and $[\mathbf{4\text{-}CH_3CN}]^+$, illustrating active catalyst generation, protonation-first and reduction-first pathways vs. the three-electron reduction pathway. Also included alongside are competitive Mn^0-Mn^0 dimer formation and Mn^I-H formation side reactions. For the C–OH bond cleavage steps, TFE is used as the Brønsted acid. The free energy changes (ΔG) and activation free energies (ΔG) are in units of kcal/mol and reduction potentials are in units of volts (V) vs. $Fc^{+/0}$.

TABLE 6 | Computed reduction potentials (V vs. $Fc^{+/0}$), free energy changes (ΔG, kcal/mol) and activation free energies ($\Delta G^{\ddagger}$, kcal/mol), and pK_a's relevant for electrocatalytic reduction of CO_2 to CO for Mn^I polypyridyl complexes **[1-CH$_3$CN]$^+$**, **[2-CH$_3$CN]$^+$**, and **[4-CH$_3$CN]$^+$**, shown in **Scheme 2**, comparing the *protonation-first* and *reduction-first* pathways vs. the *three-electron* reduction pathway.

	[1-CH$_3$CN]$^+$	**[2-CH$_3$CN]$^+$**	**[4-CH$_3$CN]$^+$**
E_2	−1.45 V	−1.49 V	−1.21 V
ΔG_2	−11.5 kcal/mol	−13.4 kcal/mol	−1.2 kcal/mol
E_5	−1.79 V	−1.83 V	−1.50 V
E_7	−2.04 V	−2.12 V	−1.52 V
pK_{a1}	24.8	25.2	17.3
ΔG_3	8.6 kcal/mol	8.7 kcal/mol	–
pK_{a2}	23.7	24.3	–
E_8	−2.71 V	−2.53 V	−2.25 V
ΔG_4	1.5 kcal/mol	5.2 kcal/mol	10.8 kcal/mol
pK_{a3}	30.0	29.6	29.4
$\Delta G_1^{\ddagger}$	23.8 kcal/mol	22.6 kcal/mol	28.8 kcal/mol
ΔG_5	17.6 kcal/mol	16.8 kcal/mol	21.1 kcal/mol
E_9	−1.61 V	−1.70 V	−1.12 V
E_{10}	−2.03 V	−2.07 V	−1.57 V
$\Delta G_2^{\ddagger}$	18.6 kcal/mol	–	20.9 kcal/mol
ΔG_6	8.0 kcal/mol	8.5 kcal/mol	10.6 kcal/mol
E_{11}	−1.91 V	−1.88 V	−1.82 V

with CO_2 compared to $[\mathbf{1}]^-$. However, we should also note that the pK_a's of $[\mathbf{1}]^-$ (pK_a = 24.8) and $[\mathbf{1}]^{2-}$ (pK_a = 36.0) are significantly higher than their counterparts, $[\mathbf{4}]^-$ (pK_a = 17.3) and $[\mathbf{4}]^{2-}$ (pK_a = 29.0), indicating that hydride formation is not as favorable in the latter either. In the absence of a Brønsted acid as a proton source, all the catalysts are predicted to form the three-electron reduced $[\mathbf{Mn}]^{2-}$ active catalyst before binding CO_2 and subsequently producing CO and CO_3^{2-} via interaction of a second CO_2 molecule with $[\mathbf{Mn\text{-}CO_2}]^{2-}$.

CONCLUSIONS

Through a systematic variation of the polypyridyl ligand from bpy to phen to dmphen and finally bqn, both steric- and electronic-based ligand influences on the activity of a $[fac\text{-}Mn(N^\wedge N)(CO)_3(CH_3CN)]^+$ class of CO_2 reduction pre-catalysts has been established, providing critical insight into the manipulation of CO_2 binding affinities and resulting product selectivity for these catalysts. Through a combination of IR-SEC and computational studies, the combined electronic and steric influences of the π-extended bqn ligand have been probed in **[4-CH$_3$CN]$^+$**, where formation of the $[\mathbf{4\text{–}4}]^0$ dimer is hindered and a concerted two-electron *ECE* mechanism for the generation of $[\mathbf{4}]^-$ is favored. Computations have revealed how the lower lying π*-orbitals of the bqn ligand have rendered this pentacoordinate $[\mathbf{4}]^-$ intermediate inactive with respect to CO_2, even in the presence of a Brønsted acid. In contrast to the bpy, phen, and dmphen derived catalysts, this has resulted in a shift in product selectivity for the **[4-CH$_3$CN]$^+$** pre-catalyst to favor H_2 evolution in the presence of excess TFE. However, electrochemical and computational investigations have established successful CO_2 activation following *in-situ* generation of a three-electron reduced $[fac\text{-}Mn^{(-1)}(N^\wedge N^{\bullet-})(CO)_3]^{2-}$ active catalyst, a first for any $[fac\text{-}Mn(N^\wedge N)(CO)_3(CH_3CN)]^+$ pre-catalyst. Although at the cost of additional overpotential, this *three-electron* pathway results in increased reactivity toward CO_2 to generate the previously established $[fac\text{-}Mn^{(I)}(CO_2H)(N^\wedge N^{\bullet-})(CO)_3]^-$ intermediate, which subsequently propagates the catalytic cycle via the standard *reduction-first* pathway involving rate-determining, proton-coupled C–OH bond cleavage.

MATERIALS AND METHODS

Acetonitrile (ACS reagent grade, 99.5%), bromopentacarbonylmanganese(I) (98%), potassium carbonate (>99%), silver trifluoromethanesulfonate (>99%), tetrahydrofuran (anhydrous, 99.9%) and 2,2,2-trifluoroethanol (>99%) were purchased from Sigma Aldrich and used as received. Dichloromethane (ACS reagent grade, >99.9%) and diethyl ether were purchased from Pharmco-Aaper (ACS reagent grade, >99.9%) and used as received. The water content in ACS reagent grade acetonitrile was confirmed by Karl-Fisher titration to be 0.17 M (0.3%). Tetrabutylammonium hexafluorophosphate (99%, Sigma Aldrich) was recrystallized thrice from ethanol and dried under vacuum prior to electrolyte preparation. Steady-state FTIR spectra were recorded on a Thermo Nicolet 670 FTIR spectrophotometer using a liquid cell with CaF_2 windows in spectrophotometric grade acetonitrile (99.5%, Sigma Aldrich) solvent. NMR spectra were recorded on an Agilent spectrometer operated at 399.80 MHz for ^1H nuclei. CD_3CN was used as received from Sigma Aldrich and its residual ^1H solvent signal used as an internal reference for reporting the chemical shift (δ = 1.96 ppm). Voltammetry and bulk electrolysis were carried out on a CH Instruments 620E potentiostat. A custom three-electrode cell was used for both voltammetry and bulk electrolysis experiments allowing airtight introduction of working, counter and reference electrodes as well as septa for gas purging. For cyclic voltammetry, glassy carbon (3 mm diameter) and Pt wire were used as working and counter electrodes, respectively, with 0.1 M $[Bu_4N][PF_6]$ in ACS reagent grade acetonitrile as the supporting electrolyte. A non-aqueous reference electrode was used to minimize ohmic potential drop at the solvent interface. This consisted of a Ag wire in 0.10 M $[Bu_4N][PF_6]$ acetonitrile supporting electrolyte isolated by a vycor frit and was calibrated *in-situ* using the ferricenium/ferrocene redox couple as an internal reference. Redox potentials (E) were determined from cyclic voltammetry as $(E_{pa} + E_{pc})/2$, where E_{pa} and E_{pc} are the anodic and cathodic peak potentials, respectively. Where E could not be calculated due to irreversible behavior, E_{pc} or E_{pa} are reported accordingly. For CO_2 concentration dependent studies, gas cylinders were ordered from Airgas containing pre-mixed ratios of Ar:CO_2 (100:0, 80:20, 60:40, 50:50, 40:60, 20:80, 0:100). For controlled potential bulk electrolysis experiments a vitreous carbon (Duocell) working electrode soldered to a copper wire was used. A Pt gauze counter electrode was used, isolated from

the main compartment by a fine porosity vycor tube+frit to minimize mass transfer resistance. Gas chromatography data were recorded on a custom Shimadzu GC-2014 instrument where a Ni "methanizer" catalyst was used to convert CO to CH_4 prior to quantification of CH_4 by the thermal conductivity detector. H_2 was simultaneously monitored by a flame ionization detector during the same injection. The GC was pre-calibrated for CO and H_2 quantification by mimicking bulk electrolysis conditions (i.e., 5 mL supporting electrolyte in the same cell, with electrodes, under 1 atm CO_2). Standard curves for H_2 and CO were generated using this cell where known volumes of the analyte gas (H_2 or CO) were injected and the solution stirred for 30 min to allow equilibration of the analyte between the electrolyte and headspace prior to GC injection.

General Synthesis of [*fac*-Mn(N^N)(CO)$_3$(OTf)] Complexes 1-4

Bromopentacarbonyl manganese(I) (100 mg, 0.36 mmol) and silver trifluoromethanesulfonate (93.5 mg, 0.36 mmol) were charged to a 50-mL round bottomed flask with approximately 25 mL of degassed dichloromethane under 1 atmosphere of argon. The solution was allowed to mix in the dark for 1 h at room temperature after which the AgBr precipitate was removed by filtration through celite. The dichloromethane solvent was subsequently removed by a rotary evaporator. After confirming quantitative transformation to the [*fac*-Mn(OTf)(CO)$_5$] intermediate by FTIR spectroscopy, the solid was transferred to a 10-mL microwave vial with 3 mL of tetrahydrofuran. To this solution was added a slight deficit of the appropriate ligand (0.33 mol). The vial was then sealed and reacted in a CEM Discovery microwave reactor at 70°C for 10 min. Each reaction afforded a bright yellow-orange solution. The tetrahydrofuran was reduced in volume to roughly 0.5 mL on a rotary evaporator at which point the pure product was immediately precipitated by addition of excess diethyl ether. The solid was isolated via vacuum filtration, rinsed with diethyl ether and dried under vacuum. No further purification was necessary.

[*fac*-Mn(OTf)(bpy)(CO)$_3$] (1) FTIR (CH_3CN) ν(CO): 2,050, 1,958 cm^{-1}. ^{1}H-NMR (CD_3CN) δ: 7.70–7.73 (2H, m), 8.21–8.25 (2H, m), 8.40 (2H, d, $J = 8.0$ Hz), 9.14 (2H, d, $J = 5.6$ Hz) ppm. Anal. Calcd. for $C_{14}H_8F_3MnN_2O_6S$: C, 37.85; H, 1.82; N, 6.31. Found: C, 38.27; H, 1.99; N, 6.02.

[*fac*-Mn(OTf)(phen)(CO)$_3$] (2) FTIR (CH_3CN) ν(CO): 2,050, 1,958 cm^{-1}. ^{1}H-NMR (CD_3CN) δ: 8.04 (2H, dd, $J_1 = 4.0$, $J_2 = 5.2$ Hz), 8.20 (2H, s), 8.78 (2H, dd, $J_1 = 1.2$, $J_2 = 8.0$ Hz), 9.49 (2H, dd, $J_1 = 1.2$, $J_2 = 4.8$ Hz) ppm. Anal. Calcd. for $C_{16}H_8F_3MnN_2O_6S$: C, 41.04; H, 1.72; N, 5.98. Found: C, 41.36; H, 1.88; N, 5.42.

[*fac*-Mn(OTf)(dmphen)(CO)$_3$] (3) FTIR (CH_3CN) ν(CO): 2,046, 1,959, 1,944(sh) cm^{-1}. ^{1}H-NMR (CD_3CN) δ: 3.30 (6H, s), 7.90 (2H, d, $J = 8.0$ Hz), 8.04 (2H, s), 8.57 (2H, d, $J = 8.0$ Hz). Anal. Calcd. for $C_{18}H_{12}F_3MnN_2O_6S$: C, 43.56; H, 2.44; N, 5.64. Found: C, 44.05; H, 2.69; N, 5.18.

[*fac*-Mn(OTf)(bqn)(CO)$_3$] (4) FTIR (CH_3CN) ν(CO): 2,047, 1,959 cm^{-1}. ^{1}H-NMR (CD_3CN) δ: 7.90 (2H, dd, $J_1 = J_2 = 8.0$ Hz), 8.12 (2H, dd, $J_1 = J_2 = 8.0$ Hz), 8.21 (2H, d, $J = 8.0$ Hz), 8.61 (2H, d, $J = 8.0$ Hz), 8.83 (2H, d, $J = 8.0$ Hz), 8.88 (2H, d, $J = 8.0$ Hz) ppm. Anal. Calcd. for $C_{22}H_{12}F_3MnN_2O_6S$: C, 48.54; H, 2.22; N, 5.15. Found: C, 49.10; H, 2.60; N, 4.91.

Computational Methods

Density Functional Theory

All geometries were fully optimized at the M06 level of density functional theory (Zhao and Truhlar, 2008a,b, 2010) with the SMD continuum solvation model (Marenich et al., 2009) for acetonitrile as solvent using the Stuttgart [8s7p6d2f | 6s5p3d1f] ECP10MDF contracted pseudopotential basis set (Dolg et al., 1987) on Mn and the 6-31G(d) basis set on all other atoms (Hehre et al., 1986). Non-analytical integrals were evaluated using the integral = grid = ultrafine option as implemented in the Gaussian 16 software package (Frisch et al., 2016). The nature of all stationary points was verified by analytic computation of vibrational frequencies, which were also used for the computation of zero-point vibrational energies, molecular partition functions, and for determining the reactants and products associated with each transition-state structure (by following the normal modes associated with imaginary frequencies). Partition functions were used in the computation of 298 K thermal contributions to the free energy employing the usual ideal-gas, rigid-rotator, harmonic oscillator approximation (Cramer, 2004). Free-energy contributions were added to single-point, SMD-solvated M06 electronic energies computed at the optimized geometries obtained with the initial basis with the SDD basis set on Mn and the larger 6-311+G(2df,p) basis set on all other atoms to arrive at final, composite free energies.

Solvation and Standard Reduction Potentials

As mentioned above, solvation effects for acetonitrile were accounted for by using the SMD continuum solvation model. A 1 M standard state was used for all species in solution (except for acetonitrile as solvent for which the standard state was assigned as 19.14 M). Thus, the free energy in solution is computed as the 1 atm gas-phase free energy, plus an adjustment for the 1 atm to 1 M standard-state concentration change of RT ln (24.5), or 1.9 kcal/mol, plus the 1 M to 1 M transfer (solvation) free energy computed from the SMD model. Standard reduction potentials were calculated for various possible redox couples to assess the energetic accessibility of different intermediates at various oxidation states. For a redox reaction of the form

$$O_{(\mathrm{soln})} + n\,e^-_{(\mathrm{g})} \rightarrow R_{(\mathrm{soln})} \tag{4}$$

where O and R denote the oxidized and reduced states of the redox couple, respectively, and n is the number of electrons involved in redox reaction, the reduction potential $E^{\mathrm{o}}_{O|R}$ relative to SCE was computed as

$$E^{\mathrm{o}}_{O|R} = -\frac{\Delta G^{\mathrm{o}}_{O|R}}{nF} - \Delta E^{\mathrm{o}}_{ref} \tag{5}$$

where $\Delta G^{\mathrm{o}}_{O|R}$ is the free energy change associated with Equation 1 (using Boltzmann statistics for the electron) and $\Delta E^{\mathrm{o}}_{ref}$

is taken as 0.141 V (Keith et al., 2013), which is required for the conversion of calculated $E^{o}_{O|R}$ vs. normal hydrogen electrode (NHE) in aqueous solution ($E_{NHE} = -4.281$ V) (Kelly et al., 2006) to $E^{o}_{O|R}$ vs. the saturated calomel electrode (SCE) in acetonitrile ($E_{SCE} = -4.422$ V) (Isse and Gennaro, 2010). We obtained reduction potentials referenced to the ferricenium/ferrocene couple by using a shift of −0.384 V from $E^{o}_{O|R}$ vs. SCE.

DATA AVAILABILITY STATEMENT

All datasets generated for this study are included in the manuscript/**Supplementary Files**.

AUTHOR CONTRIBUTIONS

MM, VB, and JR contributed to the synthesis, spectroscopic, and electrochemical characterization of all complexes studied. KN and DG contributed IR-SEC studies. ME contributed all computational studies. MM, ME, DG, and JR contributed equally to manuscript preparation.

FUNDING

JR thanks the National Science Foundation for support under Grant No. CHE-1800062. This work at BNL (DG and ME) was supported by the U.S. Department of Energy (DOE), Office of Science, Office of Basic Energy Sciences, Division of Chemical Sciences, Geosciences & Biosciences, under Contract No. DE-SC0012704. KN was grateful to the DOE for an Office of Science Graduate Student Research (SCGSR) award.

SUPPLEMENTARY MATERIAL

The Supplementary Material for this article can be found online at: https://www.frontiersin.org/articles/10.3389/fchem.2019.00628/full#supplementary-material

Scan rate dependent voltammetry studies under inert and catalytic conditions; experimental and computational IR-SEC spectra; catalyst, acid and CO_2 concentration dependence; controlled potential electrolysis plots; computational spin-density plots, total electron density difference plots, and cartesian coordinates. These materials are provided in the supporting information document.

REFERENCES

Appel, A. M., and Helm, M. L. (2014). Determining the overpotential for a molecular electrocatalyst. *ACS Catal.* 4, 630–633. doi: 10.1021/cs401013v

Arakawa, H., Areasta, M., Armor, J. N., Barteau, M. A., Beckman, E. J., Bell, A. T., et al. (2001). Catalysis research of relevance to carbon management: progress, challenges, and opportunities. *Chem. Rev.* 101, 953–996. doi: 10.1021/cr000018s

Bard, A., and Faulkner, L. (2001). *Electrochemical Methods: Fundamentals and Applications.* Oxford: John Wiley & Sons, Inc.

Bourrez, M., Molton, F., Chardon-Noblat, S., and Deronzier, A. (2011). Mn(bipyridyl)$(CO)_3$Br: an abundant metal carbonyl complex as efficient electrocatalyst for CO_2 reduction. *Angew. Chem. Int. Ed.* 50, 9903–9906. doi: 10.1002/anie.201103616

Bourrez, M., Orio, M., Molton, F., Vezin, H., Duboc, C., Deronzier, A., et al. (2014). Pulsed-EPR evidence of a manganese(II) hydroxycarbonyl intermediate in the electrocatalytic reduction of carbon dioxide by a manganese bipyridyl derivative. *Angew. Chem. Int. Ed.* 53, 240–243. doi: 10.1002/anie.201306750

Cramer, C. J. (2004). *Essentials of Computational Chemistry: Theories and Models.* Chichester: John Wiley & Sons.

Dolg, M., Wedig, U., Stoll, H., and Preuss, H. (1987). Energy-adjusted Ab initio pseudopotentials for the first row transition elements. *J. Chem. Phys.* 86, 866–872. doi: 10.1063/1.452288

Francke, R., Schille, B., and Roemelt, M. (2018). Homogeneously catalyzed electroreduction of carbon dioxide—methods, mechanisms, and catalysts. *Chem. Rev.* 118, 4631–4701. doi: 10.1021/acs.chemrev.7b00459

Frisch, M. J., Trucks, G. W., Schlegel, H. B., Scuseria, G. E., Robb, M. A., Cheeseman, J. R., et al. (2016). *Gaussian 16 Rev. A.03*. Wallingford, CT: John Wiley & Sons.

Grice, K. A., Gu, N. X., Sampson, M. D., and Kubiak, C. P. (2013). Carbon monoxide release catalysed by electron transfer: electrochemical and spectroscopic investigations of [Re(bpy-R)$(CO)_4$](OTf) complexes relevant to CO_2 reduction. *Dalton Trans.* 42, 8498–8503. doi: 10.1039/c3dt50612f

Grills, D. C., Ertem, M. Z., McKinnon, M., Ngo, K. T., and Rochford, J. (2018). Mechanistic aspects of CO_2 reduction catalysis with manganese-based molecular catalysts. *Coord. Chem. Rev.* 374, 173–217. doi: 10.1016/j.ccr.2018.05.022

Hartl, F., Rossenaar, B. D., Stor, G. J., and Stufkens, D. J. (1995). Role of an electron-transfer chain reaction in the unusual photochemical formation of five-coordinated anions $[Mn(CO)_3(\alpha\text{-diimine})]^-$ from *fac*-$[Mn(X)(CO)_3(\alpha\text{-diimine})]$ (X = halide) at low temperatures. *Recl. Trav. Chim.* 114, 565–570. doi: 10.1002/recl.19951141123

Hehre, W. J., Radom, L., Schleyer, P. V. R., and Pople, J. A. (1986). *Ab Initio Molecular Orbital Theory.* New York, NY: Wiley.

Isse, A. A., and Gennaro, A. (2010). Absolute potential of the standard hydrogen electrode and the problem of interconversion of potentials in different solvents. *J. Phys. Chem. B* 114, 7894–7899. doi: 10.1021/jp100402x

Kaim, W., and Fiedler, J. (2009). Spectroelectrochemistry: the best of two worlds. *Chem. Soc. Rev.* 38, 3373–3382. doi: 10.1039/b504286k

Keith, J. A., Grice, K. A., Kubiak, C. P., and Carter, E. A. (2013). Elucidation of the selectivity of proton-dependent electrocatalytic CO_2 reduction by fac-Re(bpy)$(CO)_3$Cl. *J. Am. Chem. Soc.* 135, 15823–15829. doi: 10.1021/ja406456g

Kelly, C. P., Cramer, C. J., and Truhlar, D. G. (2006). Aqueous solvation free energies of ions and ion–water clusters based on an accurate value for the absolute aqueous solvation free energy of the proton. *J. Phys. Chem. B* 110, 16066–16081. doi: 10.1021/jp063552y

Kurtz, D. A., Dhakal, B., Hulme, R. J., Nichol, G. S., and Felton, G. A. N. (2015). Correlations between photophysical and electrochemical properties for a series of new Mn carbonyl complexes containing substituted phenanthroline ligands. *Inorg. Chim. Acta* 427, 22–26. doi: 10.1016/j.ica.2014.12.009

Lam, Y. C., Nielsen, R. J., Gray, H. B., and Goddard, W. A. (2015). A Mn bipyrimidine catalyst predicted to reduce CO_2 at lower overpotential. *ACS Catal.* 5, 2521–2528. doi: 10.1021/cs501963v

Machan, C. W., Sampson, M. D., Chabolla, S. A., Dang, T., and Kubiak, C. P. (2014). Developing a mechanistic understanding of molecular electrocatalysts for CO_2 reduction using infrared spectroelectrochemistry. *Organometallics* 33, 4550–4559. doi: 10.1021/om500044a

Marenich, A. V., Cramer, C. J., and Truhlar, D. G. (2009). Universal solvation model based on solute electron density and on a continuum model of the solvent defined by the bulk dielectric constant and atomic surface tensions. *J. Phys. Chem. B* 113, 6378–6396. doi: 10.1021/jp810292n

Matsubara, Y., Grills, D. C., and Kuwahara, Y. (2015). Thermodynamic aspects of electrocatalytic CO_2 reduction in acetonitrile and with an ionic liquid as solvent or electrolyte. *ACS Catal.*, 6440–6452. doi: 10.1021/acscatal.5b00656

McKinnon, M., Ngo, K. T., Sobottka, S., Sarkar, B., Ertem, M. Z., Grills, D. C., et al. (2019). Synergistic metal–ligand redox cooperativity for electrocatalytic CO_2 reduction promoted by a ligand-based redox couple

in Mn and Re tricarbonyl complexes. *Organometallics* 38, 1317–1329. doi: 10.1021/acs.organomet.8b00584

Neri, G., Donaldson, P. M., and Cowan, A. J. (2019). *In situ* study of the low overpotential "dimer pathway" for electrocatalytic carbon dioxide reduction by manganese carbonyl complexes. *Phys. Chem. Chem. Phys.* 21, 7389–7397. doi: 10.1039/c9cp00504h

Ngo, K. T., McKinnon, M., Mahanti, B., Narayanan, R., Grills, D. C., Ertem, M. Z., et al. (2017). Turning on the protonation-first pathway for electrocatalytic CO_2 reduction by manganese bipyridyl tricarbonyl complexes. *J. Am. Chem. Soc.* 139, 2604–2618. doi: 10.1021/jacs.6b08776

Pegis, M. L., Roberts, J. A. S., Wasylenko, D. J., Mader, E. A., Appel, A. M., and Mayer, J. M. (2015). Standard reduction potentials for oxygen and carbon dioxide couples in acetonitrile and N,N-dimethylformamide. *Inorg. Chem.* 54, 11883–11888. doi: 10.1021/acs.inorgchem.5b02136

Riplinger, C., and Carter, E. A. (2015). Influence of weak brønsted acids on electrocatalytic CO_2 reduction by manganese and rhenium bipyridine catalysts. *ACS Catal.* 5, 900–908. doi: 10.1021/cs501687n

Riplinger, C., Sampson, M. D., Ritzmann, A. M., Kubiak, C. P., and Carter, E. A. (2014). Mechanistic contrasts between manganese and rhenium bipyridine electrocatalysts for the reduction of carbon dioxide. *J. Am. Chem. Soc.* 136, 16285–16298. doi: 10.1021/ja508192y

Sampson, M. D., Nguyen, A. D., Grice, K. A., Moore, C. E., Rheingold, A. L., and Kubiak, C. P. (2014). Manganese catalysts with bulky bipyridine ligands for the electrocatalytic reduction of carbon dioxide: eliminating dimerization and altering catalysis. *J. Am. Chem. Soc.* 136, 5460–5471. doi: 10.1021/ja501252f

Scheiring, T., Kaim, W., and Fiedler, J. (2000). Geometrical and electronic structures of the acetyl complex $Re(bpy)(CO)_3(COCH_3)$ and of $[M(bpy)(CO)_4](OTf)$, M=Mn,Re. *J. Organomet. Chem.* 598, 136–141. doi: 10.1016/S0022-328X(99)00691-9

Sinopoli, A., La Porte, N. T., Martinez, J. F., Wasielewski, M. R., and Sohail, M. (2018). Manganese carbonyl complexes for CO_2 reduction. *Coord. Chem. Rev.* 365, 60–74. doi: 10.1016/j.ccr.2018.03.011

Smieja, J. M., Sampson, M. D., Grice, K. A., Benson, E. E., Froehlich, J. D., and Kubiak, C. P. (2013). Manganese as a substitute for rhenium in CO_2 reduction catalysts: the importance of acids. *Inorg. Chem.* 52, 2484–2491. doi: 10.1021/ic302391u

Stanbury, M., Compain, J.-D., Trejo, M., Smith, P., Gour,é, E., and Chardon-Noblat, S. (2017). Mn-carbonyl molecular catalysts containing a redox-active phenanthroline-5,6-dione for selective electro- and photoreduction of CO_2 to CO or HCOOH. *Electrochim. Acta* 240, 288–299. doi: 10.1016/j.electacta.2017.04.080

Stanbury, M., Compain, J. D., and Chardon-Noblat, S. (2018). Electro and photoreduction of CO_2 driven by manganese-carbonyl molecular catalysts. *Coord. Chem. Rev.* 361, 120–137. doi: 10.1016/j.ccr.2018.01.014

Tignor, S. E., Kuo, H.-Y., Lee, T. S., Scholes, G. D., and Bocarsly, A. B. (2018). Manganese-based catalysts with varying ligand substituents for the electrochemical reduction of CO_2 to CO. *Organometallics* 38, 1292–1299. doi: 10.1021/acs.organomet.8b00554

Zhao, Y., and Truhlar, D. G. (2008a). Density functionals with broad applicability in chemistry. *Acc. Chem. Res.* 41, 157–167. doi: 10.1021/ar700111a

Zhao, Y., and Truhlar, D. G. (2008b). The M06 suite of density functionals for main group thermochemistry, thermochemical kinetics, noncovalent interactions, excited states, and transition elements: two new functionals and systematic testing of four M06-class functionals and 12 other functionals. *Theor. Chem. Acc.* 120, 215–241. doi: 10.1007/s00214-007-0310-x

Zhao, Y., and Truhlar, D. G. (2010). The minnesota density functionals and their applications to problems in mineralogy and geochemistry. *Rev. Mineral. Geochem.* 71, 19–37. doi: 10.2138/rmg.2010.71.2

Conflict of Interest: The authors declare that the research was conducted in the absence of any commercial or financial relationships that could be construed as a potential conflict of interest.

Copyright © 2019 McKinnon, Belkina, Ngo, Ertem, Grills and Rochford. This is an open-access article distributed under the terms of the Creative Commons Attribution License (CC BY). The use, distribution or reproduction in other forums is permitted, provided the original author(s) and the copyright owner(s) are credited and that the original publication in this journal is cited, in accordance with accepted academic practice. No use, distribution or reproduction is permitted which does not comply with these terms.

frontiers in Chemistry

ORIGINAL RESEARCH
published: 17 December 2019
doi: 10.3389/fchem.2019.00860

On-Surface Modification of Copper Cathodes by Copper(I)-Catalyzed Azide Alkyne Cycloaddition and CO_2 Reduction in Organic Environments

*Ryota Igarashi, Ryuji Takeuchi, Kazuyuki Kubo, Tsutomu Mizuta and Shoko Kume**

Department of Chemistry, Graduate School of Science, Hiroshima University, Higashihiroshima, Japan

In this study, organic structures were introduced onto copper cathodes to induce changes in their electrocatalytic CO_2 reduction activity. Poorly soluble organic polymers were distributed onto the copper surface as a thin layer by polymerizing monomeric precursors *via* a copper(I)-catalyzed azide-alkyne cycloaddition (CuAAC) activated by anodization of the copper substrate. The resulting structure possesses copper surface atoms that are available to participate in the CO_2 reduction reaction—comparable to close-contact organic structures—and stabilize the adsorption of organic layers through the CO_2 reduction process. The CO_2 reduction performance of the on-surface modified copper cathode exhibited improved CO_2 reduction over H_2 evolution compared with traditional cast modification systems. Preventing organic moieties from forming densely packed assemblies on the metal surface appears to be important to promote the CO_2 reduction process on the copper atoms. The suppression of H_2 evolution, a high methane/ethylene ratio, and the influence of stirring demonstrate that the improved CO_2 reduction activity is not only a result of the copper atom reorganization accompanied by repeating anodization for modification; the organic layer also apparently plays an important role in proton transfer and CO_2 accumulation onto the copper surface.

Keywords: CO_2 reduction, copper cathode, CuAAC, organic modification, hydrocarbons

OPEN ACCESS

Edited by:
Hitoshi Ishida,
Kitasato University, Japan

Reviewed by:
Enrico Andreoli,
Swansea University, United Kingdom
Tomohiko Inomata,
Nagoya Institute of Technology, Japan

***Correspondence:**
Shoko Kume
skume@hiroshima-u.ac.jp

Specialty section:
This article was submitted to Inorganic Chemistry, a section of the journal Frontiers in Chemistry

Received: *30 January 2019*
Accepted: *26 November 2019*
Published: *17 December 2019*

Citation:
Igarashi R, Takeuchi R, Kubo K, Mizuta T and Kume S (2019) On-Surface Modification of Copper Cathodes by Copper(I)-Catalyzed Azide Alkyne Cycloaddition and CO_2 Reduction in Organic Environments. Front. Chem. 7:860. doi: 10.3389/fchem.2019.00860

INTRODUCTION

The reduction of CO_2 on metal copper cathodes has been of interest since it was first reported by Hori in 1985 (Hori et al., 1985, 1986). The specific character of copper allows highly reduced hydrocarbons to be obtained at relatively large negative potentials, unlike other catalysts, which mainly afford formate and CO (Gattrell et al., 2006; Peterson and Nørskov, 2012; Zhang et al., 2014; Feaster et al., 2017).

Since common polycrystalline copper surfaces can yield various types of hydrocarbons, product distribution is difficult to control, especially for the selective formation of valuable C2-C3 products such as ethylene and ethanol. Product distribution is known to be highly influenced by the applied potential (Hori et al., 2003; Gattrell et al., 2006; Kuhl et al., 2012), Cu crystal facet (Hori et al., 2003; Gupta et al., 2006; Schouten et al., 2012; Huang et al., 2017; Qiu et al., 2017), and proton transfer conditions (Hori et al., 1997; Singh et al., 2016; Varela et al., 2016; Ooka et al., 2017). Oxide-derived Cu nanostructures are of current interest (Kas et al., 2014; Ren et al., 2015; Dutta et al., 2016; Handoko et al., 2016; Mistry et al., 2016; Huang et al., 2017; Mandal et al., 2018); however, their

high C2-C3 selectivity has not been fully elucidated, as these materials typically include multiple Cu facets endowing various activities. Furthermore, their nano-scale morphology influences local pH, and the remaining oxygen atoms are considered to influence the electronic nature of the surface. Other nanostructured Cu materials synthesized *via* various preparation methods (Tang et al., 2011; Li and Kanan, 2012; Reske et al., 2014; Ma et al., 2015; Kim et al., 2017; Zhao et al., 2017; Jeon et al., 2018; Luna et al., 2018) and alloys comprising copper and other elements are reported to show excellent performance in C2-C3 product formation (Long et al., 2017; Ma et al., 2017; Zhang et al., 2017).

The introduction of organic structures onto catalytically active metal surfaces has recently received attention, particularly the preparation of self-assembled monolayers (SAMs). Traditionally, the adsorption of organic molecules has been used to deactivate pristine metal surfaces and is often exploited to achieve higher selectivity, as demonstrated by the Lindlar catalyst. Recent developments have shown that organic molecules have a positive impact on enhancing selectivity and activity (Schoenbaum et al., 2014). Regarding CO_2 reduction, several groups have introduced organic molecules onto copper surfaces as SAMs to improve the reaction selectivity of CO and CO_2 reduction (Xie et al., 2016; Gong et al., 2017; Ahn et al., 2018). In these studies, phase-separated and densely packed structures of organic molecules on metal surfaces are carefully avoided, and the design of open-surface metal centers with neighboring organic structures to allow their cooperation seems to be a prerequisite for a productive reaction environment. To obtain the right reaction environment, similar to coordination catalysts, in which vacant metal centers can cooperate with organic ligands, requires that specific strategies be adopted in relation to contact-surface preparation.

Herein, we have developed a new method to modify metallic copper cathodes with organic layers, in contrast to SAM adsorption routes. To place open metal surface atoms in the neighborhood of the organic structure and to enhance stability, we adopted a rigid organic polymer structure. These polymers are poorly soluble in common solvents and are difficult to distribute homogeneously on the surface without aggregation. To distribute the polymer structure across the surface as a thin layer, the monomeric precursors were polymerized on the copper electrode by exploiting the Cu(I)-catalyzed azide-alkyne cycloaddition (CuAAC) catalytic activity response to surface oxidation (**Figure 1**). In this report, the copper modification achieved *via* the on-surface CuAAC approach was studied, and an efficient CO_2 reduction activity, specific to the polymer-modified electrode, was observed.

LAYER PREPARATION AND CHARACTERIZATION

Preparation

Electrochemical on-surface modification was performed in an electrolyte solution containing ethynyl and azide monomers (**Figure 2**). The redox activity of the surface copper was observed by repetitive anodic scanning of the polycrystalline copper electrode. In the absence of organic additives, the dissolution of oxidized copper from the surface proceeded continuously with an onset potential of *ca.* −0.6 V (**Figure 3A**). The first anodic scan exposed a fresh surface, making the current double afterward, and the anodic current profile was constant without decrease in the subsequent scans. When **1E** or **3E** was present in the solution, the onset potential of the copper anodization shifted positively, indicating that the ethynyl moieties promoted adsorption on the copper surface and thus inhibited copper stripping (**Figures 3B–E**). The appearance of a negatively shifted cathodic peak at *ca.* −1 V indicates coordination of the dissolved copper ion species. The ethynyl moiety likely formed insoluble coordination polymers with copper(I) through sigma- and pi-coordination bonds (Abrantes et al., 1984), and the anodic scanning appeared to first dissolve the copper(I) species into the solution (Ahrland, 1982), with subsequent coordination of ethynyl moieties. When azide precursors coexisted, these peaks were less recognizable (**Figures 3B,D**), implying that ethynylcopper(I) was consumed in the subsequent CuAAC

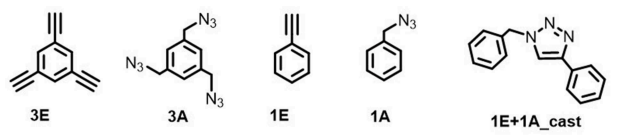

FIGURE 2 | Ethynyl and azide precursors.

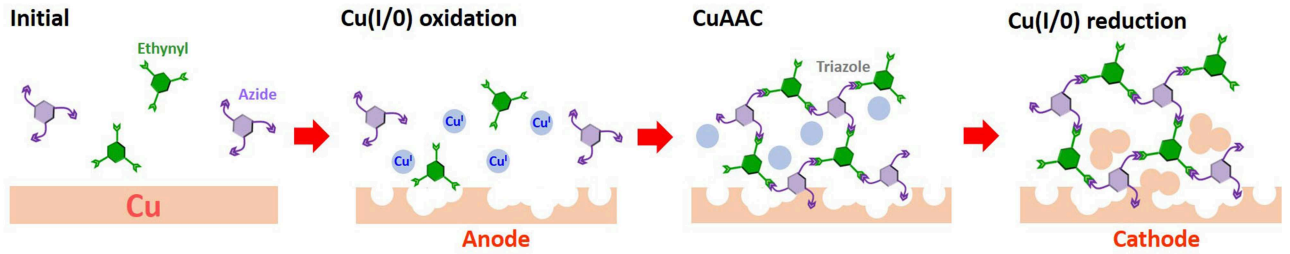

FIGURE 1 | On-surface CuAAC modification scheme.

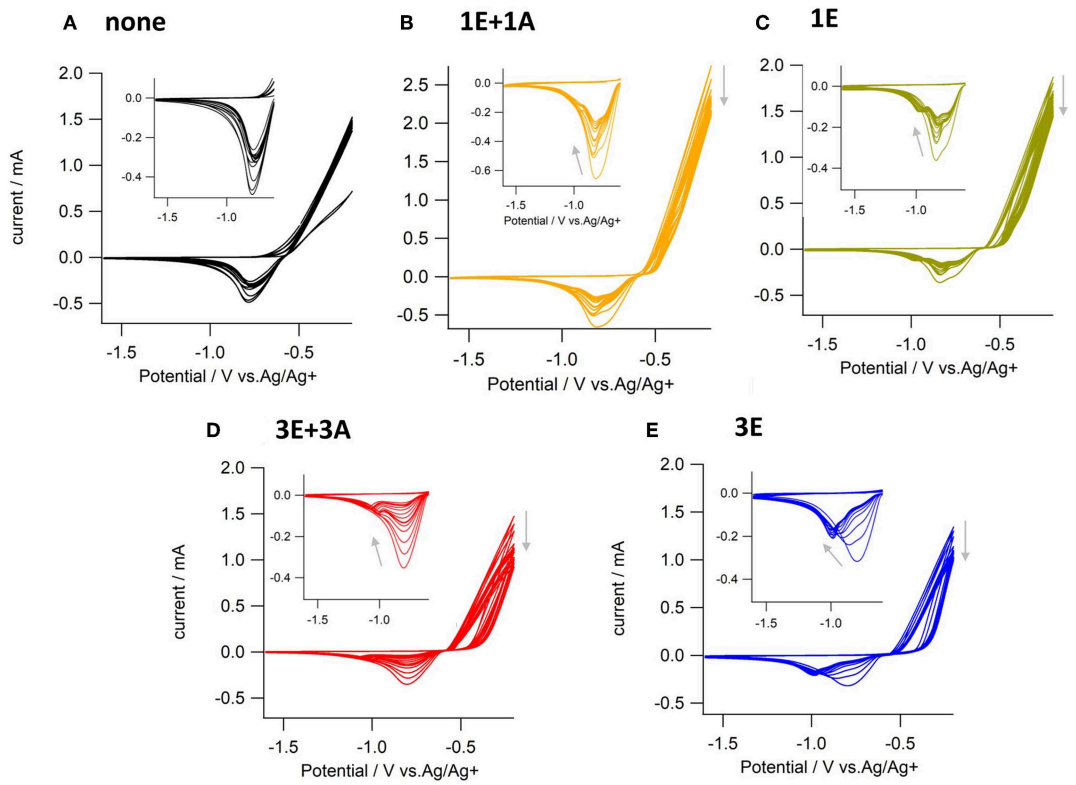

FIGURE 3 | Cyclic voltammograms of copper electrodes scanned 15 times in electrolyte solution containing **(A)** no additives, **(B) 1E** and **1A, (C) 1E, (D) 3E** and **3A,** and **(E) 3E**. Electrolyte solution; 0.1 M $^{n}Bu_4NPF_6$-acetonitrile, scan rate; 0.1 Vs^{-1}.

reaction. Upon scanning, the anodic current gradually decreased, and an anti-corrosive growth layer was observed on the surface. The current decrease was prominent in **3E+3A**, and to a smaller degree, when the solution contained **3E**, **1E** alone or **1E+1A**. The covalent polymers composed of **3E+3A**, via the CuAAC reaction, appear to induce strong adsorption compared with **3E** without covalent bond formation. The anodic scanning of **1E+1A** is expected to afford monomeric 1,2,3-triazoles because they contain only one reaction point for each, resulting in very weak adsorption. These features show that the anticorrosive layer efficiently covered the Cu surface by anodization with **3E+3A**.

X-Ray Photoelectron Spectroscopy (XPS)

XPS analysis of the **Cu_3E+3A**-modified Cu surface showed that a fair amount of nitrogen was introduced onto the surface (**Figure 4**). The binding energy associated with the introduced N species does not indicate an azide moiety, as this exhibited a peak located at ∼405 eV (Collman et al., 2006; Chisholm et al., 2016). The majority of the nitrogen, when affixed to the surface, appeared in the form of a triazole. Conversely, in addition to the Cu 2p peaks, **Cu_1E+1A** also exhibited a small nitrogen peak upon modification (**Figure S1**). These nitrogen features correspond to the difference in adsorption of polymeric and monomeric structures, as discussed in the on-surface preparation section, showing a significant and robust organic modification in polymeric **Cu_3E+3A**.

Scanning Electron Microscopy (SEM)

During the on-surface preparation, a significant amount of grain structures grew from an initially smooth polished Cu polycrystal surface (**Figure 5**). Additionally, the structures of **Cu_3E+3A**, **Cu_1E+1A**, and **Cu_1E** were similar. Anodic scans of the copper surface result in dissolution and re-deposition of Cu^+ in acetonitrile in the presence of phenylacetylene, and insoluble copper phenylacetylide is introduced as a stable intermediate (Ahrland, 1982). The grain structures seemed to grow through an oxidation–coordination–reduction process in repetitive anodization cycles, similar to the preparation of copper nanostructures derived from copper oxide CO_2-reduction catalysts. When the number of scan cycles was reduced to seven, the surface was covered by a smaller structure in the early stage of growth (**Figure S2**). XPS showed that **Cu_3E+3A** contained a higher amount of organic groups on its surface than **Cu_1E+1A**. However, these structures had very similar appearances, implying that the organic moieties were uniformly dispersed on copper grains. The thickness of the rough surface structure is estimated to have been hundreds of nanometers from the cross-sectional SEM image (**Figure S3**). When molecular triazole was cast on the copper surface (**Figure 5E**), platelet crystals were formed on the surface.

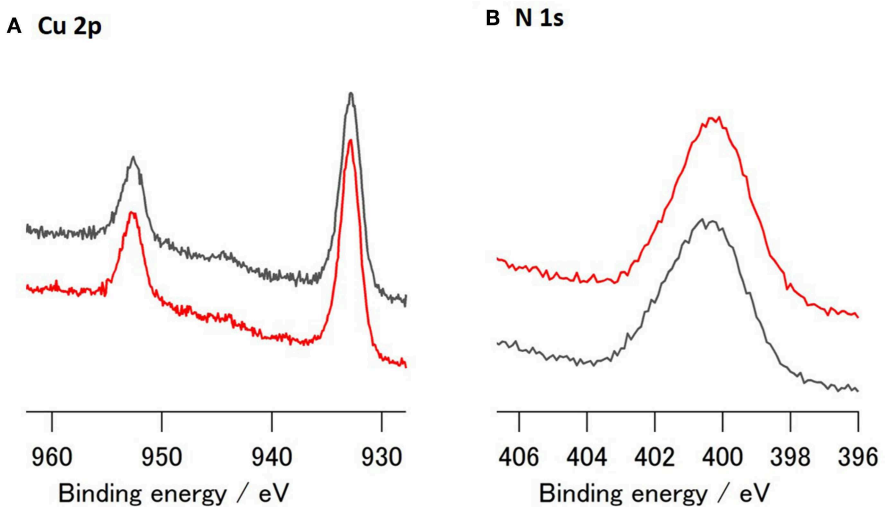

FIGURE 4 | XPS spectra of modified Cu; **(A)** Cu2p and **(B)** N1s region of **Cu_3E+3A** before (red) and after (gray) CO_2 reduction (−1.4 V vs. RHE, 40 min).

Additionally, the basal copper itself was observed to be slightly roughened by casting (**Figure S4**), as discussed in the roughness factor section.

Roughness Factor

The roughness of the electrodes was calculated from the double-layer capacitance (**Figure S5**, **Table S1**). **Table 1** details the roughness factors of the Cu electrodes, with the unmodified electrode as the reference. **Cu_1E+1A** and **Cu_1E** exhibited a high degree of roughness, which is consistent with the apparent surface topology observed in the SEM micrographs. Despite the apparent granular morphology, the roughness of **Cu_3E+3A** was similar to that of the smooth unmodified electrode. The surface of the Cu electrode may have been partially insulated by the presence of a thick organic layer film. When the triazole molecule was cast onto the surface, the surface area slightly increased, although no anodization of the copper was achieved. The adsorption of densely packed triazole, and the subsequent cathodization, may result in the re-construction of the surface copper (Gunathunge et al., 2017), as observed in the SEM micrographs.

Underpotential Deposition (UPD)

The amount of exposed Cu atoms on the electrode surface was estimated by UPD analysis (**Figure 6**). There were fewer exposed Cu atoms in the **Cu_3E+3A** electrode than estimated on the basis of the SEM micrograph and roughness factor. The surface of **Cu_3E+3A** is considered to have been largely covered by the organic layer, which inhibited the approach and deposition of Pb^{2+}; however, the system maintained its function as an electrode, as the layer could almost be considered as a monolayer in terms of thickness (Bandyopadhyay et al., 1998; Feng et al., 2017). The size of the redox wave was significantly larger in **Cu_1E+1A**, as the monomeric triazole was not able to strongly adsorb onto the surface. Furthermore, the majority of the grain structure was composed of copper. In **Cu_1E+1A_cast,** the organic moieties seemed to be aggregated to form massive crystals that inhibited the Pb deposition process on the electrode surface.

CO_2 REDUCTION

The formation of carbon products by CO_2 reduction at −1.4 V (vs. reversible hydrogen electrode, RHE, solution resistance uncorrected, **Figure 7**) showed that **Cu_3E+3A** had the highest amount of carbonaceous product formation. The products demonstrate two remarkable effects of modification: (i) ethylene formation was enhanced by anodic scanning in the presence of the ethynyl precursors; (ii) only the **Cu_3E+3A** electrode exhibited improved methane formation as a result of modification, while the other electrodes appeared to compensate for ethylene formation with methane formation.

Comparison of the Faradaic efficiency (**Figure 8**) reveals that the high CO_2 reduction performance of **Cu_3E+3A** did not result simply from an increase in total current with increasing roughness of the electrode surface. Besides the increase in methane and ethylene formation, **Cu_3E+3A** exhibited remarkably low hydrogen production, which is undesirable for the proton-consuming side reaction. Also, the control experiment under argon only bore hydrogen from **Cu_3E+3A** at the potential range, showing that the modified organics were not the source of hydrocarbons (**Figure S6**).

The linear sweep voltammetry (LSV) curves (**Figure 9**) of the electrodes provide additional information on reaction selectivity. At low current densities (−0.4 to −0.8 V), the current ratio appears to largely depend on the roughness factor. Further reducing the negative potential to under −1.0 V resulted in similar current densities for all electrodes (*ca.* −2 $mAcm^{-2}$),

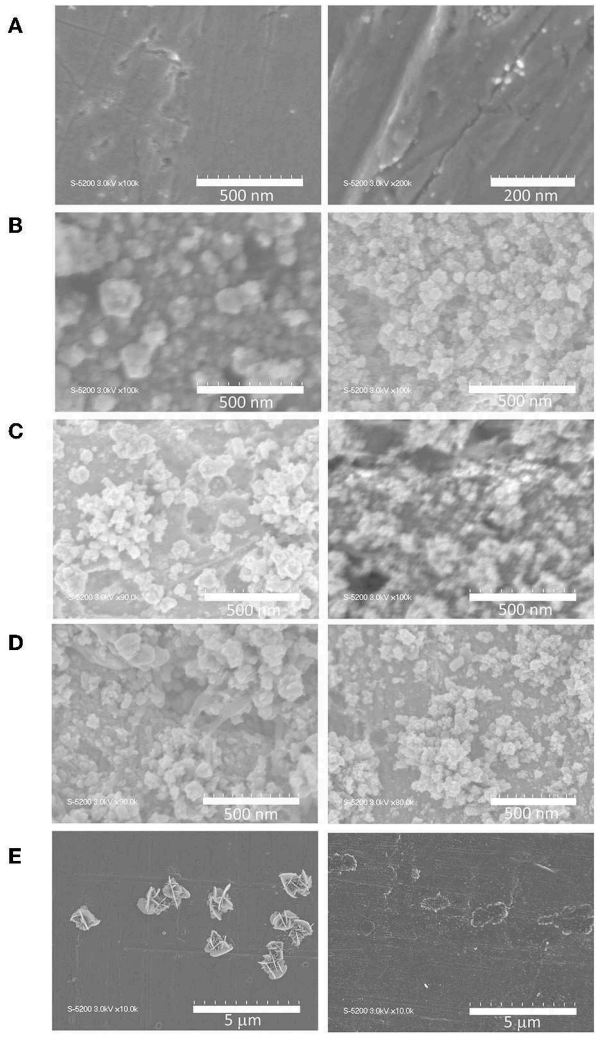

FIGURE 5 | SEM images of copper electrodes; (left) as prepared and (right) after electrolysis for 40 min at −1.4 V vs. RHE, 0.1 M $KHCO_3$aq saturated with CO_2. **(A) Unmodified, (B) Cu_3E+3A, (C) Cu_1E+1A, (D) Cu_1E**, and **(E) Cu_1E+1A_cast**.

TABLE 1 | Roughness factors of copper electrodes.

	Unmodified	Cu_3E+3A	Cu_1E+1A	Cu_1E	Cu_1E+1A_cast
	1.0	1.8	4.0	3.7	1.4
After EL[a]	0.9	1.9	4.3	3.9	1.7

[a]*Electrolysis was carried out for 50 min from −1.0 to −1.4 V vs. RHE with a stepwise increment of −0.1 V in every 10 min.*

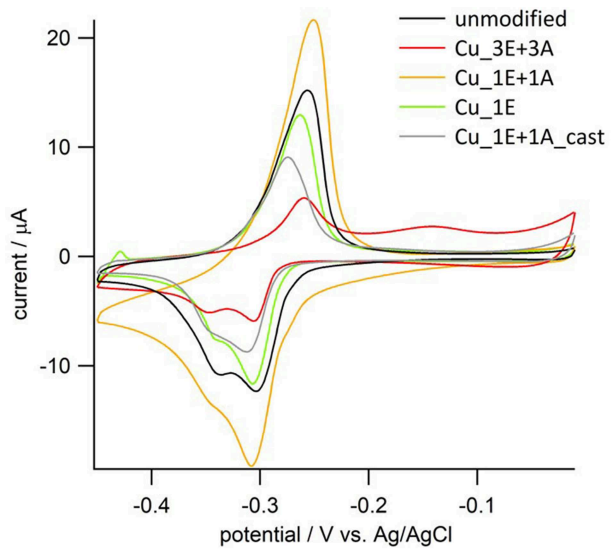

FIGURE 6 | Cyclic voltammograms of copper electrodes in the solution containing 0.5 mM $PbCl_2$. Electrolyte; 0.5 mM HCl/0.01 M $HClO_4$aq, scan rate; 10 mVs^{-1}.

despite observed differences in the roughness factor. At high current densities, the thickness of the CO_2 and proton diffusion layer increased beyond the scale of the thickness of the deposited surface structures. Therefore, the reaction is limited by the transportation properties. The polarization involves multiple electrochemical processes. By incrementally increasing the potential, the onset of CO_2 reduction to CO and hydrogen evolution was observed to first emerge at approx. −0.4 V, and the reduction of adsorbed CO into hydrocarbons was further enhanced when the potential was under −1.0 V. The current in **Cu_3E+3A** displayed slow increments despite of a relatively positive current onset, indicating that significant CO adsorption results in a current drop until the potential reaches −1.0 V, as CO_2 reduction is significantly more efficient than H_2 evolution. Thereafter, the current rapidly increased below −1.0 V as the adsorbed CO was removed through further reduction into hydrocarbons followed by dissociation, consistent with the potential dependence of Faradaic efficiency for H_2 and CO (**Figure 8**).

The effect on CO_2 reduction is influenced by how the organic moieties contact with the copper surface. In repeated cast modifications of the polished Cu electrode, the total current density was not observed to decrease; however, the formation of carbonaceous products decreased depending on the number of times the copper electrode was subjected to the cast process and was even surpassed by hydrogen production (**Figure 10**). The casting of molecular triazole typically forms densely packed crystalline structures that inhibit the adsorption of CO_2 on the surface. Conversely, this is not the case for H_2 production, as H_2 evolution requires significantly smaller surface vacancies to adsorb H atoms, and it may even be possible on the adsorbed organic molecules.

An ethylene increase was observed for the electrodes that were subjected to repetitive anodic scanning in the presence of the ethynyl precursor. The existence of the insoluble copper(I) acetylide intermediate on the surface is important for copper reorganization. This observed trend is similar to the high ethylene formation efficiency observed for nanostructured CO_2-reduction catalysts that are prepared by the formation of an insoluble copper oxide layer on the surface followed by reduction to Cu(0) (Kas et al., 2014; Ren et al., 2015; Dutta

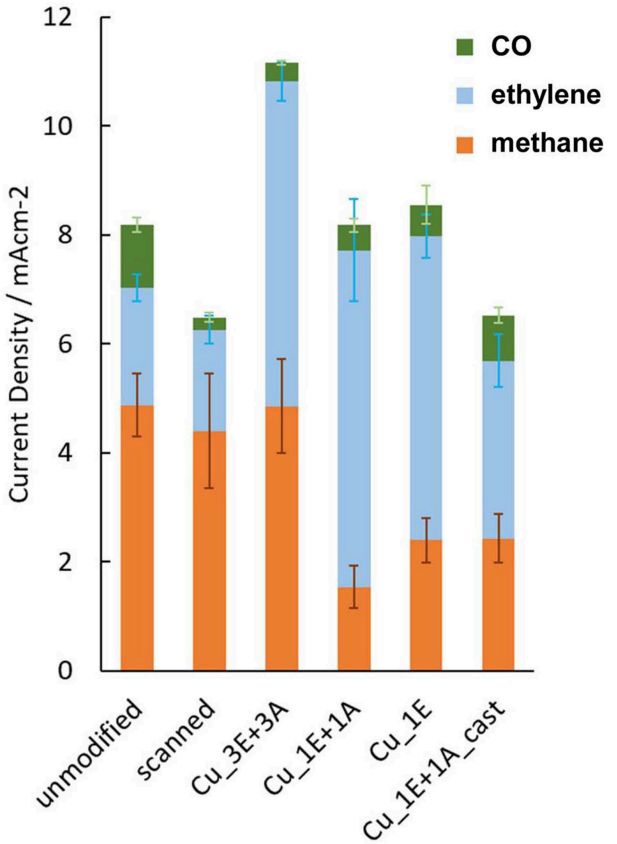

FIGURE 7 | The partial current density for the gas-phase carbonaceous products from electrolysis at −1.4 V vs. RHE; Electrolyte; CO_2-saturated 0.1 M $KHCO_3$. Error bars are placed at the top of each component. The scanned electrode was prepared by the same anodic scanning process as for on-surface preparation, without the addition of ethynyl or azide precursors.

et al., 2016; Handoko et al., 2016; Mistry et al., 2016; Mandal et al., 2018). During anodization in the absence of the ethynyl precursor ("scanned" in **Figure 7**), CO_2 reduction resulted in a decrease in the efficiency of ethylene formation. Continuous dissolution of copper into acetonitrile, without the precursor, may remove the copper atoms at the defect site of the copper crystal facet.

In the majority of Cu electrocatalytic processes, there is a trade-off in the efficiency of methane and ethylene selectivity. Additionally, the pH of the electrolyte influences the ratio of methane and ethylene, as the reduction process is related to competition of the dimerization of the adsorbed CO and the proton-coupled reduction (Schouten et al., 2011, 2013; Huang et al., 2017). The potential dependence of the ethylene/methane ratio also shows that methane formation is dominant with increased current density, as the reduction rate surpasses CO dimerization. Further increasing the current density results in an increase in pH on the surface due to H^+ consumption, resulting in dominant H_2 production through H_2O reduction because CO_2 is not stable in alkaline media (Singh et al., 2016). This trend appears to hold true in the case of **Cu_1E+1A** and **Cu_1E**, as the total CO_2 reduction efficiency remained at a similar level to that of the unmodified electrode. In **Cu_3E+3A**, both methane and ethylene increased with remarkably low hydrogen production. Hence, the organic layers play a role in increasing the total CO_2 reduction efficiency.

Stirring the electrolyte solution also changes the transport conditions. When stirring of the solution was stopped (**Figure 11**), the amount of dissolved components in the electrolyte (most likely formate) decreased for both the unmodified and **Cu_3E+3A** electrodes. Hydrogen was observed to increase for the unmodified electrode, but with the **Cu_3E+3A** electrode, the decrease of the soluble product content appeared to be compensated for by hydrocarbon formation, especially methane. Under a high current-flow condition without stirring, a pH increase at the electrode surface was observed to occur, as every electron transfer was accompanied by a proton transfer. Furthermore, the depletion of CO_2 was more severe for two reasons: (i) CO_2 possesses a lower diffusion coefficient than H^+, and (ii) CO_2 transforms to HCO_3^- in basic media. The suppression of hydrogen evolution by modification of the electrode appears to result from the preference of CO_2 reduction and adsorption over the reduction of H_2O. CO_2 selectivity is affected by the competition between CO_2 reduction and proton reduction forming surface-adsorbed H, and the latter process tends to lead to the formation of H_2 and formate. Several recent reports have demonstrated that hydrophobic modification of the surface improves the supply of CO_2 relative to H^+, which leads to better selectivity to CO and hydrocarbons (Buckley et al., 2019; Li et al., 2019). Moreover, the three-way triazole moiety was reported to have specific affinity in MOF CO_2 storage (Wang et al., 2013). In our case, the introduction of the organic layer made the surface more hydrophobic (**Figure S7**). The presence of the organic layer seems to create a CO_2-rich environment on the electrode surface, possibly by improved proton transfer and better CO_2 affinity with the layer than with the bare electrode surface.

CONCLUSIONS

A novel method has been designed to modify the surface of a metal electrode to enhance surface catalytic activity by anodization. The metal-organic contact structure formed offers unique properties over those of traditional cathodes prepared *via* the cast method by inducing a thin layer of organic moieties that are accessible to surface copper atoms. The influence of the modified electrode on CO_2 reduction reveals that the contact surface has a preference toward CO_2 reduction over H_2 evolution, contrary to the observed results from surfaces modified by the cast method. The organic layer appears to enhance the environment to achieve improved CO_2 affinity and proton transport ability at the surfaces of the copper atoms. The re-organization of copper atoms upon modification did influence CO_2 reduction selectivity, as in copper oxide-derived electrocatalysis. However, this property is not the sole factor governing the observed CO_2 reduction selectivity, because a large total CO_2 reduction efficiency and high methane formation are observed, even at low potentials. The method herein

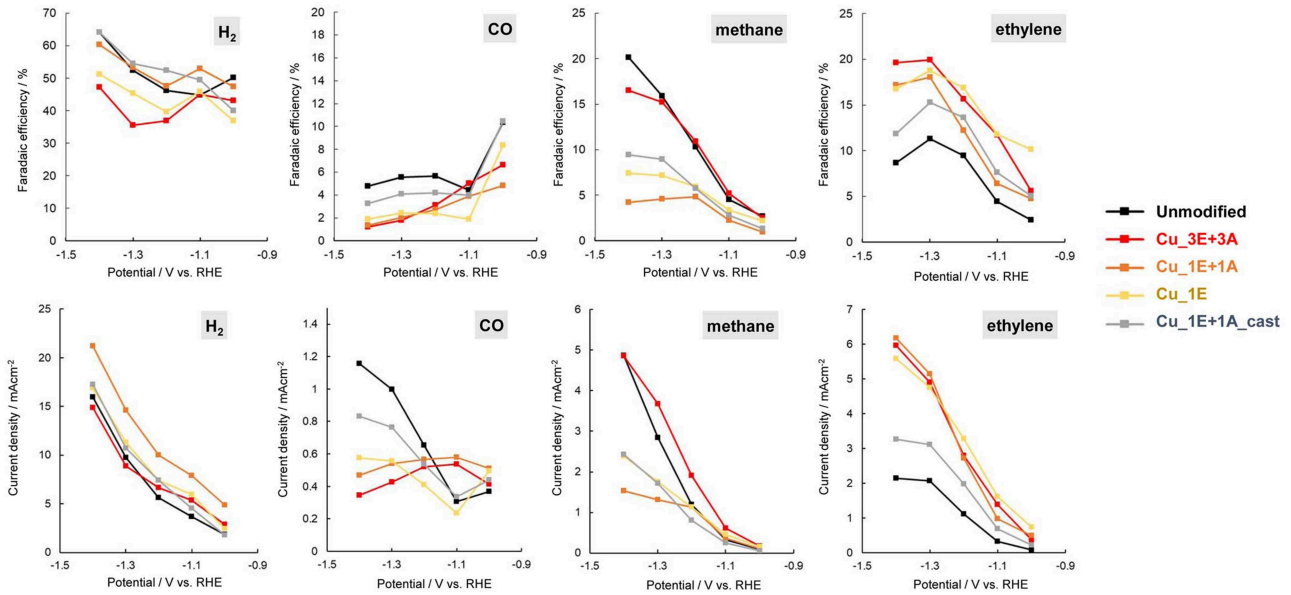

FIGURE 8 | Potential dependence of current density Faradaic efficiency **(top)** and current density **(bottom)** for product of CO_2 reduction.

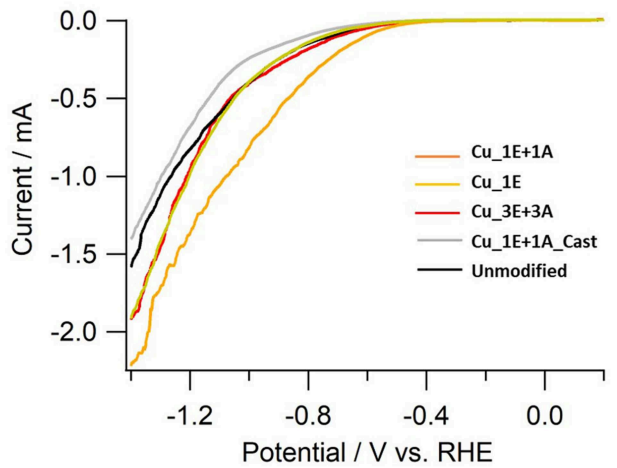

FIGURE 9 | LSV of copper electrodes. Electrolyte; CO_2-saturated 0.1 M $KHCO_3$, scan rate; 20 mVs^{-1}.

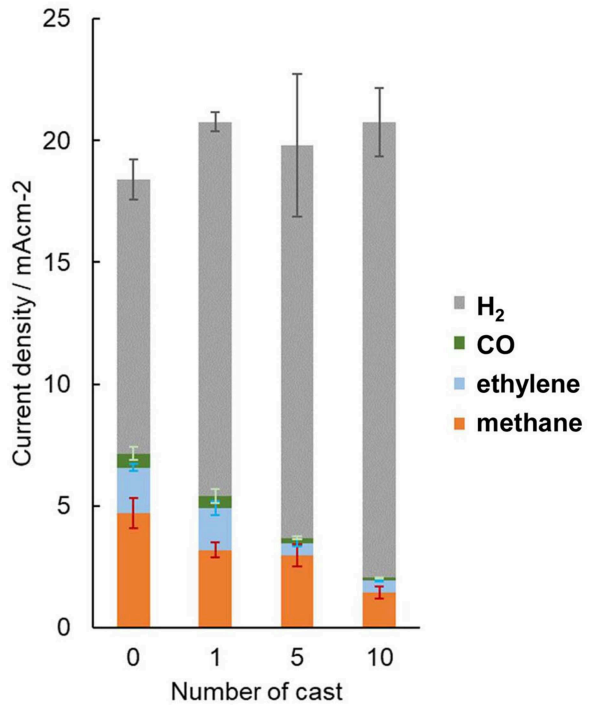

FIGURE 10 | Dependence of partial current density of the gaseous product from cast-modified electrodes with the number cast processes. Error bars are placed at the top of each component.

can readily introduce various types of organic substituents to the organic-open metal contact surface. Studies are underway to investigate controlling the CO_2 reduction based on the discussion in this report. Furthermore, the introduction of an organic functional center, such as ligands and dyes, would allow for CO_2 reduction with cooperated activation or light-driven functionality.

METHODS

Electrode Modification

A disc copper electrode (3 mmφ) was made from the cross-section of a polycrystalline rod embedded in a glass tube and polished with Bicalox0.05CR (0.05 μm alumina abrasive). Modification was performed in 5 mL electrolyte (0.1 M $^{n}Bu_4NPF_6$-acetonitrile) containing ethynyl (6.6 mM) and azide (6.6 mM) precursors under an argon atmosphere. A potential

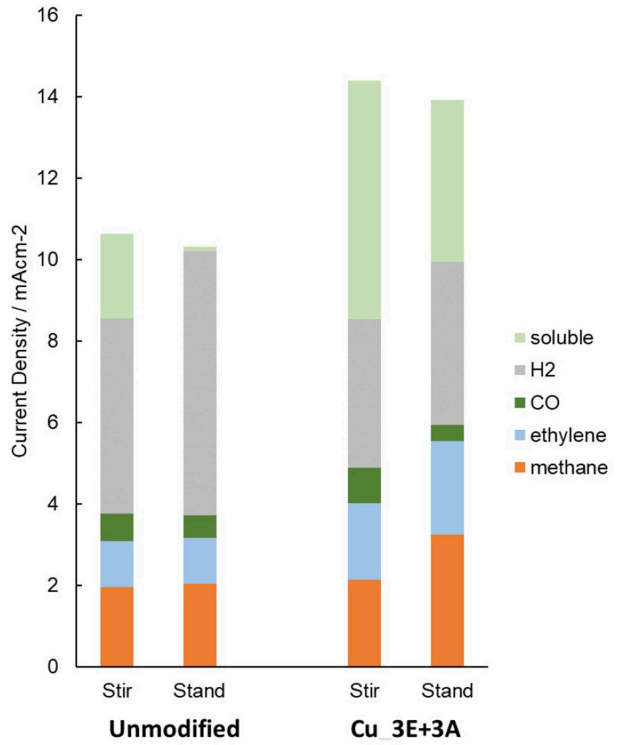

FIGURE 11 | Partial current density of the reduction products. The current density of the soluble product was estimated from the remaining component of the total current density after subtracting the gaseous components.

scan was repeated 15 times (from −0.2 to −1.0 V vs. Ag/Ag^+, 0.1 Vs^{-1}) using an ALS 650D potentiostat, followed by washing with acetonitrile. For cast modification, 0.7 μL of acetonitrile solution containing 1-benzyl-4-phenyl-1,2,3-triazole (4.3 mM) was dropped on the copper disc and air-dried. Modified copper substrates for XPS and SEM measurements were prepared using 5 mm square copper foil instead of copper discs.

Characterization of Surface Structure

SEM images were collected with a Hitachi FE-SEM S-5200. XPS data were collected using a KRATOS ESCA 3400 with an Al-*K*α source. Double-layer capacitance was measured in CO_2 saturated 0.1M $KHCO_3$aq on the basis of the current dependence upon the potential scan rate in the region of −0.6 V to −0.7 V vs. Ag/AgCl. UPD was achieved by immersing the modified electrode in electrolyte-containing lead salt (0.5 mM $PbCl_2$, 0.5 mM HCl/10 mM $HClO_4$aq, scan rate; 10 mVs^{-1}).

CO_2 Reduction

The CO_2 reduction activity on copper electrodes was investigated in CO_2-saturated 0.1 M $KHCO_3$aq (pH 6.8). The three-electrode setup was connected to a potentiostat (ALS 650D). Ag/AgCl was used as a reference electrode, and Pt mesh was used as the counter electrode. The applied potential was converted to RHE according to the equation $E_{RHE} = E_{Ag/AgCl} + 0.197\,V + 0.0591 \times pH$.

The experiments were performed in a two-compartment cell. A copper working electrode and Ag/AgCl electrode were placed in the gas-tight cathodic compartment. It was separated from the open anodic compartment, which was equipped with a Pt mesh counter electrode, by a 10 mmφ ion-exchange membrane (Selemion^{TM} AMV). Electrolysis was performed for 10 min with stirring (ca. 600 rpm), without additional supply of CO_2. Depletion of CO_2 by electrolysis did not exceed a few % of the amount of CO_2 in solution (34 mM, 6.2 mL), which is estimated from the charge flow (typically 1 C). For the quantification of gaseous products, 0.1 mL of gas product was collected from the head space (9.9 mL) of the gas-tight compartment and introduced in a gas chromatograph (Shimazu-2010) equipped with a 2.0 m × 1.0 mm ID column packed with SHINCARBON ST and a BID-2010 detector. Copper electrodes were first cathodized at −1.6 V vs. Ag/AgCl for 1 h to remove weakly physisorbed materials and reduce oxidized copper species prior to the collection of CO_2RR products. The current density was calculated according to the geometric area of the Cu electrode (3 mm φ). CO_2 reduction data are provided as averages from at least three separately prepared electrodes.

AUTHOR CONTRIBUTIONS

SK, KK, and TM contributed the overall concept of the study. SK and RT developed the experimental apparatus for electrolysis. RT and RI performed the experiments and analysis of the collected data. All authors contributed to manuscript revision and read and approved the submitted version.

FUNDING

This work was supported by JSPS KAKENHI Grant Number: JP16K05723.

ACKNOWLEDGMENTS

The authors acknowledge Dr. M. Maeda for support in SEM image collection and Dr. H. Dote for assistance in XPS measurements. We thank the Edanz Group (www.edanzediting.com/ac) for editing a draft of this manuscript.

SUPPLEMENTARY MATERIAL

The Supplementary Material for this article can be found online at: https://www.frontiersin.org/articles/10.3389/fchem.2019.00860/full#supplementary-material

REFERENCES

Abrantes, L., Fleischmann, M., Hill, I., Peter, L., Mengoli, M., and Zotti, G. (1984). An investigation of Cu(I) acetylide films on Cu electrodes: Part I. Electrochemical and Raman spectroscopic analysis of the film formation. *J. Electroanal. Chem. Interfacial Electrochem.* 164, 177–187. doi: 10.1016/S0022-0728(84)80238-7

Ahn, S., Klyukin, K., Wakeham, R. J., Rudd, J. A., Lewis, A. R., Alexander, S., et al. (2018). Poly-amide modified copper foam electrodes for enhanced

electrochemical reduction of carbon dioxide. *ACS Catal.* 8, 4132–4142. doi: 10.1021/acscatal.7b04347

Ahrland, S. (1982). Solvation and complex formation. Competing and cooperative processes in solution. *Pure Appl. Chem.* 54, 1451–1468. doi: 10.1351/pac198254081451

Bandyopadhyay, K., Patil, V., Sastry, M., and Vijayamohanan, K. (1998). Effect of geometric constraints on the self-assembled monolayer formation of aromatic disulfides on polycrystalline gold. *Langmuir* 14, 3808–3814. doi: 10.1021/la980088i

Buckley, A., Lee, M., Cheng, T., Kazantsev, R. V., Larson, D. M., Goddard, W. A., et al. (2019). Electrocatalysis at organic-metal interfaces: identification of structure-reactivity relationships for CO_2 reduction at modified Cu surfaces. *J. Am. Chem. Soc.* 141, 7355–7364. doi: 10.1021/jacs.8b13655

Chisholm, R., Parkin, J. D., Smith, A. D., and Hahner, G. (2016). Isothiourea-mediated organocatalytic michael addition-lactonization on a surface: modification of SAMs on silicon oxide substrates. *Langmuir* 32, 3130–3138. doi: 10.1021/acs.langmuir.5b04686

Collman, J. P., Devaraj, N. K., Eberspacher, T. P. A., and Chidsey, C. E. D. (2006). Mixed azide-terminated monolayers: a platform for modifying electrode surfaces. *Langmuir* 22, 2457–2464. doi: 10.1021/la052947q

Dutta, A., Rahaman, M., Luedi, N. C., Mohos, M., and Broekmann, P. (2016). Morphology matters: tuning the product distribution of CO_2 electroreduction on oxide-derived Cu foam catalysts. *ACS Catal.* 6, 3804–3814. doi: 10.1021/acscatal.6b00770

Feaster, J. T., Shi, C., Cave, E. R., Hatsukade, T., Abram, D. N., Kuhl, K. P., et al. (2017). Understanding selectivity for the electrochemical reduction of carbon dioxide to formic acid and carbon monoxide on metal electrodes. *ACS Catal.* 7, 4822–4827. doi: 10.1021/acscatal.7b00687

Feng, Y., Dionne, E. R., Toader, V., Beaudoin, G., and Badia, A. (2017). Odd-even effects in electroactive self-assembled monolayers investigated by electrochemical surface plasmon resonance and impedance spectroscopy. *J. Phys. Chem. C* 121, 24626–24640. doi: 10.1021/acs.jpcc.7b08053

Gattrell, M., Gupta, N., and Co, A. (2006). A review of the aqueous electrochemical reduction of CO_2 to hydrocarbons at copper. *J. Electroanal. Chem.* 594, 1–19. doi: 10.1016/j.jelechem.2006.05.013

Gong, M., Cao, Z., Liu, W., Nichols, E. M., Smith, P. T., Derrick, J. S., et al. (2017). Supramolecular porphyrin cages assembled at molecular–materials interfaces for electrocatalytic CO reduction. *ACS Cent. Sci.* 3, 1032–1040. doi: 10.1021/acscentsci.7b00316

Gunathunge, C. M., Li, X., Li, J., Hicks, R. P., Ovalle, V. J., and Waegele, M. M. (2017). Spectroscopic observation of reversible surface reconstruction of copper electrodes under CO_2 reduction. *J. Phys. Chem. C* 121, 12337–12344. doi: 10.1021/acs.jpcc.7b03910

Gupta, N., Gattrell, M., and MacDougall, B. (2006). Calculation for the cathode surface concentrations in the electrochemical reduction of CO_2 in $KHCO_3$ solutions. *J. Appl. Electrochem.* 36, 161–172. doi: 10.1007/s10800-005-9058-y

Handoko, A. D., Ong, C. W., Huang, Y., Lee, Z. G., Lin, L., Panetti, G. B., et al. (2016). Mechanistic insights into the selective electroreduction of carbon dioxide to ethylene on Cu_2O-derived copper catalysts. *J. Phys. Chem. C* 120, 20058–20067. doi: 10.1021/acs.jpcc.6b07128

Hori, Y., Kikuchi, K., Murata, A., and Suzuki, S. (1986). Production of methane and ethylene in electrochemical reduction of carbon dioxide at copper electrode in aqueous hydrogencarbonate solution. *Chem. Lett.* 15, 897–898. doi: 10.1246/cl.1986.897

Hori, Y., Kikuchi, K., and Suzuki, S. (1985). Production of CO and CH_4 in electrochemical reduction of CO_2 at metal electrodes in aqueous hydrogencarbonate solution. *Chem. Lett.* 14, 1695–1698. doi: 10.1246/cl.1985.1695

Hori, Y., Takahashi, I., Koga, O., and Hoshi, N. (2003). Electrochemical reduction of carbon dioxide at various series of copper single crystal electrodes. *J. Mol. Cat. A* 199, 39–47. doi: 10.1016/S1381-1169(03)00016-5

Hori, Y., Takahashi, R., Yoshinami, Y., and Murata, A. (1997). Electrochemical reduction of CO at a copper electrode. *J. Phys. Chem. B* 101, 7075–7081. doi: 10.1021/jp970284i

Huang, Y., Handoko, A. D., Hirunsit, P., and Yeo, B. S. (2017). Electrochemical reduction of CO_2 using copper single-crystal surfaces: effects of CO* coverage on the selective formation of ethylene. *ACS Catal.* 7, 1749–1756. doi: 10.1021/acscatal.6b03147

Jeon, H. S., Kunze, S., Scholten, F., and Roldan Cuenya, B. (2018). Prism-shaped Cu nanocatalysts for electrochemical CO_2 reduction to ethylene. *ACS Catal.* 8, 531–535. doi: 10.1021/acscatal.7b02959

Kas, R., Kortlever, R., Milbrat, A., Koper, M. T. M., Mul, G., and Baltrusaitis, J. (2014). Electrochemical CO_2 reduction on Cu_2O-derived copper nanoparticles: controlling the catalytic selectivity of hydrocarbons. *Phys. Chem. Chem. Phys.* 16, 12194–12201. doi: 10.1039/C4CP01520G

Kim, D., Kley, C. S., Li, Y., and Yang, P. (2017). Copper nanoparticle ensembles for selective electroreduction of CO_2 to C_2-C_3 products. *Proc. Natl. Acad. Sci. U.S.A.* 114, 10560–10565. doi: 10.1073/pnas.1711493114

Kuhl, K. P., Cave, E. R., Abram, D. N., and Jaramillo, T. F. (2012). New insights into the electrochemical reduction of carbon dioxide on metallic copper surfaces. *Energy Environ. Sci.* 5, 7050–7059. doi: 10.1039/c2ee21234j

Li, A., Cao, Q., Zhou, G., Schmidt, B. V. K., Zhu, W., Yuan, X., et al. (2019). Three-phase photocatalysis for the enhanced selectivity and activity of CO_2 reduction on a hydrophobic surface. *Angew. Chem. Int. Ed.* 58, 14549–14555. doi: 10.1002/anie.201908058

Li, C. W., and Kanan, M. W. (2012). CO_2 Reduction at low overpotential on Cu electrodes resulting from the reduction of thick Cu2O films. *J. Am. Chem. Soc.* 134, 7231–7234. doi: 10.1021/ja3010978

Long, R., Li, Y., Liu, Y., Chen, S., Zheng, X., Gao, C., et al. (2017). Isolation of Cu atoms in Pd lattice: forming highly selective sites for photocatalytic conversion of CO_2 to CH_4. *J. Am. Chem. Soc.* 139, 4486–4492. doi: 10.1021/jacs.7b00452

Luna, P. D., Quintero-Bermudez, R., Dinh, C. D., Ross, M. B. R., Bushuyev, O. S., Todorović, P., et al. (2018). Catalyst electro-redeposition controls morphology and oxidation state for selective carbon dioxide reduction. *Nat. Catal.* 1, 103–110. doi: 10.1038/s41929-017-0018-9

Ma, M., Djanashvili, K., and Smith, W. A. (2015). Selective electrochemical reduction of CO_2 to CO on CuO-derived Cu nanowires. *PCCP* 17, 20861–20867. doi: 10.1039/C5CP03559G

Ma, S., Sadakiyo, M., Heima, M., Luo, R., Haasch, R. T., Gold, J. I., et al. (2017). Electroreduction of carbon dioxide to hydrocarbons using bimetallic Cu–Pd catalysts with different mixing patterns. *J. Am. Chem. Soc.* 139, 47–50. doi: 10.1021/jacs.6b10740

Mandal, L., Yang, K. R., Motapothula, M. R., Ren, D., Lobaccaro, P., Patra, A., et al. (2018). Investigating the role of copper oxide in electrochemical CO_2 reduction in real time. *ACS Appl. Mater. Interfaces* 10, 8574 −8584. doi: 10.1021/acsami.7b15418

Mistry, H., Varela, A. S., Bonifacio, C. S., Zegkinoglou, I., Sinev, I., Choi, Y., et al. (2016). Highly selective plasma-activated copper catalysts for carbon dioxide reduction to ethylene. *Nat. Commun.* 7:12123. doi: 10.1038/ncomms12123

Ooka, H., Figueiredo, M. C., and Koper, M. T. M. (2017). Competition between hydrogen evolution and carbon dioxide reduction on copper electrodes in mildly acidic media. *Langmuir* 33, 9307–9313. doi: 10.1021/acs.langmuir.7b00696

Peterson, A. A., and Nørskov, J. K. (2012). Activity descriptors for CO_2 electroreduction to methane on transition-metal catalysts. *J. Phys. Chem.* 3, 251–258. doi: 10.1021/jz201461p

Qiu, Y., Zhong, H., Zhang, T., Xu, W., Li, X., and Zhang, H. (2017). Copper electrode fabricated via pulse electrodeposition: toward high methane selectivity and activity for CO_2 electroreduction. *ACS Catal.* 7, 6302–6310. doi: 10.1021/acscatal.7b00571

Ren, D., Deng, Y., Handoko, A. D., Chen, C. S., Malkhandi, S., and Yeo, B. S. (2015). Selective electrochemical reduction of carbon dioxide to ethylene and ethanol on Copper(I) oxide catalysts. *ACS Catal.* 5, 2814–2821. doi: 10.1021/cs502128q

Reske, R., Mistry, H., Behafarid, F., Cuenya, B. R., and Strasser, P. (2014). Particle size effects in the catalytic electroreduction of CO_2 on Cu nanoparticles. *J. Am. Chem. Soc.* 136, 6978–6986. doi: 10.1021/ja500328k

Schoenbaum, C. A., Schwartz, D. K., and Medlin, J. W. (2014). Controlling the surface environment of heterogeneous catalysts using self-assembled monolayers. *Acc. Chem. Res.* 47, 1438–1445. doi: 10.1021/ar500029y

Schouten, K. J. P., Gallent, E. P., and Koper, M. T. M. (2013). Structure sensitivity of the electrochemical reduction of carbon monoxide on copper single crystals. *ACS Catal.* 3, 1292–1295. doi: 10.1021/cs4002404

Schouten, K. J. P., Kwon, Y., van der Ham, C. J. M., Qin, Z., and Koper, M. T. M. (2011). A new mechanism for the selectivity to C1 and C2 species in the

electrochemical reduction of carbon dioxide on copper electrodes. *Chem. Sci.* 2, 1902–1909. doi: 10.1039/c1sc00277e

Schouten, K. J. P., Qin, Z., Gallent, E. P., and Koper, M. T. M. (2012). Two pathways for the formation of ethylene in CO reduction on single-crystal copper electrodes. *J. Am. Chem. Soc.* 134, 9864–9867. doi: 10.1021/ja302668n

Singh, M. R., Kwon, Y., Lum, Y., Ager, J. W., and Bell, A. T. (2016). Hydrolysis of electrolyte cations enhances the electrochemical reduction of CO_2 over Ag and Cu. *J. Am. Chem. Soc.* 138, 13006–13012. doi: 10.1021/jacs.6b07612

Tang, W., Peterson, A. A., Varela, A. S., Jovanov, Z. P., Bech, L., Durand, W. J., et al. (2011). The importance of surface morphology in controlling the selectivity of polycrystalline copper for CO_2 electroreduction. *Phys. Chem. Chem. Phys.* 14, 76–81. doi: 10.1039/C1CP22700A

Varela, A. S., Kroschel, M., Reier, T., and Strasser, P. (2016). Controlling the selectivity of CO_2 electroreduction on copper: the effect of the electrolyte concentration and the importance of the local pH. *Catal. Today* 260, 8–13. doi: 10.1016/j.cattod.2015.06.009

Wang, X., Li, P., Chen, Y., Zhang, Q., Zhang, H., Chan, X. X., et al. (2013). A rationally designed nitrogen-rich metal-organic framework and its exceptionally high CO_2 and H_2 uptake capability. *Sci. Rep.* 3:1149. doi: 10.1038/srep01149

Xie, M. S., Xia, B. Y., Li, Y., Yan, Y., Yang, Y., Sun, Q., et al. (2016). Amino acid modified copper electrodes for the enhanced selective electroreduction of carbon dioxide towards hydrocarbons. *Energy Environ. Sci.* 9, 1687–1695. doi: 10.1039/C5EE03694A

Zhang, F., Sheng, T., Tian, N., Liu, L., Xiao, C., Lu, B., et al. (2017). Cu overlayers on tetrahexahedral Pd nanocrystals with high-index facets for CO_2 electroreduction to alcohols. *Chem. Commun.* 53, 8085–8088. doi: 10.1039/C7CC04140C

Zhang, Y., Sethuraman, V., Michalsky, R., and Peterson, A. A. (2014). Competition between CO_2 reduction and H_2 evolution on transition-metal electrocatalysts. *ACS Catal.* 4, 3742–3748. doi: 10.1021/cs5012298

Zhao, J., Sun, L., Canepa, S., Sun, H., Yesibolati, M. N., Sherburne, M., et al. (2017). Phosphate tuned copper electrodeposition and promoted formic acid selectivity for carbon dioxide reduction. *J. Mater. Chem. A* 5, 11905–11916. doi: 10.1039/C7TA01871A

Conflict of Interest: The authors declare that the research was conducted in the absence of any commercial or financial relationships that could be construed as a potential conflict of interest.

Copyright © 2019 Igarashi, Takeuchi, Kubo, Mizuta and Kume. This is an open-access article distributed under the terms of the Creative Commons Attribution License (CC BY). The use, distribution or reproduction in other forums is permitted, provided the original author(s) and the copyright owner(s) are credited and that the original publication in this journal is cited, in accordance with accepted academic practice. No use, distribution or reproduction is permitted which does not comply with these terms.

Advantages of publishing in Frontiers

OPEN ACCESS
Articles are free to read for greatest visibility and readership

FAST PUBLICATION
Around 90 days from submission to decision

HIGH QUALITY PEER-REVIEW
Rigorous, collaborative, and constructive peer-review

TRANSPARENT PEER-REVIEW
Editors and reviewers acknowledged by name on published articles

Frontiers
Avenue du Tribunal-Fédéral 34
1005 Lausanne | Switzerland

Visit us: www.frontiersin.org
Contact us: info@frontiersin.org | +41 21 510 17 00

REPRODUCIBILITY OF RESEARCH
Support open data and methods to enhance research reproducibility

DIGITAL PUBLISHING
Articles designed for optimal readership across devices

FOLLOW US
@frontiersin

IMPACT METRICS
Advanced article metrics track visibility across digital media

EXTENSIVE PROMOTION
Marketing and promotion of impactful research

LOOP RESEARCH NETWORK
Our network increases your article's readership